Partial melting and phase relations in metapelitic granulites.

Damian Peter Carrington

A thesis submitted for the degree of Doctor of Philosophy.

University of Edinburgh
1993.

Abstract.

The dehydration (vapour-absent) melting of biotite is considered to be a fundamental process governing the evolution of metapelites in high-grade metamorphism. Melts produced by this process may segregate and hence allow for the low water-activity characteristic of granulite terrains. Previously, experimental constraints on the theoretical reaction grids were very scarce. This thesis develops and constrains a petrogenetic grid for high-grade metapelites and links biotite dehydration melting reactions (BDMR's) to phase relations above the stability of biotite.

The cornerstone of the thesis is the set of sixty four experiments carried out on three synthetic, mineral-mix, KFMASH (K_2O-FeO-MgO-Al_2O_3-SiO_2-H_2O) compositions, with bulk X_{Mg}'s of 0.62, 0.74 and 0.86. Magnesian compositions are used so that univariant equilibria, many of which do not act on iron-rich compositions, can be constrained. The experiments were conducted in the pressure-temperature range 5-12.5 kilobars and 840-1000°C. The assemblages stable in this range were subsets of garnet-cordierite-biotite-osumilite-orthopyroxene-sillimanite-K-feldspar-quartz-melt.

The results of the experiments represent a close approach to equilibrium and several key reactions were reversed. The results are used to derive a petrogenetic grid of KFMASH univariant reactions and pseudosections for each of the bulk compositions. In the KFMASH system, the position of reactions on the grid does not depend on the rock bulk composition or the activity of water. This provides an excellent, fixed reference for consideration of lower crustal processes and mineral assemblages. In particular, the fundamental granulite-facies KFMASH invariant point, which involves the BDMR's and the reaction separating garnet-cordierite and orthopyroxene -sillimanite-quartz assemblages, has been positioned between 890-910°C, 8.7-9.5kb.

The current and previous data on BDMR's are accounted for by a simple model in which the melting interval is inversely proportional to the bulk X_{Mg} and its absolute position in temperature is controlled by the concentration of titanium and fluorine in biotite. The reaction separating garnet-cordierite and orthopyroxene-sillimanite-quartz assemblages has been constrained to run from 900°C, 8.8kb to 1000°C, 7.8kb. This is at lower pressure than previous estimates as it accounts for vapour-undersaturation in cordierite and the fact that melt must be produced when the hydrous cordierite breaks down. Osumilite has a large stability field at temperatures above approximately 900°C and is likely to be more common than is currently thought. Recent KFMASH system experimental data at high temperature (Audibert et al. 1994) is used to extend the petrogenetic grid to 1100°C, but only after their underestimated friction correction, detected by cross-calibration experiments conducted in this study, has been accounted for.

The grids replicate natural rocks extremely well and provide hitherto unavailable constraints on the conditions of high-grade metamorphism in several terrains. The constraints are particularly valuable in determining the peak conditions of metamorphism as these are often unobtainable from conventional cation exchange geothermometers and geobarometers which suffer from low closure temperatures.

Acknowledgements.

Every student hopes for a supervisor who gives help when it is needed and doesn't when it isn't. Simon Harley trod this fine line to perfection and with his irrepressible enthusiasm ensured that this project was a pleasure to do - my warmest thanks to him. Many other people were invaluable in the completion of this project, most importantly my XP comrades who helped keep me going during six dark months of failed runs. Steve Elphick taught me how to use the experimental petrology laboratories and offered much expert advice on how not to break experiments. Bob Brown provided unstinting technical support. Nic Odling and Harriet Randle are thanked for their help and their shoulders to cry on. I also thank Dave Draper, Keith Harris, Marion Holness, Colin Graham, Olivier Paillat and Paul Thomas for their help in the lab. Ian Parsons and Colin Graham provided K-feldspar gel and quartz respectively.

Discussion of my work with Bas Hensen and Ian Fitzsimons helped clarify many of my ideas and undoubtedly improved this study. I am grateful to Nathalie Audibert for sharing her work with me and for buying me pancakes and cider in Paris. Francois Holtz provided pre-prints and advice regarding melts and provided the home-made Schnapps which enabled the Spanish field meeting to go with a bang. Mark Pownceby introduced me to the platinum wire technique of fO_2 measurement. Michael Brown, John Clemens, Alberto Patino Douce, Giles Droop, Nigel Harris, John Holloway, Peter Mirwald, Gary Stevens, Dave Waters, Gordon Watt and Daniel Vielzeuf have all provided stimulating conversations at conferences I have attended in San Francisco, Strasbourg, Central Spain and Leeds.

I thank the people who proof-read my chapters for their prompt and useful contributions: Pauline Collins, Harriet Randle, Paul Thomas, Gordon Watt and particularly Ian Fitzsimons and his fine-tooth comb. The staff at Edinburgh have given me much assistance for which I am grateful. The electron microprobe work was almost pleasurable thanks to the patience and expertise of Stuart Kearns and Pete Hill. Diana Baty helped produce the plates and Shane Voss, Ian Chisolm and Cliff Ford kept the computers going. Helen McKeating typed some of the references and Bob Pringle helped in the stores.

My friends in the department have made the last three years a happy time and have all played their part in getting me this far: Kevin Stephen, Trevor Williams, Babs Page, Nicky Allison and Ned Pegler. My family have been very understanding during my long stretch in higher education and I appreciate that very much. Finally, Ciara Shine has supported me emotionally, financially and even physically from time to time. She provided the sense of proportion which kept me sane in the last few months and this thesis is dedicated to her.

This project was funded by the Natural Environment Research Council of Great Britain.

Partial melting and phase relations in metapelitic granulites.

An experimental study in the KFMASH system.

CONTENTS

Chapter Three. Experimental results.

Chapter Four. Interpretation of equilibrium phase assemblages.

Plates. Back-scattered electron photomicrographs.

Chapter Five. Reversal experiments and assessment of the equilibration of the experiments.

Chapter Six. Derivation of phase diagrams.

Chapter Seven. Geological implications of grids and pseudosections.

Chapter Eight. Applications of phase diagrams to natural rocks.

Chapter Nine. Summary of Conclusions.

Appendices.

References.

Inserts (inside back cover).

List of figures and tables.

CHAPTER ONE.

CHAPTER TWO.

CHAPTER THREE.

CHAPTER FOUR.

PLATES.

CHAPTER FIVE.

CHAPTER SIX.

CHAPTER SEVEN.

CHAPTER EIGHT.

APPENDICES.

APPENDIX ONE.
Table A1.1. Ideal and actual melting temperatures of salt in the solid-media cells.

APPENDIX TWO.
Table A2.1. Summary of platinum wire experimental data.

APPENDIX THREE.
AFM Projections of experiments: D41-13/14/15, D43-13/14, D48-14/15/17, D49-16/17/18, D66-18A, D51-16/17, D52-17/18, D54-16/17/18, D55-16/17/18, D56-17/18, D57-16/17/18, D60-16A/17A/18A, D64-16A/17A/18A
KFM Projections of experiments: D47-16/17/18, D59-17/18, D62-16A/18A, D65-16A/17A/18A.
HFM Projections of experiments: D40-13/14/15, D61-16A/17A, D63-16A/18A, D67-16A.

Symbols and abbreviations.

PHASES

als	Al_2SiO_5	**fs**	(ortho)ferrosilite	**phl**	phlogopite
an	anorthite	**grt, gt**	garnet	**plag**	plagioclase
ab	albite	**kfs**	K-feldspar	**prp**	pyrope
alm	almandine	**L**	silicate melt	**qz**	quartz
bt	biotite	**mus**	muscovite	**sa, spr**	sapphirine
cor	corundum	**opx**	orthopyroxene	**sil**	sillimanite
crd, cd	cordierite	**or**	orthoclase	**spl**	spinel
en	enstatite	**os**	osumilite	**V**	volatile fluid

ABSENT-PHASE NOTATION FOR EQUILIBRIA

(a, b,...)	univariant or divariant reaction or assemblage not involving phases a, b,...
[p, q,...]	invariant reaction or assemblage not involving phases p, q,..

EXPERIMENT NOTATION

e.g. D51-16.		**e.g. DS43-14**	
51	run number	**43**	run number
16	mix number	**14**	mix number
		S	solid-media

Mixes

13, 14, 15	mixes of bulk X_{Mg} = 0.62, 0.74, 0.86 respectively, contain sillimanite as mineral
16, 17, 18	mixes of bulk X_{Mg} = 0.62, 0.74, 0.86 respectively, contain sillimanite as gel
16A,17A,18A	repeat batches of mixes 16, 17, 18

M62, M74 and M86	generic labels for mixes with bulk X_{Mg}'s of 0.62, 0.74 and 0.86 respectively, i.e. 13, 16, 16A and 14, 17, 17A and 15, 18, 18A.

Apparatus (optional label)

S	solid-media apparatus used
G	gas-media apparatus used

CHEMICAL SYSTEM ABBREVIATIONS

Components:

S	SiO_2	**C**	CaO
A	Al_2O_3	**N**	Na_2O
M	MgO	**K**	K2O
F	FeO	**H**	H_2O

e.g. KFMASH K_2O-FeO-MgO-Al_2O_3-SiO_2-H_2O

THREE-COMPONENT PROJECTIONS

AFM	projection onto the plane Al_2O_3-FeO-MgO from quartz, K-feldspar and melt
KFM	projection onto the plane K_2O-FeO-MgO from quartz, sillimanite and melt
HFM	projection onto the plane H_2O-FeO-MgO from quartz, K-feldspar and sillimanite

MISCELLANEOUS

A/AFM	molecular $Al_2O_3/Al_2O_3 + FeO + MgO$
Al[4]	aluminium cation in tetrahedral co-ordination
Al[6]	aluminium cation in octahedral co-ordination
a_Q	activity of species Q
a-x	activity-composition
atm	atmosphere
BDMR	biotite dehydration melting reaction
C_p	specific heat capacity
dP/dT	gradient of a line in pressure-temperature space
°C	degrees centigrade
ΔG	difference in molar Gibb's free energy
ΔH	difference in molar enthalpy
ΔS	difference in molar entropy
ΔV	difference in molar volume
e.m.f.	electromotive force (voltage measured on thermocouple)
fO_2	fugacity of oxygen
f_{H2O}	fugacity of water
IBC	isobaric cooling
K_D	partitioning coefficient
K_w	partitioning coefficient of water between melt and cordierite, = H_2O^L/H_2O^{crd}
n	number
NC	Napier Complex, Antarctica
P-T	pressure-temperature
P-T-t	pressure-temperature-time
kb	kilobar
SHBPGI	Sand Hill Big Pond Gabbronorite Intrusion
SIMS	Secondary ion mass spectrometry
vol%	percentage by volume
wt%	percentage by weight
X_{Mg}	molecular MgO/MgO + FeO
XRD	X-ray diffraction
XRF	X-ray fluorescence

BUFFER ASSEMBLAGES

HM	haematite-magnetite
NNO	nickel-nickel oxide
QFM	quartz-fayalite-magnetite
IW	iron-wustite
TTO	tantalum-tantalum oxide

Chapter One

INTRODUCTION

Chapter One. Introduction.

1.1 THE FORMATION OF GRANULITES: MECHANISMS AND SIGNIFICANCE.

Granulites and retrograded granulite-facies rocks make up a large part of cratonic areas and are believed to constitute a significant part of the lower crust. However, the processes which form these rocks and their role in the evolution of the continental crust are still incompletely understood. Granulite terrains are characterised by rocks with water-poor phase assemblages and consequently reflect conditions of low water activity (a_{H2O}). Mechanisms by which the a_{H2O} can be lowered are central to processes of granulite-formation and three principal mechanisms have been suggested (for a recent review, see Stevens and Clemens, 1993). Dilution of a water-rich fluid-phase with a pervasive and voluminous CO_2-rich fluid would lead to a lowered a_{H2O} (Touret 1971, Newton et al. 1980, Newton 1990), as would the removal of a water-rich silicate melt (e.g. Fyfe 1973). Both these mechanisms would result in a relatively dry lower crust and a net upward transport of melt-forming components. The third mechanism envisages a water-poor metamorphic protolith (Lamb and Valley 1985).

Recently, the production of granulites through the fluxing of the terrain by a CO_2-rich fluid has lost favour as a general model in the face of contradictions between fluid inclusion data, frequently CO_2-rich, and independent fluid compositional indicators. These independent indicators include mineral assemblages (Lamb et al. 1987) which show that CO_2 rich inclusions formed after the peak of metamorphism. Also, fluid flow is unlikely to be pervasive in the lower crust given the gradients in fluid composition inferred in the Adirondacks (Valley et al. 1990). Dihedral angle studies raise a more fundamental objection in suggesting that pervasive flow of CO_2 through granulites is unlikely (Watson and Brenan 1987, Holness 1992, 1993). The metamorphism of a water-poor metamorphic protolith does not explain the frequent production of pelitic granulites from rocks rich in hydrous micas.

Heterogeneity in the stable isotope compositions of minerals from adjacent granulite lithologies (Valley and O'Neill 1984) suggests that granulites may form under fluid-absent conditions. Fluid-absent partial melting and segregation is a process which can be envisaged to operate on a variety of scales and independently in different lithologies. It is currently the most plausible general model of granulite formation.

The lowering of a_{H2O} by partial melting was discussed by Powell (1983). As the hydrous assemblage experiences increasing temperature, dehydration occurs raising the a_{H2O}, assuming the fluid is internally buffered. This leads to a premature intersection with the solidus relative to an externally buffered case. The first melt to form is water-undersaturated and absorbs any free water. Further temperature increases give more melt and more of the anhydrous product assemblage via the dehydration melting reaction. The a_{H2O} decreases as the water from the hydrous minerals reacts straight into the melt and the melt segregates.

The importance of dehydration melting reactions in metapelitic rocks in producing migmatitic features, controlling a_{H2O} and the mineral assemblage evolution has been emphasised by recent work. Several criteria have been used; textural data from rocks from the Arunta Complex, Australia (Vernon and Collins 1988); geochemical data from rocks from Cameroon (Barbey et al. 1990); mineralogical data from rocks from Namaqualand, South Africa (Waters and Whales 1984) and Broken Hill, Australia (Phillips 1980). These studies and others (Stuwe and Powell 1989, Waters 1988) have also shown that the most important dehydration melting reaction in metapelites is the breakdown of biotite.

A principal criticism of the partial melting mechanism of granulite formation is that the silicic, water-undersaturated melts required would be too viscous to segregate efficiently. Instead, they should remain in-situ and retrogressively rehydrate the rock on crystallisation (Warren 1983, Peterson and Newton 1989). Furthermore, few granulite terrains have a chemical and mineralogical composition consistent with the extraction of large melt volumes (Clemens 1990, Vielzeuf et al. 1990). However, the scale of segregation need only be a few centimetres, as seen in Namaqualand (Waters and Whales 1984, Waters 1988), and other studies suggest the segregation of granitic magmas can be efficient at melt fractions as low as 5% (Jurewicz and Watson 1985, Wickham 1987, Holtz and Barbey 1991). Even if the melts do recrystallise in-situ the consequent fluid-loss is likely to be channelised and will not affect the bulk mineralogy of the rocks.

Whilst the formation of metapelitic granulites will not contribute to intra-crustal granitic intrusions except when extreme temperatures of metamorphism are reached (Clemens and Vielzeuf 1987), they will have a role in the evolution and elemental distribution of the lower crust. A better understanding of this can be gained from fuller knowledge of the partial melting process and the phase compositions and

assemblages associated with it. Minerals in metapelite phase assemblages exhibit limited solid solution, relative to mafic rocks, leading to the formation of distinctive, low-variance mineral assemblages. These assemblages may provide pressure-temperature information unavailable from conventional exchange geothermobarometry where uncertainties in calibrations may be large or where only closure temperatures are retrieved. Distinctive phase assemblages are particularly useful in constraining peak metamorphic conditions as this is when exchange geothermobarometry is most uncertain. For example, the co-existence of sapphirine and quartz in the Napier complex of Antarctica requires temperatures above 1025°C (Hensen and Green 1973, Chatterjee and Schreyer 1972) but conventional geothermometry only rarely produces maximum temperature estimates of 1000°C (Harley and Hensen 1990). Quantitative assessment of the pressure-temperature evolution of granulites allows tectonic models to be constrained.

The use of phase relations in gaining a greater understanding of the nature of the lower crust has been given impetus from the development of a theoretical framework in the form of a series of petrogenetic grids (see next section). However, the implementation of these grids has been seriously hindered by the paucity of experimental pressure-temperature constraints on the postulated topologies.

1.2 THEORETICAL PHASE RELATIONS IN METAPELITIC GRANULITES.

The theoretical phase relations of metapelitic granulites have received considerable attention in the last ten years (Thompson 1982, Vielzeuf and Boivin 1984, Grant 1985, Hensen 1986, Powell and Downes 1990, Hensen and Harley 1990, Mouri et al. 1993). The requirements of a petrogenetic grid[1] for the amphibolite- to granulite-facies transition in metapelites are ideally met by the biotite dehydration melting reactions. This is because, whilst a_{H2O} is a fundamental parameter in granulite petrogenesis and will vary in time and space, the pressure-temperature locations of the biotite dehydration melting reactions are independent of it. The phase rule requires that the a_{H2O} is fixed at any point along a given reaction which is univariant in pressure-temperature space (Hensen and Harley 1990).

---

[1] A short review of the theoretical principles of petrogenetic grids is given in section 6.2.

The first step in deriving a grid is choosing a chemical system. Ideally this would be the natural system but its large number of components make constructing and constraining such a petrogenetic grid extremely difficult. Most experiments to date have been conducted in very simple systems such as $FeO-Al_2O_3-SiO_2-H_2O$ (FASH), $MgO-Al_2O_3-SiO_2-H_2O$ (MASH) or $K_2O-Al_2O_3-SiO_2-H_2O$ (KASH). However, the system most frequently chosen for theoretical studies of metapelites is the KFMASH system as this offers the best compromise between the natural system, and therefore applicability, and simplicity, and therefore reliability .

Some authors, in order to derive grids in KFMASH, combine the topologies of the end member systems, as will be seen below. This requires some caution. In general, consideration of the topologies of end member systems has no predictive value in determining the stable topology of the multisystem (Hensen and Harley 1990). This is fundamentally due to the requirement that stable, non-degenerate reactions must become metastable through an invariant point and vice versa. In particular, a reaction stable in between two invariant points in a multisystem cannot be stable in either end member system. However, when only the end member system is considered, the reaction may well be stable. Predicting the *stable* topology of the multisystem requires data from either careful study of metamorphic assemblages, where the recognition of unique assemblages can distinguish stable topologies from residuals (e.g. Hensen 1986), or from experimental work on end member or multisystems, (Hensen and Harley 1990).

It is therefore crucial in assessing a proposed diagram to consider the quality of the constraints used in specifying the stable topology. It is also very important assess assumptions made about phase compositions as variations in these can alter the topology of a grid. The salient features of the recent petrogenetic grids are considered below.

Appraisal of published grids.

The first grid considered here is that of Thompson (1982) which extended the work of Grant (1973) in the light of new experimental data (figure 1.1). A KFMASH biotite dehydration melting reaction, bt + sil + qz = grt + crd + kfs + L, is shown on the grid as (63) and is stable from 750°C, 3kb to 830°C, 8.5kb. The diagram was constructed by combining KFASH and KMASH system diagrams and extrapolating to water-undersaturated conditions. The biotite dehydration melting reaction has only

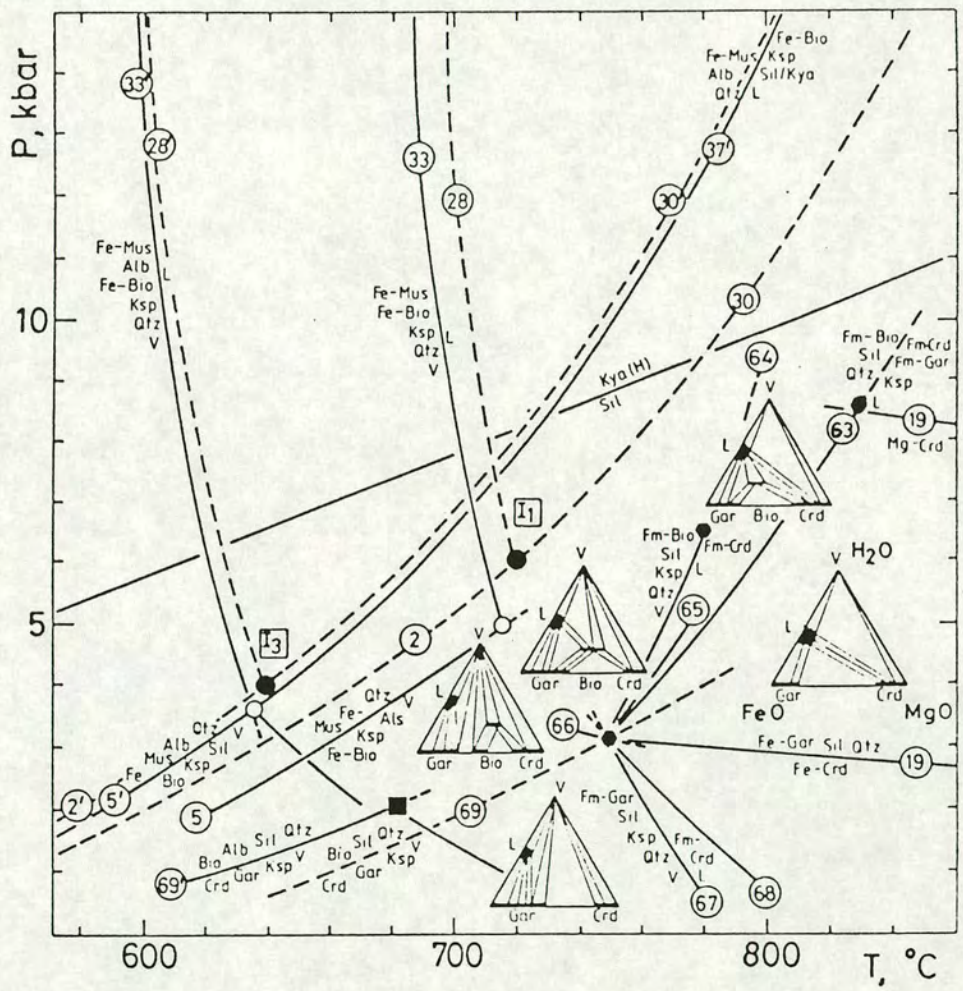

Figure 1.1. Pressure-temperature diagram reproduced from Thompson (figure 7, 1982). The diagram shows the extrapolation of the than available data into the systems KFMASH, KNFASH, KNFMASH. The KFMASH reactions are shown emanating from the solid hexagons.

one constraint: its lower grade end is positioned at the intersection of the analogous dehydration reaction (69) and the water-saturated minimum melting curve (e.g. Luth 1976). The former reaction was positioned experimentally by Holdaway and Lee (1977). The slope of the biotite dehydration melting reaction is estimated here. The high-pressure breakdown of cordierite, here to garnet-sillimanite-quartz, is shown in the KFASH and KMASH end member systems (19).

In constructing figure 1.1 the assumption was made that the first formed melt is always more iron rich than co-existing silicate crystals (figure 1.2). More recent experimental work (Ellis 1986) suggests that below 900°C at 10kb this is not true and that garnet is the most iron-rich silicate phase. This does not affect the stoichiometry of the biotite dehydration melting reaction (63) discussed above but does change some reactions on the water-saturated solidus leading to eutectic melting in the assemblage bt + grt + sil + ksp + qz. A more important implication is that metapelites of intermediate bulk composition would melt before iron- or magnesium-rich ones.

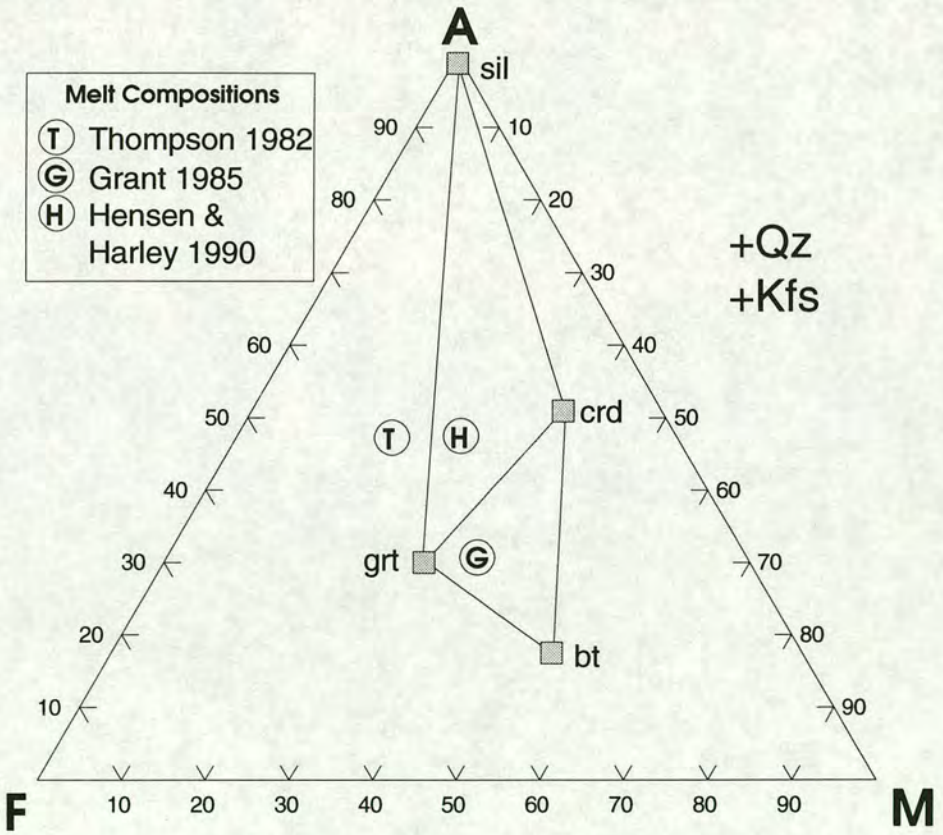

Figure 1.2. Schematic AFM diagram showing the relative melt compositions chosen by various authors in constructing petrogenetic grids. Thompson (T, 1982) chose a melt with a lower X_{Mg} than co-existing garnet and with a higher A/AFM than the garnet-cordierite tie-line. Hensen and Harley (1990) chose a melt with a higher X_{Mg} than garnet, as did Grant (1985) whose melt also had a lower A/AFM. The differences affect the phase relations under water-saturated conditions.

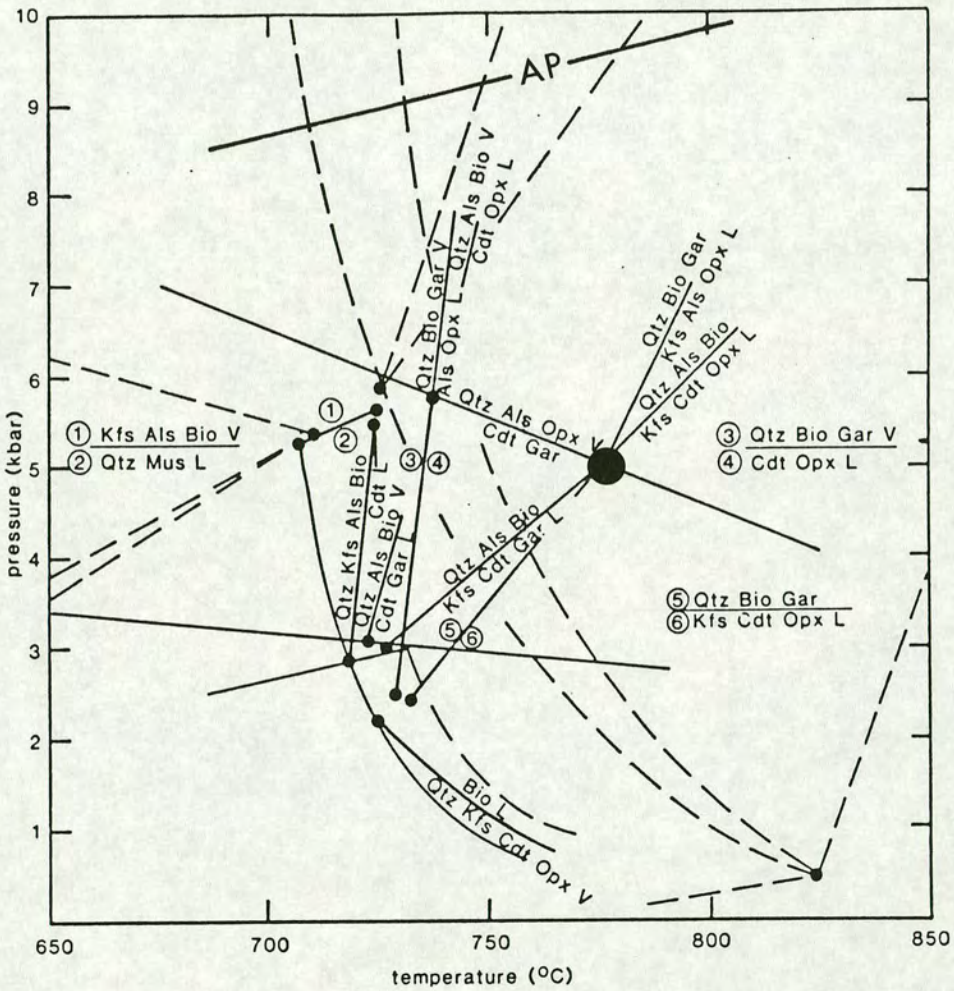

Figure 1.3. Pressure-temperature diagram reproduced from Grant (figure 3.15, 1985). The grid shows the inferred stable univariant and invariant equilibria in KFMASH (heavy lines), tentatively positioned in P-T space on a base of KFASH and KMASH reactions. The large circle is the invariant point referred to in the text and is equivalent to that labelled [spr, spl] in Hensen and Harley (1990). The line at high pressure labelled AP is the position of the reaction Cdt + Gar = Qtz + Als + Opx + V of Grant (1985) as later determined by Aranovich and Podlesskii (1989).

The grid derived by Grant (1985) assumed garnet was the most iron-rich phase during biotite dehydration melting (figure 1.3), in agreement with Ellis (1986). Here KFMASH reactions considered stable under conditions of reduced a_{H2O} have been taken from a complex grid for $P_{H2O} = P_{Tot}$ and positioned with "considerable temerity" in pressure-temperature space. The relationship between the KFMASH equilibria and the base grid is unclear. The biotite dehydration melting reaction (of the same form as Thompson 1982, figure 1.1) runs from 725°C, 3kb to 775°C, 5kb. This is too restricted a range, given the widespread recognition of the reaction in experiments and in the field (e.g. Waters 1988, Vielzeuf and Holloway 1988, Le Breton and Thompson 1988). The reason for this inconsistency is the misplacement in the grid of Grant (1985) of the degenerate reaction crd + grt = opx + als + qz + V at only 5kb at 775°C and with a negative slope. More recently, this reaction has been differently positioned in the FMASV system at pressures above 8.5kb and with a positive slope (figure 1.3, Aranovich and Podlesski 1989, Bertrand et al. 1991). Also, the temperatures estimated by Grant (1985) for the univariant biotite dehydration melting reaction seem rather low in the light of experimental studies published since (Vielzeuf and Holloway 1988, Patino Douce and Johnston 1991).The high pressure-temperature invariant point emphasised in figure 1.3 is vapour-absent and is central to phase relations related to biotite dehydration melting in the KFMASH system (e.g. Powell and Downes 1990).

As melt compositions were not well known, Grant (1985) had to choose a relative alumina content in order to derive a grid topology. He chose the melt composition such that it was less aluminous than the AFM garnet-cordierite tie line (figure 1.2). However, more recent experimental data (Ellis 1986, Vielzeuf and Holloway 1988, Le Breton and Thompson 1988, Patino Douce and Johnston 1991) suggest a peraluminous melt. Though low-alumina rocks formed from melts do occur, this may be due to fractionation. The assumption of a low-alumina melt rather than a peraluminous one does not directly affect the biotite dehydration melting reactions but it does alter the water-saturated equilibria at lower grade and more importantly would alter the phase relations at higher grade above the stability of biotite.

The most recent grid, presented by Hensen and Harley (1990, figure 1.4), is topologically consistent with that of Grant (1985) except that the experimental data of Bertrand et al. (1991) was used in positioning the grt + crd = opx + sil + qz

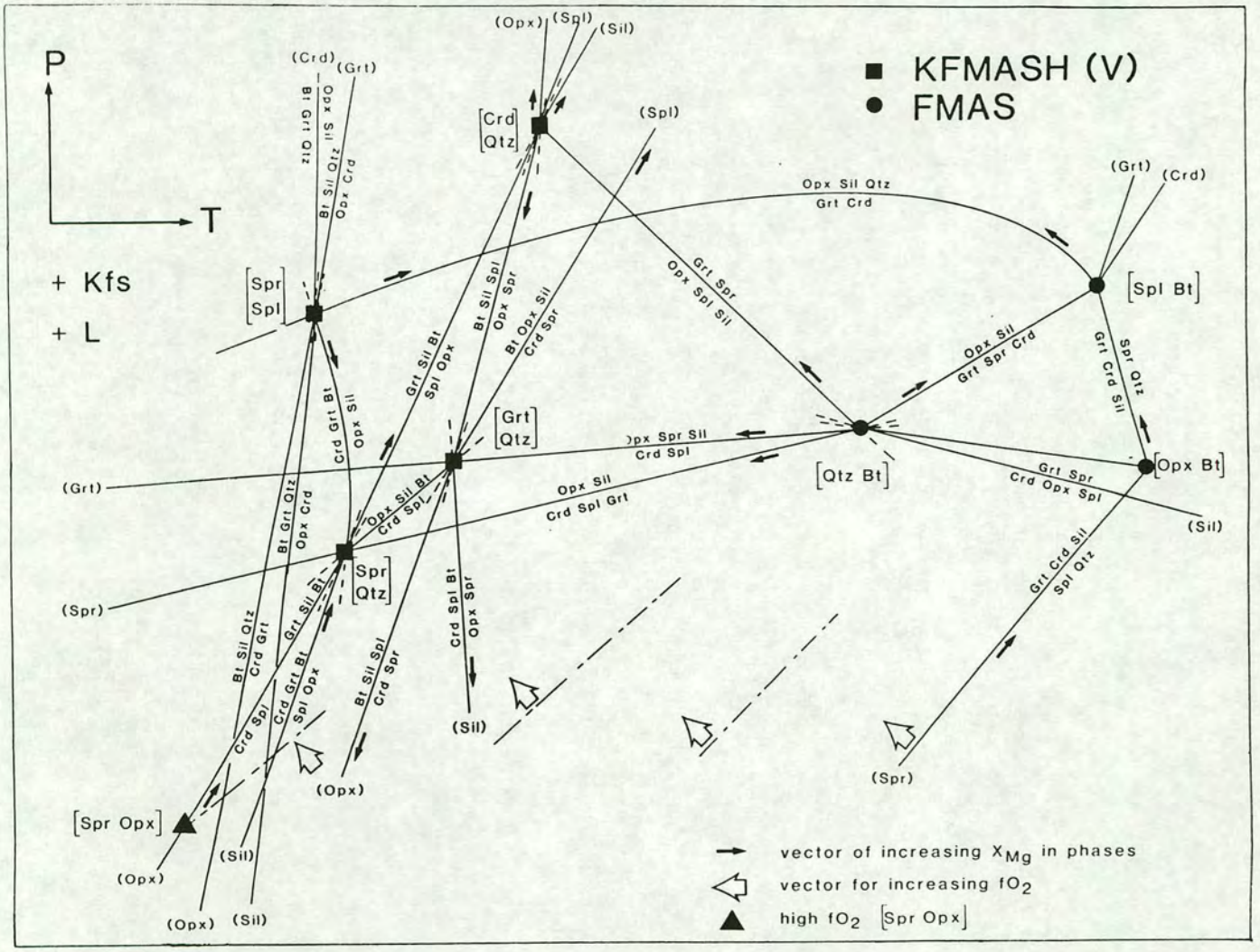

Figure 1.4 Pressure-temperature diagram reproduced from Hensen and Harley (figure, 2.17, 1990). The diagram is a theoretical grid for vapour absent dehydration melting reaction in the system KFMASH(O). Both quartz-absent and quartz-present conditions are represented.

reaction. Hensen and Harley (1990) include the same important invariant point as Grant (1985), which they label [spr, spl]. The topology of their grid assumes a melt composition close to the AFM garnet cordierite tie-line and more magnesian than co-existing garnet (figure 1.2). They also specify that the water/iron + magnesium ratio of the melt is much higher than that for biotite. The grid of Hensen and Harley (1990) is wider in scope than previous grids, accounting for silica-saturated and silica-undersaturated compositions and varying oxygen fugacity. Insufficient experimental constraints were available to enable Hensen and Harley (1990) to position their grid in pressure-temperature space and they stressed the need for such data. They did, however, predict that the [spr, spl] point would lie in the range 850-900°C, 9-10kb.

1.3 EXPERIMENTAL CONSTRAINTS ON PHASE RELATIONS IN METAPELITIC GRANULITES.

Biotite dehydration melting reactions.

Experimental work on biotite dehydration melting reactions in metapelitic lithologies was conducted by Vielzeuf and Holloway (1988), Patino Douce and Johnston (1991) and Le Breton and Thompson (1988). The experiments in these studies were carried out primarily at 10kb though the first two studies also ran experiments at 7kb and 12 or 13kb. None of the studies included reversal experiments. The main aim of all the studies was to determine the fertility of metapelites as sources of granitic melts and to ascertain at what temperatures significant melting occurred. The results of the experiments are summarised in table 1.1.

	No. of experiments.	**Pressure (kb)**	**Beginning of melting (°C)**	**Loss of biotite (°C)**
Vielzeuf and Holloway (1988)	15	10	-	850-862
Le Breton and Thompson (1988)	3	10	750-800	-
Patino Douce and Johnston (1991)	10	10	-	975-1000
Patino Douce and Johnston (1991)	8	7	-	950-975

Table 1.1. Summary of experimental data of three studies of biotite dehydration melting. None of the experiments were reversed. Each of the studies used a single, natural bulk composition based on an average pelite.

All the experiments were done using natural starting materials modelled on average pelite compositions. In each case only one bulk composition was used; $X_{Mg} = 0.41$ in Vielzeuf and Holloway (1988), $X_{Mg} = 0.44$ (0.39 in one mix) in Le Breton and Thompson (1988) and $X_{Mg} = 0.36$ in Patino Douce and Johnston (1991). The studies achieve their aims with varying degrees of success and provide useful insights as to which lithologies are likely to produce the most melt on heating. However, they are of limited use in developing or constraining petrogenetic grids based on univariant reactions and applicable over a broad range of bulk compositions. Only a single biotite dehydration melting reaction was intersected in their experiments because

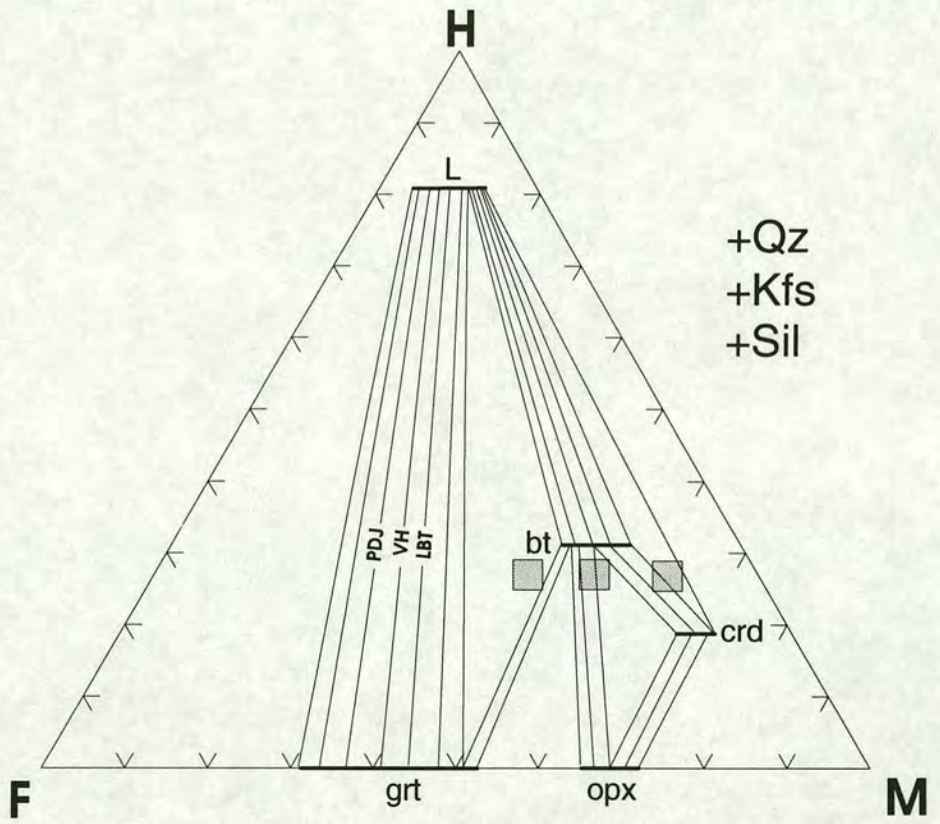

Figure 1.5. Schematic AFM diagram illustrating why previous studies on biotite dehydration melting (PDJ, VH, LBT represent the work of Patino Douce and Johnston 1991, Vielzeuf and Holloway 1988, Le Breton and Thompson 1988) have failed to intersect univariant equilibria. Iron-rich bulk compositions lose biotite at lower temperatures than the terminal stability of biotite and are therefore not affected by the KFMASH univariant reaction bt + grt + kfs + qz = opx + sil + L, i.e. when the rock has risen to the temperature where the last biotite of any composition is stable, iron-rich compositions already lie in the garnet-melt trivariant field. More magnesium-rich bulk compositions would retain biotite to this temperature and would therefore react via the univariant reaction to produce an opx-grt-sil-kfs-qz-L assemblage. Garnet-absent assemblages would see the KFMASH univariant reaction bt + sil + kfs + qz = opx + crd + L at higher temperatures. The compositions used in the present study are shown (grey boxes). The experiments in the current study show that this diagram represents pressure-temperature conditions of about 890°C, 9kb.

only one, iron-rich bulk composition was used and that reaction is at least divariant in the KFMASH system (figure 1.5).

The pressure-temperature position of divariant (or sliding) reactions are dependent on bulk composition and so the results of the experiments only apply to the bulk compositions used. For example, the persistence of biotite to relatively high temperatures (950-975°C) in the experiments of Patino Douce and Johnston (1991, table 1.1) may be due to differences in bulk water contents, differences in the titanium and fluorine contents of biotites or the different alkali contents of the melt. Univariant reactions, by contrast, operate for a range of bulk compositions in pressure-temperature space and so can be used to develop a truly general grid, applicable to all bulk compositions within the system considered. In addition, the positions of divariant reactions, the most common type of reaction operating on rocks, are limited by the positions of the univariant reactions. Figure 1.5 shows that more magnesian bulk compositions would be required to intersect the univariant reactions involving the dehydration melting of biotite.

Experimental phase relations at high temperatures, above the stability of biotite.

In the past biotite-melting reactions in natural or model systems have generally been considered in isolation. However, they must link in with higher-temperature reactions involving phases stable beyond the stability of biotite and for this reason it is necessary to consider the available experimental constraints on high-temperature phase relations and grids.

The pioneering experimental work on the phase relations of metapelitic granulites was done by Hensen and Green (figure 1.6, 1970, 1971, 1972, 1973) and were interpreted in terms of FMAS system reactions, although the experiments were performed on bulk compositions containing small but significant amounts of CaO, K_2O, Na_2O and, particularly important, H_2O (table 7.2). Their work principally concerns very high temperature assemblages such as sapphirine-quartz and is still widely used (e.g. Harley et al. 1990, Waters 1991, Harley and Fitzsimons 1991, Bertrand et al. 1992). The experiments of Hensen and Green (*as above*) position the important granulite-facies reaction crd + grt = opx + sil + qz at 950°C, 10kb and with a negative slope (figure 1.6). Bertrand et al. (1991) positioned the same reaction at 11kb, 950°C in the system FMASV and although their experiments gave a positive slope for the reaction (see figure 7.7), they confirmed the high pressure nature of the

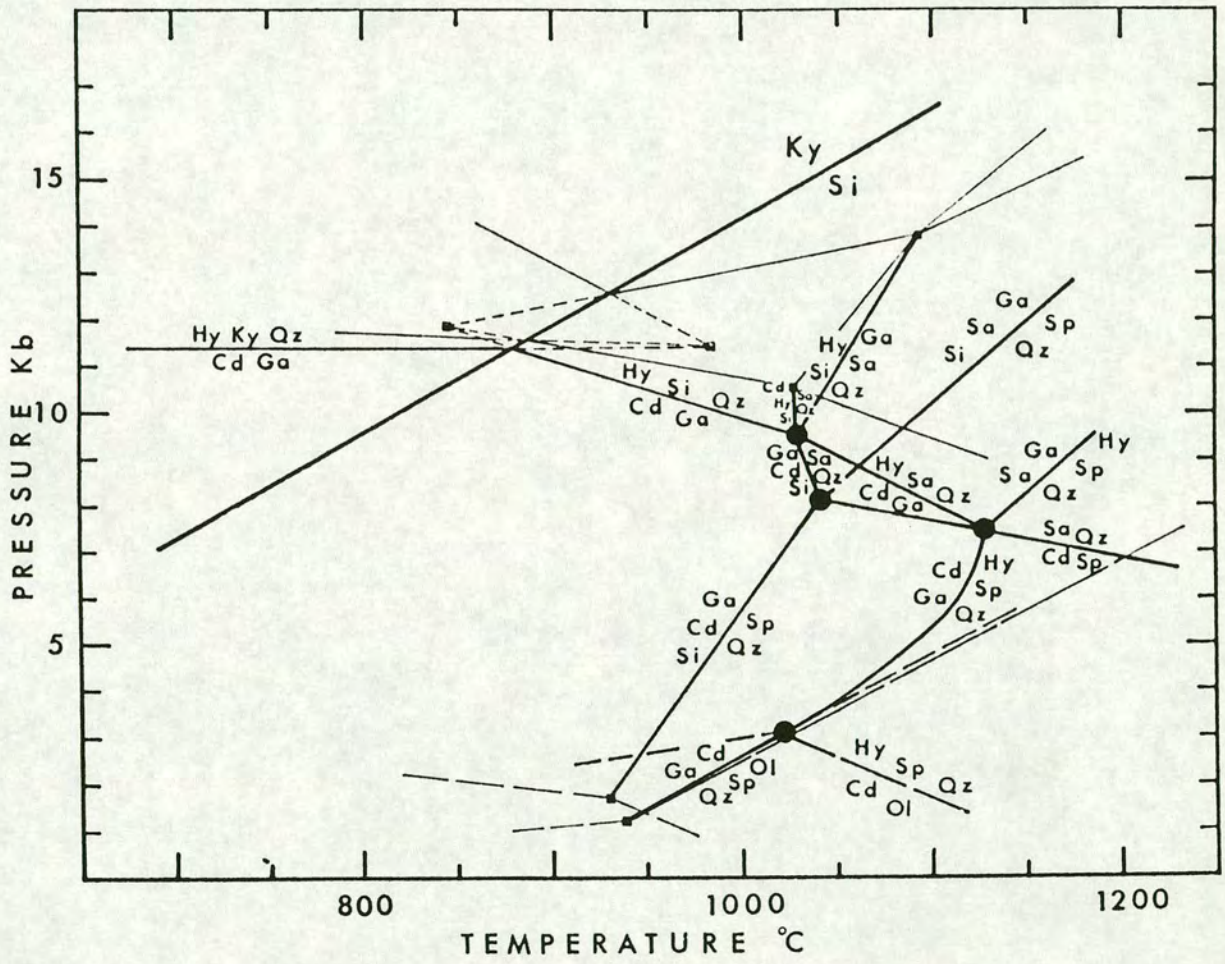

Figure 1.6. Pressure-temperature diagram reproduced from Hensen and Green (1973). The grid shows the best-fit pressure-temperature positions of FMAS univariant reactions (heavy lines) as constrained by the experiments of Hensen and Green (1970, 1971, 1972, 1973). MAS and FAS system reactions are shown as light lines. The reaction Hy + Si + Qz = Ga + Cd (opx + sil + qz = grt + crd, in the notation used here) is discussed in the text.

orthopyroxene-sillimanite-quartz assemblage. The only other experimental work useful in constraining phase relations in metapelitic granulites was done by Annersten and Seifert (1981) but applied to the alternative topology of Hensen (1971) because the fO_2 was controlled at the haematite-magnetite buffer.

Pseudosections.

The grids of Hensen and Green (1970, 1971, 1972, 1973) were developed concurrently with a new approach to the interpretation of phase assemblage histories in rocks. The phase assemblage evolution of a rock of particular bulk composition is controlled principally by the operation of divariant reactions, rather than univariant ones. This is because a larger number of divariant phase assemblages are accessible to a particular bulk composition than the number of univariant reactions that could be intersected, fundamentally because divariant reactions require the presence of one fewer phase. Only rocks in a restricted range of bulk composition will be altered by the operation of a univariant reaction at a particular pressure and temperature. A very useful type of phase diagram is a pseudosection, originally used by Hensen (1971). A pseudosection shows the divariant *and* univariant reactions which a particular bulk composition may experience and are therefore powerful tools in the interpretation of phase assemblage histories (e.g. Powell and Downes 1990, Jones and Brown 1990). The experiments conducted by Hensen and Green (1970, 1971, 1972, 1973) used several different bulk compositions and allowed a range of pseudosections to be drawn, reflecting the range of natural rock bulk compositions.

1.4 THE STABILITY OF OSUMILITE.

It was shown above (figure 1.5) that to intersect univariant reactions in KFMASH relatively magnesian metapelite compositions must be used. This raises the possibility of stabilising osumilite, which has been found in magnesian metapelites from several localities. Osumilite is a predominantly a KFMAS system phase with a crystal structure very like cordierite[2], although osumilite never contains volatiles. It was first reported by Miyashiro (1956) from Sakkabira, Japan from vesicles in a volcanic rock. Since then at least twenty six occurrences have been reported (Berg

---

[2] General formula, $(K,Na)^{XII}(Mg,Fe)_2^{VI}(Al,Mg,Fe)_3^{IV}(Si,Al)_{12}^{IV}O_{30}$. For example, $(K_{0.93}Na_{0.14})(Mg_{1.49}Fe_{0.46})(Al_{2.69}Mg_{0.23}Fe_{0.08})(Si_{10.37}Al_{1.63})O_{30}$, "Norway", table 1, Armbruster and Oberhansli (1988).

and Wheeler 1976, Maijer et al. 1977, Ellis et al. 1980, Grew 1982, Waters 1988, 1991, Arima and Gower 1991, Audibert et al. 1993 and Schreyer et al. 1986 and references therein) from a variety of environments: volcanic formations, buchites, volcanic xenoliths, contact-metamorphosed sedimentary rocks and granulite facies regionally-metamorphosed rocks.

Experimental work on the stability of osumilite is limited but Hensen (1977) showed that the mineral was not only stable at very low pressures but could exist in the bulk compositions used[3] at 3.6 to 7.2kb, 1000°C and 5.4 to 7.2kb, 1100°C. Olesch and Seifert (1981) demonstrated that osumilite could not be stable above 0.8kb in the presence of a hydrous fluid. Their findings are consistent with the fact that all high-pressure occurrences of osumilite are interpreted to have formed under conditions of low water activity.

The discovery of osumilite in the Napier Complex, Antarctica lead to disagreement over the relative stabilities of osumilite and sapphirine in quartz-bearing rocks. Ellis et al. (1980) developed a theoretical KFMAS system grid in which osumilite was only stable inside the stability limits of the sapphirine-quartz assemblage (figure 1.7a). In contrast, the theoretical grid developed by Grew (1982) allowed for a larger stability field of osumilite, extending below the low temperature stability limit of sapphirine-quartz (figure 1.7b).

An experimental study of osumilite phase relations in the KFMASH system in the pressure-temperature range 1000-1100°C, 8-13kb was presented by Audibert et al. (1994). This study confirmed the stability of osumilite at high pressure and temperature and suggests that the high pressure stability limit of the garnet-osumilite assemblage is 11kb. The data of Audibert et al. (1994) also showed that osumilite could be stable outside the stability field of sapphirine-quartz and was therefore consistent only with the grid of Grew (1982) and not that of Ellis et al. (1980).

Osumilite may well be more common than is currently thought for two reasons. Firstly, it is not distinctive in thin section, having a first order grey interference colour, moderate relief and a single weak cleavage. Secondly, it is a high temperature mineral and is often replaced retrogressively by symplectites of quartz-K-feldspar

---

[3] The experiments of Hensen and Green (1970, 1971, 1972, 1973) stabilised osumilite in some cases and it is these results that Hensen (1977) reports.

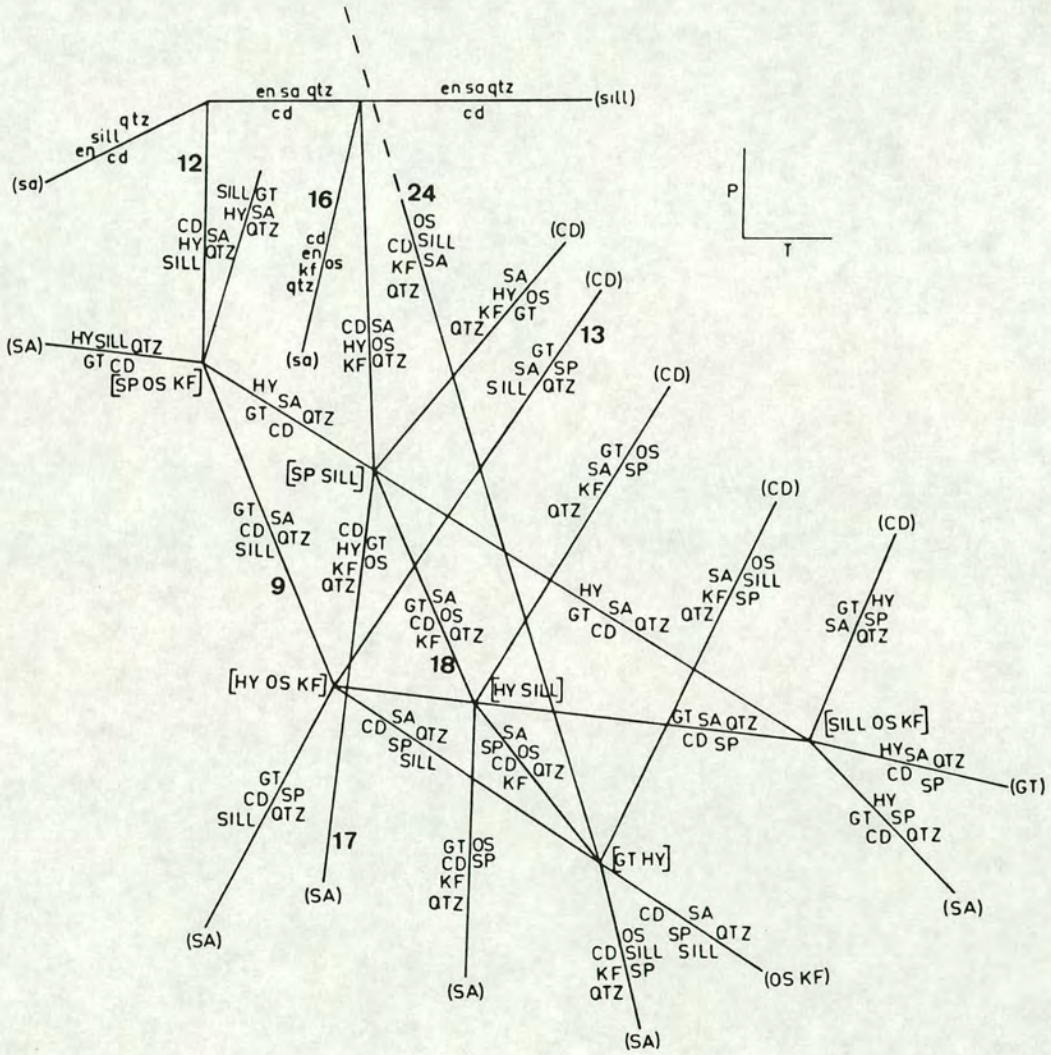

Figure 1.7a. Pressure-temperature diagram reproduced from Ellis et al. (figure 20, 1980). The diagram shows a theoretical KFMAS system grid of univariant reactions. The reactions in written in lower case letters are in the KMAS system. The reactions emanating from the [SP OS KF] point limit the stability of sapphirine-quartz. The positioning of this point at a *lower* temperature than the [SP SILL] point, which is formed by reactions limiting the stability of osumilite, means that osumilite is only stable within the stability field of sapphirine-quartz, at moderate pressures. Compare with figure 1.7b. (Phase abbreviations: KF = K-feldspar, OS = osumilite, SILL = sillimanite, SP = spinel)

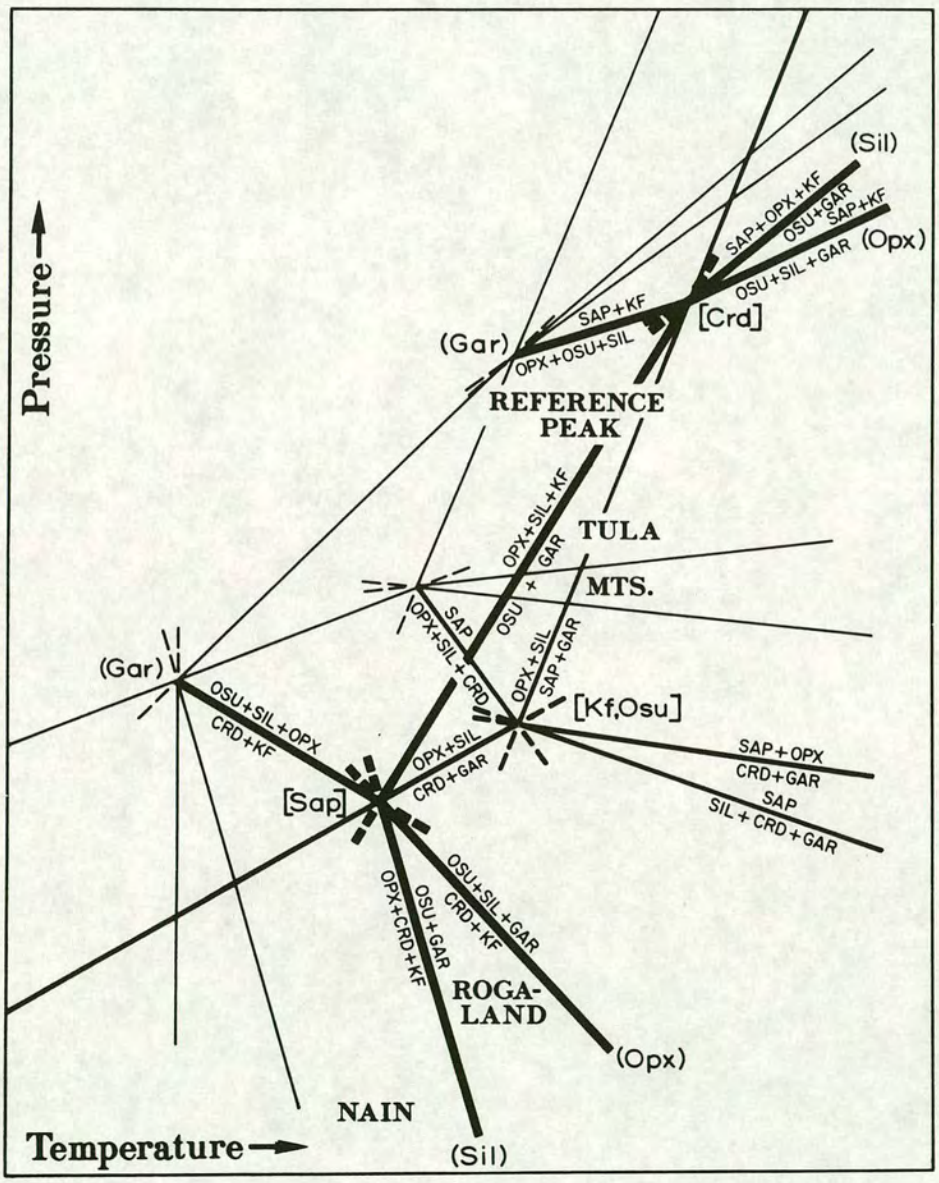

Figure 1.7b. Pressure-temperature diagram reproduced from Grew (figure 12, 1982). The diagram shows a theoretical grid of KFMAS system reactions (heavy lines) and FMAS reactions (lighter lines) with quartz present in all assemblages. The [Kf, Osu] point is analogous to the [SP OS KF] point of Ellis et al. (1980) but here lies at a *higher* temperature than the reactions limiting the stability of osumilite, which emanate from the [Sap] and [Crd] points. Therefore, on this grid, osumilite can be stable outside the stability field of sapphirine-quartz.
(Phase abbreviations: Crd = cordierite, KF = Kf = K-feldspar, OS = Osu = osumilite, Sap = sapphirine, SP = spinel)

cordierite ± orthopyroxene (e.g. Maijer et al. 1981, Audibert et al. 1993) which may not have been recognised as forming after osumilite. Osumilite potentially has an important role to play in the phase relations of magnesian metapelites at high temperatures. To date, there has been no study which constrains the phase relations involving osumilite at conditions below 1000°C or which considers its importance in the melting of magnesian metapelites via the breakdown of biotite.

1.5 AIMS OF STUDY.

This project aims to increase the understanding of the processes of partial melting in the lower crust which lead to the formation of granulites. It endeavours to do this by taking a different approach to those previously chosen. Experimental data from KFMASH system metapelite compositions are used to determine the univariant reactions stable around the invariant point upon which the biotite dehydration melting reactions centre (figures 1.2 and 1.4, labelled [spr, spl]). A petrogenetic grid is derived by positioning these reactions in pressure-temperature space. In the KFMASH system considered, this grid is independent of bulk composition and therefore provides an excellent framework for the consideration of lower crustal processes.

Distinctive low-variance assemblages can provide invaluable pressure-temperature information in the absence of reliable cation exchange geothermobarometers only if sufficient experimental constraints are available. Extending the determination and positioning of stable KFMASH univariant reactions and invariant points to higher temperatures than the stability of biotite will produce a KFMASH multi-grid which will provide these constraints.

The use of several different KFMASH bulk compositions not only enables closer constraints to be placed on the univariant grid by producing a wider range of assemblages but allows pseudosections to be produced for each of those bulk compositions. The pseudosections are very useful in the interpretation of phase assemblage histories of rocks with similar bulk compositions, and are applied to a number of published examples.

Particular areas of interest that this study also hopes to illuminate are:

1. Univariant biotite dehydration melting reactions - pressure-temperature positions and the controls they provide on partial melting in different bulk compositions.

2. The reaction garnet + cordierite = orthopyroxene + sillimanite + quartz - the true form, pressure-temperature position and dP/dT gradient of this reaction in the KFMASH and other systems.

3. Osumilite - the extent of stability of this mineral, the assemblages in which it can occur and its role in melting equilibria.

4. The use of carefully determined univariant petrogenetic grids and pseudosections in defining the pressure-temperature conditions of metamorphism - application to natural examples, some already well-constrained and some still poorly constrained.

1.6 STRUCTURE OF THESIS.

The cornerstone of this thesis is the series of sixty four experiments conducted in the pressure-temperature range 840-1000°C, 5-12.5kb. The experiments were run in solid-media apparatus, using salt cells, and in internally-heated gas-media apparatus. The experimental procedure and assessment of uncertainties is described in **Chapter Two**. Three different bulk compositions were used in the experiments in order to, firstly, produce as many different assemblages as possible and thereby constrain the univariant grid as closely as possible and, secondly, enable the construction of different pseudosections. The bulk compositions chosen were magnesium-rich to ensure that the univariant KFMASH reactions were intersected and were composed of a mixture of natural and synthetic minerals. The method of production of the experimental mixes is also given in **Chapter Two**.

The results of the experiments are presented in **Chapter Three**. The product assemblages of all the experiments are given along with the phase compositions. The experimental products must be well characterised to warrant confident interpretation of the results and so the phase chemistry is evaluated in some detail. The compositions of individual phases and the partitioning of iron and magnesium between ferromagnesian phases is considered and compared to data from the

literature. Water is a vital component in the KFMASH system but is frequently ignored. **Chapter Three** describes the attempts made to constrain the water contents of the hydrous phases, which involve mass balance calculations, theoretical modelling and direct analysis of one experiment by Secondary Ion Mass Spectrometry.

The interpretation of the experiments is considered in **Chapter Four**. The majority of the experiments produced what was interpreted to be an equilibrium assemblage. However, some experiments were interpreted to contain extra phases and some to have phases missing. The methodology by which the interpretations were made is carefully stated. The data from all the experiments are presented in the form of three-component projections in **Chapter Four** and **Appendix Three**. The positions of hydrous phases on the three-component projections depends on their water contents, which in general is not well known. The final section of **Chapter Four** considers whether reasonable variations in phase water contents could alter the interpreted phase relations.

It is an essential duty of experimentalists to give an assessment of how closely their experiments approach equilibrium and this is done in **Chapter Five**. Successful reversal experiments are a compelling indication of a close approach to equilibrium and five such experiments are reported. Consideration of these and other criteria for equilibrium lead to the conclusion that the experiments were close to equilibrium.

The end product of the experimental data are a well-constrained grid of univariant and invariant KFMASH system reactions and three KFMASH pseudosections. **Chapter Six** firstly contains a review of the theoretical basis of such diagrams and then describes the derivation of them in this study. The role of K-feldspar in biotite dehydration melting reactions is evaluated and accounted for in the topology of the diagrams. The implications of experimental interpretations alternative to those given in **Chapter Four** are considered.

The geological implications of the phase diagrams are examined in **Chapter Seven**. The main conclusions drawn are:

- The temperature range over which biotite dehydration melting reactions operate depends on the bulk X_{Mg} of the rock concerned and the pressure at which melting occurs. The position of that melting range in temperature

depends on the amount of stabilising components (titanium and fluorine) in the biotite.

- The correct form of the reaction relating garnet-cordierite and orthopyroxene-sillimanite-quartz assemblages in a water-undersaturated KFMASH system is,

garnet + cordierite + K-feldspar + quartz =
orthopyroxene + sillimanite + melt,

and this reaction runs from 8.8kb, 900°C to 7.8kb, 1000°C, i.e. a negative dP/dT.

- Osumilite should be stable in metapelites with bulk X_{Mg}'s of greater than 0.62 if temperatures have exceeded 875°C at 5kb and 940°C at 8kb. The high pressure stability limit of the garnet-osumilite assemblage is 9kb at 1000°C. This limit is 2kb lower than that determined by Audibert et al. (1994). A solid-media run using a talc-pyrex cell very similar in design to that used by Audibert et al. (1994) shows that the pressure discrepancy is very likely to have been the result of an underestimate of the friction correction required by the talc-pyrex cell. When a suitable correction is made to the results of Audibert et al. (1994) they become compatible with the results of the current study.

The application to natural rocks of the phase diagrams derived in this study is illustrated in **Chapter Eight**. Examples are taken from five localities and the constraints of the phase diagrams allow improvements in the pressure-temperature estimates or in the understanding of the history of the rocks in all cases.

The conclusions of the thesis are summarised in **Chapter Nine**.

Chapter Two

EXPERIMENTAL METHODOLOGY

Chapter Two. Experimental methodology

2.1 INTRODUCTION and SYNOPSIS OF CHAPTER.

The primary objectives of this thesis were outlined in section 1.5. The experiments performed to accomplish these objectives required reproduction of the conditions of high-grade metamorphism in the lower crust, 800 to 1000°C and 5 to 12kb (see review of granulite pressure-temperature conditions by Harley, 1989). To achieve these conditions in the experimental petrology laboratories at Edinburgh it is necessary to use both the solid-media piston-cylinder apparatus and the internally-heated gas-media vessels (gas bombs).

The aim of this chapter is to describe the way in which the experiments were conducted and to assess the uncertainty and variation in the experimental conditions.

The design of the apparatus, and the way in which it is used, determines how tightly the experimental conditions are constrained. Salt-cells are used in the solid-media apparatus and these very closely approximate the hydrostatic pressure conditions produced in the gas-bombs. One run was conducted in a talc-pyrex cell, and the results of the experiments it contained showed that, when used at 10kb, talc-pyrex cells require a much larger friction correction (at least 20%) than is usually applied.

The pressure and temperature uncertainties in the experiments deserve careful attention as they determine how closely the phase relations derived later are constrained. The uncertainties are summarised in table 2.1.

Uncertainty in:	**Pressure (kb)**	**Temperature (°C)**
Solid Media - Salt-cell	± 0.5	± 5
Solid Media - Talc-pyrex	n.a.*	± 5
Gas bombs	±0.19	±5.3
Cold-seals	±0.05	± 5

Table 2.1. Summary of the pressure and temperature uncertainties associated with each apparatus used in this study. * Not Applicable - only one talc-pyrex run was done and the pressure could only be constrained to be less than 8kb.

The fugacity of oxygen (fO_2) in the experiments could be a significant parameter, particularly if it varied by a large amount. As the operation of standard buffer assemblies is not guaranteed in these fluid-absent experiments, the fO_2 is constrained by two other methods. Firstly, very large variation in fO_2 between the experiments is ruled out by comparison of the current phase assemblages with studies in the literature in which the fO_2 was controlled. This comparison shows the fO_2 in all the experiments to lie between the nickel-nickel oxide and iron-wustite buffers. Smaller variations probably do occur and these are evidenced by different compositions of some phases when runs are performed at the same pressure and temperature but in different apparatuses. A new technique of fO_2 measurement was attempted but was only partially successful. This involved placing platinum or palladium wires in the charge, which dissolved iron from the mix to form Pt-Fe alloys during the run. This allows the calculation of the activity of iron and from that the fO_2.

The kinetic rate[1] of an experiment must be sufficient to allow the equilibrium assemblage to form, for a given run time. Two factors determine the kinetic rate in these experiments; (a) the presence/absence of melt and (b) which apparatus the experiments were run in: the solid-media salt-cells produce a higher kinetic rate than the gas bombs as a result of their enhanced proton fugacity (Graham and Elphick 1990).

The success of an experiment depends fundamentally on the use of appropriate and well-characterised starting materials. It was decided that mixes of natural and synthetic minerals constituted in the K_2O-MgO-FeO-Al_2O_3-SiO_2-H_2O (KFMASH) system would give the best results. However, it was apparent that in some circumstances mineral-sillimanite persists metastably and that its lack of reaction prevents other phases from forming. For this reason a second set of mixes was made in which the mineral-sillimanite was replaced by an AlSiO gel. The bulk compositions calculated from the phase compositions and proportions compare favourably with those derived from electron probe analysis of glasses made from the mixes.

[1] The "kinetic rate" is taken here to mean the average rate of reaction at a given pressure and temperature. Equilibration rates and diffusivities of individual phases will affect the kinetic rate as a function of modes, initial composition, grain size etc.

2.2 EXPERIMENTAL APPARATUS.

2.2.1 Solid media apparatus.

The piston-cylinder equipment used at Edinburgh University is the Boyd and England (1960) design. A large piston creates a confining pressure under which the cell, which contains the experimental charge, is pumped to higher pressure using a smaller internal piston. All but one of the solid media runs in this study were performed using the 19mm diameter salt-cell illustrated in figure 2.1. The exception was a run carried out in a 12.7mm diameter talc-pyrex cell (figure 2.2) for the purpose of interlaboratory comparison. The salt-cell design was adapted from the one in use at Edinburgh to meet the requirements of this study. The use of different bulk compositions is an integral part of this study and so it was important to design a cell in which three capsules could be run simultaneously. The total experimental run-time is reduced by two-thirds by running the three bulk compositions at the same time. The many teething problems encountered

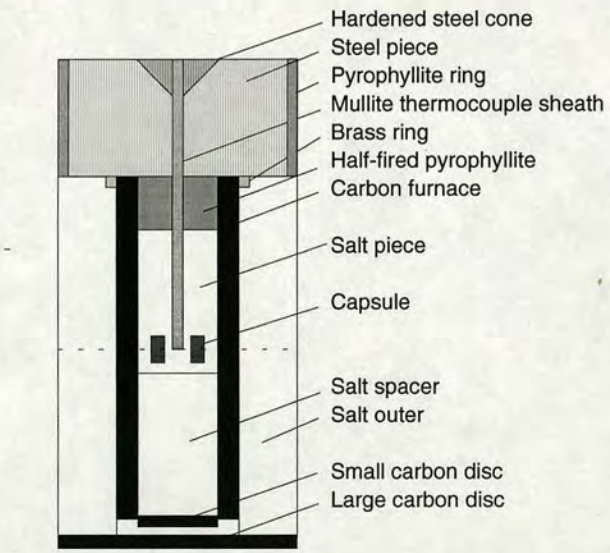

Figure 2.1. A schematic section of the salt-cell used in the solid-media experiments. The cell is 19.0mm in diameter. The outer surface of the cell is thoroughly lubricated with MoS grease, though no lead foil is used[2]. To allow for differential compaction, the salt outer is made 0.25mm longer than the furnace and the sum of the inner pieces is 0.13mm longer than the furnace. Therefore, initially there is a small void space at the bottom of the cell between the carbon discs.

[2] The absence of lead foil is not thought to increase the friction between the cell and the bore of the bomb. The cell used by Johannes (Johannes et al, 1971) was not wrapped in lead foil but that cell was believed by the author and by Bohlen (1984) to be essentially frictionless. Newton (in Johannes et al, 1971) produced very similar results to Johannes with a similar cell, but using lead foil.

in the development of this cell are detailed in Appendix One. The talc-pyrex cell was also adapted to run two capsules simultaneously.

Run-up procedure - salt-cell runs.

The salt-cell runs were brought to pressure and temperature in the following way. At room temperature, the pressure was brought to the target value; the apparatus was left overnight to allow the void space in the cell and the salt to compact[3]; the run was pumped back up to about 90% of the target and then heated; the pressure rose as the salt expanded and when it reached the target, it was bled back to the 90% value; this was repeated, seven times, until the target temperature was reached; the final pressure was set by bleeding back the piston by a couple of hundred bars.

The run reached its final temperature in less than half-an-hour. The run was checked twice daily and the e.m.f., pressure, temperature and power values recorded. The runs were quenched by simply switching off the power and so the temperature and pressure fell concurrently. The temperature dropped to less than 100°C in a few seconds.

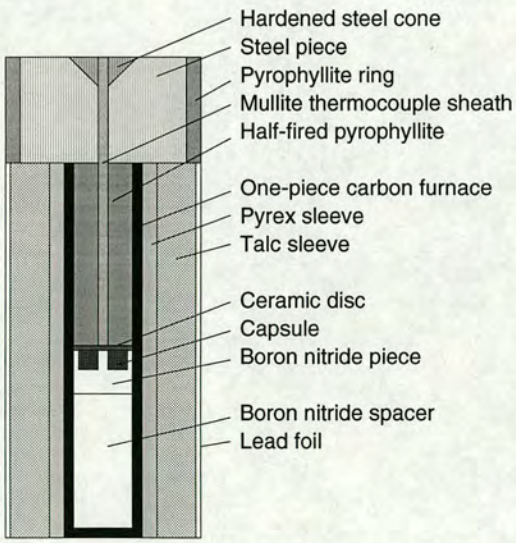

Figure 2.2. A schematic section of the talc-pyrex cell used in the solid media experiments. The cell is 12.7 mm in diameter. The outer surface of the cell is thoroughly lubricated with MoS grease.

[3] The initial density of the salt is about 95% of the theoretical value. The overnight compaction was typically between 5 and 13%.

The run-up procedure is ostensibly a "piston-out" technique, but this is equivocal. The run temperatures are very close to the melting point of salt and so the cell is not robust. Consequently, the final pressure drop must be small, necessitating a small retraction of the piston which could be negated: it was often necessary to advance the piston during the run as additional cell compaction can occur in the early stages and the hydraulic lines which pump the pistons can leak slightly. Furthermore, daily laboratory temperature fluctuations can necessitate advancing or retracting the piston as the metal bombs expand or contract. The position of the piston during the run is therefore essentially unconstrained, as in virtually all piston-cylinder runs except those in which the piston position is gauge monitored.

Run-up procedure - talc-pyrex cell.

The one talc-pyrex run was brought to pressure and temperature in the following way. The run was pumped to the target pressure and left for a few hours[4]; the run was heated and as the cell components softened the cell compacted and the pressure dropped; the piston was continually advanced to keep the pressure constant at the target level; when the target temperature was reached the piston was advanced a final time by a few hundred bars. The run-maintenance and quench routine was the same as for the salt-cell runs.

The run-up procedure for the talc-pyrex run is ostensibly "piston-in" but this is subject to the same uncertainties as the salt-cell runs. The friction correction used for this cell in the laboratory at Edinburgh is a standard -10%, but this is queried and discussed below (section 2.3.1 and section 7.4.2)

Pressure and temperature measurement.

The applied pressure was measured using an oil-filled Heise gauge with scale gradations of 40 bars. The temperature was measured using $Pt/Pt_{87}Rh_{13}$ thermocouples with a cold-junction maintained at a reference temperature of 0°C using an ice-water mixture. No correction was made for the effect of the pressure on the e.m.f. Eurotherm electronic controllers were used.

[4] The talc-pyrex cell compacts very little at room temperature due to the strength of the materials.

2.2.2 Internally-heated pressure vessels (gas-bombs).

The gas-bomb apparatus follows the design of Holloway (1971). The layout of the gas lines is described by Edgar (1973). The pressure medium used is argon. Inside the furnace ceramic there are two near-axial $Pt/Pt_{87}Rh_{13}$ thermocouples with the beads separated by about 1cm along the length of the bomb. The capsules were arranged in the can between the thermocouple beads and this allowed any thermal gradient to be measured and reduced by altering the tilt of the apparatus. The void space in the sample holder was filled with silica wool and tantalum metal chips. The tantalum was used to reduce the fO_2 in the bomb (see section 2.3.4) and thereby also preserve the molybdenum furnace. The tantalum was not allowed to be in contact with the thermocouples or the capsules.

Run-up procedure.

The run was pumped to 80% of the target pressure and then heated to the target temperature. The run was left to settle for fifteen minutes and then the pressure and the tilt of the bomb, which affects the position of the hot-spot, were adjusted.

The run reached its final temperature in less than forty-five minutes. As with the solid-media runs, the e.m.f., pressure, temperature and power values were recorded twice daily. Again, the run was quenched by switching off the power and so the pressure and temperature fell together. The gas-bomb quench rate is considerably slower than that for the solid-media apparatus. The highest temperature run (D65, 1000°C) fell through the solidus (900°C) within 15 seconds and reached 260°C in 150 seconds. All the other runs quenched at a faster rate.

Pressure and temperature measurement.

The pressure was measured using Harwood manganin-wire pressure gauges attached to each pressure vessel (Edgar 1973). The gauges were calibrated against the melting pressure of mercury at 0°C (7565 bars). They were found to be accurate to ± 20 bars. The pressures were read using a Wheatstone-bridge (Ford 1972). The temperature was measured using the two thermocouples referred to above. One of these was connected to a Eurotherm controller. No correction was made for the effect of pressure on the emf.

2.2.3 Externally-heated gas-media vessels.

The externally-heated gas-media vessels (cold-seal bombs) are vertical "Tuttle" cold-seal vessels. The pressure medium is argon. The cold-seal bombs were used only for the synthesis of k-feldspar.

The procedure used for operation of the cold-seal bombs is the same as for the gas bombs. The only major difference is the quench rate, which is considerably slower than that for the gas bombs. As the syntheses were successful (section 2.4.2), this was not a matter for concern.

2.2.4 The preparation of capsules.

All the capsules used in the experiments were fabricated from 2mm $silver_{70}$-$palladium_{30}$ tube. This alloy was chosen for its ability to contain experimental mixes for lengthy periods without absorbing iron[5]. The capsules used in the solid-media runs were pin-pressed into a cylindrical shape about three to four millimetres long. The capsules used in the gas-bomb runs were not pin pressed and were up to seven millimetres long.

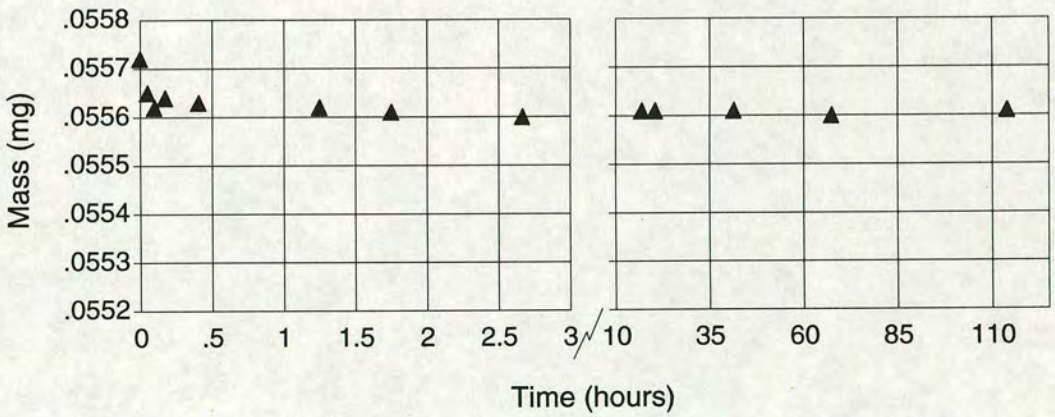

Figure 2.3. A graph of mass versus time for an open capsule kept in an oven at 120°C. Note the change of scale between three and ten hours. On this evidence a drying time of two hours is deemed to be sufficient to drive off all the adsorbed water.

[5] Ellis (1986) states that Ag_{75}-Pd_{25} alloy can run at temperatures of up to 1000°C for up to a week without significant absorption of iron.

The absence of water vapour is a very important requirement of the experiments as its presence, even in small amounts, will lead to the production of relatively large amounts of melt, which could obscure the position of the dehydration-melting solidus and alter other phase relations. Therefore, considerable care was taken to ensure conditions of vapour-absence were approached as closely as possible.

The mixes were stored permanently in an oven at 125°C, contained in small jars inside a large, covered beaker. The mixes were removed when required and eight to ten milligrams of mix was loaded into a pre-annealed capsule. The open capsule was then placed back in the oven for at least two hours. This was sufficient to drive off any water that had been absorbed during the few minutes it took to fill the capsules (figure 2.3). The capsule was then crimped in the oven and immediately welded shut. At each stage of this procedure the capsule was weighed.

A few capsules appear to have been contaminated with water (see section 4.1). It is believed that the drying technique removes all the possible water vapour[6]. A more likely source of contamination is the method by which the capsule is welded closed. In order to prevent oxidation of the metal during welding, a wet strip of tissue paper is wound around the capsule. When the capsule gets hot, a small cloud of steam is produced about the weld, which prevents oxidation. However, for this to be effective the tissue must be near the rim of the capsule and if the tissue rises too high there is a chance that water will be drawn into the dry mix. The weighing of capsules failed to identify this as all the capsules used were the same mass or lighter after the weld. The loss of small blobs of metal could cause a weight loss which overcompensates for the gain from any water contamination.

The integrity of the capsule welds was checked by submerging the capsule in acetone for several hours and observing any change in the mass of the capsule. Even tiny holes are detected by the low viscosity solvent and, if one is present, the capsules can be returned to the oven to drive off the acetone and the capsule can be rewelded.

Despite this care, some capsules failed in the course of a run. The solid-media run failure-rate at 18% (n=27) was higher than that for the gas bombs, 12% (n=57). Perhaps

[6] A tiny amount of water may remain trapped in the mix, but, if so, it is presumably a constant amount given that the capsule-filling procedure is the same in all cases.

this is due to pin-pressing or a corrosive property of hot salt. Both failure rates are rather high and probably reflect the long run durations.

2.3 ESTIMATION OF EXPERIMENTAL CONDITIONS.

2.3.1 Estimation of pressure and temperature uncertainties for the solid-media apparatus.

Salt cells: Temperature.

The temperature is automatically controlled within ± 2°C and is measured with high precision (± 1°C) against a fixed reference point. The most important factor which could affect temperature accuracy in solid-media runs is the presence of temperature gradients.

The thick size of the furnace wall (1.2mm) used in the salt-cell runs will lengthen the hot-spot plateau region along the axis of the assembly. The centre of the capsules are at the same level as the bead of the thermocouple (unlike many other designs where the capsule sits under the thermocouple). As the length of capsule extending above and below the thermocouple bead is less than two millimetres, longitudinal temperature gradients are very unlikely. Radial temperature gradients could affect the experiments as the capsules in the salt-cell runs are off-axis. Bohlen (1984), using a 25.4 mm diameter salt-cell otherwise identical to that used in this study, laid a capsule radially from one wall of the furnace to the other and determined that the radial gradient was less than 5°C. No evidence of thermocouple drift or extrusion was observed.

The estimate of the uncertainty in temperature is ± 5°C.

Salt cells: Pressure.

The accurate estimation of pressure in solid-media runs has concerned many experimental petrologists, though it is worth repeating the note of Bohlen (1984) that in experiments designed to locate boundaries with high dP/dT gradients, the pressure uncertainty is less important.

Pressure uncertainties result from two effects:

1. The first effect is a diverse collection of phenomena grouped under the term friction. These include frictional drag between the piston and the chamber walls and between the pressure medium and the chamber walls. These are minimal if the chamber walls are hard, smooth and well-lubricated as in the experiments here. The shear strength of the pressure medium can lead to pressure reduction away from the piston and this varies from one pressure medium to another.

2. The second effect is an inhomogeneity of shear strength in the cell, resulting from the use of components of various materials. These effects were termed "anvil effects" by Bell and Mao (1971). If the part of the cell outside the furnace has a greater shear strength than that inside, then the outer part may support more of the piston load. The capsules, in the inner part of the cell, would therefore be subject to lower pressures than the nominal pressure (piston pressure). This was termed a negative anvil effect. A positive anvil effect is possible if the central part of the cell has a higher shear strength than the outer part.

These two effects can occur simultaneously, either augmenting each other or tending to cancel each other out.

The relative merits of approaching the final pressure from the high-pressure side (piston-out) or low-pressure side (piston-in) techniques has been disputed. For example, Newton (in Johannes et al. 1971) advocates piston-out whilst Bohlen (1984) suggests that piston-in is better. The technique used in the present experiments is undetermined. Therefore, the matter will not be discussed further, except to say that the friction effects of (1) above, if any are present, are thought to be equal in magnitude but opposite in sign for the piston-in and piston-out techniques: the anvil effect, (2) above, is likely to be much more important in affecting pressure accuracy. As shown below, the salt-cell used suffers from neither (1) nor (2) and so whether the run is performed piston-in or -out is unlikely to make a difference.

Obviously the anvil effect cannot occur in cells in which the inner and outer parts are made of the same material[7]. The salt cell design used in this study (figure 2.1) satisfies this criterion. It is very similar to the cells used by Johannes (in Johannes et al. 1971), Newton (in Johannes et al. 1971), Mirwald et al. (1975) and Bohlen (1984). None of

[7] The carbon furnaces cannot support a significant load as evidenced by the furnace breaking when it is overlong (Appendix One).

	Bohlen (1984)	Mirwald et al. (1975)	Johannes (*)	Newton (*)
Pressure uncertainty (kb)	±0.1	±0.3	±0.5	±0.45
Pressure Range	5-20kb	10-60kb	15-18kb	15.5-18kb
Temperature Range	700-1200°C	300-1400°C	@ 600°C	@ 600°C
Cell diameter (mm)	25.4	12.7	25.4	25.4

Table 2.2. Summary of the pressure uncertainties from published salt-cell studies. The studies marked (*) both appear in Johannes et al. (1971).

these authors report a requirement for a friction correction, i.e. they believe the pressure on the capsule is the same as the piston pressure. The pressure uncertainties reported are summarised in table 2.2.

The diameter of the salt cell used in this study is 19.0 mm, between that of Mirwald et al. (1975) and the others (table 2.2). Bohlen (1984) and Mirwald et al. (1975) both calibrated their cells against the hydrostatic, polybaric, melting-point experiments on eight alkali halides, performed by Clark (1959). The temperatures of Mirwald et al. (1975) and Clark (1959), both determined by differential thermal analysis, coincide. Bohlen (1984) reports temperatures higher by about 10°C, employing a direct physical method (the falling-ball technique) to infer the occurrence of melting. The direct physical method seems more reliable and so I believe the results of Bohlen (1984) to be more accurate. This means that the 12.7mm diameter cell of Mirwald et al. (1975) does require a small, negative friction correction (<5%). However, Bohlen (1984) includes a persona! communication from M.Engi reporting that down-sizing Bohlen's cell to 19.0mm does not affect its "frictionless" properties.

In the present experiments the cells were run very close to the melting point of the salt. Under these conditions the salt is extremely soft and this corroborates the assumption that in these experiments the salt has a negligible shear strength.

Finally, other potential errors, e.g. pressure fluctuation or gauge error, are small compared to the errors quoted in table 2.2.

It is therefore confidently stated that the pressure experienced by the capsules in the salt-cell runs lies within a ± 0.5kb bracket of the nominal pressure.

Talc-pyrex run.

The results of the experiments from the talc-pyrex run contradict all the other experimental data (see section 7.4.2). The nominal run pressure was 10kb and the standard friction correction applied in the Edinburgh laboratory is -10%, thereby giving a pressure estimate of 9kb. A gas-bomb run was performed at 9kb and the same temperature, 1000°C. The critical assemblages produced were garnet-cordierite-osumilite (talc-pyrex run) and orthopyroxene-sillimanite-quartz (gas-bomb run). The consideration of KFMASH phase relations (INSERT A) require these two assemblages to separated by two invariant reactions. These reactions are constrained by other gas-bomb runs, which allow a maximum stability of the garnet-cordierite-osumilite assemblage to be 8kb. Therefore, the pressure estimate for the talc-pyrex cell is at least 1kb too high. No other factors (e.g. variable fO_2) are envisaged which could explain this result.

The diagram of the talc-pyrex cell (figure 2.2) shows that a negative anvil effect is possible. The two outer cylinders are made of talc and pyrex, whilst the inner parts are boron nitride. Talc has a higher shear strength than either pyrex or boron nitride at high temperatures (e.g. Boettcher et al. 1981), and so will support more of the end-load. The negative anvil effect (type 2 effect, above), possibly combined with the effect of internal friction (type 1 effect), could lead to the -20% (minimum) friction correction implied by the phase assemblage comparison with the gas-bomb experiments.

A friction correction of -20% is larger than those routinely reported in the literature, though a wide range of friction corrections are used in different laboratories (illustrated in Johannes et al., 1971) and a few extreme examples exist[8]. In all the studies which report a calibrated friction correction of less than -20%, the experiments have been done at considerably higher pressures than 10kb, although at comparable temperatures. I conclude that at low pressures the shear strength of talc is relatively large and for that reason, the friction correction must be larger. Bohlen (1984) notes that, although the shear strength of cell materials will change with pressure and temperature (and time), few calibrations are done under variable pressure-temperature conditions or even under the conditions at which the cell is to be used.

---

[8] A cell used by Richardson et al. (1968) with fired pyrophyllite inners and boron-nitride/talc outers was shown to have suffered a positive anvil effect of 20% at 12kb, 850°C. An even more extreme example of 40% positive anvil effect has been reported at 25kb, 25°C (Bell et al., 1971) using a very similar cell to Richardson et al. (1968).

2.3.2 Estimation of pressure and temperature uncertainties for the gas bombs.

The assessment of pressure and temperature uncertainties in the gas bomb runs is rather different to that in the solid-media runs. The pressure medium is a gas and so the pressure on the capsules is hydrostatic. However, as gases at high pressures are difficult to contain, some leakage occurs in the course of a run. Periodically replacing this lost gas (topping up the pressure), means that the pressure may step up and then drift down several times during a run. Convection currents are present in the gas in the bomb and if these change through time, there may be variations in temperature.

Each measurement of pressure and temperature was made with a precision of $\pm$ 10 bars and $\pm$ 0.1°C respectively and the accuracy is believed to be at least $\pm$ 50 bars and $\pm$ 1°C (see section 2.2.2 for the calibrations). No evidence of thermocouple drift was seen. The uncertainty in the pressure and temperature of each experiment resulting from the individual measurements is small, compared to that resulting from the fluctuation of pressure and temperature through time as described in the last paragraph. The maximum and minimum measurements of pressure and temperature recorded during each run have been used to calculate the maximum ranges of these parameters. Then, the mean maximum ranges of pressure and temperature for all the runs were determined;

Mean maximum pressure range = 0.20kb, Standard deviation =0.09, (n=16),
Mean maximum temperature range = 5.6°C, Standard deviation =2.5, (n=18).

The pressure and temperature conditions assigned to each gas-bomb run are calculated as follows;

P or T = (mid point of range) $\pm$ 0.5 (mean range + 2 (standard deviations))

i.e. $\pm$ 0.19 kb,
or $\pm$ 5.3°C.

The pressure ranges of runs D53 and D54 are not included in the above calculations of the means. During the course of those runs the pressure intensifier was not able to reach high pressures because of a leak. Therefore, after the initial high pressures were reached

after heating, gas leaks from the bomb could not be replaced. The pressure drifted down monotonically throughout these runs[9]. The pressure uncertainties for these experiments are calculated as above, but using the actual range not the mean range;

D53, P = (mid point of range) ± 0.36kb
D54, P= (mid point of range) ± 0.44kb

2.3.3 Estimation of pressure and temperature uncertainties for the cold-seal bombs.

The cold-seal bombs were only used for synthesis of k-feldspar at 2kb and 800°C. Following Pawley (1989), the errors are estimated at ± 50 bars for pressure and ± 5°C for temperature. The platinum capsules were less than four centimetres long and will experience thermal gradients of less than 5°C.

2.3.4 The fugacity of oxygen in the experiments.

Measuring/controlling fO_2 in the experiments.

The fugacity of oxygen (fO_2) has largely been ignored in fluid-undersaturated experiments because of the difficulties in controlling it under such conditions. It is, nonetheless, an important parameter which should be constrained as closely as possible, particularly in studies where more than one set of apparatus is used: different results have been reported from experiments run at the same pressure and temperature in different machines, probably resulting from differences in fO_2[10].

The traditional method of buffering fO_2 is the use of a double-capsule arrangement. The buffer assemblage is in the outer capsule, the sample in the inner, and the two are separated by a hydrogen-permeable metal capsule[11]. The buffer will not operate efficiently unless it co-exists with a vapour (water in this case). However, for the fO_2 in

---

[9] The stage of the run at which the assemblage produced was formed is debatable - perhaps during initial heating and melting or perhaps the partially molten charge is responsive enough to change continuously with changing pressure.

[10] For example, Patino Douce and Johnston (1991) report two solid-media experiments at 10kb and 975°C. One was done in a barium carbonate cell, and stabilised ilmenite. The other was done in a salt cell and did not produce ilmenite.

[11] Both silver-palladium and platinum are very permeable to hydrogen but impermeable to other gases (Holloway and Wood, 1988).

the sample to be that of the buffer, the vapour co-existing with the sample must be the same, i.e. free water. This is not the case in water-undersaturated experiments.

Puziewicz and Johannes (1990) noted the difficulties outlined above in their study of water-saturated and water-undersaturated biotite-bearing granites. In their experiments the a_{H2O} was constrained (using the water solution model of Burnham, see references in Puziewicz and Johannes 1990) and this allowed them to calculate the fO_2 in the sample despite no free water phase being present. In my experiments the a_{H2O} has not been constrained and would indeed be difficult as most of the experiments have at least two hydrous phases.

An innovative way of measuring fO_2 has been devised by Gudmundsson and Holloway (1989, 1993) and developed by Jamieson et al. (1992). The approach requires the placement of a very thin platinum (or palladium) wire directly in the sample. Through the duration of the experiment, iron from the mix diffuses into the platinum wire, and an iron-platinum alloy forms. As the activity-composition relationships are well known for Fe-Pt alloys, writing an O_2-dependent reaction involving iron-metal and ferric-iron in a co-existing phase[12] allows the calculation of fO_2. The wires equilibrate very rapidly and the results are very precise. It is important to realise that the fO_2 is not being controlled here, but simply monitored.

This approach has previously only been used at temperatures above 1300°C and in mantle-simulation experiments, but here the use of Pt-wire fO_2 monitors has been tested in a low-temperature quartz-bearing system. A number of problems have been encountered and, whilst I believe it still to be possible and a very exciting prospect, there has not been enough success to date to be confident of the results gained. A fuller discussion of the implementation of the approach is given in Appendix Two. The current, tentative estimates, subject to the provisos given in Appendix Two, are;

$\log fO_2$ (solid-media, salt cell) = 1 to 2 log units below QFM
$\log fO_2$ (gas bombs, with tantalum) = 0 to 1 log units below QFM.

Effect of fO_2 on phase relations and compositions.

As the fO_2 in the experiments and how it might vary during and between runs is

[12] e.g. $Fe + SiO_2 + {}^1/_2\ O_2 = FeSiO_3$.

uncertain, consideration must be given to what effect this might have on the experimental products. Very large differences in fO_2 can have fundamental consequences for the phase assemblages produced for a given bulk composition.

By comparing high-fO_2 experimental work (HM buffer[13], Annersten and Seifert, 1981) and low-fO_2 experimental work (below the QFM buffer (QFM), Hensen and Green 1971, 1972, 1973), Hensen (1986) showed that the topology of the pressure-temperature grid in the FMAS system is inverted at high- and low-fO_2's. At high fO_2's the stability-field of spinel is considerably enlarged and the [grt] and [crd] invariant points (metastable at low-fO_2 conditions) become stable. This occurs because, if the fO_2 can change, then the oxidation state of iron becomes an extra variable. At high fO_2's, phases into which ferric iron partitions (e.g. spinel) are stabilised.

At the beginning of this study the runs performed in the gas-bombs did not have tantalum metal packed around the capsules in the can. These experiments produced significant spinel, even at relatively high pressures, and the high cation-totals suggested a significant ferric-iron content. A spinel from D25-10[14] had a composition of $spinel_{40}$-$hercynite_{45}$-$magnetite_{15}$ (calculated from electron microprobe analyses by correcting the high cation-total to the theoretical total, following Droop, 1987). This evidence shows that the "ambient" fO_2 of the gas bombs is high and so tantalum was packed around the capsules in subsequent experiments. The oxidation of the tantalum metal during the run leads to a very reducing atmosphere outside the capsules, which may have some effect inside the capsules (also see section 2.3.5 below). Experiment D47-16, run at the same pressure, temperature and bulk composition as D25-10, but with tantalum in the can, produced no spinel and no high cation-totals, suggesting the fO_2 had been successfully lowered. Experiments from gas-bomb runs were only used in the derivation of phase diagrams (Chapter Six) if tantalum had been present in the can, i.e. they had been run at low fO_2. In fact, one such experiment (D51) did produce spinel as a trace but, at 5kb, is at sufficiently low pressure for spinel to be stable under low-fO_2 conditions (Waters, 1990, Shulters and Bohlen, 1989).

---

[13] The buffers are referred to by the following abbreviations; HM, hematite-magnetite; NNO, nickel-nickel oxide; QFM, quartz-fayalite-magnetite; IW, iron-wustite; TTO, tantalum-tantalum oxide. The fO_2's of the buffer assemblages decreases in the order HM>>NNO>QFM>>IW>TTO for a given pressure and temperature.

[14] This run was done at 7kb and 940°C in a gas bomb with no tantalum in the can. The mix had a bulk X_{Mg} of 0.62.

Puziewicz and Johannes[15] (1990) attempted an fO_2 reversal run, initially running their mix at the iron-wustite buffer (IW), then at the nickel-nickel oxide buffer (NNO). The first stage of the run produced olivine-orthopyroxene-glass. The second stage produced biotite-orthopyroxene-magnetite. Neither olivine nor iron metal was observed in the current experiments and, as discussed above, magnetite (spinel) is only present in one of the used runs.

The phase assemblages produced in the present experiments allow some constraints to be put on the fO_2 they experienced. The virtual absence of spinel implies that the fO_2 during the experiments was less than the HM buffer (Hensen, 1986). The absence of olivine or iron metal implies that the fO_2 is above the IW buffer (Puziewicz and Johannes, 1990) and that the actual fO_2 inside the capsules in the tantalum-present gas-bomb runs is much higher than the level of the tantalum-tantalum oxide equilibrium (TTO). The presence of magnetite in the NNO runs of Puziewicz and Johannes suggest that the present runs are at lower fO_2 than that buffer. Therefore, the fO_2 in these runs lies between the NNO and IW buffers, (c.f. the platinum wire approach (Appendix Two) which may constrain the fO_2 to just below QFM).

However, the difference in fO_2 between the NNO and IW buffers is about four log units at a given pressure and temperature. Variation in fO_2 on the order of one or two log units is much more likely than the large variations discussed above. Whilst these small variations will not alter the phase relations fundamentally, they may well alter the phase compositions and thus cause changes in the pressure and temperature position of equilibria. A gas-bomb experiment was duplicated in a solid-media salt-cell run and the phase assemblages and compositions are given in table 2.3.

All the phase compositions are reproduced well in the salt-cell experiment, except that of biotite, which has a higher X_{Mg} in the salt-cell. Wones and Eugster (1965) investigated experimentally the relationship between f_{H_2O}, fO_2, and biotite composition. They derived an equation relating these parameters (plus the activities of the components $KAlSi_2O_5$ and Fe_3O_4) which was subsequently revised by Wones (1972). Their data at 875°C (e.g. their figure 4) and equation indicate that a change in biotite X_{Mg} of -0.06 (solid-media to gas bomb, table 2.3) could result from a reduction in fO_2 of

[15] The bulk composition used by Puziewicz and Johannes (1990) is similar to that used here though it included sodium as well as the KFMASH components.

	bt	os	crd	L	opx	grt
D49-18 Gas Bomb	0.81	0.92	0.88	?[a]	absent	unreacted seed
D66-18 Salt-Cell	0.87	0.92	0.89	0.61	0.80[b]	absent

Table 2.3. The assemblages and phase compositions of two experiments run at 875°C and 7kb, using mixes with bulk X_{Mg}'s of 0.86. [a] Melt was present, but in too small a quantity to be analysed. [b] A very small amount of metastable orthopyroxene was formed in this experiment.

about one log unit[16]. This suggests that the gas-bombs with tantalum are more reducing than the solid-media salt-cells, in contrast to the results of the platinum-wire technique. The fact that other phase compositions are reproduced well suggests that they do not incorporate significant ferric iron.

Variation of fO_2 on a small scale does appear to occur and alters some phase compositions measurably. Whilst cordierite and osumilite are unaffected by the fO_2 contrast between the solid-media salt-cells and the gas bombs, biotite, garnet and perhaps the melt will be.

2.3.5 Kinetic rate variation in the experiments and run times.

The experimental results indicate that kinetic rate (as previously defined) in the experiments is somewhat variable. It is well known that experiments involving only solid phases have much lower reaction rates than those with a liquid phase. This is because solid-state diffusion is a much slower process than diffusion through a liquid. If a liquid is present, the redistribution of components necessary for reaction occurs more rapidly and the experiment will approach equilibrium more closely in a given time. The experiments reported here are water-undersaturated and so only the supersolidus experiments involve a liquid. Evidence for the catalytic effect of the presence of melt can be found by comparing the products of the two-step solidus-reversal runs with the one-step subsolidus runs (e.g. D65 with D50). In contrast with experiments only run below the solidus, in the experiments which were heated above the solidus and then

[16] As described in the next section, solid-media salt-cells give better equilibrated products than the gas-bombs, particularly at low temperatures, and if this were a partial cause for the observed discrepancy in composition, then the implied fO_2 difference between the two apparatuses will be less. However, the initial biotite composition in both D49 and D66 was 0.90, so the gas-bomb experiment has changed more suggesting that, if anything, it has equilibrated more fully.

cooled below it, the phases originally present have adjusted their compositions, seed rims are better formed and new phases have formed freely (e.g. compare plates 1a and 2b).

The apparatus in which an experiment was run also affected the kinetic rate. The solid-media runs gave better equilibrated products than the gas-bomb runs for similar run times. For example, the re-growth of biotite in gas-bomb reversals was much poorer than in the solid-media runs (e.g. compare plates 1a and 8a). Graham and Elphick (1990) published a study of the role of hydrogen in Al-Si interdiffusion in feldspars, conducted in the laboratories in Edinburgh. They established that ordering in feldspars is dependent on the activity of the H^+ species of hydrogen, i.e. protons. They also showed that capsules run in solid-media salt-cells enjoy a much higher proton flux than in those run in gas-bombs, even if the experiments in the gas-bombs are surrounded by salt. Furthermore, they demonstrate that tantalum metal behaves as a vigorous water "getter", thereby reducing the a_{H+}. Tantalum metal is used here in the gas-bombs. An enhanced rate of interdiffusion can easily be envisaged to aid equilibration in all phases and so the faster kinetic rates inferred for the salt-cell runs are ascribed to a higher a_{H+} relative to the gas bombs.

If the kinetic rate is slower in a particular type of experiment then the run time should be proportionally longer. The data which permitted the comparison of the kinetic rates given above was not available until near the end of the study, however. Initially, the run times used were similar to those of published studies of related work (Le Breton and Thompson 1988, Vielzeuf and Holloway 1988, Patino Douce and Johnston 1990, Puziewicz and Johannes 1988, 1990), i.e. a week to ten days. This time was sufficient for the initial work done with the solid-media salt-cells. The gas-bombs require longer run times of over two weeks. The three reversal experiments were each run for a month. How closely these run times allow the experiments to approach equilibrium is considered in Chapter Five.

2.4 STARTING MATERIALS FOR THE EXPERIMENTS.

The correct choice of starting material is crucial to the success of any experiment. The first choice to be made is what chemical system to use. As discussed in the section 1.2, the compromise between simplicity and applicability offered by the KFMASH system is deemed best for the present study.

2.4.1 Bulk compositions and choice of starting material type.

The KASH components were modelled on the representative natural pelites used in Vielzeuf & Holloway (1988) and Le Breton & Thompson (1988). The iron and magnesium contents were altered from those in the quoted studies to give three higher bulk X_{Mg}'s (MgO/MgO+FeO); approximately 0.60, 0.75 and 0.90, whilst keeping the molar total of iron and magnesium constant. Table 2.7 lists the bulk compositions used.

It is next necessary to decide what form the mixes will take. Possible choices are mineral mixes, gels, glasses or some combination of these[17]. It is preferable to use mineral-mixes in phase equilibrium studies, if possible, as this simulates natural rocks more closely. Nevertheless, the correct choice must balance the potential for sluggishness of reaction of mineral starting-materials against the production of metastable phases which frequently results from the use of very reactive glasses and gels. Mineral-seeds may be used for phases which nucleate with difficulty. The experimental results show that all the minerals encountered in this study are sufficiently reactive for mineral mixes to be used with the exception of sillimanite. Some of the mixes used had the mineral-sillimanite replaced by an AlSiO gel. This will be considered further in section 2.4.4.

2.4.2 Minerals

Synthetic minerals.

It was not possible to obtain natural specimens of pure KFMASH biotites [18] or K-feldspars. Therefore, these minerals were synthesised from gels. The biotite gels were made in Edinburgh following the procedure described by Holloway and Wood (1988) and the K-feldspar gel was made by Dr J.Rushton and provided by Professor I.Parsons (University of Edinburgh).

---

[17] Sintered oxide mixes are another possibility but, whilst easy to prepare, they are rather unreactive and are only usually successful at high temperatures.

[18] Deer, Howie and Zussman (1966) define the arbitrary division between phlogopites and biotites to be where the Mg:Fe ratio is 2:1. For simplicity all the biotites and phlogopites used in this study (X_{Mg}=0.6, 0.75 and 0.90) will be referred to as biotites.

Table 2.4. Synthetic Biotites.

XMg=0.60 Phlogopite

	S2-4	S6-112	S7-34	S7-36	S8-15	Mean (27)	Target
SiO2	36.562	37.491	36.813	36.028	35.574	36.431	36.580
Al2O3	16.727	17.048	17.065	16.570	15.996	16.657	16.920
FeO	17.180	15.938	16.305	16.467	17.382	16.394	17.490
MgO	15.709	14.805	14.818	14.840	14.662	15.030	14.720
CaO	na	na	0.028	0.028	0.064	0.034	0.000
K2O	9.948	9.699	9.994	9.699	9.421	9.773	10.420
Na2O	na	0.059	0.024	0.036	0.062	0.049	0.000
TOTAL	96.126	95.041	95.048	93.668	93.161	94.343	96.130
XMg	0.620	0.623	0.618	0.616	0.601	0.620	0.600

XMg=0.75 phlogopite

	S2-3	S6-108	S7-25	S7-27	S7-28	Mean (17)	Target
SiO2	38.097	38.753	37.035	36.764	37.042	37.445	37.670
Al2O3	17.300	17.260	16.761	16.718	16.822	17.017	17.430
FeO	10.764	9.597	11.181	10.932	10.963	10.288	11.250
MgO	19.058	19.829	18.507	19.769	18.753	19.275	18.950
CaO	na	na	0.006	0.049	0.015	0.027	0.000
K2O	10.208	9.859	10.069	9.916	10.061	9.882	10.740
Na2O	na	0.287	0.071	0.054	0.030	0.140	0.000
TOTAL	95.427	95.586	93.631	94.202	93.685	94.015	96.040
XMg	0.759	0.786	0.747	0.763	0.753	0.770	0.750

XMg=0.90 phlogopite

	S2-15	S7-6	S7-9	S7-11	S8-1	Mean (22)	Target
SiO2	40.492	39.104	39.006	40.015	39.763	39.135	38.840
Al2O3	18.171	17.521	17.453	17.927	18.318	17.479	17.960
FeO	4.367	4.665	4.593	5.070	4.612	4.544	4.640
MgO	23.082	23.034	23.198	23.410	22.583	22.869	23.450
CaO	na	0.042	0.050	0.042	0.101	0.046	0.000
K2O	10.333	10.059	10.163	10.174	9.972	10.170	11.060
Na2O	na	0.055	0.044	0.181	0.030	0.056	0.000
TOTAL	96.445	94.480	94.507	96.819	95.378	94.276	95.950
XMg	0.904	0.898	0.900	0.892	0.897	0.900	0.900

Table 2.4. A selection of individual electron probe analyses of the synthetic biotites, with the means of all the analyses (total number in parentheses) and the original target compositions. Each analysis label shows which synthesis it came from, e.g. S6-108 comes from synthesis six. "na" signifies that that element was not analysed for.

Biotite is the only ferromagnesian mineral (apart from garnet seeds) in the starting mixes so its composition controls the bulk X_{Mg}. Therefore, three biotite gels were made with target X_{Mg}'s of 0.60, 0.75 and 0.90. The aluminium content of the biotites was chosen to be halfway between the eastonite and phlogopite end-members, i.e. $K_2(Mg,Fe)_{5.5}Al_{0.5}(Si_{5.5}Al_{2.5}O_{20})(OH)_4$), to reflect the aluminous character of natural high-grade phlogopites and biotites. The K-feldspar is a pure end-member orthoclase composition.

The biotite gels were first run for twenty hours in a gas mixing furnace at 900°C and an fO_2 of -17 log units, in order to reduce the ferric-iron to ferrous-iron. The fO_2 was controlled by an H_2-CO_2 mix in 30:70 volume ratio. The reduced biotite gels were then run for seven days in a gas-bomb at 850°C and 5kb with 10wt% distilled water, using 3mm $Ag_{70}Pd_{30}$ capsules. A total of nine synthesis runs were done. In these synthesis runs the gas-bombs did not have tantalum in the can and so the biotites may contain some ferric iron, but this should be re-reduced when the mixes are used in experiments. The crystals produced in the syntheses were small, about 5μm by 5μm by 1μm. Mixing some of the biotite crystals with more gel did not increase the product crystal size in repeat syntheses.

The crystalline biotites were analysed by x-ray diffractometry (XRD) and no other minerals were detected. The small crystal size made electron probe analysis difficult but it was attempted and the results are given in table 2.4.

	S1C1-6	S1C1-11	S1C2-16	S1C2-18	S2-14	Mean (14)	Ideal
NA2O	0.031	0.054	0.102	0.044	0.03	0.043	0.000
MGO	0.061	0.048	0.017	0.003	0.005	0.031	0.000
AL2O3	17.411	18.025	18.114	17.543	17.95	17.828	17.600
SIO2	67.959	66.581	67.608	67.537	66.055	67.069	66.200
K2O	13.845	15.539	14.308	14.434	15.357	14.705	16.200
CAO	0.021	0.027	0.004	0.000	0.003	0.016	0.000
FEO	0.001	0.058	0.027	0.000	0.021	0.020	0.000
TOTAL	99.330	100.332	100.180	99.563	99.421	99.711	100.000

Table 2.5. A selection of individual electron probe analyses of the K-feldspar syntheses, with the means of all the analyses (number in brackets) and an ideal composition. Each analysis label shows which synthesis it came from, e.g. S1C2-18 comes from synthesis one, capsule two.

The K-feldspar was synthesised hydrothermally at 800°C and 2kb in the cold-seal bombs with 5wt% distilled water and in 4mm-diameter platinum capsules. Three such syntheses were conducted. The crystals produced were fairly large (10-15μm square) and equant. Analysis by XRD revealed no other phases and the composition determined by electron probe is given in table 2.5. The reason for the apparently low potassium content is not known, though it could be due to potassium loss under the electron probe beam. The K-feldspar is in the high structural state as indicated by a $2\Theta\ \bar{2}04\ Cu_{\alpha 1}$ XRD reflection at 50.85° (Wright 1968). The experiments were run at supersolvus conditions and so the mineral has been synthesised in the appropriate structural state.

Natural Minerals.

Quartz and sillimanite are quite easy to obtain as pure phases. An Antarctic sillimanite was used and the quartz was supplied by Professor C.M.Graham (University of Edinburgh). The minerals were broken up into small fragments and clear pieces were hand-picked. When the sillimanite had been ground up, a magnet was passed through the powder to remove any iron oxides. The mineral powders were analysed by XRD and in neither case were other minerals detected.

Garnet is stable in many of the experiments and can be a difficult phase to nucleate. Therefore, the mixes are seeded with a natural Antarctic garnet (SH-218, Harley and Fitzsimons, 1991) which has a high X_{Mg} (0.69) appropriate to these experiments. The composition of the garnet is given in table 2.6. It has a very low grossular content (1.1wt% CaO). This slight contamination of the KFMASH mix with calcium was acceptable given the advantages of using a natural (and therefore well ordered and defect-free) high X_{Mg} garnet as a seed.

	SH-218	37-10-13
SiO2	41.866	41.524
Al2O3	23.288	23.367
FeO	15.028	15.258
MgO	18.053	18.698
CaO	1.175	1.206
K2O	0.080	0.055
Na20	0.022	0.003
TOTAL	99.512	100.110
XMg	0.682	0.686

Table 2.6. Selected electron probe analyses of the garnet used as seeds in the mixes.

2.4.3 Preparation and characterisation of mixes.

The mixes were prepared by combining the minerals in the proportions given in table 2.7. Each of the minerals was ground under acetone using an agate mortar and pestle. No evidence of silica contamination was seen in the bulk compositions (table 2.7). In order to try and ensure that grain-size effects did not influence the experiments all the mineral powders were sieved under acetone through an ultra-fine 10μm nylon mesh. Then each mineral was weighed by difference into a clean mortar and the mixes homogenised by grinding. Each batch of mix weighed 150mg. The mixes were stored permanently in an oven at 125°C, in small glass jars inside a large, covered glass beaker. The mixes were not used until they had spent at least one week in the oven.

Knowledge of the bulk composition of the mixes is very important and, in order to check the calculated compositions, the mixes were glassed and then analysed with the electron-microprobe (table 2.7). Small beads of glass were produced by mixing the mineral powders with polyvinyl-acetate, scooping up a small amount with a looped platinum wire and then passing a current through the wire. If the current is increased slowly then first the solvent is driven off and then the mix melts. The first couple of beads produced with a particular piece of wire were discarded as some iron could be lost from the mix to the platinum. I assume that the wire became saturated with iron after a couple of beads had been glassed. At least two beads of glass were analysed for each mix.

Comparing the calculated compositions and the normalised probe compositions the overall correspondence is good. However, the amount of iron measured in the glasses is systematically higher and the aluminium content is quite low in a few cases (table 2.8).

Iron is certainly not lost from the mixes in the glassing process as in all six cases it is higher in the probed-glass analyses. The aluminium is low in half the cases. The reason why these elements differ when the others do not is uncertain. Therefore, when the bulk compositions are plotted on three-component projections (section 4.1, Appendix Three), the error bars are drawn so as to include both the calculated and the probed glass bulk compositions.

Table 2.7. Mineral and bulk compositions of mixes.

Mix	13	14	15
WEIGHT PROPORTION OF MATERIAL ADDED			
bt (synthetic)	0.230	0.221	0.210
sil	0.180	0.179	0.180
qz	0.380	0.390	0.400
AlSiO gel	none	none	none
kfs (synthetic)	0.156	0.170	0.144
grt (seed)	0.040	0.041	0.040

BULK COMPOSITIONS

wt% oxides	Calculated	Probed glass	Calculated	Probed glass	Calculated	Probed glass
SiO2	66.275	66.027	67.277	66.105	68.329	68.423
Al2O3	18.888	18.665	18.858	19.111	18.739	18.193
FeO	4.470	4.947	2.907	3.621	1.544	1.886
MgO	4.378	4.387	5.049	5.302	5.849	5.812
CaO	0.049	0.074	0.049	0.076	0.049	0.074
K2O	5.022	4.893	4.960	4.813	4.618	4.644
H2O	0.890	0.890	0.871	0.871	0.875	0.875
Total	99.972	99.883	99.971	99.899	100.003	99.907
XMg	0.636	0.613	0.756	0.723	0.871	0.846

Mix	16	17	18
WEIGHT PROPORTION OF MATERIAL ADDED			
bt (synthetic)	0.230	0.221	0.209
sil (seed)	0.013	0.013	0.014
qz	0.336	0.349	0.357
AlSiO gel	0.210	0.214	0.210
kfs (synthetic)	0.170	0.170	0.169
grt (seed)	0.040	0.040	0.039

BULK COMPOSITIONS

wt% oxides	Calculated	Probed glass	Calculated	Probed glass	Calculated	Probed glass
SiO2	66.275	65.429	67.277	67.864	68.249	68.768
Al2O3	18.888	18.914	18.858	18.089	18.724	17.930
FeO	4.470	5.055	2.907	3.170	1.497	1.684
MgO	4.378	4.538	5.049	4.684	5.681	5.577
CaO	0.049	0.175	0.049	0.076	0.049	0.071
K2O	5.022	4.850	4.960	5.132	4.921	5.055
H2O	0.890	0.890	0.871	0.871	0.851	0.851
Total	99.972	99.851	99.971	99.886	99.972	99.936
XMg	0.636	0.615	0.756	0.725	0.871	0.855

Table 2.7. A table showing the mineral and bulk compositions of the nine mixes used in the experiments. Mixes 13, 14 and 15 have only mineral-sillimanite. Mixes 16,17,18 and 16A, 17A, 18A contain the AlSiO gel. The calculated compositions are derived from the weight proportions of the phases added and the compositions of those phases as given in tables 2.4, 2.5 and 2.6.
The biotite data was normalised to oxide totals equivalent to two moles of water per mole of biotite.
The bulk water content is calculated from the normalised biotite composition.
The glasses were analysed wtih the probe beam scanning over an area of 100 um. Each composition given is a mean of at least six analyses. The mean glass analyses are normalised to the calculated water content. The raw glass analyses were all more than 98%.

/continued

Table 2.7. Mineral and bulk compositions of mixes.

Mix	16A	17A	18A
WEIGHT PROPORTION OF MATERIAL ADDED			
bt (synthetic)	0.230	0.220	0.217
sil (seed)	0.013	0.014	0.015
qz	0.338	0.349	0.358
AlSiO gel	0.208	0.208	0.208
kfs (synthetic)	0.169	0.168	0.169
grt (seed)	0.047	0.041	0.040

BULK COMPOSITIONS

wt% oxides	Calculated	No glass	Calculated	No glass	Calculated	No glass
SiO2	66.722		67.420		68.612	
Al2O3	19.027		18.851		18.943	
FeO	4.552		2.931		1.607	
MgO	4.387		5.086		5.787	
CaO	0.055		0.048		0.047	
K2O	4.775		4.691		4.731	
H2O	0.884		0.858		0.874	
Total	100.403		99.887		100.601	
XMg	0.632		0.756		0.865	

Table 2.7 continued. A table showing the mineral and bulk compositions of the nine mixes used in the experiments. Mixes 13, 14 and 15 have only mineral-sillimanite. Mixes 16,17,18 and 16A, 17A, 18A contain the AlSiO gel. The 16A, 17A and 18A mixes are simply repeats batches of mixes 16, 17 and 18. The calculated compositions are derived from the weight proportions of the phases added and the compositions of those phases as given in tables 2.4, 2.5 and 2.6. The biotite data was normalised to oxide totals equivalent to two moles of water per mole of biotite. The bulk water content is calculated from the normalised biotite composition. The glasses were analysed wtih the probe beam scanning over an area of 100 um. Each composition given is a mean of at least six analyses. The mean glass analyses are normalised to the calculated water content. The raw glass analyses were all more than 98%.

Oxide	SiO_2	Al_2O_3	K_2O	MgO	FeO
Sum of Deviations (wt%)	0.066	2.050	0.096	0.084	-2.568

Table 2.8. The sums of the deviations of the glass probe-analyses from the calculated values for each oxide. The sum of the deviations is determined for each oxide by subtracting the probed-glass weight-percentage from the calculated weight-percentage (table 2.7) for each mix and then adding them all.

The original target X_{Mg}'s were 0.60, 0.75, 0.90 but the addition of garnet seeds and the high iron content described above have resulted in the mixes having X_{Mg}'s of 0.62, 0.74 and 0.86, (the mixes will be referred to as M62, M74 and M86. respectively). These X_{Mg}'s are sufficiently close to the targets for the purposes of the phase equilibrium experiments.

2.4.4 Sillimanite: mineral or gel?

Previous work suggests that in this KFMASH system, at elevated temperatures, the low-pressure assemblage garnet-cordierite will become unstable relative to the high-pressure assemblage orthopyroxene-sillimanite-quartz somewhere in the range 8-11kb (Bertrand et al., 1991, Hensen and Green 1971, Newton 1972). The pilot experiments in this study conducted at 7kb, 940°C using the mixes containing only minerals produced the high-pressure assemblage, with little or no sign of resorption of sillimanite. As sillimanite is notoriously slow to react, evidenced by the relatively common occurrence of two or three Al_2SiO_5 polymorphs together in natural rocks, this result was checked using mixes in which the sillimanite was replaced by an AlSiO gel, whilst keeping the bulk composition the same. This second run produced the low pressure-assemblage thereby demonstrating that in the first run the mineral-sillimanite had persisted metastably, preventing the cordierite from forming.

Previous experience suggested that if the gel added was of exactly sillimanite composition it might, as a result of its highly reactive nature, simply "snap" into sillimanite crystals which would then be difficult to resorb. Therefore a gel was made which was silica-rich and the amount of quartz crystals was reduced accordingly. The gel used was actually a homogenised mixture of two gels: a pure silica gel and a gel which was 34wt% SiO_2 and 66wt% Al_2O_3. The two gels were combined in 35:65 weight proportion respectively, which resulted in a composition equivalent to $sil_{80}qz_{20}$.

One weight-percent mineral-sillimanite was retained to act as seeds in case of any nucleation difficulties.

The majority of the experiments were done at pressures where cordierite is stable and these always used mixes with the AlSiO gel. Obviously, the inability of the mixes containing mineral-sillimanite to form cordierite or osumilite means that these mixes cannot be used to determine the position of the high-pressure stability limits of those phases. Near the terminal stability of cordierite and osumilite, mineral-sillimanite mixes and the AlSiO-gel mixes of the same bulk composition were run simultaneously (see runs D41, D43 and D52, tables 3.1 and 4.1). In experiments where the assemblage produced by the AlSiO-gel mix did not contain cordierite or osumilite, those assemblages and phase compositions matched very well with those from the equivalent mineral-sillimanite mixes. Therefore, in cases where sillimanite, but not cordierite or osumilite, is stable the alternative mixes give the same experimental results.

This result is useful because the orthopyroxene alumina contents are less variable when mineral-sillimanite is used, both in individual experiments and between experiments (See section 3.3). Orthopyroxene crystals form very readily, occasionally metastably, in both types of mixes used and with apparently disequilibrium alumina contents. The use of a reactive gel encourages this metastable behaviour. Thus, it is beneficial to use mineral-sillimanite mixes in the runs above the stability of cordierite and osumilite.

The behaviour of the mineral-sillimanite seems to be ambivalent. It cannot be completely inert as aluminous orthopyroxene, melts and garnet do form from mixes containing it. Indeed, the (higher-pressure) melts produced by the mineral-sillimanite mixes have higher alumina contents than those produced with the AlSiO-gel mixes. However, the mineral-sillimanite mixes cannot produce cordierite or osumilite when experiments are conducted within the stability range of these minerals, probably because only a small proportion of the mineral-sillimanite is able to react in run durations used here. When only a little sillimanite is required to react or, indeed, sillimanite grows, the true equilibrium assemblage can be formed. This would be the case when the initial modal proportion of sillimanite is less than or only slightly greater than the equilibrium proportion, such as in the high pressure experiments. When sillimanite is not stable or the modal proportion is required to be greatly reduced, it cannot react rapidly enough and the resultant alumina deficiency prevents the formation of other aluminous phases. This is the thought to be the case in the lower-pressure runs.

Chapter Three

EXPERIMENTAL RESULTS

Chapter Three. Experimental Results.

3.1 INTRODUCTION AND SYNOPSIS OF CHAPTER.

This chapter reports the results of the experiments. The run conditions and product phases are listed in section 3.3 but first the method of sample preparation and electron microprobe analysis is given, in section 3.2. The phase chemistry is considered in sections 3.4, 3.5 and 3.6. As the experimental products must be well characterised to allow confident interpretation of the experiments, it is important that the phase chemistry is described and evaluated in some detail.

The phase compositions are compared to published data and are generally found to be in good accordance. There are points of difference, some of which are believed to be genuine differences and some which are due to metastability. The orthopyroxene produced in the experiments has a metastably high alumina-content thought to be due to the high alumina activity resulting from the use of an AlSiO gel in place of mineral-sillimanite. The biotite also has a high alumina content but this is consistent with a previously identified substitution of octahedral aluminium cations for iron and magnesium (Patino Douce et al. 1993). The cordierite has a small but significant potassium content of 0.6-0.8 wt%. This is thought to be stable and therefore the previously published interpretation of potassic cordierite as characteristic of very low pressure environments (Schreyer et al. 1990) is considered incorrect. Indialite, the high-temperature hexagonal polymorph of cordierite, may have formed in the experiments but it is unlikely to affect the phase relations to any significant extent. Osumilite in the experiments is aluminous due to the operation of the Tschermak substitution.

Partitioning of iron and magnesium between the ferromagnesian phases is also considered in detail in this chapter. Comparison with the literature shows that whilst the cordierite, orthopyroxene and osumilite have reached equilibrium partitioning, the biotite may not have and the garnet certainly has not. The melt is believed to have achieved equilibrium partitioning but demonstrates a higher degree of Fe-Mg partitioning with most phases than previously reported (Ellis 1986).

Evaluation of the melt chemistry is complicated by the effect of potassium-volatilisation during electron microprobe analysis, but it is shown that under certain

conditions reliable measurements of K_2O can be obtained. The melt compositions compare favourably with other water-undersaturated peraluminous melts in the literature. The normative feldspar-content increases with pressure and decreases with temperature. The normative corundum-content of the melts increases with temperature but is independent of pressure.

Finally the water-contents of the hydrous phases are estimated by a mass-balance/point-counting method, by modelling and by Secondary Ion Mass Spectrometry analysis of one experiment. The main reason for deriving these estimates is because the position of the hydrous phases on the three-phase projections, used in Chapter Four to interpret the experimental phase assemblages, depends partly on their water-content. As the projected position of a hydrous phase determines the interpreted phase relations, it is important to assess the uncertainty in its position. Each of the methods produces estimates with fairly large relative uncertainties but these estimates are sufficient to demonstrate that the hydrous phases and bulk compositions can be plotted with adequate precision to enable the phase relations to be confidently derived (see section 4.1).

3.2 THE METHODOLOGY OF ELECTRON MICROPROBE ANALYSIS.

3.2.1 Sample preparation.

For each experiment the entire cylindrical charge was mounted in araldite and polished so that a longitudinal cross-section was available for probing. This section was chosen as it gives the maximum surface area for analysis and for recognition of any heterogeneity within the charge. A few initial runs were broken in two and half of the charge mounted and half ground and analysed in the XRD. However, even half the charge was not a sufficient amount of product to give a clear XRD trace which is necessary for the identification of minor products.

The mounts were polished using carborundum grits and then diamond paste or alumina powder. The use of diamond paste leads to less relief on the polished sample. Both methods were much less effective with subsolidus-experiment products than with supersolidus-experiment products. The relative softness and anisotropic shape of the biotite coupled with the absence of melt, which is thought to act as a "glue" in supersolidus experiments, results in the subsolidus products polishing

poorly and being difficult to probe. The biotite appeared to suffer particularly badly and in experiments even well below the solidus, the apparent amount of biotite sometimes decreased as a consequence of the polishing.

The polished mounts were coated with carbon.

3.2.2 Electron microprobe analytical conditions.

The experiments were analysed using the Cameca CAMEBAX Microbeam microprobe in the Department of Geology and Geophysics at the University of Edinburgh. The very small crystal-size (1-10μm) of the experimental products made it very important to reduce the X-ray excitation volume to a minimum. Consequently, the accelerating potential used was 15kV and the beam current was 10nA. Count times were thirty seconds for all elements except potassium for which the count time was ten seconds. The precision of the analyses under these conditions is still ± 1% relative for each oxide. Potassium in silicic melts and feldspars is unstable under too powerful an electron beam (section 3.5.1). The beam diameter on the sample under these conditions is less than one micron.

Quantitative analysis was performed using the wavelength-dispersive system. The energy-dispersive system was invaluable in enabling a rapid assessment of whether a particular sample-volume of a crystal was contaminated by overlap with an adjacent phase. The count data was reduced using an on-line PAP[1] correction. Mineral standards were used for all elements, except for iron where the metal was used.

3.2.3 Phase morphology, analysis contamination and data selection.

If the sample volume is not entirely within a single phase the analysis will be contaminated. It was generally quite easy to obtain consistent analyses of new, easily-grown, equant phases; orthopyroxene (e.g. plates 3b, 4b, 6a&b), cordierite (e.g. plates 8a and 9a), osumilite (e.g. plate 9a). However, the low contrasts between some phases on the back-scattered electron image occasionally made it difficult to distinguish a particular crystal and therefore to position the beam centrally[2]. This was particularly true of the magnesium-rich bulk compositions because of the atomic

---

[1] This is a Cameca software package based on the $\phi(\rho z)$ model of count data reduction (Reed 1993).
[2] The following phase pairs were often hard to distinguish; cordierite-quartz (e.g. plates 7a and 8a), osumilite-melt (e.g. plates 5a and 7a), quartz-sillimanite (e.g. plates 1a and 2b).

weight of magnesium is lower than that of iron.

More commonly, contamination resulted from very small analysable areas being presented by thin garnet rims (e.g. plates 2a and 6a), thin biotite crystals (e.g. plates 1a, 2b and 8a&b) and low-volume partial melts (e.g. plates 2b and 6a). Selecting data as "uncontaminated" may introduce a bias towards ideal compositions and obscure a true variation in composition between experiments. This is important because variation in phase compositions may cause changes in the phase relations if a reaction is close to degeneracy. To try and combat any bias, about ten analyses of every phase in each experiment were done, from all parts of the charge. Analyses (usually about 50% of those done) showing variations which were significantly detrimental to the cation totals or obviously the result of overlap with a specific phase were discarded. The variations in the remaining data was generally unsystematic, i.e., showed no compositional trends but scattered randomly around the mean.

There is a general correlation between a phase being present as large, equant crystals and the compositional data being consistent. When the phase is present as smaller crystals, the compositional data is less consistent. Thus, in these cases, the poorer data is thought to be partly the result of poor analyses. It is shown in the following sections that the compositional data for orthopyroxene, cordierite, osumilite and to a lesser extent, melt are consistent and can be confidently assumed to reflect equilibrium. The garnet and biotite data are less good and it is shown that this is due to the difficulties of analysis and a lack of equilibration.

The electron microprobe analyses are plotted individually in Appendix Three. The phase compositions generally scatter randomly about their means and so these have been used as best estimates of the phase composition in the following sections. Garnet is an exception. Garnet seeds were used and in cases where large rims grew, analysis was straightforward and means could be used. Sometimes, however, the rims were rather thin (<2μm) and the analyses were often contaminated by the core. This caused some difficulty in determining the X_{Mg} of the new garnet in the rim. A solution to this problem was possible because the seed garnets contained 1.1wt% CaO, a contaminant in a KFMASH system, and this could be used as a tracer of

Table 3.1. Supersolidus experiment results. Subscript numbers are the X_{Mg}'s of the mean phase analyses (see table 3.3 for assessment of uncertainties). All the experiments have quartz present.

Run (Run-mix)[1]	P (kb)	T (°C)	Time (hours)	Major Products[2]	Minor Products[3]
DG51-16	5	875	185	os_{72}, crd_{68}, grt_{40}	kfs, L_{29}, spinel*
DG51-17	5	875	185	os_{78}, crd_{76}, grt^{na}	kfs, L^{na}, opx_{61}
DG60-16A	6	900	288	os_{75}, crd_{74}, grt_{47}, kfs, L_{31}	
DG60-17A	6	900	288	os_{82}, grt^{na}, L_{36}	crd_{80}, kfs*, opx_{65}*
DG60-18A	6	900	288	os_{88}, crd_{88}, L_{56}	opx_{77}, kfs,
DS66-17A	7	875	263	crd_{84}, grt_{64}, L_{39}	opx_{74}
DS66-18A	7	875	263	bt_{87}, os_{92}, crd_{89}, L_{61}	opx_{80}*, kfs
DG49-16	7	875	260	crd_{79}, grt_{42}, kfs	bt_{65}, L*
DG49-17	7	875	260	crd_{83}, grt_{53}, kfs	bt_{69}, opx_{72}*, L*
DG49-18	7	875	260	crd_{88}, kfs	bt_{88}, os_{92}, L*
DG56-16[a]	7	900	312/328[4]	crd_{79}, L_{33}	opx_{64}, grt_{na}
DG56-17	7	900	312/328[4]	crd_{82}, $grt_{<56}$, L_{40}, kfs	opx_{70}
DG56-18	7	900	312/328[4]	os_{90}, crd_{88}, kfs	L_{67}, opx_{77}
DG47-16	7	940	244	os_{79}, grt_{52}, L_{33},	kfs, sil*
DG47-17	7	940	244	os_{81}, grt^{na}, L_{54},	crd_{80}, sil
DG47-18	7	940	244	os_{91}, crd_{88}, L_{51}, opx_{79}	
DS62-16[b]	<8	1000	242	os_{81}, crd_{82}, grt_{46}, L_{45}	sil
DS62-18[b]	<8	1000	242	crd_{91}, L_{68}	opx_{87}
DG57-16	8	910	195/355[4]	grt_{55}, L_{40}, kfs	opx_{70}, crd_{84}, sil
DG57-17	8	910	195/355[4]	crd_{86}, grt_{65}, L_{na}, kfs	sil, opx_{75},
DG57-18	8	910	195/355[4]	os_{92}, opx_{85}, kfs	L_{60}, crd_{90}
DG64-17A	8	910	259	crd_{87}, grt_{62}, L_{44}, kfs	opx_{78},, sil*
DG59-17	8	965	212	os_{86}, $grt_{<64}$, kfs	opx_{76}, L^{na}, sil
DG59-18	8	965	212	os_{92}, L_{81}	opx_{81}, sil
DG55-16	8.5	950	210	opx_{71}, grt_{53}, L_{40}, sil, kfs	
DG55-17	8.5	950	210	opx_{78}, L_{43}, kfs	os_{92}*, grt_{70}, sil,
DG55-18	8.5	950	210	opx_{84}, L_{69}, kfs	os_{91}*, sil

Continued/

[a] DG56-16 suffered serious contamination by water - no quartz was present in the run products.

[b] DS62 was run in the solid-media apparatus using a talc-pyrex cell. Comparison of the assemblages produced with those from gas-bomb runs implies that the friction correction is much larger than previously thought (see Chapter Two). The pressure can only be constrained to be less than 8kb.

Note - Other superscripts explained on next page.

Table 3.1. (Continued.) Supersolidus experiment results. Subscript numbers are phase XMg's (see table 3.3 for assessment of uncertainties). All the experiments have quartz present.

Run (Run-mix)[1]	P (kb)	T (°C)	Time (hours)	Major Products[2]	Minor Products[3]
DG61-16	8.75	895	288	grt_{49}, kfs	bt_{77}, crd_{87}, opx_{74}, L^*, sil
DG54-16	9.2/8.5[5]	925	264	grt_{52}, L_{49}, kfs	opx_{76}, sil
DG54-17	9.2/8.5[5]	925	264	opx_{81}, grt_{67}, L_{50}, kfs	crd_{88}, sil
DG54-18	9.2/8.5[5]	925	264	crd_{91}, opx_{88}, L_{60}, kfs	sil
DG64-16A[6]	8⇒9	910	259⇒424	grt_{50-53}, kfs	crd_{86}^*, opx_{70-77}, L_{44}, sil
DG64-18A[6]	8⇒9	910	259⇒424	crd_{91}, kfs	opx_{83-86}, L_{59}, sil
DG65-16A	9	1000	291	grt_{60}, L_{42}, sil	kfs*[7]
DG65-17A	9	1000	291	opx_{79}, grt_{70}, L_{49}, sil	kfs*[7]
DG65-18A	9	1000	291	opx_{89}, L_{63}, sil	os_{94}
DS43-13	10	900	264	grt_{51}, L_{51}, sil, kfs	opx_{83},
DS43-14	10	900	264	opx_{85}, grt_{60}, L_{55}, sil, kfs	
DS52-17	10	910	263	opx_{86}, grt_{61}, L_{56}	sil
DS52-18	10	910	263	opx_{88}, L_{66}, sil	
DS40-13	12.5	900	140	bt_{85}, grt_{51}, sil, kfs	L_{58}
DS48-14	12.5	925	294	grt_{77}, L_{68}, sil, kfs	opx_{87}^*
DS48-17	12.5	925	294	grt_{77}, L_{65}, sil, kfs	opx_{88}^*
DS48-15	12.5	925	294	opx_{91}, L_{75}, kfs	grt_{78}, sil
DS41-13	12.5	950	148	grt_{55}, L_{55}, sil, kfs	
DS41-14	12.5	950	148	grt_{67}, L_{64}, sil, kfs	
DS41-15	12.5	950	148	opx_{90}, L_{70}, sil, kfs	grt_{80}

[1] e.g. DG52-18. "DG" - gas-bomb apparatus used, "DS" - solid-media apparatus used, "52" - run number, "18" - Mix number.
[2] Estimated modal abundance ≥ 10%.
[3] Estimated modal abundance < 10%.
[4] Run quenched by a power failure at an unknown time. Therefore, the first run time is the minimum, the second the maximum.
[5] The pressure could not be topped up during this run due to a leak in the intensifier. The pressure drifted down during the run from the first value to the second.
[6] Two-step reversal run.
[7] Selvedge of K-feldspar present at edge of capsule.
[na] Phase could not be reliably analysed, usually because of too small a crystal size.
[*] Trace amount of phase present. Analysis not always possible.

Table 3.2. Subsolidus experiment results. Subscript numbers are the X_{Mg}'s of the mean phase analyses (see table 3.3 for an assessment of uncertainties). All the experiments have quartz present.

Experiment (Run-Mix)	P (kb)	T (°C)	Time (hours)	Major Products[1]	Minor Products[2]
D50-16	7	840	188	bt_{76}, grt_{45}, crd^{na}, kfs, sil	opx*
D50-17	7	840	188	bt^{na}, grt^{na}, kfs, sil	
D50-18	7	840	188	bt^{na}, crd^{na}, kfs, sil	grt^{na}
D63-16A[3]	7	890⇒ 855	253 ⇒ 424	grt_{50}, crd_{80}, kfs	bt_{61}, sil
D63-18A[3]	7	890⇒ 855	253 ⇒ 424	crd_{88}, kfs	bt_{82}, opx_{80}
D53-17	8.5	875	265	bt_{78}, kfs, sil	$grt_{<56}$
D53-18	8.5	875	265	bt_{89}, kfs, sil	grt^{nr}
D61-17A	8.75	895	288	bt_{82}, grt_{61}, kfs	crd_{88}, sil
D37-13	10	825	400	bt_{66}, kfs, sil	grt_{39}
D37-14	10	825	400	bt_{77}, kfs, sil	$grt_{55\text{-}60}$
D37-15	10	825	400	bt_{86}, kfs, sil	
D67-16A[3]	10	900⇒ 875	188⇒ 580	bt_{65}, sil, kfs	grt_{39}
D38-13	12.5	840	284	bt_{66}, kfs, sil	grt_{41}
D38-14	12.5	840	284	bt_{78}, kfs, sil	grt_{53}
D38-15	12.5	840	284	bt_{89}, kfs, sil	grt^{nr}
D40-14	12.5	900	140	bt_{80}, kfs, sil	grt_{58}
D40-15	12.5	900	140	bt_{89}, kfs, sil	grt^{nr}

[1] Estimated modal abundance ≥ 10%.
[2] Estimated modal abundance < 10%.
[3] Two-step reversal run.
[na] Phase not analysed, usually because of a too small crystal size.
[*] Trace amount of phase present. Analysis not always possible.

reaction[3]. In fact, it is shown below, on the basis of comparisons with published Fe-Mg partitioning data, that even when a good analysis of a rim is made the composition is frequently a metastable one.

3.3 EXPERIMENTAL RESULTS.

Two tables presented in this section record the pressure, temperature, run duration and product phase assemblages of the experiments, and the mean X_{Mg}'s of the ferromagnesian phases. Table 3.1 gives the results of the supersolidus experiments and table 3.2 the results of the subsolidus experiments. There is a small range of X_{Mg} in the individual analyses of each ferromagnesian phase and these ranges are summarised in table 3.3. These values are taken as estimates of the uncertainty in the X_{Mg} values.

	Opx	Crd	Os	Melt	Biotite
Mean Range	0.020	0.014	0.021	0.032	0.010
Standard deviation	0.013	0.008	0.013	0.014	0.006
No. of experiments	31	25	17	29	11

Table 3.3. Mean ranges of X_{Mg} in the ferromagnesian phases produced in the experiments. The number of experiments each phase occurred in is given and for each of these occurrences at least four good analyses were done. Garnet is omitted because the contamination of the analyses by the seed invalidates the use of the range in X_{Mg} as a guide to the uncertainty in composition.

3.4 PHASE CHEMISTRY: SOLID PHASES.

The cation contents of the phases are considered in section 3.4.1 and in particular the variation in aluminium, potassium and silicon cations is evaluated. The most variable and important compositional parameter is the X_{Mg} of the ferromagnesian phases and section 3.4.2 compares the phase-pair partitioning data obtained in this study with that in the literature. The melt phase data is considered in section 3.5. The available

[3] Entirely new garnet should have no CaO at all. When the rims were large enough to analyse or where new garnet crystals have formed which were large enough, this was the case. When this was not the case, the amount of CaO was often intermediate between zero and the original 1.2wt% and a linear correlation existed between the X_{Mg} and the CaO content. Extrapolating this correlation back to zero CaO gives an estimate of the rim X_{Mg}. The data used in the following sections are from "pure" (CaO-free) analyses, or sometimes from an extrapolation back to zero CaO.

constraints on the water-content of the hydrous phases are evaluated in section 3.6, and best estimates are derived.

It should be noted that this study intended to constrain the phase relations of the system as closely as possible and so the experiments were not always carried out at regular intervals in pressure and temperature. Therefore, there are not always convenient sets of isothermal or isobaric data enabling the straightforward comparison of the current data to the literature.

3.4.1 Variation in the cation contents of the experimental phases.

The phases produced in the present experiments which have the potential to vary in composition are garnet, orthopyroxene, biotite, cordierite, osumilite and melt. The quartz, sillimanite and K-feldspar do not vary in composition and are not considered further. The total number of probe analyses is over 800 and so, for clarity, in the following sections mean analyses have been used for each phase in each experiment. The use of means is justified, in general, by the random scatter exhibited by the data around the means in the three-component projections presented in Appendix Three. However, where necessary, the individual analyses for phases are also presented to enable an assessment of the variability of the data and, in particular, to evaluate the validity of interpreted trends.

Garnet.

The garnet analyses are generally good (table 3.4) in so far as the oxide totals, cation totals and site occupancies are all close to, and scattered above and below, the ideal required by stoichiometry. In the majority of cases the garnets are virtually pure pyrope-almandine mixes. The maximum grossular content (residual from the seeds) is less than two mole per cent. The only non-stoichiometric feature of the data is a tendency towards high silica-content and concomitant low cation totals, e.g. D41-14, D47-17 and D54-17 (table 3.4). As the garnet analyses are of seed rims, overlap with other phases is a common problem and this is most likely to cause the high silica-contents: most of the other phases present in the experiments have higher silica-contents than garnet.

Table 3.4. Garnets.

	D38-10	D38-11	D39-13	D40-13	D40-14	D41-13	D41-14	D41-15	D43-13	D43-14
n	3	3	5	7	5	8	3	4	5	4
Oxides										
SiO2	39.251	41.617	39.249	41.076	41.279	41.567	42.228	45.500	40.214	41.248
Al2O3	21.735	22.226	21.513	21.785	22.789	22.090	22.472	23.245	22.391	22.394
FeO	27.572	21.757	27.620	23.115	19.737	21.512	16.980	9.456	22.892	18.842
MgO	10.534	14.096	10.775	13.232	15.584	14.502	17.713	21.682	13.647	15.650
CaO	0.286	0.499	0.259	0.131	0.292	0.098	0.331	0.306	0.085	0.199
K2O	0.098	0.129	0.065	0.219	0.128	0.234	0.095	0.184	0.078	0.074
Na2O	0.012	0.028	0.004	0.015	n.a	0.014	0.011	0.028	0.007	0.004
TOTAL	**99.488**	**100.352**	**99.486**	**99.572**	**99.810**	**100.016**	**99.830**	**100.400**	**99.313**	**98.410**
Cations										
Si	3.018	3.076	3.019	3.080	3.039	3.078	3.067	3.160	3.023	3.066
Al	1.970	1.936	1.950	1.925	1.978	1.928	1.924	1.903	1.984	1.962
Fe(2+)	1.773	1.345	1.777	1.450	1.215	1.332	1.031	0.549	1.439	1.171
Mg	1.207	1.553	1.236	1.479	1.711	1.601	1.918	2.245	1.529	1.734
Ca	0.024	0.040	0.021	0.011	0.023	0.008	0.026	0.023	0.007	0.016
Total VI	3.004	2.938	3.034	2.940	2.949	2.941	2.975	2.817	2.975	2.921
Na	0.002	0.004	0.001	0.002	n.a.	0.002	0.002	0.004	0.001	0.001
K	0.010	0.012	0.006	0.021	0.012	0.022	0.009	0.016	0.008	0.007
Total	**8.004**	**7.966**	**8.010**	**7.968**	**7.978**	**7.971**	**7.977**	**7.900**	**7.991**	**7.957**
XMg	0.405	0.536	0.410	0.505	0.585	0.545	0.650	0.803	0.515	0.597

	D47-16	D47-17	D48-14	D48-17	D48-15	D49-16	D50-16	D51-16	D54-16	D54-17
n	3	3	4	3	5	4	4	3	2	4
Oxides										
SiO2	40.535	43.108	43.665	43.503	43.032	40.287	39.905	39.538	40.395	42.970
Al2O3	22.539	23.237	23.493	23.787	23.509	22.423	22.814	22.741	22.996	22.703
FeO	22.850	16.755	11.850	11.264	10.794	24.978	25.082	27.409	22.924	17.543
MgO	13.837	16.626	21.310	21.603	22.223	12.063	12.160	10.669	14.028	16.407
CaO	0.111	0.576	0.106	0.055	0.134	0.189	0.202	0.068	0.084	0.142
K2O	0.144	0.193	0.096	0.104	0.063	0.060	0.042	0.144	0.054	0.264
Na2O	0.018	0.010	n.a.	n.a.	n.a.	0.009	n.a.	0.016	0.013	0.015
TOTAL	**100.034**	**100.506**	**100.528**	**100.316**	**99.756**	**100.010**	**100.203**	**100.585**	**100.494**	**100.043**
Cations										
Si	3.024	3.101	3.069	3.056	3.038	3.034	3.003	2.998	2.998	3.115
Al	1.981	1.970	1.946	1.970	1.956	1.990	2.023	2.032	2.012	1.940
Fe(2+)	1.425	1.008	0.697	0.662	0.637	1.573	1.578	1.738	1.423	1.064
Mg	1.539	1.783	2.233	2.263	2.339	1.354	1.364	1.206	1.552	1.773
Ca	0.009	0.044	0.008	0.004	0.010	0.015	0.016	0.006	0.007	0.011
Total VI	2.973	2.835	2.938	2.929	2.986	2.942	2.958	2.950	2.982	2.848
Na	0.003	0.001	n.a.	n.a.	n.a.	0.001	n.a.	0.002	0.002	0.002
K	0.014	0.018	0.009	0.009	0.006	0.006	0.004	0.014	0.005	0.024
Total	**7.995**	**7.925**	**7.962**	**7.964**	**7.986**	**7.973**	**7.988**	**7.996**	**7.999**	**7.929**
XMg	0.519	0.639	0.762	0.774	0.786	0.463	0.463	0.409	0.522	0.625

Table 3.4. Mean garnet analyses, in weight-percent oxides and cations per 12 oxygens.
"n" - number of analyses. "n.a." - element not analysed for. All iron as Fe2+.

Table 3.4. Garnets.

	D56-17	D57-16	D57-17	D59-17	D60-16	D60-17	D61-16	D61-17	D62-16	D63-16
n	4	6	6	4	4	3	4	5	5	6
Oxides										
SiO2	40.473	40.521	41.682	42.350	40.412	40.411	40.080	41.017	39.065	40.360
Al2O3	23.092	23.219	22.960	23.203	22.324	23.339	22.797	23.297	22.355	23.115
FeO	20.830	22.043	16.658	15.927	24.347	21.559	23.547	18.905	25.271	23.509
MgO	15.072	14.430	17.331	17.654	12.688	13.911	12.699	16.430	11.954	13.165
CaO	0.120	0.127	0.949	0.856	0.183	0.149	0.156	0.435	0.096	0.203
K2O	0.054	0.085	0.103	0.067	0.052	0.069	0.055	0.058	0.099	0.101
Na2O	0.017	0.020	0.012	0.013	0.005	0.020	0.010	0.014	0.016	n.a.
TOTAL	**99.658**	**100.445**	**99.694**	**100.069**	**100.010**	**99.458**	**99.344**	**100.157**	**98.855**	**100.453**
Cations										
Si	3.001	2.997	3.035	3.055	3.035	3.011	3.019	3.001	2.990	3.005
Al	2.018	2.024	1.970	1.973	1.976	2.049	2.024	2.009	2.017	2.029
Fe(2+)	1.292	1.363	1.014	0.961	1.529	1.343	1.483	1.157	1.618	1.464
Mg	1.666	1.591	1.881	1.899	1.420	1.545	1.426	1.792	1.364	1.461
Ca	0.010	0.010	0.074	0.066	0.015	0.012	0.013	0.034	0.008	0.016
Total VI	2.968	2.964	2.969	2.926	2.964	2.900	2.922	2.983	2.990	2.941
Na	0.002	0.003	0.002	0.002	0.001	0.003	0.002	0.002	0.002	n.a.
K	0.005	0.008	0.010	0.006	0.005	0.007	0.005	0.005	0.010	0.010
Total	**7.994**	**7.996**	**7.986**	**7.962**	**7.981**	**7.970**	**7.972**	**8.000**	**8.009**	**7.985**
XMg	0.563	0.538	0.650	0.664	0.482	0.535	0.490	0.608	0.457	0.499

	D64-16	D64-17	D65-16	D65-17	D66-17	D67-16
n	7	3	5	6	5	5
Oxides						
SiO2	40.210	44.014	22.445	24.169	42.681	39.750
Al2O3	22.785	22.734	42.625	42.788	22.928	22.381
FeO	23.418	17.104	19.039	14.921	17.504	27.358
MgO	13.570	16.806	16.328	18.840	17.564	9.815
CaO	0.253	0.233	0.154	0.787	0.046	0.699
K2O	0.066	0.177	0.058	0.135	0.316	0.048
Na2O	n.a.	n.a.	n.a.	n.a.	n.a.	0.013
TOTAL	**100.302**	**101.069**	**100.648**	**101.641**	**101.039**	**100.064**
Cations						
Si	3.000	3.145	3.093	3.024	3.068	3.031
Al	2.004	1.915	1.919	2.013	1.942	2.011
Fe(2+)	1.461	1.022	1.155	0.882	1.052	1.745
Mg	1.509	1.790	1.766	1.985	1.882	1.116
Ca	0.020	0.018	0.012	0.060	0.004	0.057
Total VI	2.990	2.830	2.933	2.927	2.938	2.918
Na	n.a.	n.a.	n.a.	n.a.	n.a.	0.002
K	0.006	0.016	0.005	0.012	0.029	0.005
Total	**8.000**	**7.906**	**7.950**	**7.976**	**7.977**	**7.967**
XMg	0.508	0.637	0.604	0.692	0.641	0.390

Table 3.4 continued. Mean garnet analyses, in weight-percent oxides and cations per 12 oxygens.
"n" - number of analyses. "n.a." - element not analysed for. All iron as Fe2+.

Table 3.5. Orthopyroxenes.

	D41-15	D43-13	D43-14	D47-18	D48-15	D51-17	D54-16	D54-17	D54-18	D55-16
n	5	5	5	4	5	2	4	4	3	4
Oxides										
SiO2	51.669	51.559	50.738	51.457	52.487	48.588	49.154	48.665	50.218	47.777
Al2O3	12.219	10.640	11.258	9.295	10.658	7.767	13.533	14.140	14.381	12.320
FeO	5.582	9.091	9.148	12.799	5.676	23.154	13.387	10.368	6.743	16.919
MgO	30.380	27.907	28.004	26.730	30.955	20.448	24.177	26.182	29.063	22.786
CaO	0.014	0.007	0.016	0.029	0.015	0.038	0.026	0.007	0.021	0.009
K2O	0.126	0.165	0.043	0.061	0.026	0.076	0.218	0.086	0.044	0.195
Na2O	0.021	0.017	0.015	0.008	n.a.	0.011	0.022	0.009	0.003	0.004
TOTAL	**100.011**	**99.386**	**99.223**	**100.377**	**99.817**	**100.080**	**100.517**	**99.458**	**100.472**	**100.009**
Cations										
Si	1.771	1.806	1.782	1.816	1.802	1.812	1.738	1.717	1.723	1.731
Al(4)	0.229	0.194	0.218	0.184	0.198	0.188	0.262	0.283	0.277	0.269
Total (4)	2.000	2.000	2.000	2.000	2.000	2.000	2.000	2.000	2.000	2.000
Al (6)	0.265	0.245	0.248	0.203	0.233	0.153	0.302	0.305	0.305	0.257
Fe(2+)	0.160	0.266	0.269	0.378	0.163	0.722	0.396	0.306	0.194	0.513
Mg	1.553	1.458	1.466	1.407	1.585	1.137	1.275	1.377	1.487	1.231
Total (6)	1.978	1.969	1.983	1.988	1.981	2.012	1.973	1.988	1.986	2.001
Ca	0.001	0.000	0.001	0.001	0.001	0.002	0.001	0.000	0.001	0.000
Na	0.001	0.001	0.001	0.001	n.a.	0.001	0.002	0.001	0.000	0.000
K	0.006	0.007	0.002	0.003	0.001	0.004	0.010	0.004	0.002	0.009
Total	**3.986**	**3.977**	**3.987**	**3.993**	**3.983**	**4.019**	**3.986**	**3.993**	**3.989**	**4.010**
XMg	0.907	0.845	0.845	0.788	0.907	0.611	0.763	0.818	0.885	0.706

	D55-17	D55-18	D56-17	D56-18	D57-16	D57-17	D64-17	D57-18	D59-17	D59-18
n	4	4	4	5	3	4	4	4	4	5
Oxides										
SiO2	49.765	48.994	48.502	49.930	48.927	49.766	48.751	51.958	48.858	50.057
Al2O3	10.790	16.063	10.431	8.803	13.750	13.585	13.922	11.433	16.010	16.364
FeO	12.923	8.621	17.185	13.913	15.869	13.081	12.026	8.554	13.102	9.003
MgO	26.386	26.339	22.899	26.385	21.137	23.441	24.903	28.282	22.498	24.030
CaO	0.023	0.035	0.019	0.041	0.025	0.027	0.020	0.015	0.006	0.032
K2O	0.049	0.152	0.084	0.074	0.502	0.274	0.052	0.278	0.210	0.513
Na2O	0.014	0.013	0.024	0.001	0.015	0.012	n.a.	0.016	0.009	0.013
TOTAL	**99.948**	**100.218**	**99.144**	**99.148**	**100.226**	**100.184**	**99.673**	**100.535**	**100.692**	**100.011**
Cations										
Si	1.769	1.699	1.774	1.799	1.755	1.760	1.727	1.795	1.718	1.738
Al(4)	0.231	0.301	0.226	0.201	0.245	0.240	0.273	0.205	0.282	0.262
Total (4)	2.000	2.000	2.000	2.000	2.000	2.000	2.000	2.000	2.000	2.000
Al (6)	0.221	0.356	0.224	0.173	0.336	0.326	0.308	0.261	0.381	0.408
Fe(2+)	0.384	0.250	0.526	0.419	0.476	0.387	0.356	0.247	0.385	0.262
Mg	1.398	1.362	1.249	1.418	1.130	1.236	1.315	1.457	1.179	1.244
Total (6)	2.003	1.968	1.999	2.010	1.942	1.949	1.979	1.965	1.945	1.914
Ca	0.001	0.001	0.001	0.002	0.001	0.001	0.001	0.001	0.000	0.001
Na	0.001	0.001	0.002	0.000	0.001	0.001	n.a.	0.001	0.001	0.001
K	0.002	0.007	0.004	0.003	0.023	0.012	0.002	0.012	0.009	0.023
Total	**4.007**	**3.977**	**4.006**	**4.015**	**3.967**	**3.963**	**3.982**	**3.979**	**3.955**	**3.939**
XMg	0.785	0.845	0.704	0.772	0.704	0.762	0.787	0.855	0.754	0.826

Table 3.5. Mean orthopyroxene analyses, in weight-percent oxides and cations per 6 oxygens.
Tetrahedral aluminium calculated as 2-Si. Octahedral aluminium calculated as Al-(2-Si).
"n" - number of analyses. "n.a." - element not analysed for. All iron as Fe2+.

Table 3.5. Orthopyroxenes.

	D60-17	D60-18	D61-16	D63-18	D64-16	D64-18	D65-17	D65-18	D66-17	D66-18
n	3	5	5	4	4	6	4	4	4	3
Oxides										
SiO2	48.242	51.435	48.001	51.452	47.920	50.461	46.895	49.454	48.746	52.124
Al2O3	9.132	8.174	11.966	8.654	13.817	11.922	17.556	15.513	11.911	7.735
FeO	20.268	13.552	14.955	12.381	14.745	9.131	11.850	6.784	14.655	12.200
MgO	20.535	26.431	23.589	27.239	23.508	28.369	24.424	28.545	23.699	27.751
CaO	0.019	0.041	0.014	0.049	0.015	0.033	0.010	0.012	0.009	0.028
K2O	0.069	0.116	0.115	0.057	0.131	0.084	0.098	0.118	0.057	0.048
Na2O	0.014	0.005	0.022	n.a.	n.a.	n.a.	n.a.	n.a.	n.a.	n.a.
TOTAL	**20.637**	**99.755**	**98.662**	**99.832**	**100.136**	**99.999**	**100.832**	**100.425**	**99.077**	**99.886**
Cations										
Si	1.799	1.835	1.746	1.824	1.714	1.760	1.643	1.699	1.760	1.845
Al(4)	0.201	0.165	0.254	0.176	0.286	0.240	0.357	0.301	0.240	0.155
Total (4)	2.000	2.000	2.000	2.000	2.000	2.000	2.000	2.000	2.000	2.000
Al (6)	0.204	0.179	0.259	0.186	0.297	0.250	0.368	0.327	0.267	0.168
Fe(2+)	0.638	0.404	0.455	0.367	0.441	0.266	0.347	0.195	0.443	0.361
Mg	1.152	1.406	1.279	1.440	1.254	1.475	1.276	1.462	1.276	1.464
Total (6)	1.994	1.989	1.993	1.993	1.992	1.991	1.991	1.984	1.986	1.993
Ca	0.001	0.002	0.001	0.002	0.001	0.001	0.000	0.000	0.000	0.001
Na	0.001	0.000	0.002	n.a.	n.a.	n.a.	n.a.	n.a.	n.a.	n.a.
K	0.003	0.005	0.005	0.003	0.006	0.004	0.004	0.005	0.003	0.002
Total	**3.999**	**3.996**	**4.001**	**3.998**	**3.999**	**3.996**	**3.995**	**3.989**	**3.989**	**3.996**
XMg	0.644	0.777	0.738	0.797	0.739	0.847	0.786	0.882	0.743	0.802

Table 3.5 continued. Mean orthopyroxene analyses, in weight-percent oxides and cations per 6 oxygens. Tetrahedral aluminium calculated as 2-Si. Octahedral aluminium calculated as Al-(2-Si).
"n" - number of analyses. "n.a." - element not analysed for. All iron as Fe2+.

Orthopyroxene.

Again the oxide totals and the cation totals are very close to, and scattered above and below the ideal (table 3.5). However the alumina contents are inconsistent with natural rocks and experiments. Figure 3.1 shows the measured aluminium contents of the orthopyroxenes are consistently greater than that predicted by Harley (1984b), whose calibration is taken to accurately model equilibrium conditions[4].

It is common in metapelite experiments to obtain metastably high alumina contents in orthopyroxenes (e.g. Bertrand et al. 1991[5]). This may be caused by the exceptionally fast growth of orthopyroxene, which is suggested by a large crystal size and occasional rosettes of crystals seen in the experiments (see plate 3b). The determination of stable assemblages in section 4.1 shows that orthopyroxene itself

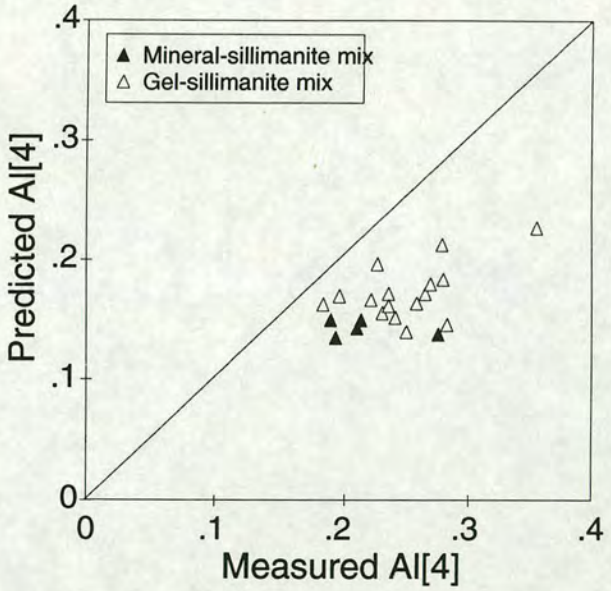

Figure 3.1. Measured tetrahedral aluminium cations in orthopyroxene (Al[4]) versus that predicted by the calibration of Harley (1984b) for a given pressure, temperature and X_{Mg}. The "mineral-sillimanite mixes" contained natural sillimanite. The "gel-sillimanite mixes" were of the same composition as the "mineral-sillimanite" mixes (table 2.7). Measured Al[4] calculated from (2-Si) (table 3.4).

[4] In his review of geothermobarometry, Essene (1988) recommends the orthopyroxene aluminium content calibration of Harley (1984b), amongst others.

[5] Bertrand et al. (1991) suggest that this high alumina content could be the result of tiny sillimanite inclusions, but in the current experiments there are numerous occurrences of orthopyroxene in the absence of sillimanite which still display a high alumina content.

frequently forms metastably[6], further evidence of its ease of crystal growth. Another factor can be deduced from two layer-experiments in which pelites and tonalites are juxtaposed, producing a gradient in alumina activity (Skjerle et al. 1993). These experiments produced orthopyroxenes with different alumina-contents at different points on the gradient indicating that the alumina content of orthopyroxene (in experiments at least) is controlled predominantly by the availability of alumina. It is concluded that experimental orthopyroxenes have high alumina-contents and a tendency towards metastable formation because of easy crystal growth, particularly in mixes in which alumina gels are used.

Figure 3.2 shows that alumina site occupancy is certainly related to the Tschermak substitution but deviates, particularly at high total aluminium, to an octahedral excess and hence non-stoichiometry. The deviation from stoichiometry is also manifested in low cation totals (table 3.5).

The orthopyroxenes formed from mixes containing mineral sillimanite are less

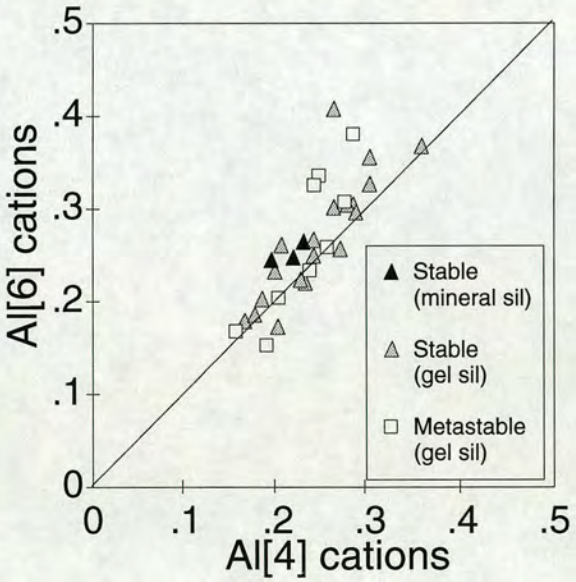

Figure 3.2. Measured tetrahedral aluminium cations (Al[4]) versus measured octahedral aluminium cations (Al[6]) for orthopyroxene, as calculated in table 3.4. The orthopyroxenes interpreted as stable and metastable are distinguished. Only gel-sillimanite mixes produced metastable orthopyroxene.

[6] The interpretation of orthopyroxene as metastable is based on comparison of phase and bulk compositions. See section 4.1.

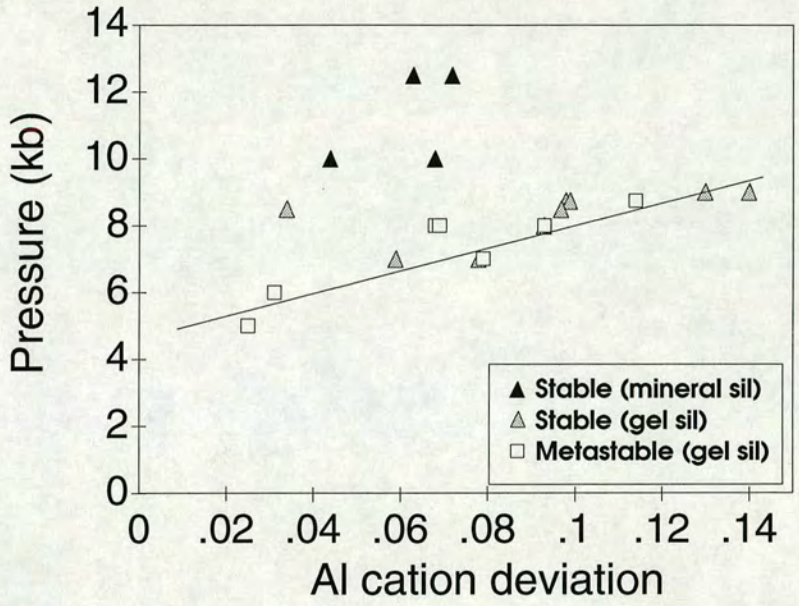

Figure 3.3. The variation of aluminium cation deviation in the orthopyroxenes with pressure. The deviation is calculated by subtracting the predicted value of tetrahedral aluminium cations (calculated from Harley (1984) for a given pressure, temperature and X_{Mg} from the measured value.

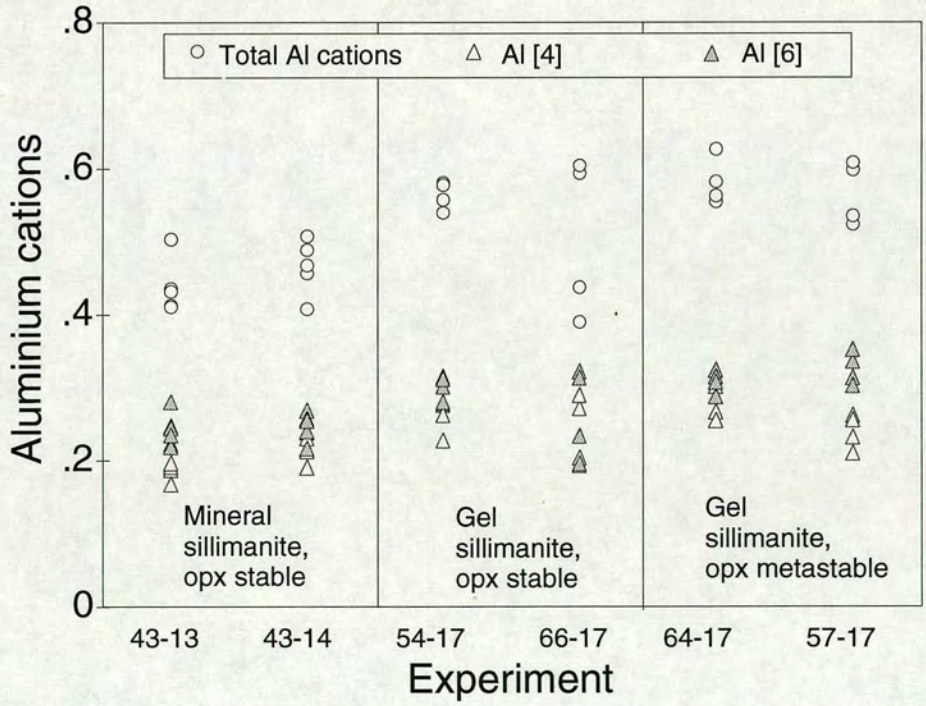

Figure 3.4. Orthopyroxene aluminium cation contents for individual analyses from six representative experiments.

dispersed (though there are fewer data) than those mixes in which the sillimanite component was added as a gel. There is no difference in the distribution of alumina contents for orthopyroxenes interpreted as stable or metastable. Interestingly, the metastable excess of alumina in orthopyroxenes from the gel-sillimanite mixes is a linear function of pressure over and above the expected increase in aluminium with pressure. The deviation from the equilibrium value is 0.02 at 5kb but increases linearly to 0.14 cations at 9kb (figure 3.3). It should be noted, however, that multiple orthopyroxene analyses from the same experiment have a large variation in aluminium contents (figure 3.4).

Biotite.

The biotite data shows some variation in oxide totals and cation totals (table 3.6). This is most probably related to the difficulty of analysing the tiny, thin crystals (e.g. plates 1a and 2a&b). Nonetheless, the oxide totals only vary between 94 and 97 wt% (the ideal is approximately 96 wt%). The cation totals vary between 15.3 and 15.6 cations per twenty two oxygens which is certainly within the range of natural biotites.

The operation of the substitution Al[6] + vacancy = -0.66(Fe, Mg) on the biotite compositions is demonstrated in figure 3.5. This substitution was identified by Patino Douce et al. (1993) and their data are also plotted. The trend is certainly more obvious in the current data but Patino Douce et al. (1993) used a natural pelite which contained significant titanium probably in octahedral co-ordination: the current KFMASH system can only have Al, Mg and Fe in the octahedral sites and so the linearity of the fit of the data plotted in figure 3.5 is enhanced by a constant-sum effect[7]. The gradient of the data is the crucial parameter in assessing whether the substitution has occurred and figure 3.5 shows that the data very closely approaches the ideal. Patino Douce et al. (1993) concluded that pressure was the predominant factor in the operation of the substitution. The pressures of the two sets of experiments are very similar (figure 3.6).

The total aluminium content of the biotites in both sets of experiments are very similar. The variation of the total (Fe+Mg) cations with pressure is also matches well between the experiments. A disparity arises in the distribution of the aluminium

[7] It should be remembered, though, that biotite frequently exists in a state intermediate between dioctahedral and trioctahedral and will often contain vacancies.

Table 3.6. Biotites.

	D38-10	D38-11	D38-12	D39-14	D39-15	D40-13	D40-14	D40-15	D49-16	D49-17
n	4	3	4	2	3	2	5	6	4	3
Oxides										
SiO2	40.727	41.158	42.036	40.234	39.932	41.430	40.707	41.918	40.295	39.204
Al2O3	21.380	20.300	20.240	18.414	18.310	20.671	20.390	20.507	21.100	19.970
FeO	11.495	7.940	3.931	10.799	4.603	5.523	7.230	4.213	12.591	11.619
MGO	12.215	15.758	17.909	18.744	22.724	18.114	16.409	18.725	12.851	15.583
CaO	0.000	0.000	0.120	0.046	0.007	0.000	0.009	0.005	0.009	0.002
K2O	9.704	9.346	9.893	8.145	8.986	10.298	9.938	10.075	9.497	9.749
Na2O	0.077	0.224	0.169	0.051	0.069	n.a.	n.a.	n.a.	0.052	0.043
TOTAL	**95.597**	**94.726**	**94.298**	**96.432**	**94.631**	**96.035**	**94.681**	**95.442**	**96.394**	**96.170**
Cations										
Si	5.843	5.860	5.911	5.700	5.640	5.784	5.803	5.838	5.768	5.640
Al(4)	2.157	2.140	2.089	2.300	2.360	2.216	2.197	2.162	2.232	2.360
Total(4)	8.000	8.000	8.000	8.000	8.000	8.000	8.000	8.000	8.000	8.000
Al(6)	1.458	1.267	1.266	0.775	0.688	1.185	1.229	1.204	1.328	1.026
Fe	1.379	0.945	0.462	1.279	0.544	0.645	0.862	0.491	1.507	1.398
Mg	2.613	3.345	3.755	3.959	4.785	3.770	3.487	3.888	2.742	3.342
Total (6)	5.450	5.557	5.483	6.013	6.017	5.600	5.578	5.583	5.577	5.766
Ca	0.000	0.000	0.018	0.007	0.001	0.000	0.001	0.001	0.001	0.000
Na	0.021	0.062	0.046	0.014	0.019	n.a.	n.a.	n.a.	0.014	0.012
K	1.776	1.698	1.775	1.472	1.619	1.834	1.807	1.790	1.734	1.789
Total A	1.797	1.760	1.839	1.493	1.639	1.834	1.808	1.791	1.749	1.801
Total	**15.247**	**15.317**	**15.322**	**15.506**	**15.656**	**15.434**	**15.386**	**15.374**	**15.326**	**15.567**
XMg	0.654	0.780	0.890	0.756	0.898	0.854	0.802	0.888	0.646	0.705

	D49-18	D50-16	D50-18	D61-16	D61-17	D63-16	D63-18	D66-18	D67-16i	D67-16ii
n	3	4	3	3	4	4	4	4	5	5
Oxides										
SiO2	39.818	40.495	41.232	42.573	39.671	37.913	39.841	40.845	38.454	38.786
Al2O3	19.838	20.897	19.766	21.062	20.178	19.693	21.127	19.294	20.885	20.805
FeO	7.457	9.071	5.337	8.064	7.001	14.887	7.228	5.407	13.597	12.246
MGO	18.982	16.455	20.131	15.618	17.919	13.234	18.348	20.132	13.024	13.869
CaO	0.012	0.005	0.008	0.004	0.003	0.005	0.004	0.004	0.013	0.011
K2O	9.975	9.557	9.883	9.417	9.705	9.119	9.489	9.937	9.383	9.440
Na2O	0.127	n.a.	n.a.	0.013	0.062	n.a.	n.a.	n.a.	0.056	0.059
TOTAL	**96.207**	**96.479**	**96.355**	**96.773**	**94.538**	**94.851**	**96.037**	**95.619**	**95.411**	**95.217**
Cations										
Si	5.625	5.705	5.734	5.912	5.673	5.611	5.601	5.735	5.615	5.638
Al(4)	2.375	2.295	2.266	2.088	2.327	2.389	2.399	2.265	2.385	2.362
Total(4)	8.000	8.000	8.000	8.000	8.000	8.000	8.000	8.000	8.000	8.000
Al(6)	0.928	1.175	0.974	1.359	1.074	1.046	1.102	0.928	1.209	1.202
Fe	0.881	1.069	0.621	0.937	0.837	1.843	0.850	0.635	1.660	1.489
Mg	3.997	3.456	4.174	3.233	3.820	2.920	3.845	4.214	2.835	3.005
Total (6)	5.806	5.700	5.769	5.529	5.731	5.809	5.797	5.777	5.704	5.696
Ca	0.002	0.001	0.001	0.001	0.001	0.001	0.001	0.001	0.002	0.002
Na	0.035	n.a.	n.a.	0.004	0.017	n.a.	n.a.	n.a.	0.016	0.017
K	1.798	1.718	1.753	1.668	1.771	1.722	1.702	1.780	1.748	1.750
Total A	1.835	1.719	1.754	1.673	1.789	1.723	1.703	1.781	1.766	1.769
Total	**15.641**	**15.419**	**15.523**	**15.202**	**15.520**	**15.532**	**15.500**	**15.558**	**15.470**	**15.465**
XMg	0.819	0.764	0.870	0.775	0.820	0.613	0.819	0.869	0.631	0.669

Table 3.6. Mean analyses of biotites produced in the experiments, in weight-percent oxides and cations per 22 oxygens. Tetrahedral aluminium cations calculated as 8-Si. Octahedral aluminium cations calculated as Al-(8-Si). "n" - number of analyses. "n.a." - element not analysed for. D67-16i, D67-16ii - from garnet-absent and garnet-bearing parts of charge respectively. All iron as Fe2+.

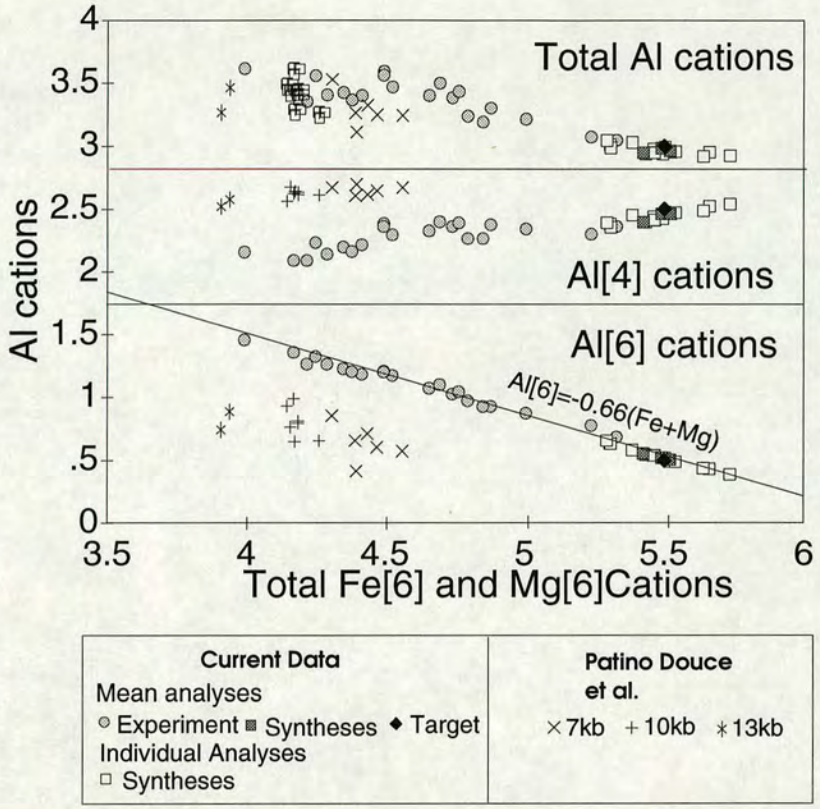

Figure 3.5. Total iron and magnesium cations versus tetrahedral, octahedral and total aluminium cations for biotite analyses from this study and that of Patino Douce et al. (1993). All points are means including the data of Patino Douce et al. (1993), except for the white squares which are individual analyses of the products of biotite syntheses. The sloping line is the ideal position of the substitution shown. The horizontal lines simply divide the three types of aluminium cation.

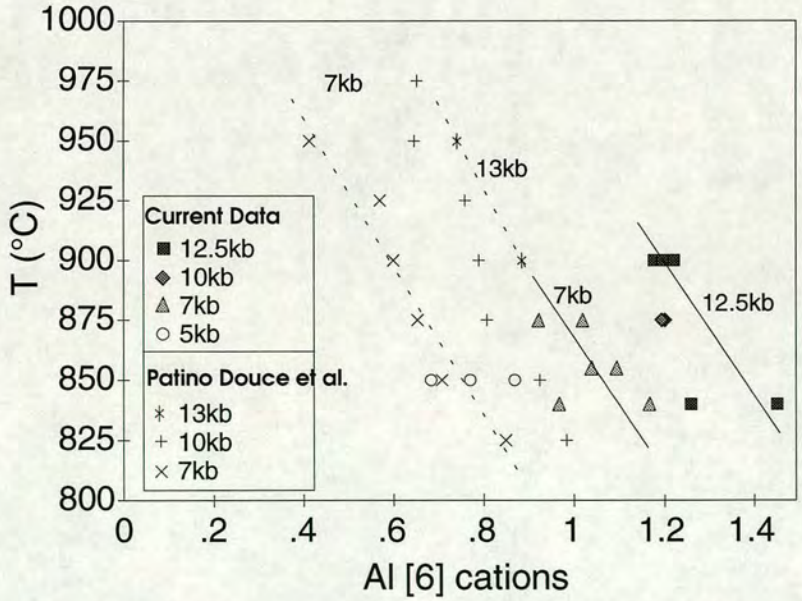

Figure 3.6. Octahedral aluminium cations (Al[6]) versus temperature for isobaric data sets of mean biotite analyses. The lines highlighting the trends were drawn by eye.

cations on the tetrahedral and octahedral sites. The probable explanation is a systematic underestimate (by Patino Douce et al., 1993) or overestimate (by this study) of the silica content of the biotite, which would raise or lower the estimate of tetrahedral aluminium cations respectively. Natural high-grade (pressure) biotites tend to be more aluminous and correspondingly more silica-poor than those listed in table 3.5 and thus it is more likely that this study has overestimated the silica. Patino Douce et al. (1993) did systematically reject all analyses with more than 39wt% silica and, so, it remains possible that the current data set is closer to equilibrium. The partial-melting study of Puziewicz and Johannes (1990) produced biotites with around 40wt% silica but was conducted at a pressure of 2kb.

Figure 3.6 shows that the pressure-temperature variation of the octahedral aluminium is analogous for both sets of experiments but one is displaced from the other. This mismatch could most simply be explained by a silica under/overestimate.

Cordierite.

The weight-percent oxide totals vary between 96 and 99 percent as would be expected from a mineral which can contain variable amounts of water. The cation totals are consistently above 11 (per 18 oxygens) by up to 0.1 cation, despite the silicon, aluminium and iron and magnesium site occupancies all being very closely

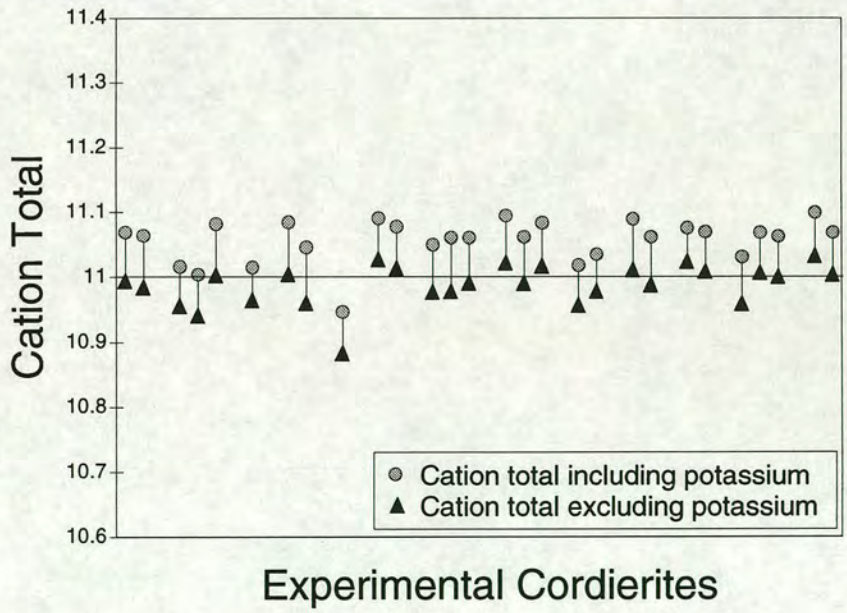

Figure 3.7. Pairs of cation totals (mean analyses) for all the cordierites produced in the experiments. The higher cation totals were calculated including the measured potassium, the lower totals were calculated without the potassium.

Table 3.7. Cordierites.

	D47-16	D47-17	D49-16	D49-17	D49-18	D50-16	D51-16	D51-17	D54-18	D56-17
n	4	4	3	5	3	4	4	3	3	5
Oxides										
SiO2	49.213	49.934	48.681	50.359	48.992	50.387	48.315	49.977	51.525	48.101
Al2O3	33.356	33.541	33.832	32.514	33.394	32.871	33.864	32.161	32.886	32.907
FeO	4.671	2.753	4.391	3.809	2.707	4.246	7.527	5.482	1.911	4.139
MgO	10.533	11.690	9.805	10.741	11.846	10.233	8.734	10.053	11.178	11.035
CaO	0.017	0.025	0.036	0.040	0.131	0.027	0.037	0.057	0.035	0.016
K2O	0.771	0.809	0.536	0.592	0.593	0.518	0.735	0.828	0.627	0.598
Na2O	0.015	0.020	0.036	0.023	0.056	n.a.	0.046	0.025	0.017	0.031
TOTAL	**98.576**	**98.770**	**97.317**	**98.079**	**97.718**	**98.281**	**99.258**	**98.582**	**98.179**	**96.828**
Cations										
Si	4.990	5.009	4.982	5.097	4.968	5.094	4.931	5.083	5.155	4.956
Al	3.986	3.965	4.081	3.879	3.991	3.950	4.073	3.855	3.878	3.996
Fe(2+)	0.396	0.231	0.376	0.322	0.230	0.359	0.643	0.466	0.160	0.357
Mg	1.592	1.748	1.496	1.621	1.791	1.542	1.329	1.524	1.667	1.695
Total FM	1.988	1.979	1.872	1.943	2.021	1.901	1.972	1.990	1.827	2.052
Ca	0.002	0.003	0.004	0.004	0.014	0.003	0.004	0.006	0.004	0.002
Na	0.003	0.004	0.007	0.005	0.011	n.a.	0.009	0.005	0.003	0.006
K	0.100	0.104	0.070	0.076	0.077	0.067	0.096	0.107	0.080	0.079
Total	11.069	11.064	11.016	11.004	11.082	11.015	11.085	11.046	10.947	11.091
Total-K	**10.995**	**10.985**	**10.956**	**10.942**	**11.004**	**10.965**	**11.005**	**10.961**	**10.884**	**11.028**
XMg	0.801	0.883	0.799	0.834	0.886	0.812	0.674	0.766	0.912	0.826

	D56-18	D57-16	D57-17	D57-18	D60-16	D60-17	D60-18	D61-16	D61-17	D62-16
n	4	4	4	4	5	5	5	4	3	6
Oxides										
SiO2	48.427	49.459	49.314	49.526	48.065	48.712	48.792	49.108	48.835	48.507
Al2O3	32.402	32.827	32.980	33.585	33.062	32.593	33.345	32.918	34.412	33.633
FeO	2.819	3.800	3.103	2.235	6.086	4.544	2.875	3.007	2.680	4.156
MgO	11.833	10.966	11.299	12.016	9.868	10.481	11.813	10.892	11.101	10.821
CaO	0.059	0.028	0.040	0.066	0.050	0.026	0.057	0.025	0.033	0.023
K2O	0.557	0.676	0.758	0.632	0.666	0.703	0.623	0.562	0.502	0.779
Na2O	0.031	0.040	0.052	0.028	0.023	0.018	0.021	0.031	0.036	0.026
TOTAL	**96.128**	**97.795**	**97.545**	**98.087**	**97.820**	**97.077**	**97.526**	**96.542**	**97.599**	**97.944**
Cations										
Si	4.993	5.030	5.017	4.988	4.947	5.012	4.961	5.035	4.947	4.943
Al	3.937	3.935	3.954	3.987	4.011	3.952	3.996	3.977	4.109	4.040
Fe(2+)	0.243	0.323	0.264	0.188	0.524	0.391	0.245	0.258	0.227	0.354
Mg	1.819	1.663	1.714	1.804	1.514	1.608	1.791	1.665	1.676	1.644
Total FM	2.062	1.986	1.978	1.992	2.038	1.999	2.036	1.923	1.903	1.998
Ca	0.007	0.003	0.004	0.007	0.006	0.003	0.006	0.003	0.004	0.003
Na	0.006	0.008	0.010	0.006	0.005	0.004	0.004	0.006	0.007	0.005
K	0.073	0.088	0.098	0.081	0.088	0.092	0.081	0.074	0.065	0.101
Total	11.078	11.050	11.061	11.061	11.095	11.062	11.084	11.018	11.035	11.090
Total-K	**11.014**	**10.978**	**10.979**	**10.992**	**11.023**	**10.991**	**11.018**	**10.958**	**10.979**	**11.012**
XMg	0.882	0.837	0.866	0.906	0.743	0.804	0.880	0.866	0.881	0.823

Table 3.7. Mean cordierite analyses, in weight-percent oxides and cations per 18 oxygens. The "Total-K" is the cation total calculated without potassium, which is thought to be situated in the channels, not the lattice.
"n" - number of analyses. "n.a." - element not analysed for. All iron as Fe2+.

Table 3.7. Cordierites.

	D62-18	D63-16	D63-18	D64-16	D64-17	D64-18	D66-17	D66-18
n	5	4	5	3	3	5	5	6
Oxides								
SiO2	50.247	48.493	49.098	49.006	49.137	48.688	48.338	49.681
Al2O3	33.665	33.596	33.901	34.317	32.892	33.654	33.452	33.331
FeO	1.989	4.454	2.656	3.035	2.988	2.069	3.859	2.687
MgO	12.252	10.848	11.871	10.629	11.755	11.900	11.307	12.023
CaO	0.015	0.040	0.123	0.046	0.036	0.066	0.025	0.052
K2O	0.806	0.521	0.539	0.739	0.642	0.610	0.697	0.657
Na2O	n.a.	n.a.	n.a.	n.a.	n.a.	n.a.	n.a.	n.a.
TOTAL	**98.975**	**97.951**	**98.188**	**97.771**	**97.449**	**96.986**	**97.677**	**98.430**
Cations								
Si	5.012	4.941	4.951	4.967	5.000	4.957	4.933	4.998
Al	3.957	4.035	4.029	4.100	3.945	4.038	4.024	3.952
Fe(2+)	0.166	0.380	0.224	0.257	0.254	0.176	0.329	0.226
Mg	1.822	1.648	1.784	1.606	1.783	1.806	1.720	1.803
Total FM	1.988	2.028	2.008	1.863	2.037	1.982	2.049	2.029
Ca	0.002	0.004	0.013	0.005	0.004	0.007	0.003	0.006
Na	0.000	0.000	0.000	0.000	0.000	0.000	0.000	0.000
K	0.103	0.068	0.069	0.096	0.083	0.079	0.091	0.084
Total	11.062	11.076	11.070	11.031	11.069	11.063	11.100	11.069
Total-K	**10.988**	**11.025**	**11.009**	**10.959**	**11.007**	**11.001**	**11.034**	**11.005**
XMg	0.917	0.813	0.889	0.862	0.875	0.911	0.839	0.889

Table 3.7 continued. Mean cordierite analyses, in weight-percent oxides and cations per 18 oxygens. The "Total-K" is the cation total calculated without potassium, which is thought to be situated in the channels, not the lattice. "n" - number of analyses. "n.a." - element not analysed for. All iron as Fe2+.

stoichiometric (table 3.7). The high totals result from the incorporation of small amounts of potassium into the cordierite. The cation totals are brought closer to the ideal 11 when the potassium cations are excluded from the calculation of the cation total (figure 3.7). This indicates that the potassium cations are not part of the crystal structure of the cordierite but occur in the channels, causing the slight charge imbalance indicated by the high cation total.

The phenomenon of potassic cordierites was investigated by Schreyer et al. (1990) who reported examples from three different localities[8] and stated that potassic cordierites are characteristic of high-temperature and very low-pressure environments. These environments result in rapid growth and the rapid cooling of the cordierite crystals. The cordierites are either the high-temperature hexagonal cordierite-polymorph, indialite (Si-Al disordered[9]), or have Miyashiro distortion indices intermediate between indialite and orthorhombic, low-cordierite (implying some long-range Si-Al ordering). Schreyer et al. (1990) state that the predominant substitution mechanism leading to alkali incorporation is $K^{[channel]} + Al^{[4]} = vacancy^{[channel]} + Si^{[4]}$. Daniels et al. (in press) ran an experiment containing a potassic cordierite at 1290°C for 290 days, during which time its composition did not change but its structure changed from hexagonal to orthorhombic. From this Schreyer et al. (1990) argue that potassic cordierites are chemically stable on a time-scale appropriate to a volcanic origin, though not structurally stable as hexagonal cordierite. Potassic cordierites have also been reported from metamorphic terrains[10] suggesting that they are also stable on a much longer time scale.

Whilst containing potassium, the cordierites in the current study show no evidence for either the substitution of Schreyer et al. (1990) (figure 3.8) or any other obvious substitution[11]. Since the microprobe analyses show that the Si:Al ratio in the cordierites is the ideal 5:4, there is no disruption of the ratio and there is no

---

[8] The localities were; 1. the products of the Bellerberg and Herchenberg volcanoes in the Eastern Eifel, Germany, 2. buchites from Blaue Kuppe, Germany, 3. fused shales from Bokaro coal field, India.

[9] While hexagonal cordierite can have no long-range Si-Al order, it can have significant short-range order (Putnis and Holland 1986). It is called disordered here for simplicity.

[10] Sodium is the alkali found most commonly in metamorphic cordierite. Deer, Howie and Zussman (1986) state "Na_2O and K_2O are commonly up to 0.8wt% and 0.6wt% respectively".

[11] The potassium cations are apparently not charge balanced. Another possible substitutions is K + vacancy = (Mg/Fe) (Mottana et al. 1983) but again this is not supported by the current data. Perhaps there are OH anions in the channels balancing the potassium cations but they have never been reported, despite the fact that they would manifest in Infra-Red spectroscopy. Furthermore, Schreyer and Yoder (1964) refuted previous suggestions of channel OH, at least for synthetic cordierites.

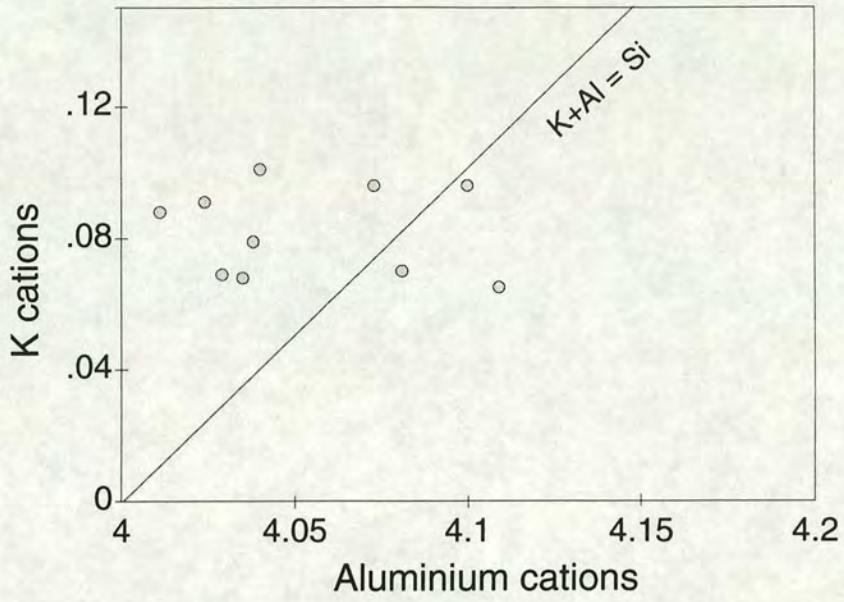

Figure 3.8. Aluminium cations versus potassium cations for mean cordierite analyses. The line shows the ideal position of the substitution marked.

requirement for Si:Al disorder on the grounds of stoichiometry. Disorder could, of course still be present.

As reported potassic cordierites mostly have, or have had, a hexagonal structure, it may be that the hexagonal cordierite better accommodates potassium. However, the experimental result of Daniels et al. (in press) above shows that the structure can change *independently* of the potassium content. It is more likely that the potassic chemistry and hexagonal structure of the cordierites are *both* results of the manner of crystallisation, i.e. crystals quickly grown (thus hexagonal) in an environment with a high mobility of potassium (thus potassic) and quickly quenched, such as the current experiments and the formation environments of the samples of Schreyer et al. (1990). Therefore, the evidence of the current experiments implies that potassic cordierites are not restricted to low-pressure environments (as Schreyer et al. state, 1990) but to environments where potassium is easily available and where crystallisation and cooling are relatively rapid: potassic cordierites have been reported from relatively high-pressure potassium-rich contact aureoles and pegmatites (Deer, Howie and Zussman, 1986). The current experiments show that the potassium content of the cordierite correlates positively with temperature (figure 3.9). It is invariant with pressure (figure 3.10).

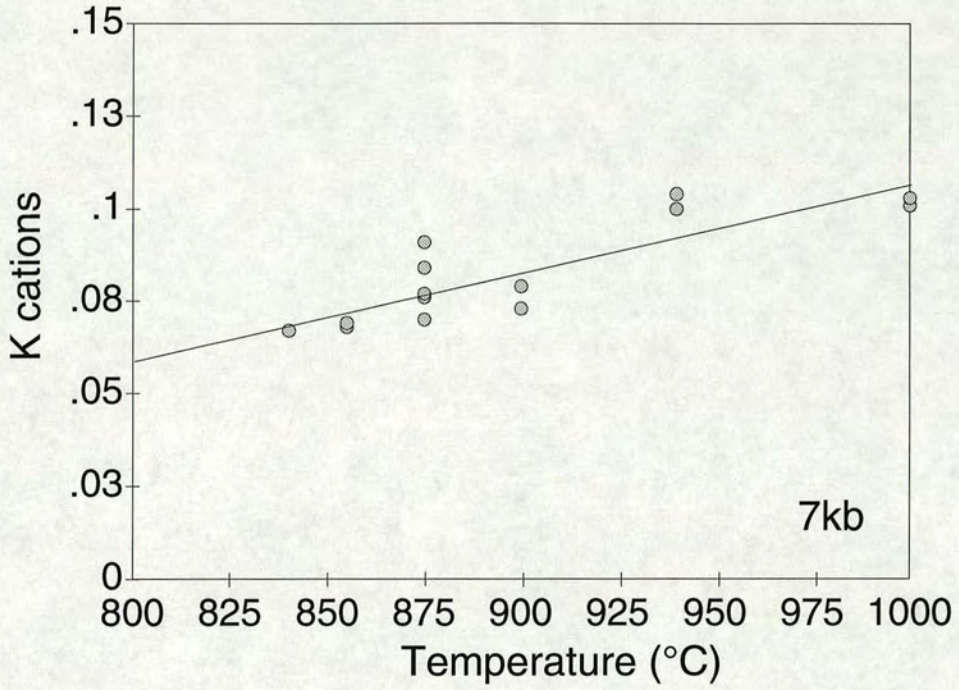

Figure 3.9. Temperature versus potassium cation content for cordierites (mean analyses) formed at 7kb. The line highlighting the trend is a linear regression line.

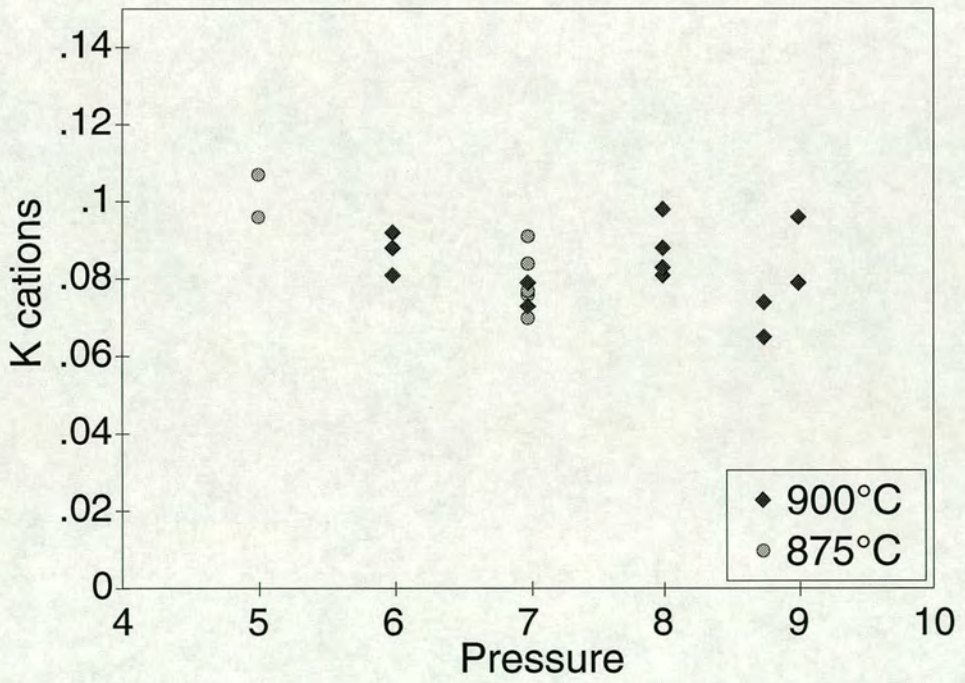

Figure 3.10. Pressure versus potassium cation content for cordierites (mean analyses) formed at 900°C and 875°C.

Putnis and Holland (1986) argued that the formation of indialite below 1450°C at atmospheric pressures is metastable and with time Si-Al ordering will increase and it will become orthorhombic. Indialite may form metastably because, as a disordered phase, it is kinetically favoured relative to the ordered low-cordierite. However, Kitamura and Hiroi (1982) report the co-existence of indialite and cordierite, with different Fe:Mg ratios from a pelitic hornfels in Japan, suggesting that indialite may be stable at crustal temperatures. Many experimental cordierites initially form as indialite. Schreyer et al. (1990) infer from their data that potassic cordierites may exhibit a hexagonal nature because the substitution to which they ascribe alkali incorporation disrupts the Si:Al ratio from the ideal and so precludes total ordering.

The structural state of the cordierite formed in the current experiments is of interest as, if it were metastable indialite, then the pressure-temperature positions for the reactions derived in later chapters could be significantly different to those for low-cordierite (Putnis and Holland, 1986). How different depends on the size of the pressure-temperature overstep required to form metastable indialite. Putnis and Holland (1986) calculated a pressure overstep of 3kb at temperatures of granulite metamorphism. Furthermore, the combination of temperatures and run times used in the current experiments are not sufficient to convert indialite to low-cordierite, if indialite were to form first (Putnis et al. 1987). Too little experimental material is produced to obtain an XRD trace which could determine the distortion index of the cordierite.

If indialite is metastable below 1450°C, the pressure-temperature overstep required for its formation would result in a different Fe-Mg partitioning between the indialite and co-existing phases than that for low-cordierite and co-existing phases (Putnis and Holland, 1986). The Fe-Mg partitioning described in section 3.3.2 below for garnet-cordierite pairs in the current experiments is consistent with a calibration based on natural rock data (Thompson, 1976) and which was confirmed experimentally (Ellis, 1986). This consistency suggests that, even if indialite does form, the overstep required is not large enough to change the Fe-Mg partitioning noticeably and therefore much smaller than the calculated overstep of Putnis and Holland (1986).

In summary; the cordierites in the current experiments are chemically straightforward with the exception of a high potassium content. This is ascribed to the easy availability of potassium and the fast growth and quench of the crystals in the

experiments. Whether the cordierite is hexagonal or orthorhombic cannot be determined but the Fe-Mg partitioning, which is consistent with natural rock and experimental data, suggests that whichever polymorph is present, the phase stability has not been significantly affected.

Osumilite.

The osumilite data is given in Table 3.8 and shows that the oxide totals and cation totals are both very good. The osumilite is remarkably stoichiometric as has been noted previously for both natural and synthetic osumilites (Grew 1982). However, the osumilites here show high alumina-contents which are variable within and between experiments (figure 3.11), though the effect is less dramatic than for the experimental orthopyroxenes. No correlation of the osumilite alumina-content and the co-existing phase assemblage was noted.

The Tschermak substitution is seen to account for the high alumina-contents (figure 3.12). Grew (figure 7, 1982) also noted this correlation in natural osumilites. The potassium content of the C sites (channel-necks) can be variable in natural osumilites (Figure 5, Armbruster and Oberhansli, 1988). Figure 3.13 shows that whilst a negative correlation exists between potassium and octahedral aluminium, it cannot be explained by the substitution which Armbruster and Oberhansli (1988) observed, $Al^{[6]} + vacancy^{[C]} = K^{[C]} + (Mg/Fe)^{[6]}$. The only osumilites reported by Armbruster

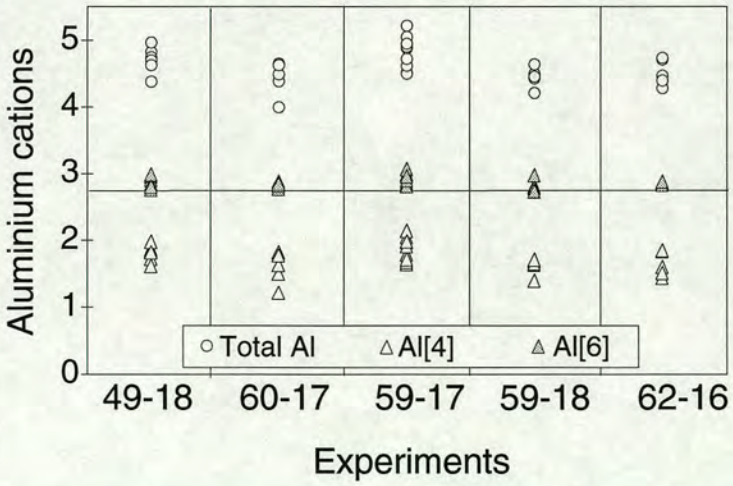

Figure 3.11. Aluminium cations for individual osumilite analyses from five representative experiments. The horizontal line is the maximum octahedral aluminium (Al[6]) content reported for natural osumilite (Grew 1982). Synthetic osumilites have been reported with Al[6] up to the theoretical maximum of three cations (Schreyer and Seifert 1961).

Table 3.8. Osumilites.

	D39-13	D47-16	D47-17	D47-18	D49-18	D51-16	D51-17	D55-17	D55-18	D56-18
n	5	5	4	4	7	3	3	3	4	4
Oxides										
SiO2	61.600	60.932	62.539	62.326	62.154	61.873	61.754	61.833	61.886	62.893
Al2O3	22.577	23.643	23.605	22.701	24.308	23.328	23.629	23.881	23.090	22.199
FeO	3.674	3.324	2.942	1.461	1.480	4.660	3.604	1.307	1.146	1.552
MgO	7.080	6.991	7.071	8.027	7.890	6.261	6.910	8.273	8.377	7.709
CaO	0.007	0.011	0.006	0.020	0.019	0.015	0.023	0.004	0.006	0.029
K2O	4.291	4.302	4.230	4.425	4.320	4.292	4.275	4.330	4.303	4.332
Na2O	0.051	0.043	0.024	0.030	0.041	0.042	0.042	0.040	0.027	0.051
TOTAL	**99.281**	**99.248**	**100.416**	**98.989**	**100.212**	**100.471**	**100.235**	**99.665**	**98.836**	**98.763**
Cations										
Si	10.293	10.175	10.278	10.339	10.184	10.255	10.214	10.186	10.268	10.444
Al (4)	1.707	1.825	1.722	1.661	1.816	1.745	1.786	1.814	1.732	1.556
Total (4)	12.000	12.000	12.000	12.000	12.000	12.000	12.000	12.000	12.000	12.000
Al (6)	2.739	2.828	2.850	2.777	2.878	2.812	2.820	2.822	2.783	2.789
Fe2+	0.513	0.464	0.404	0.203	0.203	0.646	0.499	0.180	0.159	0.216
Mg2+	1.764	1.740	1.732	1.985	1.927	1.547	1.704	2.032	2.072	1.908
Total M	2.277	2.204	2.136	2.188	2.130	2.193	2.203	2.212	2.231	2.124
Ca	0.001	0.002	0.001	0.004	0.003	0.003	0.004	0.001	0.001	0.005
Na	0.017	0.014	0.008	0.010	0.013	0.014	0.014	0.013	0.009	0.016
K	0.915	0.916	0.887	0.937	0.903	0.908	0.902	0.910	0.911	0.918
Total C1	0.933	0.932	0.896	0.951	0.919	0.925	0.920	0.924	0.921	0.939
TOTAL	**17.949**	**17.964**	**17.882**	**17.916**	**17.927**	**17.930**	**17.943**	**17.958**	**17.935**	**17.852**
XMg	0.775	0.790	0.811	0.907	0.905	0.705	0.774	0.919	0.928	0.899

	D57-18	D59-17i	D59-17ii	D59-18	D60-16	D60-17	D60-18	D62-16	D65-18	D66-18
n	3	6	4	7	5	7	5	5	3	4
Oxides										
SiO2	62.216	61.243	62.211	62.857	61.119	61.569	62.696	62.189	23.990	63.164
Al2O3	25.222	25.660	23.446	22.938	23.941	24.096	22.231	23.029	62.034	22.392
FeO	1.109	2.035	2.096	1.632	3.848	2.806	1.913	2.674	0.997	1.441
MgO	7.008	7.304	7.515	7.817	6.346	7.160	8.415	6.835	8.432	8.406
CaO	0.027	0.007	0.014	0.014	0.023	0.006	0.028	0.008	0.017	0.003
K2O	4.190	4.203	4.368	4.403	4.303	4.263	4.544	4.282	4.365	4.501
Na2O	0.043	0.035	0.043	0.049	0.049	0.032	0.035	0.056	n.a.	n.a.
TOTAL	**99.815**	**100.486**	**99.693**	**99.710**	**99.629**	**99.932**	**99.863**	**99.072**	**99.835**	**99.906**
Cations										
Si	10.192	10.031	10.273	10.352	10.183	10.176	10.346	10.347	10.187	10.382
Al (4)	1.808	1.969	1.727	1.648	1.817	1.824	1.654	1.653	1.813	1.618
Total (4)	12.000	12.000	12.000	12.000	12.000	12.000	12.000	12.000	12.000	12.000
Al (6)	3.061	2.984	2.836	2.804	2.884	2.870	2.670	2.863	2.830	2.720
Fe2+	0.152	0.279	0.290	0.225	0.536	0.388	0.264	0.372	0.137	0.198
Mg2+	1.711	1.783	1.850	1.919	1.576	1.764	2.070	1.695	2.064	2.060
Total M	1.863	2.062	2.140	2.144	2.112	2.152	2.334	2.067	2.201	2.258
Ca	0.005	0.001	0.003	0.003	0.004	0.001	0.005	0.001	0.003	0.001
Na	0.014	0.011	0.014	0.016	0.016	0.010	0.011	0.018	n.a.	n.a.
K	0.876	0.878	0.920	0.925	0.915	0.899	0.957	0.909	0.915	0.944
Total C1	0.895	0.890	0.937	0.944	0.935	0.910	0.973	0.928	0.918	0.945
TOTAL	**17.819**	**17.936**	**17.913**	**17.892**	**17.931**	**17.932**	**17.977**	**17.858**	**17.949**	**17.923**
XMg	0.918	0.865	0.865	0.895	0.746	0.820	0.887	0.820	0.938	0.912

Table 3.8. Mean osumilite analyses, in weight-percent oxides and cations per 30 oxygens.
Tetrahedral aluminium calculated as 12-Si. Octahedral aluminium calculated as Al-(12-Si).
"n" - number of analyses. "n.a." - element not analysed for. All iron as Fe2+.
D59-17i, D59-17ii - high and low alumina analyses respectively.

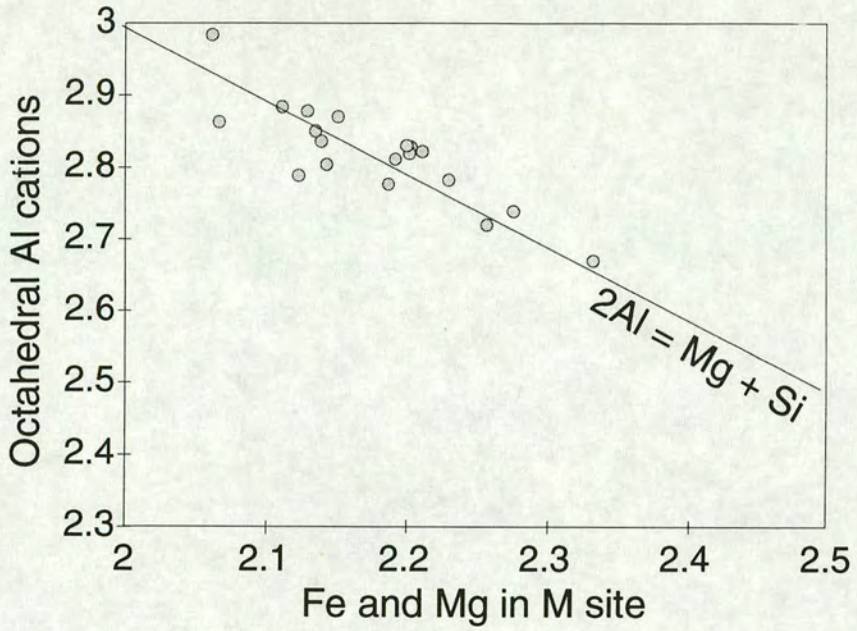

Figure 3.12. Iron and magnesium in the octahedral M site (i.e. total iron and magnesium) versus aluminium in the octahedral site for mean osumilite analyses. The ideal position of the Tschermak substitution is marked by a line.

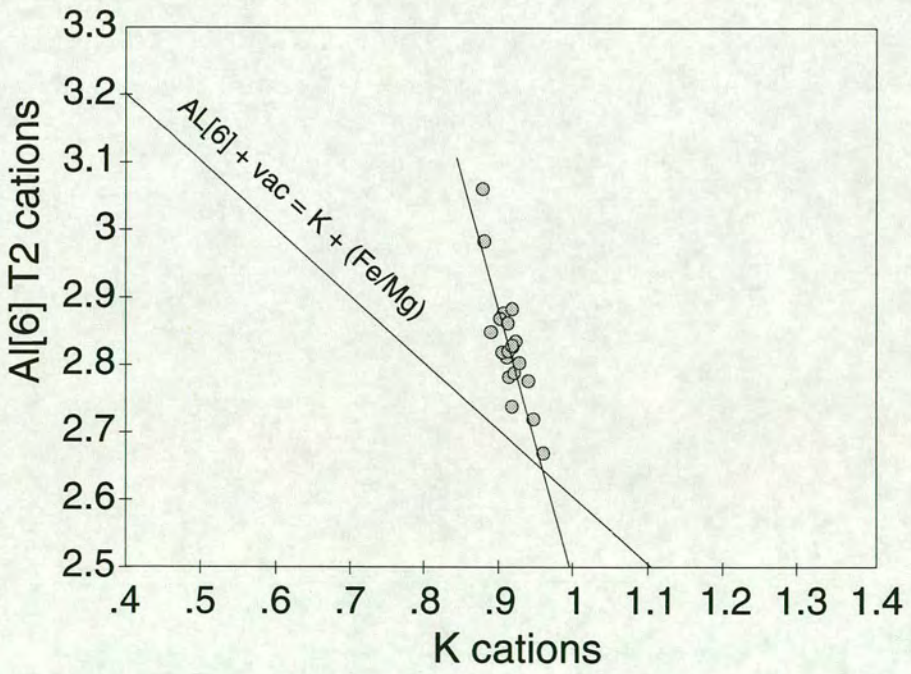

Figure 3.13. Potassium cations versus octahedral aluminium (T2 site) for mean osumilite analyses. The ideal position of the substitution marked is shown. The trend of the data is emphasised with a linear regression line and projects back to the ideal potassium cation value of one.

and Oberhansli (1988) with C-site occupancies of less than 0.9 (and varying down to 0.35) were from very low-pressure environments, suggesting that the substitution only operates at near-surface conditions. The substitution giving rise to the correlation observed in the current data is not properly understood.

3.4.2 Partitioning of iron and magnesium amongst the experimental phases.

Geologists long have found the variation in partitioning of iron and magnesium between mineral pairs useful as an indicator of past rock-temperatures (e.g. Kretz 1959, Albee 1965b, Thompson 1976). This has lead to a good deal of data being available for certain mineral pairs. By comparing the partitioning observed in these experiments with that in the literature the probable extents of equilibration of the phases can be evaluated.

Garnet-orthopyroxene Fe-Mg partitioning.

The garnet-orthopyroxene data are shown on figure 3.14. The review of thermo-barometry by Essene (1989) states that the work of Harley (1984a), used here, is in

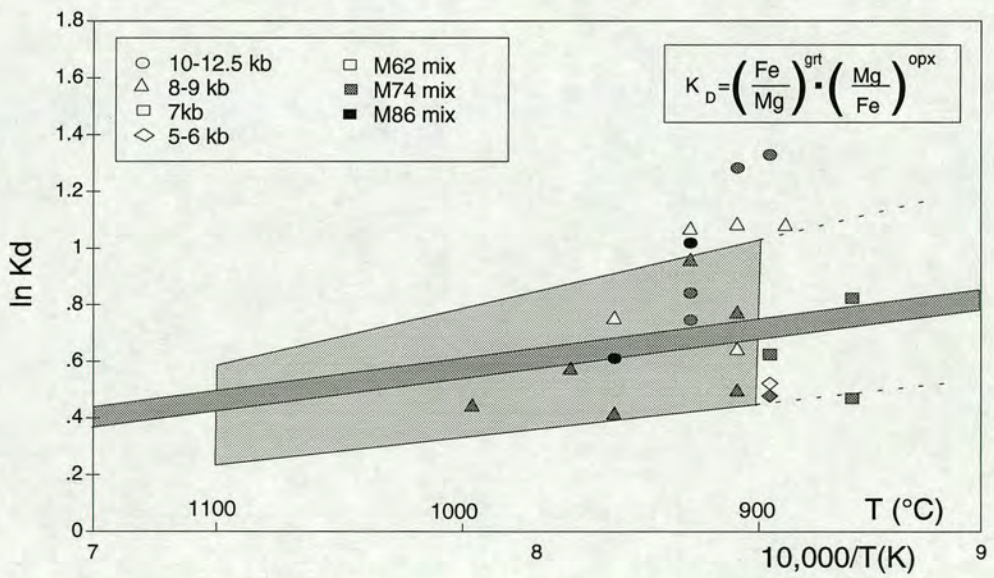

Figure 3.14. Inverse temperature versus ln K_D for garnet-orthopyroxene pairs formed at various pressures and temperatures in experiments using different mixes. Also shown for comparison are; thin, dark grey band - the calibration of Harley (1984a), the upper line of the band is the position of the equilibrium at 12.5kb, the lower that at 5kb; pale grey area - field of data scatter from the studies of Bertrand et al. (1991) and Hensen and Green (1971, 1972).

broad agreement with other available calibrations (Sen and Bhattacharya 1984, Lee and Ganguly, 1988) at the temperatures of interest (<1000°C). The calibrations diverge at higher temperatures and Eckert and Bohlen (1992) recently presented reversed experiments which support the data of Lee and Ganguly (1988) above 1000°C.

The data from the current experiments are spread along the linear relation of Harley (1984a) and scattered equally above and below it, quite considerably in some cases. However, virtually all of the data are within the spread of the data from comparable phase equilibrium studies (Hensen and Green 1971, 1972, Bertrand et al. 1991). The data becomes more widely spread at lower temperatures as might be expected, given that reaction rates are slower at low temperature. This effect is also observable in the field drawn for the other experiments. Variation in pressure cannot explain the scatter of the data as the distribution of the experiments from each pressure is too inconsistent and the magnitude of the scatter is too large. The width of the dark grey band in figure 3.14 represents the predicted variation in K_D from 5kb to 12.5kb (Harley 1984a). The bulk composition of the experiment exerts no obvious control.

The data from this study is similar to that from other phase equilibrium studies but has a very large scatter compared to Fe-Mg exchange studies. The reasons for this are considered below.

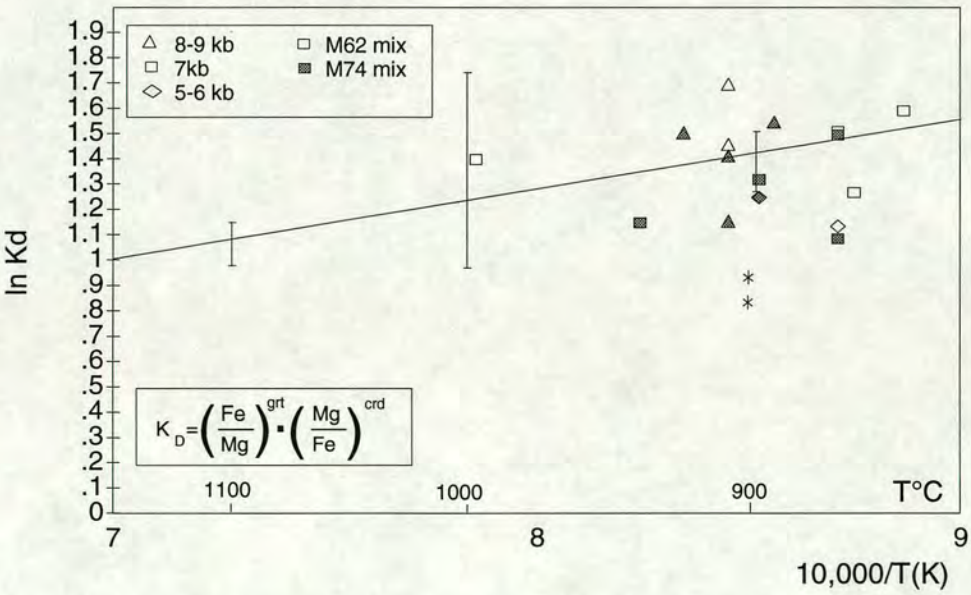

Figure 3.15. Inverse temperature versus ln K_D for garnet-cordierite pairs formed at various pressures and temperatures in experiments using various mixes. The linear relation shown was derived by Thompson (1976) from natural rock data and reproduced by Ellis (1986) experimentally. The brackets shown encompass the data from the phase equilibrium studies of Hensen and Green (1971,1972) and Bertrand et al (1991), except the asterixes which are also from Bertrand et al. (1991).

Garnet-cordierite Fe-Mg partitioning.

The garnet-cordierite partitioning data from the current experiments are compared with literature values in figure 3.15. The data are distributed along the linear relation of Thompson (1976) and are scattered equally above and below it. The data is consistent with the other experimental data plotted. No evidence could be found in the data for the Fe-Mg partitioning being affected by pressure or the X_{Mg} of the cordierite, though this is perhaps because the scatter is too broad.

The calibration of Bhattacharya et al. (1988) was also tested but gave K_D's lower than all the data on figure 3.15. The temperatures of the current experiments are mostly outside the stated range of validity (620°C to 860°C) of that study.

Garnet-biotite Fe-Mg partitioning.

Essene (1988) recommends the data of Ferry and Spear (1978) for the Fe-Mg partitioning between garnet and biotite. Their linear relation is extrapolated to higher temperatures (there is no other high-temperature data available) in figure 3.16 which

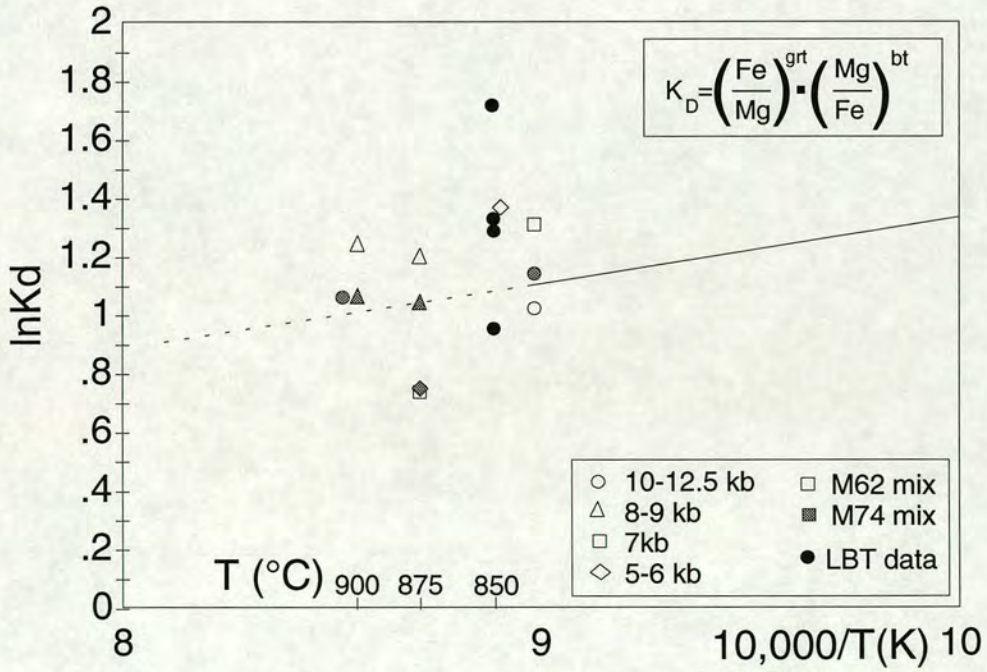

Figure 3.16. Inverse temperature versus ln K_D for garnet-biotite pairs formed at various pressures and temperatures in experiments using various mixes. The linear relation plotted is from Ferry and Spear (1978) and is extrapolated above 850°C (dashed line). "LBT data" refers to the 10kb data of Le Breton and Thompson (1988).

also shows the data from these experiments and that from Le Breton and Thompson (1988). The pattern of scatter of the data obtained here is similar to that of the garnet-orthopyroxene data and the garnet-cordierite data: the data shows a similar scatter to other phase equilibrium studies, but are not sufficiently consistent to provide additional support for the linear Fe-Mg exchange relation used.

Variable equilibration of different phases.

At this point, it is appropriate to ask why the data are rather widely scattered about the published partitioning study data. As noted above, the analyses of the garnet inspire less confidence than those of other phases because of the small analysable area presented by the reaction rims and the consequent possibility of overlap. However, if this were the only factor the measured garnet X_{Mg}'s would be expected to be too high in general, as the seeds are more magnesian than the product crystals (except rarely at the highest pressures). The X_{Mg}'s would also be too high if the crystal had not reacted sufficiently.

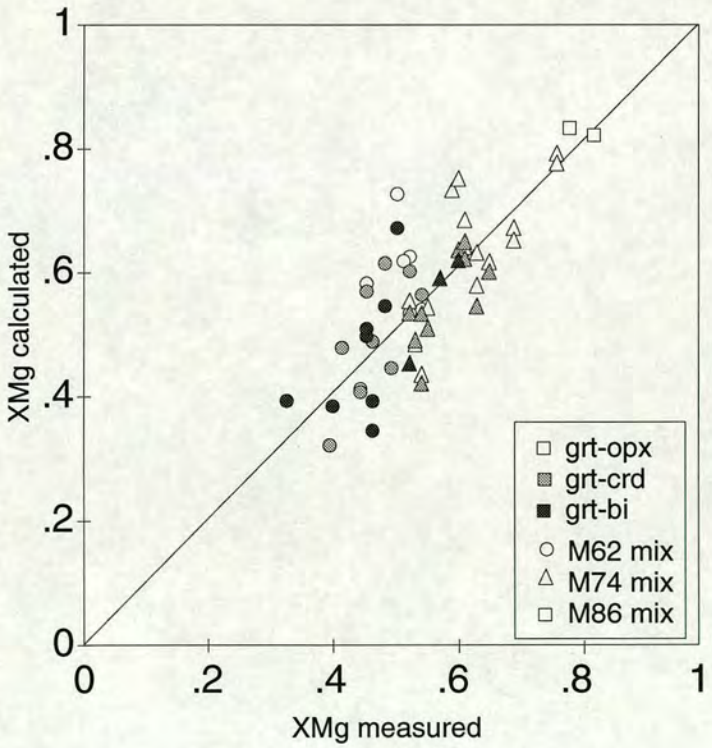

Figure 3.17. Measured garnet X_{Mg} versus garnet X_{Mg} calculated from X_{Mg} of co-existing orthopyroxene (Harley, 1984a), cordierite (Thompson 1976, Ellis 1986) or biotite (Ferry and Spear, 1978) and the experimental pressure and temperature.

The data presented above is summarised in figure 3.17. It plots the measured garnet compositions against the garnet compositions which the calibrations above *predict* for a given orthopyroxene or cordierite composition, pressure and temperature. It shows that the measured compositions deviate from those predicted on both the high- and low-magnesium sides. In the latter case the garnet rims are too iron-rich, showing that the crystal has reacted but "overshot" the equilibrium composition. This phenomenon of compositional "overshooting" has been reported in other experimental work (Ferry and Spear 1978, Pattison and Newton 1989). Given this, it is likely that even those garnets with relatively high measured X_{Mg}'s reacted and that overlap of the electron beam with the garnet core caused the pyrope-rich composition. It is significant that the measured X_{Mg}'s of the majority of the M74-mix garnets are higher than the predicted values (triangles, figure 3.17): the M74 mix formed less new garnet than the M62 mixes and therefore thinner rims, the analyses of which are more prone to core contamination, and therefore produce systematically high measured X_{Mg}'s.

So, overall, the garnet compositional data suffers from lack of homogenisation but not lack of reaction. Indeed, in the M86 mixes garnet was not stable (except at the highest pressure) and the seeds dissolved away completely. The compositional data

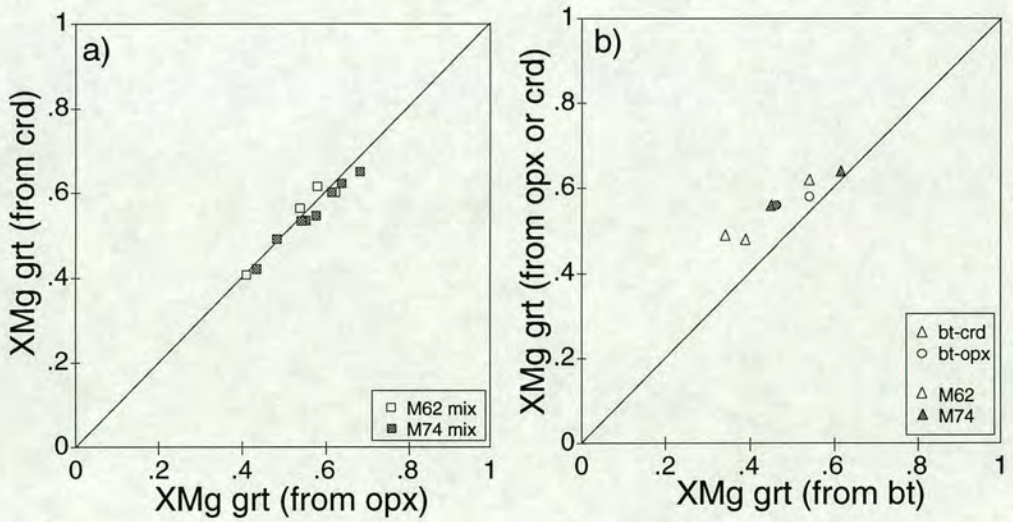

Figure 3.18. A comparison of the garnet X_{Mg}'s predicted from the X_{Mg}'s of two other co-existing phases.
a) garnet X_{Mg} predicted from orthopyroxene composition versus garnet X_{Mg} predicted from cordierite composition (grt-opx-crd assemblages).
b) garnet X_{Mg} predicted from biotite composition versus garnet X_{Mg} predicted from orthopyroxene or cordierite composition (grt-crd-bt and grt-opx-bt assemblages).

for cordierite, orthopyroxene and osumilite was believed to be much better as these were newly-grown phases which were large and well formed and easily analysed. To test the validity of this belief, garnet X_{Mg}'s calculated from cordierite and coexisting orthopyroxene X_{Mg}'s were plotted against each other (figure 3.18a). The excellent agreement of two independent Fe-Mg partitioning calibrations suggests that the cordierite and orthopyroxene crystals are at equilibrium and that the X_{Mg} for garnet predicted is an accurate estimate of the equilibrium composition.

The same approach was taken to assess the biotite data (figure 3.18b), which, like the garnet data, was difficult to collect as the crystals were rarely even as wide as 1μm. The plot shows a much poorer correlation than that in figure 3.18a. The garnet X_{Mg}'s calculated from the biotite data are consistently less magnesian than those calculated from co-existing cordierite or orthopyroxene and always further from the measured garnet composition. This may be the result of disequilibrium biotite X_{Mg}'s, as the cordierites and orthopyroxenes appear to be in equilibrium. If this were the case, then the biotite compositions should be consistently lower than their equilibrium value in order to produce less magnesian garnet X_{Mg} estimates. The biotite in all but one of the experiments increased its X_{Mg}. Therefore it seems that the experiments were quenched before the biotite could react to high enough X_{Mg}'s. This is likely given that the experiments which contained biotite were the lowest temperature runs and predominantly subsolidus, conditions which hinder full equilibration.

The discrepancy between the calculated garnet X_{Mg}'s could alternatively be due to a systematic mismatch between the biotite Fe-Mg calibration and the other calibrations: the data in figure 3.18b does seem to show a trend of higher discrepancies at lower X_{Mg}'s. However the lower X_{Mg}'s also correlate with the lowest temperatures and so an increased possibility of disequilibrium. In fact, the Fe-Mg partitioning for biotite-garnet was calibrated at lower temperatures than used in this study (Ferry and Spear 1978) and would be expected to be more reliable at those low temperatures. Therefore, it is concluded that the most likely reason for the difference in the calculated X_{Mg}'s in figure 3.18b is biotite X_{Mg} disequilibrium due to low run temperatures and the absence of melt.

Osumilite Fe-Mg partitioning.

Osumilite was first reported relatively recently (Miyashiro 1956) and is still considered a rare mineral though at least twenty-six occurrences have now been

reported (Schreyer et al., 1986, Arima and Gower, 1991, Audibert et al 1993). Consequently, very little experimental data exists on the Fe-Mg partitioning between osumilite and other phases. Figure 3.19 plots the X_{Mg}'s of osumilite and co-existing phases in the present experiments.

There is an excellent correlation between the X_{Mg}'s of the mineral pairs cordierite-osumilite and orthopyroxene-osumilite. The data presented above (figure 3.18a) shows that the cordierite and orthopyroxene in the experiments have reached Fe-Mg exchange equilibrium and so, given the excellent correlation shown in figure 3.19, the same conclusion can be extended to osumilite.

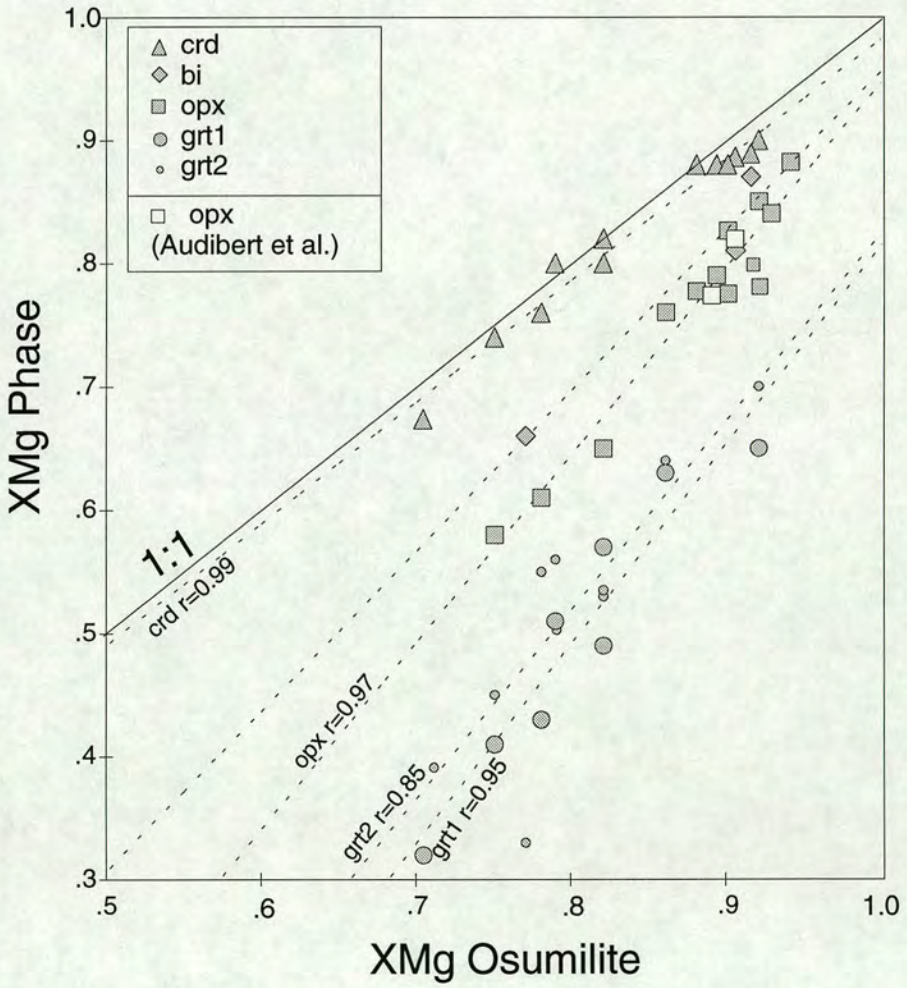

Figure 3.19. Osumilite X_{Mg} versus the X_{Mg} of co-existing phases. Linear regression lines are drawn for each set of mineral-pair data and the residuals (r) are shown. (A perfect, positive correlation has a residual of exactly one. A random scatter has a residual of zero.. The residual for the biotite-osumilite data is 0.98 but is omitted as it is based on only three data points.) "grt 1" are garnet-osumilite data points using the garnet X_{Mg}'s predicted from coexisting cordierite or orthopyroxene compositions. "grt 2" are data points using the measured garnet X_{Mg}'s. The only experimental data in the literature, two orthopyroxene-osumilite pairs from Audibert et al. (1993) are also plotted.

The larger scatter on figure 3.19 for the osumilite-grt2 (measured X_{Mg}) pairs reflects the poorer equilibration of garnet. The marked improvement in the fit of the data if the grt1 (calculated X_{Mg}) values are used suggests these values represent the equilibrium X_{Mg}'s more closely. The scarcity of biotite-osumilite pairs (three) precludes any conclusion further to that made above regarding the level of equilibration of the biotite.

Melt-crystal Fe-Mg partitioning.

The work of Ellis (1986) allows the partitioning between the melt phase and garnet, cordierite and orthopyroxene in the current experiments to be assessed (figure 3.20). The current data displays acceptable linear correlations for all the mineral-melt pairs. The data for the garnet-melt pairs uses the garnet X_{Mg}'s calculated from the X_{Mg}'s of co-existing orthopyroxene or cordierite (grt1, figure 3.21 and 3.18a).

In all three cases, the trends are significantly displaced from those reported by Ellis (1986). The present experiments imply larger values of K_D and so greater Fe-Mg partitioning. The variation of K_D with temperature is much lower than in Ellis' (1986) experiments. Furthermore, the current cordierite-melt data suggests a decrease, rather than an increase, in the Fe-Mg partitioning between those phases with increasing temperature, though this inference depends heavily on two data points at 1000°C.

The most important conclusion of Ellis (1986) was that there was a reversal in Fe-Mg partitioning between garnet and melt below 900°C at 10kb and at 1000°C at 30kb. The data shown on figure 3.20 is not consistent with this, and figure 3.22 shows how reasonable errors cannot explain the differences between the two data sets. The cause of the difference between the current work and that of Ellis (1986) is unlikely to be due to a systematic error in analysing the melt in the current experiments. Firstly, some melts could be analysed very easily when, fortuitously, large pools had segregated and these analyses were consistent with all the other data and secondly, contamination of the melt analysis with any other ferromagnesian phase would increase the X_{Mg}, not decrease it, as would be required to explain the higher K_D's of the current study. Ellis used a mix of $X_{Mg} = 0.7$ in addition to the mixes more iron-rich than in the current experiments and noted no change in K_D with X_{Mg}. It is difficult to take the discussion further without further information on Ellis' (1986) data and so the discrepancy can only be noted.

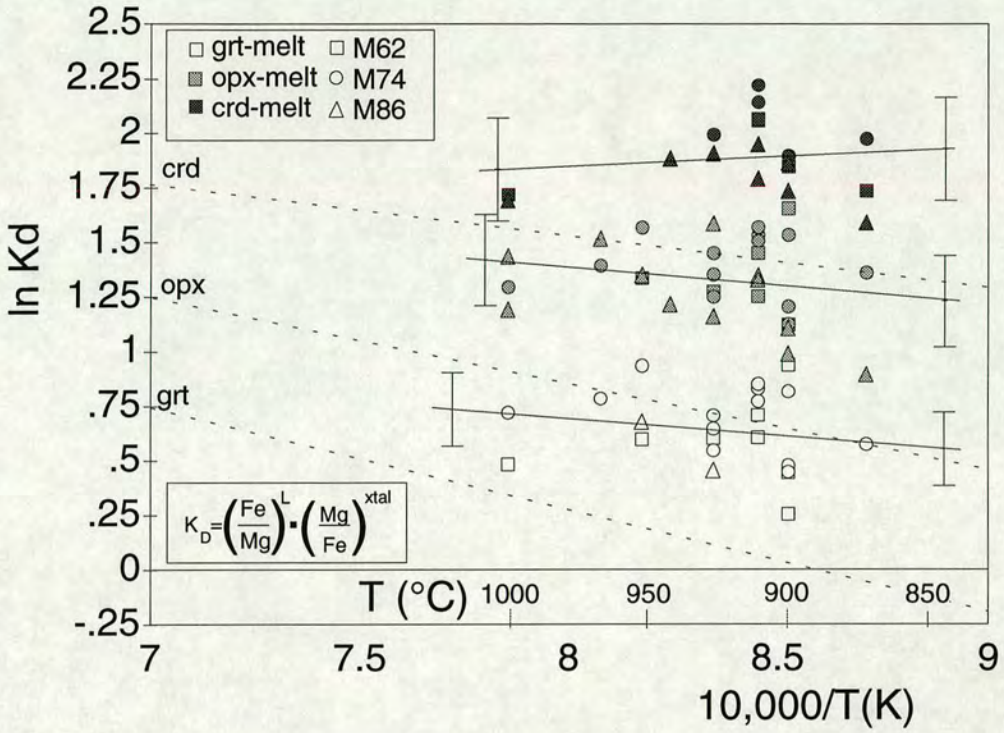

Figure 3.20. Inverse temperature versus ln K_D for co-existing garnet-melt, orthopyroxene-melt and cordierite-melt pairs. The solid lines are linear regression lines of the current data. The error bars represent an uncertainty in the X_{Mg} of each phase of ± 0.02 (c.f.table 3.3). The error in temperature is small (± 5°C) relative to the error in ln K_D and is not shown. The dashed lines are the linear trends reported by Ellis (1986) for garnet-melt, orthopyroxene-melt and cordierite-melt pairs.

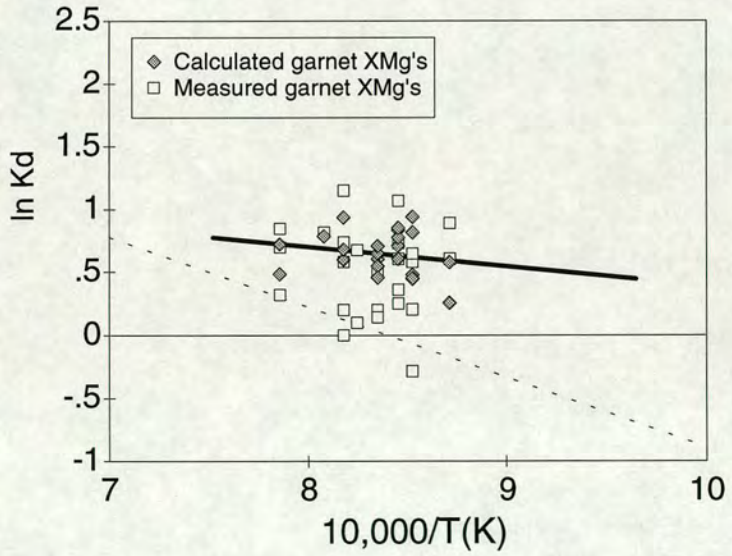

Figure 3.21. Inverse temperature versus ln K_D for Fe-Mg partitioning between garnet-melt pairs using either measured garnet X_{Mg}'s or garnet X_{Mg}' calculated from co-existing cordierite or orthopyroxene. The full line shows the trend of the data which used the calculated garnet X_{Mg}'s, and which is less scattered. The dashed line is linear relation reported by Ellis (1986) for garnet-melt pairs.

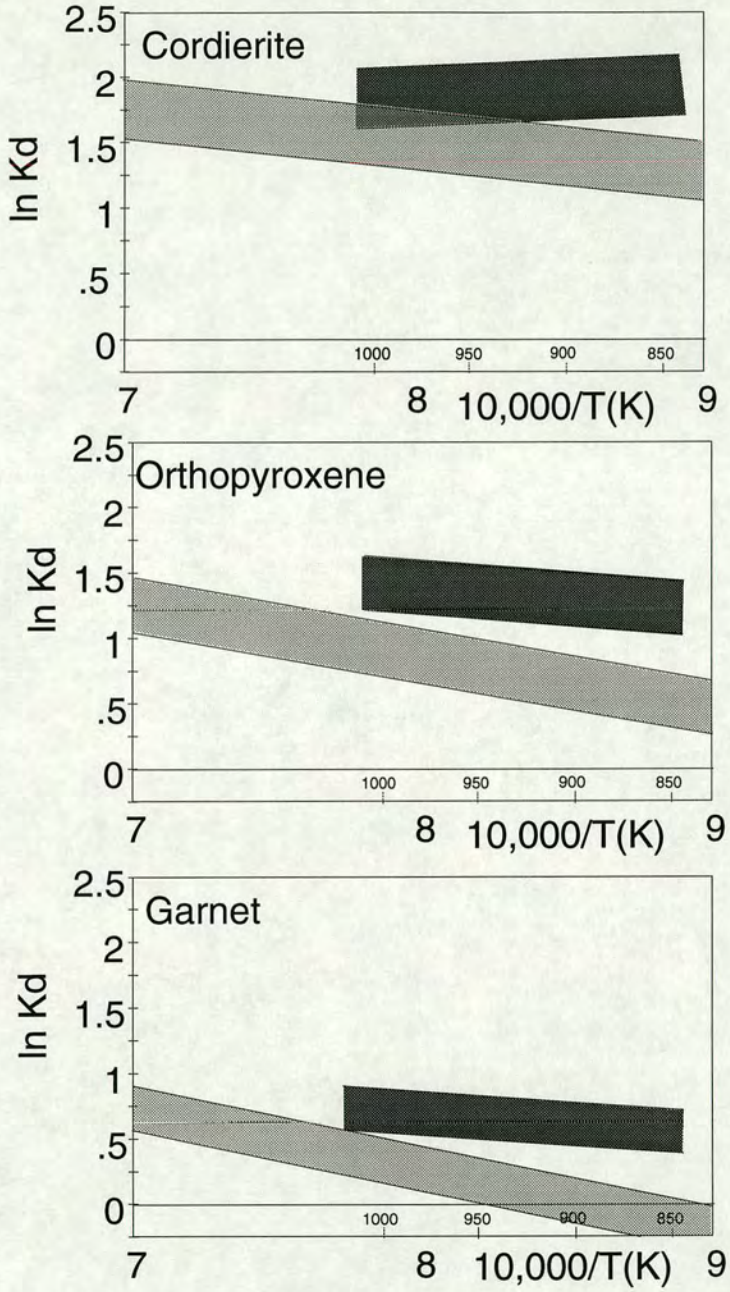

Figure 3.22. Inverse temperature versus ln K_D for cordierite-melt, orthopyroxene-melt and garnet-melt pairs. The dark-shaded areas represents the trend and error of the current data and was drawn by enclosing the area within error of the interpolated linear trend, as shown on figure 3.20. The error in temperature is much smaller than that in ln K_D. The same uncertainty was applied to the trends Ellis (1986) reported (the author gives no estimate of the uncertainty) and the resultant areas are shown lightly-shaded. No overlap at all occurs for the orthopyroxene-melt and garnet-melt pairs. A small overlap occurs for the cordierite-melt pairs.

3.5. PHASE CHEMISTRY: MELTS.

This section describes the KFMAS-component chemistry of the melts produced in the experiments and compares them to the literature. The melt compositions are similar to those in comparable studies, in particular that of Patino Douce and Johnston (1991). This suggests that the melts have equilibrated well and have been adequately analysed. Melt water-contents are considered in section 3.6.

Difficulties in analysing small volume partial-melts are a common experience and this study is not an exception. Fortunately, in this study many of the experiments produced areas of melt which could be analysed without contamination by overlapping phases. However, as these areas were small the measurement of potassium was not always reliable due to volatilisation under too powerful an electron beam. Six experiments formed very large melt-segregations which enabled the reliable measurement of potassium. There were a few experiments in which analysis of the melt phase was not possible or was seriously affected by contamination by other phases.

3.5.1 The measurement of potassium in the melt.

Before considering the melt chemistry in detail it is necessary to assess the extent to which potassium-loss affects the probe analyses. There are three aspects of the electron microprobe analytical set-up which can be varied to try and minimise potassium-loss:

1. beam current - the lower the beam current, the lower the potassium-loss;
2. counting time - the shorter the counting time, the lower the potassium-loss;
3. scanned area - the larger the scanned area, the lower the potassium-loss.

However, each of these can only be changed so far before the count rate is reduced to a such a low level that the statistical precision of the measurement is unacceptable. The maximum area that can be scanned reliably is a 10k raster[12]. The lowest reliable beam-current achievable on the electron microprobe used is 10nA.

---

[12] A 10k raster is produced by scanning the beam over a set area at 10,000-times magnification, which corresponds to an area of 10μm by 10μm. A 20k raster therefore corresponds to a 5μm by 5μm area and so on.

Figure 3.23 illustrates the relationship between counting time and scanned area. It shows that for a 10k raster there is no loss in potassium, if the count time is less than twenty seconds. Therefore all the melts in the experiments were analysed using a count time for potassium of ten seconds. Figure 3.23 suggests that analyses done with a 20k raster also may not lose potassium over the first twenty seconds. To test this, the melt in experiment D66-18 was analysed using a 10k raster (twelve individual analyses) and 20k raster (eight individual analyses). The mean weight-percent K_2O for the analyses was 9.155 compared to 8.841 respectively. This demonstrates that some potassium-loss occurs even when using a 20k raster with a count time of ten seconds and a beam current of 10nA to analyse the melt.

Whilst many of the experiments produced melt segregations which could be analysed without contamination by other phases, only a few produced segregations large enough to enable the melt to be analysed without potassium-loss, i.e. using a 10k raster. In Chapter Four (and Appendix Three) many of the phase diagrams are derived by projecting phase compositions from the melt composition. Therefore it is necessary to correct for the potassium-loss in the analyses where the melt

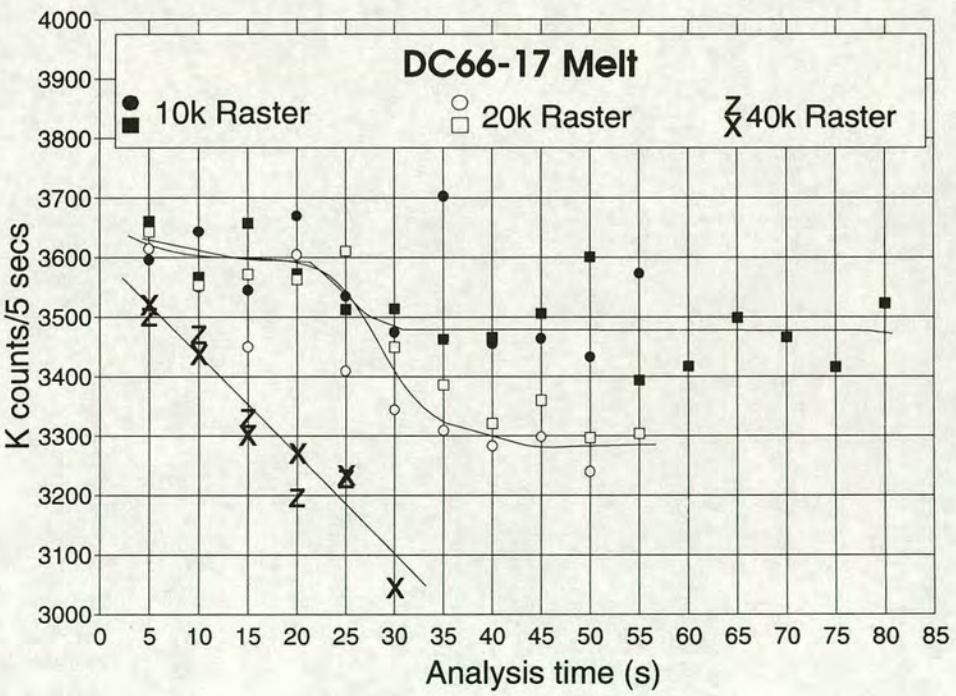

Figure 3.23. Electron microprobe counts for potassium in the melt per five seconds versus time, for various beam rasters. The melt from experiment D66-17 was used for all the data. Each symbol represents one sequence of five-second analysis-intervals on the same area of melt.

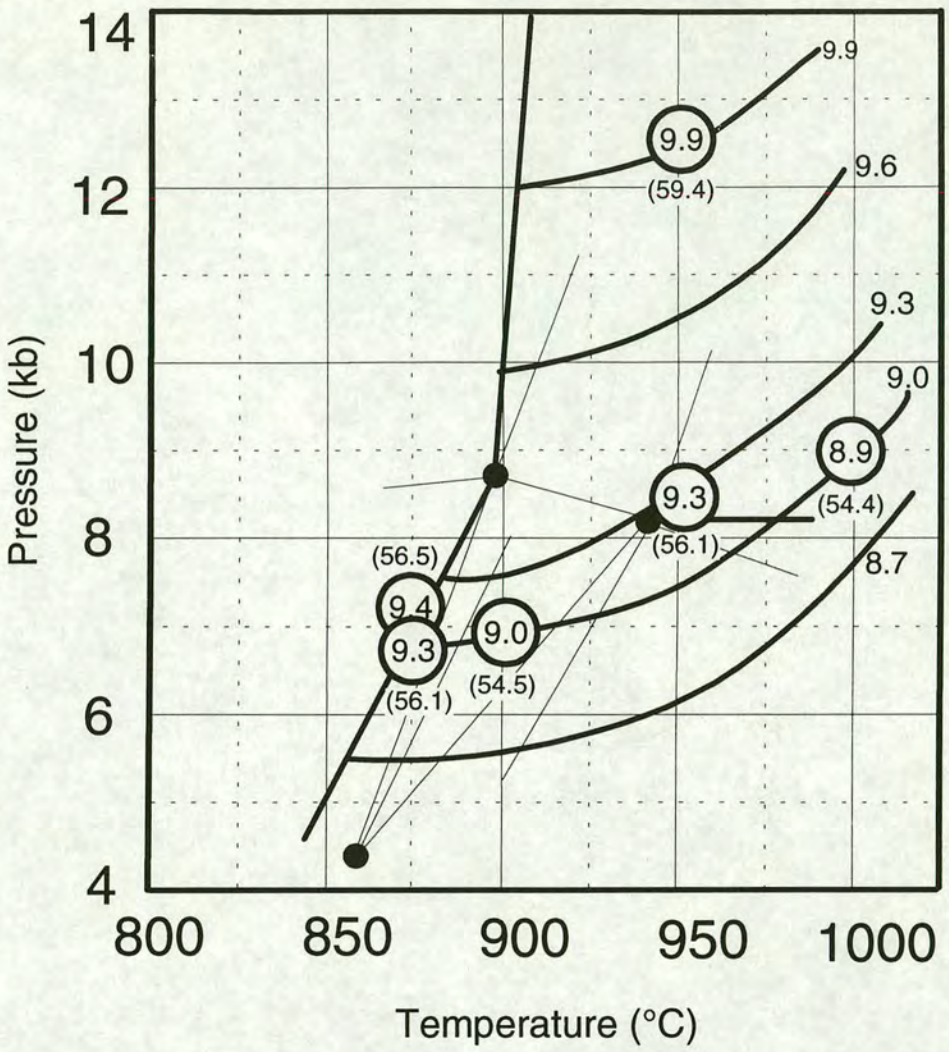

Figure 3.24. Weight percent K_2O in the melts (figures in circles) from 10k raster analyses plotted on a pressure-temperature diagram. The weight percents are from mean analyses normalised to 100% (i.e. anhydrous). On the basis of these the pressure-temperature space has been contoured (curves with figures). The figures in parentheses are the normative orthoclase contents of the melts. The straight lines and points are the univariant grid derived in Chapter Six (INSERT A), the heavier lines being the univariant solidus.

segregations were small. To do this, the pressure-temperature range of the experiments was contoured for potassium using the data collected using a 10k raster (figure 3.24). This diagram was then used to give potassium-content estimates for the melts. Given the small number of data points on figure 3.24 the estimates must be considered to have a large uncertainty, perhaps ± 0.5wt%. However, this uncertainty translates into very small differences in the positions of the projected phases in Chapter Four and these are not enough to alter the interpretation of the phase relations (see figures 4.6 and 4.7).

Table 3.9. Melts.

	D41-13*	D55-16*	D56-17*	D62-16*	D65-16*	D66-17*	D66-18*
n	7	8	7	5	6	10	12
Temperature (°C)	950	950	900	1000	1000	875	875
Pressure (kb)	12.5	8.5	7	7?	9	7	7
Oxides							
SiO2	74.271	74.329	76.462	75.568	74.895	76.705	76.825
Al2O3	14.055	13.983	12.760	13.532	14.285	12.601	12.615
FeO	1.129	1.674	1.205	1.076	1.292	0.935	0.499
MgO	0.679	0.661	0.494	0.781	0.547	0.382	0.453
CaO	0.027	0.081	0.088	0.088	0.069	0.068	0.139
K2O	9.838	9.271	8.990	8.955	8.912	9.310	9.469
Na2O	n.a.	n.a.	n.a.	n.a.	n.a.	n.a.	n.a.
Anhydrous Total	90.162	100.000	91.010	91.045	91.088	90.691	90.532
Raw Total	**95.984**	**95.142**	**94.927**	**96.484**	**95.249**	**97.578**	**96.690**
CIPW Norm							
Quartz	37.23	39.60	42.59	41.89	41.40	41.47	40.670
Corundum	3.42	3.89	2.92	3.75	4.60	2.43	2.130
Orthoclase	59.21	56.10	54.05	53.92	53.65	55.75	56.500
Albite	n.a.	n.a.	n.a.	n.a.	n.a.	n.a.	0.000
Anorthite	0.14	0.41	0.44	0.44	0.35	0.34	0.700
Norm total	100.00	100.00	100.00	100.00	100.00	99.99	100.000
XMg	0.517	0.413	0.422	0.453	0.430	0.422	0.618

	D41-14	D41-15	D43-13	D43-14	D44-15	D47-16	D47-17
n	4	3	5	5	4	4	4
Temperature (°C)	950	950	900	900	940	940	940
Pressure (kb)	12.5	12.5	10	10	7	7	7
Oxides							
SiO2	75.858	75.162	76.136	76.076	76.572	75.331	75.410
Al2O3	13.708	14.334	13.400	13.399	13.334	14.268	14.159
FeO	0.664	0.455	0.978	0.845	1.007	1.557	1.540
MgO	0.758	0.589	0.578	0.598	0.646	0.451	0.999
CaO	0.026	0.046	0.012	0.042	0.228	0.057	0.082
K2O	8.892	9.026	8.806	8.939	8.083	8.265	7.743
Na2O	0.093	0.387	0.089	0.101	0.129	0.070	0.067
Anhydrous Total	91.015	90.587	91.104	90.960	91.787	91.665	92.190
Raw Total	**94.177**	**94.378**	**94.985**	**94.419**	**95.560**	**96.326**	**98.006**
CIPW Norm							
Quartz	41.83	38.67	42.55	41.79	45.14	44.06	46.390
Corundum	3.94	3.88	3.76	3.53	4.02	5.21	5.660
Orthoclase	53.31	53.90	52.86	53.60	48.57	49.84	46.950
Albite	0.80	3.31	0.77	0.87	1.11	0.60	0.580
Anorthite	0.13	0.23	0.06	0.21	1.15	0.29	0.420
Norm total	100.01	99.99	100.00	100.00	99.99	100.00	100.000
XMg	0.670	0.697	0.514	0.558	0.527	0.340	0.535

Table 3.9. Mean melt analyses, in weight percent oxides normalised to 100% anhydrous total. The raw (un-normalised) total is also given. The CIPW normative phase abundances (%) are calculated ignoring the FeO and MgO content of the melt. The first seven analyses (marked with *) were obtained using a large area electron beam scan (10k raster) and have reliable K2O values. The other analyses were obtained using smaller area scans and may have suffered potassium loss.
"n" - number of analyses. "n.a." - element not analysed for. All iron as Fe2+.

Table 3.9. Melts.

	D47-18	D48-14	D48-15	D48-17	D51-16	D52-17	D52-18
n	4	3	4	3	3	5	5
Temperature (°C)	940	925	925	925	875	910	910
Pressure (kb)	7	12.5	12.5	12.5	5	5	10
Oxides							
SiO2	77.199	75.874	76.667	76.432	78.792	76.626	76.246
Al2O3	13.208	13.841	13.627	14.958	13.523	13.634	13.772
FeO	0.835	0.783	0.402	0.545	1.814	0.871	0.550
MgO	0.524	0.885	0.709	0.618	0.372	0.646	0.599
CaO	0.159	0.034	0.053	0.039	0.097	0.060	0.121
K2O	7.996	8.583	8.542	7.406	5.309	8.101	8.634
Na2O	0.079	n.a.	n.a.	n.a.	0.094	0.063	0.077
Anhydrous Total	91.925	91.417	91.458	92.593	94.597	91.837	91.289
Raw Total	**97.509**	**94.910**	**94.879**	**95.714**	**96.673**	**96.356**	**96.086**
CIPW Norm							
Quartz	46.43	43.68	44.35	48.57	59.01	45.82	42.99
Corundum	4.19	4.56	4.33	6.95	7.61	4.72	4.13
Orthoclase	47.90	51.58	51.05	44.28	32.08	48.61	51.62
Albite	0.68	n.a.	n.a.	n.a.	0.81	0.54	0.66
Anorthite	0.80	0.17	0.27	0.20	0.49	0.30	0.61
Norm total	100.00	99.99	100.00	100.00	100.00	99.99	100.01
XMg	0.527	0.668	0.759	0.669	0.267	0.570	0.660

	D54-16	D54-17	D54-18	D55-17	D55-18	D56-16*	D56-18
n	4	4	2	3	2	5	2
Temperature (°C)	925	925	925	950	950	900	900
Pressure (kb)	10	8.75	8.75	8.5	8.5	7	7
Oxides							
SiO2	74.523	73.571	74.243	71.287	74.182	77.081	76.387
Al2O3	17.663	17.731	17.132	19.724	16.702	12.622	12.947
FeO	1.097	0.910	0.691	1.202	0.727	3.202	0.820
MgO	0.548	0.503	0.597	0.497	0.927	0.870	0.529
CaO	0.047	0.064	0.199	0.102	0.237	0.078	0.299
K2O	6.046	7.139	7.076	7.113	7.130	6.148	8.889
Na2O	0.075	0.082	0.063	0.076	0.095	0.000	0.129
Anhydrous Total	93.878	92.780	92.862	92.812	92.774	93.852	90.982
Raw Total	**95.916**	**95.675**	**96.571**	**97.189**	**95.789**	**94.059**	**94.228**
CIPW Norm							
Quartz	51.70	46.29	46.97	44.15	46.60	55.65	41.54
Corundum	11.09	9.89	9.12	11.92	8.54	6.07	2.60
Orthoclase	36.33	42.79	42.36	42.76	42.84	37.87	53.25
Albite	0.65	0.70	0.54	0.65	0.82	0.00	1.11
Anorthite	0.24	0.32	1.00	0.51	1.20	0.40	1.50
Norm total	99.99	99.99	100.00	100.00	99.99	100.00	100.00
XMg	0.470	0.497	0.606	0.425	0.694	0.326	0.535

Table 3.9 continued. Mean melt analyses, in weight percent oxides normalised to 100% anhydrous total. The raw (un-normalised) total is also given. The CIPW normative phase abundances (%) are calculated ignoring the FeO and MgO content of the melt. The analyses were obtained using smaller area scans and may have suffered potassium loss. Experiment DC56-16 (marked *) contained more initial water than the other experiments (see section 3.6.3) and consequently melted more.
"n" - number of analyses. "n.a." - element not analysed for. All iron as Fe2+.

Table 3.9. Melts.

	D57-16	D57-17	D57-18	D59-17	D59-18	D60-16	D60-17
n	1	2	2	4	4	3	4
Temperature (°C)	910	910	910	965	965	900	900
Pressure (kb)	8	8	8	8	8	6	6
Oxides							
SiO2	74.323	70.721	78.425	77.181	76.521	76.483	77.166
Al2O3	20.802	23.466	14.962	15.519	13.441	13.058	12.789
FeO	1.014	1.230	0.719	1.102	0.947	1.775	1.280
MgO	0.386	0.466	0.633	0.499	0.555	0.444	0.433
CaO	0.039	0.081	0.293	0.084	0.269	0.167	0.090
K2O	3.387	3.865	4.897	5.563	8.156	7.972	8.178
Na2O	0.050	0.171	0.072	0.051	0.112	0.102	0.065
Anhydrous Total	96.564	95.963	95.031	94.385	91.732	91.926	91.757
Raw Total	**98.365**	**97.985**	**95.046**	**94.541**	**96.835**	**96.470**	**95.687**
CIPW Norm							
Quartz	61.85	55.71	59.44	56.32	44.75	46.04	46.09
Corundum	17.22	19.18	9.13	9.41	4.00	4.05	3.73
Orthoclase	20.30	23.23	29.34	33.41	48.93	48.18	49.17
Albite	0.43	1.47	0.62	0.44	0.96	0.88	0.56
Anorthite	0.20	0.41	1.47	0.42	1.35	0.85	0.45
Norm total	100.00	100.00	100.00	99.99	100.00	100.00	100.00
XMg	0.405	0.403	0.610	0.446	0.511	0.308	0.376

	D60-18	D62-18	D64-16	D64-17	D64-18	D65-17	D65-18
n	3	5	3	3	3	3	4
Temperature (°C)	900	1000	910	910	910	1000	1000
Pressure (kb)	6	7?	9	8	9	9	9
Oxides							
SiO2	77.155	77.008	75.106	74.472	75.612	76.113	76.385
Al2O3	12.892	12.858	15.065	16.476	14.054	14.714	14.299
FeO	0.790	0.574	1.183	1.203	0.714	0.972	0.603
MgO	0.573	0.654	0.548	0.531	0.581	0.553	0.602
CaO	0.244	0.106	0.160	0.144	0.335	0.062	0.132
K2O	8.275	8.800	7.939	7.175	8.703	7.587	7.980
Na2O	0.071	n.a.	n.a.	n.a.	n.a.	n.a.	n.a.
Anhydrous Total	91.654	91.200	92.062	92.826	91.296	92.413	92.020
Raw Total	**95.260**	**97.358**	**94.190**	**96.089**	**93.892**	**97.846**	**97.484**
CIPW Norm							
Quartz	45.16	43.64	45.16	47.53	42.13	47.67	46.12
Corundum	3.42	3.18	6.29	8.60	4.08	6.49	5.49
Orthoclase	49.58	52.65	47.74	43.15	52.11	45.53	47.73
Albite	0.61	n.a.	n.a.	n.a.	n.a.	n.a.	n.a.
Anorthite	1.23	0.53	0.81	0.73	1.68	0.31	0.66
Norm total	100.00	100.01	100.00	100.00	100.00	99.99	100.00
XMg	0.564	0.670	0.452	0.441	0.592	0.504	0.640

Table 3.9 continued. Mean melt analyses, in weight percent oxides normalised to 100% anhydrous total. The raw (un-normalised) total is also given. The CIPW normative phase abundances (%) are calculated ignoring the FeO and MgO content of the melt. The analyses were obtained using smaller area scans and may have suffered potassium loss.
"n" - number of analyses. "n.a." - element not analysed for. All iron as Fe2+.

3.5.2 Melt chemistry and comparison to the literature.

The mean melt analyses from the experiments are presented in table 3.9, normalised to 100% anhydrous. Also given are the CIPW normative mineral-contents calculated ignoring the iron and magnesium, which generally total less than two weight percent of the melt. In the following, the current data is compared with several other studies, some conducted on natural compositions, some on synthetic compositions, all at a variety of pressures, temperatures and activities of water. The purpose of this comparison is to assess whether the current melts are realistic equilibrium melts, not to diagnose the chemical behaviour of the melt, and so the differences in the various studies do not prevent useful comparison. The most similar study to the current one is that by Patino Douce and Johnston (1991). The pressure and temperature ranges are very similar, both are water-undersaturated and whilst Patino Douce and Johnston (1991) used a less-siliceous/more-aluminous natural metapelite with a lower X_{Mg}, the bulk compositions are broadly similar (see below). The fact that synthetic bulk compositions and natural bulk compositions give very similar melt compositions is particularly encouraging[13].

The melts from this study are plotted on a normative mineral diagram in figure 3.25a. The analyses cluster along a trend of increasing normative-quartz and -corundum. The position of the arrow indicating the trend of increasing potassium-loss shows that these normative increases are mostly due to potassium-loss during analysis. However, the 10k raster scan melts parallel this trend for a short way showing that there is some genuine variation also, from $kfs_{60}qz_{37.5}cor_{2.5}$ to $kfs_{54}qz_{42}cor_{4}$.

The melts produced in five other studies of melting of metapelitic compositions are also plotted in figure 3.25 and all show similar trends, with the exception of the data of Le Breton and Thompson (1998). Their experiments were all done at 850°C, 10kb but the data is so wildly scattered that the experiments must either have been very far from equilibrium or, more probably, poorly analysed. There are differences in detail between the studies but the overall comparability of all the data is good suggesting that the analysed SiO_2-Al_2O_3-K_2O contents of the melts in the current study are reasonable. The data from this study suggests that the trends seen are partly due to

[13] The natural rock used by Patino Douce and Johnston (1991) had significant CaO, Na_2O, TiO_2, F and MnO in addition to the KFMASH components of the synthetic system used in the current experiments.

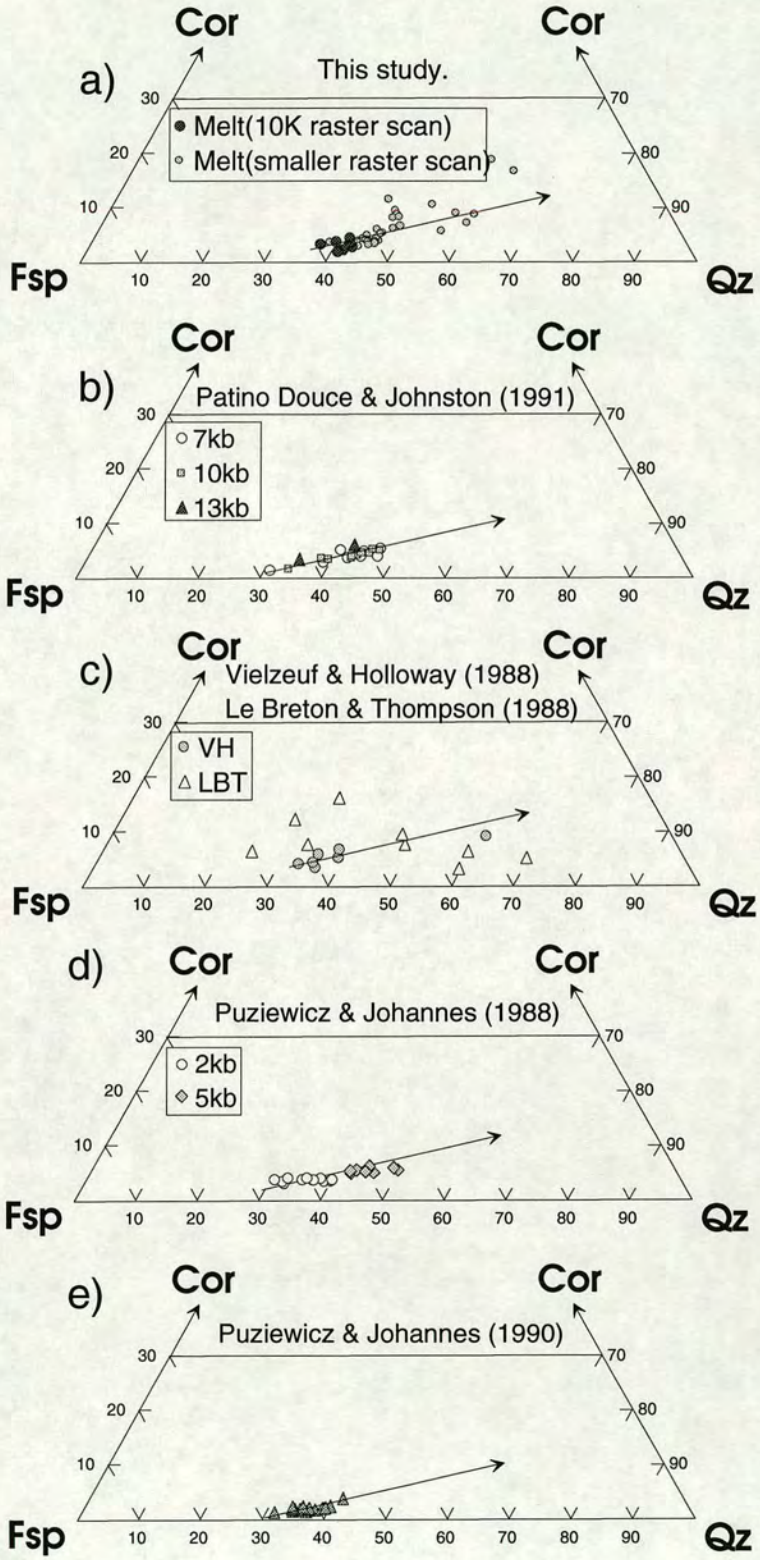

Figure 3.25. Normative mineral abundances in melts (as calculated in table 3.9) plotted on a quartz-corundum-feldspar diagram. The percentage feldspar is the total normative feldspar (i.e. orthoclase + albite + anorthite). The arrow on each diagram represents the direction in which a melt composition would evolve if it suffered potassium-loss during electron-microprobe analysis. Data from the literature is plotted as labelled.

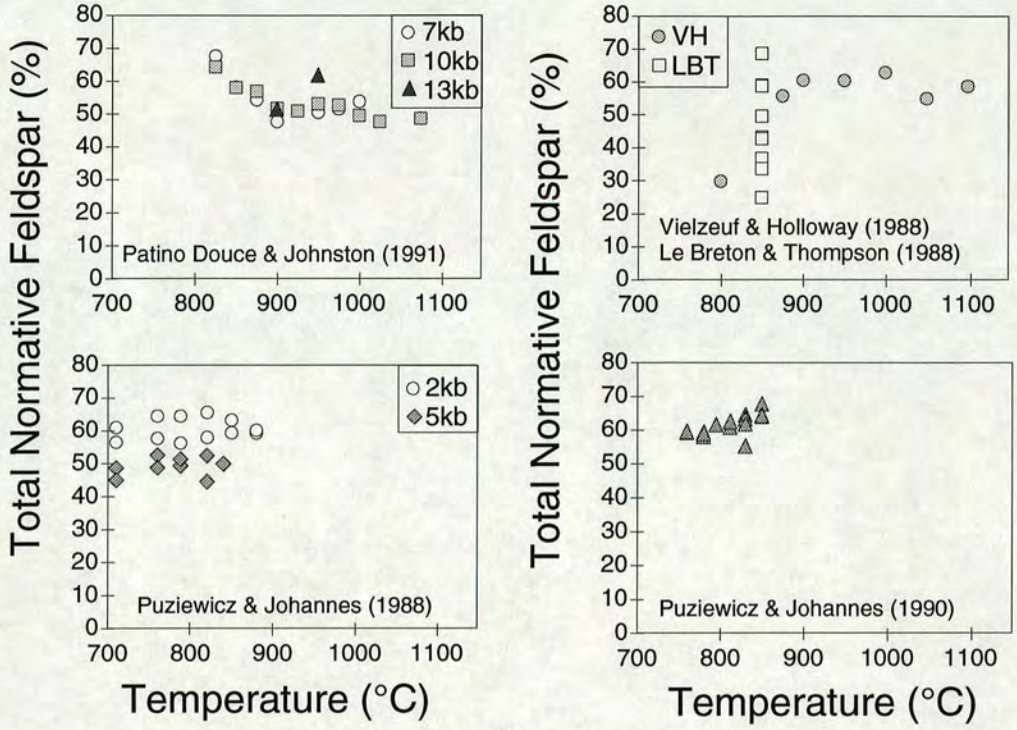

Figure 3.26. Total normative feldspar in melts (i.e. orthoclase + albite + anorthite) versus temperature for various published studies. Compare with figure 3.24.

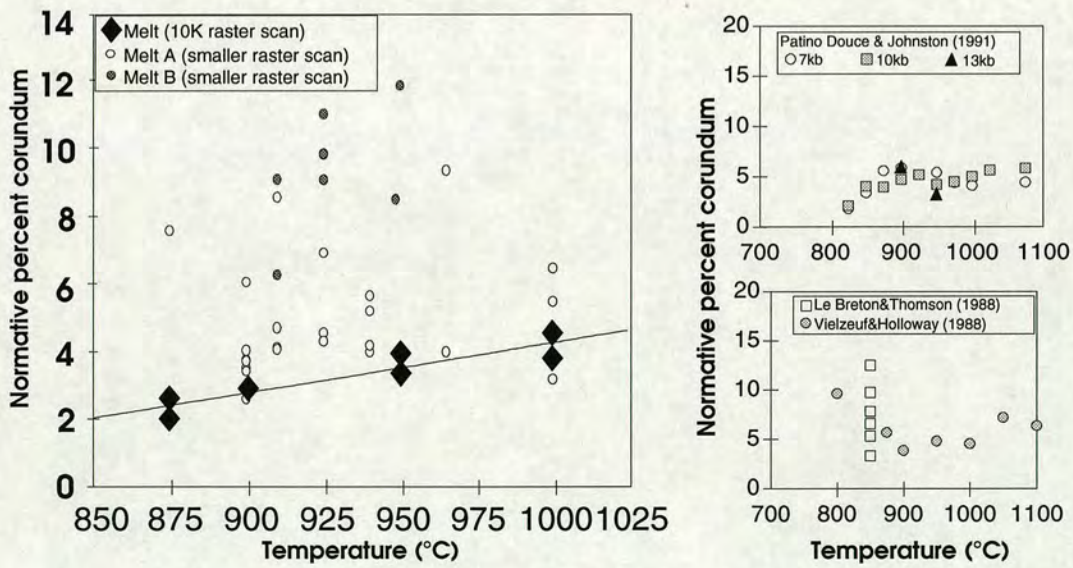

Figure 3.27. Normative corundum in the melts versus temperature, for all pressures. The data from the current study is plotted on the larger graph. The high normative corundum from melts analysed using small area scans is a result of potassium loss. "Melt B" signifies a mean melt analysis with higher than normal Al_2O_3 (see table 3.9) - potassium-loss and aluminium contamination have combined to give a very high normative corundum content. These melts are usually the smallest volume fraction melts, i.e. the most difficult to analyse. "Melt A" signifies a mean melt analysis which has a normal Al_2O_3 content, and so has a high corundum content solely as a result of potassium-loss. Data from the literature is shown for comparison.

potassium-loss during electron probe analysis: only Patino Douce and Johnston (1991) comment on potassium-loss at all.

The total normative feldspar in the melts is plotted versus temperature in figure 3.26 and the data of Patino Douce and Johnston (1991) shows a decrease with temperature, as does the current data (illustrated in figure 3.24). The small but significant increase in normative feldspar with pressure in the current melts (figure 3.24) is not reproduced by any of the studies in figure 3.26 but has been demonstrated for water-saturated melts (e.g. Luth 1976).

The peraluminosity (normative-corundum content) of the melt is a linear function of temperature but is independent of pressure (figure 3.27). These features are also seen

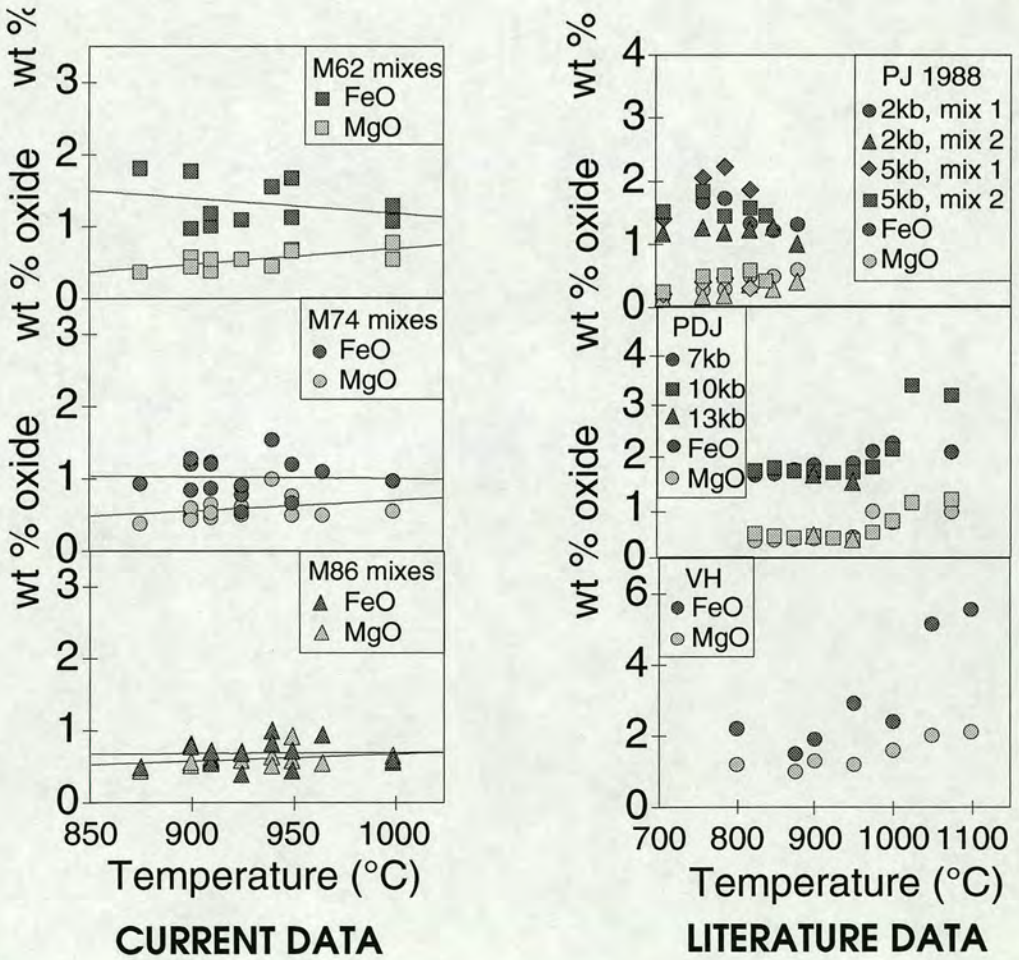

Figure 3.28. Weight percent FeO and MgO in the melts versus temperature, for all pressures. The graphs on the left present the current data, for each bulk composition used. There was insufficient data at any one pressure to produce isobaric plots. The graphs on the right present data from the literature - "PJ 1988" - Puziewicz and Johannes (1988), "PDJ" - Patino Douce and Johnston (1991), "VH" - Vielzeuf and Holloway (1988).

in the data of Patino Douce and Johnston (1991). Holtz et al. (1992b) found their melt coexisting with phlogopite to contain three percent normative corundum. The two to four percent normative corundum-content of the melts (analysed with a 10k raster) in this study of is likely to be close to the equilibrium value.

The iron and magnesium contents of the melt are low (figure 3.28) and of the same magnitude as the other studies, though Vielzeuf and Holloway (1988) report rather higher amounts of iron and magnesium. In the current experiments the variation in FeO and MgO contents of the melts corresponds to the X_{Mg} of the melt and so with increasing pressure (figure 3.29) and temperature (figure 3.28) the amount of FeO decreases or remains approximately the same while the amount of MgO increases. In contrast, the data of Patino Douce and Johnston (1991) does not vary in this way but remains approximately constant until biotite is lost at about 1000°C. The data of Vielzeuf and Holloway (1988) shows a gradual increase of MgO with temperature, though the FeO data is less consistent. The apparent indifference of the

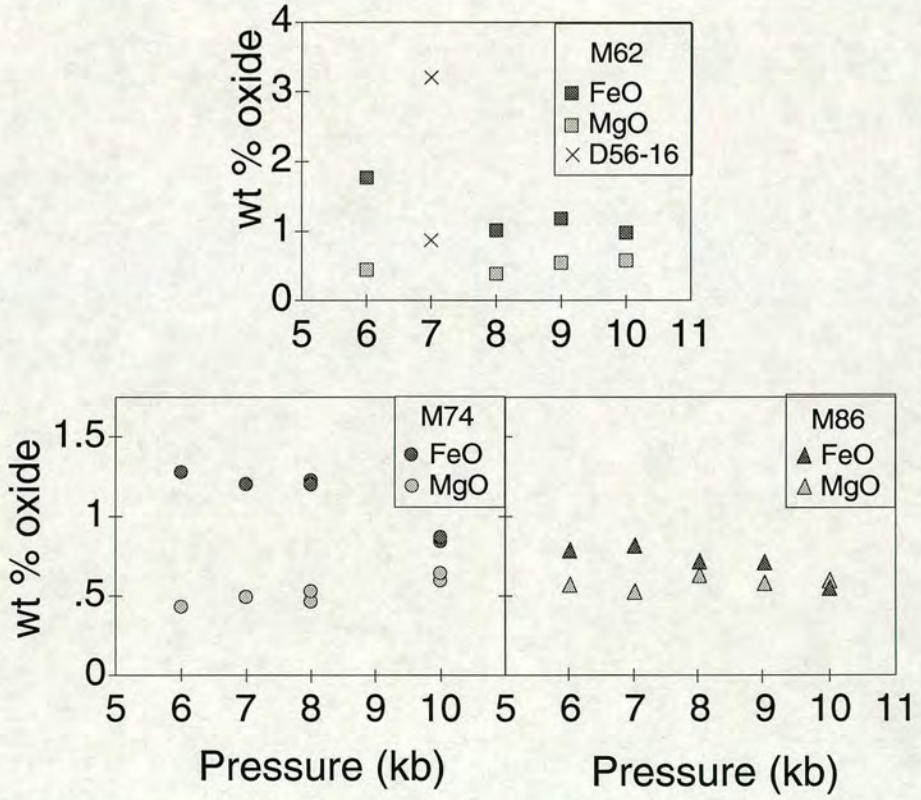

Figure 3.29. Weight percent FeO and MgO in the melts versus pressure for experiments run between 900 and 910°C. The data is shown for each bulk composition. Experiment D56-16 contained more water than the others. It therefore melted to a greater extent, leaving an assemblage of cordierite, orthopyroxene and melt only.

ferromagnesian content of the current melts to variations in phase assemblage demonstrates that no one phase is dominating the chemistry of the melt. The consistency of the data suggests a close approach to equilibrium. In the study of Patino Douce and Johnston (1991) the biotite (which finally reacts out at 975°C) controls the chemistry of the co-existing melt more strongly because these are the most abundant ferromagnesian phases.

3.6 PHASE CHEMISTRY: WATER-CONTENTS OF THE HYDROUS PHASES.

The experimental phases were analysed by electron microprobe, the only technique with sufficient resolution, and so water was not measured directly. Three hydrous phases occur in the experiments - melt, cordierite and biotite - and in only two of these is water content likely to be highly variable - melt and cordierite. Water-contents *were* measured directly in one, atypical experiment, by Dr S.Harley using Secondary Ion Mass Spectrometry (see section 3.6.3).

The reason for estimating the water-contents is to enable that component to be accounted for in the three-component projections used in Chapter Four. It will be shown later that, for the most of the projections used, the water-contents are sufficiently constrained for the phase relations to be confidently derived.

Water-content estimates are commonly made by equating the weight-percent deficiency (from 100%) in an electron microprobe analysis directly with the amount of water present. In this study the data thus derived are inconsistent over the investigated pressure-temperature range and usually significantly higher than other estimates (e.g. compare raw melt totals in table 3.9 with figure 3.32 below) and are therefore not used. The lack of consistency in the data results from the very small size of the phases and the analytical difficulties associated with this. Deriving water-contents from low probe totals is particularly dangerous for the melts, which, if not analysed over a sufficiently large area, will suffer potassium-loss.

3.6.1 Water-content of biotite.

Biotite is frequently assumed to have ideal water-contents (i.e. four moles of water per twenty-two oxygens) and indeed this assumption is made here, in the absence of any evidence to the contrary. However, recent work (Dyar et al. 1993) has shown the

imprudence of assuming a standard water stoichiometry for biotites. Substitutions and de-hydroxylation can occur, lowering the water-content of the biotite from the ideal, but biotites are also reported which have higher water-contents than the ideal. The biotites used in the current experiments were synthesised under water-saturated conditions but, given the lack of data, it would be unwise to speculate on whether this would lead to a high water-content. It is important to be aware of the uncertainty in the water-content of the biotite because this leads to uncertainty in the bulk-water contents of the mixes, as biotite is the only source of water in these. The uncertainty in the water-content of the biotite is estimated at ± 10% relative, about 0.4wt% or 0.4 moles of water per twenty-two oxygens. This uncertainty is taken into account in the modal abundance calculations in the following section (figure 3.30).

3.6.2 Water-content of the melt.

This is the most important phase water-content in this study. This is because it is potentially the most variable and is most likely to affect the three-component projections used to define and interpret the phase relations.

Estimation of melt water-content by modal analysis..

Estimates of the water-contents of some melts were possible using a mass-balance approach combined with point-counting, illustrated and explained in figure 3.30. The only compositional parameters which are unknown are the water-contents of the hydrous phases and so, if only one hydrous phase is present (i.e. melt) modal abundances can be calculated for a range of water-contents[14]. As the modal abundance of the melt, quartz and K-feldspar vary significantly with the melt water content, modal abundances obtained from point-counting of back-scattered electron photomicrographs (table 3.10) can then be used to estimate the water-content of the melt. Limiting the application of this method is the poor quality of many of the photomicrographs - many of the experiments contain phases which are too close in contrast or too small in size to be imaged with sufficient resolution for point-counting. The five experiments for which estimates have been made (table 3.11) were chosen because they produced the best photomicrographs.

[14] If two hydrous phases co-exist in the experiment, e.g. D60-17 (table 3.10), then a water partitioning coefficient must be assumed (see section 3.6.3).

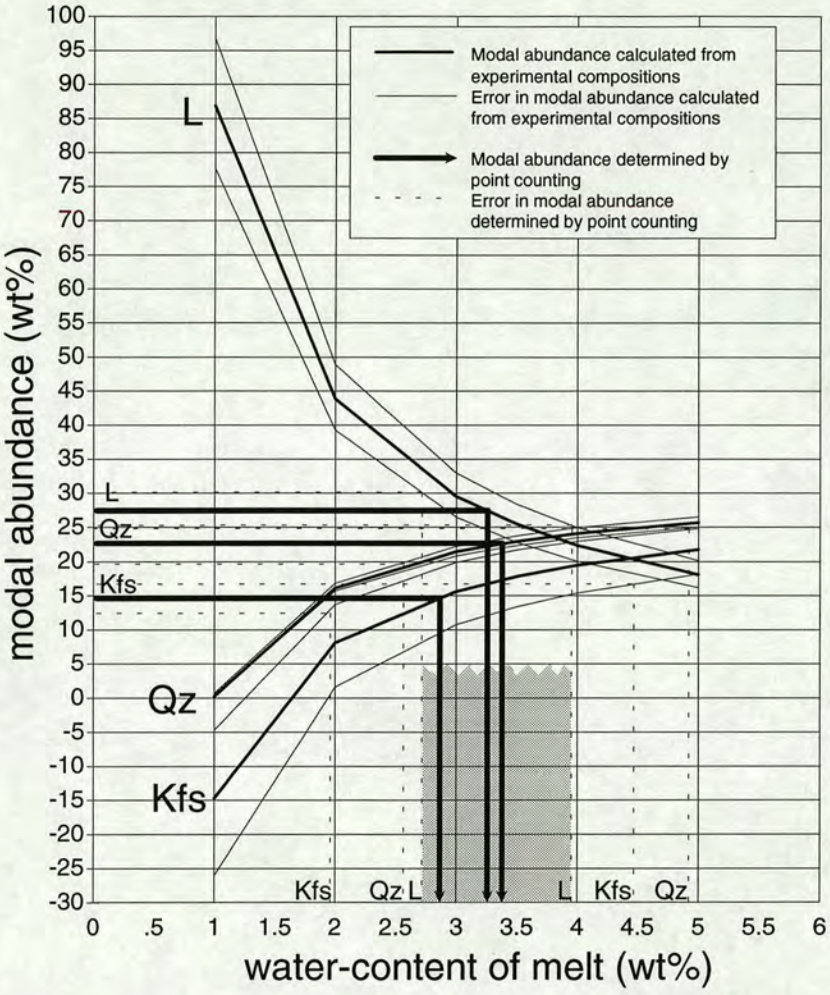

EXAMPLE OF MELT WATER-CONTENT ESTIMATION BY MODAL ANALYSIS.

Figure 3.30. Modal abundance of phases versus water-content of the melt (both in weight percent) for experiment D48-14. Except for the water-content of the melt, all the compositional parameters of the phases are known, as is the bulk composition of the experiment. Therefore modal abundances can be calculated by mass balance for a range of water-contents. The arrowed, heaviest lines show how point-counted modes (table 3.10) can then be used to estimate the water-content of the melt phase. The estimate of the melt water-content derived here is 3.3 ± 0.65 wt% and is illustrated by the shaded area. The uncertainty in the estimate is taken to be the maximised combination of the uncertainties in the point-counted mode and the calculated mode for the melt; this encompasses the estimates derived from quartz and feldspar.

Note on uncertainties. Each compositional parameter has an associated uncertainty but calculations are only significantly sensitive to the largest, which are:

a) uncertainty in water-content of starting mix (± 10% relative),

b) uncertainty in potassium-content of starting mix (± 10% relative),

c) uncertainty in potassium-content of melt (± 5% relative).

Therefore these are taken to account for all the uncertainty and are combined to maximise the uncertainty margins (thinnest curves) in the figure. The modes have zero residuals as six phases exist in a six component system (KFMASH).

The uncertainty in the point-counted modes (table 3.10) is taken to be ± 2.5%.

Garnet, orthopyroxene and sillimanite occur in the experiment but do not vary significantly with the water-content of the melt and so are left off the diagram, to enhance the clarity.

The phase composition data required for the calculation of modal abundances are given in tables 3.4 to 3.9.

Table 3.10. Modal Abundances

	D43-13	D43-14A	D43 14B	D48-14	D48-15
Points counted	844	817	814	848	842
VOLUME PERCENT					
Garnet	19.3	12.7	10.8	20.1	6.1
Orthopyroxene	5.8	11.4	11.8	2.2	15.4
K-feldspar	5.8	15.3	16.1	18.5	22.0
Quartz	22.0	24.5	22.5	22.7	0.0
Sillimanite	6.8	8.2	7.9	11.8	14.4
Melt	40.0	27.9	30.9	24.6	41.3
WEIGHT PERCENT					
Garnet	26.0	16.1	13.8	25.8	8.0
Orthopyroxene	6.5	13.2	13.8	2.5	17.6
K-feldspar	5.0	13.6	14.4	16.2	20.4
Quartz	19.7	22.6	20.9	20.6	0.0
Sillimanite	7.5	9.2	9.0	13.1	16.3
Melt	35.3	25.2	28.1	21.9	37.6
Mean Density	2.95	2.88	2.86	2.93	2.86

	D51-16		D60-17
Points counted	769		776
VOLUME PERCENT			
Garnet	7.8	Garnet	7.2
K-feldspar	5.8	Cordierite	5.3
Osumilite	41.5	Quartz	19.7
Quartz/cordierite	12.0	Osumilite	39.6
Melt	32.9	Melt	28.2
WEIGHT PERCENT			
Garnet	11.6	Garnet	10.6
K-feldspar	5.5	Cordierite	5.0
Osumilite	40.4	Quartz	19.2
Quartz/cordierite	11.0	Osumilite	38.0
Melt	31.9	Melt	27.0
Mean Density	2.68		2.71

Table 3.10. Modal abundances point-counted from photomicrographs for six experiments. The weight percent is calculated from the volume percent using the following densities (g/cm3); pyrope 3.58, almandine 4.32, enstatite 3.21, orthoferrosillite 3.96, K-feldspar 2.56, quartz 2.65, sillimanite 3.25, Mg-cordierite 2.53, Fe-cordierite 2.78, osumilite 2.6, melt (i.e. glass), 2.6. All from Deer, Howie and Zussman (1968) except osumilite, from Grew (1982).
In experiment D51-16, it was not possible to distinguish the quartz and cordierite crystals and so they were counted together. D43-14A and D43-14B are repeat counts of the same photograph to test the precision of the data.

Estimation of the melt water-content by modelling.

Using the experimental work from other studies in which the water-content of the melt has been determined directly, with some theoretical considerations, a model can be derived which applies to the current experiments. It is unlikely that the small amounts of iron and magnesium in the melts will significantly affect the SiO_2-Al_2O_3-K_2O-H_2O chemistry of the melts and so a eutectic quartz-orthoclase-water (qz-or-H_2O) system is considered. As long as quartz and orthoclase coexist with the melt, the diagram will be applicable: if one phase is absent, there will be less melt with a higher water-content. Holtz and Johannes (figure 2, 1993) derive a diagram which shows liquidus curves for haplogranitic (i.e. qz-or-H_2O *and* albite) eutectic melts with specified water-contents[15]. These curves give the water-contents of melts produced in water-undersaturated conditions and are calculated from a knowledge of three sets of data;

1. the pressure-temperature position of the water-saturated solidus,
2. the solubility of water in eutectic melts at a given pressure and temperature,
3. the amount of water in the melt at the liquidus.

An analogous diagram to that of Holtz and Johannes (1993) is derived in figure 3.31 for the qz-or-H_2O system and serves as a model for the water-contents of the melts in the experiments.

	Pressure (kb)	**Temperature (°C)**	**Melt-water content**
D51-16	5	875	2.4 ± 0.4
D60-17A	6	900	2.0 ± 0.5
D43-13	10	900	2.6 ± 0.5
D43-14	10	900	2.9 ± 0.8
D48-14	12.5	925	3.3 ± 0.6

Table 3.11. Melt water-contents from modal abundance analysis as described in the text and illustrated in figure 3.30. D43-13 and D43-14 are different experiments from the same run. The mixes are identical except for the magnesium/iron ratio and if, as expected, the ferromagnesian components do not significantly affect the melt chemistry, the estimates should be the same: they are consistent within the uncertainties. N.B. D60-17A did not have K-feldspar (due to water-contamination) and so the melt is not a eutectic one. The melt-volume may be lower than for a eutectic melt and the water-content may be correspondingly high. Cropped versions of the photomicrographs counted for experiments D43-14, D48-14, D51-16 and D60-17A are reproduced as plates 2b, 3a, 9a and 9b.

[15] The model of Nekvasil and Burnham (1987) and Nekvasil (1988) might be used to calculate similar data but Johannes and Holtz (1990) and Holtz et al. (1992b) found that their experimental results, used in part in Holtz and Johannes (1993), were different from the predictions.

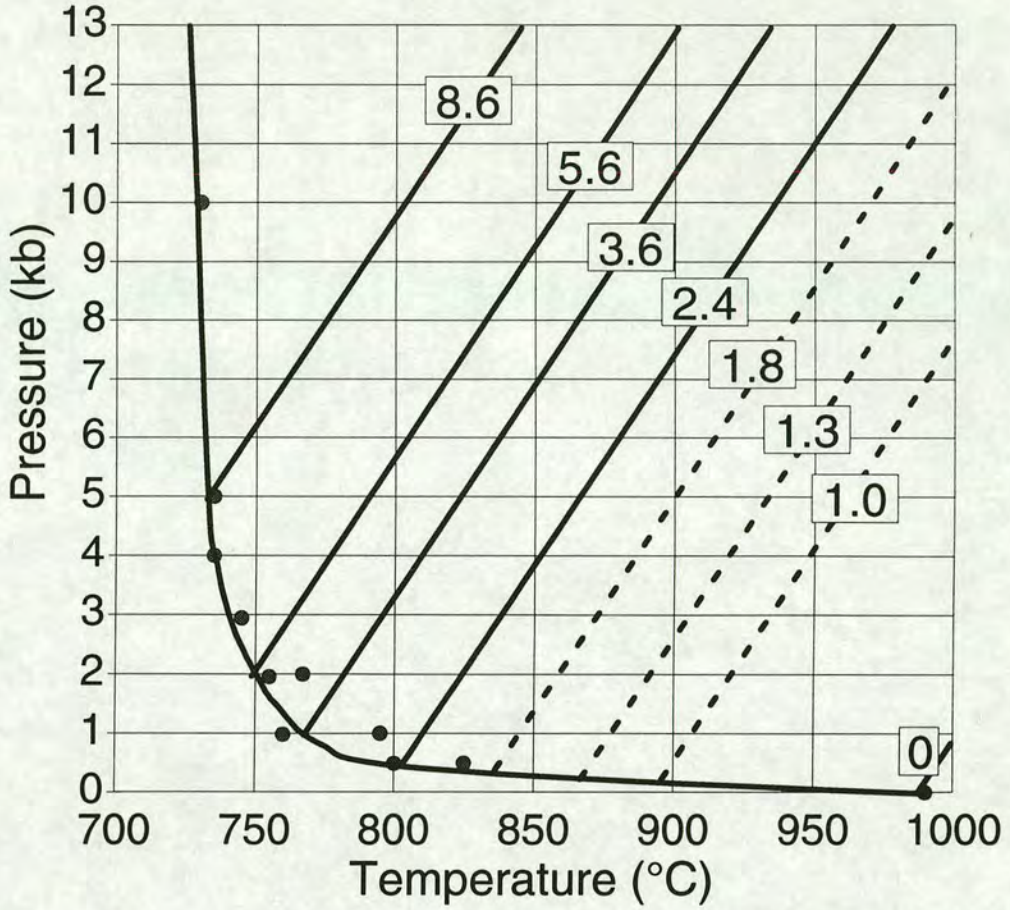

MELT WATER-CONTENT MODEL DERIVED FROM PUBLISHED EXPERIMENTS.

Figure 3.31. Liquidus contours for given water-contents (lines with boxes, wt%) in pressure-temperature space in the quartz-orthoclase-water system. Eutectic melts produced at a given pressure and temperature will have the water-content shown. Note that the change in melt-water content for a given change in pressure and temperature is greater at higher pressures and lower temperatures. The data used to define the water-saturated solidus (circles) is from the compilation of Luth (1976). The following solidus melt water-solubility data was kindly provided by Dr F.Holtz (taken or extrapolated from Huang and Wyllie 1975, Ebadi and Johannes 1991, Holtz et al. 1992a, 1993):

Pressure (bars)	**Water solubility at 900°C (weight percent)**	**Temperature dependence (wt% H_2O/100°C)**
1	0	0
500	2.3	0.15
1000	3.4	0.15
2000	5.4	0.15
5000	9.0	-0.25

This data enables the calculation of the water-content of a melt on the water-saturated solidus at the given pressures - the temperature dependence is used to adjust the solubility at a given pressure from 900°C to the solidus temperature. The slope of the lines (effectively the melt water-content at the liquidus) is taken to be parallel to those in figure 2 of Holtz and Johannes (1993). The dashed lines in the diagram are interpolations from the above data. No information on the uncertainties in the data used in this diagram is available but Holtz and Johannes (1993) quote an uncertainty of ± 0.2wt% H_2O for their qz-or-ab-H_2O system diagram and there is no reason to suspect the uncertainty in the present diagram to be significantly worse.

Comparison of melt water-content estimates.

The two approaches to estimating melt water-contents described above are compared in figure 3.32. The estimates from modal analysis differ with those from the model by at most 0.3wt%, which is well within the associated uncertainties. Therefore, when the melts are projected from in the diagrams in Chapter Four, the melt water-content is taken from figure 3.32. The water-content estimates have quite large

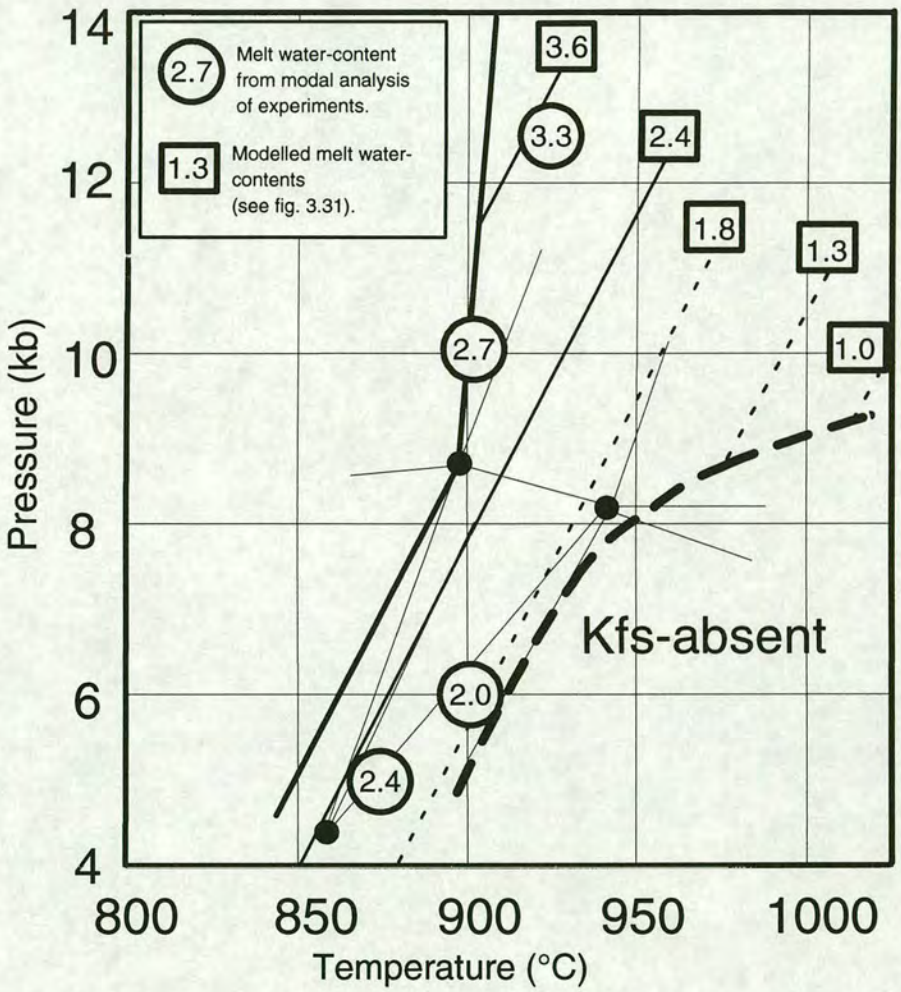

Figure 3.32. Comparison of melt water-content estimates (weight percent) derived from modal analysis of the experiments (points in circles, c.f. table 3.11 and figure 3.30) and by modelling based on data in the literature (lines with rectangles, c.f. figure 3.31). The uncertainties in the estimates from modal analysis are between ± 0.4wt% and ± 0.8wt% (see table 3.11). The assumed uncertainty for the modelled water-content contours is ± 0.2 wt%. The estimate given at 10kb, 900°C is the mean of the two estimates for that pressure-temperature position. The K-feldspar-absent field is delineated by a heavy line and shows the pressure-temperature space in which the melts are no longer eutectic and therefore no longer constrained by the model (see text for further discussion). The thin lines and solid circles are the univariant KFMASH grid derived in Chapter Six (INSERT A): the univariant solidus is highlighted with a heavy line. The dashed lines are interpolations of the data given in figure 3.31.

associated uncertainties but they are sufficient to adequately constrain nineteen out of the twenty three-component projections diagrams used in Chapter Four and Appendix Three.

The water-contents indicated for the melts in figure 3.32 are significantly lower than those of Patino Douce and Johnston (1991) who calculated their melt water-contents by mass balance (along with sodium-contents). Their data is not very consistent but does show a general decline with rising temperature and a general increase with rising pressure (table 3.12). Recent work has shown that albite-rich haplogranitic melts contain more water than an orthoclase-rich melt at the same pressure and temperature (Holtz et al., 1992a, Pichavant et al. 1992)[16]. However, the magnitude of this effect is to small too explain all the discrepancy between the current data and that of Patino Douce and Johnston (1991).

Figures 3.31 and 3.32 only apply to eutectic melts, i.e. those melts co-existing with quartz and K-feldspar. In the high-temperature, low-pressure quadrant of the investigated range K-feldspar is lost (figure 3.32). When a eutectic phase is lost, further increases in temperature will not produce as much further melting as would have occurred had all the eutectic phases been present. The water-content of the melt will therefore decrease less with increasing temperature if it is not eutectic. Estimates of melt water-content made from diagram 3.32 for non-eutectic melts will be too low.

Pressure (kb)	**Temperature (°C)**	**Melt water-content (wt%)**
7kb	875	4.09
7kb	1000	3.13
10kb	825	4.67
10kb	1025	2.79
13kb	900	7.14
13kb	950	5.33

Table 3.12. Melt water-content data from the experiments of Patino Douce and Johnston (1991).

[16] For example, a $Qz_{35}Ab_{60}Or_{05}$ melt dissolved 6.49 ± 0.2 wt% water at 2kb and 800°C, whereas a $Qz_{35}Ab_{10}Or_{55}$ melt dissolved 5.5 ± 0.15 wt% water at the same pressure and temperature (Holtz et al. 1992a).

Four experiments were run in the K-feldspar-absent region (D47, D59, D62, D65)[17]. The absence of K-feldspar not only introduces an additional uncertainty about the water-content of the melt but also prevents the use of an AFM projection (projected from quartz, K-feldspar and melt). Instead, a KFM projection must be used (projected from quartz, sillimanite and melt, Appendix Three). This is unfortunate because the KFM projection is the only one used here which is significantly sensitive to the water-content of the phases and the bulk composition. Whilst this prevents the diagrams from being used in interpreting the phase assemblages of those experiments it enables the diagrams to be used as rough estimate of melt water-content. This is illustrated in Appendix Three, experiment D59. As garnet and osumilite do not contain water, the tie-line between the two phases is fixed on a KFM projection. The bulk composition does vary its position as the melt from which it is projected varies its water-content. If garnet and osumilite are the only phases from the assemblage which plot on the diagram (i.e. the assemblage is trivariant) then the bulk composition must lie on the tie-line. Therefore, the water-content of the melt which projects the bulk composition on to the tie-line can be used as an estimate. This is effectively a graphical mass-balance approach. For D59 and D47 the appropriate melt water-contents are about two weight percent. This amount suggests, when compared to figure 3.32, that when the melts become non-eutectic their water-content decreases very little with increasing temperature, implying that further melting is very limited for those bulk compositions[18].

3.6.3 Water-content of cordierite.

Cordierite is one of the few framework silicates which can hold a variable amount of water and carbon dioxide (though carbon dioxide is not present in the current experiments). Volatile-saturation of cordierite requires one mole of water, 2.99wt% for Mg-cordierite (Johannes and Schreyer 1981), to be held in the channels of the crystal structure, but many natural, high-grade cordierites are found to contain less than this amount. In this study, the probe totals are only very rarely below 97wt% which would allow for water-saturation. This water-deficiency could be explained if the volatile-contents of the cordierite reflect equilibrium with water-undersaturated

---

[17] Some experiments run at pressures and temperatures outside the region depicted on figure 3.32 produced K-feldspar-absent assemblages but this was because of water-contamination. See Chapter Four.

[18] The role of cordierite, which also contains water, is uncertain. If the partitioning of water between melt and cordierite increases with temperature, this would enable the production of more melt without lowering the water content, if this were required.

melts rather than a free-vapour phase (Harley et al. 1992). This implies the operation of partitioning of water between the melt and the cordierite.

No experimental data is available in the literature on the water-contents of water-undersaturated cordierites. Therefore, the best method of obtaining a cordierite water-content estimate is to determine the partitioning-coefficient for water between melt and cordierite ($K_w=H_2O^L/H_2O^{crd}$) using the data presented below and then use the melt water-content estimate to give the water-content of the cordierite. In fact, the position of hydrous cordierite on a diagram projected from a hydrous melt depends only on K_w and not on the absolute water-contents. This is because it is the relative amounts of water in the melt and cordierite which determines the angle of projection and thus how far a hydrous cordierite is moved from the position of an equivalent but anhydrous cordierite.

Under water-saturated conditions K_w is estimated to be between five and seven for crustal, high-grade conditions[19]. The only data available on the value of K_w in water-undersaturated conditions is from one, atypical experiment in this study. D56-16 was run at 900°C, 7 kb but had been contaminated by excess water, which seeped in during the welding process (see section 2.2.4). This caused much more extensive melting than observed in the other experiments from the same run (D56-17, D56-18). The assemblage produced was cordierite (about 40% by volume), melt (60%) and orthopyroxene (trace). Quartz was absent. The cordierite crystals (5-15μm) were considerably larger than in the other experiments and large pools of melt (≈20μm) were also present. The large size of the phases enabled direct analysis using Secondary Ion Mass Spectrometry (SIMS). The analysis was performed by Dr S.L.Harley[20]. The results are given in table 3.13.

Phase	**Water Content (wt%)**	**Uncertainty (wt%)**
Cordierite	1.7	±0.1
Melt	5.4	±0.4

Table 3.13. Results of SIMS analysis of D56-16: water-contents of co-existing cordierite and melt.

[19] These figures are calculated from the cordierite water-content data of Mirwald et al. (1979) and Vry et al. (1990) and melt water-content data of Holtz and Johannes (1993).

[20] SIMS analysis for H^+ referenced against ^{28}Si was carried out using an O- primary beam (20μm diameter) and positive secondary beam, with an 8μm aperture inserted. Isotope ratios in the experimental cordierite and melt were calibrated against $H^+/^{28}Si$ in standard cordierites and felsic glasses.

The K_w calculated from this data is 3 ± 0.3, considerably lower than the values predicted for water-saturated conditions. This may be due to fewer water-solubility mechanisms being available in the melt at low water-contents. As D56-16 was enriched in water this K_w may be slightly higher than that appropriate for the other experiments. However this uncertainty is small when it is demonstrated that whatever value of K_w is used, as long as it is greater than one, the phase relations derived in the next chapter are the same (figure 4.5).

If the concept of a partitioning coefficient for water between cordierite and melt is valid, it follows necessarily, that if one phase is present, the other must also be, if there are no other hydrous phases. It is theoretically possible that an anhydrous or CO_2-filled cordierite could exist in the absence of a melt, but it is very unlikely that any natural cordierite would be completely free of water. Therefore, if cordierite is present in a rock it is very likely that a melt also co-existed.

Chapter Four

INTERPRETATION OF EQUILIBRIUM PHASE ASSEMBLAGES

Chapter Four. Interpretation of equilibrium phase assemblages.

This chapter presents the equilibrium phase assemblages interpreted from the experimental data. The majority of the experiments produced what are interpreted to be equilibrium assemblages. For a variety of reasons, some of the experiments produced assemblages not interpreted to be at equilibrium. These result from water-contamination, metastability or sluggish nucleation/growth of phases, or the failure to identify rare phases. The method of interpretation is illustrated in this chapter and all the projections used are presented in Appendix Three.

The interpretation of the supersolidus experiments is considered first, followed by subsolidus assemblages. An assessment is given of the effect of uncertainties in the phase compositions (particularly water-contents) on the interpretation of phase assemblages.

4.1 INTERPRETATION OF EQUILIBRIUM PHASE ASSEMBLAGES.

The product assemblage of an experiment does not necessarily represent the equilibrium phase assemblage, though a successful study should achieve this frequently. Potential problems which could alter the result of the experiment from that required at equilibrium are metastability of a phase, sluggish nucleation, contamination of the mix or a very small modal abundance of a phase leading to difficulties in its identification. A powerful method of assessing whether these problems have occurred is available if the bulk composition of the mix is known. If the assemblage produced is plotted on a suitable three-component projection[1] then the bulk composition should lie between the plotted phases. If this is the case, and the phases are close to equilibrium, then the product assemblage can be taken as the equilibrium assemblage. For the majority of the supersolidus experiments in this study (twenty-eight out of forty-seven), this was the case (e.g. figure 4.1). Three-component projections for all the experiments are given in Appendix Three and a summary of the interpretations is given in tables 4.1 and 4.2. The self-consistency of the data set as a whole can also be a guide to the equilibrium assemblages and this is employed for some of the more equivocal interpretations, as described below.

---

[1] Three simple projections are used; AFM, projected from quartz (SiO_2), K-feldspar (K_2O) and the melt (H_2O); KFM, projected from quartz (SiO_2), sillimanite (Al_2O_3) and the melt (H_2O); HFM projected from quartz (SiO_2), K-feldspar (K_2O) and sillimanite (Al_2O_3).

Table 4.1. Interpretation of equilibrium assemblages for the supersolidus experiments. All the experiments have quartz present. The product assemblages of the experiments are given in table 3.1. The interpretation of the product assemblages is discussed in the text.

Run (Run-mix)	P (kb)	T (°C)	Interpretation of Product Assemblage	Equilibrium assemblage
DG51-16	5	875	Metastable spinel	os, crd, grt, kfs, L
DG51-17	5	875	As univariant assemblage	os, crd, grt, kfs, L, opx
DG60-16A	6	900	As equilibrium assemblage	os, crd, grt, kfs, L
DG60-17A	6	900	As univariant assemblage	os, crd, grt, kfs, L, opx
DG60-18A	6	900	As equilibrium assemblage	os, crd, opx, kfs, L
DS66-17A	7	875	Water contaminated	bt, crd, grt, kfs, L
DS66-18A	7	875	Metastable orthopyroxene	bt, os, crd, kfs, L
DG49-16	7	875	As equilibrium assemblage	bt, crd, grt, kfs, L
DG49-17	7	875	Unidentified melt	bt, crd, grt, kfs, L
DG49-18	7	875	Unidentified melt	bt, os, crd, kfs, L
DG56-16	7	900	Water contaminated	crd, opx, grt, L (no qz)
DG56-17	7	900	As equilibrium assemblage	crd, opx, grt, L, kfs
DG56-18	7	900	As equilibrium assemblage	os, crd, opx, kfs, L
DG47-16	7	940	As equilibrium assemblage	os, grt, kfs, sil, L
DG47-17	7	940	As equilibrium assemblage	os, crd, grt, sil, L
DG47-18	7	940	As equilibrium assemblage	os, crd, opx, L,
DS62-16A	<8	1000	As equilibrium assemblage	os, crd, grt, sil, L
DS62-18A	<8	1000	Water contaminated	crd, opx, L
DG57-16	8	910	Metastable orthopyroxene	crd, grt, kfs, sil, L
DG57-17	8	910	Metastable orthopyroxene	crd, grt, kfs, sil, L
DG57-18	8	910	As equilibrium assemblage	os, crd, opx, kfs, L
DG64-17A	8	910	Metastable orthopyroxene	crd, grt, kfs, sil, L
DG59-17	8	965	Metastable orthopyroxene	os, grt, kfs, sil, L
DG59-18	8	965	As equilibrium assemblage	os, opx, sil, L
DG55-16	8.5	950	As equilibrium assemblage	opx, grt, kfs, sil, L
DG55-17	8.5	950	Quasi-univariant assemblage	os, opx, grt, kfs, sil, L
DG55-18	8.5	950	As equilibrium assemblage	os, opx, kfs, sil, L
DG61-16	8.75	895	As invariant assemblage	bt, crd, opx, grt, kfs, sil, L
DG54-16	9.2/8.5	925	As equilibrium assemblage	opx, grt, kfs, sil, L

Continued./

Sorry about the column switch between Table 4.1 and 4.2!

Table 4.1. Continued. Interpretation of equilibrium assemblages for the supersolidus experiments. All the experiments have quartz present. The product assemblages of the experiments are given in table 3.1. The interpretation of the product assemblages is discussed in the text.

Run (Run-mix)	P (kb)	T (°C)	Interpretation of Product Assemblage	Equilibrium Assemblage
DG54-17	9.2/8.5	925	Quasi-univariant assemblage	crd, opx, grt, kfs, sil, L
DG54-18	9.2/8.5	925	As equilibrium assemblage	crd, opx, kfs, sil, L
DG64-16A	9	910	Metastable cordierite	opx, grt, kfs, sil, L
DG64-18A	9	910	As equilibrium assemblage	crd, opx, kfs, sil, L
DG65-16A	9	1000	As equilibrium assemblage	grt, kfs, sil, L
DG65-17A	9	1000	As equilibrium assemblage	opx, grt, kfs, sil, L
DG65-18A	9	1000	As equilibrium assemblage	os, opx, sil, L,
DS43-13	10	900	As equilibrium assemblage	opx, grt, kfs, sil, L
DS43-14	10	900	As equilibrium assemblage	opx, grt, kfs, sil, L
DS52-17	10	910	Water contaminated	opx, grt, sil, L
DS52-18	10	910	Water contaminated	opx, sil, L
DS40-13	12.5	900	As equilibrium assemblage	bt, grt, kfs, sil, L
DS48-14	12.5	925	As equilibrium assemblage	opx, grt, kfs, sil, L
DS48-17	12.5	925	As equilibrium assemblage	opx, grt, kfs, sil, L
DS48-15	12.5	925	As equilibrium assemblage	opx, grt, kfs, sil, L
DS41-13	12.5	950	As equilibrium assemblage	grt, kfs, sil, L
DS41-14	12.5	950	As equilibrium assemblage	grt, kfs, sil, L
DS41-15	12.5	950	As equilibrium assemblage	opx, grt, kfs, sil, L

Table 4.2. Interpretation of equilibrium assemblages for the subsolidus experiments. All the experiments have quartz present. The products assemblages of the experiments are given in tabie 3.2.

Experiment (Run-Mix)	P (kb)	T (°C)	Equilibrium Assemblage	Interpretation of Product Assemblage
D50-16	7	840	bt, grt, crd , kfs, sil	Metastable orthopyroxene
D50-17	7	840	bt, grt, crd, kfs, sil	Cordierite not formed
D50-18	7	840	bt, crd, opx, kfs, sil	Orthopyroxene not formed
D63-16A	7	855	bt, grt, crd, kfs, sil	As equilibrium assemblage
D63-18A	7	855	bt, opx, crd, kfs	As equilibrium assemblage
D53-16	8.5	875	bt, grt, crd, kfs, sil	Cordierite not formed
D53-17	8.5	875	bt, grt, crd, kfs, sil	Cordierite not formed
D53-18	8.5	875	bt, crd, kfs, sil	Cordierite not formed
D61-17A	8.75	895	bt, grt, kfs, crd, sil	As equilibrium assemblage
D37-13	10	825	bt, grt, kfs, sil	As equilibrium assemblage
D37-14	10	825	bt, grt, kfs, sil,	Orthopyroxene not formed
D37-15	10	825	bt, kfs, sil	Orthopyroxene not formed
D67-16A	10	875	bt, grt, sil, kfs,	As equilibrium assemblage
D38-13	12.5	840	bt, grt, kfs, sil	As equilibrium assemblage
D38-14	12.5	840	bt, grt, kfs, sil	As equilibrium assemblage
D38-15	12.5	840	bt, kfs, sil,	As equilibrium assemblage
D40-14	12.5	900	bt, grt, kfs, sil,	As equilibrium assemblage
D40-15	12.5	900	bt, kfs, sil	Orthopyroxene not formed

The phase rule shows that in a six component system, such as the KFMASH system used here, a six phase assemblage is divariant, a seven phase assemblage is univariant and an eight phase assemblage is invariant. Natural univariant and invariant assemblages are rare (except in cases of fluid buffering) as they are only stable at pressures and temperatures representing a line and a point respectively in pressure-temperature space. The probability of finding a rock of the right composition which equilibrated at the required pressure and temperature is extremely small. In experimental studies apparently low-variance product assemblages are rather more common, for two possible reasons. Firstly, the persistence of metastable phases is common and secondly, the pressure-temperature fluctuation inherent in the experimental apparatus could enable an experiment to straddle a univariant boundary and produce a "genuine" univariant assemblage. Whilst both of these factors could operate simultaneously, it is important to determine which is the dominant one.

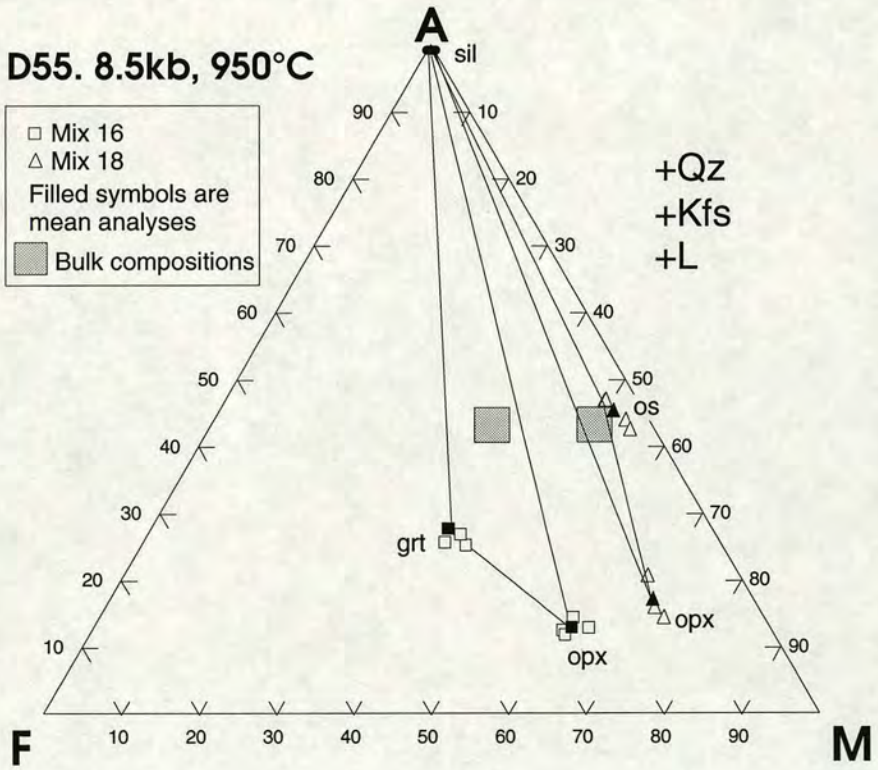

Figure 4.1. AFM projection of experiments D55-16 and D55-18. In each of these experiments the product assemblage consisted of six phases (table 3.1). Three phases are used to project from (qz, kfs, L) and the other three define a divariant field on the diagram,. The projected bulk composition for each experiment lies within the divariant field. Therefore the product assemblage is equated with the equilibrium assemblage. The size of the bulk composition symbol represents the uncertainty and is discussed in Appendix Three.

Following the methodology outlined above, if the bulk composition projects onto the tie-line which divides the two divariant fields defined by the product phases then the product assemblage is equated with a univariant equilibrium assemblage (e.g. figure 4.2). This occurred in four supersolidus experiments out of forty-seven (table 4.1). It transpires later, that when the univariant KFMASH grid is constructed (figure 6.11) two of the experiments interpreted as having univariant assemblages (D54-17, D55-17) do not lie on or near univariant reactions. In fact, the experiments straddle narrow trivariant fields which separate two divariant fields (figure 6.14) and could be called "quasi-univariant". In one further case (D61-16A) the product assemblage contained eight phases. The data from all the other experiments implied that an invariant point was indeed in that region of pressure-temperature space and so the product assemblage was taken as the equilibrium assemblage, i.e. as invariant.

When the product assemblage has more than six phases but the bulk composition does not lie in an appropriate place for a low-variance assemblage, one of the phases

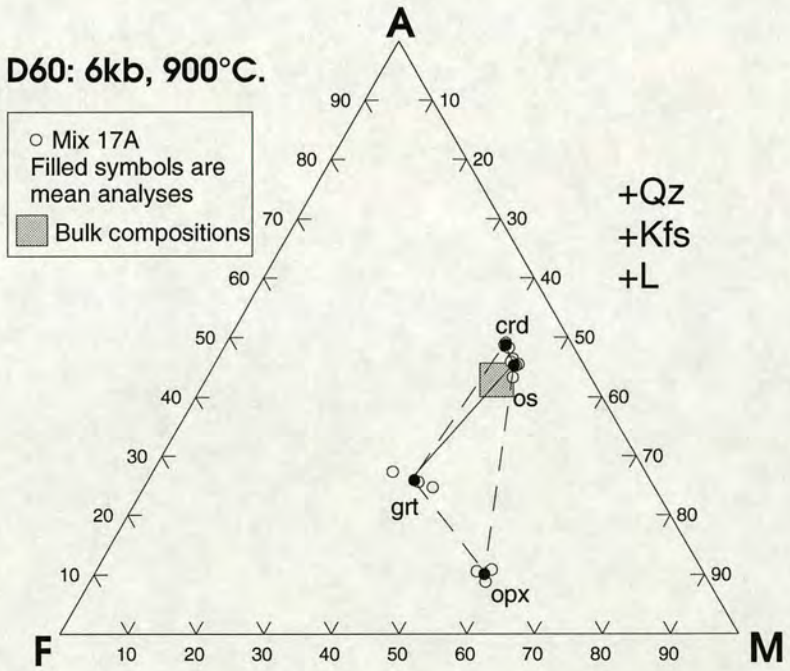

Figure 4.2. AFM projection of D60-17. The product assemblage of the experiment contained seven phases (table 3.1), three of which are used to project from. The remaining four phases define two divariant fields, grt-crd-os and grt-opx-os, and the bulk composition lies on the grt-os tie-line which divides them. Therefore, the product assemblage is taken to be equilibrium assemblage and is thus univariant. This four phase assemblage cannot determine whether the grt-os or the crd-opx tie-line is stable but D60-16A produced a divariant grt-crd-os assemblage which indicates the stability of the grt-os tie-line.

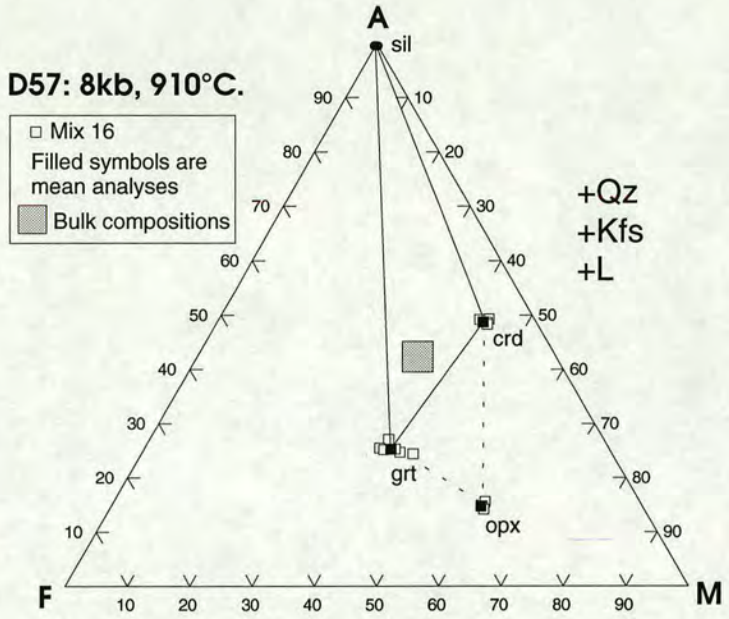

Figure 4.3. AFM projection of D57-16. The product assemblage of the experiment contained seven phases, three of which are used to project from. Other experiments show the grt-crd tie-line to be stable. The bulk composition projects within the grt-crd-sil divariant field and so the orthopyroxene is taken to be metastable.

is interpreted as being metastable[2] (e.g. figure 4.3). This occurs in seven supersolidus experiments and in five cases the phase interpreted as metastable is orthopyroxene. It is well known by experimentalists that orthopyroxene forms very easily (the phase is never seeded for) but this is enhanced here by the metastably high aluminium-contents of the orthopyroxenes and the easy availability of alumina from the AlSiO gel (see section 3.4.1). Furthermore, the bulk compositions lie close to the AFM-projection garnet-cordierite tie-line, which divides the diagram into sillimanite- and orthopyroxene-bearing assemblages. Therefore, even when orthopyroxene is not stable, the bulk composition will not be far from its stability field and thus requires little equilibrium overstepping to form. The ease of formation of metastable

[2] There are situations in which this method would not predict the presence of a metastable phase. The diagnostic method is based on the mass-balance constraint of the bulk composition and the fact that, even if a metastable phase forms, the compositions of the equilibrium phases will remain the same. However, the presence of the metastable phase necessarily alters the bulk composition from which the equilibrium phases form. The presence of a metastable phase will reduce the modal abundances of the equilibrium phases. It is possible that a sufficient amount of the metastable phase could form to cause the loss of one of the equilibrium phases. In this situation, a divariant assemblage would be present and mass-balance constraints would mean that the bulk composition would plot in that field on a three-component projection. Therefore, the diagnostic method used here would not predict the presence of a metastable phase. Fortunately, this situation is unlikely to occur as in most situations metastable phases do not have large modal abundances.

orthopyroxene, contrasted with the fact that sillimanite is very slow to nucleate, creates the possibility of orthopyroxene forming and sillimanite not forming when the equilibrium case is the opposite (as determined by the position of the bulk composition), i.e. metastable orthopyroxene forms and stable sillimanite does not form. However, the experiments were seeded with sillimanite and these seeds were lost when sillimanite was not stable, even when the experiment was close to the sillimanite stability field (e.g. D56-17, Appendix Three). Therefore, if the garnet-cordierite tie-line is stable, the presence or absence of sillimanite is a guide to whether the orthopyroxene is metastable; if sillimanite is present then the orthopyroxene is most likely metastable and vice versa.

The other phases interpreted as metastable are spinel in D51-16 (5kb, 875°C) and cordierite in D64-16A. Spinel is not found in any other experiment in the study but a stability field at low pressure (<5kb) is expected (Waters 1991, Shulters and Bohlen 1989). Excluding spinel, D51-16 contains a divariant assemblage which encloses the bulk composition and is consistent with all the other experiments and so D51-16 is interpreted as close to, but outside, the stability field of spinel. D64-16A was a reversal run and during the first step of the run was in the garnet-cordierite-K-feldspar-quartz stability field. After the second step of the run the M86 mix in the same run, D64-18A, stabilised orthopyroxene-sillimanite-melt which must lie at higher pressures than the garnet-cordierite-K-feldspar-quartz stability field, and so the cordierite in D64-16A must be a metastable remnant (see section 5.2 and INSERT A).

Another situation in which the product assemblage is not considered to be the equilibrium assemblage is if the mix is thought to have been contaminated by water (section 2.2.4 discusses sources of contamination). If extra water is present in an experiment, additional melting will occur and the phases principally contributing to the melt will decrease in modal abundance or be lost. The melt is formed predominantly from quartz, K-feldspar and biotite. A fairly small amount of water contamination could lead to the consumption of K-feldspar and biotite (when these phases are stable), as they have lower abundances than quartz.

An extreme example of water-contamination, in which even quartz was lost, is experiment D56-16 in which the product assemblage was cordierite-orthopyroxene-melt. This is the only experiment in the whole study which lost quartz but was run 100°C below the highest temperature experiment. From the Secondary Ion Mass

Spectrometry analysis of the water-content of the hydrous phases in D56-16 (described in section 3.6.3) it can be deduced that the bulk water-content of that experiment must have been about four weight-percent[3], which is over four times the original water content of the mix (table 2.7). This excess water would have caused the extreme melting and loss of quartz.

Less severe water-contamination is interpreted for four other experiments (table 4.1), in three cases because K-feldspar is absent from the assemblage whilst being present in the other experiments from the same run. For example, runs D49 (gas-bomb) and D66 (solid-media salt cell) were both done at 7kb and 875°C. Comparison of the M86 mixes from both experiments shows that the same phase assemblage is produced, with the only differences being a slightly higher X_{Mg} for biotite and a trace of metastable orthopyroxene in D66-18A (figure 4.4). However, the M74 mixes from D66-17A and D49-17 did not produce the same assemblage. Whilst D49-17 produced the assemblage biotite-garnet-cordierite-quartz-K-feldspar-melt (plus

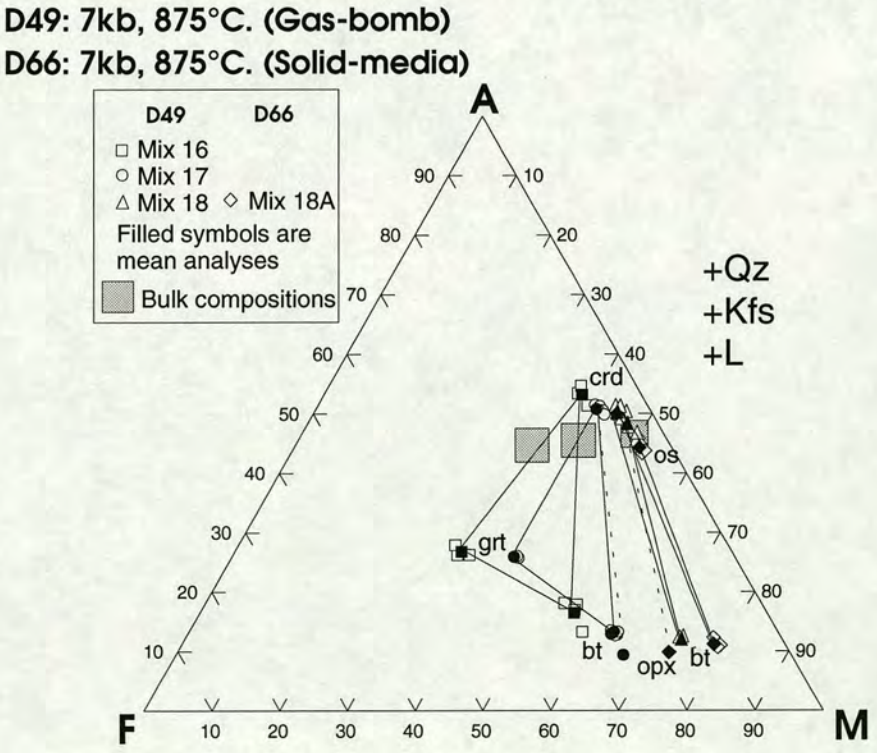

Figure 4.4. AFM projection of runs D49 and D66. See text for discussion. D66-17A is not shown as it did not contain K-feldspar and cannot therefore be legitimately projected (see table 3.1).

[3] The cordierite contains 1.7 ± 0.1 wt% water and comprises about 40 vol% of the experiment. The melt contains 5.4 ± 0.4 wt% water and comprises about 60 vol% of the experiment. The orthopyroxene is only present as a trace.

orthopyroxene, interpreted as metastable), D66-17A produced garnet-cordierite-quartz-melt and orthopyroxene, but no K-feldspar or biotite. So, although all four experiments shown on figure 4.4 retained biotite and K-feldspar, D66-17A did not. If the data set is to be self-consistent the lack of biotite and K-feldspar cannot represent the equilibrium condition of the original mix and is therefore attributed to water contamination.

Experiment D62-18A (1000°C, <8kb) was interpreted to have lost osumilite, as a result of water contamination, because all eight other experiments using M86 mixes above 875°C and below 9kb contained osumilite. K-feldspar was not present but is not expected to be stable at the high temperature of the experiment.

Finally, in experiments D49-17 and D49-18 the melt interpreted to be present was not positively identified. The interpretation that these experiments had been run at supersolidus conditions is based on a repeat run, D66, using the solid-media apparatus. Reaction rates are faster in the solid-media experiments than in the gas-bomb experiments (section 2.3.5) and D66 produced analysable melt. This suggests that D49 was run above the solidus but produced too small a fraction of melt to be identified, because of the proximity of the solidus and the sluggish kinetics of the gas-bombs. It is possible that small fO_2 differences between the apparatuses (section 2.3.4) could shift the temperature of the solidus but experiments below the solidus contain sillimanite (table 4.2) which is absent from D49-17 and D49-18.

All the experiments discussed so far were run at supersolidus conditions. Seventeen subsolidus runs were done and in nine cases the product assemblage and the interpreted equilibrium assemblage were the same (table 4.2). Importantly, this nine included the four subsolidus experiments closest to the solidus. A further seven experiments contained fewer phases than the other experiments suggested should be stable. This is likely to be the result of a lack of reaction at low temperature, liquid-absent conditions. For example, in experiment D50-17 (7kb, 840°C) no new phases formed giving a product assemblage of biotite-garnet-sillimanite-K-feldspar-quartz. D50-16, D61-17 and D63-16A all have that product assemblage, but with cordierite as well, and this is interpreted to be the equilibrium assemblage. One subsolidus experiment was interpreted to have metastable orthopyroxene (table 4.2).

4.2 THE EFFECT OF UNCERTAINTIES IN PHASE WATER-CONTENTS AND MELT COMPOSITION ON THE INTERPRETATION OF EQUILIBRIUM PHASE ASSEMBLAGES.

The interpretations in the last section depend primarily on the plotted position of the bulk composition relative to the phases. The uncertainties in the water-contents of the phases are much larger than the uncertainties in the KFMAS components and this is manifested in much larger uncertainties in the position of the hydrous phases. The potential of these uncertainties to invalidate the interpretations made must be assessed. The phase water-content estimates are derived in section 3.6.

The uncertainties associated with the AFM projection, where the melt is a projecting phase, are illustrated in figure 4.5. The partitioning coefficient of water between melt and cordierite, K_w, determines the position of the cordierite on the AFM plot. Section 3.6.3 showed that K_w is 3 ± 0.3 for D56-16. In fact, except in the improbable event of a reversal in the partitioning, any value of K_w will give the same relative phase positions for the experiments shown (figure 4.5a). The uncertainty in the position of the bulk compositions on the AFM projection would not significantly alter the interpretation. Also shown on figure 4.5a is a sillimanite-osumilite tie-line. This is not stable in the experiment shown but illustrates the near collinearity of osumilite, sillimanite and cordierite. This means that the stoichiometry of reactions involving those three phases and garnet or orthopyroxene may depend on K_w (see section 6.3.2). The sillimanite-osumilite tie-line passes through position for cordierite where $K_w = 3.0$. As this value is likely to be a maximum (D56-16 contained four times as much water as the other experiments) the projected position of cordierite is assumed to be more magnesian than the sillimanite-osumilite tie-line (see figure 6.10 for further discussion).

Other uncertainties in the melt composition affect the positions of the hydrous phases on the AFM projection. The potassium-content of the melt is not very well known (see section 3.5.1). However, figure 4.6 shows that the uncertainty in the position of the cordierite resulting from the uncertainty in the melt potassium-content is negligible.

In contrast to the AFM projections which show small shifts in position associated with the compositional uncertainties of the phases, the phase and bulk composition positions on KFM projections show a large dependence on the water-contents (figure

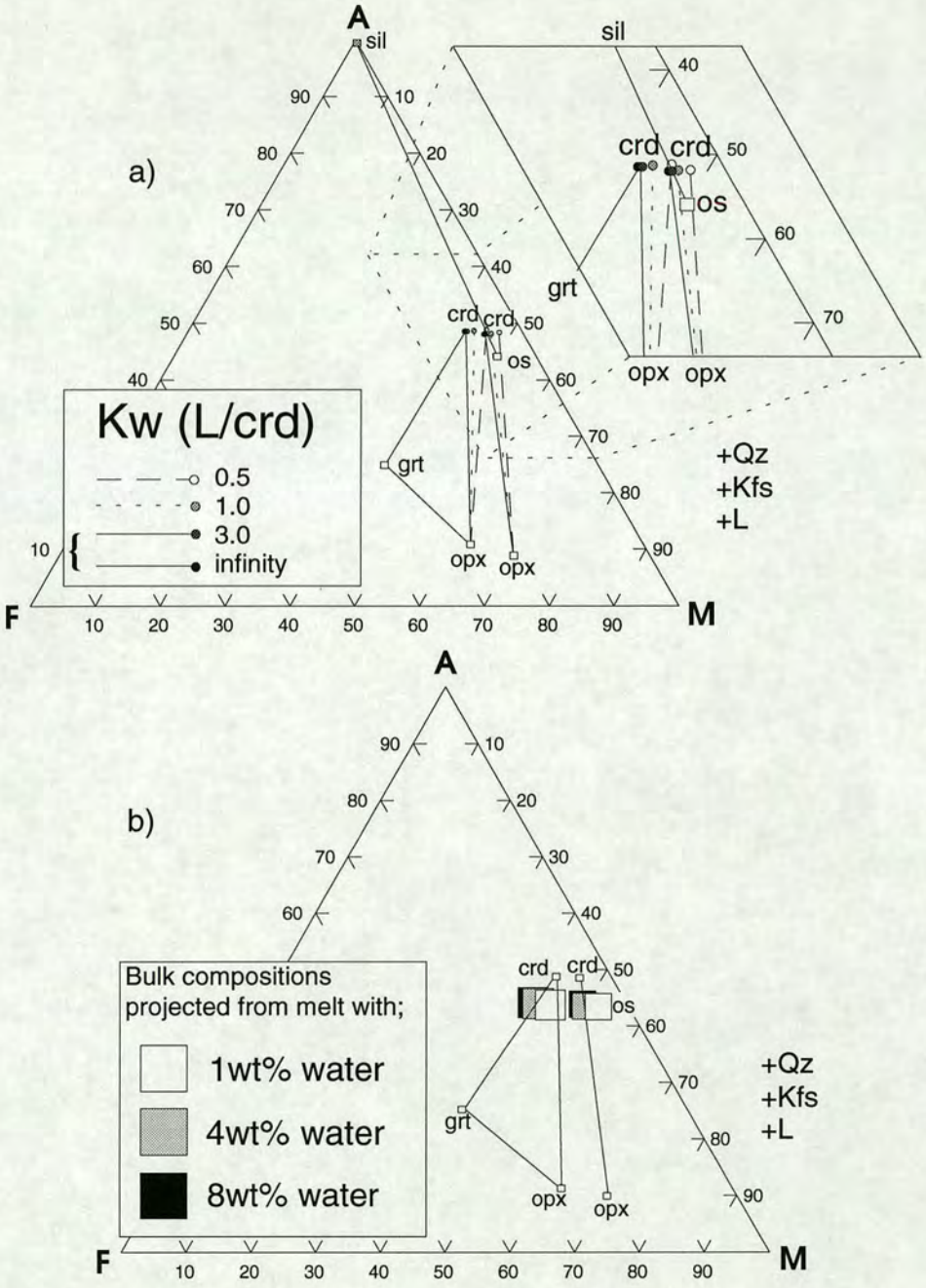

Figure 4.5. Uncertainties in the AFM positions of phases and bulk compositions.

a) Phases from experiments D56-17 and D56-18 plotted on an AFM projection for different values of K_w. Cordierite is the only hydrous phase which plots on the diagram. The measured value of K_w is 3.0 ± 0.3 for D56-16 (section 3.6.2). As the melt is more iron-rich than the cordierite, the cordierite plots to more magnesian positions for lower values of K_w. The relative phase relations in this experiment only change when the melt-cordierite water partitioning is reversed (K_w<1) which results in the cordierite-orthopyroxene tie-line lying on the magnesian side of the osumilite. An infinite value for K_w is equivalent to treating all the phases as anhydrous. Sillimanite is not present in D56-18 but is included to show that sillimanite, cordierite and osumilite are nearly co-linear leading to near degeneracy in the reactions (bt, grt) and (bt, opx) (see text and figure 6.10 for further discussion).
b) An AFM projection showing the variation in the plotted position of the bulk compositions with varying water-content estimates for the melt. All the melts in this study are estimated to have a water-content in the range 1.0-3.7wt% with a maximum error of ± 0.8wt%. Therefore, the uncertainty in the position of the bulk composition projected from a particular melt will be small and will not affect the interpretation of equilibrium assemblages. The phases plotted are from D56-17 and D56-18.

4.7). This means that equilibrium assemblages cannot be interpreted from these diagrams without significant uncertainty. Fortunately, only two out of the ten experiments which have to be plotted on the KFM projections (D59-17, D62-18A) produced product assemblages inconsistent with the data set as a whole. To be consistent with the other experiments, D59-17, requires the interpretation of the orthopyroxene as metastable. This interpretation is only usually made if the bulk composition can be shown to be outside the appropriate field, but this is not possible here. Therefore, experiment D59-17 is treated with caution. D62-18A is interpreted as water-contaminated primarily on the basis of comparison with other experiments (see above). So, for the KFM projections, the position of the bulk composition is not used as an interpretative tool, but the sensitivity of the projected positions of the bulk compositions may be utilised as a constraint on the melt water-content. This is described in section 3.6.2.

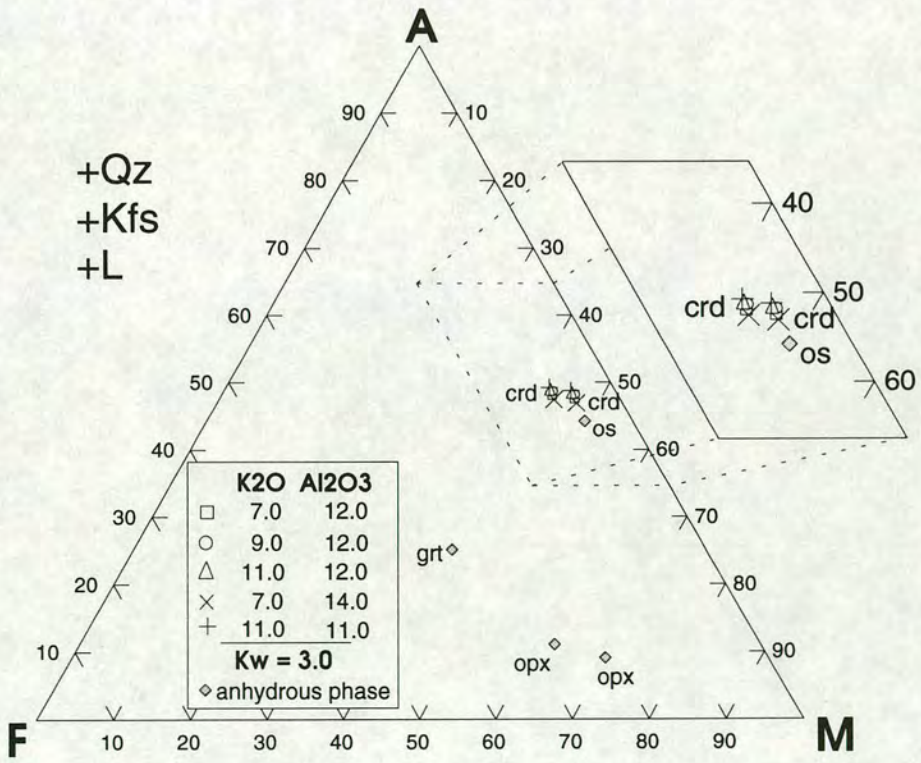

Figure 4.6. An AFM projection showing phases from D56-17 and D56-18 projected from melts with varying potassium- and aluminium-contents. The oxide weight percents are given for a melt with 2wt% water. The potassium-content estimates are given in section 3.5.1 and for all experiments are between 8.5 and 10.0wt% anhydrous, with an uncertainty of about ± 0.5wt%. This diagram shows that this uncertainty has a negligible effect on the position of the phases.

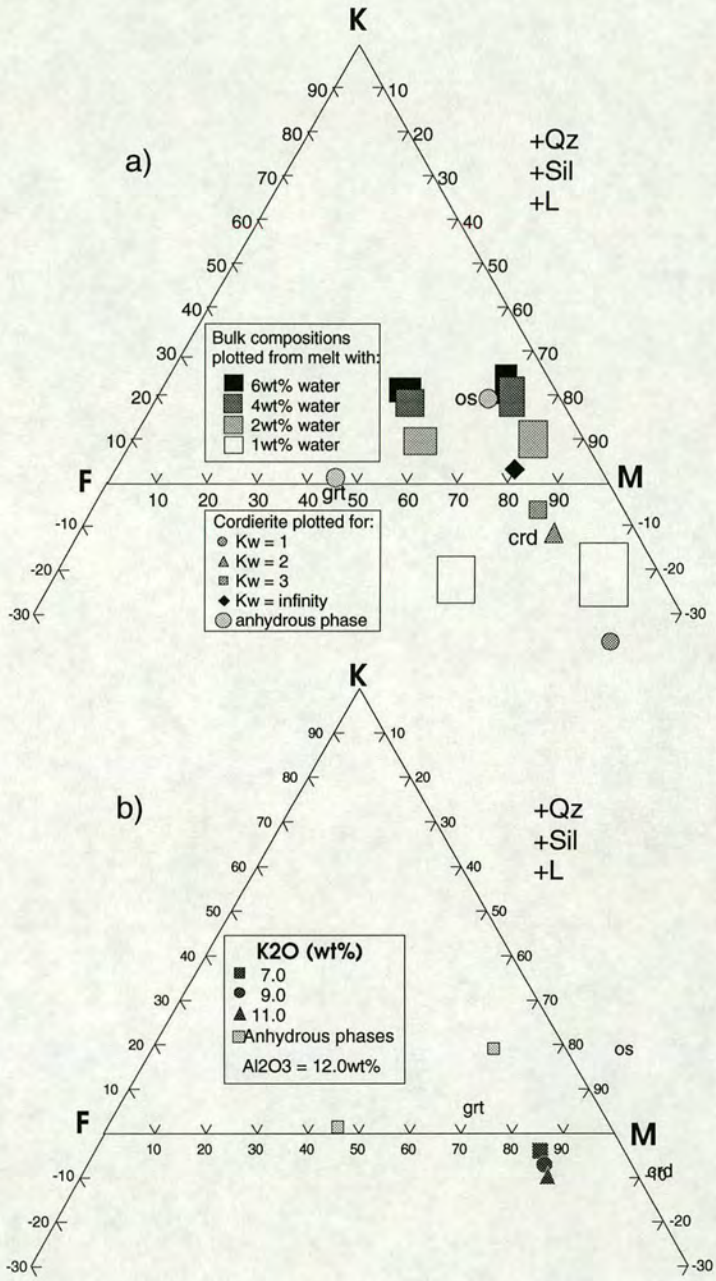

Figure 4.7.

a) Bulk compositions and cordierites plotted on a KFM projection for various melt-water contents and K_w's respectively. The phases plotted are from experiment D62-16A. All the melts in this study are estimated to have a water-content in the range 1.0-3.7wt% with a maximum error of ± 0.8wt%, which leads to considerable uncertainty in the position of the bulk composition, particularly at low water-contents. The K_w for experiment D56-16 (section 3.6.3) is 3 ± 0.3, but may be lower for other experiments. The consequent uncertainty in the position of the cordierite is smaller than that for the bulk compositions, though still significant.

b) Cordierite position on a KFM projection plotted for different potassium-contents of the melt. Data from D62-16A. The diagram is drawn for K_w=3.0. The potassium-content estimates for the melts in all the experiments are between 8.5 and 10.0wt% anhydrous, with an uncertainty of about ± 0.5wt%. The consequent uncertainty in the position of the cordierite is significant but small compared to that resulting from the uncertainty in K_w (figure 4.7a).

PLATES

Plate 1. Back-scattered electron photomicrographs.

a) D67-16A. Reversal run: 900⇒875°C, 10kb in solid-media salt cell. Product assemblage: *biotite-garnet-sillimanite-K-feldspar-quartz*, interpreted as equilibrium assemblage. The charge exhibits plentiful re-growth of biotite (small bright laths) which would have been absent during the first step of the run (c.f. D43-13, table 3.1). This re-growth shows that the dehydration melting reaction has been reversed and also gives the equilibrium subsolidus assemblage. The garnet crystals show iron-rich rims. The biotite crystals are rarely wider than 1μm, which is the same as the smallest electron-probe beam-size, and so they are difficult to analyse without contamination. Thin growth rims on garnet crystals can be similarly difficult to analyse, though in this experiment the long run duration (580 hours) has produce large growth rims. 10μm scale as marked.

b) D43-14. 900°C, 10kb in solid media salt cell. Product assemblage: *garnet-orthopyroxene-sillimanite-K-feldspar-quartz-melt*, interpreted as equilibrium assemblage. This assemblage is important at high pressures and temperatures in this study. Both the orthopyroxene and the sillimanite have tabular, elongate forms. The sillimanite is the same contrast as the quartz but can be distinguished by its brighter outline. The melt is easily distinguished, having a contrast intermediate between the K-feldspar and sillimanite/quartz and occurring interstitially. 10μm scale as marked.

Plate 1

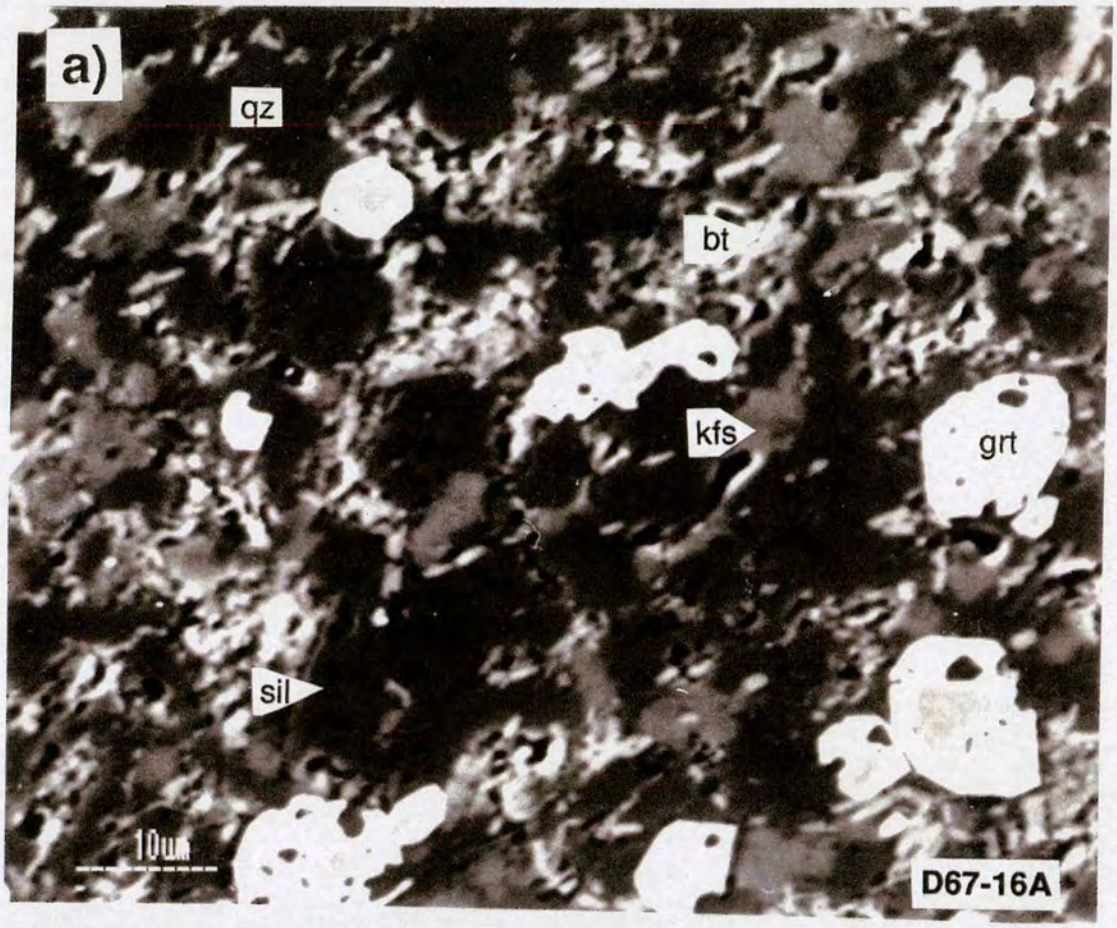

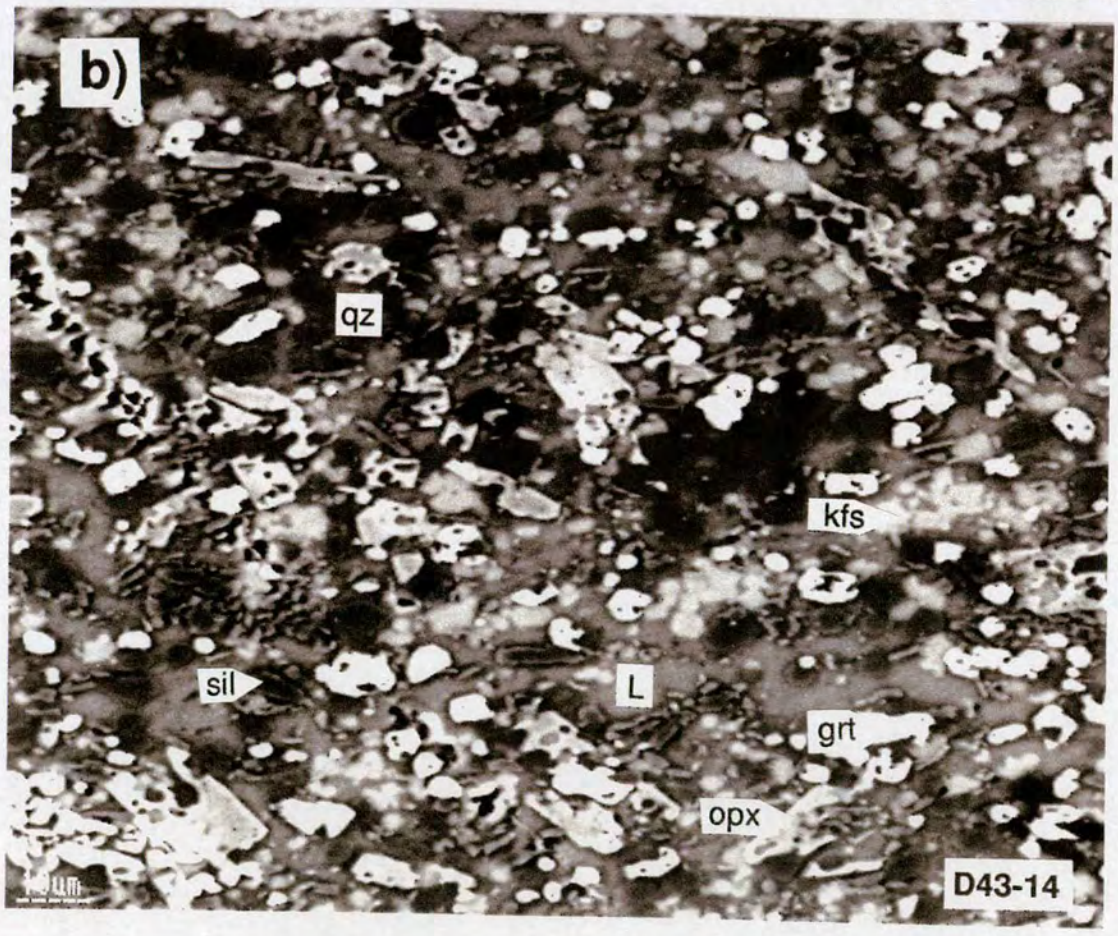

Plate 2. Back-scattered electron photomicrographs.

a) D40-13. 900°C, 12.5 kb in solid-media salt cell. Product assemblage: *biotite-garnet-sillimanite-K-feldspar-quartz-melt*, interpreted as equilibrium assemblage. This experiment illustrates the divariant melting of biotite, which has become quite magnesium-rich and hence rather dark in contrast. Compare with D40-14 (Plate 2b) which did not melt. 10μm scale as marked.

b) D40-14. 900°C, 12.5 kb in solid-media salt cell. Product assemblage: *biotite-garnet-sillimanite-K-feldspar-quartz*, interpreted as equilibrium assemblage. In the M74 bulk compositions at this pressure and temperature the divariant melting field of biotite is not stable and so the assemblage contains no melt (compare with D40-13, Plate 2a). The solidus for this composition is the (os, crd) reaction (INSERT D). The dark void space, where the charge has not fully compacted, is characteristic of unmelted experiments in the solid media runs. 10μm scale as marked.

Plate 2

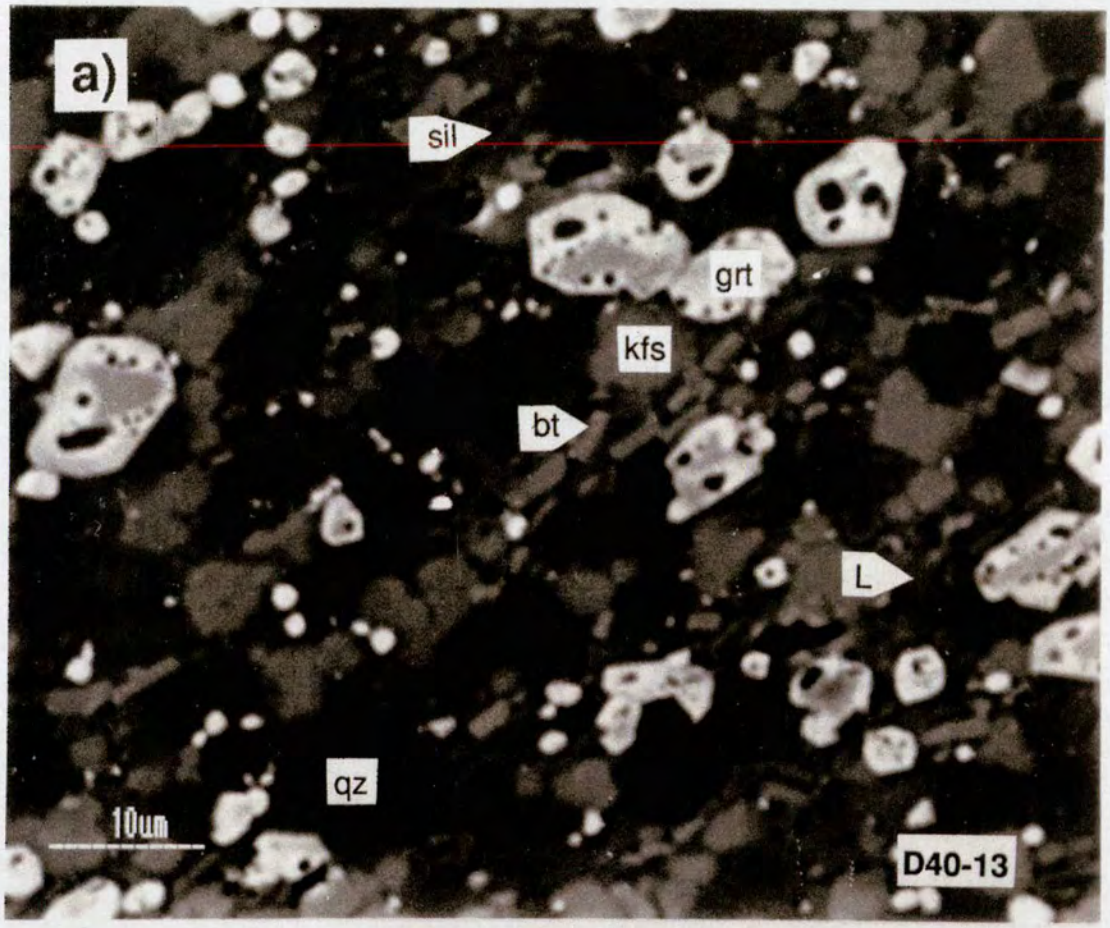

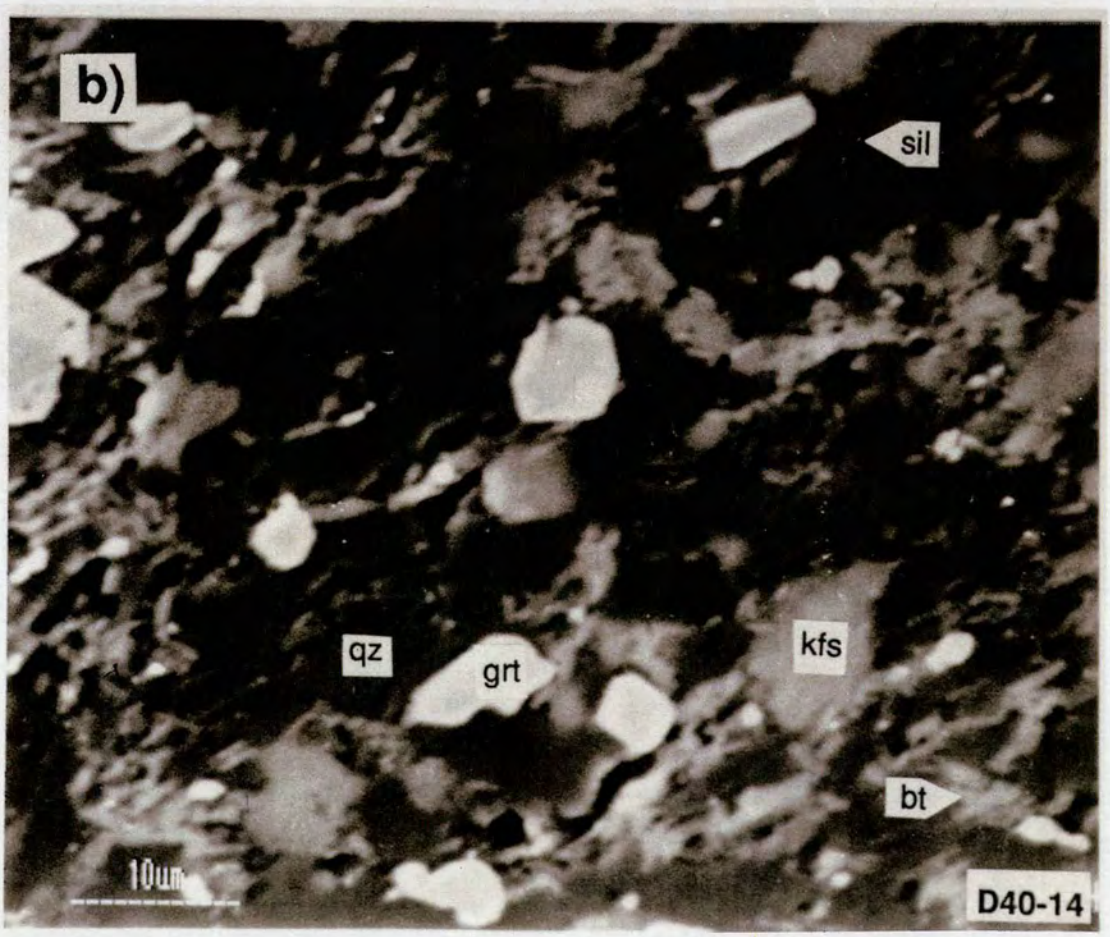

Plate 3. Back-scattered electron photomicrographs.

a) D48-14. 925°C, 12.5kb in solid-media salt cell. Product assemblage: *orthopyroxene-garnet-K-feldspar-sillimanite-quartz-melt*, interpreted as equilibrium assemblage. The orthopyroxene crystals have a contrast intermediate between the melt and K-feldspar, and are larger and brighter than the sillimanite crystals. Compare with D48-15 (Plate 3b) which has the same assemblage but with different modal abundances of phases. 10μm scale as marked.

b) D48-15. 925°C, 12.5kb in solid-media salt cell. Product assemblage: *orthopyroxene-garnet-K-feldspar-sillimanite-quartz-melt*, interpreted as equilibrium assemblage. This experiment produced the same assemblage as D48-14 (Plate 3a) but contained more orthopyroxene and less garnet due to the higher X_{Mg} of the bulk composition (see three-component projection in Appendix Three). The large, tabular shape of the orthopyroxene crystals shows the ease with which that phase grows, particularly compared to the sillimanite crystals. 50μm scale as marked.

Plate 3

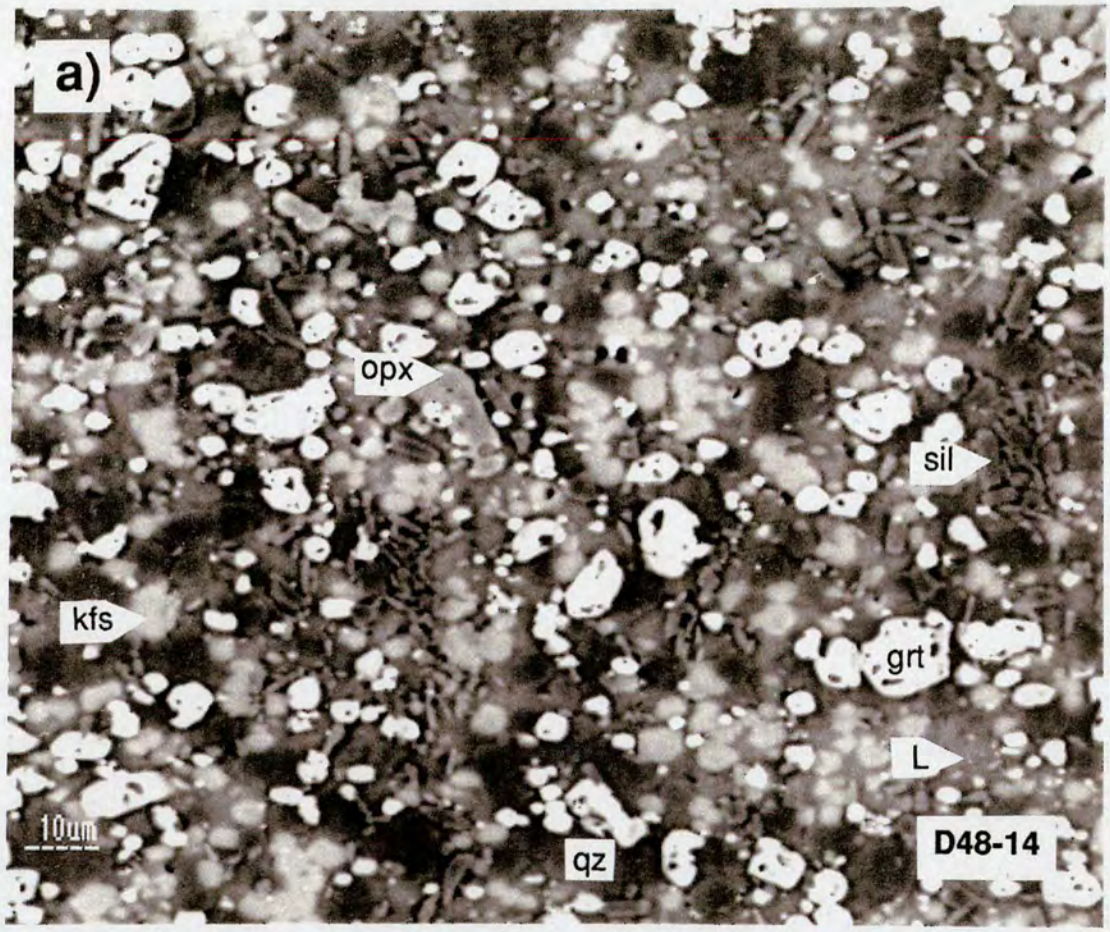
a)
opx
sil
kfs
grt
L
10µm
qz
D48-14

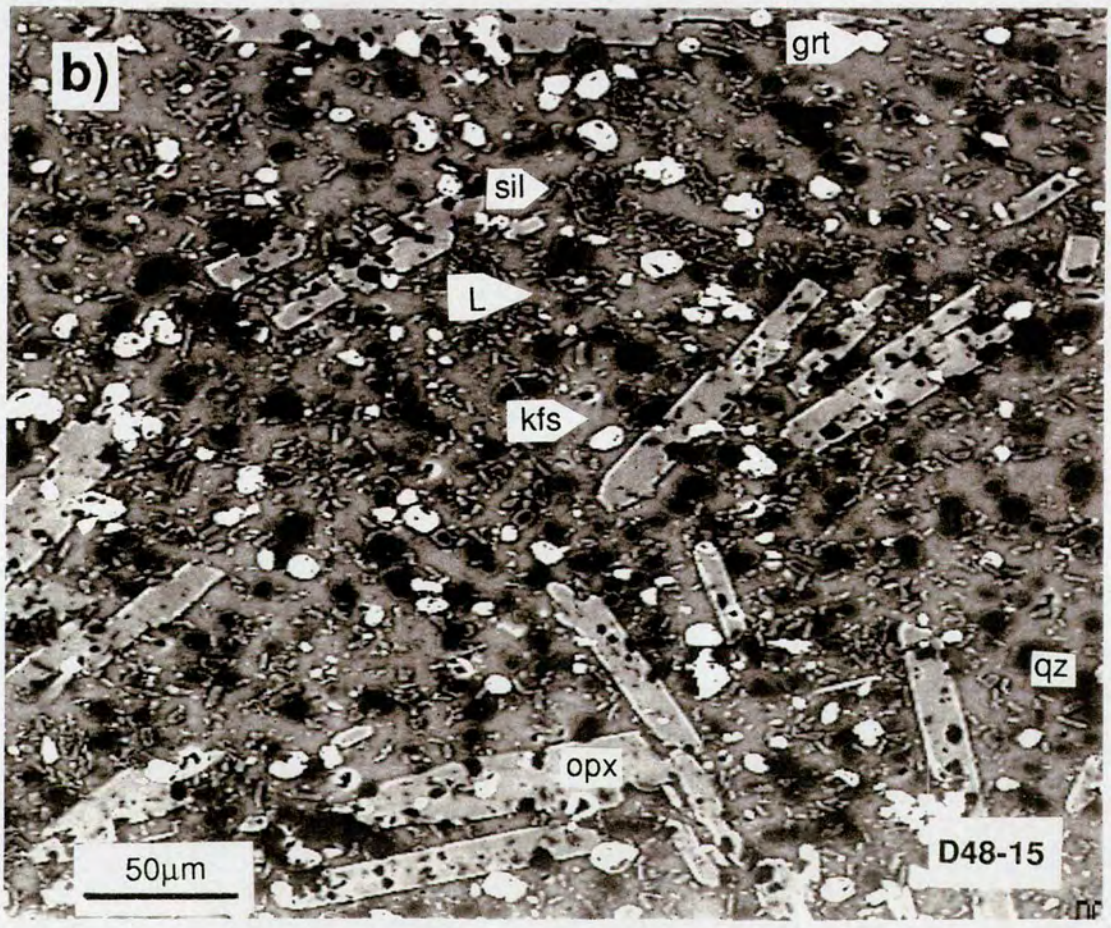
b)
grt
sil
L
kfs
qz
opx
50µm
D48-15

Plate 4. Back-scattered electron photomicrographs.

a) D65-16A. 1000°C, 9kb, in gas-bomb apparatus. Product assemblage: *garnet-K-feldspar-sillimanite-quartz-melt*, interpreted as equilibrium assemblage. The K-feldspar is concentrated in a selvedge next to the edge of the charge, and is quite rare in the centre. This may be due to the K-feldspar preferring to nucleate or grow on the capsule metal. The selvedges also occur in D59-18, D60-18A and D65-18A. The K-feldspar selvedges are discussed in section 5.4. The round, black, void spaces are characteristic of the gas-bomb runs both above and below the solidus. The gas filling the voids is not known. It cannot be water as, if that were present, melting would be much more extensive (see qz-absent D56-16, table 3.1) and there is no reason to suspect the presence of carbon dioxide as no graphite is used in the capsule preparation. The air which is in the sealed capsule to begin with should compress to negligible volume at the high run pressures, as it does in the solid-media super-solidus runs. Argon is the pressure medium used in the gas bombs and could be detected in some failed capsules but these had also lost all their water (no hydrous phases at all). Perhaps the void space appears when the run is quenched and the charge contracts. 10μm scale as marked.

b) D65-18A. 1000°C, 9kb, in solid-media salt cell. Product assemblage: *orthopyroxene-garnet-K-feldspar-sillimanite-quartz-melt*, interpreted as equilibrium assemblage. The high proportion of melt seen in this experiment, and D65-16A, is commensurate with the high temperature they were run at. The garnet and orthopyroxene crystals are the same shade in this photomicrograph but can be distinguished by their contrasting shapes, round and tabular respectively. See Plate 4a for a discussion of the dark void spaces. 10μm scale as marked.

Plate 4

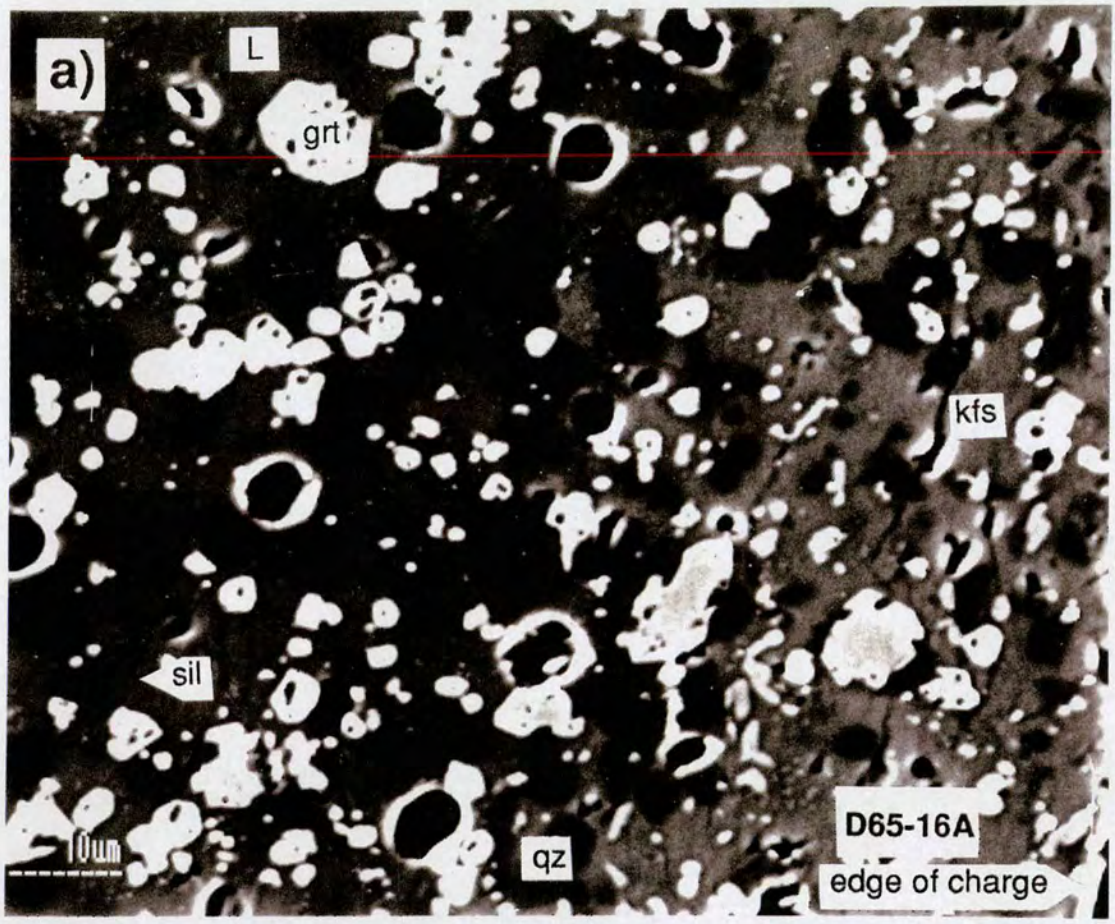
a)
L
grt
kfs
sil
qz
10um
D65-16A
edge of charge

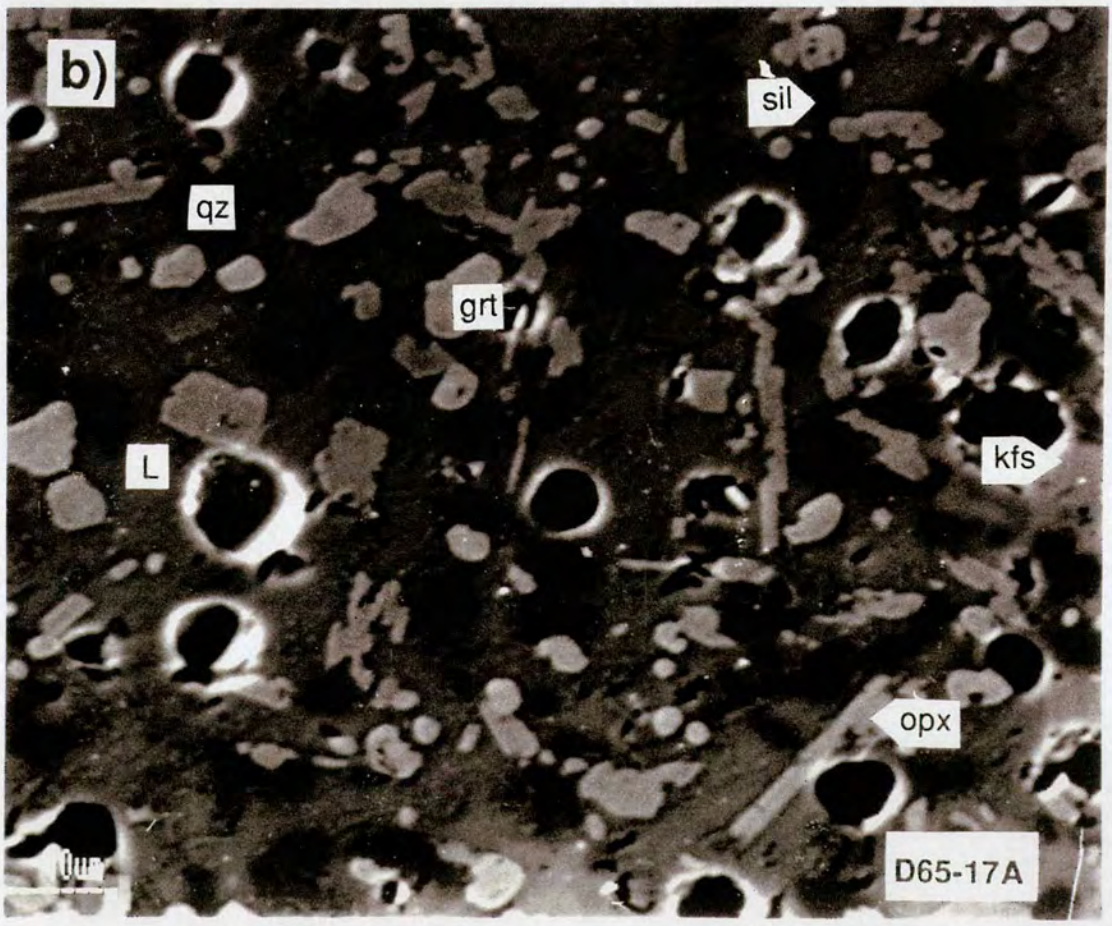
b)
sil
qz
grt
L
kfs
opx
0um
D65-17A

Plate 5. Back-scattered electron photomicrographs.

a) D59-18. 965°C, 8kb in the gas-bomb apparatus. Product assemblage: *osumilite-orthopyroxene-sillimanite-K-feldspar-melt*, interpreted as equilibrium assemblage. Iron is a much heavier element than the other elements in the system and so the iron-poor bulk compositions have a lower mean-atomic-number contrast between the phases, as in this photomicrograph. See Plate 4a for a discussion of the dark void spaces. 10μm scale as marked.

b) D57-16. 910°C, 8kb in the gas-bomb apparatus. Product assemblage: *cordierite-orthopyroxene-garnet-sillimanite-K-feldspar-melt*, orthopyroxene interpreted as metastable on the basis of bulk compositional constraints (figure 4.3). The quartz, cordierite and melt are rather difficult to distinguish in this photomicrograph. See Plate 4a for a discussion of the dark void spaces. 10μm scale as marked.

Plate 5

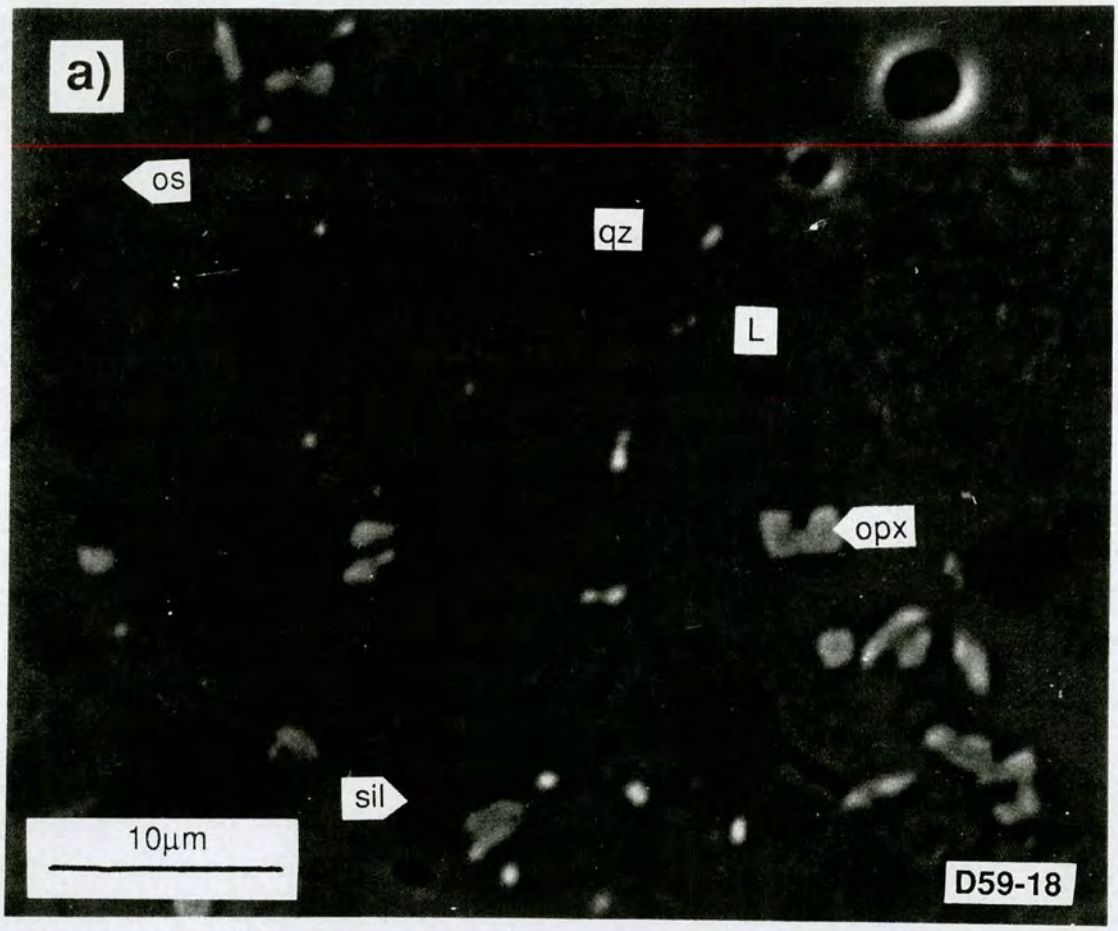

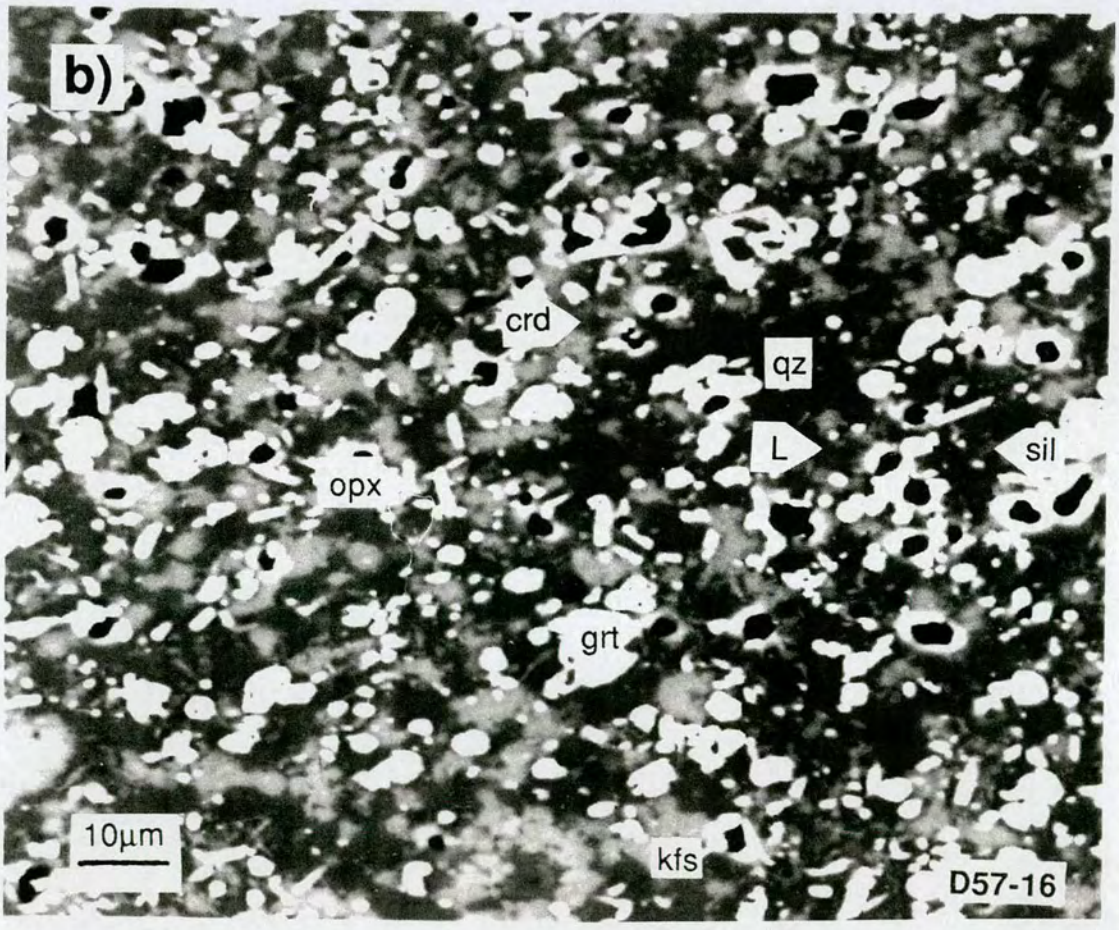

Plate 6. Back-scattered electron photomicrographs.

a) **D64-16A**. Reversal run: 910°C, 8⇒9kb in the gas-bomb apparatus. Product assemblage: *garnet-orthopyroxene-cordierite-sillimanite-K-feldspar-quartz-melt*, cordierite is interpreted as being metastable. Only a trace of cordierite remained in this experiment and there is none in the photomicrograph. Experiment D64-18A lies unambiguously at higher pressures than the (os, bt) reaction (INSERT A) and so D64-16A is also interpreted to be so, therefore requiring the metastability of the cordierite (see sections 4.1 and 5.2). The thin nature of the garnet rims in some experiments, which caused difficulty in their analysis, is illustrated here, where they are at most 2μm wide. See Plate 4a for a discussion of the dark void spaces. 10μm scale as marked.

a) D64-18A. Reversal run: 910°C, 8⇒9kb in the gas-bomb apparatus. Product assemblage: *orthopyroxene-cordierite-sillimanite-K-feldspar-quartz-melt*, interpreted as equilibrium assemblage. The cordierite can be distinguished from the quartz in this photomicrograph by its slightly lighter contrast. This results from the use of the electron microprobe's X-ray detector facility, set to magnesium, which gives an added brightness to phases containing magnesium. See Plate 4a for a discussion of the dark void spaces. 10μm scale as marked.

Plate 6

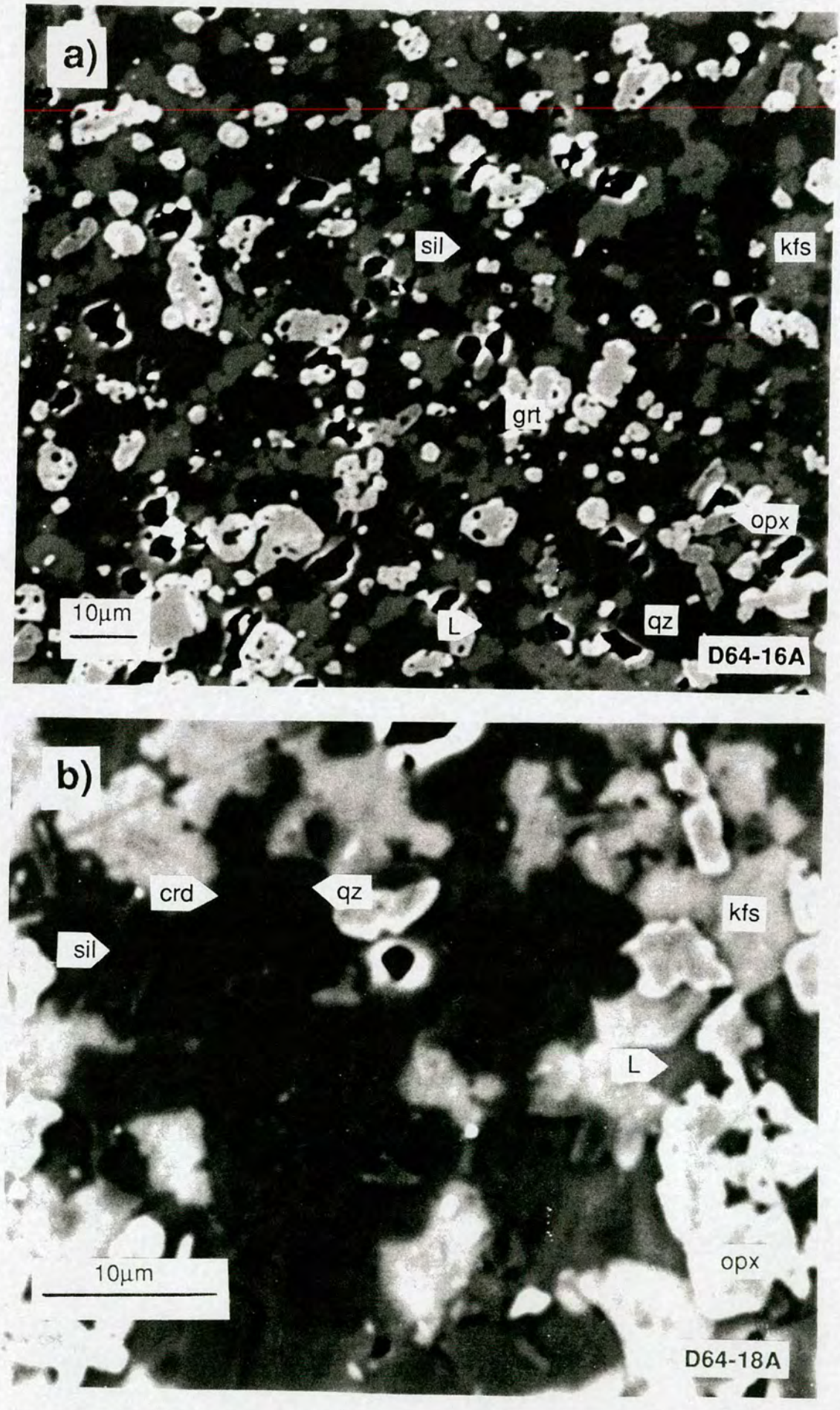
a)
sil
kfs
grt
opx
10µm
L
qz
D64-16A
b)
crd
qz
sil
kfs
L
10µm
opx
D64-18A

Plate 7. Back-scattered electron photomicrographs.

a) D47-18. 940°C, 7kb in the gas-bomb apparatus. Product assemblage: *osumilite-cordierite-orthopyroxene-quartz-melt*, interpreted as equilibrium assemblage. The osumilite can be identified in this photomicrograph by its tabular shape, bright outline and slightly darker contrast compared to the melt. The cordierite contrast is enhanced using the electron microprobe's X-ray detector (see Plate 6b). See Plate 4a for a discussion of the dark void spaces. 10μm scale as marked.

b) D49-16. 875°C, 7kb in the gas bomb apparatus. Product assemblage: *biotite-cordierite-garnet-K-feldspar-quartz-melt*, interpreted as equilibrium assemblage. This assemblage represents the divariant biotite melting field present between the (os, opx) and (os, sil) reactions (INSERTS C and D). See Plate 4a for a discussion of the dark void spaces. 10μm scale as marked.

Plate 7

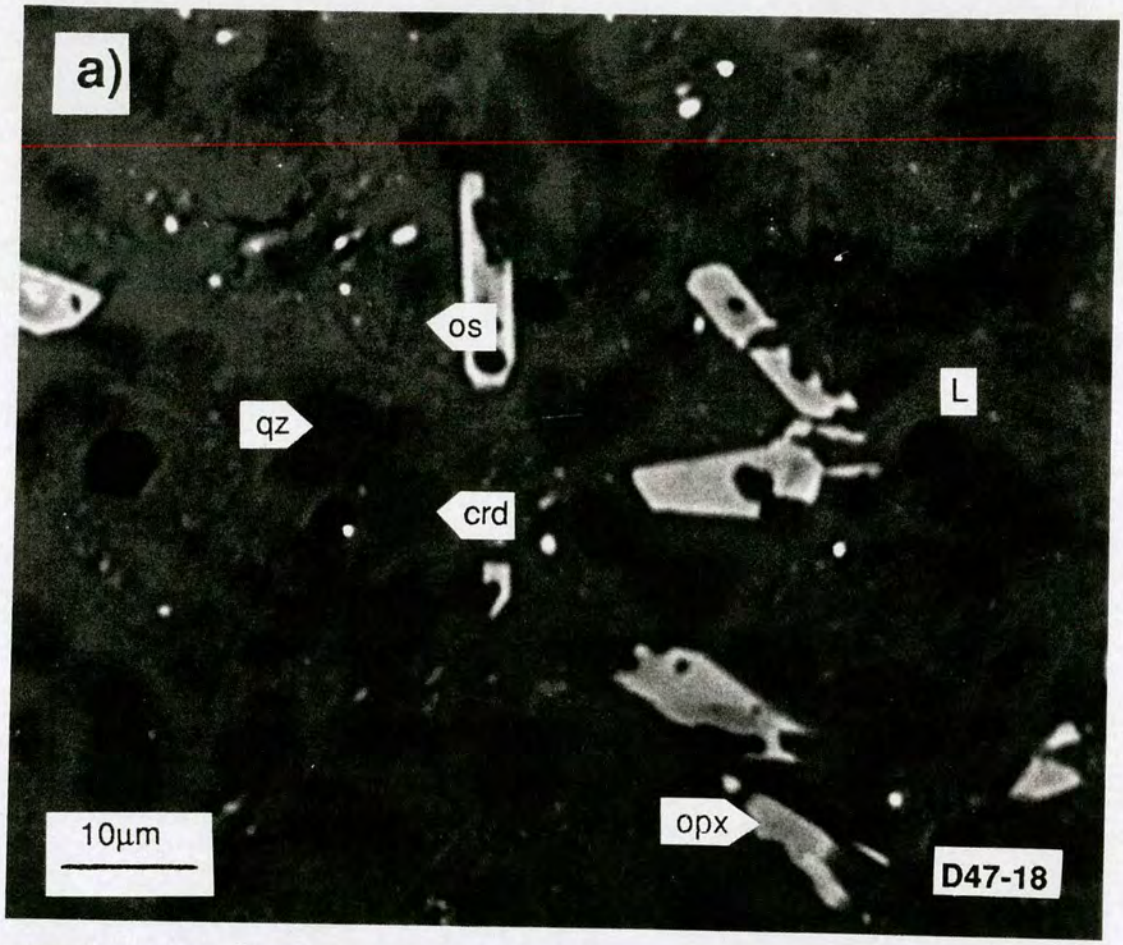

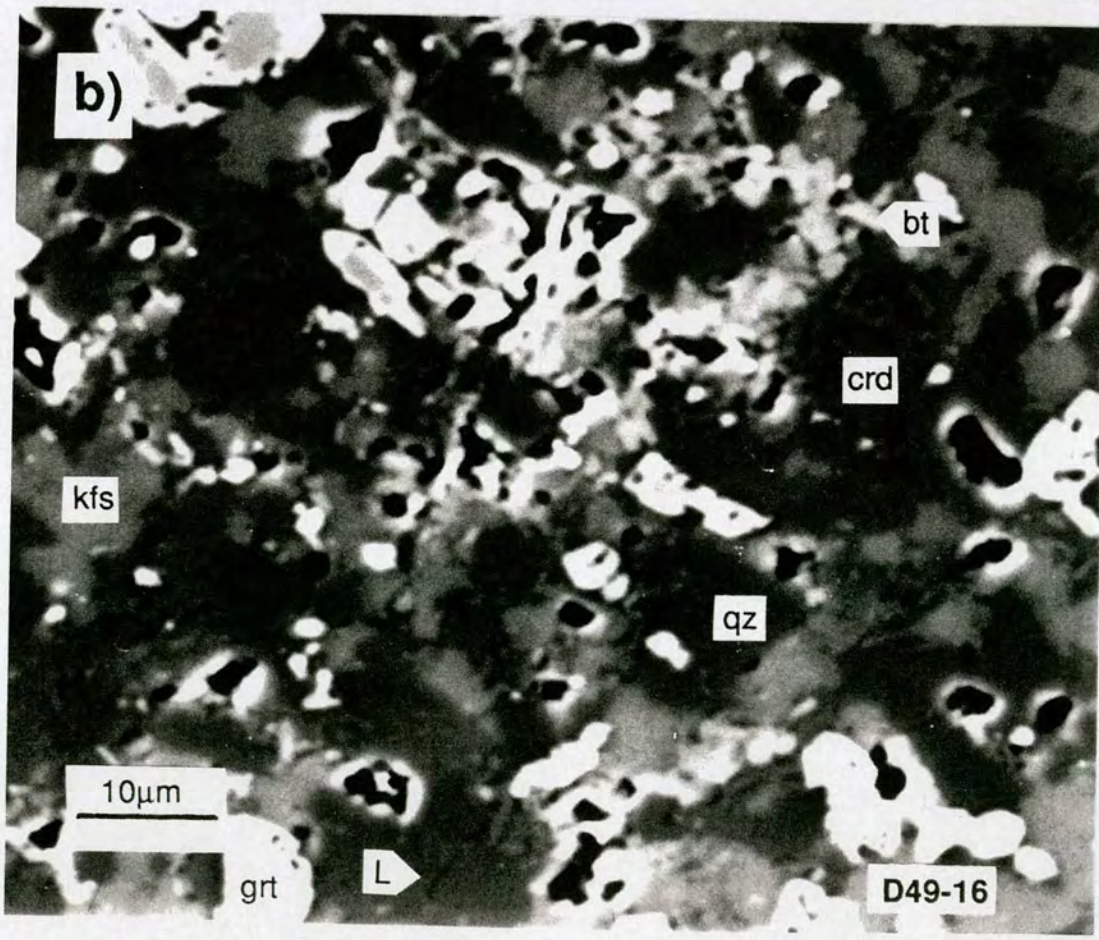

Plate 8. Back-scattered electron photomicrographs.

a) D63-16A. Reversal run: 890⇒855°C, 7kb in the gas-bomb apparatus. Product assemblage: *biotite-cordierite-garnet-sillimanite-K-feldspar-quartz*, Interpreted as equilibrium assemblage. This subsolidus assemblage reverses the biotite dehydration melting reactions through which biotite is exhausted up temperature. The limited re-growth of biotite is partly due to the fact that a large amount of water-bearing cordierite is present. A good deal of the water, originally in biotite, is now contained in the cordierite. The cordierite is clearly distinguishable from the quartz due to the use of the electron microprobe's X-ray detector (see Plate 6b). See Plate 4a for a discussion of the dark void spaces. 10μm scale as marked.

b) D63-18A. Reversal run: 890⇒855°C, 7kb in the gas-bomb apparatus. Product assemblage: *biotite-cordierite-orthopyroxene-K-feldspar-quartz*, interpreted as equilibrium assemblage. The biotite growth in this melt-absent experiment reverses the biotite dehydration melting reactions which consume biotite up temperature. As in D63-16A, a large amount of cordierite is present and the re-growth of biotite is rather limited. The cordierite (with enhanced contrast, see Plate 6b) crystal labelled has grown into a large poikoblast during the long duration of the two step run (table 3.2). See Plate 4a for a discussion of the dark void spaces. 10μm scale as marked.

Plate 8

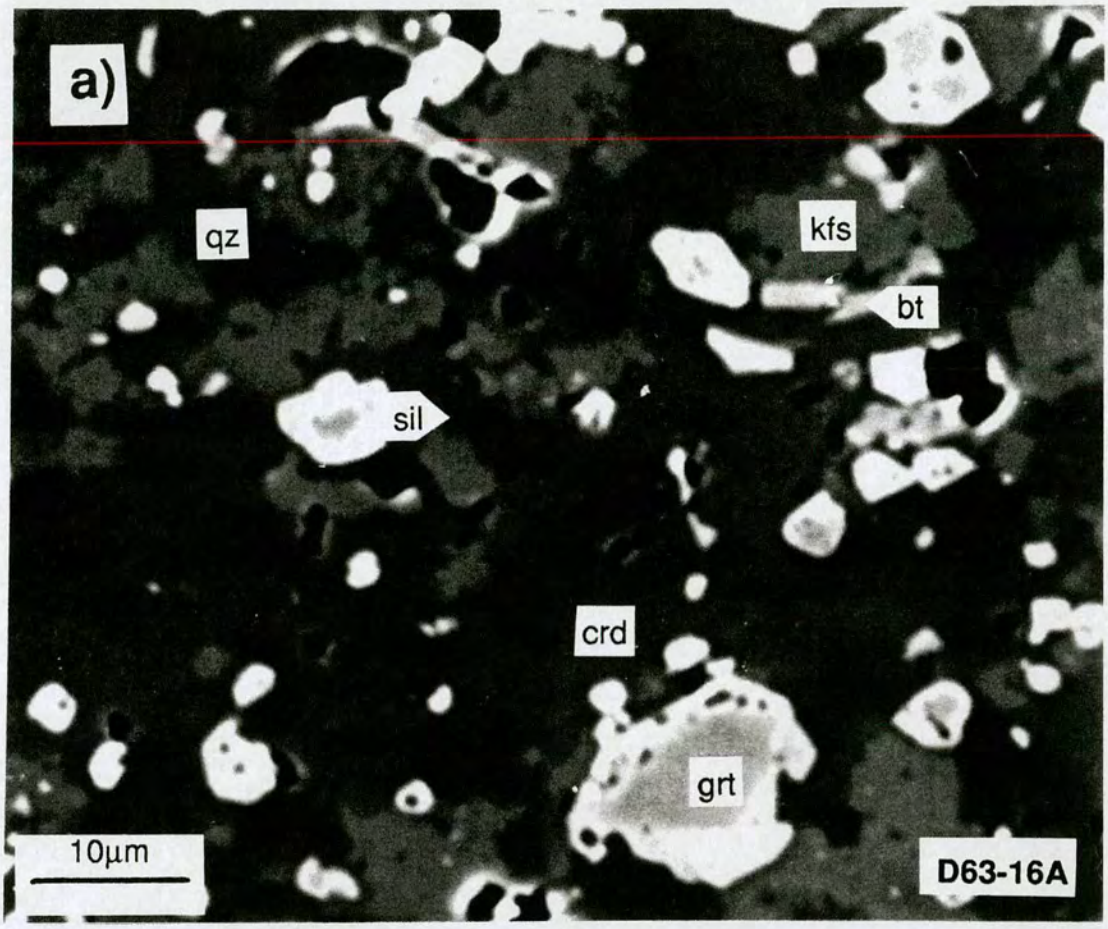
a)
qz
kfs
bt
sil
crd
grt
10µm
D63-16A

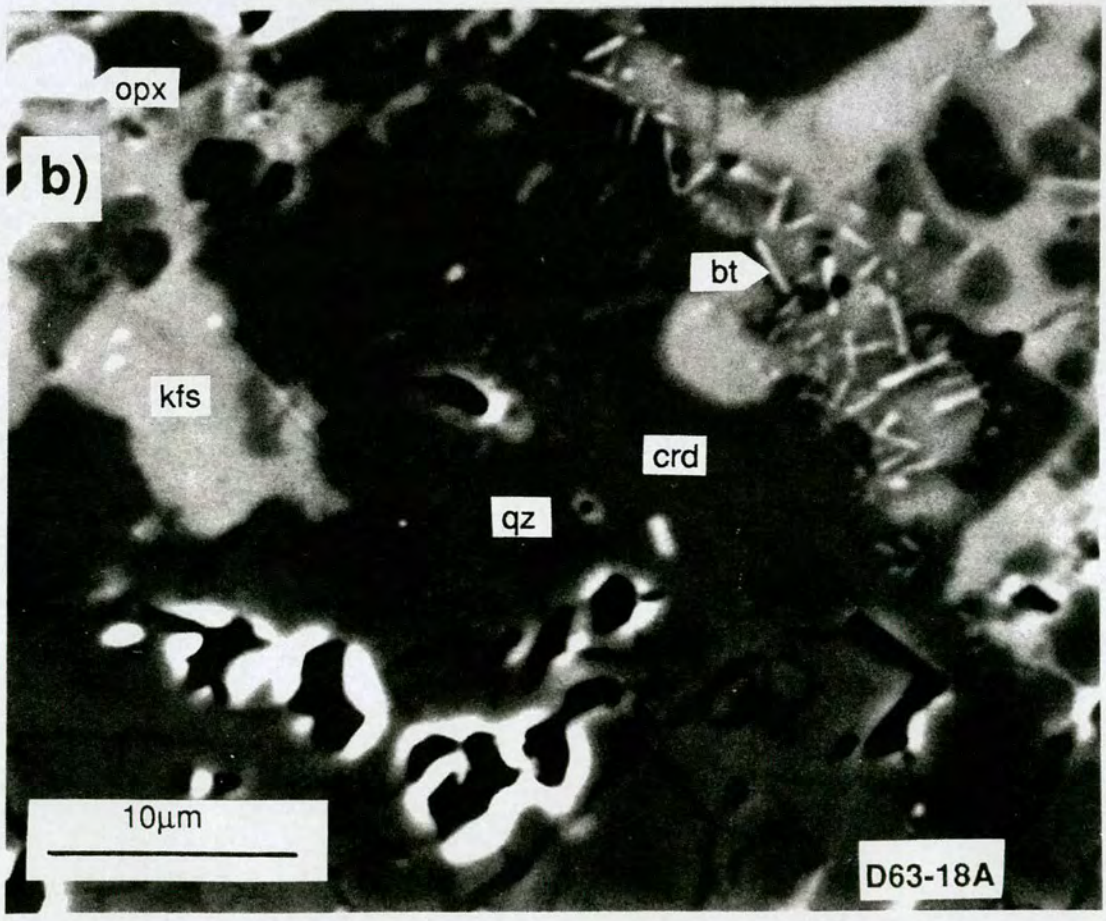
opx
b)
bt
kfs
crd
qz
10µm
D63-18A

Plate 9. Back-scattered electron photomicrographs.

a) D60-17A. 900°C, 6kb in the gas-bomb apparatus. Product assemblage: *osumilite-cordierite-orthopyroxene-garnet-quartz-K-feldspar-melt*, interpreted as a univariant equilibrium assemblage. The seven phase assemblage is interpreted to lie on the univariant KFMASH reaction (os, sil) (INSERT A). Osumilite is abundant in this experiment and its euhedral shape and large crystal size suggest it grows easily in these experiments. The cordierite and quartz are easily distinguished in this photomicrograph. The dark void spaces in this run have bright rims. See Plate 4a for a discussion of the dark void spaces. 25μm scale as marked.

b) D51-16. 875°C, 5kb in the gas-bomb apparatus. Product assemblage: *osumilite-cordierite-garnet-spinel-quartz-K-feldspar-melt*, spinel interpreted as metastable. The tiny, bright crystals of spinel were only seen in this experiment, which is from the lowest pressure run. The easy growth of osumilite (Plate 9b) is also well illustrated in this photomicrograph. See Plate 4a for a discussion of the dark void spaces. 25μm scale as marked.

Plate 9

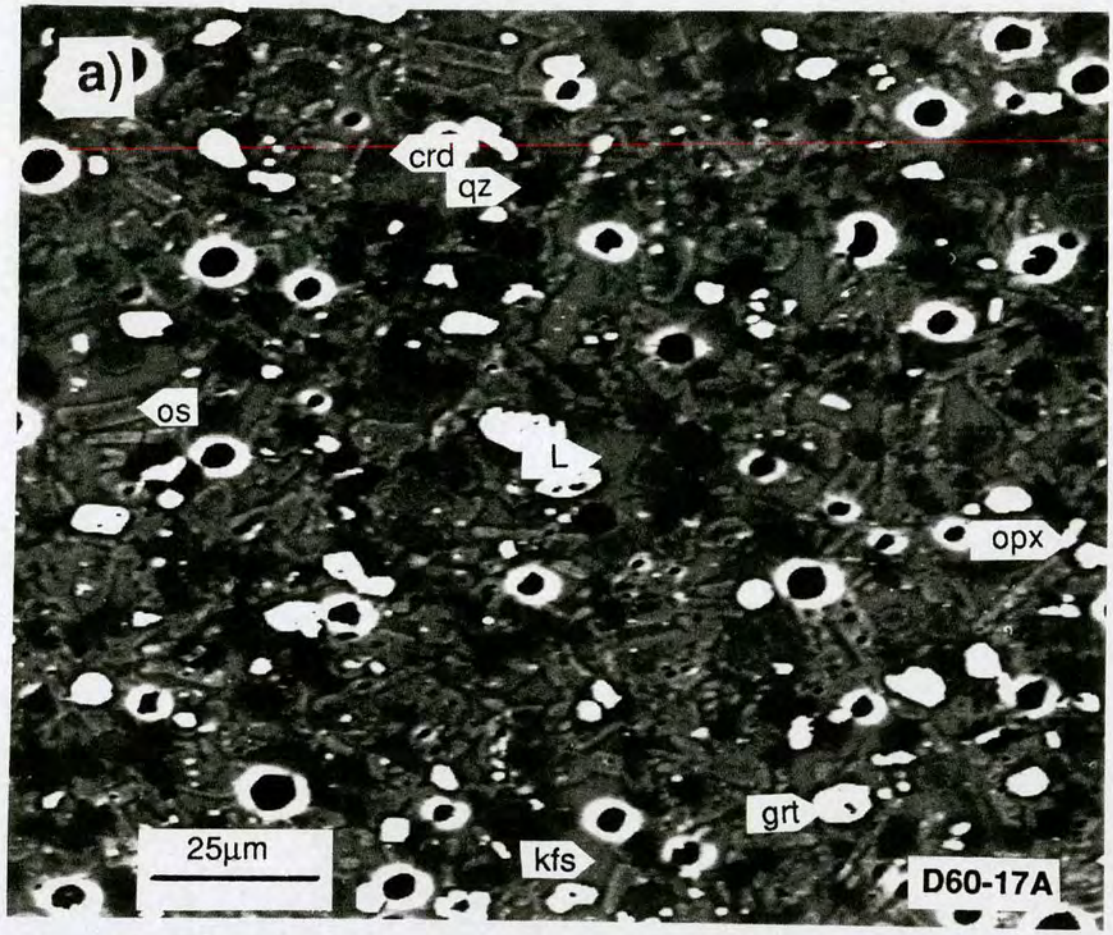
a)
crd
qz
os
L
opx
grt
kfs
25µm
D60-17A

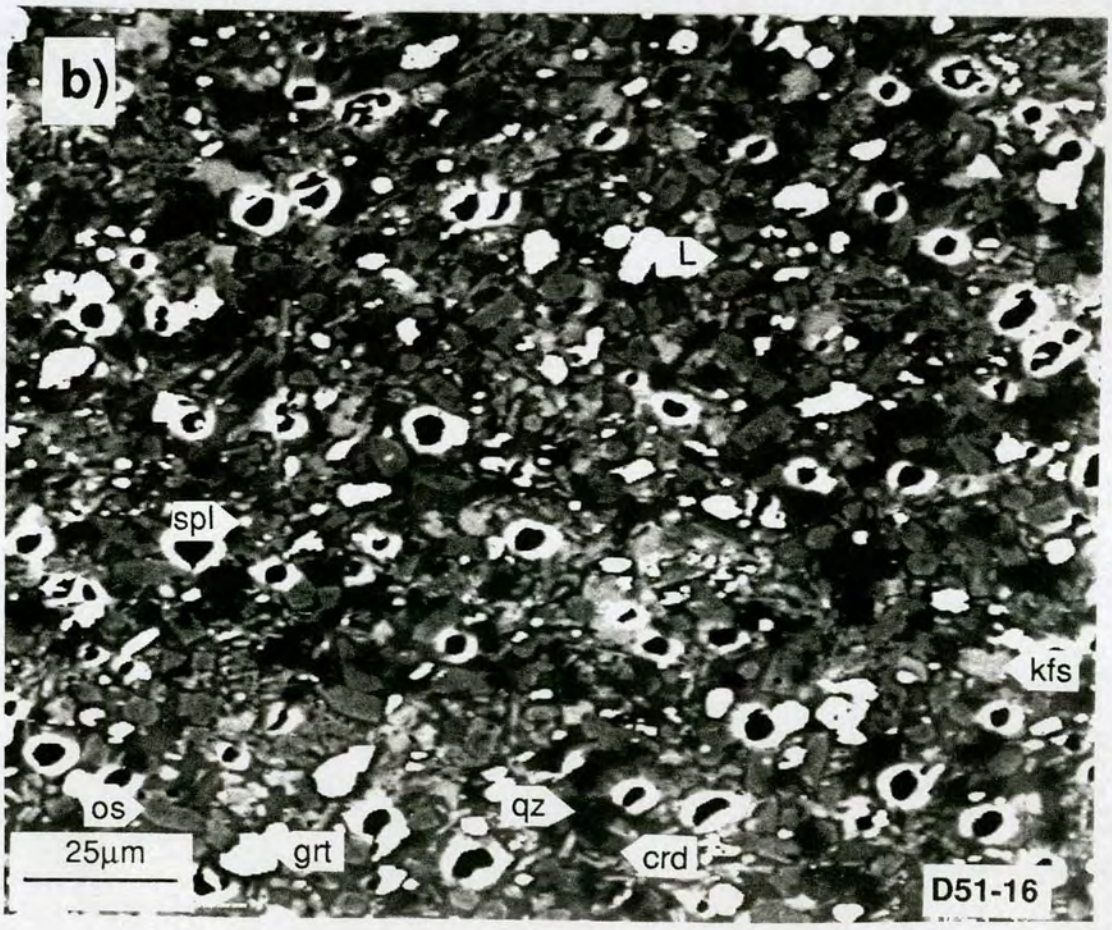
b)
L
spl
kfs
os
qz
grt
crd
25µm
D51-16

Plate 10. Back-scattered electron photomicrographs.

a) Platinum wire in D44-13. 940°C, 7kb in gas-bomb apparatus. The wire is originally pure platinum, circular and 25μm in diameter. The wire is relatively undeformed. The minerals surrounding the wire cannot be seen because of their very low contrast relative to the wire. During the run, iron alloys with the platinum and this experiment produced a zoned wire. The zoning is not gradual, but occurs over a sharp boundary, suggesting that there is not a continuous solid solution between iron and platinum at these temperatures. The pits produced by the electron beam during the analysis are shown. 10μm scale as marked.

b) Platinum wire in D41-13. 950°C, 12.5kb in the solid-media salt-cell. The wire is originally pure platinum, circular and 25μm in diameter. The wire has been severely desegregated during the course of the run, which might help it to equilibrate. The contrast has been adjusted to show the silicate phase and so no zoning is seen in the wire. In fact, in this case, there is no zoning. There is a halo around the wire from which the iron has been removed in order to alloy with the platinum. 50μm scale as marked.

Plate 10

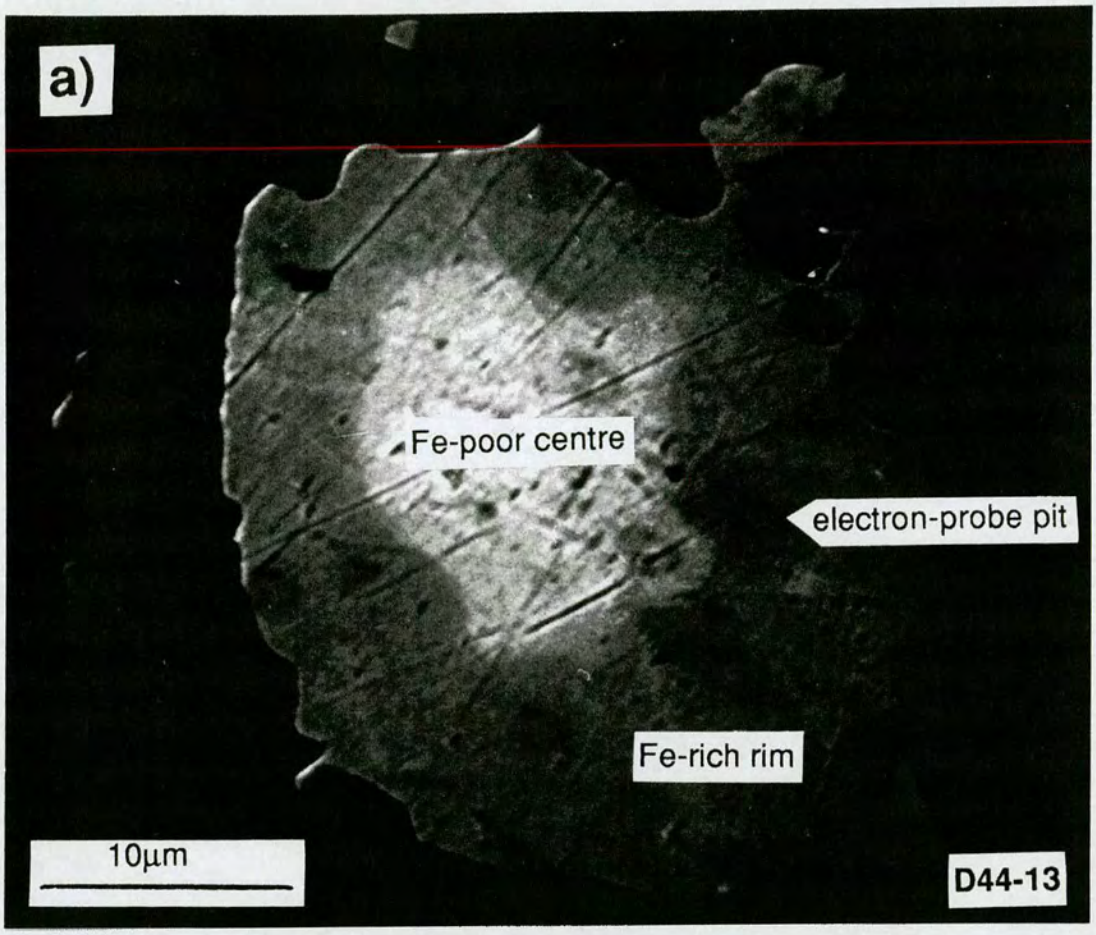
a)
Fe-poor centre
electron-probe pit
Fe-rich rim
10μm
D44-13

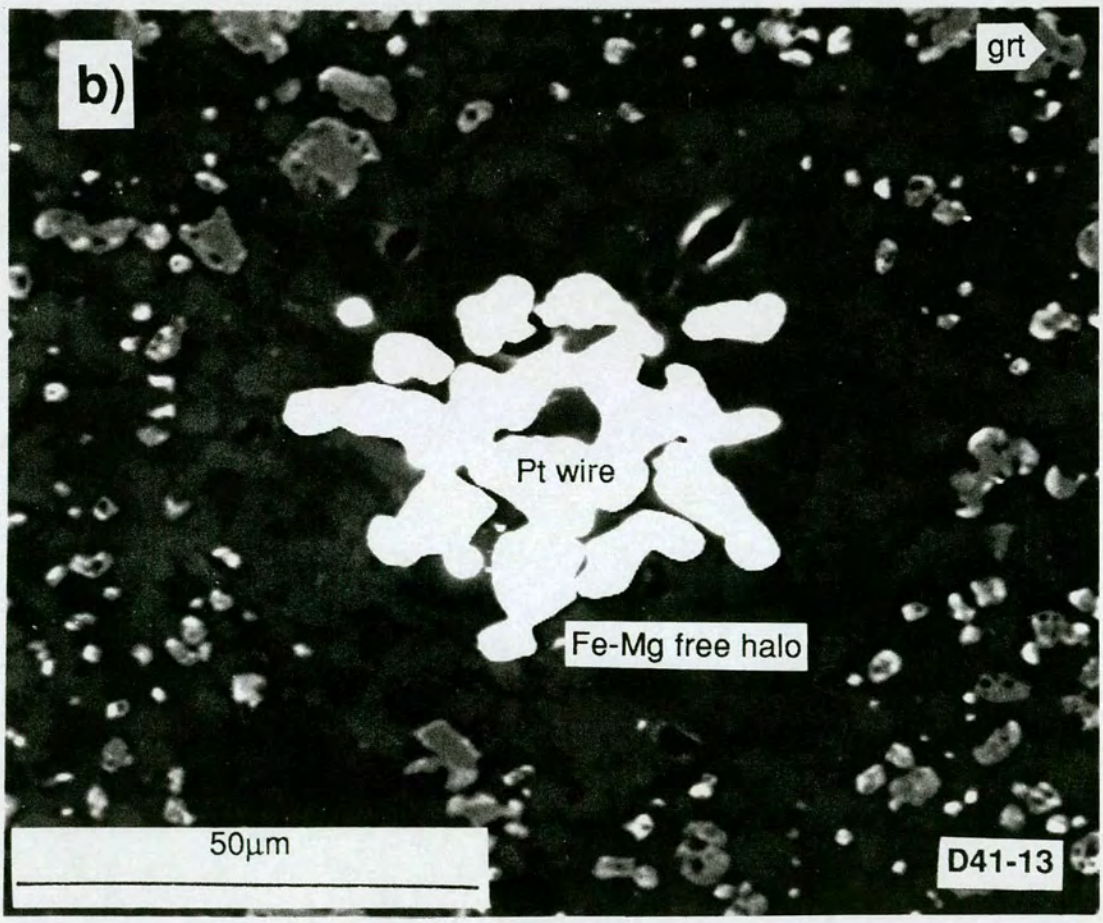
b)
grt
Pt wire
Fe-Mg free halo
50μm
D41-13

Chapter Five

REVERSAL EXPERIMENTS AND ASSESSMENT OF THE EQUILIBRATION OF THE EXPERIMENTS

Chapter Five. Reversal experiments and assessment of the equilibration of the experiments.

5.1 INTRODUCTION AND SYNOPSIS OF CHAPTER.

It is an essential duty of experimentalists to give a assessment of how closely their experiments approach equilibrium, i.e. how near the Gibb's free energy of the assemblages produced are to their minimum. It is impossible to *prove* that an assemblage is at equilibrium: the possibility always remains that, if run for a longer time, another phase with a lower free energy could form, or a phase present could disappear, thereby giving a different assemblage. Nonetheless, the successful consideration of a range of necessary criteria can allow the assumption of equilibrium for a set of experiments. These criteria include data presented in previous chapters, such as homogeneity of phase compositions and equilibrium partitioning between phases, and others described in this chapter such as the results of reversal experiments. Comparison with natural rock data is also a useful guide of the closeness of an experiment to equilibrium.

The pressure-temperature reversals are a very important, necessary condition of equilibrium, demonstrating that the reactant assemblage can be recovered from the product assemblage. The reversal of a reaction in pressure-temperature space *proves* the reaction occurs in that pressure-temperature interval. Of course, if the product or reactant assemblages are metastable then the reaction is also metastable; it is quite possible to reverse a metastable equilibrium (Holloway and Wood, 1988).

Three of the four pressure-temperature reversal runs were successful and these determined the position of the some of the most important reactions in the study. The compositional reversals were successful in the solid-media apparatus but less so in the gas-bomb runs. These reversals, combined with the other considerations, lead to the conclusion that the experiments represent an acceptably close approach to equilibrium.

5.2. PRESSURE-TEMPERATURE REVERSALS.

One of the primary objectives of this study is to locate the pressure-temperature position of the [os] invariant point, which forms at the intersection of the sub-parallel

univariant biotite dehydration melting reactions[1] (steep positive dP/dT's) and the (os, bt) reaction[1] (shallow negative dP/dT) (INSERT A). This point and these reactions are fundamental in subdividing metamorphic conditions in the metapelitic granulite facies (e.g. Powell and Downes, 1990). The single-step experiments, which form the bulk of this study, indicate the position of these reactions, but as discussed above, only reversals can prove their occurrence in a given pressure-temperature interval. The details of the reversals attempted are given in table 5.1. It is necessary to be confident that the product assemblage has formed in the first step of the experiment before it is reversed to the reactants. Therefore, the first step of each reversal was at a pressure and temperature for which there was already a single-step experiment. After the first step of each isobaric reversal the temperature was lowered gradually, over a period of several hours, to try and enable some biotite to nucleate in the small divariant melting interval. In run D58 the temperature was dropped instantaneously and the unsuccessful results suggested that the biotite had problems nucleating in the liquid-absent, subsolidus environment.

The biotite dehydration melting reaction reversal experiment run at 10kb, D67-16A (plate 1a), is illustrated in figure 5.1, in which it is compared with D43-13 and D43-14. The starting assemblage was garnet-biotite-sillimanite-K-feldspar-quartz. The

Experiment	Reaction	Pressure (kb)	Temperature (°C)	Time (hours)	Result
D67-16A	BDMR	10kb	900⇒875	188⇒580	successful
D63-16A	BDMR	7kb	890⇒855	253⇒424	successful
D63-18A	BDMR	7kb	890⇒855	253⇒424	successful
D58-16,17,18	BDMR	7kb	900⇒875	268⇒293	unsuccessful
D64-16A	(os, bt)	8⇒9kb	910	259⇒424	successful
D64-18A	(os, bt)	8⇒9kb	910	259⇒424	successful

Table 5.1. Summary of the two-step reversal experiments over the biotite dehydration melting reactions (BDMR's) and the (os, bt) reaction, grt + crd + kfs + qz = opx + sil + L. These experiments are illustrated and described below. The reversals were considered successful if they produced an assemblage which lay on the required side of the reaction involved. The reactions reversed are considered in further in Chapter Six (see INSERT A, univariant grid). See tables 3.1, 3.2, 4.1 and 4.2 for further details of experiments and assemblages.

[1] There are four biotite dehydration melting reactions, two at higher pressures than the [os] invariant point and two at lower pressures. However, for some of the bulk compositions used there is a narrow divariant melting interval associated with the univariant reaction. Furthermore, if more than one univariant reaction is stable then the reactions are very close together. Therefore, for the purposes of the reversals, the system is treated as if the biotite breaks down over a single reaction.

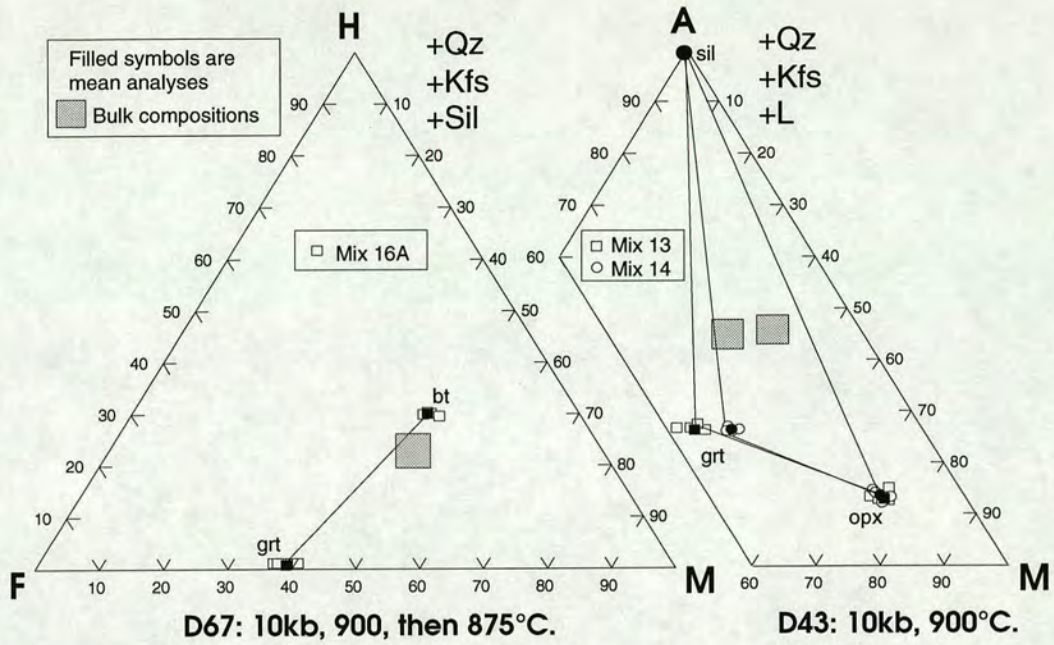

Figure 5.1. Isobaric reversal experiment D67-16A plotted on an HFM diagram. D43-13 and D43-14 (shown on an AFM diagram) are the single-step experiments run at the same pressure and temperature as the first step of the reversal. All the experiments were run in salt-cells in the solid-media apparatus.

first step of the reversal would have produced the biotite-absent assemblage garnet-orthopyroxene-sillimanite-K-feldspar-quartz-melt (D43-13). As the final assemblage of the reversal was garnet-biotite-sillimanite-K-feldspar-quartz, the same as the starting assemblage, the BDMR is considered to have been successfully reversed over the interval 900-875°C. The X_{Mg} of the garnet in D67-16A is significantly lower than that in D43-13 (0.39 versus 0.51) but it was shown in section 3.4.2 that the garnet is often not in Fe-Mg equilibrium.

The BDMR's were also successfully reversed at 7kb (figure 5.2 and plates 8a and 8b). The bracket used, 895-855°C, in fact crosses several reactions (see INSERTS A, C, D, E) but this is necessary if biotite is to be completely consumed in the first step of the reversal, because there is a narrow divariant biotite melting interval. A reasonably large reversal bracket is necessary because of the slow rates of reaction close to a given equilibrium[2]. This factor was probably part of the reason

[2] The rate of reaction is approximately proportional to the free energy difference driving the reaction, and this tends to zero on the reaction.

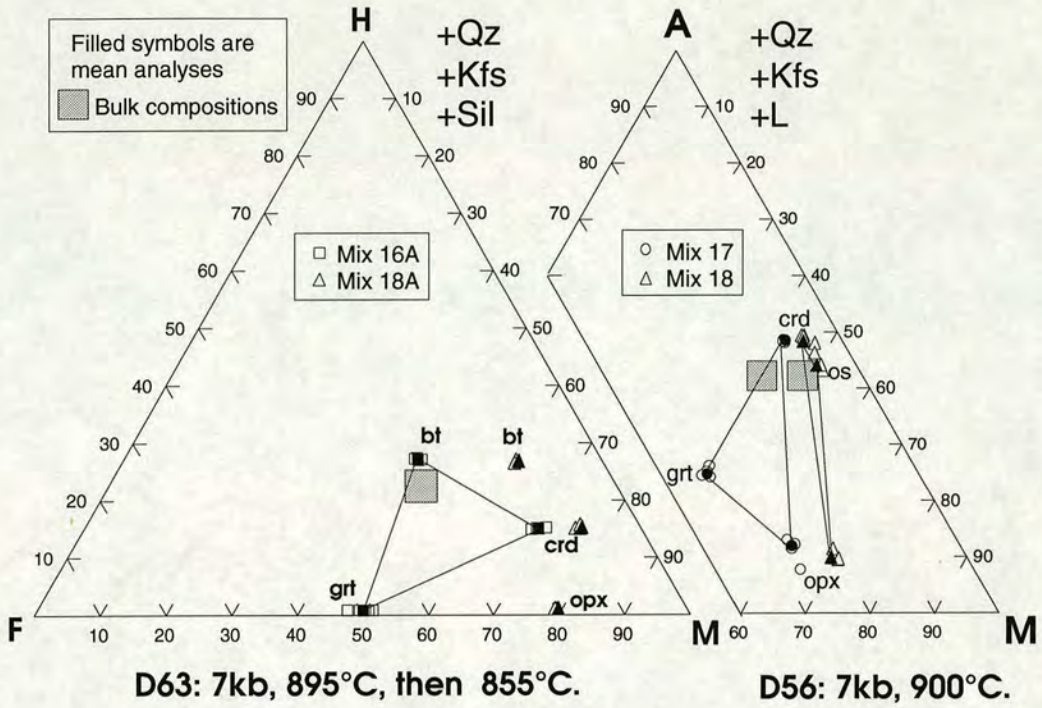

Figure 5.2. Isobaric reversal experiments D63-16A and D63-18A plotted on an HFM diagram. D63-18A did not contain sillimanite and therefore cannot be legitimately plotted on an HFM diagram but the phases are shown to illustrate the assemblage. D56-17 and D56-18 (shown on an AFM diagram) are the single step experiments run at the same pressure and (virtually the same) temperature as the first step of the reversal. Runs D49 and D66, run at 875°C, 7kb (diagrams in Appendix Three), illustrate the divariant biotite melting field which exists in the reversal interval.

why the reversal (D58- 16, 17, 18) attempted at 7kb over the bracket 900-875°C was unsuccessful, i.e. produced no biotite. The reversal at 10kb was successful over the same temperature interval but was run in a solid-media salt cell, which enhances reaction relative to the gas-bombs (section 2.3.5). Also, the single step runs at 7kb and 875°C (D49 and D66) show that, at that pressure and temperature, all the bulk compositions are in a divariant biotite melting field, and so the amount of biotite is considerably less than the original 20-23 wt% (table 2.7). Therefore, the D58 reversal is thought to have failed because of the relatively poor reaction rates experienced in the gas bombs, the small amount of biotite stable at the lower temperature, the small temperature interval of the reversal and also, perhaps most importantly, the relatively short second-step run time.

Alternatively, the negative result of D58 could be taken as evidence that the results of runs D49 and D66 at 875°C, 7kb are metastable and that all the biotite would have

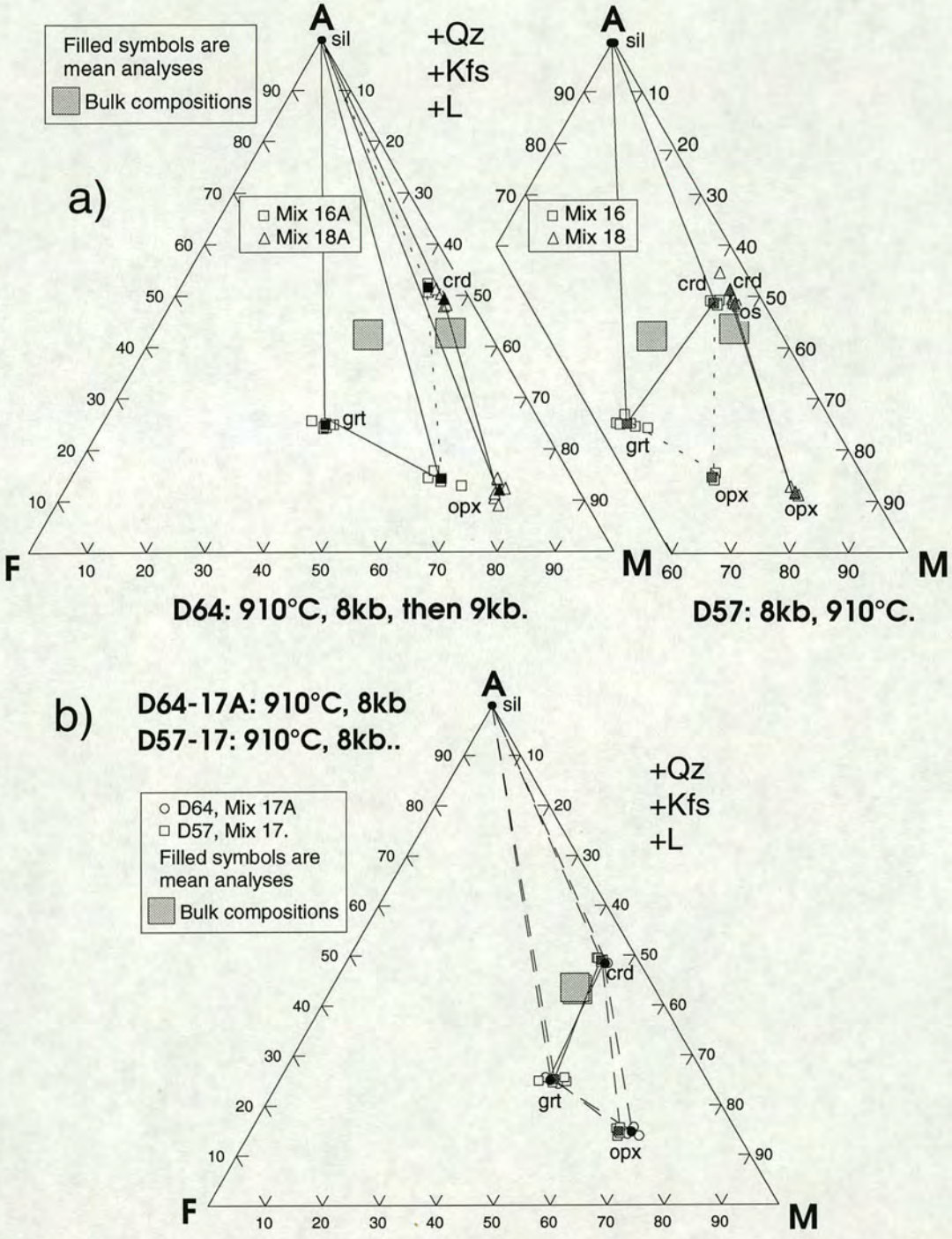

Figure 5.3.
a) Isothermal reversal experiments D64-16A and D64-18A plotted on an AFM diagram. D57-16 and D57-18 (also shown on an AFM diagram) are the single step experiments run at the same pressure and temperature as the first step of the reversal.
b) Experiments D64-17A and D57-17 plotted on an AFM diagram. D64-17A was removed after the first step of the two-step run. The assemblages are virtually identical and were interpreted in Chapter Four as containing metastable orthopyroxene. The garnet-cordierite tie-line is shown to be stable by experiment D57-16.

been consumed in these had the runs been left for longer. This is not accepted on the grounds that the entropy change of the biotite dehydration melting reactions strongly favours the breakdown of biotite to melt over the reverse. Indeed, D63-16A and D63-18A formed only a small amount of biotite despite being inside a region where all the original biotite should re-form (plates 8a and 8b). In contrast, the full amount of biotite was present in D67-16A (plate 1a) showing that the absence of biotite from the gas-bomb reversal of D58 was not an equilibrium effect but a kinetic one.

The reversal of the (os, bt) reaction was attempted from low to high pressure in run D64 (figure 5.3a). In this run, the M74 mix (17A) capsule was removed after the first step of the run, to ensure the low-pressure assemblage had formed before the other two capsules (16A and 18A) were reversed: comparison of experiment D64-17A with D57-17, the single-step run at 910°C, 7kb, shows that virtually identical assemblages were formed (figure 5.3b). This also demonstrates that the experiments are repeatable.

D64-18A was a successful reversal, as the assemblage changed from one unequivocal six-phase assemblage to another, cordierite-osumilite-orthopyroxene-K-feldspar-quartz-melt (D57-18) to cordierite-sillimanite-orthopyroxene-K-feldspar-quartz-melt (D64-18A) (figure 5.3a). The high pressure assemblage of the (os, bt) reaction is orthopyroxene-sillimanite-melt and so D64-18A must lie above it (INSERT A). This is important because experiment D64-16A retained a trace of the cordierite which formed during the first step of the run, and was therefore equivocal. However, as D64-18A lies above the (os, bt) reaction, the other capsule from that run, D64-16A must also do so. The fact that the amount of cordierite in D64-16A was reduced to a trace (compared to D57-16) also suggests that it is a metastable remnant.

5.3 COMPOSITIONAL REVERSALS.

Bulk composition, along with pressure and temperature, determines the equilibrium assemblage of an experiment. Therefore, producing the same assemblage, with the same phase compositions, from different bulk compositions can be considered a reversal. The phase compositions must be the same if the assemblage is divariant (i.e. six phases in this six component system) because the assemblage then has only two degrees of freedom, pressure and temperature, and so all the compositional parameters must be fixed. Compositional reversals are usually conducted so that the

equilibrium X_{Mg} values of the phases are approached from low and high sides. In effect, a divariant Fe-Mg exchange reaction is being reversed, for a particular pressure and temperature. This is the case for the biotite in experiments D49-16 and D49-17 (see figure 5.5 below). In this case, the true equilibrium phase compositions must lie between the phase compositions from each experiment. In the other two compositional reversals shown here, the biotite is exhausted. Nonetheless, if the same assemblage forms in two different bulk compositions at the same pressure and temperature, it is a necessary condition of equilibrium that the phase compositions are the same. That this is the case is shown in figure 5.4.

The two experiments from D43 and the three from D48 (figure 5.4) match almost perfectly with the exception of the garnets in D43, which have not equilibrated fully. This may be due to a relatively low run-temperature or the relatively large difference between the seed garnet composition (X_{Mg}= 0.69) and that produced in the

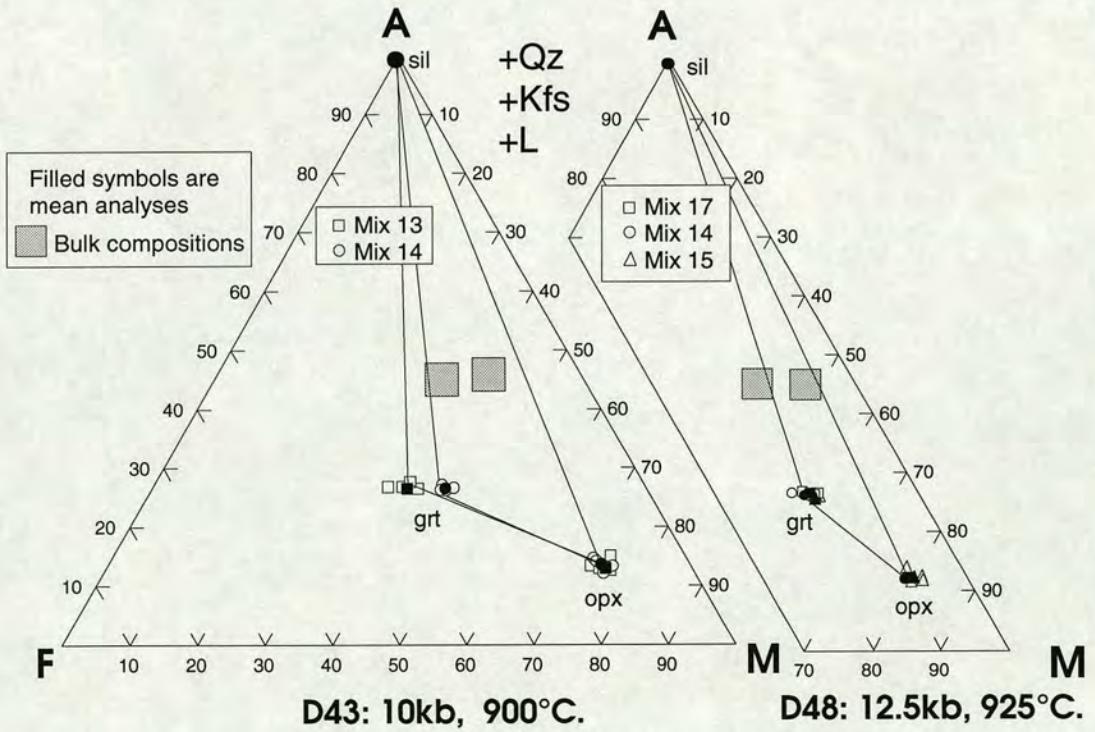

Figure 5.4. Experiments from runs D43 and D48 shown on an AFM diagram. In all cases the assemblage is garnet-orthopyroxene-sillimanite-K-feldspar-quartz-melt. In most cases the same phase compositions have been produced with mixes of different bulk composition, a compositional reversal. The position of the bulk compositions relative to the three-phase triangle shows that the more magnesian mixes should have a higher modal proportion of orthopyroxene than the more iron rich mixes, which will have correspondingly more garnet. This is indeed the case (see table 3.10 and plates 3a and 3b).

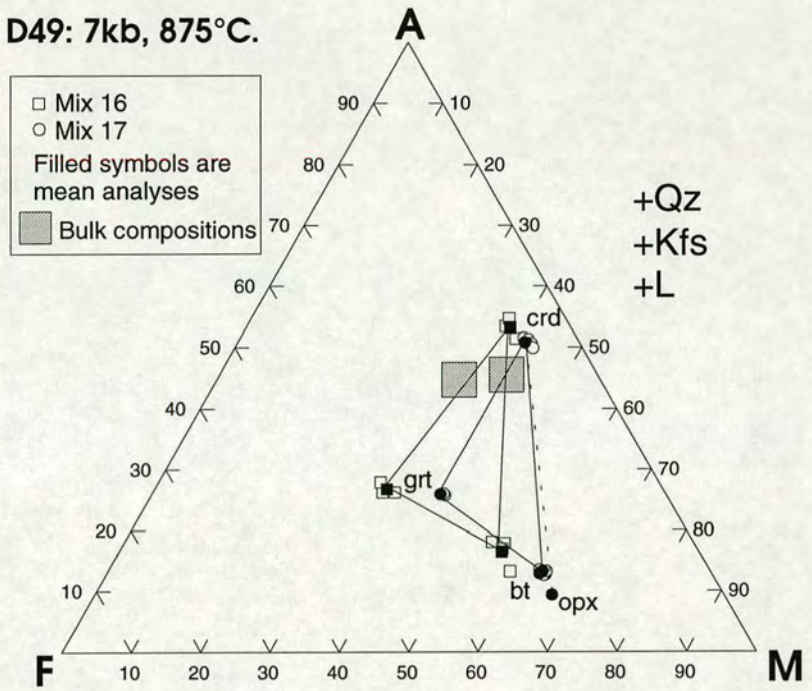

Figure 5.5. Experiments D49-16 and D49-17 plotted on an AFM diagram. Both experiments produced the same assemblage, apart from a trace of metastable orthopyroxene in D49-17. The phase compositions should be the same in each of the experiments, but are slightly different. See text for discussion.

experiment (also see section 3.4.2). It is interesting to note that in D48 mixes 14 and 17, identical except for containing mineral-sillimanite and gel-sillimanite respectively, produce precisely the same assemblage.

The true compositional reversal, D49, does not match quite as well (figure 5.5). The biotite and cordierite in D49-17 (M74) are slightly more magnesian (ΔX_{Mg}=0.04) than those in D49-16 (M62). These differences are only slightly larger than the uncertainties in the measured X_{Mg}'s (table 3.3) and so these phases are likely to be close to equilibrium. However, the garnet compositions are again problematic; the discrepancy between the garnet compositions is large (ΔX_{Mg}=0.10). Reasons for this are discussed above and in section 3.4.2. Compositional reversals D43 and D48 are more consistent than D49 and this is probably due to combination of the latter run being conducted at lower temperatures, nearer the solidus and in the gas-bomb apparatus rather than a solid-media salt-cell.

5.4 OTHER NECESSARY CRITERIA OF EQUILIBRIUM.

As discussed in the introduction, no sufficient criteria for the achievement of equilibrium exist but there are many necessary ones, the contravention of which would prove metastability. The most important of these are the reversals described above and these provide good evidence of a close approach to equilibrium of the assemblages and they determine the position of the reactions involved.

Other criteria are listed below, some of which are discussed by Edgar (1973) and Holloway and Wood (1988).

Increasing run times.

One method previous workers have used to indicate the attainment of an equilibrium assemblage is to run repeat experiments for successively longer times. This is not really a very good indicator as, particularly near reaction boundaries and below the solidus, reactions rates can be very slow and equilibrium may be unattainable on a laboratory time-scale. For these reasons, time-consuming repeat runs were not conducted but some comparisons are available. The second step of the reversal runs, were around twice as long as the normal run times of 200-300 hours (tables 3.1, 3.2). Though no shorter, single-step experiments were conducted at exactly the pressures and temperatures of the second steps of the reversals, there was often a run close to those conditions. For example, the reversal experiments D64-16A, D64-18A (9kb, 910°C, second step) and D54-16, D54-18 (about 8.8kb, 925°C) produce the same assemblages despite the former running for 424 hours and the latter only 264 hours. So, whilst increasing the run time of an experiment without a change in assemblage is only a minor indication of a close approach to equilibrium, the present experiments do not contradict this criterion.

Homogeneity of phase composition.

A frequent indicator of a lack of equilibration in experimental studies is zoned or inhomogeneous crystals or departures from accepted partitioning values between phases. Chapter Three dealt with these matters in detail. The phase are remarkably

homogeneous in each experiment, within single crystals and between them[3]. The Fe-Mg partitioning data is less consistent, predominantly due to problems with garnet equilibration. The scatter of the partitioning data is of the same magnitude as other phase equilibrium studies (e.g. figure 3.14). The partitioning between phases other than garnet is reasonably consistent (e.g. figure 3.19). Overall, these experiments satisfy the criterion of homogeneity of phase composition.

Homogeneity of assemblage.

As the experimental charge is perhaps a thousand times larger than the individual phases it is possible that different parts of the charge could have different assemblages. This would be an indicator of disequilibrium. This criterion is especially important in phase-equilibrium studies, such as this one, where many different assemblages are produced in a relatively small region of pressure-temperature space. Therefore, when studying the experiments care was taken to observe and analyse phases from all parts of the polished section.

In only six cases out of the sixty-seven experiments was there any variation of assemblage in the charge. In four experiments, D59-18, D60-18A, D65-16A and D65-17A, K-feldspar was absent from the centre of the charge, whilst being abundant in a selvedge around the edge of the charge[4]. The selvedges are between 15 and 60 μm wide (plate 4a). The reason for this behaviour of K-feldspar is not understood, but may be related to preferential nucleation or growth near the capsule metal. There was a K-feldspar-absent area in experiment D43-13 but this was a sector at the edge of the charge, not concentrically arranged. Finally, in experiment D67-16A there was a small garnet-absent area in which the biotite had a lower X_{Mg} than that in the garnet-present area[5].

It is believed that the complete homogeneity of assemblage in sixty-one of the experiments is a good record and compares very favourably to many other studies.

---

[3] See table 3.3 for mean values of the range of X_{Mg} in measured phase compositions in each experiment. Garnet is not included in table 3.3 because, as a seeded phase, the problem of rim/core overlap means that the measured compositions will not reflect the homogeneity of the new garnet growth.

[4] Two other experiments, D64-16A and D66-18A, exhibited a marked decrease in the abundance of K-feldspar from the edge of the charge to the centre, though the phase is present throughout.

[5] The biotite co-existing with garnet of $X_{Mg} = 0.39$ has an X_{Mg} of 0.66. The biotite in the garnet-absent area has an X_{Mg} of 0.63. This difference is consistent with the local assemblage reflecting the same overall bulk composition, which therefore has an X_{Mg} of about 0.63.

The six heterogeneous experiments have lost a phase which is elsewhere present, rather than formed a new phase, and this perhaps makes these discrepancies less serious. The overall homogeneity of the assemblages vouches for a high level of interdiffusion on the scale of the whole capsule which would enable most kinetic problems to be overcome. However it is, of course, possible to have a homogeneous assemblage which is metastable.

Phase rule constraints.

These were considered in Chapter Four and only a brief summary is given here. In a synthetic system the number of components is controlled and known. Here it is six, KFMASH. The phase rule therefore demands that a divariant assemblage has six phases. If there are more than six then either the assemblage is univariant (rare in natural rocks but more common in experiments) or contains a metastable phase. Six of the supersolidus experiments fall into the latter category (tables 4.1 and 4.2), as interpreted in Chapter Four, and are therefore not at equilibrium. As specific, plausible reasons can be found for the metastability of these phases it is believed that the disequilibrium demonstrated can be accounted for and the true equilibrium assemblage accurately predicted. Around half of the subsolidus assemblages have too few phases (as interpreted in Chapter Four) and this represents a more serious departure from equilibrium, caused by the lack of reaction in the liquid-absent, subsolidus domain. The subsolidus phase relations cannot be determined from these experiments with great confidence, although it is stressed that the biotite dehydration melting reactions have been successfully reversed and so must lie in the given brackets.

Comparison to natural rocks.

It is tempting to use comparisons between natural rock data and experiments as evidence of the experiments' high degree of equilibration. This is reasonable as natural rocks have formed on geologic time-scales and peak metamorphic assemblages will not, in general, suffer from problems of disequilibrium. However, there is the danger of a circular argument, if the experiments are to be used to interpret natural rocks. One might argue that a set of experiments are in equilibrium because they closely reproduce some natural rock data, and then claim that because the experiments are in equilibrium, one can use them to interpret other natural rocks. This reasoning fails if the natural rock assemblage or phase compositions have been

wrongly interpreted, as might happen if the rock contained zoned phases or had undergone partial retrogression.

For these reasons, it is preferred not to stress the similarity of the experiments to natural data but to argue for the near-equilibrium state of the experiments on the basis of the other evidence discussed in this chapter. Nonetheless, the excellent applicability to natural rocks of the grids derived from the experiments is taken as implicit confirmation of a closeness to equilibrium (Chapter Eight).

5.5 CONCLUSIONS OF THE ASSESSMENT OF EQUILIBRATION.

The evidence presented and summarised in this chapter is believed to constitute strong grounds for the assumption of a close approach to equilibrium for the experiments above the solidus, in terms of both the phase assemblages and the phase compositions produced. There are the following important exceptions:

a) garnet compositions,
b) occasional orthopyroxene metastability,
c) occasional heterogeneous distribution of K-feldspar.

Any assertions based on these phases in the relevant experiments will be made more cautiously. However, one of the advantages of this study is the fact that three bulk compositions were used and this frequently allows an independent assessment of an ambiguous experiment, so that as a whole, the data set is a good representation of equilibrium conditions. Two examples illustrate this point. Firstly, experiments D51-16 and D60-16A both show that the garnet-osumilite tie-line is stable, not the cordierite-osumilite tie-line, a situation which is ambiguous in the M74-mix experiments from the same runs (See Appendix Three). Secondly, the presence of orthopyroxene-sillimanite-melt in D64-18A showed that D64-16A must also lie above the (os, bt) reaction, despite preserving metastable cordierite (see section 5.2).

The single-step experiments below the solidus are not as near to equilibrium and can only be used tentatively as indicators of the phase relations. However, the success of the reversal experiments suggests that these are better equilibrated and can provide more reliable data on the equilibrium subsolidus assemblages and phase compositions.

Chapter Six

DERIVATION OF PHASE DIAGRAMS

Chapter Six. Derivation of phase diagrams.

6.1 INTRODUCTION AND SYNOPSIS OF CHAPTER

In this chapter two types of phase diagram are derived which summarise the experimental data and allow them to be applied to natural rocks. The first type is a grid of KFMASH univariant reactions, or a petrogenetic grid, which is applicable to rocks of all bulk compositions. Initially, the topology of the grid is derived qualitatively, based on the assemblages produced in the experiments and on published data. The topology of the grid depends on the relative compositions of the phases and some of these change continuously through the pressure-temperature range investigated. The changes in topology which could occur as a result of changing phase compositions are considered fully. In particular, it is considered whether K-feldspar is a product or reactant in the biotite dehydration melting reactions. It is concluded that in this study it is a reactant, but that it could be a product in other systems, depending principally on the water/potassium ratio of the melt produced.

The univariant KFMASH grid is positioned in pressure-temperature space using the constraints which the experiments provide and Schreinemakers' rules. The large number of experiments, their close spacing in pressure-temperature space and the duplication of pressure-temperature conditions with mixes of different bulk compositions provide constraints which allow very little lee-way in the positioning of the grid. The invariant point involving the biotite dehydration melting reactions and the reaction separating garnet-cordierite and orthopyroxene-sillimanite-melt assemblages, which is fundamental in dividing high-grade metapelite metamorphic conditions, has been positioned in the range 890-910°C, 8.7-9.5kb.

The second type of diagram derived are pseudosections, one for each of the three bulk compositions used. These diagrams not only show the univariant reactions which will be stable for that bulk composition but also the divariant reactions which are the dominant mechanism of phase changes in natural rocks. Pseudosections are very powerful in the interpretation of phase assemblage histories in rocks. They are derived here by using the univariant grid as a template, determining the possible divariant reactions and then defining self-consistent divariant fields to account for the assemblages produced in the experiments. In Chapter Four it was shown that some of

the experiments had probably produced assemblages which were not the equilibrium assemblages. The potential effects of alternative interpretations of the equilibrium assemblages on the topology of the pseudosections is considered in detail.

The chapter begins with a short section giving the theoretical background to the diagrams produced in the following sections.

6.2 BACKGROUND TO THE PHASE DIAGRAMS.

A wide range of diagrams are available for depicting the phase relations in any system. This section will show how the diagrams used here are derived and how they relate to one another.

Phase diagrams are used essentially in order to present thermodynamic data in an easy-to-interpret, graphical form. The fundamental tool in linking thermodynamic data and graphical representations is the phase rule,

$$P = C - F + 2,$$

where P is the number of phases in the system, C is the number of chemical components and F is the number of independently variable parameters (sometimes called the degrees of freedom). The lowest variance assemblages (i.e. minimum F) commonly observed in natural rocks are divariant (F=2), i.e. the phase assemblage can exist over a range of pressures and temperatures for a given bulk composition[1]. Through this range, the phase compositions will change until a phase is lost: this process is the operation of a divariant reaction and this is the commonest type of reaction observed in natural rocks. Divariant reactions are also called continuous reactions as they can operate continuously over a range of pressure and temperature. The pressure-temperature range of a divariant reaction is dependent on the bulk composition under consideration. This is illustrated in figure 6.1a.

The pressure-temperature location of univariant reactions (F=1) is not dependent on bulk composition and therefore a univariant reaction applies to *all* bulk compositions which stabilise the appropriate phases (figure 6.1b). As univariant assemblages have

[1] Other intensive parameters such as fO_2 and a_{H2O} are assumed to be constant.

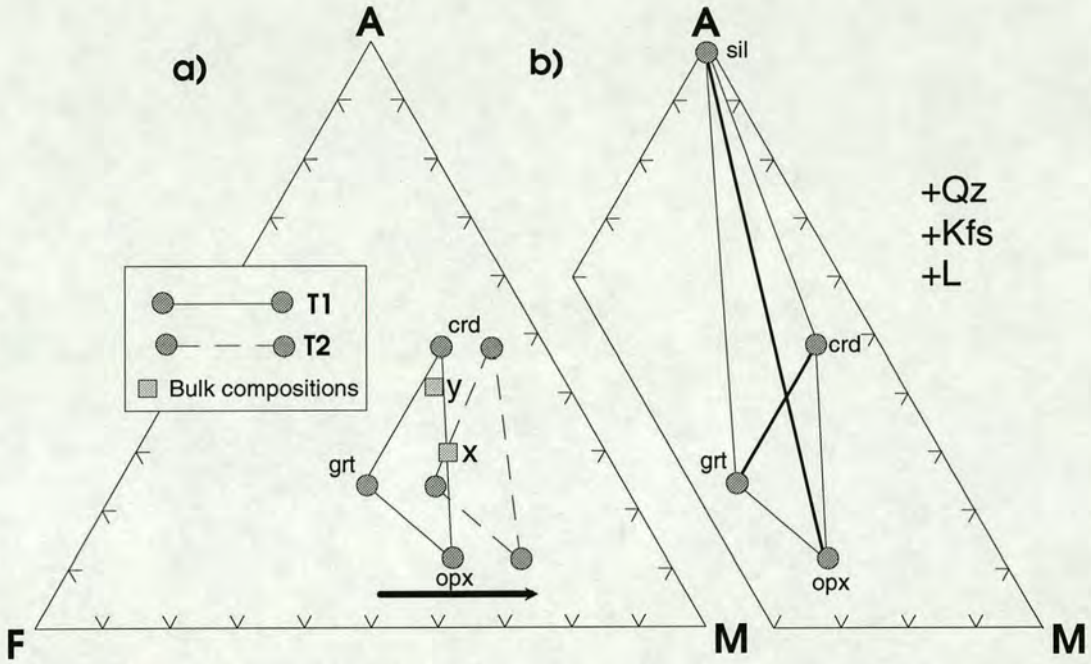

UNIVARIANT AND DIVARIANT ASSEMBLAGES AND REACTIONS

Figure 6.1.
a) Divariant KFMASH assemblage (six phases) projected on to an AFM diagram from quartz, K-feldspar and melt. The garnet-cordierite-orthopyroxene three-phase triangle which represents the assemblage will translate to a more magnesian position (the direction of the arrow) as the temperature rises, because the equilibrium compositions of the phases become more magnesian at higher temperatures. This translation represents the operation of the divariant reaction, which is crd + opx (+ qz + kfs) = grt (+ L) in this case. The pressure is taken to be constant and so, with rising temperature and for composition X, the divariant reaction first operates at T1 and forms garnet from the trivariant assemblage cordierite-orthopyroxene. At T2 the divariant reaction consumes the last orthopyroxene, leaving the trivariant assemblage garnet-cordierite. Between T1 and T2, the phase compositions are changing continuously via the divariant reaction. The divariant reaction will operate over a different pressure-temperature range for each bulk composition. For example, for composition Y, the divariant reaction will begin operating at a lower temperature and continue for a shorter interval than for composition X. The pressure-temperature range for divariant reactions involving two Fe-Mg solid solutions depends only on the bulk X_{Mg}. If all three phases exhibit Fe-Mg solid solution then the range will also depend on the A/AFM ratio (Hensen, 1971).

b) Univariant KFMASH assemblage (seven phases) projected on to an AFM diagram from quartz, K-feldspar and melt. Univariant assemblages have only one degree of freedom and therefore, for a given pressure, the assemblage is only stable at a single temperature. The operation of a univariant reaction is manifested on three-component diagrams by a change in the tie-line topology. On the diagram the univariant reaction grt + crd + (kfs +qz) = opx + sil (+ L) involves the destabilisation of the garnet-cordierite tie-line and the stabilisation of the orthopyroxene-sillimanite tie-line. The reaction will occur at this temperature for all bulk compositions. However, only those rocks with bulk compositions inside the quadrilateral defined by the phases will be changed by its operation, as only those rocks will have all the required phases. Those outside the quadrilateral do not "see" the reaction. The reaction illustrated is "non-terminal" (Niggli, 1954), that is it does not limit the stability of a particular phase, and the reaction results only in a change in the topology of the diagram. Terminal reactions do limit the stability of a particular phase, and the reaction results in the appearance or dissappearance of that phase. This is shown on a three-component diagram when a phase present between three others appears or disappears.

only one degree of freedom the locus of their stable pressure-temperature conditions is a line. This is the reason why univariant assemblages are very rare in natural rocks[2] - the probability of a rock with an appropriate bulk composition equilibrating at the precise pressure, temperature and all other intensive parameters required is extremely small. Despite the rarity of natural evidence for univariant reactions, they are very important because they bracket the stability fields of the common divariant assemblages. Knowledge of the position of a divariant reaction gained from a particular rock can only be applied to rocks of the same bulk composition. Univariant reactions can provide a framework in which all rocks in that system can be studied, with each bulk composition having a different set of divariant reactions stable.

The idea of a petrogenetic grid, in which pressure-temperature space is divided into distinctive fields by univariant reactions, was conceived by Bowen (1940) but the first KFMASH grid was not published until much later (Albee, 1965a). Petrogenetic grids can be used to give estimates of the pressure-temperature-time evolution of a rock or suite of rocks, from the assemblages and reaction textures the rocks preserve. The construction of a theoretical grid is relatively straightforward: only a knowledge of the compositional (or chemographic) relationships of the phases is required and from this all possible reactions and stoichiometric coefficients may be derived. In a system with (C+2) phases there will be (C+2) univariant reactions. There will also be one invariant assemblage, i.e. an assemblage which contains all the phases in the system and has no degrees of freedom. Consequently, this assemblage can only exist at a point in pressure-temperature space and the univariant reactions must cross at this point. If there are more than (C+2) phases, then there will be more than one invariant point - a multisystem (Korzhinskii, 1959). The topology of the points and reactions must conform to a number of constraints collectively known as Schreinemakers' rules.

The thermodynamic principles which underlie the construction of grids were summarised by F.A.H. Schreinemakers in a number of geometric rules, which were published in a series of twenty nine articles between 1915 and 1925. Schreinemakers' methods were popularised rather later (e.g. Niggli 1954, Korzhinskii 1959, Zen 1966) but have since become an integral part of metamorphic petrology. The rules are not repeated here. For a given invariant point, Schreinemakers' rules enable the univariant reactions to be positioned in two possible relative orders around the

[2] Univariant assemblages can be common in rocks which have an internally-buffered fluid composition.

invariant point, one being the mirror image of the other. In a multisystem, all the possible points and all the reactions around each can be determined, all solely from a knowledge of the chemographic relations. However, the *relative* positions of the reactions is all that is determined. Further information is required to ascertain which of the mirror image bundles is stable and the orientation of that bundle in pressure-temperature space. If all the invariant points in a multisystem are stable, then it is impossible to construct a grid with a closed topology (i.e. all points connected to each other) without extreme curvature of some of the reactions. Therefore, some of the points will be metastable and again further information is required to determine which these are. If two invariant points are known to be stable and two reactions in each of these are positioned in pressure-temperature space then the topology of the rest of the multisystem grid follows from Schreinemakers' rules. The invariant points

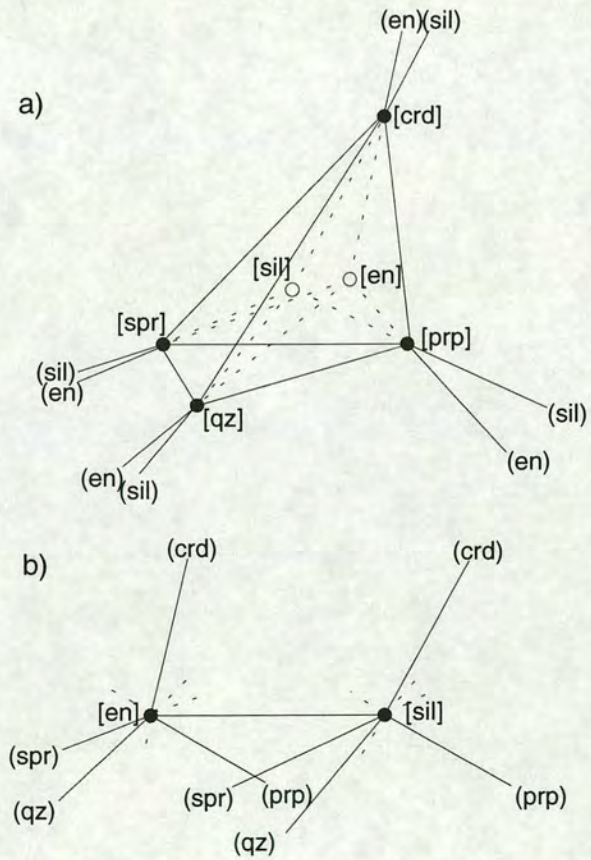

Figure 6.2. Example of a stable univariant grid (a) and its metastable residual (or alternative) grid (b). The example is taken from the MgO-Al_2O_3-SiO_2 system, involving the phases pyrope, sapphirine, cordierite, enstatite, sillimanite, and quartz, investigated by Hensen and Essene (1971). The divariant assemblages (spr, crd, prp), (spr, prp, qz), (spr, crd, qz) and (crd, prp, qz) are only stable in grid a), between the appropriate invariant points. There is no position in grid b) where these assemblages are stable. The reactions are labelled using the absent-phase notation. (After Hensen and Harley 1990).

which are not stable form a residual (or alternative) topology[3] (figure 6.2).

The pressure-temperature gradient of a reaction can be determined from a knowledge of molar volumes (V) and entropies (S) of the phases involved, via the Clausius-Clapyeron equation:

$$dP/dT = \Delta S/\Delta V.$$

Whilst molar volumes are well constrained for many common phases, high quality entropy data are scarce. However, certain useful generalisations can be made and in the construction of qualitative grids it is frequently assumed that dehydration or melting reactions (large entropy changes) have steep gradients with the fluid/melt on the high-temperature side. Similarly, solid-solid reactions which involve large volume changes are assumed to have shallow gradients with the denser assemblage on the high-pressure side (Thompson 1955, Albee 1965a). The actual gradients of equilibria involving melts are particularly difficult to constrain thermodynamically, as those properties of the melt phases are poorly known.

Both natural rock and experimental data can constrain the stability of invariant points in a multisystem. Experimental data are directly applicable and may allow the positioning of the grid in pressure-temperature space. Natural rock data can be used to choose between grids and their residuals, because any grid with three or more invariant points will have divariant assemblages which are unique to that topology and which cannot occur in the residual topology[4] (figure 6.2). For example, Hensen (1971) determined the stable topology of the FMAS-system grid for high-grade metapelites from the results of an experimental study (Hensen and Green 1971, 1972). Phase assemblages unique to the grid proposed by Hensen (1971) were found in natural rocks (e.g. Harley 1986) but also found were natural rock assemblages which were unique to the residual (e.g. Caporuscio and Morse 1978). This paradox was resolved when Hensen (1986) showed that the inversion from one topology to the other occurs in response to changes in fO_2. Recent experimental work confirmed that the original topology (Hensen, 1971) was stable for low values of fO_2 (Bertrand et al. 1991).

---

[3] The absent-phase notation is used in this study, for its brevity. Any assemblage or reaction is referred to by the phases in the system which are not involved. Invariant assemblages are given in square brackets, higher variance assemblages in round brackets.

[4] All the univariant and invariant assemblages are also unique to that grid but are very rarely found in natural rocks.

Figure 6.3. DERIVATION OF PSEUDOSECTIONS

a) Seven-phase KFMASH univariant reaction depicted in pressure-temperature space. It is assumed that no KFMASH invariant points are stable and therefore the reaction can occur from the iron end-member system (KFASH) to the magnesium end-member system (KMASH). The KFMASH reaction terminates in these end-member systems and because the same number of phases still occur but in a system with one fewer component, the ends of the reactions are end-member system invariant points. Emanating from these are end-member univariant reactions (involving six phases). The KFMASH divariant assemblages are stable somewhere between the equivalent end-member univariant assemblages. For example, the assemblage bt-sil-qz-grt-kfs-L (crd) is stable on the low-temperature side of the KFMASH univariant reaction and between the two (crd) end-member system univariant reactions.

b) Three-component HFM projection for the divariant assemblage (crd). As described in figure 6.1, the three-phase triangle will translate across the projection with increasing temperature, with the operation of the divariant reaction bt + sil (+ qz) = grt + (kfs + L) causing the required compositional changes. For the bulk composition X the divariant assemblage will only be stable between T1 and the higher temperature, T2, at a given pressure. At T1, the first liquid forms, at T2 the last biotite reacts. Therefore, the divariant assemblage cannot be stable over the whole compositional range, from one end-member system to the other, but rather, just part of that range.

c) Simplified T-X_{Mg} section for the KFMASH divariant assemblage (crd). The shaded ellipse shows the maximum possible temperature range of the assemblage's stability, from one end member-system to the other. The white area in the ellipse shows the temperature range in which the divariant assemblage is stable for the bulk composition X.

d) KFMASH divariant field (crd) and univariant reaction depicted in P-T space for the bulk composition X. The temperatures T1 and T2 are shown, corresponding to the limits of the divariant assemblage at the pressure of figures a and b. The univariant reaction will only be crossed if it is approached via the P-T region in which the divariant assemblage is stable. If it is approached from outwith this region it will not have the phases required by the univariant reaction and though the univariant reaction is still stable it is not "seen" by this bulk composition. This diagram is a pseudosection because it shows only those reactions which will affect the bulk composition under consideration.

e) Pseudosection for the KFMASH univariant reaction showing all the stable divariant reactions for composition X. Experiments shiw that four of the possible five divariant reactions (figure a) are stable. The (grt) reaction requires a more magnesian composition to be stable. Again, the univariant reaction will only be "seen" when it is crossed from a divariant field.

f) Pseudosection for the KFMASH univariant reaction for two bulk compositions. The dark grey divariant fields correspond to the more magnesian bulk composition Y (figure b), and are therefore shifted to higher temperatures (i.e. the three-phase triangle in figure b has to move to more magnesian compositions before crossing composition Y). The arrow shows how an isobarically-heated rock may not react on crossing a univariant boundary. Composition X would only react through the divariant reaction (crd) whereas, at exactly the same pressure, composition Y would only react through the divariant reaction (sil).

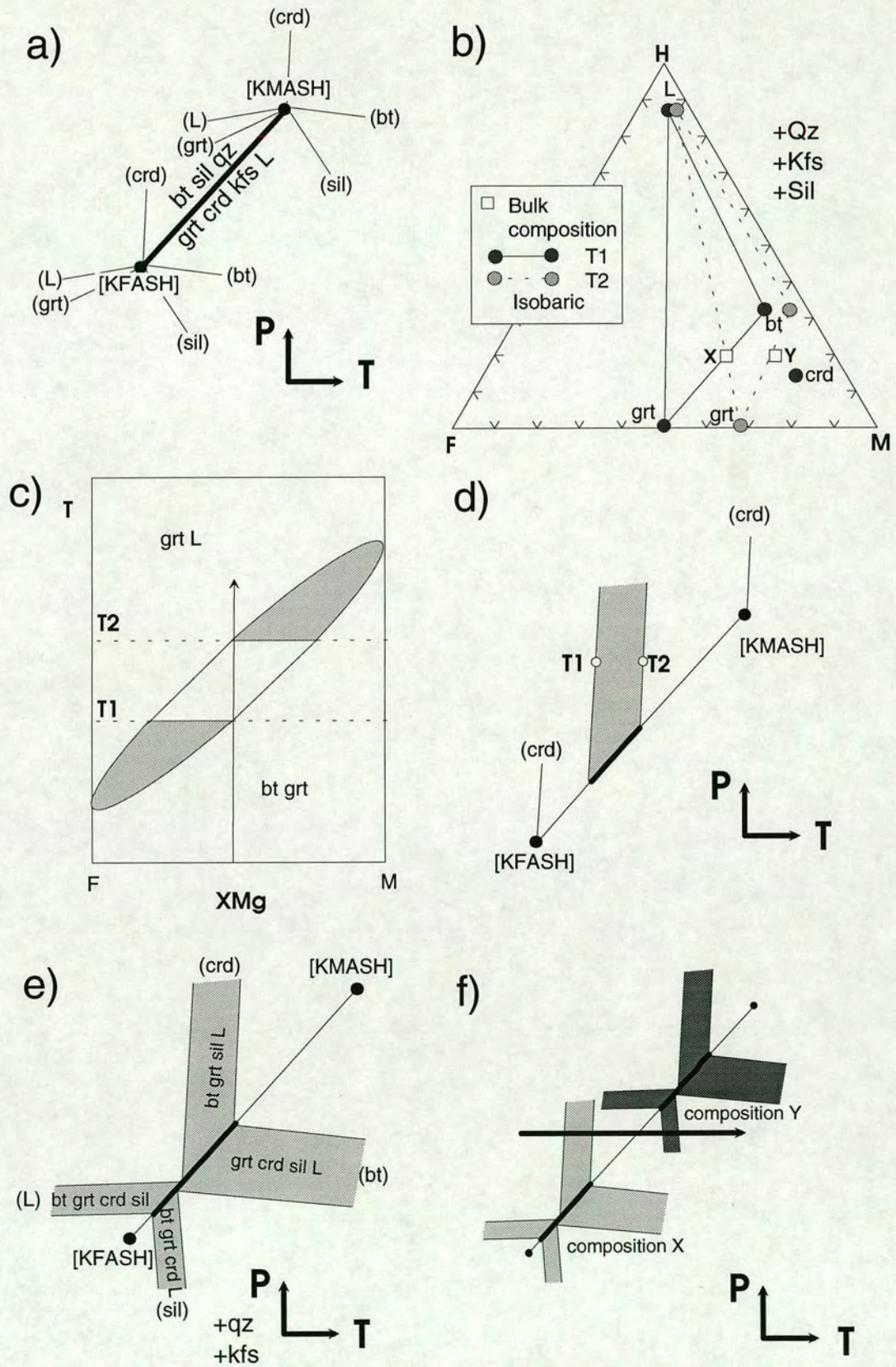

DERIVATION OF PSEUDOSECTIONS (see caption opposite).

Petrogenetic grids composed from univariant reactions are important because they apply to all bulk compositions in the system. However, univariant reactions only sometimes cause changes in the phase assemblages in a rock, because bulk compositions often lie outside the compositional range defined by the phases in the reaction (figure 6.1b). Most phase changes are the result of divariant reactions. A powerful way of depicting the phase relations of a given rock is in a pseudosection (Hensen 1971). These diagrams show the univariant *and* divariant reactions which are stable for a given bulk composition and are therefore extremely useful in the interpretation of a given natural rock. Pseudosections are usually drawn in pressure-temperature space but can be drawn for other parameters. Figure 6.3 shows how pseudosections can be derived and how they relate to the three-component projections and the univariant grids.

6.3 A UNIVARIANT GRID AND PSEUDOSECTIONS FROM THE EXPERIMENTS.

6.3.1 Derivation of the univariant grid.

The experiments in this study can be considered in terms of an "n+3" multisystem (Korzhinskii, 1959), i.e. a system with three more phases than components. The components are K_2O-FeO-MgO-Al_2O_3-SiO_2-H_2O (KFMASH) and the phases are quartz, K-feldspar, sillimanite, melt, garnet, orthopyroxene, biotite, cordierite and osumilite. As each invariant point has an assemblage with one phase absent, this multisystem has nine possible points, though the [qz] point is not considered because all the experiments were quartz-saturated. Ignoring the quartz-absent assemblages, there are a maximum of twenty-eight possible univariant assemblages. The chemographic relations of the phases are required to determine the reactions associated with each of these assemblages.

The compositions of the phases vary over the pressure-temperature range considered but, with the possible exception of the melt phase, the compositional relations between them remain constant. In particular the relative Fe-Mg partitioning is constant, with the relative magnesium content increasing in the order; melt, garnet, orthopyroxene, biotite, cordierite, osumilite (see figures 3.19 and 3.20). This order of relative partitioning is the same as that of Hensen (1971), though that study did not include osumilite or melt. The relative melt composition found in the current

experiments is also the same as that used in the theoretical study of Thompson (1982). Since Ellis (1986) showed that garnet was more iron-rich than co-existing melt below 900°C at 10kb, it has been commonly assumed that garnet is the most iron-rich phase when deriving high grade metapelite phase relations (e.g. Waters 1988). The current experiments contradict the conclusions of Ellis (1986, see figure 3.20), but are mostly conducted above 900°C. In any case, because garnet and melt are the two most iron-rich phases and have the lowest and highest H/FM ratios in the system respectively, the phase relations are the same whichever is the more iron-rich. This would not be the case if a free-fluid phase was present.

The reactions were determined by solving simultaneous equations[5] constructed for each reaction from a set of standard mineral compositions. The set of standard mineral compositions, set A (table 6.1), is based on experiment D66-18A which contained all the phases except garnet and sillimanite. The set was completed by constructing a garnet composition which was consistent with the partitioning data given in figure 3.20. The solutions to the equations are the stoichiometric coefficients for the reactions (table 6.1). To test the robustness of the calculated phase relations, a second set of mineral compositions was used, set B, based on D47-18 and with artificially high water-contents (table 6.2). Once the univariant grid has been derived for set A, the possible variations implied by set B are considered. The phase compositions are illustrated graphically in figure 6.4. Three-component projections could have been used to derive the phase relations but many different projections would be required and any one of these can only deal with four phases at a time - the reactions would still require balancing. The method employed is much less time-consuming and though potential degeneracies are not seen graphically, careful consideration of phase composition variation will reveal them and allow them to be accounted for.

Firstly, it is necessary to select two invariant points as being stable. The KFMASH invariant point formed by the intersection of four biotite dehydration melting reactions and the reaction which divides the garnet-cordierite and orthopyroxene-sillimanite-quartz fields is central to many natural and experimental studies of metapelitic granulites (e.g. Grant 1985, point [mus, V], figure 3.14; Powell and Downes 1990, point 1, figure 5.3; Hensen and Harley 1990, point [spr, spl], figure

[5] The equations were solved using the MODES programme, written by Dr C.E.Ford, of the University of Edinburgh. As seven equations (i.e. phase compositions) existed for six variables (i.e. phase components) the equations could be solved with zero residuals.

Table 6.1. KFMASH Univariant Reactions (Set A)

Phase Compositions (Set A)

	grt	crd	L	opx	os	bi	qz	kfs	sil
SiO2	40.00	49.68	74.28	52.12	63.16	40.84	100.00	66.20	38.60
Al2O3	22.93	33.33	12.20	7.73	22.39	19.29	0.00	17.60	61.40
FeO	14.00	2.69	0.48	12.20	1.44	5.41	0.00	0.00	0.00
MgO	23.00	12.02	0.44	27.75	8.41	20.13	0.00	0.00	0.00
K2O	0.00	0.66	9.16	0.05	4.50	9.94	0.00	16.20	0.00
H2O	0.00	1.04	2.60	0.00	0.00	4.00	0.00	0.00	0.00
Total	59.93	49.74	24.87	47.73	36.74	58.77	0.00	33.80	61.40
XMg	0.75	0.89	0.62	0.80	0.91	0.87	n.a.	n.a.	n.a.

Calculated Univariant Reactions (arranged by invariant point)

[sil]

	grt	crd	L	opx	os	bi	qz	kfs
(grt)		-124.00	122.30	16.28	232.39	-47.61	-99.36	-100.00
(crd)	-140.62		345.88	230.29	148.15	-225.77	-257.93	-100.00
(L)	76.95	-191.67		-100.86	278.14	49.96	-12.51	-100.01
(opx)	10.68	-133.36	105.31		238.68	-34.04	-87.28	-99.99
(os)	-391.31	220.01	744.03	611.91		-543.67	-540.97	-100.00
(bi)	37.60	-157.06	62.61	-40.92	254.74		-56.97	-100.00
(Kfs)	-88.65	78.08	140.92	134.93	-52.94	-112.35	-99.99	

[bt]

	grt	crd	L	opx	os	qz	kfs	sil
(grt)		600.98	-239.86	-37.47	-727.42	189.18	314.60	-100.01
(crd)	143.60		-0.02	-193.89	247.56	-28.99	-68.26	-100.00
(L)	143.70	-0.40		-193.99	248.21	-29.09	-68.44	-99.99
(opx)	-34.40	745.03	-297.34		-961.13	241.48	406.36	-100.00
(os)	107.06	152.63	-60.89	-154.12		26.38	28.93	-99.99
(Kfs)	117.92	107.25	-42.73	-165.94	73.60	9.90		-100.00
(sil)	37.60	-157.06	62.61	-40.92	254.74	-56.97	-100.00	

[kfs]

	grt	crd	L	opx	os	bi	qz	sil
(grt)		211.04	144.68	13.55	3.34	-149.46	-123.15	-100.00
(crd)	239.55		-236.11	-351.05	146.46	154.10	147.05	-100.00
(L)	91.04	130.93		-125.02	57.56	-34.08	-20.43	-100.00
(opx)	8.89	203.23	130.54		8.61	-138.17	-113.10	-100.00
(os)	-6.02	216.21	154.19	22.71		-157.12	-129.98	-99.99
(bt)	117.92	107.25	-42.73	-165.94	73.60		9.90	-100.00
(sil)	-88.65	78.08	140.92	134.93	-52.94	-112.35	-212.34	

Table 6.1. Univariant KFMASH equilibria calculated by mass balance from the compositions given. The numbers are stoichiometric coefficients derived for an arbitrary consumption (negative) of K-feldspar or sillimanite of 100 weight units. Five of the six ferromagnesian phases coexisted in D66-18A, garnet being the absent phase, and these are the phase compositions used. The phase compositions are illustrated in figure 6.4. The garnet composition was constructed in accordance with the grt-L Fe-Mg partitioning shown in figure 3.20. The quartz, K-feldspar and sillimanite are taken to be pure. Table 6.2 presents repeat calculations for different phase compositions (set B). The implications of variation in phase compositions are considered in the text.

Table 6.1. KFMASH Univariant Reactions (Set A)

Calculated Univariant Reactions (arranged by invariant point)

[os]

	grt	crd	L	opx	bi	qz	kfs	sil
(grt)		212.83	143.23	13.44	-148.97	-121.89	1.38	-100.02
(crd)	378.58		-577.80	-578.72	377.27	401.96	98.71	-100.00
(L)	75.12	170.59		-104.14	-44.43	-17.85	20.71	-100.00
(opx)	8.52	208.03	126.73		-136.96	-109.95	3.62	-99.99
(bt)	107.06	152.63	-60.89	-154.12		26.38	28.93	-99.99
(kfs)	-6.02	216.21	154.19	22.71	-157.12	-129.98		-99.99
(sil)	-391.31	220.01	744.03	611.91	-543.67	-540.97	-100.00	

[grt]

	crd	L	opx	os	bi	qz	kfs	sil
(crd)		352.70	41.12	398.83	-230.28	-292.12	-170.25	-100.00
(L)	357.91		-5.63	-271.90	-93.24	-5.59	118.44	-99.99
(opx)	314.39	42.73		-190.35	-109.81	-40.34	83.38	-100.00
(os)	212.83	143.23	13.44		-148.97	-121.89	1.38	-100.02
(bt)	600.98	-239.86	-37.47	-727.42		189.18	314.60	-100.01
(kfs)	211.04	144.68	13.55	3.34	-149.46	-123.15		-100.00
(sil)	-124.00	122.30	16.28	232.39	-47.61	-99.36	-100.00	

[opx]

	grt	crd	L	os	bi	qz	kfs	sil
(grt)		314.39	42.73	-190.35	-109.81	-40.34	83.38	-100.00
(crd)	25.17		291.04	372.33	-190.04	-246.10	-152.40	-100.00
(L)	-4.31	368.60		-287.40	-96.00	-4.89	124.01	-100.01
(os)	8.52	208.03	126.73		-136.96	-109.95	3.62	-99.99
(bt)	-34.40	745.03	-297.34	-961.13		241.48	406.36	-100.00
(kfs)	8.89	203.23	130.54	8.61	-138.17	-113.10		-100.00
(sil)	10.68	-133.36	105.31	238.68	-34.04	-87.28	-99.99	

[crd]

	grt	L	opx	os	bi	qz	kfs	sil
(grt)		352.70	41.12	398.83	-230.28	-292.12	-170.25	-100.00
(L)	143.59		-193.90	247.56	0.02	-28.99	-68.29	-99.99
(opx)	25.17	291.04		372.33	-190.04	-246.10	-152.40	-100.00
(os)	378.58	-577.80	-578.72		377.27	401.96	98.71	-100.00
(bt)	143.60	-0.02	-193.89	247.56		-28.99	-68.26	-100.00
(kfs)	239.55	-236.11	-351.05	146.46	154.10	147.05		-100.00
(sil)	-140.62	345.88	230.29	148.15	-225.77	-257.93	-100.00	

[L]

	grt	crd	opx	os	bi	qz	kfs	sil
(grt)		361.88	-6.68	-280.39	-90.71	-3.19	119.09	-100.00
(crd)	143.59		-193.90	247.56	0.02	-28.99	-68.29	-99.99
(opx)	-4.31	368.60		-287.40	-96.00	-4.89	124.01	-100.01
(os)	75.12	170.59	-104.14		-44.43	-17.85	20.71	-100.00
(bt)	143.70	-0.40	-193.99	248.21		-29.09	-68.44	-99.99
(kfs)	91.04	130.93	-125.02	57.56	-34.08	-20.43		-100.00
(sil)	76.95	-191.67	-100.86	278.14	49.96	-12.51	-100.01	

Table 6.1 continued. See caption on previous page.

Table 6.2. KFMASH Univariant Reactions (Set B)

Phase Compositions (Set B)

	grt	crd*	L*	opx	os	bt	qz	kfs	sil
SiO2	43.23	49.57	73.51	51.31	63.11	40.71	100.00	66.20	38.60
Al2O3	23.30	33.29	12.58	9.27	22.65	20.35	0.00	17.60	61.40
FeO	16.80	2.73	0.80	12.76	1.71	5.66	0.00	0.00	0.00
MgO	16.67	11.60	0.50	26.66	7.97	19.53	0.00	0.00	0.00
K2O	0.00	0.80	7.61	0.00	4.56	9.75	0.00	16.20	0.00
H2O	0.00	2.00	5.00	0.00	0.00	4.00	0.00	0.00	0.00
TOTAL	56.77	50.43	26.49	100.00	36.89	59.29	0.00	33.80	61.40
XMg	0.64	0.88	0.53	0.79	0.89	0.86	n.a	n.a.	n.a.

Calculated Univariant Reactions (arranged by invariant point)

[sil]

	grt	crd	L	opx	os	bt	qz	kfs
(grt)		-166.08	89.73	3.10	296.96	-29.12	-94.60	-100.00
(crd)	338.26		-731.64	-754.73	-376.59	914.13	710.57	-100.00
(L)	36.95	-147.88		-79.70	223.28	73.96	-6.61	-100.00
(opx)	1.38	-165.40	86.36		294.20	-25.24	-91.30	-100.00
(os)	149.01	-92.77	-272.18	-330.81		386.52	260.22	-100.00
(bt)	10.45	-160.97	64.37	-20.30	276.19		-69.74	-100.00
(kfs)	-42.00	-20.67	101.99	94.11	83.71	-117.14	-100.00	

[bt]

	grt	crd	L	opx	os	qz	kfs	sil
(grt)		1166.95	-466.26	3.54	-1679.97	441.56	634.17	-100.00
(crd)	76.81		-0.01	-144.17	321.42	-63.59	-90.45	-100.00
(L)	76.77	0.06		-144.15	321.34	-63.59	-90.43	-100.00
(opx)	2.59	1143.42	-457.32		-1640.47	431.84	619.93	-100.00
(os)	64.63	187.34	-74.93	-120.54		17.57	25.93	-100.00
(kfs)	67.35	145.59	-58.24	-125.81	71.62	-0.51		-100.00
(sil)	10.45	-160.97	64.37	-20.30	276.19	-69.74	-100.00	

[kfs]

	grt	crd	L	opx	os	bt	qz	sil
(grt)		112.41	105.36	25.13	205.92	-187.90	-160.92	-100.00
(crd)	-229.16		661.71	538.45	662.05	-826.78	-706.27	-100.00
(L)	43.36	133.80		-72.07	119.42	-66.89	-57.61	-100.00
(opx)	11.20	117.95	78.11		183.55	-156.61	-134.21	-100.00
(os)	103.28	163.28	-145.52	-206.33		100.23	85.06	-100.00
(bt)	67.35	145.59	-58.24	-125.81	71.62		-0.51	-100.00
(sil)	-42.00	-20.67	101.99	94.11	83.71	-117.14	-100.00	

Table 6.2. Univariant KFMASH equilibria calculated by mass balance from the compositions given, as in table 6.1. Again, the numbers are stoichiometric coefficients derived for an arbitrary consumption (negative) of K-feldspar or sillimanite of 100 weight units. Five of the six ferromagnesian phases coexisted in D47-18, garnet being the absent phase, and these are the phase compositions used. The phase compositions are illustrated in figure 6.4. The garnet composition was invented in accordance with the grt-L Fe-Mg partitioning shown in figure 3.20. The quartz, K-feldspar and sillimanite are taken to be pure. * The water-contents of these phases have been raised to artificially high levels to assess the effects of their variation.

Table 6.2. KFMASH Univariant Reactions (Set B)

Calculated Univariant Reactions (arranged by invariant point)

[os]

	grt	crd	L	opx	bt	qz	kfs	sil
(grt)		227.58	43.13	22.98	-167.71	-95.32	69.34	-100.00
(crd)	365.51		-624.43	-788.58	780.59	543.04	-176.12	-100.00
(L)	23.60	212.89		-29.45	-106.44	-54.08	53.48	-100.00
(opx)	10.34	221.14	24.23		-140.85	-77.25	62.39	-100.00
(bt)	64.63	187.34	-74.93	-120.54		17.57	25.93	-100.00
(kfs)	103.28	163.28	-145.52	-206.33	100.23	85.06		-100.00
(sil)	149.01	-92.77	-272.18	-330.81	386.52	260.22	-100.00	

[grt]

	crd	L	opx	os	bt	qz	kfs	sil
(crd)		165.94	27.16	406.92	-207.49	-224.86	-67.67	-100
(L)	307.52		21.51	-142.92	-153.74	-49.83	117.46	-100
(opx)	1232.43	-503.76		-1797.13	14.88	480.94	672.63	-100
(os)	227.58	43.13	22.98		-167.71	-95.32	69.34	-100
(bt)	1166.95	-466.26	3.54	-1679.97		441.56	634.17	-100
(kfs)	112.41	105.36	25.13	205.92	-187.9	-160.92		-100
(sil)	-166.08	89.73	3.1	296.96	-29.12	-94.6	-100	

[opx]

	grt	crd	L	os	bt	qz	kfs	sil
(grt)		1232.43	-503.76	-1797.13	14.88	480.94	672.63	-100
(crd)	12.19		139.68	393.35	-174.61	-199.31	-71.3	-100
(L)	9.95	267.55		-82.55	-133.77	-51.63	90.44	-100
(os)	10.34	221.14	24.23		-140.85	-77.25	62.39	-100
(bt)	2.59	1143.42	-457.32	-1640.47		431.84	619.93	-100
(kfs)	11.2	117.95	78.11	183.55	-156.61	-134.21		-100
(sil)	1.38	-165.4	86.36	294.2	-25.24	-91.3	-100	

[crd]

	grt	L	opx	os	bt	qz	kfs	sil
(grt)		165.94	27.16	406.92	-207.49	-224.86	-67.67	-100
(L)	76.78		-144.16	321.44	0	-63.6	-90.46	-100
(opx)	12.19	139.68		393.35	-174.61	-199.31	-71.3	-100
(os)	365.51	-624.43	-788.58		780.59	543.04	-176.12	-100
(bt)	76.81	-0.01	-144.17	321.42		-63.59	-90.45	-100
(kfs)	-229.16	661.71	538.45	662.05	-826.78	-706.27		-100
(sil)	338.26	-731.64	-754.73	-376.59	914.13	710.57	-100	

[L]

	grt	crd	opx	os	bt	qz	kfs	sil
(grt)		307.52	21.51	-142.92	-153.74	-49.83	117.46	-100
(crd)	76.78		-144.16	321.44	0	-63.6	-90.46	-100
(opx)	9.95	267.55		-82.55	-133.77	-51.63	90.44	-100
(os)	23.6	212.89	-29.45		-106.44	-54.08	53.48	-100
(bt)	76.77	0.06	-144.15	321.34		-63.59	-90.43	-100
(kfs)	43.36	133.8	-72.07	119.42	-66.89	-57.61		-100
(sil)	-42	-20.67	101.99	94.11	83.71	-117.14	-100	

Table 6.2 continued. See caption on previous page.

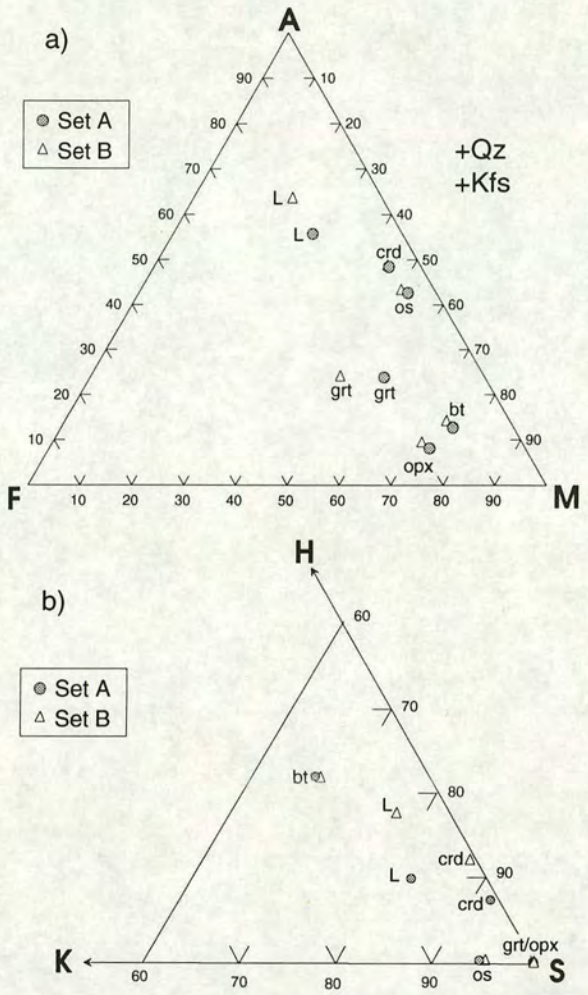

Figure 6.4.
a) An AFM diagram showing the chemographic relations of the phases in sets A and B (tables 6.1 and 6.2). The phases are projected from quartz and K-feldspar only, water is ignored.
b) A partial H(H_2O)-K(K_2O)-S(SiO_2) plot showing the chemographic relations of the phases in sets A and B (tables 6.1 and 6.2). The components MgO, FeO and Al_2O_3 are ignored in this plot.

2.17). In this study the point is labelled [os] (INSERT A). The biotite dehydration melting reactions involved at this point, both univariant and divariant are even more widely cited (e.g. Thompson 1982, Waters and Whales 1984, Le Breton and Thompson 1988, Vielzeuf and Holloway 1988, Waters 1988). The stability of this point has not been demonstrated experimentally before but the evidence cited above strongly implies it is stable. Additionally, the stability of the [os] point considerably reduces the pressure-temperature range over which osumilite can be stable, in keeping with the relative rarity of the mineral in high-temperature metamorphic rocks.

The second invariant point chosen as being stable is [bt]. The consequence of the biotite dehydration melting reactions running to completion must be biotite-absent assemblages. Several experimental and natural rock studies have demonstrated the stability of analogous points in various systems (Motoyoshi et al. 1993, labelled [spr], KMAS; Grew 1982, [sap], KFMAS; Arima and Gower 1991, I1, KMASH, Audibert et al. 1994, [sa], KFMASH). The strength of the evidence is considered to be sufficient for the safe assumption of the stability of the [os] and [bt] points.

The assumption of stability of the two points in the system is sufficient to constrain the grid topology if the slopes of the reactions are estimated. This need only be done approximately here as a better estimate of the reaction gradients can be made when the grid is fitted to the experiments. The following assumptions were made in constructing the grid;

a) biotite lies on the low-temperature side of melting reactions, melt on the high-temperature side and the slopes are steep (melting involves a large entropy change),

b) osumilite has a low high-pressure stability limit (Harley and Hensen 1990, Motoyoshi et al. 1993, Audibert et al. 1994) due to its low density and will therefore occur on the low-pressure side of reactions,

c) cordierite will also lie on the low-pressure side of reactions for the same reasons that osumilite does (e.g. Newton 1972), except if osumilite also occurs in the reaction,

d) orthopyroxene-sillimanite-quartz is a high-pressure assemblage (Hensen and Green 1973, Bertrand et al. 1991).

The grid drawn using these assumptions and the [os] and [bt] points is shown in figure 6.5. The [sil], [opx] and [L] points can also be stable[6] in the given topology but the [grt], [crd] and [kfs] points cannot be, and the latter form a residual grid (figure 6.6). A few reactions have stoichiometries which are sensitive to the variation in phase compositions and could potentially be degenerate. These are discussed below and the conclusions have been incorporated into figure 6.5.

[6] Although the [sil], [opx] and [L] points can be topologically stable in the derivation given here, they do not have to be stable in reality - the reactions may not converge to a point.

Figure 6.5. The KFMASH, univariant multisystem grid for the phases quartz, K-feldspar, sillimanite, melt, garnet, orthopyroxene, biotite, cordierite and osumilite, positioned qualitatively in pressure-temperature space. The reactions not labelled were outside the range of pressure, temperature and bulk composition used in the current experiments, but are listed in table 6.1. The grid is based on;
i) reactions calculated by mass-balance from phase compositions listed in table 6.1 (set A) and illustrated in figure 6.4,
ii) the assumption of the stability of the [os] and [bt] points,
iii) the assumptions on the slopes of reactions given in the text above.
Given these assumptions the [kfs], [crd] and [grt] points (grey circles) must be metastable: the residual grid is given in figure 6.6. The experiments in this study show that [os] and [bt] are stable. The [sil], [opx] and [L] points *may* be stable but are not necessarily so.

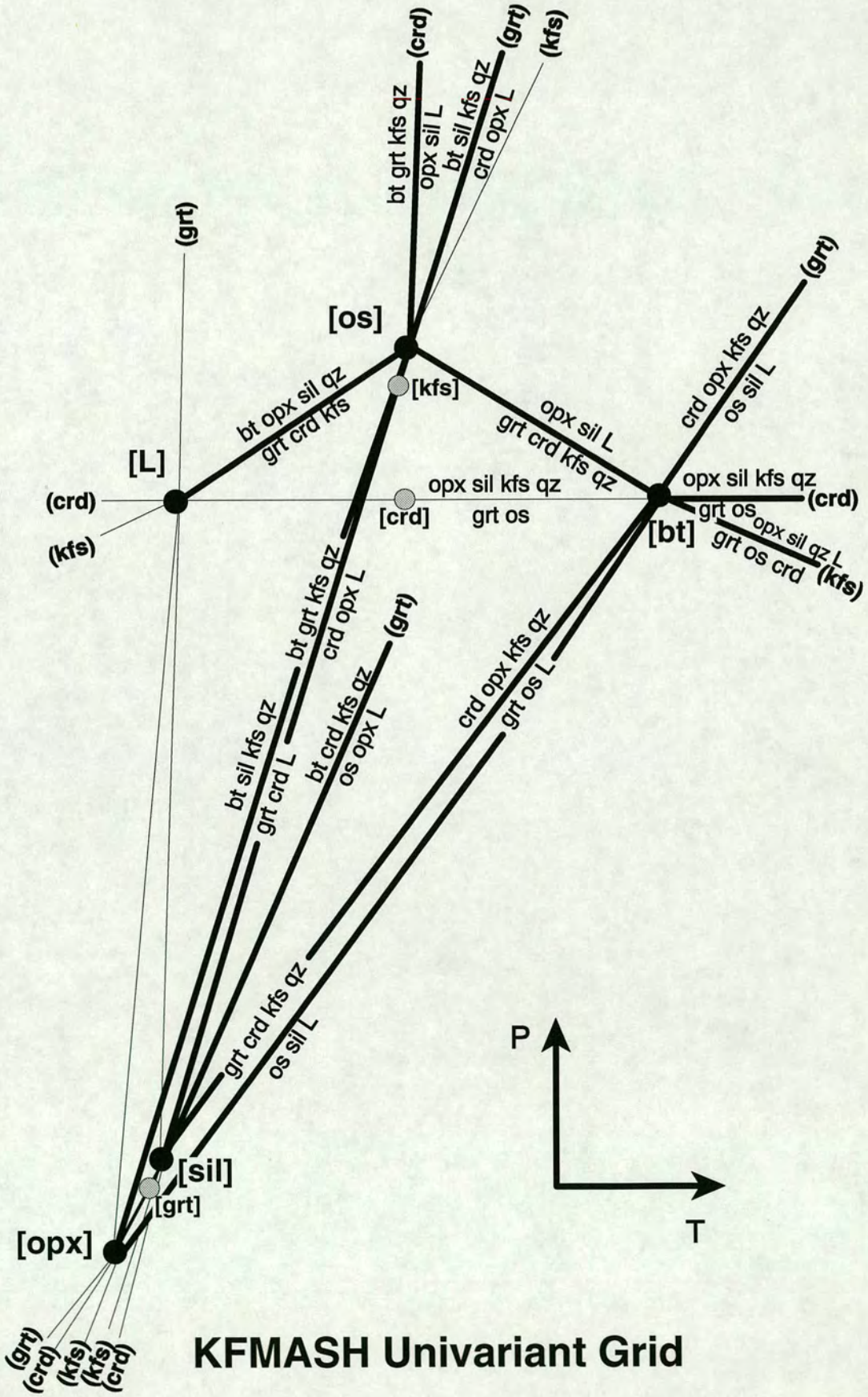
[os]
[L]
[bt]
[sil]
[opx]
[kfs]
[crd]
[grt]
bt grt kfs qz
opx sil L
bt sil kfs qz
crd opx L
(crd)
(grt)
(kfs)
bt opx sil qz
grt crd kfs
opx sil L
grt crd kfs qz
crd opx kfs qz
os sil L
opx sil kfs qz
grt os
grt os crd
opx sil qz L
bt grt kfs qz
crd opx L
bt sil kfs qz
grt crd L
bt crd kfs qz
os opx L
crd opx kfs qz
grt os L
grt crd kfs qz
os sil L
P
T
KFMASH Univariant Grid

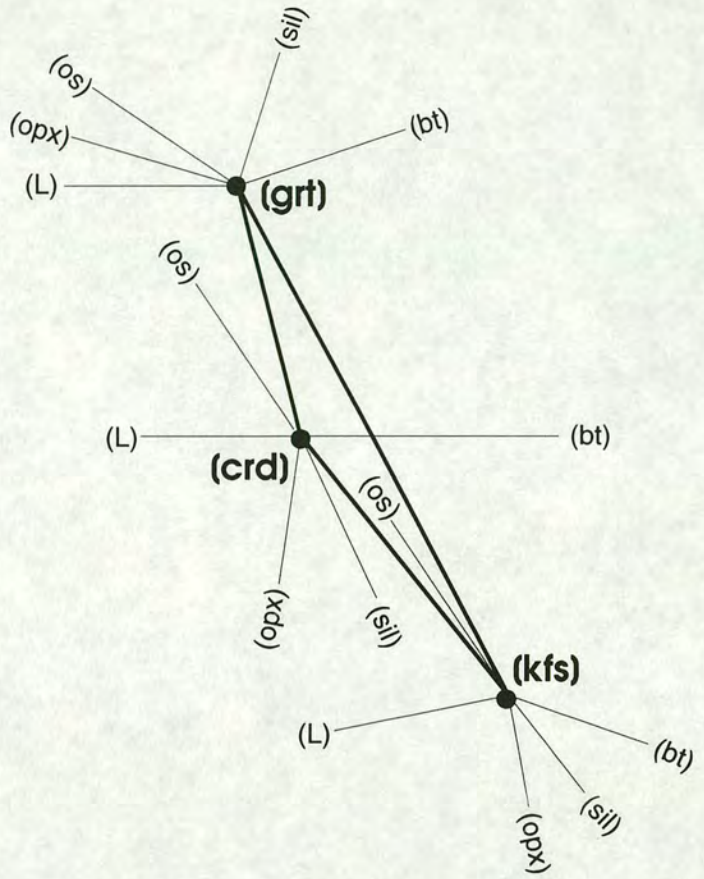

Figure 6.6. Sketch of the residual grid to that with the [os] and [bt] points stable (figure 6.5). Here the [kfs], [crd] and [grt] points are stable and the [os], [bt], [sil], [opx] and [L] points must be metastable. The reaction stoichiometries are given in table 6.1.

A powerful way of determining the stability of a chosen grid, relative to its residual, is to demonstrate the stability of the divariant assemblages unique to it[7]. This method was described in section 6.1 and used by Hensen (1986) to distinguish high and low fO_2 FMAS grids, (see sections 2.3.4 and 6.1). The ten divariant assemblages unique to the grid in figure 6.5 and the one unique to its residual grid (figure 6.6) are given in table 6.3. Three of the ten divariant assemblages (those with both biotite and liquid absent) are not accessible to the bulk compositions used. This is because the only remaining hydrous phase is cordierite which has a water content of the approximately the same magnitude as the bulk composition's one weight-percent, therefore requiring a bulk composition very close to cordierite to stabilise the assemblage. Of the remaining seven assemblages, five were produced in the experiments (table 6.3), some more than once. The fact that two were not produced again reflects the fact that

[7] The demonstration of the stability of a grid's unique divariant assemblages does not prove its stability relative to any other grid which could have been derived, had different invariant points been chosen initially.

Unique to grid in figure 6.4;	**Experiments assemblage formed in.**	**Unique to residual grid;**	**Experiments assemblage formed in.**
(os, L opx)	63-16A*	(grt, crd, kfs)	none
(os, bt, sil)	56-17*		
(os, bt, opx)	57-16		
(os, sil, opx)	49-16, 49-17, 66-18A*		
(bt, sil, opx)	51-16, 60-16A*		
(os, L, sil)	none		
(L, sil, opx)	none		
(L, bt, sil)	not accessible		
(L, bt, opx)	not accessible		
(L, bt, os)	not accessible		

Table 6.3. Unique divariant assemblages of the stable grid (figure 6.5) and its residual grid (figure 6.6). An asterix denotes that the unique assemblage was present in that experiment as the product assemblage, i.e. those phases and no others formed. The others are *interpreted* to have formed the unique assemblages, i.e. the product assemblage was not the interpreted equilibrium assemblage (see tables 4.1 and 4.2). Three of the assemblages are thought not to accessible to the bulk compositions used (see text).

the bulk compositions were not appropriate for those assemblages at the pressures and temperatures used. The divariant assemblage unique to the residual grid (bt-os-sil-opx-qz-L) was not produced. Of course, this may have been because no appropriate bulk composition was used but this seems unlikely as all the other melt-present assemblages were found.

6.3.2 The sensitivity of reaction stoichiometry to varying phase compositions.

The evidence of table 6.3 and the fact that the grid and pseudosections can describe the experiments with very few contradictions (see pseudosections below) supports the grid constructed. However, some of the univariant reaction stoichiometries are rather sensitive to the phase compositions used in their calculation. This is demonstrated by comparing the original calculated reactions (set A) with those in table 6.2, which used a second set of phase compositions (set B) which has higher water-contents for the melt and the cordierite and different values of X_{Mg} for the ferromagnesian phases. The differences between the two sets indicate that further consideration should be given to;

i) the role of K-feldspar in the biotite dehydration melting reactions,

ii) implications of near-degeneracy of the (bt, grt) and (bt, opx) reactions,

iii) other sensitive reactions.

The set B calculations (high melt water-content) suggest that K-feldspar is a product for all the osumilite-absent, biotite dehydration melting reactions. However, the set A data (low melt water-content), which are the best estimate of phase compositions in this study, show that K-feldspar is a reactant for the (os, sil) and (os, crd) reactions. The different H_2O/K_2O ratios of the melts are responsible for this contradiction (figure 6.7). The water- and potassium-contents of the melts both increase with pressure and decrease with temperature, but figure 6.8 shows that the H_2O/K_2O ratio

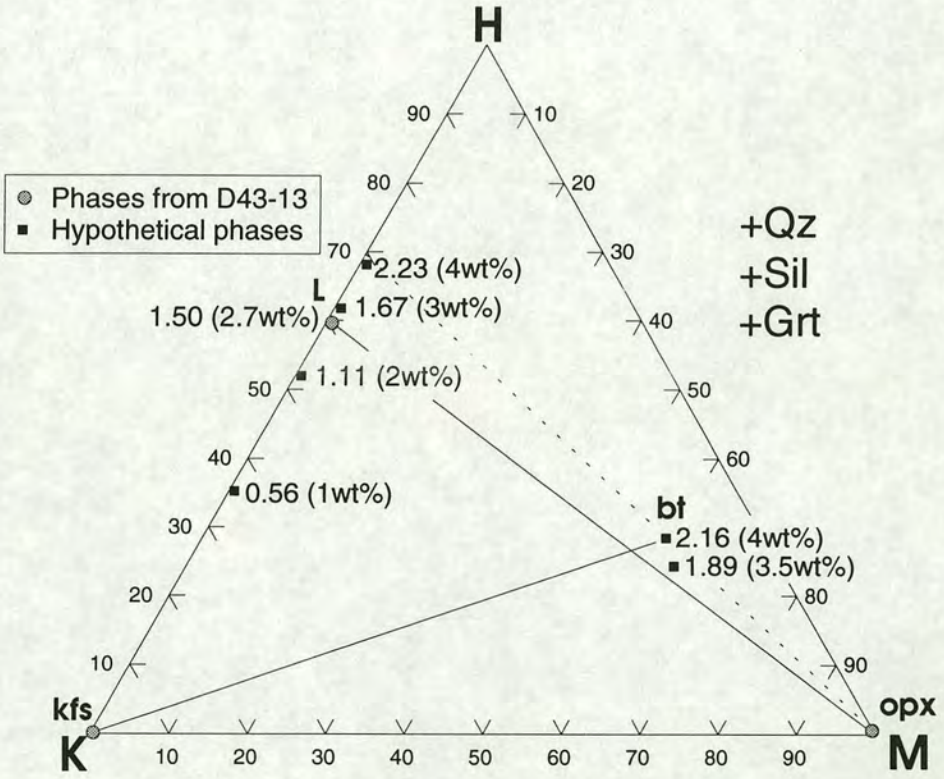

Figure 6.7. HKM projection (from quartz, sillimanite and garnet) for D43-13 showing how K-feldspar can be a product or a reactant of a biotite dehydration melting reaction, in this case (os, crd). At high H_2O/K_2O ratios for the melt, the orthopyroxene-melt tie-line lies above the biotite and thus K-feldspar must be a product of the breakdown of biotite. At low H_2O/K_2O ratios for the melt, the tie-line crosses the biotite-K-feldspar tie-line and therefore the K-feldspar must be a reactant. The reaction will be degenerate when the orthopyroxene, biotite and melt are collinear. The melt H_2O/K_2O for degeneracy will be about 2.20 for a biotite with 4wt% water, but lower if dehydroxylation has decreased the water-content of the biotite.
The H_2O/K_2O molar ratios are given next to the plotted phases with the water-contents given in brackets in weight percent. The hypothetical melts are calculated for a constant potassium content. The estimated melt water-content for D43-13 is 2.7 ± 0.5 wt% (fig 3.32) which gives a H_2O/K_2O ratio of 1.5 and therefore K-feldspar should be a product. A similar diagram was published by Patino Douce and Johnston (1991) and is discussed in the text.

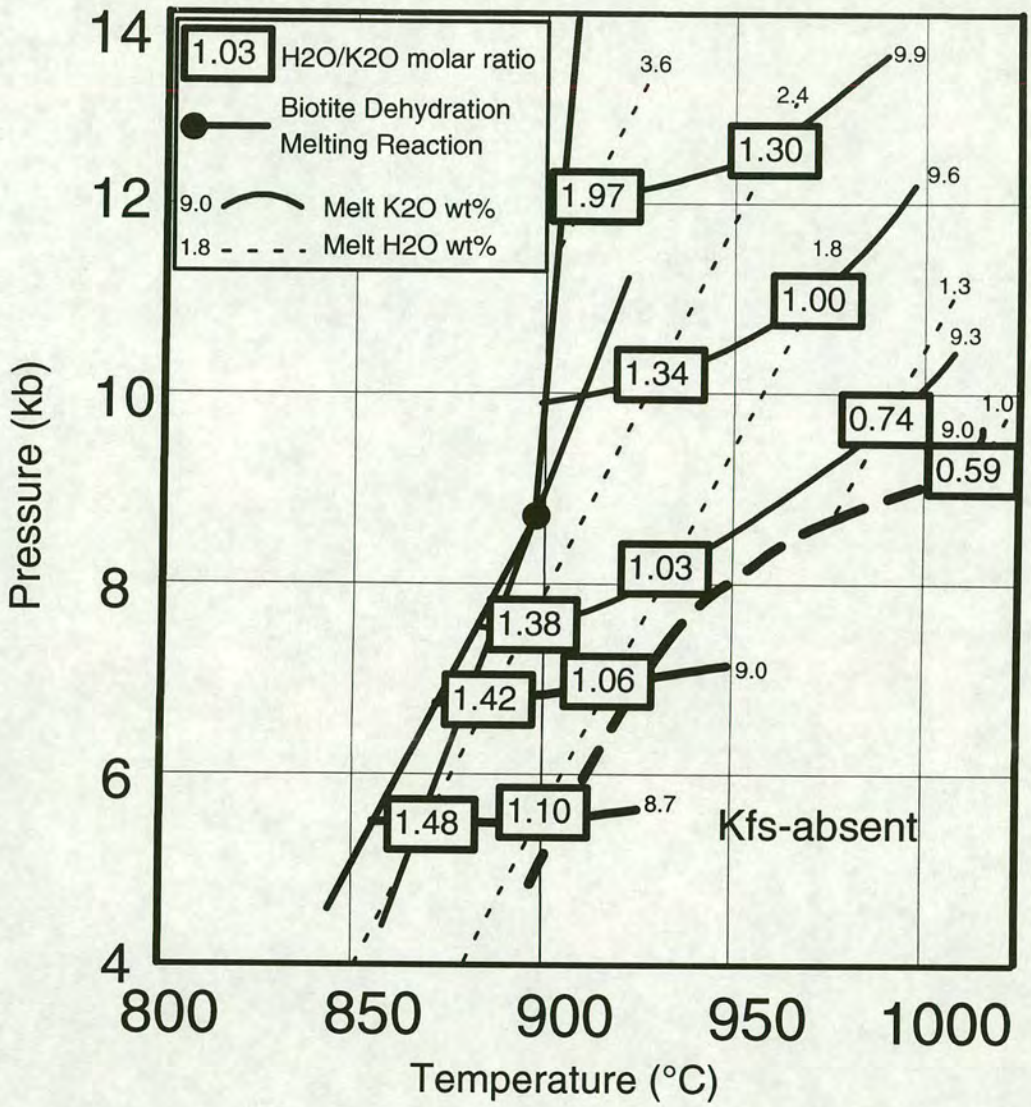

VARIATION OF THE H_2O/K_2O RATIO FOR MELTS IN THIS STUDY

Figure 6.8 Pressure-temperature diagram showing the H_2O/K_2O molar ratio for melts in this study. The ratios are calculated from the estimated water and potassium contents, taken from figures 3.32 and 3.24 respectively. If the uncertainty in the water and potassium contents is taken to be ± 0.5wt%, the error in the molar H_2O/K_2O ratio is ± 0.4.

The biotite dehydration melting reactions referred to in figures 6.7 and 6.9 and in the text are also shown. For the (os, crd) reaction to be degenerate (figure 6.7) the melt H_2O/K_2O ratio must be greater than about 2.2 for a biotite with 4wt% water. This is within the estimated uncertainty at the highest pressures and lowest temperatures investigated in this study. If the biotite has undergone some dehydroxylation to, say, 3.5wt% water, then the required H_2O/K_2O ratio is 1.9. The melt H_2O/K_2O ratio is likely to be this high at the highest pressures investigated in the study.

is highest at the highest pressures and lowest temperatures used in the study. Comparison with the H_2O/K_2O ratio required for degeneracy (about 2.2 for a biotite with 4wt% water) shows that K-feldspar could only be a product in reactions (os, sil) and (os, crd) at, or above, the highest pressures in this study. Therefore, the (os, sil) and (os, crd) reactions are both taken to have the reactant assemblages biotite-garnet-quartz-K-feldspar. The phase compositions are changing continuously and so the reaction will only be degenerate at a single point on the reaction, usually termed a singular point. The stoichiometry will reverse at this point, i.e. the K-feldspar will lie on one side of the reaction below the point and on the other side above it. Truly degenerate reactions are degenerate along all their length because they require fewer than C components to describe the phases involved, e.g. the anhydrous reaction (crd, bt, L) (figure 6.5).

The other two osumilite-absent, biotite dehydration melting reactions, (os, opx) and (os, grt) are closer to degeneracy, though they still require K-feldspar as a reactant. This is because a lower melt H_2O/K_2O ratio is required for degeneracy, as a result of the involvement of cordierite which contains some water (figure 6.9). The stoichiometric coefficients for set A data (table 6.1) show that the (os, grt) and (os, opx) reactions have a small amount of K-feldspar as a *product*, but are nearly degenerate with the (os, kfs) reaction, which only involves a little orthopyroxene and garnet. The discrepancy between the generalised data (set A, table 6.1) and the single experiment data (figure 6.9), which implies that K-feldspar is a *reactant* emphasises how close these reactions are to degeneracy. Whichever the case, K-feldspar, garnet and orthopyroxene are not volumetrically important phases in these reactions, which must predominantly involve biotite-sillimanite-quartz producing cordierite and melt. The value of the melt-cordierite water-partitioning coefficient[8] can also affect the stoichiometry of the reaction; the lower K_w, the lower the melt H_2O/K_2O ratio required for degeneracy (figure 6.9).

In summary, the current data suggest that the role of K-feldspar depends primarily on the H_2O/K_2O ratio of the melt phase which is determined by pressure and temperature for a given bulk composition. It may also be affected by the level of melt-cordierite water-partitioning or the occurrence of dehydroxylation in biotite.

[8] $Kw = H_2O^L/H_2O^{crd}$. See section 3.6.3.

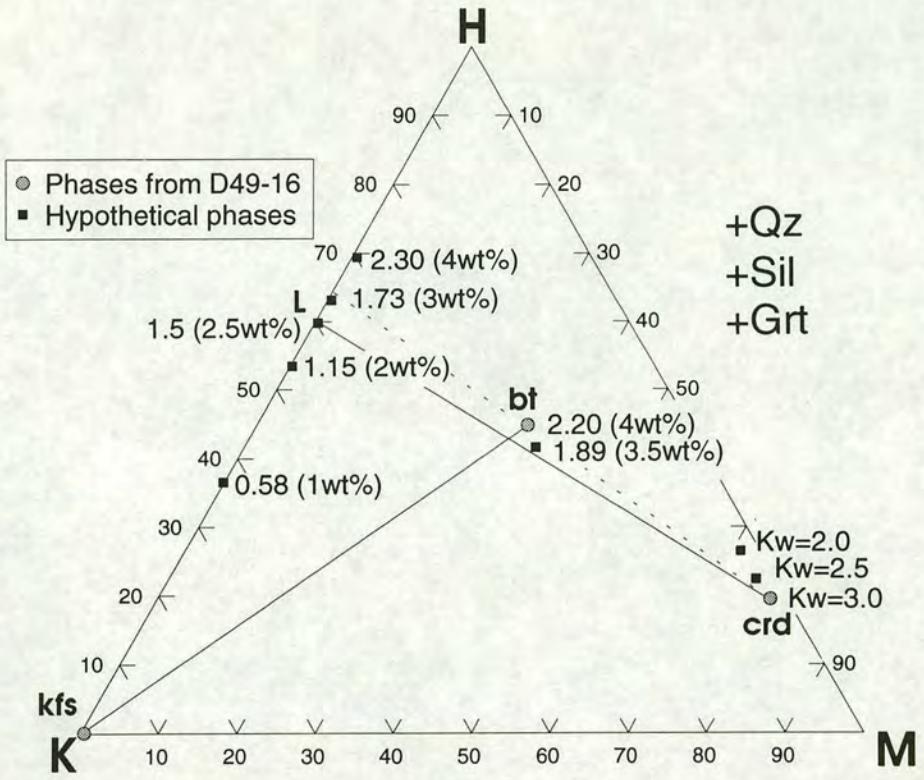

Figure 6.9. HKM projection (from quartz, sillimanite and garnet) for D49-16 showing how K-feldspar can be a product or a reactant of a biotite dehydration melting reaction, in this case (os, opx). Comparison with figure 6.7 shows that the (os, opx) reaction is closer to degeneracy than the (os, crd) reaction, particularly if the distribution coefficient of water between melt and cordierite (Kw) is less than the maximum value of 3.0 derived in section 3.6.3. This is because the cordierite involved in the (os, opx) reaction contains some water and therefore plots nearer the H apex. If the H_2O/K_2O ratio for the melt is such that the melt, biotite and cordierite are co-linear then K-feldspar will not be involved and the (os, opx) reaction will be degenerate. The estimated melt water-content for D49-16 is 2.5 ± 0.5 wt% (fig 3.32) with an H_2O/K_2O ratio of 1.5. A similar diagram was published by Patino Douce and Johnston (1991) and is discussed in the text.

Previous theoretical and natural rock studies argue that biotite dehydration melting reactions should produce K-feldspar (e.g. Thompson and Algor 1977, Thompson 1982, Vielzeuf and Holloway 1988, Stevens and van Reenen 1992) but this has not been demonstrated experimentally either in this study[9] or in others involving mica dehydration melting with excess quartz (e.g. Peterson and Newton 1989, Vielzeuf and Holloway 1988, Patino Douce and Johnston 1991). However, K-feldspar was reported as a product of biotite dehydration melting reaction by Bohlen et al. (1983) and Le Breton and Thompson (1988). The arguments presented above suggest that the H_2O/K_2O ratio of the melt controls the role of K-feldspar and that variations in

[9] Table 3.10 shows that in several experiments the proportion of K-feldspar has decreased from that originally present.

this ratio could explain the discrepancies noted: for a given potassium content, water-rich melts result in the production of K-feldspar, water-poor melts result in the consumption of K-feldspar. It should be remembered that natural rocks will contain sodium and this will partition strongly into the melt. Therefore, the potassium-contents in natural or complex-system melts may be lower than in the current experiments and this would raise the H_2O/K_2O ratio, thereby favouring the production of K-feldspar in biotite dehydration melting reactions.

No K-feldspar was observed in the experiments of Patino Douce and Johnston (1991)[10], but the melt compositions produced unequivocally suggest that K-feldspar should have been a product of their melting reaction (see their figure 10, analogous to figures 6.7 and 6.9). It was concluded from this that the biotite must have undergone dehydroxylation, thereby allowing the formation of melt but no K-feldspar. However, Patino Douce and Johnston do not consider uncertainties in their water-content estimates nor make any allowance for the variation of melt water-content with changing pressure and temperature. It was noted previously that the melt water-content estimates given by Patino Douce and Johnston (1991) were significantly higher than those made here (table 3.12). They calculated the water- and sodium-contents by mass balance. If their water contents were overestimated by only a percent or two then the contradiction that they explained by biotite dehydroxylation, i.e. that no K-feldspar was produced when their estimate of the melt composition required it, would not exist.

Variations in the H_2O/K_2O ratio of the melt phase adequately explain how the (os, crd) and (os, sil) reactions could cause the reduced K-feldspar abundance in all the point-counted experiments[11], with the (os, grt) and (os, opx) reactions not affecting the abundance of K-feldspar significantly. However, it is important to note that part of the change in the phase abundances will occur via divariant reactions. In particular, the univariant reaction may produce K-feldspar but any further temperature increase beyond the limit of biotite stability will start to consume the K-feldspar. This is because all of the biotite-absent divariant reactions operating above the limit of biotite consume K-feldspar (table 6.4). This is inevitable in biotite- and osumilite-absent reactions as there are then only two potassic phases, K-feldspar and

[10] Unlike the present study, the starting mix of Patino Douce and Johnston (1991) contained no K-feldspar at all. They used natural starting materials and therefore their melts contained sodium.
[11] Phase modal abundances were estimated by eye for every experiment and none showed an increase in K-feldspar.

Bulk composition	Reaction	Reaction label
a) with biotite		
M62, M74, M86	bt + sil = grt + kfs + L	(os, crd, opx)
M62, M74	bt + crd + kfs = grt + L*	(os, sil, opx)
M86	bt + sil = opx + kfs +L	(os, grt, crd)
M86	bt = crd + opx +kfs + L	(os, grt, sil)
M86	bt + crd + kfs = os + L	(sil, grt, opx)
b) without biotite		
M62, M74	crd + kfs = grt + sil + L	(os, opx, bt)
M62, M74	opx + crd + kfs = grt + L	(os, sil ,bt)
M86	opx + crd + kfs = os + L	(sil, grt, bt)
M86	crd + kfs = opx + sil + L	(os, grt, bt)

Table 6.4. Divariant melting reactions operating in the divariant fields adjacent to the biotite dehydration melting reactions (see pseudosections presented in figures 6.13, 6.14 and 6.15).
a) Reactions involving biotite, i.e. below the terminal stability of biotite. b) Reactions not involving biotite, i.e. above the terminal stability of biotite. All reactions also involve quartz.
*This reaction is almost degenerate with a K-feldspar-absent reaction.

melt, and the melt must be produced with increasing temperature.

It is not practical to perform the experiments closer than 10°C apart as the temperature uncertainty is ± 5°C. However, even in this small temperature range, several reactions affecting the abundance of K-feldspar could occur. If the temperature range straddles a univariant reaction it will also include a divariant biotite-present reaction and a biotite-absent divariant reaction. Such complexities cannot be resolved by the current experiments.

The hypothesis presented above can explain all the observed data, in this study and in the literature, by ascribing control of the role of K-feldspar in biotite dehydration melting reactions to the water-potassium ratio in the melts. This is a simple and flexible model but cannot be applied to natural rocks unless good estimates of the melt composition are available. The ongoing experimental work on granites and tonalites by Dr F.Holtz, Prof. W.Johannes and Dr M.Pichavant (see reference list) and the potential of water-undersaturated cordierite as an indicator of co-existing melt water-contents in natural rocks, currently being developed by Dr S.Harley (Harley et al. 1992), suggest this may be the case in the future.

Degeneracy of (bt, grt) and (bt, opx) reactions.

The two sets of data (tables 6.1 and 6.2) suggest that reactions (bt, grt) and (bt, opx) are close to degeneracy. Figure 6.10 illustrates the degeneracy, which depends on the relative water-contents of the melt and cordierite (i.e. the partitioning coefficient, K_w), as this controls the position of cordierite on the AFM diagram. If the cordierite is co-linear with osumilite and sillimanite then the reaction will be degenerate and will not involve a more iron-rich phase, whether that is garnet or orthopyroxene. When the experimental data are plotted for a K_w=3.0 the reaction is very close to degeneracy (see figure 4.5 and Appendix Three). However, because the experiment from which the value of K_w=3.0 was derived contained approximately four times the water of the normal mix, the value must be considered a maximum (see section 3.6.3). If the K_w is less than 3.0 then the reaction will be have garnet or orthopyroxene as a reactant (form C, figure 6.10). The degeneracy is caused by

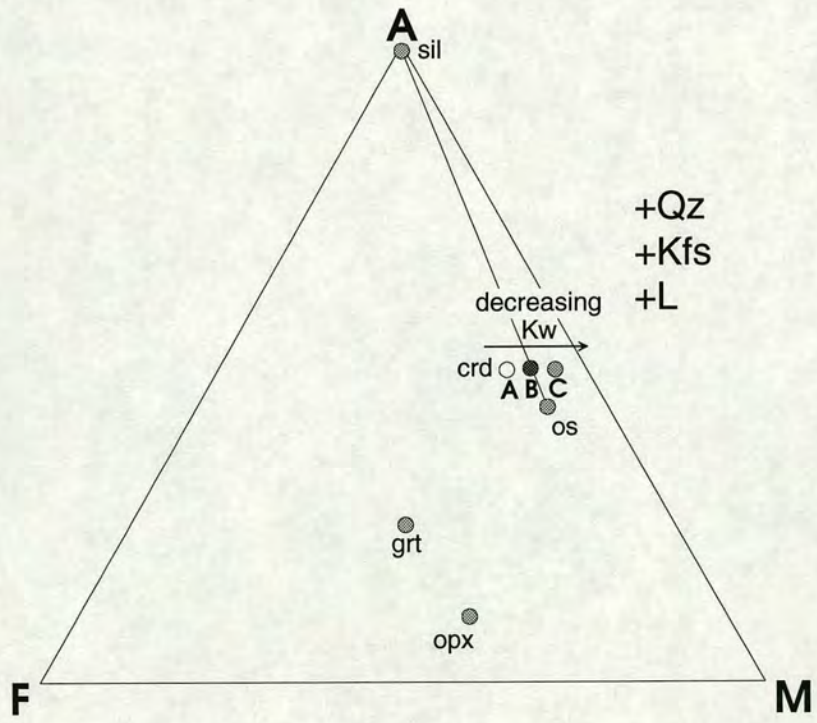

Figure 6.10. Schematic AFM projection illustrating the three potential forms of the (bt, grt) and (bt, opx) reactions. The stoichiometry of the reaction depends on the projected position of the cordierite, which is determined by the melt-cordierite water partitioning coefficient, K_w (see figure 4.5 and section 3.6.3).
A - crd + kfs + qz = os + grt/opx + sil + L (higher K_w)
B - crd + kfs + qz = os + sil + L (degenerate)
C - crd + grt/opx + kfs +qz = os + sil + L (lower K_w).
The only reliably measured water contents in this study (section 3.6.3) give a value for K_w of 3.0, which would make the reactions virtually degenerate. This value is a maximum, however, and therefore C is the most probable stoichiometry.

changing phase compositions, like the biotite dehydration melting reactions above, not by the absence of a component and so there could be a singular point. As the water-content of the melt increases down temperature and the water-content of the cordierite decreases down pressure, the highest values of K_w will be found at low pressures and temperatures. Therefore the singular point, if stable in this system, will most probably occur on the (os, opx) reaction (figure 6.5).

Other sensitive reactions.

There are several more reactions which are sensitive to the phase compositions used. However, these reactions, listed below, are either unstable in the current grid (i.e. only stable in its residual) or are outside the range of pressure, temperature and composition investigated (see INSERT A). These reactions are:

(kfs, crd) - only stable on residual grid,
(opx, grt) - outside range of experiments,
(sil, kfs) - outside range of experiments,
(L, grt), (L, opx) - possible degeneracy, but outside P-T range.

6.3.3 Positioning of the univariant grid in pressure-temperature space.

Once the topology of the KFMASH univariant grid has been derived (previous section), the next step in the development of applicable diagrams is to position the grid in pressure-temperature space using the experimental data and Schreinemakers' rules. The reactant and product assemblages of a univariant reaction are only stable on their respective sides of the reaction, i.e. they are characteristic to that side. For example, any experiment containing the stable assemblage osumilite-sillimanite-melt must be at higher temperatures than the (bt, opx) and (bt, grt) reactions (figure 6.5). Therefore, the characteristic assemblages that may be present in each experiment allow the pressure-temperature position of the univariant reactions to be constrained. The fact that three bulk compositions were used at most of the run pressures and temperatures means that more than one characteristic assemblage may be available at each pressure and temperature for constraining the position of the reactions. For example, D57-16 contained the assemblage garnet-cordierite-K-feldspar-quartz and D57-18 contained the assemblage osumilite-orthopyroxene-melt: the former requires that the (os, bt) reaction lies at higher pressures than the experiment and the latter that the (sil, grt) reaction lies at lower temperatures.

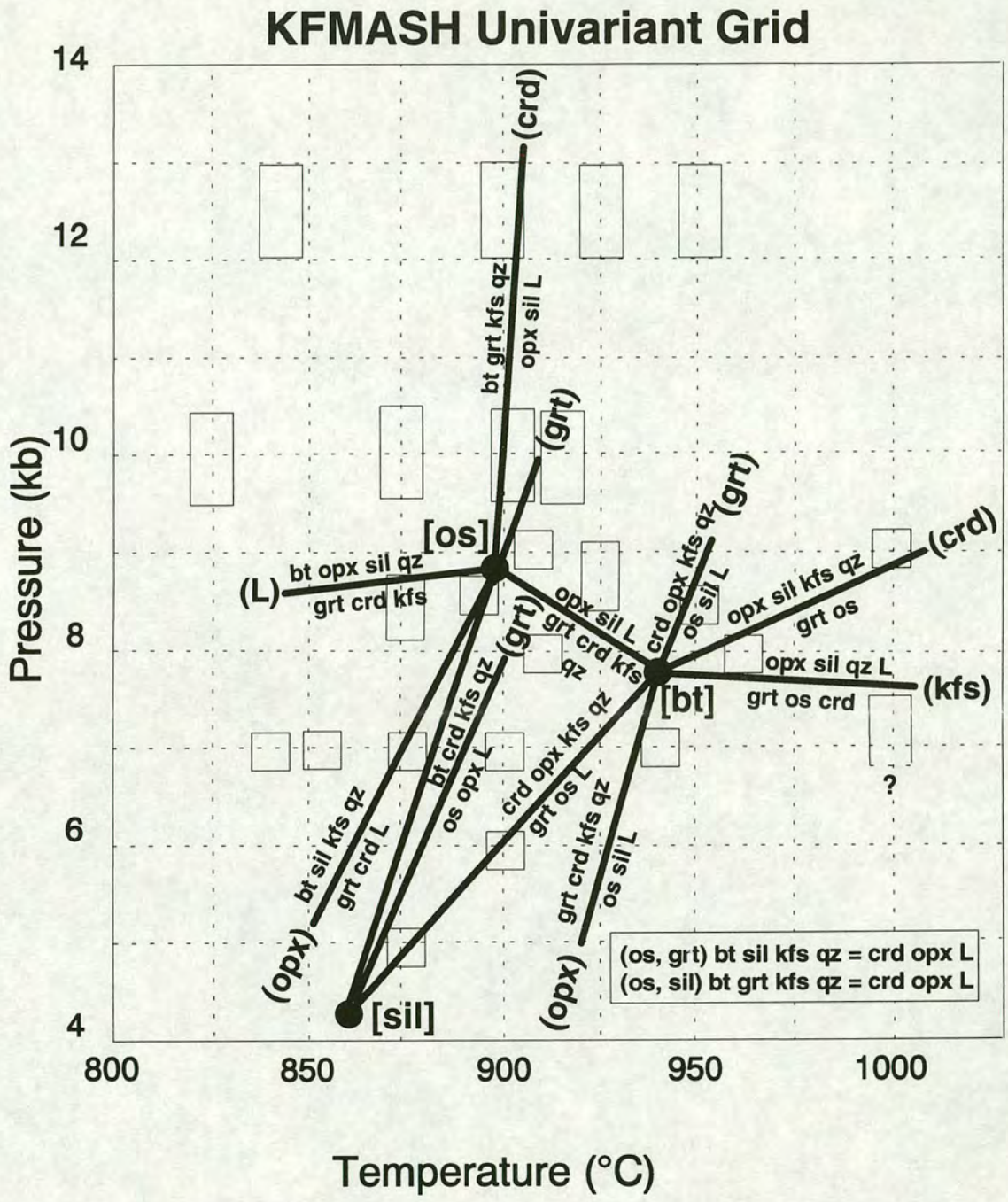

Figure 6.11. Univariant reaction pressure-temperature grid for the KFMASH system. The grid is positioned on the basis of the current experimental data and is fully consistent with Schreinemakers' rules. The methods by which the experimental constraints were applied is discussed in the text, as is the uncertainty in the positioning of the grid. The run conditions of the experiments are shown as rectangles. The size of the rectangles represent the uncertainty in the run conditions (see Chapter Two). Figure 6.12 gives the run numbers of the experiments for reference. Note: (os, kfs) is left off as all assemblages in that region involve K-feldspar. (os, qz) and (bt, qz) are not considered as all assemblage involve quartz. This diagram is reproduced as INSERT A.

The reaction positioning must be done in such a way that the grid is still consistent with Schreinemakers' rules. This provides additional, and sometimes powerful, constraints on reactions, as they must form invariant points at appropriate positions and their metastable extensions through the invariant points must lie in appropriate fields. Figure 6.11 shows the "best-fit" positioning of the grid in pressure-temperature space and is discussed further below. Figure 6.12 shows the pressure-temperature positions of the runs, for reference.

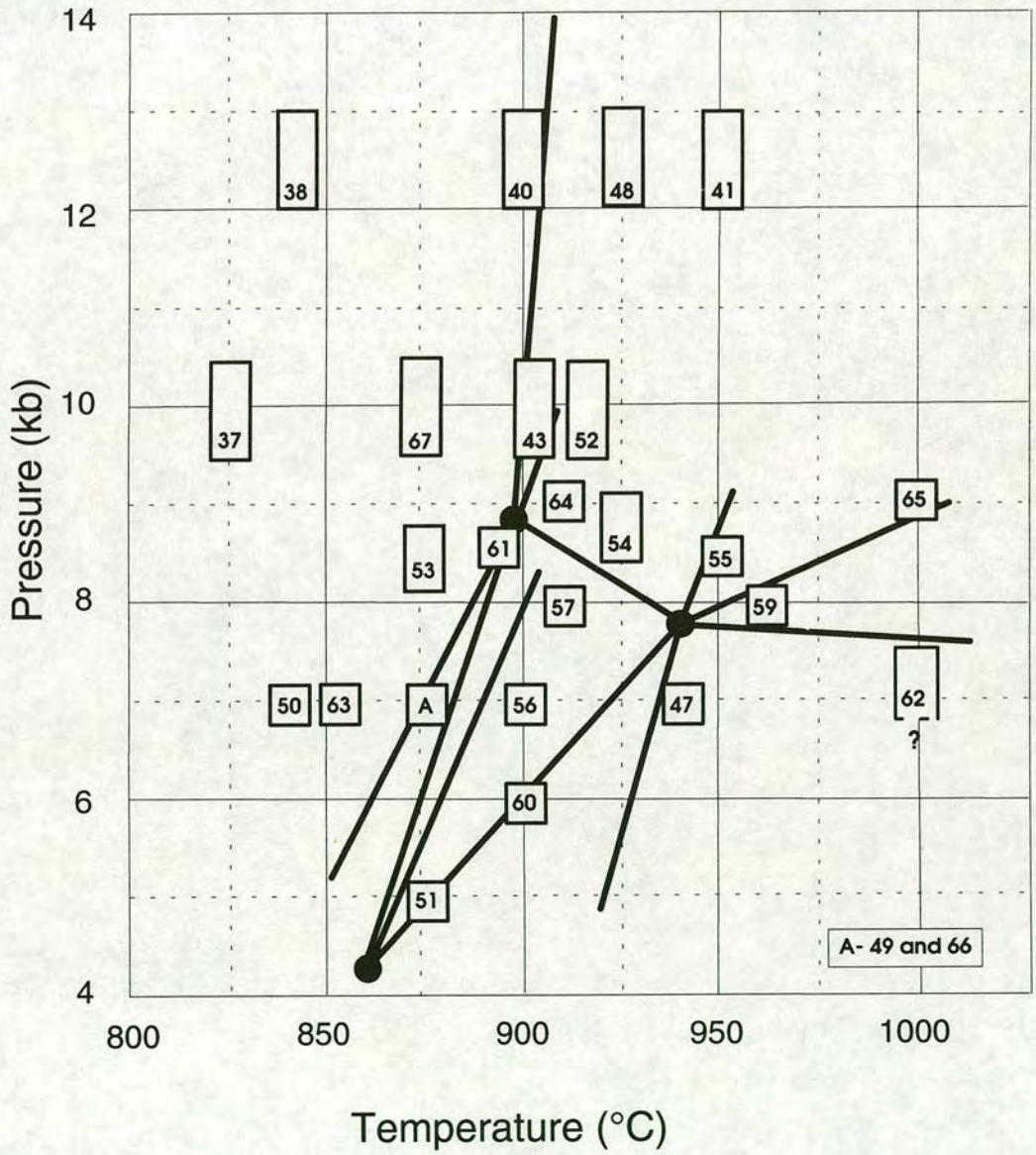

Figure 6.12. Pressure-temperature plot showing the positions of the runs. The run numbers are in the rectangles. The size of the rectangles represents the uncertainty in the pressure-temperature positions (see Chapter Two). Note: D64-17A was removed after the first step of the reversal run, an equivalent pressure-temperature condition to D57. This diagram is reproduced as INSERT B.

The [os] point is tightly positioned at the intersection of four well constrained reactions; the (os, crd) reaction (constrained by runs D40, D48, D43 and D67), the (os, opx) reaction (D49, D66, D61, D63, D56), the (os, bt) reaction (D64, D54, D57), and the (os, sil) reaction (D51, D49, D66, D56, D61, D57). Satisfying all the constraints on the reactions allows only a very small range of pressure-temperature positions for the invariant point. As runs D40 and D61 lie at lower temperatures than the (os, crd) reaction, but D43 lies above it, the [os] point must lie very close to 900°C. The [os] point cannot lie at lower pressure than D61 and can be no higher than the (os, bt) reaction allows. The maximum pressure for the [os] point will be when the (os, bt) reaction has its maximum negative gradient. The gradient is constrained by runs D64 and D57 and allows a maximum pressure of the [os] point of approximately 9.5kb. So, the experiments constrain the [os] point to lie in the range 890-910°C, 8.7-9.5kb. The position of the [bt] point is constrained in an analogous way to 930-945°C, 7.0-8.1kb.

The only reactions in the grid which are not well constrained by the experiments and the positions of the invariant points are the (os, grt), (bt, grt) and the (bt, kfs) reactions. Fortunately, the Schreinemakers' requirement for the metastable extension of a reaction to lie between two reactions which produce the absent phase allows close constraints to be placed on the first two reactions: the metastable extension of the (os, grt) reaction through the invariant point must lie between the (os, opx) and (os, sil) reactions and the metastable extension of the (bt, grt) reaction through the invariant point must lie between the (bt, opx) and (bt, sil) reactions.

The (bt, kfs) reaction is drawn in its maximum pressure position. Its low pressure limit is provided by run D62, the talc-pyrex run, but because the pressure correction is not known for this cell, the true pressure of this experiment could have been much lower (see sections 2.3.1 and 7.4) and the reaction could have a much steeper negative gradient. The position of the [sil] point is implied by the gradients of reactions (os, sil), (grt, sil) and (bt, sil), as shown, but has no direct experimental low-temperature or low-pressure constraint. The [opx] point was potentially stable in figure 6.5, where the gradients were qualitative. In figure 6.11, where the gradients are experimentally constrained, the (bt, opx) and (os, opx) reactions diverge, implying that the [opx] point is metastable. However, the divergence is slight and the reactions could be moved so as to converge without contradicting any of the experimental data. Therefore, the current data give no information on the stability of the [opx] point.

Different interpretation of the minority of experiments in which the product assemblage was not thought to be the equilibrium assemblage could alter the positioning of the grid, though by no more than a 10 or 20°C or a few hundred bars. These possibilities are discussed in detail in section 6.3.5, also with reference to the pseudosections derived below.

6.3.4 Derivation of pseudosections for each bulk composition.

A pseudosection (Hensen 1971) is drawn for a given bulk composition and will show the univariant and divariant reactions which can modify the phase assemblages available to that composition. The pseudosections are constructed here on the principle of parsimony, i.e. the simplest grid which accounts for all the data is drawn.

Firstly all the divariant reactions were evaluated[12]. Each univariant reaction has seven possible divariant fields associated with it, and therefore seven divariant reactions, but it is rare to require more than two or three to account for the data. Using the pressure-temperature position of the univariant grid (figure 6.11, INSERT A) as a template, the associated divariant assemblages required to account for the experimental assemblages are drawn in, attempting to achieve maximum consistency. The resulting diagrams are presented in figures 6.13 (M62 mixes), 6.14 (M74 mixes) and 6.15 (M86 mixes). An example of the method of construction is given in figure 6.16.

The pseudosections for M62 and M74 bulk compositions (figures 6.13 and 6.14) are broadly similar in topology. In going from the more magnesian (M74) to the less magnesian (M62) bulk compositions the important divariant assemblage bt-grt-sil-kfs-qz-L (os, crd, opx) expands down temperature. This divariant assemblage represents the reaction by which many natural metapelites melt. Natural metapelites most commonly have a relatively low value of X_{Mg} (about 0.45) and have wide divariant melting intervals (Vielzeuf and Holloway 1988, Patino Douce and Johnston 1991, Le Breton and Thompson 1988). This reflects the bt-grt-sil-kfs-qz-L divariant

[12] These were not calculated. A divariant reaction involving Fe-Mg exchange can be considered as two reactions - an end-member system (Fe- or Mg-absent) univariant reaction coupled with an Fe-Mg exchange reaction. The end-member univariant reactions involve one fewer component and therefore one fewer phase and are thus easier to represent on three-component projections than KFMASH univariant reactions. There are a large number of possible divariant reactions and as determining the reactions graphically is quicker in this case, this method was used. Just as with univariant reactions around invariant points, the divariant reactions must occur in a specific order around the univariant reaction.

Figure 6.13. Pressure-temperature pseudosection drawn for M62 mixes (i.e. those with bulk X_{Mg}=0.62), as described in the text. The heavy lines are univariant reactions, the divariant fields are shaded white and are separated from the grey-shaded trivariant fields by lighter lines. The divariant assemblages are labelled and all assemblages also have quartz. The position of the experiments is also shown and the different symbols refer to the different interpretations of the product assemblages made in Chapter Four (tables 4.1 and 4.2). The "product assemblage" and "univariant assemblage" markers refer to experiments where the phases produced in the experiment were believed to be the equilibrium assemblage, effectively where no interpretation was made. The implications of alternative interpretations of the other experiments are considered fully in the text. The P-T positions where no M62-mix experiments were run, but other mixes were, are marked by small white squares. The experiment at 7.5kb, 1000°C is D62-16A and was run in a talc-pyrex cell, for which the friction correction is only constrained to be >20%. Therefore, the pressure of the experiment is only constrained to be <8kb. This diagram is reproduced as INSERT C.

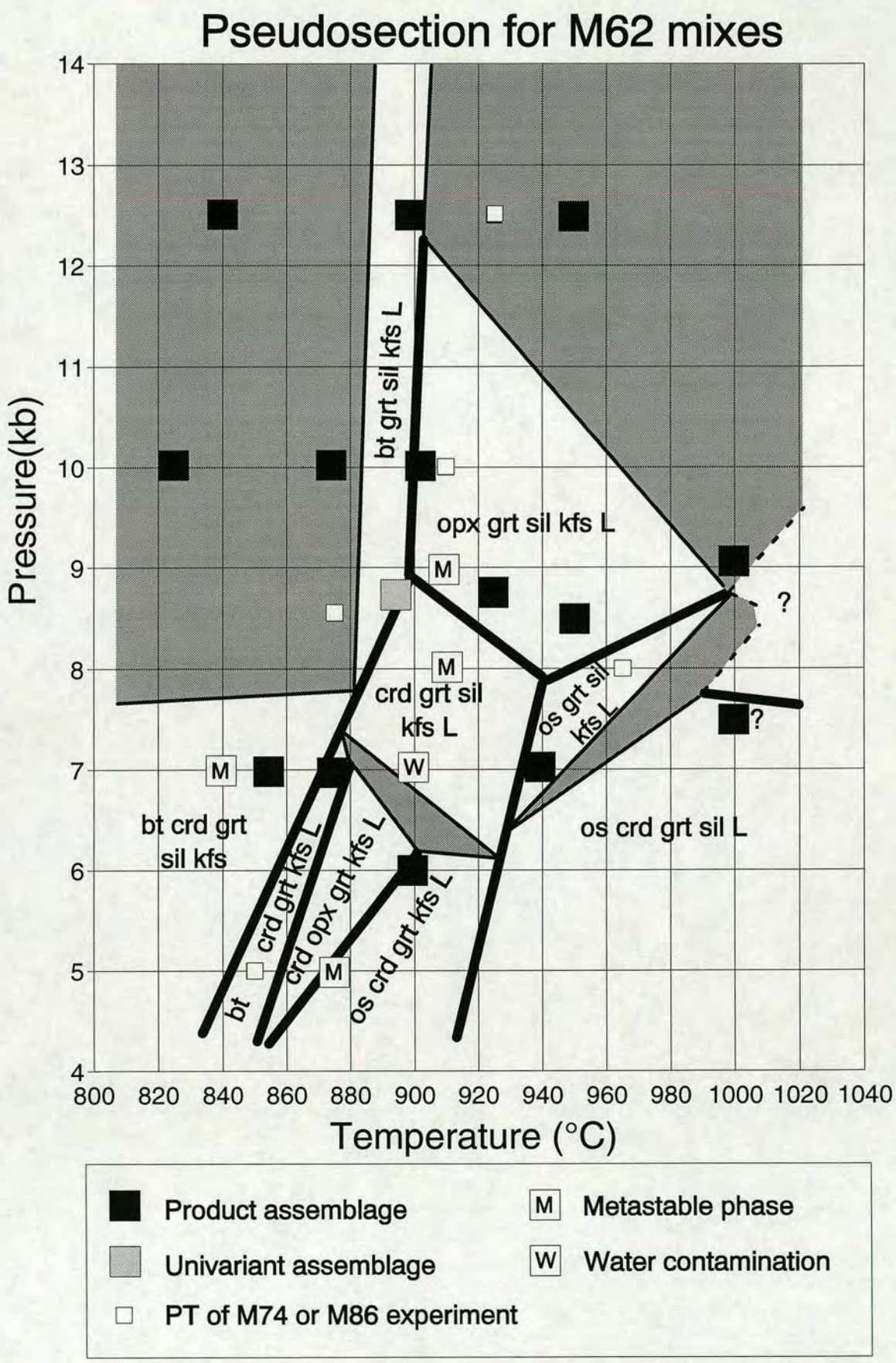
Pseudosection for M62 mixes
Pressure(kb)
Temperature (°C)
14
13
12
11
10
9
8
7
6
5
4
800
820
840
860
880
900
920
940
960
980
1000
1020
1040
bt grt sil kfs L
opx grt sil kfs L
crd grt sil kfs L
os grt sil kfs L
os crd grt sil L
bt crd grt sil kfs
crd grt kfs L
crd opx grt kfs L
os crd grt kfs L
bt
M
W
?
Product assemblage
Univariant assemblage
PT of M74 or M86 experiment
Metastable phase
Water contamination

Figure 6.14. Pressure-temperature pseudosection drawn for M74 mixes (i.e. those with bulk X_{Mg}=0.74), as described in the text. The heavy lines are univariant reactions, the divariant fields are shaded white and are separated from the grey-shaded trivariant fields by lighter lines. The divariant assemblages are labelled and all assemblages also have quartz. The position of the experiments is also shown and the different symbols refer to the different interpretations of the product assemblages made in Chapter Four (tables 4.1 and 4.2). The "product assemblage" and "univariant assemblage" markers refer to experiments where the phases produced in the experiment were believed to be the equilibrium assemblage, effectively where no interpretation was made. The implications of alternative interpretations of the other experiments is considered fully in the text. The P-T positions where no M74-mix experiments were run but other mixes were are marked by small white squares.
"Two experiments" - D49-17 and D66-17A were both run at 875°C, 7kb. In D49-17 the presence of melt was interpreted whilst not positively identified. D66-17A was interpreted as being water-contaminated. This diagram is reproduced as INSERT D.

Pseudosection for M74 mixes

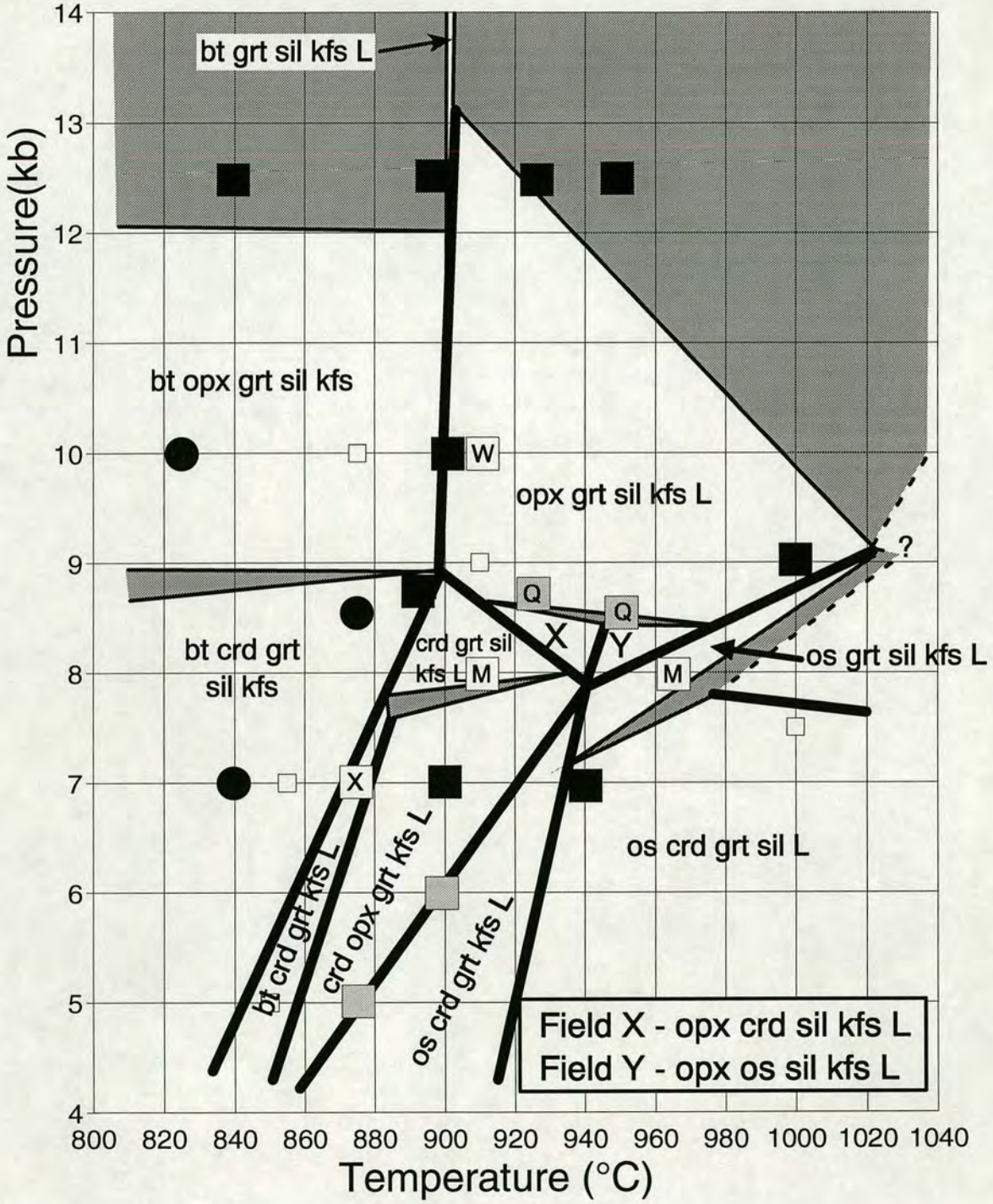

■	Product assemblage	●	Phase Not Produced
▒	Univariant assemblage	M	Metastable phase
Q	Quasi-univariant assemblage	W	Water contamination
□	PT of M62 or M86 experiment	X	Two exps., see caption.

Figure 6.15. Pressure-temperature pseudosection drawn for M86 mixes (i.e. those with bulk X_{Mg}=0.86), as described in the text. The heavy lines are univariant reactions, the divariant fields are shaded white and are separated from the grey-shaded trivariant fields by lighter lines. The divariant assemblages are labelled and all assemblages also have quartz. The position of the experiments is also shown and the different symbols refer to the different interpretations of the product assemblages made in Chapter Four (tables 4.1 and 4.2). The "product assemblage" and "univariant assemblage" markers refer to experiments where the phases produced in the experiment were believed to be the equilibrium assemblage, effectively where no interpretation was made. The implications of alternative interpretations of the other experiments is considered fully in the text. The P-T positions where no M86-mix experiments were run but other mixes were are marked by small white squares.
The experiment at 7.5kb, 1000°C is D62-16A and was run in a talc-pyrex cell, for which the friction correction is only constrained to be >20%. Therefore, the pressure of the experiment is only constrained to be <8kb.
"Two experiments" - D49-18 and D66-18A were both run at 875°C, 7kb. In D49-18 the presence of melt was interpreted whilst not positively identified. D66-17A was interpreted as having produced the equilibrium assemblage.
This diagram is reproduced as INSERT E.

Pseudosection for M86 mixes

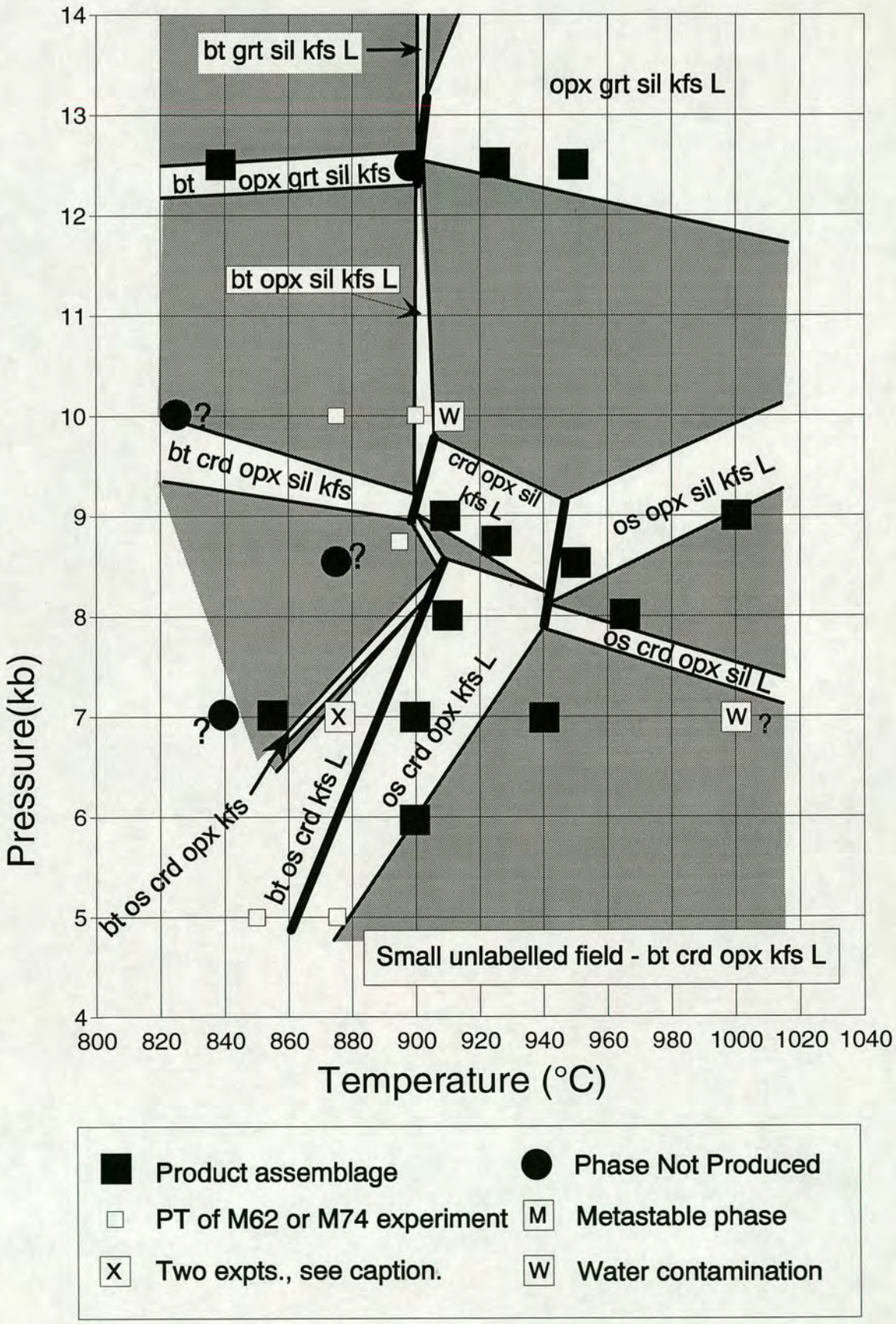

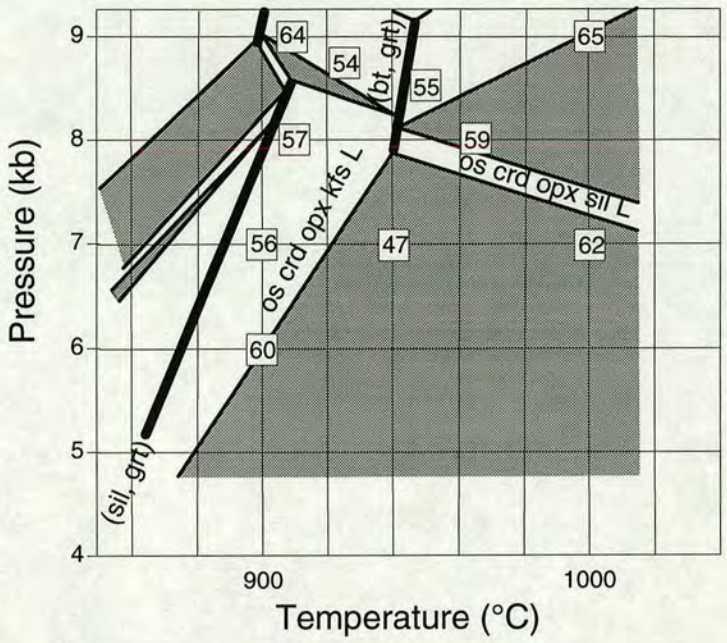

Figure 6.16. Detail of the pseudosection for M86 mixes (figure 6.15) to illustrate an example of the method of construction. The numbered boxes are experiments, with their run numbers. The assemblage osumilite-cordierite-orthopyroxene-K-feldspar-quartz-melt is produced by experiments D57-18, D56-18 and D60-18A[13]. This requires an os-crd-opx-kfs-qz-L stability field and this can occur between the (sil, grt) and (bt, grt) reactions. D47-18 and D62-18A contained the same assemblage, but without K-feldspar. The stability of the os-crd-opx-sil-qz-L field on the high-temperature side of the (bt, grt) reaction means the trivariant field in which D47-18 and D62-18A then lie is appropriately K-feldspar-absent.

field expanding even further down temperature as the bulk composition becomes more iron-rich. Furthermore, common natural metapelites show little variation in phase assemblage which results from the fact that most of the KFMASH univariant reactions will only be seen by relatively magnesian bulk compositions. This is discussed further in the section 7.2. Figure 7.4 is a predicted pseudosection for a bulk composition of $X_{Mg} = 0.45$. It is composed mostly of trivariant pressure-temperature space, in contrast to those for more magnesian compositions derived here, which are predominantly divariant space.

The pseudosection for M86 bulk compositions (figure 6.15) is very different from the other two. This is because garnet is not stable in such magnesian bulk compositions below around 12kb at these temperatures. All three pseudosections have distinctive

[13] This experiment lies on the boundary between K-feldspar-present and K-feldspar-absent assemblages (see below).

divariant assemblages with restricted pressure-temperature ranges which are largely absent from more iron-rich bulk compositions. These assemblages have an obvious use as sensitive geothermometers and geobarometers and this is demonstrated in Chapter Eight.

6.3.5 Implications of alternative interpretations of experimental results.

The pseudosections presented are believed to be the closest representation of the equilibrium situation which can be derived from the experiments, i.e. the "best-fit" pseudosections. The interpretations made for the minority of experiments in which the product assemblage was not thought to be the equilibrium assemblage (see Chapter Four) were such that the pseudosections presented are entirely consistent with the experimental data. Chapter Four justifies these interpretations on the basis of chemographic evidence and is thought to be sufficient support for the interpretations. Nonetheless, further confidence in the chosen phase relations can be obtained by considering the implications which alternative interpretations, even if unlikely, would have and showing that these alternatives result in inconsistencies. This is done, in full, below.

Supersolidus experiments.

D49-17, D49-18, D66-17A and D66-18A.

The interpretation of these experiments affects the low-pressure position of the solidus in the M74 and M86 pseudosections, though by no more than 20°C (figure 6.17). Melt was identified in D66-17A and D66-18A as well as D49-16 but not in D49-17 or D49-18. If the latter experiments are genuinely melt-absent then the solidus must lie above those reactions. It may be that the small differences in fO_2 expected between the gas-bombs (D49) and the solid-media apparatus (D66) can alter the position of the solidus slightly (see section 2.3.4). However, the solidus in the M74 mixes at 7kb is the univariant (os, opx) reaction and as D49-16 contains melt it must lie on the high-temperature side of it. Univariant reactions apply to all bulk compositions in a system and so D49-17 and D49-18 must also lie above the solidus.

The absence of K-feldspar and biotite in D66-17A was interpreted to be the result of water contamination which promoted extra melting. If this is not the case then the K-

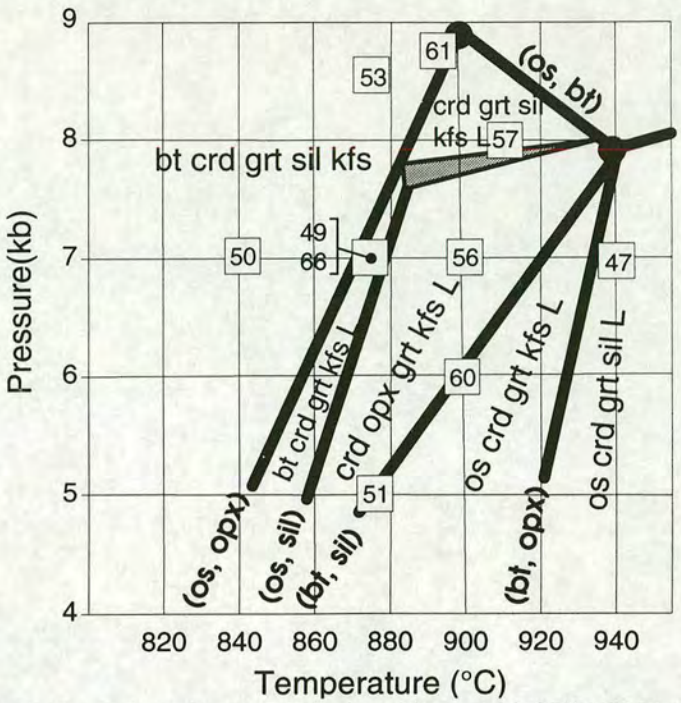

Figure 6.17. Detail of pseudosection for M74 mixes (figure 6.14, INSERT D) to illustrate the alternative interpretations of experiments D49-17, D49-18, D66-17A and D66-18A, and D57-16, D57-17 and D64-17A, as described in the text. The numbered boxes are experiments, with their run numbers. Note: D64 was a reversal run and the capsule containing mix 17A was removed after the first step, i.e. pressure-temperature conditions equivalent to run D57.

feldspar in the higher-temperature experiments D51-17, D56-17, D57-17 and D60-17A must all be metastable, which is thought to be very unlikely. Therefore the absence of biotite is also attributed to water contamination.

A trace of orthopyroxene was seen in D66-18A and was interpreted as being metastable. If it were not metastable, then either the melt or the biotite must be metastable for the experiment to remain consistent with the possible topology of divariant fields, but the chemographic relations (figure 4.4) show that this is unlikely. Furthermore, the excess alumina contents of the orthopyroxenes provides a reason for the metastability of the orthopyroxene.

D56-16, D52-17 and D52-18.

Experiment D56-16 was very clearly contaminated by water because if quartz and K-feldspar were genuinely not stable in the original bulk composition at this pressure and temperature then the quartz in all experiments run at the same or higher temperatures (e.g. D47-16, D57-16, D60-16A, D62-16) is metastable. Similarly, the

lack of K-feldspar in experiments D52-17 and D52-18 was also attributed to water contamination on the grounds that if not, the ten experiments run at higher temperatures would have to contain metastable K-feldspar.

D57-16, D57-17 and D64-17A.

All these experiments contained small amounts of orthopyroxene which was interpreted as being metastable. If it were stable then there are two possibilities (figure 6.17):
a) the sillimanite in these experiments is metastable, extending the crd-grt-opx-kfs-qz-L (os, sil, bt) field to higher pressures and eliminating the crd-grt-sil-kfs-qz-L (os, opx, bt) stability field. However, the latter assemblage has been reported as having a large stability field in other experimental studies, 900 to 1000°C and 8 to 11 kb (Hensen and Green 1971, Bertrand et al. 1991).
b) the cordierite in these experiments is metastable, indicating that the (os, bt) reaction lies at lower pressure than these experiments, i.e. less than 8kb. This requires the [os] point to be at a similarly low pressure. However, D61-16A and D61-17A (run at 8.75kb) lie below, or very close to, the [os] invariant point and would thus be inconsistent with this new interpretation. Reactions determined in other studies, analogous to the (os, bt) reaction here, occur between 10 and 12 kb (Hensen and Green 1971, Bertrand et al. 1991), see section 7.3.

D59-17.

If the orthopyroxene in D59-17 is interpreted as stable, the sillimanite must be metastable and a new divariant field is required for the assemblage; os-opx-grt-kfs-qz-L (bt, sil, crd). The new field is illustrated in figure 6.18. The chemographic relations in Chapter Four show that the orthopyroxene is most likely to be metastable.

D64-16A.

The cordierite present in the reversal experiment D64-16A is adequately explained as a metastable remnant of the cordierite which was stable during the first step of the run. If it were stable then the (bt, os) reaction must lie at higher pressures than the experiment and the sillimanite it contained would be metastable. This would contradict D64-18A which contained the assemblage opx-sil-L, characteristic of the

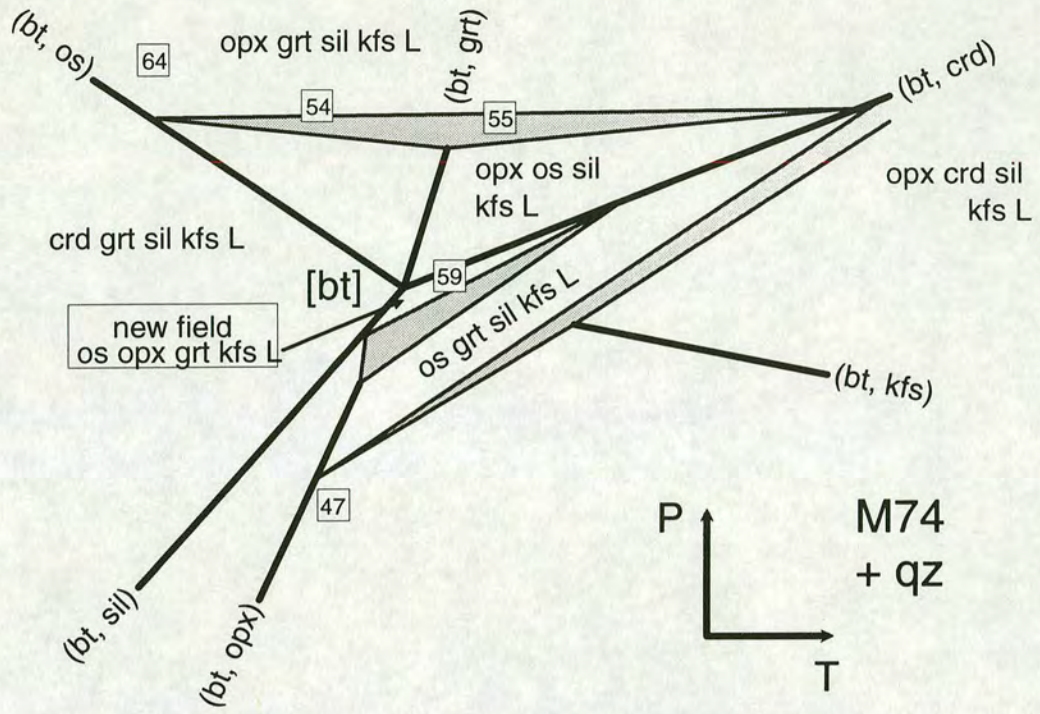

Figure 6.18. An alternative topology (schematic) for the [bt] point on the M74 pseudosection (compare with figure 6.14, INSERT D). The numbered boxes are experiments, with their run numbers. If the orthopyroxene in D59-17 is stable then the sillimanite must be metastable and a new os-opx-grt-kfs-qz-L field is required to account for the assemblage.

high-pressure side of the reaction. Also, D54-16 and D55-16 both lie above the (bt, os) reaction and so, if D64 were below it, the reaction would require an unreasonably steep, negative dP/dT slope. The position of the reactions and experiments are given in figure 6.18.

Subsolidus experiments.

The subsolidus reactions are more poorly equilibrated than the supersolidus reactions and the discrepancies are most commonly attributed to lack of reaction.

D50-17, D53-17.

Cordierite was interpreted to be stable though it did not form. If this is not the case then the higher-pressure boundary of the bt-crd-grt-sil-kfs-qz (os, opx, L) divariant field in the M74 pseudosection (figure 6.14, INSERT D) will have a steeper dP/dT.

D50-16.

Orthopyroxene interpreted as metastable formed in D50-16. The (os, opx) reaction forms the solidus at low pressures and only has one associated melt-absent field, and this does not involve orthopyroxene. It is not obvious how the assemblage from D50-16 would be accommodated if the orthopyroxene were stable but it would probably involve the (sil, L) reaction.

D37-15[14], D50-18 and D53-18.

The trivariant assemblage, bt-crd-opx-kfs-qz, was produced by the long-duration, reversal experiment, D63-18A. The assemblage was interpreted as being the

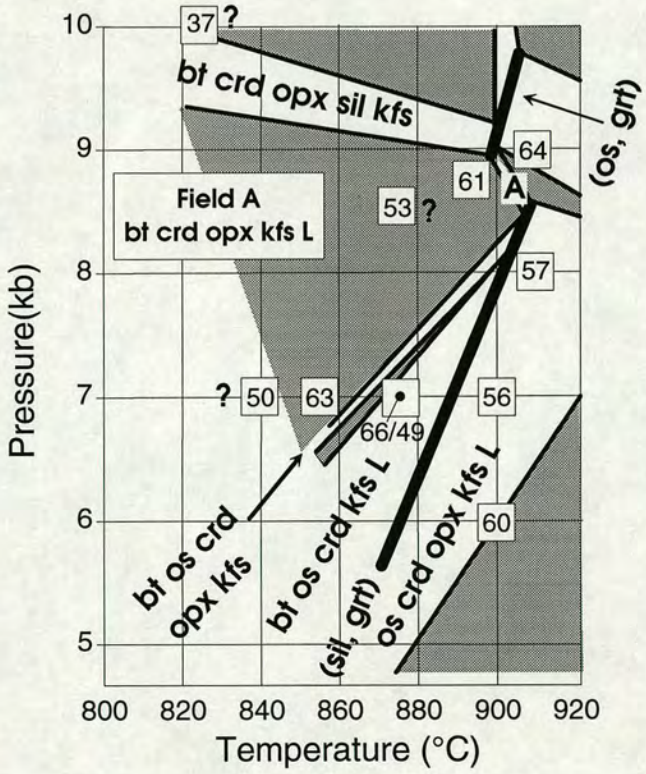

Figure 6.19. Detail of pseudosection for M86 mixes (figure 6.15, INSERT E) to illustrate the poor experimental constraints in the subsolidus region, as discussed in the text. The numbered boxes are experiments, with their run numbers.

[14] c.f. table 2.7. Mixes 13, 14 and 15 have the same bulk compositions as 16, 17 and 18 (XMg = 0.62, 0.75, 0.86, respectively) but contain mineral-sillimanite, not gel-sillimanite.

equilibrium assemblage and this requires the stability of two divariant fields for which there is no direct evidence, in order to create a suitable trivariant field between them (figure 6.19). The two divariant fields required are bt-os-crd-opx-kfs-qz (grt, sil, L) and bt-crd-opx-sil-kfs-qz (grt, os, L). The former must lie at lower pressures than D63-18A and the latter at higher pressures.

The interpretation of experiments D37-15, D50-18 and D53-18 depend on where the bt-crd-opx-sil-kfs-qz (grt, os, L) field is placed. Only D50-18 has changed its phase assemblage from the starting assemblage, forming cordierite, and so the (grt, os, L) field is only constrained to have its high pressure limit above D50-18. As the other experiments are unreacted, any interpretation of those experiments is rather meaningless. They cannot be used to constrain the phase relations. Therefore, the

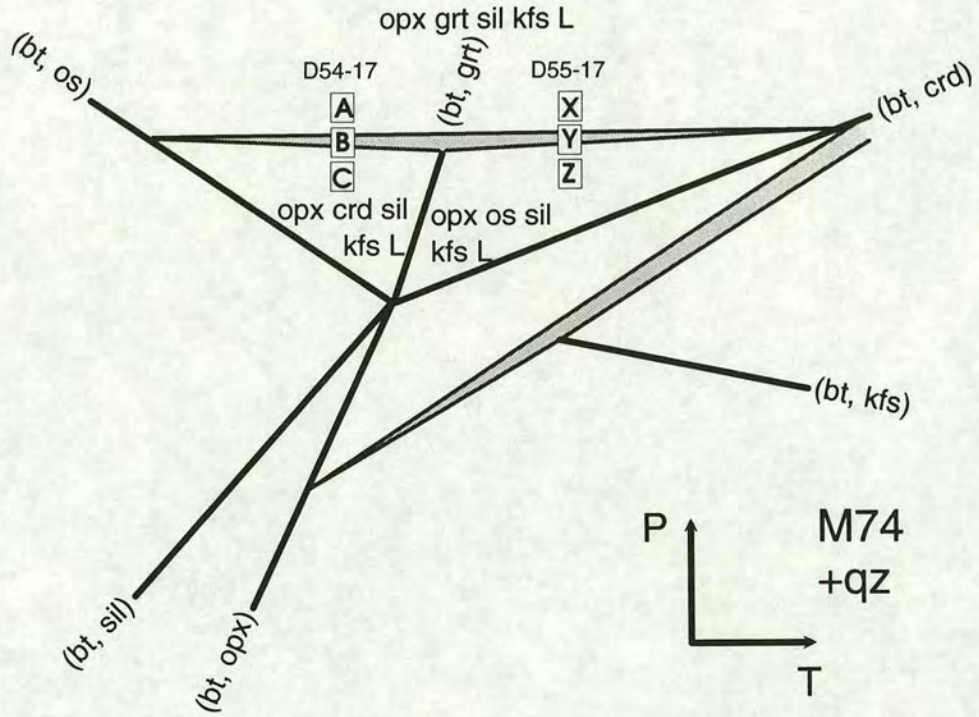

Figure 6.20. Detail (schematic) of the [bt] point from the M74 pseudosection (figure 6.14) showing how different interpretations of D54-17 and D55-17 give different positions of the divariant and trivariant fields associated with the high-pressure termination of the (bt, grt) reaction.

D54-17. Position A requires cordierite to be metastable.
Position C requires garnet to be metastable.

D55-17 Position X requires osumilite to be metastable.
Position Z requires garnet to be metastable.

Positions B and Y are the positions required for the trivariant assemblage, opx-sil-kfs-L, which require the metastability of cordierite and garnet (D54-17) and osumilite and garnet (D55-17). This is the preferred position of the experiments in this study and these experiments are interpreted as quasi-univariant, i.e. straddling a narrow trivariant field.

subsolidus topology of the M86 pseudosection is quite poorly constrained.

Univariant or quasi-univariant experiments.

Alternative interpretations of this group of experiments can only result in small changes in the pressure-temperature position of the reactions involved, as the experiments necessarily lie close to those reactions.

D54-17 and D55-17.

The interpretation of these quasi-univariant assemblage experiments[15] determines the position of the slim trivariant field which terminates the (bt, grt) reaction at high pressures (figure 6.20). The trivariant field separates the low- and high-pressure assemblages and garnet, cordierite and osumilite are all absent. In D54-17, choosing garnet or cordierite as metastable determines the whether the trivariant field should lie above or below the experiment respectively. D55-17 is entirely analogous but with osumilite replacing cordierite.

D61-16A.

This experiment contained eight of the nine phases in the system and if all of these were stable it would represent the invariant point [os]. The probability of achieving this by chance is exceedingly small and some of the phases are probably metastable,

but it is believed that D61-16A must be very close to the invariant point for this to have occurred. D61-17A gave a divariant assemblage bt-crd-grt-sil-kfs-qz (os, opx, L), stable at lower pressure and temperature than the [os] point. The divariant assemblage on the M62 pseudosection which would form at the same pressure and temperature is bt-grt-sil-kfs-L (os, crd, opx), suggesting that cordierite and orthopyroxene are the phases most likely to be metastable in D61-16A. Because the other possible fields are all nearby in pressure-temperature space, any choice of assemblage will not cause a significant change in the position of the [os] point (figure 6.21).

---

[15] Section 4.1 described these experiments and explained how straddling a narrow trivariant field between two divariant fields could produce an apparently univariant assemblage. As these reactions were not close to any univariant reactions, they could not be *genuinely* univariant and were termed quasi-univariant.

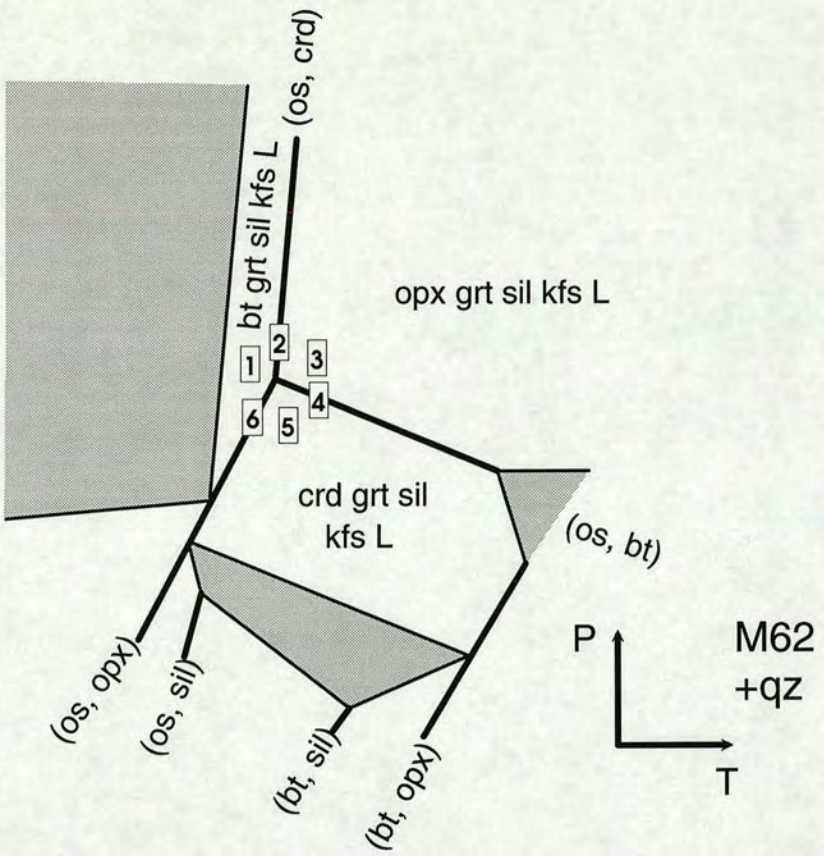

Figure 6.21. Detail (schematic) of the [os] invariant point from the M62 pseudosection showing the implications of alternative interpretations of D61-16A. Experiment D61-16A contained biotite, garnet, orthopyroxene, cordierite, sillimanite, K-feldspar, quartz and melt.
1 - divariant assemblage, requires metastability of orthopyroxene and cordierite,
2 - univariant assemblage, requires metastability of cordierite,
3 - divariant assemblage, requires metastability of cordierite and biotite,
4 - univariant assemblage, requires metastability of biotite,
5 - divariant assemblage, requires metastability of orthopyroxene and biotite,
6 - univariant assemblage, requires metastability of orthopyroxene.
D61-17A produced an assemblage analogous to position 1 and this is the interpreted position of D61-16A.

D51-17 and D60-17A.

These are the last experiments for which the product assemblages are not considered to be the equilibrium assemblages, but are the first for which a simple and plausible explanation cannot be found for the contradictions they present.

D51-17 and D60-17A appear to be truly univariant (figure 4.2) and lie on the (bt, sil) reaction (figure 6.22). D60-16A contained the grt-os-L assemblage, showing it must lie on the high-temperature side of (bt, sil) as did D51-16, although that experiment

also contained metastable spinel. In contrast, D60-18A produced the crd-opx-kfs-qz assemblage characteristic of the low-temperature side of the (bt, sil) reaction, although K-feldspar was rare. The reaction stoichiometry is too robust to be affected by feasible changes in phase compositions.

The (bt, sil) reaction is not stable on the M86 pseudosection (figure 6.15), because garnet does not form, but the low-temperature assemblage of that reaction, crd-opx-kfs-qz, is stable. To prevent the stability of this assemblage above the temperature of

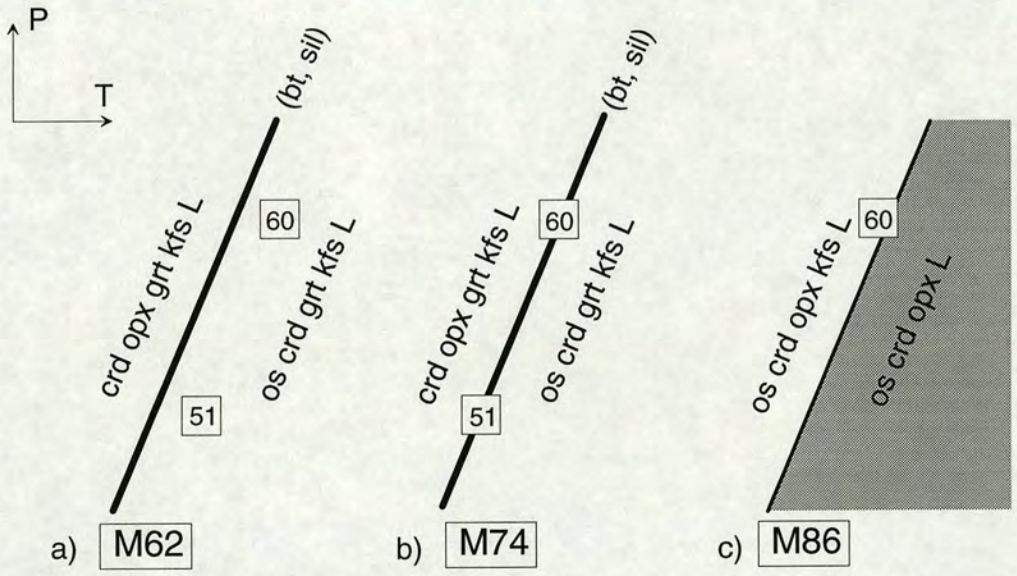

(bt, sil) crd + opx + kfs + qz = grt + os + L

Figure 6.22. Schematic pressure-temperature diagrams showing the results of runs D51 and D60 and the univariant reaction (bt, sil).
a) Experiments D60-16A and D51-16 (X_{Mg} = 0.62). These experiments produced divariant assemblages including the phases grt-os-L which occurs on the high-temperature side of the (bt, sil) reaction.
b) Experiments D60-17A and D51-17 (X_{Mg} = 0.74). These experiments produced univariant assemblages which are stable on the (bt, sil) reaction.
c) Experiment D60-18A (X_{Mg} = 0.86). This experiment produced a divariant assemblage, but with only a trace of K-feldspar. This is consistent with the trace of the (bt, sil) reaction which, though not stable in these compositions, is manifested by a transition from a divariant to a trivariant field, with the loss of K-feldspar.

the (bt, sil) reaction[16], K-feldspar is lost on the high-temperature boundary of the divariant os-crd-opx-kfs-L (grt, sil, bt) field. This divariant/trivariant boundary has the same pressure-temperature position as the (bt, sil) reaction. Therefore, if the assemblage produced by D60-18A is to be consistent with the univariant assemblage produced by D60-17A, it must lie on this boundary and therefore contain its last K-feldspar. The rare K-feldspar present in D60-18A suggests that this interpretation is correct. However, why D60-16A and D51-16 did not produce the orthopyroxene required for the (bt, sil) univariant assemblage is not known.

6.5 CONCLUSIONS.

In this chapter the experimental results of the current study, Schreinemakers' rules and previously published data were used to derive a tightly constrained and self-consistent grid of KFMASH univariant reactions. i.e. a petrogenetic grid. The grid covers the pressure-temperature range 5-12.5kb, 840-1000°C and includes the invariant points [os] (890-910°C, 8.7-9.5kb) and [bt] (930-945°C, 7.0-8.1kb). These invariant points are fundamental in dividing pressure-temperature space for high-grade metapelites. Comparison of the grid with previous work and consideration of the implications for geological problems are considered in Chapter Seven, with particular reference to;

- mechanisms of biotite dehydration melting,
- the relative stability of orthopyroxene-sillimanite-quartz and garnet-cordierite,
- the phase relations of osumilite.

Phase composition data, in combination with the phase relations derived, enabled the role of K-feldspar in biotite dehydration melting to be related to the H_2O/K_2O ratio of the melt. Low values of this ratio, compared to that for biotite, require K-feldspar as a reactant and vice versa. This is a generally applicable solution to the conflicting evidence previously reported.

---

[16] A univariant reaction which is not "seen by" a given bulk composition *must* still manifest on a pseudosection if a divariant assemblage bounded by that univariant reaction occurs, because the univariant reactions apply to all bulk compositions. If the assemblage crosses the pressure-temperature position of the univariant reaction, a phase will be lost by the transition from a divariant to trivariant assemblage, thereby preventing the occurrence of an assemblage outside its stability field.

Pressure-temperature pseudosections, which show the univariant and divariant reactions which will act on a particular composition, were derived for each of the three experimental bulk compositions. The fact that large areas of the pseudosections are occupied by divariant assemblages reflects the fact that for the relatively magnesian bulk compositions used here, many univariant reactions are operative. This means that there are many distinctive assemblages with restricted pressure-temperature ranges and that magnesian pelites are potentially very sensitive geothermometers and geobarometers. This contrasts markedly with more iron-rich bulk compositions which exhibit very few changes in phase assemblage over wide pressure-temperature ranges. The application of the pseudosections and the grid to natural rocks is given in Chapter Eight.

Chapter Seven

GEOLOGICAL IMPLICATIONS OF GRIDS AND PSEUDOSECTIONS

Chapter Seven. Geological implications of grids and pseudosections.

7.1 INTRODUCTION AND SYNOPSIS OF CHAPTER.

The phase diagrams derived in the last chapter are useful as descriptions of the stable phase relations in the KFMASH-system in that region of pressure-temperature space and in aiding the interpretation of metamorphic histories of rocks. This will be illustrated in the next chapter. The phase diagrams also have implications for specific assemblages or reactions which geologists have found to be of interest.

Biotite dehydration melting reactions are widely cited as being important in the formation of granulites. However, previous work has concentrated on the production of granitoid magmas via these reactions and has only positioned reactions specific to the particular bulk compositions used in those studies. The current experiments have positioned a set of univariant reactions applicable to all quartz-saturated KFMASH-system compositions and not dependent on a_{H2O}. These provide excellent fixed starting points in investigations of biotite dehydration melting. The current and published data can be explained by a model in which the temperature range over which biotite breaks down to produce melt is controlled by the bulk X_{Mg} and the pressure, and the temperature position of this melting interval is controlled by the concentration of titanium (and probably fluorine) in biotite. The current experiments also offer some insight into the controls on the incremental melt production, i.e. the amount of melt produced for a given increase in temperature: the narrower the melting interval, the greater the incremental melt production. Intersection of a rock's prograde path with a univariant reaction allows for the production of large amounts of melt in a small temperature interval.

The assemblage orthopyroxene-sillimanite-quartz is generally accepted as a breakdown product of cordierite at high pressures of metamorphism. Until now, the representation and interpretation of this reaction has not been systematic or rigorous. In a water-undersaturated KFMASH system the reaction is of the form;

garnet + cordierite + quartz + K-feldspar =
orthopyroxene + sillimanite + melt.

The reaction has a negative dP/dT and runs from 8.8kb at 900°C to 7.8kb at 1000°C. Calcium can significantly stabilise garnet and so move the reaction to higher pressures. An increasing level of vapour-saturation, particularly the incorporation of CO_2, stabilises the cordierite to higher pressures, again moving the reaction up pressure.

The phase relations of osumilite derived from the experiments give important new data on osumilite-bearing assemblages. They also help clarify previous theoretical work and provide powerful comparisons with new, partly overlapping data from other laboratories (Audibert et al. 1994). Whilst the phase relations and temperature estimates of an important invariant point, common to both the studies, are very similar, there is a 2-4kb discrepancy in the pressure estimates. A comparison of the talc-pyrex cell used by Audibert et al. (1994) and the gas-bomb apparatus, carried out in this study, shows that Audibert et al. (1994) seriously underestimated the friction correction necessary for their cell and therefore introduced a systematic error in pressure to their results. Having corrected for this error, the phase relations from both studies are combined to provide an experimentally constrained, KFMASH-system, univariant grid covering the pressure-temperature range 850-1100°C, 5-12.5kb. The application of the phase diagrams to natural osumilite occurrences is presented in Chapter Eight.

7.2 BIOTITE DEHYDRATION MELTING IN PELITES.

The grid of univariant KFMASH reactions derived from the experiments in this study (INSERT A) has positioned the biotite dehydration melting reactions in pressure-temperature space and these positions have been confirmed by reversal experiments (section 5.2). The reactions and their positions apply to all KFMASH-system compositions and are not dependent on the a_{H2O}[1]. Therefore, the reactions provide an excellent fixed starting point for the interpretation of biotite dehydration melting in natural rocks and the factors which may affect it, such as the effects of fluorine and titanium, which will stabilise the biotite to high temperatures. The pseudosections derived from the experiments (INSERTS C, D, E) show what reactions can occur during melting and how the rock bulk composition affects the melting process.

---

[1] It should be noted that if CO_2 were present, reactions involving cordierite may shift their pressure-temperature positions.

The previous work on the dehydration melting of natural biotite-sillimanite-quartz assemblages (Patino Douce and Johnston 1991, Vielzeuf and Holloway 1988, Le Breton and Thompson 1988) can be considered in terms of the reaction;

biotite + sillimanite + quartz = garnet + (K-feldspar) + melt.

This reaction is divariant in the KFMASH system and is illustrated on the M62 pseudosection (figure 6.13, reaction (os, opx, crd)). Figure 7.1 compares the results of the present study with those previously published. The reaction is available to a

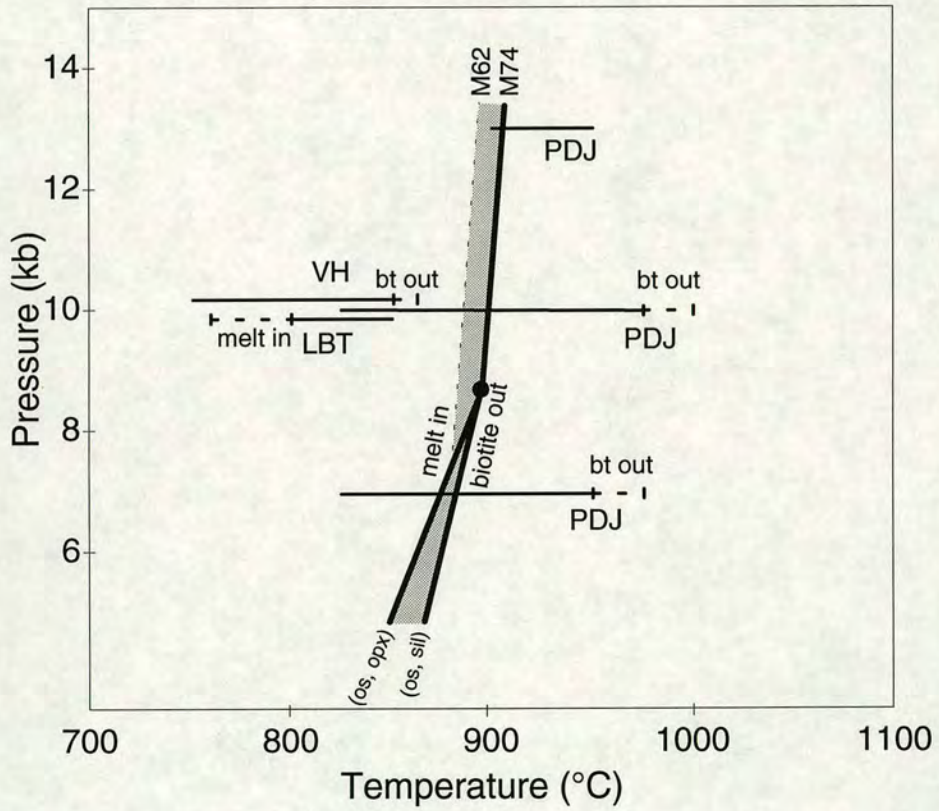

Figure 7.1. Pressure-temperature diagram showing the results of the present study and those of Patino Douce and Johnston (PDJ, 1991), Vielzeuf and Holloway (VH, 1988) and Le Breton and Thompson (LBT, 1988). The continuous horizontal lines indicate the co-existence of biotite and melt. The dashed and barred intervals span the temperature interval between the last biotite-present experiment and the first biotite-absent experiment (bt out) or the temperature interval between the last melt-absent experiment and the first melt-present experiment (melt in). The heavy lines are KFMASH univariant biotite dehydration melting reactions from this study and the shaded areas are regions of divariant biotite melting (INSERTS C and D). At higher pressures the M62 composition melts (divariant reaction) before the M74 compositions (univariant reaction). At lower pressure both compositions melt via the first univariant reaction (os, opx) and, because of the bulk compositions used, lose sillimanite. The final biotite is lost at the second univariant reaction (os, sil). In more aluminous bulk compositions, all the biotite would be lost at the first reaction.

large range of pelitic bulk compositions over a wide pressure range: this study and others (Patino Douce and Johnston 1991, Vielzeuf and Holloway 1988) show the reaction is stable for compositions with bulk X_{Mg}'s of less than 0.62 at pressures greater than 7kb. The previous studies used natural bulk compositions, containing calcium, and the reaction may also involve plagioclase as a reactant. The role of K-feldspar depends on the water/potassium ratio of the melt and, if it is involved, it may be a product or a reactant, as discussed in the last chapter (section 6.3.1, figures 6.7, 6.8 and 6.9).

Two major discrepancies are apparent between the present study and published work (figure 7.1).

1. The temperature at which the last biotite reacts out at 10kb varies widely, from between 850 and 862°C (Vielzeuf and Holloway 1988) to between 975 and 1000°C (Patino Douce and Johnston 1991).

2. The temperature interval over which the biotite co-exists with melt also varies widely at 10kb, from 20°C (this study) to 150°C (Patino Douce and Johnston 1991) .

In the simple model presented below, the biotite-out temperature depends on the concentration of stabilising elements in the biotite, i.e. titanium and fluorine, and the biotite-melting temperature-interval depends on the bulk X_{Mg} of the rock. The temperature interval can also be affected by the pressure at which melting occurs. This model can account for differing levels of incremental melt production.

It is well known qualitatively that fluorine and titanium enhance the temperature stability of biotite (e.g. Guidotti 1984) although the quantitative effect has not been constrained. Table 7.1 shows the titanium- and fluorine-contents of biotites in the studies of Patino Douce and Johnston (1991) and Vielzeuf and Holloway (1988). The significantly higher TiO_2 content of the biotites in the former study correlates with a much higher biotite-out temperature (table 7.1, figure 7.1). In a simple attempt to account for the stabilising effects of titanium and fluorine in biotite, the temperatures in each study have been "normalised" so that the temperature of the experiment containing the last existing biotite is the same as that reported by Vielzeuf and Holloway (1988), i.e. 850°C (figure 7.2). This normalisation of the temperatures is intended to enable comparison of the width of the melting intervals and of different levels of incremental melt production.

	Temperature (°C)	TiO_2	F
VH - starting biotite composition	-	1.78	n.a.
LBT - starting biotite composition	-	3.5	n.a.
LBT - highest temperature biotite	850	4.2	n.a.
PDJ - starting biotite composition	-	2.68	0.31
PDJ - last biotite at 7kb	950	6.30	1.07
PDJ - last biotite at 10kb	975	5.38	1.29

Table 7.1. Biotite titanium- and fluorine-contents (wt%) from the studies of Vielzeuf and Holloway, (VH, 1988), Le Breton and Thompson (LBT, 1988) and Patino Douce and Johnston (PDJ, 1991). The data for the latter study is taken from Patino Douce et al. (1993). VH did not give compositional data for their product biotites. "n.a." - not analysed.

Figure 7.2 shows a consistent correlation between the size of the biotite-melting temperature intervals and the bulk X_{Mg} of the mixes used, at 10kb. The largest melting interval, and the smallest rate of melt production with increasing temperature, exist for the lowest X_{Mg}, 0.36 (PDJ10). The narrowest melting interval is zero, for the M74 (X_{Mg} = 0.74) composition in the present study. The melting interval is zero because the biotite reacts via a univariant reaction (biotite + sillimanite + K-feldspar + quartz = garnet + orthopyroxene + melt, see INSERT D) and is consumed at a single temperature. The experiments of Patino Douce and Johnston (1991) and Vielzeuf and Holloway (1988) produced almost the same proportion of melt on the exhaustion of biotite. This should be expected, assuming that the melt compositions are similar, since melt is then the only hydrous phase and the experiments contained a similar bulk water-content (table 7.2).

The biotite-melting model proposed here states that the temperature range of biotite-melting, i.e. the width of the divariant reaction, is inversely proportional to the rock's bulk X_{Mg} at a given pressure. With decreasing X_{Mg}, there may be a maximum limit to this range, which would equate to the divariant band reaching a fixed width (figure 7.3a). For a given bulk water-content, the level of incremental melt production will also be proportional to the bulk X_{Mg}. A sharp change in the incremental melt production could occur if the divariant melting interval ends in a univariant reaction, as in the M62 pseudosection (figure 6.13 and figure 7.3c), because, at the univariant reaction, a finite amount of biotite would have to be consumed at a single

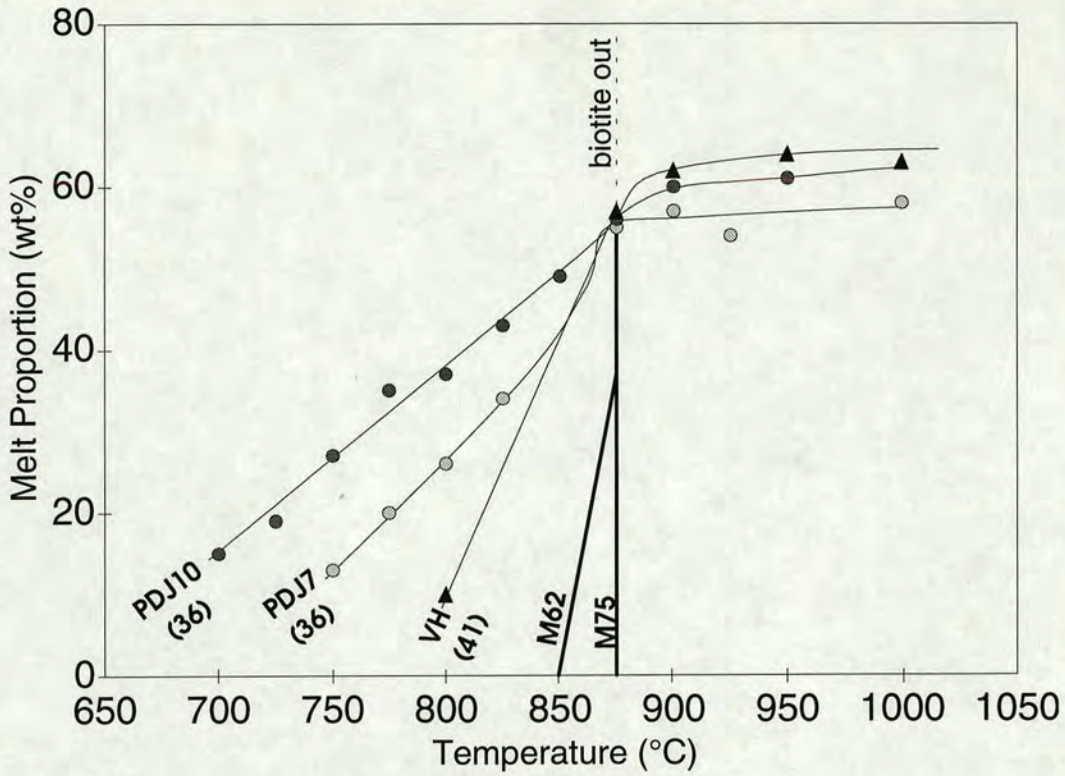

Figure 7.2. Melt proportion (wt%) versus normalised temperatures for different compositions. The bulk X_{Mg} values are given in parenthesis. The data is from Patino Douce and Johnston (PDJ, 1991), Vielzeuf and Holloway (VH, 1988) and the present study (M62, M75). The temperatures of the experiments have been altered by a constant amount, such that the **last biotite-present experiment** is at 850°C, the temperature at which Vielzeuf and Holloway (1988) reported their last biotite. The **first biotite-absent experiments** occur on the dotted line marked "biotite out". All the experiments were run at 10kb except PDJ7 which was run at 7kb. The melt proportions (VH, PDJ) are based on mass balance calculations, except for the present study where the melt proportions are hypothetical. The 10wt% melt proportion value at 800°C (VH) is an estimate only. In the experiments of Patino Douce and Johnston (1991) and Vielzeuf and Holloway (1988) the beginning of melting is obscured by the original presence of muscovite in their mixes. This breaks down, producing melt, before biotite does.

temperature. Vielzeuf and Holloway (1988) argued that the incremental melt production in their experiments was high which, according to the reasoning above, suggests the ultimate operation of a univariant reaction. However, the temperature range for the loss of their titanium-containing biotite (850-862°C) is below that of the pure KFMASH univariant reactions determined and reversed in this study (figure 7.2). The addition of titanium and fluorine to biotite should *raise* the temperatures at which the univariant reaction occurs and so it is concluded that Vielzeuf and Holloway's (1988) biotite-out temperature range must represent the end of a divariant field at a lower temperature than the univariant reaction (figure 7.3a and 7.4). Their melt volumes were not estimated quantitatively below 875°C and the melting curve

	VH	PDJ	HG1	HG2	M62	M74	M86
SiO_2	64.35	57.36	53.82	61.11	66.00	67.13	68.44
TiO_2	0.82	1.26	0	0	0	0	0
Al_2O_3	18.13	23.24	25.43	19.47	18.84	18.729	18.40
FeO	6.26	8.59	6.83	7.54	4.74	3.151	1.65
MgO	2.44	2.72	8.95	9.88	4.42	5.021	5.73
MnO	0.09	0.17	0	0	0	0	0
CaO	1.52	0.40	2.42	0	0.09	0.06	0.06
K_2O	2.56	3.63	1.35	0	4.95	4.97	4.81
Na_2O	1.66	0.48	1.18	0	0.00	0.00	0.00
F	--	0.11	0	0	0	0	0
H_2O	1.86	1.69	--	--	0.89	0.87	0.86
TOTAL	97.85	99.65	99.98	98.00	99.92	99.93	99.96
X_{Mg}	0.410	0.361	0.700	0.700	0.625	0.740	0.861

Table 7.2. Bulk compositions of mixes used in experimental studies discussed in this chapter.
VH - Vielzeuf & Holloway (1988), average of atomic absorption analysis and EDS microprobe analyses of glass, water by thermogravimetric analysis (0.29 wt% adsorbed H_2O not included); PDJ - Patino Douce and Johnston (1991), analysed by XRF except sodium by instrumental neutron-activation analysis and fluorine and water calculated from modal proportion of micas, the water content of which were calculated by difference from 100% in microprobe totals; HG1 - Hensen and Green's B_{70} (1970, 1972), method of analysis not given; HG2 - Hensen and Green's $B_{70}S$ (1972), method of analysis not given; M62, M74 and M86 - this study, means of microprobe analyses of glasses and compositions calculated from modes of phases (table 2.7).
"0" - not analysed for but presumed to be zero as compositions are synthetic.
"--" - not analysed for or estimated, but probably present.
"X_{Mg}" - MgO/(MgO + FeO).

could be broader than they show. Furthermore, the final biotite-out reaction is unlikely to have been a univariant one in the experiments of Vielzeuf and Holloway (1988) because at 10kb this would require the production of orthopyroxene, which is not seen in their experiments.

The difference between the size of the melting interval for PDJ10 (bulk X_{Mg}=0.36) and VH (bulk X_{Mg}=0.41) is about 100°C for the increase 15 to 55 wt% melt. This could indicate that the size of the melting interval is extremely sensitive to bulk X_{Mg}'s in iron-rich compositions but this is thought to be unlikely. It is more probable that the stabilising elements in biotite not only extend its stability limit up

temperature but also expand its melting range.

Other elements could also influence the onset and extent of biotite-melting. The only major pelite component missing from the KFMASH system is sodium which would occur only in the melt and in alkali-feldspar, partitioning more strongly into the melt than potassium. Sodium allows the production of true haplogranitic melts which can form at lower temperature than orthoclase-quartz-H_2O melts and consequently, in albite-orthoclase-quartz-H_2O systems, it lowers the solidus temperature by some 40°C (e.g. Luth 1976, Johannes and Holtz 1990). Calcium can be present in pelites in low concentrations and would only occur in plagioclase and as a minor constituent of garnet and the melt (e.g. Johannes and Holtz 1992). Plagioclase is a reactant in biotite dehydration melting reactions whereas garnet and melt are products and so the effect of adding of calcium to the KFMASH system could be to raise the melting temperature.

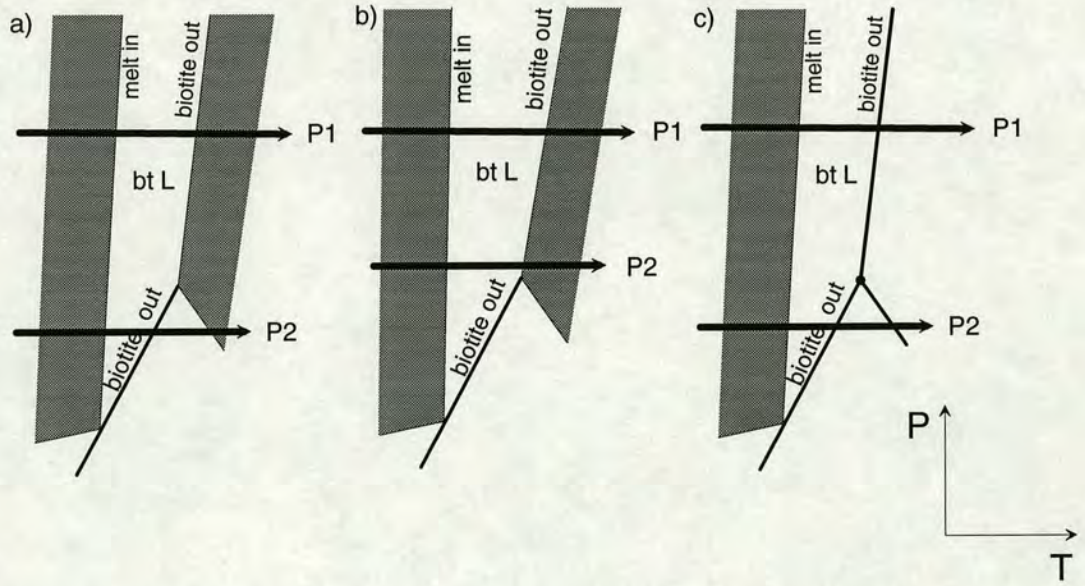

Figure 7.3. Schematic illustration of biotite-melting intervals.
a) At P1 the biotite-melting interval is defined by the limits of the divariant reaction (white area, light lines). At P2 the biotite is lost at the univariant reaction (heavy line) and therefore, the melting interval is shorter. Just above the temperature of the univariant reaction the assemblage at P2 will be involve an additional phase relative to that at P1 but they may become the same with further increases in temperature. Note that the high-temperature limit of the bt-L field at P1 is simply the edge of a divariant field and not a univariant reaction. **This will apply to relatively iron-rich rocks.**
b) As figure a) but with a divariant bt-L field which diverges up-pressure. This is an alternative reason for getting shorter melting intervals at lower pressures.
c) as figure a) but with the high-temperature limit of biotite as a univariant reaction. **This will apply to relatively magnesium-rich rocks.** Also, all biotite must be consumed at that reaction and in crossing it, there will be a sharp increase in the volume of melt.

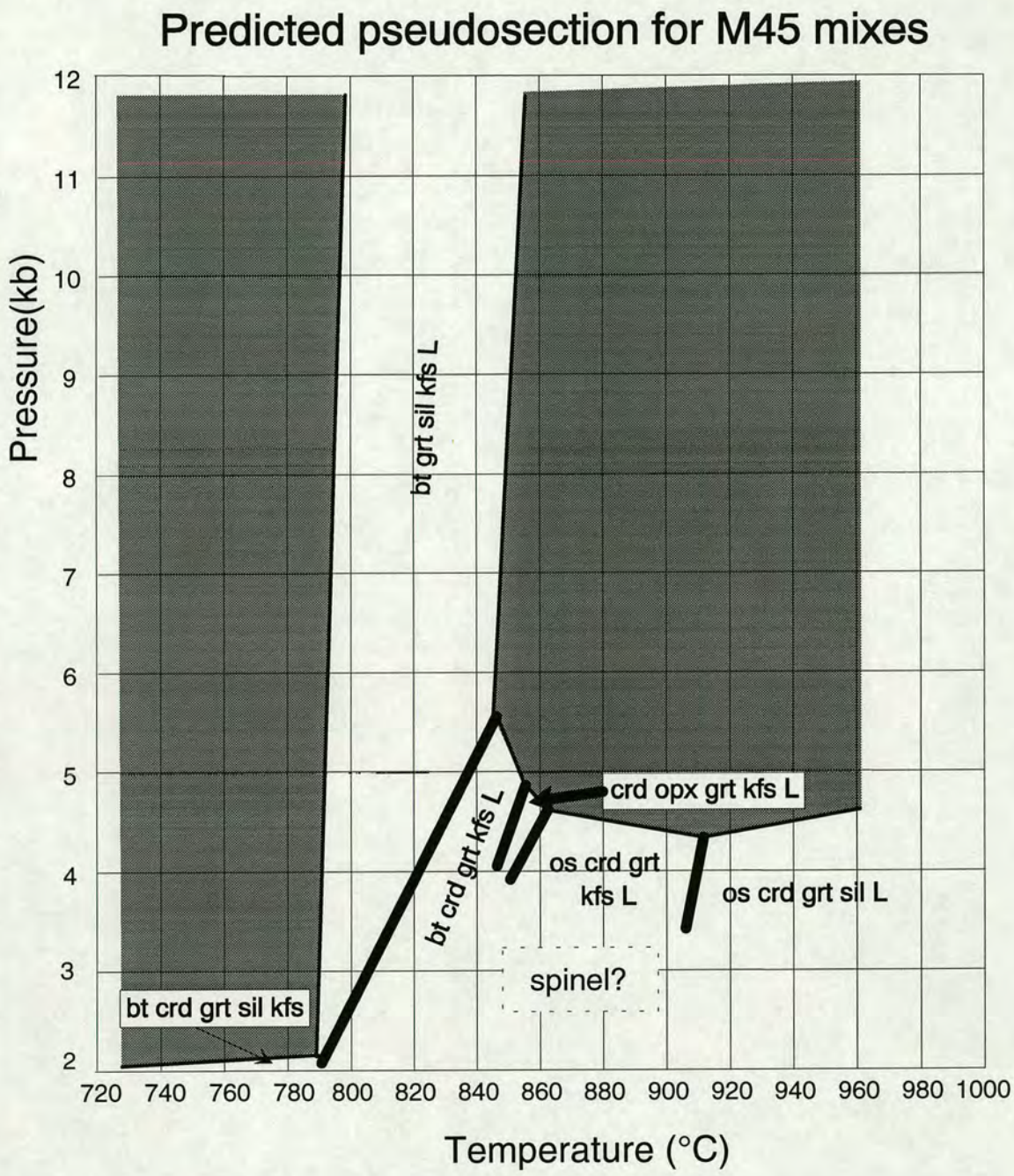

Figure 7.4. Predicted pseudosection for a KFMASH bulk composition similar to those in this study (table 7.2) but with a bulk XMg of 0.45. The heavy lines are univariant reactions, the white areas divariant reactions and the grey areas are trivariant regions. The pseudosection incorporates the 850-862°C biotite-out temperature range of Vielzeuf and Holloway (1988) and the 760-800°C biotite-in temperature range of Le Breton and Thompson (1988) both at 10kb. The titanium-contents of the biotites is not considered - the pseudosection is intended to illustrate its likely form. The phase assemblages found in the experiments of Patino Douce and Johnston (1991) and the two studies mentioned above suggest that no other phases will form other than those shown and possibly spinel. Spinel is likely to be stable above 1050°C at 10kb but is also likely to be stable at lower pressures and reactions involving spinel may replace all the postulated phase relations below 5kb.

The melting data at 7kb (PDJ7, figure 7.2) show a narrower biotite-melting range than the equivalent data at 10kb (PDJ10). This means that the lower pressure experiments meet the terminal stability of biotite at lower temperature, which would be expected when univariant reactions are stable, as they have positive dP/dT's (figure 7.3a). This effect can be seen on the M62 pseudosection (INSERT C) between 8 and 9kb. An alternative explanation is simply that the divariant biotite-melting field diverges with increasing pressure (figure 7.3b). The predicted pseudosection for bulk $X_{Mg} = 0.45$ further illustrates the point made in Chapter One that relatively iron-rich bulk compositions cannot constrain KFMASH univariant reactions, except at low pressures, as these reactions are not stable for those compositions.

In summary, the current data, in conjunction with that previously published, can all be accounted for by a simple qualitative model in which:

1. The size of the temperature range of biotite-melt co-existence is inversely proportional to the bulk X_{Mg} of the rock and may be directly proportional to the pressure at which melting occurs.
2. The temperature at which the biotite is lost, i.e. the position of the melting range in temperature, depends on the concentration of stabilising elements (titanium, fluorine) in the biotite.

These two factors may well not be independent - the presence of titanium and fluorine could affect the temperature range. The addition of sodium to a KFMASH system will lower the melting temperature.

7.3 THE RELATIVE STABILITIES OF GARNET-CORDIERITE AND ORTHOPYROXENE-SILLIMANITE-QUARTZ ASSEMBLAGES.

Since the work of Hensen (1971) and related papers[2], orthopyroxene-sillimanite-quartz-bearing assemblages have been recognised as high-pressure breakdown products of cordierite. In rocks with reasonable iron-content, garnet will also be present. This breakdown reaction has become one of the fundamental divides in the metapelitic granulite facies. The reaction is important for petrogenetic studies as it

[2] Klestov (1964), Marakushev and Kudryavtsev (1965) and Hensen and Green (1970, 1971, 1972, 1973).

	Type of Investigation	Reaction	dP/dT slope	Interpretative System	Actual System
HG	Experiment	grt + crd = opx + sil + qz	-ve	FMAS	CNKFMASH[a]
BEG	Experiment	grt + crd = opx + sil + qz	+ve[b]	FMAS	FMASH-CO_2
AP	Calculation	grt + crd = opx + sil + qz	+ve	FMAS	FMASH-CO_2
HH	Theory	grt + crd = opx + sil + qz	+ve	KFMASH	-
G	Theory	grt + crd = opx + sil + qz + V	-ve	KFMASH	-
PD	Theory/ calculation	grt + crd + qz + kfs = opx + sil + L	+ve	KFMASH	-

Table 7.3. Various representations of the high-pressure garnet-cordierite breakdown reaction from the literature. Given for each study are: the type of data used in the investigation: the form and dP/dT slope of the reaction: the chemical system used to interpret the results: the actual system the data was obtained in. All the authors consider the reactions to be stable above 700°C. K-feldspar is stable in all the studies except BEG and AP.
HG - Hensen and Green (1971, 1972, 1973) and Hensen (1971), BEG - Bertrand et al. (1991), AP - Aranovich and Podlesskii (1989), HH - Hensen and Harley (1990), G - Grant (1985), PD - Powell and Downes (1990). Chemical components: C - CaO, N - Na_2O, K - K_2O, F - FeO, M - MgO, A - Al_2O_3, S - SiO_2, H - H_2O, also CO_2.
Slopes: +ve - positive, -ve - negative.
[a] - example compositions given in table 7.2.
[b] - up to 1000°C, then negative to 1050°C where their reaction terminates.

fixes the position of the KFMASH [os] point, which controls the dehydration melting of biotite (sections 6.3.1 and 6.3.2, reaction (os, bt) INSERT A). The fact that the breakdown reaction occurs at around 30km in depth, the thickness of normal continental crust, makes it useful in studies of continental evolution.

In previous experimental and theoretical work the high-pressure breakdown reaction of the garnet-cordierite assemblage has been written and oriented in a variety of ways (table 7.3).

The reaction is most commonly given as:

garnet + cordierite = orthopyroxene + sillimanite + quartz (1)

This is only correct if the cordierite is anhydrous, i.e. in a volatile-free system, for example, the FMAS system. The high-pressure limit of anhydrous Mg-cordierite was investigated directly by Schreyer and Yoder (1960) who found it broke down at 10kb at 1100°C. However, their experiments were unseeded and they anticipated problems of overstepping the reaction up-pressure. Newton (1972) used seeded experiments to

show that their concern was well-founded. In both these studies, satisfactory results were only obtained at very high temperatures (>1200°C) where the high-pressure breakdown product of Mg-cordierite is sapphirine-quartz. Therefore, Newton (1972) extrapolated that reaction back to intersect the en + sil = sa + qz reaction of Chatterjee and Schreyer (1972). This suggests the high-pressure breakdown limit of anhydrous Mg-cordierite is 8.2kb. On this basis, reaction 1 can only be stable below 8.2kb and therefore it should not be written for reactions which involve vapour and may occur well above that pressure.

If the system also involves a vapour phase then the cordierite will contain volatile components and a free vapour is required on the high-pressure side of the reaction to balance it (compare BEG, AP, table 7.3):

garnet + cordierite = orthopyroxene + sillimanite + quartz + vapour (2).

If the vapour phase is water and K-feldspar and quartz are present then, above about 700°C, a melt must be present, which will probably consume all the free water and

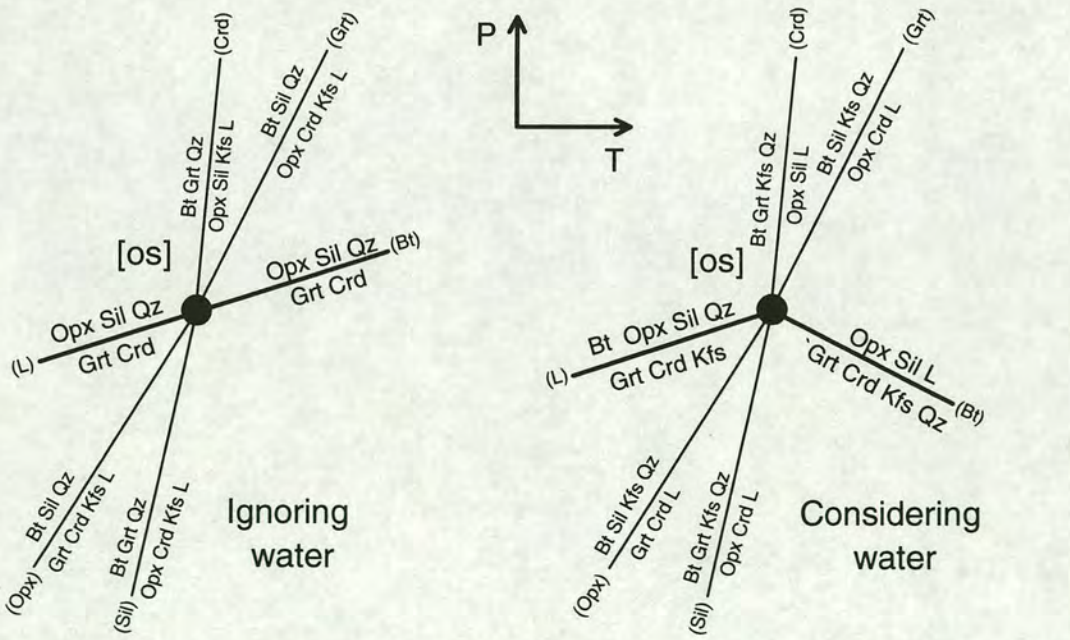

Fi

Figure 7.5. Schematic topologies of the KFMASH [os] point (INSERT A) demonstrating the different reaction stoichiometries and dP/dT gradients which result from the consideration of cordierite as anhydrous (left, shows reaction 1 in text) or water-undersaturated (right, shows reaction 2 in text). Consideration of water when balancing the reactions may result in the K-feldspar becoming a reactant in the biotite dehydration melting reactions, as shown (see figure 6.7, 6.8 and 6.9).

lead to water-undersaturation (compare G, table 7.3). The melt will be silica-rich and potassic and therefore requires quartz and K-feldspar on the low-pressure side of the reaction. Therefore, in the KFMASH-system the correct form of the reaction is (figure 7.5, compare HG, HH, table 7.3 and reaction (os, bt) INSERT A):

garnet + cordierite + quartz + K-feldspar =
orthopyroxene + sillimanite + melt (3).

The calculated breakdown reaction of Powell and Downes (1990) is therefore considered to have the correct stoichiometry for the KFMASH-system but they state that (p111) "From the calculations, cd + g +opx + L [i.e. crd + grt + kfs + qz = opx + sil + L, (os, bt)] should have a positive slope... . These conclusions are more or less inescapable, even though silicate melts cannot yet be included in the calculations." The current experiments clearly show the reaction to have a negative slope (INSERT A and figure 7.7).

Bertrand et al. (figure 5, 1991) recognised that, with vapour-bearing cordierite, the breakdown reaction was a dehydration reaction or, if melt was produced, a dehydration melting reaction in their vapour-saturated experiments. However, as they were unable to discern any systematic difference in the melt-present and melt-absent experiments, they ignored this factor and chose reaction (1) rather than the true reaction for their system, reaction (2).

The work of Bertrand et al. (1991) appears to support the earlier findings of Hensen and Green (1971, 1972, 1973), i.e. that orthopyroxene-sillimanite-quartz assemblages are only stable above at least 10kb in metapelites. However, although both groups of researchers used the FMAS system to interpret their experiments, the studies are not directly comparable: the experiments were carried out in an H_2O/CO_2-saturated FMAS-system[3] (Bertrand et al. 1991) as opposed to an H_2O-undersaturated CNKFMASH system (Hensen and Green 1971, 1972, 1973). The vapour-saturated and vapour-undersaturated systems do not relate to each other in a simple way and should not be compared (figure 7.6): it is well known that metapelitic granulite-facies assemblages cannot co-exist with a water-rich vapour.

---

[3] The experiments of Bertrand et al. (1991) certainly started with a free-fluid phase (H_2O only, a H_2O/CO_2 mixture or CO_2 only) but whether vapour was still present after the runs is not reported. If only a small amount of water was present, it could well be consumed by the melt which occurs in most of the experiments, thereby producing water-undersaturated conditions.

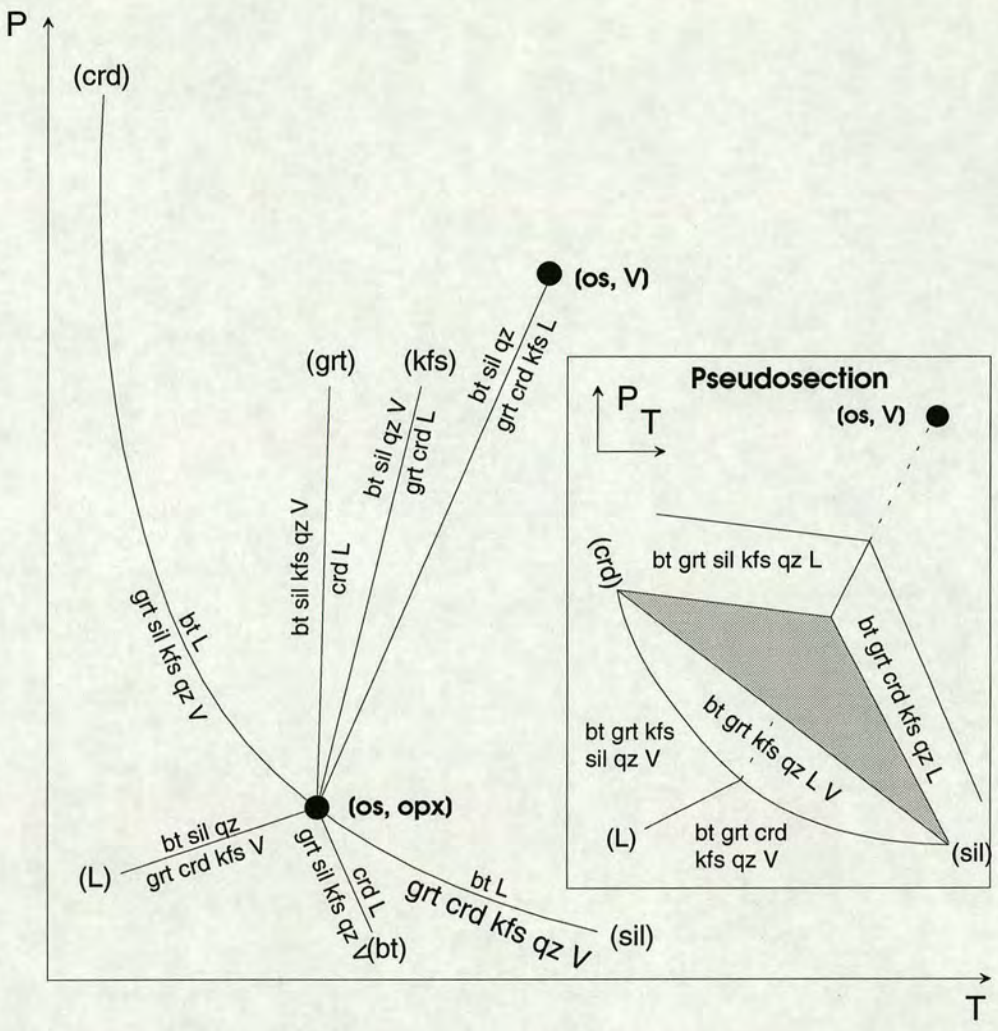

Figure 7.6. Schematic pressure-temperature diagram showing the relationship between water-saturated and water-undersaturated reactions in the KFMASH-system in which the vapour is pure water. The (crd) and (sil) reactions emanating from the [os, opx] point define the solidus for biotite-bearing rocks. If a vapour-saturated bulk-composition crosses one of these reactions up temperature, melting will occur until a phase is lost. If this phase is the vapour then the (grt) and (kfs) reactions become metastable leaving only vapour-absent (water-undersaturated) reactions stable at higher temperature. The stability field of vapour could be extended if a different phase was lost at the solidus - the inset pseudosection would be stable for a composition which lost sillimanite before vapour at the (crd) reaction. The presence of CO_2 could allow a large vapour-present field as CO_2, unlike water, scarcely dissolves in these silicate melts, thereby giving a low water activity in the vapour. The potential stabilising effect of CO_2 on cordierite would also need to accounted for.

The reaction curves from the experimental studies given in table 7.3 are shown in figure 7.7. The curve given by Hensen and Green (1970) has a very similar negative gradient to that produced in the current study above 900°C, but is approximately 2kb higher. Between 920 and 1000°C, the Bertrand et al. (1991) curve is at a higher

pressure still and has a positive gradient. As the experiments in each of the studies were conducted in a different system, differences would be expected in the position of the reaction.

In the alkali-free FMASH/CO_2 system (Bertrand et al. 1991), the garnet-cordierite breakdown reaction has a positive slope and occurs at higher pressures than the pure KFMASH system (this study, table 7.3 for bulk compositions), in which the reaction has a negative slope and exists at lower pressure. This probably results from one of two effects, or a combination of both. Firstly, the stability of cordierite is thought to depend strongly on its vapour-content (Schreyer and Yoder 1960, Newton 1972, Newton and Wood 1979, Martignole and Sisi 1981). Bertrand et al. (p69, 1991) state that "In the absence of any gas phase (H_2O or CO_2), the possibility still exists that the lower pressure stability limit of cordierite predicted by Newton (1972) [8.2kb] may

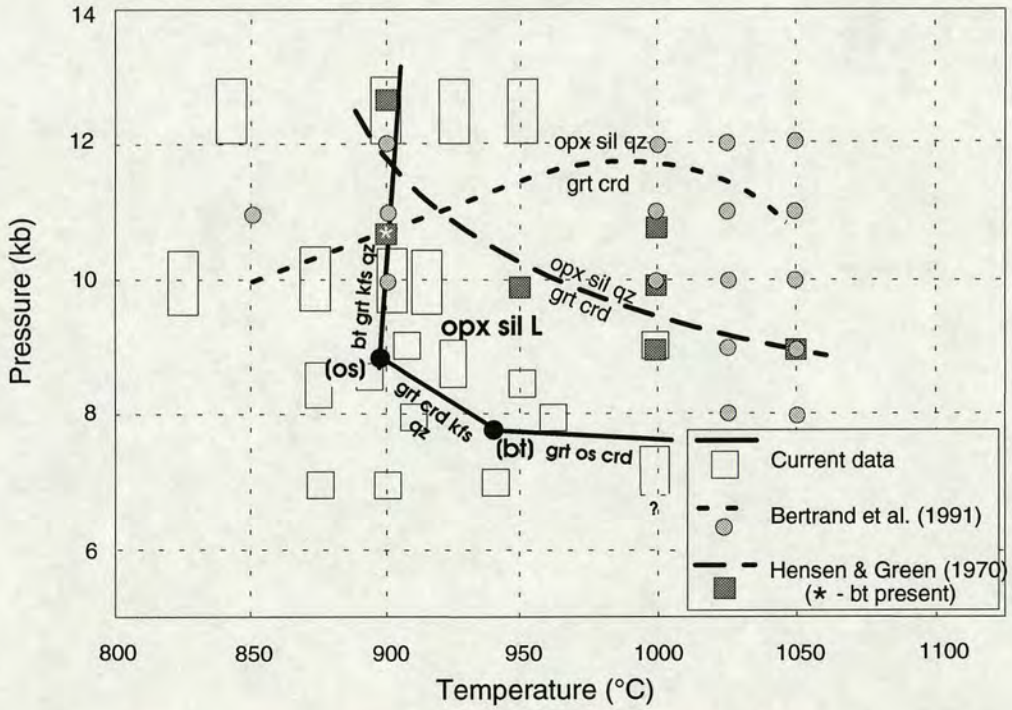

Figure 7.7. Pressure-temperature diagram showing three curves limiting the stability of orthopyroxene-sillimanite-quartz assemblages. The current data are from a quartz-present, water-undersaturated, KFMASH-system and the high-pressure assemblage includes melt. Bertrand et al. (1991) give the breakdown as reaction 1, while acknowledging reaction 2 as the true reaction (see text). The curve shown for the work of Hensen and Green (1971, 1972, 1973) and Hensen (1971) is taken from the best-documented experimental results, the B_{70} series, (Hensen and Green 1970). They report the reaction as reaction 1 despite the experimental system being CNKFMASH (table 7.3). The true reaction in their system is reaction 4. For each study, the experiments on which the curves are based are shown.

have application. However, there is no experimental evidence available to date to confirm this effect...". Presumably, water-undersaturated cordierite will have a stability limit intermediate between that of water-saturated and anhydrous cordierites. Therefore, the much lower pressure found for the breakdown reaction in the current study compared to that of Bertrand et al. (1991) may be due to fact that in the current study the cordierites are water-undersaturated whereas in Bertrand et al. (1991) the cordierites are vapour-saturated. Secondly, the presence of a hydrous, potassic melt (and K-feldspar) may lower the pressure of the breakdown as water will partition more strongly into the melt than the cordierite. However, as many of the experiments of Bertrand et al. (1991) contained melts the first factor is likely to be the most important.

In the light of the above, it seems sensible to interpret the experiments of Hensen and Green (1970, 1971, 1972, 1973) in the CNKFMASH-system in which they were done, rather than the FMAS-system they chose to report them. This is emphasised by the occurrence of biotite (10.8kb, 900°C) and osumilite (3.6 to 7.2kb, 1000°C and 5.4 to 7.2kb, 1100°C - see Hensen 1977) in the experimental products of Hensen and Green (1970, 1972). These occurrences compare favourably with the position of the KFMASH reactions derived in the current study (INSERT A and 7.7). Biotite and osumilite might have been reported from more of the experiments of Hensen and Green (1970) had the run times been longer than the 18 to 72 hours for the 900-1000°C runs. The run times in this study varied between 140 and 424 hours in the same temperature range.

In the CNKFMASH-system (Hensen and Green 1970) the reaction will be similar to that for the KFMASH-system, but will also involve plagioclase and a grossular-component in garnet:

garnet(Mg-Fe-Ca) + cordierite + quartz + alkali-feldspar =
orthopyroxene + sillimanite + plagioclase + melt (4).

The stabilising effect of minor components which occur only in one or two phases in a system is well known, e.g. titanium in biotite (e.g. Guidotti 1984), zinc in spinel (e.g. Shulters and Bohlen 1989, Nichols et al. 1992), and calcium can play this role in garnet (e.g. Harley 1984b). The grossular content of the garnets in the experiments shown in figure 7.7 (Hensen and Green 1970) are not recorded but, for an analogous

composition C_{70}[4], they lie between five and ten mole percent (figure 6, Hensen and Green 19/1). This is a large grossular component given that many garnets in metapelitic granulites contain less than five mole percent grossular (e.g. Harley and Fitzsimons 1991). The calcium-content of melts formed from this type of rock is very low (e.g. Johannes and Holtz 1992). Therefore, addition of calcium to the KFMASH-system would cause the stabilisation of garnet and the breakdown reaction would be displaced to higher pressures (figure 7.8). This provides a plausible reason for the pressure difference in the position of the breakdown reactions in the pure KFMASH-system[5] of the current study and the CNKFMASH-system[6] of Hensen and Green (1970,1973).

The possibility of the grossular component of the garnet affecting its stability was noted by Hensen and Green (1972) who attempted to evaluate the effect using a FMASH-system mix ($B_{70}S$, see table 7.2). The results of these experiments certainly showed an expansion of the stability field of garnet down pressure when it contained a grossular component, but were equivocal regarding the upper pressure limit.

Three other reasons for the higher-pressure position of the breakdown reaction of Hensen and Green (1970) are put forward here, though they are thought to be less likely than that presented above. Firstly, as mentioned before, their run durations were rather short (18-72 hours) in the range 900-1000°C. If, in their experiments, the low pressure assemblage, garnet-cordierite, was kinetically favoured over the assemblage orthopyroxene-sillimanite[7] then the reaction would be placed at too high a pressure. Secondly, the pressures quoted for the experiments have a standard -10% pressure correction applied[8] because "accurate data for the variation of the pressure correction as a function of pressure and temperature are not available as yet" (p312, Hensen and Green 1971). The possibility exists, therefore, that the pressure correction applied to these experiments is an underestimate (see also sections 2.3.1

---

[4] This composition has the same alkali- and silica-contents as the B_{70} mixes (table 7.3) and the same X_{Mg}. It is significantly more aluminous and has 30% *less* CaO than the B_{70} mixes.

[5] In fact, there is a very small amount of calcium present (<0.1wt%, see table 7.2 for comparison). In any case, most of the garnet rims are almost calcium-free (table 3.4).

[6] The sodium present in the CNKFMASH system, present in the alkali feldspar and the melt, will partition more strongly into the melt (e.g. Luth 1976, Johannes and Holtz 1990) and so is likely to counteract the breakdown reaction's upward pressure shift, relative to the KFMASH system, caused by the addition of CaO.

[7] All the experiments contain quartz, alkali- and plagioclase-feldspars and melt.

[8] The cell used is a 12.7mm diameter talc/boron-nitride cell with pyrophyllite and ceramic inners, described in Green and Ringwood (1967). They believe the talc outer to be the strongest part of the cell, implying the possibility of a negative anvil effect (section 2.3.1 and 7.4).

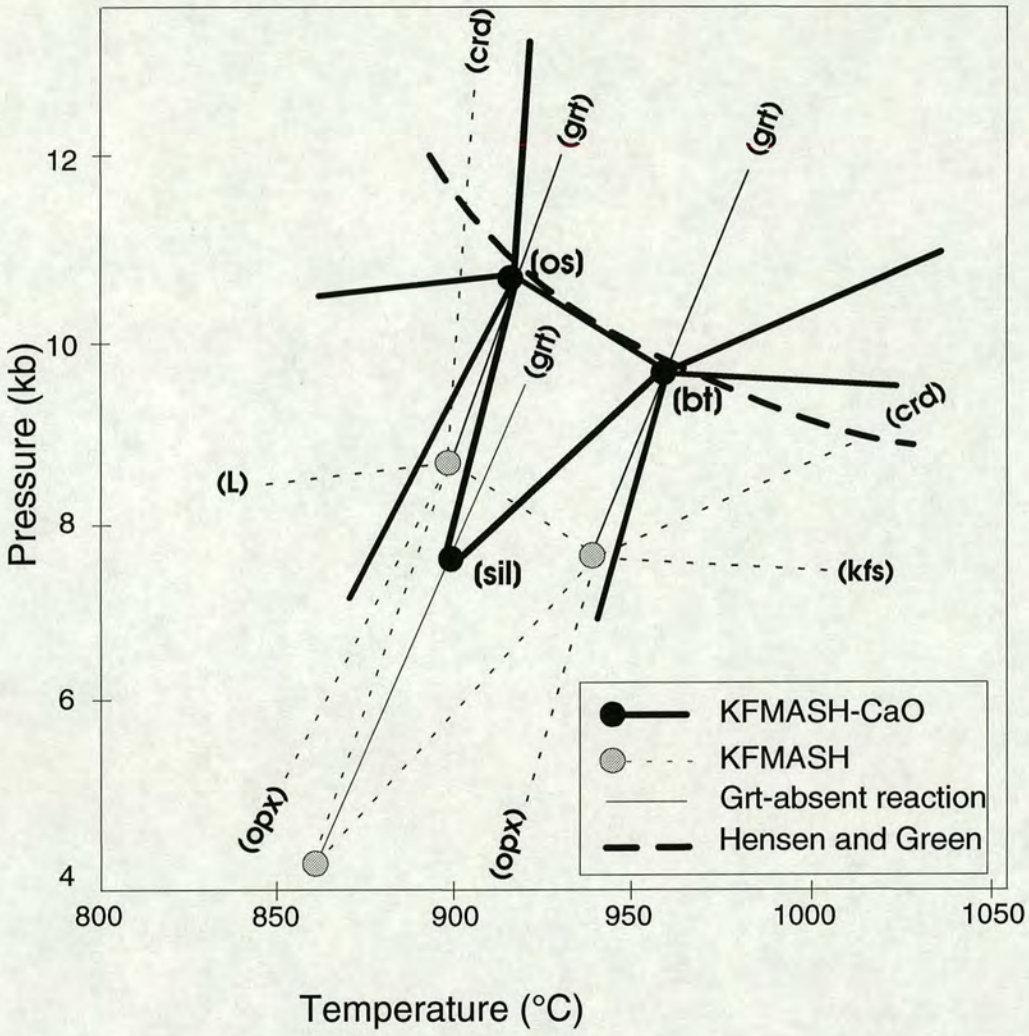

Figure 7.8. Pressure-temperature diagram showing the possible effect on reactions of the addition of CaO to the KFMASH system. The CaO is likely to stabilise the garnet and so displace the (os, bt) breakdown reaction to higher pressures. The addition of CaO will change the (os, bt) reaction from reaction 3 to reaction 4 (see text). The garnet-absent reactions will not be affected and the diagram shows how the grid derived from the current KFMASH experiments can be shifted up these reactions to coincide with the CNKFMASH reaction of Hensen and Green (1970, 1973). The dP/dT slopes of the two breakdown reactions are virtually identical. The addition of CaO to the KFMASH-system will not add a degree of freedom to the system if another phase, namely plagioclase is formed as a result. Plagioclase was present in all the experiments of Hensen and Green (1970, 1971, 1972, 1973).

and 7.4 below). Finally, if cordierite were closer to volatile-saturation this would increase its pressure stability but, as no data are reported on the water-contents of the Hensen and Green mixes (1970, 1971, 1972), this cannot be assessed.

Natural cordierites often contain some CO_2 and it is therefore important to assess the effect CO_2 may have on phase relations. CO_2 may also occur in the melt, though it

will fractionate very strongly into the cordierite. The experiments of Bertrand et al. (1991) were conducted in pure water, pure CO_2 or a mixture of both but showed no systematic differences in assemblage between them. The experiments were fluid-saturated and the cordierites should therefore have fully occupied channel-sites. It seems that water, CO_2 or a mixture of both all have approximately the same stabilising effect on cordierite. Therefore, in fluid-undersaturated cordierites it is likely that the level of channel-site occupancy will control the stability, irrespective of the particular fluid-species. This means that the influx of a CO_2-rich fluid to an initially fluid-undersaturated CO_2-poor terrain could enhance the stability of cordierite by increasing its fluid-content through the incorporation of CO_2. Other phase relations could be essentially unaffected. The stabilisation of cordierite to higher pressures would shift the breakdown reaction to higher pressures in an

FMASH **FMASH-CO_2** **FMAS-CO_2**	**grt + crd = opx + sil + qz + V**		
Fluid-saturated system	10.8kb, 900°C to 11.5kb, 1000°C +ve dP/dT	BEG	Maximum cordierite stability due to full channel occupancy.
KFMASH	**grt + crd + kfs + qz = opx + sil + L**		
Fluid-undersaturated system	8.8kb, 900°C to 7.8kb, 1000°C -ve dP/dT	This study	Cordierite undersaturation and hydrous melt reduce pressure of reaction.
CNKFMASH	**grt(Fe-Mg-Ca) + crd + kfs + qz = opx + sil + plag + L**		
Fluid-undersaturated system	11.8kb, 900°C to 9.5kb, 1000°C -ve dP/dT	HG	Stabilisation of garnet by CaO.

Table 7.4. Summary of the conclusions of section 7.3. The appropriate reaction stoichiometry for the chemical systems used in three experimental studies are given. The level of fluid-saturation in the experiments, the pressure-temperature position of the reaction, the reference and reasons for the differences are also given.
BEG - Bertrand et al. (1991).
HG - Hensen and Green (1970, 1971, 1972, 1973).

analogous way to that illustrated in figure 8.8, except that the (crd) reactions would be unaffected, rather than the (grt) reactions.

The garnet-cordierite breakdown reactions, which limit the low-pressure stability of the orthopyroxene-sillimanite-quartz assemblage, have different stoichiometries, different slopes and different pressure-temperature positions in different chemical systems. The conclusions of this section are summarised in table 7.4.

7.4 OSUMILITE PHASE RELATIONS.

7.4.1 Evidence from natural rocks.

The phase relations of osumilite in high-temperature, high-pressure metapelites were considered qualitatively by Ellis et al. (1980) and Grew (1982), based on natural-rock evidence from the Napier Complex, Antarctica. Each proposed a theoretical KFMAS-system grid (figures 1.7a and 1.7b), but there is a major topological difference between them, concerning the positioning of the FMAS-system invariant point which limits the low-temperature stability of sapphirine (figure 1.7a, [sp, os , kfs] point, Ellis et al. 1980; figure 1.7b, [os, kfs] point, Grew 1980). In the grid of Ellis et al. (1980), the point lies at lower temperatures than the reactions introducing osumilite up-temperature whereas Grew's grid (1982) places it at higher temperatures. Therefore, Grew's grid (1982) allows osumilite to be stable at lower temperatures than the stability of sapphirine-quartz, whereas Ellis et al.'s grid (1980) only allows osumilite stability above sapphirine-quartz stability. The experimental studies of Mototyoshi et al. (KMASH-system[9], 1993) and Audibert et al. (KFMASH, 1994) show that Grew's grid (1980) is topologically correct. The present experiments implicitly support this conclusion as no sapphirine was formed in any of the experiments, yet osumilite was.

7.4.2 Comparison of experimental data.

The study of Audibert et al. (1994) provides an excellent comparison for the current study - it was conducted independently, in the same chemical system and the run

[9] Though Motoyoshi et al. (1993) consider their experiments in the KMAS-system, the mixes were "moistened by breathing" to "promote reaction rates" and so some water must be present. In a totally dry system melting would not occur below 1100°C (Bohlen et al. 1983).

temperatures overlap by 50°C. Their interpreted reaction grid and a grid summarising their experimental results are reproduced from their paper as figures 7.9 and 7.10. The same phases were present as in the current study with the exception of biotite and the addition of sapphirine. For this reason, the point labelled [sa] in figure 7.9 is the same as that labelled [bt] in INSERT A, with which figure 7.9 should be compared. The topology of the [bt, sa][10] points is the same, with one exception. The stoichiometries of the (bt, sa, opx) and (bt, sa, grt) reactions are very sensitive to the relative water-content of melt and cordierite, K_w[11]. This was discussed in section 6.3.1 and figure 6.10. In this study, it was concluded that the AFM-projection position of cordierite would be slightly more magnesian than osumilite, causing garnet and orthopyroxene to be reactants up-temperature and, therefore, the (bt, sa, opx) reaction to have a steeper slope than the (bt, sa, grt) reaction. This was based on measurements and estimates of melt and cordierite water-contents and is preferred to the topology of Audibert et al. (1994), who had no information on water-contents and assumed the projected position of the cordierite would be less magnesian. The near-degeneracy of sillimanite, cordierite and osumilite on an AFM projection (figure 6.10) will not affect the higher temperature topology derived by Audibert et al. (1994) as the appropriate assemblages do not occur.

A more serious discrepancy between the two studies is the pressure-temperature locations of the [bt, sa] points (table 7.5).

	Pressure (kb)	**Temperature (°C)**
This study.	7.0 - 8.1	930 - 945
Audibert et al. (1994)	9.9 - 11.1	950 approximately

Table 7.5. Estimates of the pressure-temperature position of the [bt, sa] point. Data for this study from INSERT A and section 6.3.1. Data for Audibert et al. (1994) estimated from figure 7.10; there is only one experiment at 950°C and so the temperature of the point cannot be constrained; the low pressure limit is derived by maximising the dP/dT of the (sa, bt, crd) reaction, assuming the 1000°C, 11.1kb experiment to be above the reaction.

The temperature estimates for the points are very similar but the there is a 2-4 kb difference in the pressure estimates. The KMASH-system data of Mototyoshi et al. (1993), which place the high-pressure stability limit of Mg-osumilite at 11.5kb

[10] Henceforth, the KFMASH-system considered will include both biotite and sapphirine. The [sa] and [bt] points are therefore re-labelled [bt, sa].
[11] $K_w = H_2O^L/H_2O^{crd}$, see section 3.6.3.

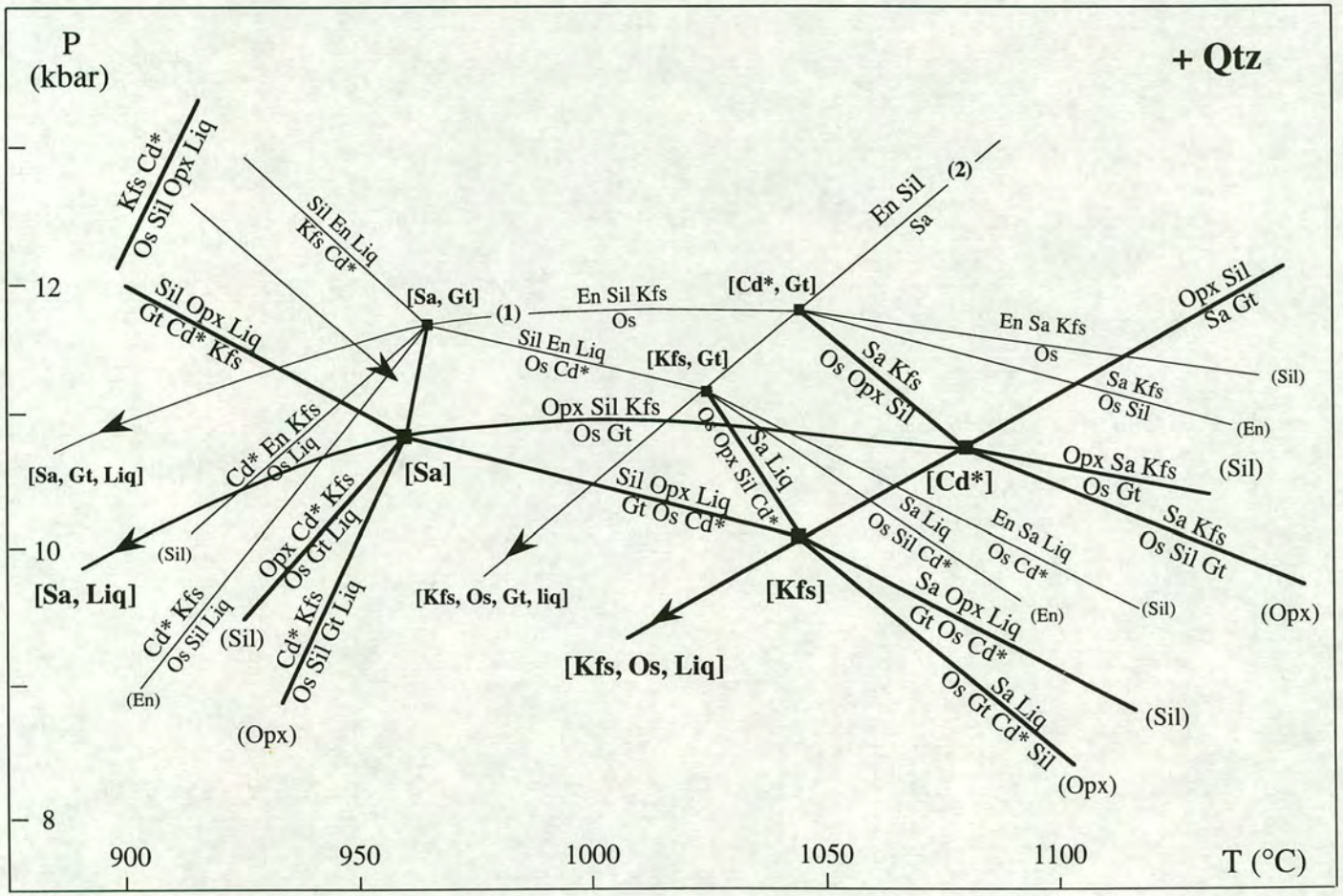

Figure 7.9. Reproduced from Audibert et al. (figure 13, 1994). Interpretative pressure-temperature diagram for quartz-saturated KFMASH (heavy lines) and KMASH (light lines) systems. The reaction (1) is from Motoyoshi et al. (1993) and reaction (2) is extrapolated from Chatterjee and Schreyer (1972). "crd*" - water-undersaturated cordierite. "crd" - anhydrous cordierite.

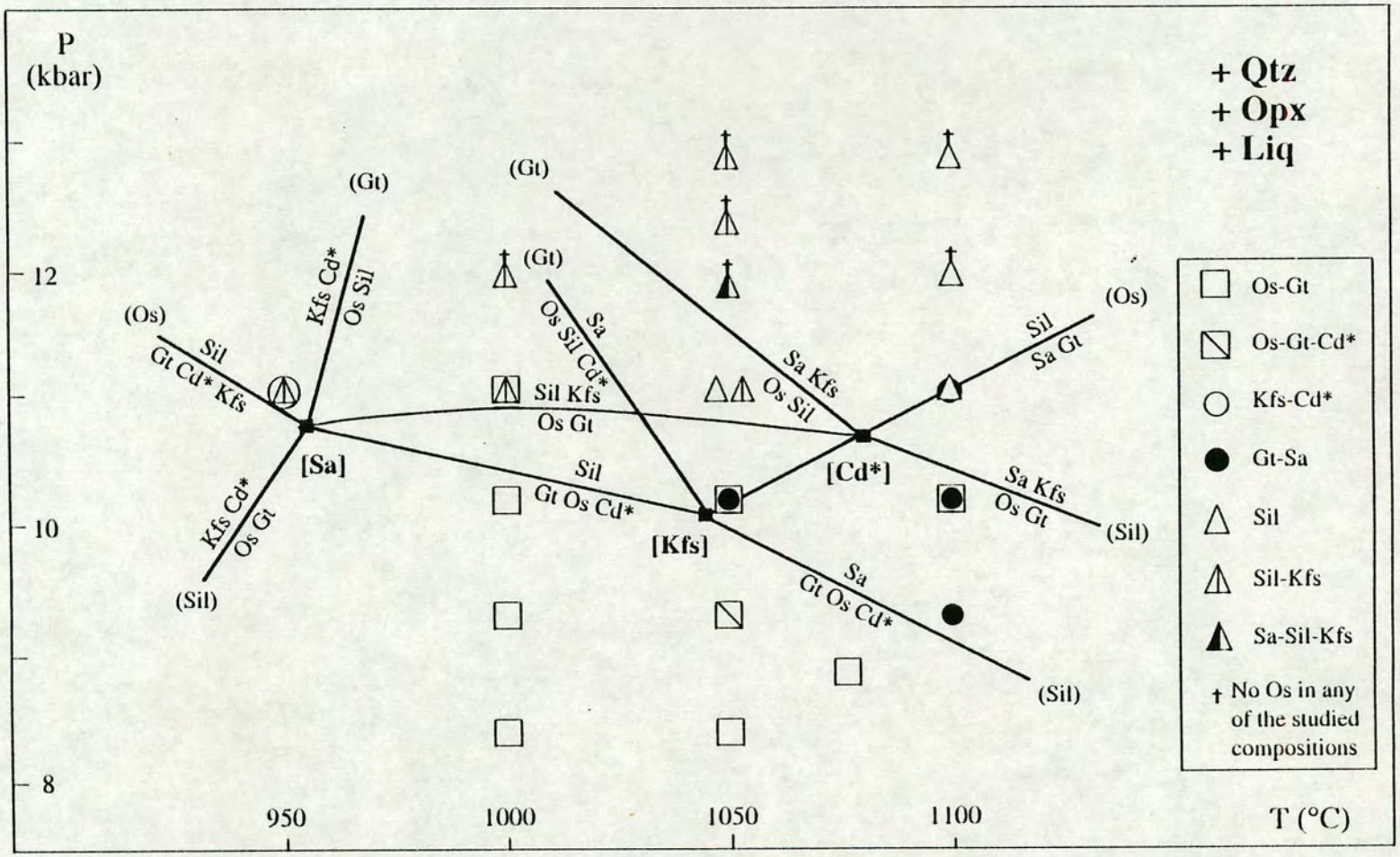

Figure 7.10. Reproduced from Audibert et al. (figure 6, 1994). Pressure-temperature diagram showing KFMASH system experimental results at 950, 1000, 1050 and 1100°C. "crd*" - water-undersaturated cordierite.

between 975 and 1100°C, are consistent with both grids (INSERT A and 7.9). It should be noted, though, that in the present study no experiments could be run above 925°C between 9 and 12 kb due to failure by melting of the salt cells.

The most important consequence[12] of the pressure discrepancy between the grids is the difference in the location of the high-pressure stability limit of the garnet-osumilite assemblage; 11kb, 950°C (Audibert et al. 1994) compared to 8kb, 950°C (this study). The studies used different experimental apparatus and a cross-calibration experiment was carried out in the current study in order to investigate whether this was the cause of the discrepancy. This study used gas-media and salt-cell solid-media apparatus. The former must give hydrostatic pressure transmission to the experimental charges and the latter almost certainly does, given the proximity of the salt to its melting temperature in these runs (see section 2.3.1). Audibert et al. (1994) and, in fact, Motoyoshi et al. (1993) both used talc-pyrex cells of the same design as illustrated in figure 2.2, but with AlSiMag internal components, rather than boron nitride. Both apply a -10% friction correction to the nominal pressures and this is also the correction used in high-pressure runs with this cell in the laboratory at the University of Edinburgh.

The talc-pyrex run in this study, D62, conducted at a nominal pressure of 10kb, produced the distinctive assemblage **garnet-osumilite-cordierite** (D62-16A, tables 3.1 and 4.1), which must lie at *lower pressures* than the (bt, kfs, sa) reaction (INSERT A). Using a -10% friction correction, the run pressure would be estimated at 9kb. This run essentially repeats the N64 run of Audibert et al. (1994) at 9.3kb, 1000°C and is fully consistent with it. However, the gas-bomb experiments in the present study (run D65) which were conducted under the same conditions (9kb, 1000°C) produced the distinctive assemblage **orthopyroxene-sillimanite-K-feldspar-quartz**. This assemblage must lie at *higher pressures* than not only the (bt, kfs, sa) reaction but also the (bt, crd, sa) reaction (INSERT A). This and other gas-bomb runs in this study (D55, D59, D47) require that, at 1000°C, the (bt, kfs, sa) reaction lies below 8kb and the (bt, crd, sa) reaction lies below 9kb. This means that the maximum pressure on the experimental charges in the talc-pyrex run (D62) was 8kb, and that the true friction correction is at least -20%.

Talc-pyrex cells with soft internal components could well suffer from a "negative-

[12] The important (os, bt, sa) reaction discussed in the last section is also implicated as it ends in the [bt, sa] point, but it is not constrained by the experiments of Audibert et al. (1993).

anvil effect" (section 2.3.1). Audibert et al. (1994) do not report a pressure calibration for their cell but state that their experimental technique is the same as Hensen and Green (1971)[13]. Those authors, in turn, used the pressure calibration of Green and Ringwood (1967) which showed a -10% friction correction was necessary. However, the transition used for the pressure-calibration was quartz-coesite, which occurs above 30kb (Smith 1984), well above the nominal 9-14kb range of the study of Audibert et al. (1994). Given the experimental comparison of the talc-pyrex and gas-bomb apparatus described in the last paragraph, is clear that the friction correction of the talc-pyrex cell must increase with decreasing pressure and that Audibert et al. (1994) have considerably underestimated it, thereby introducing a systematic pressure error into their results.

Two further points also show that Audibert et al. (1994) overestimated the pressures in their runs:

1. The gas-bomb reversal run, D64, proved that the (os, bt, sa) reaction must lie between 8 and 9kb at 910°C (section 5.2) and other gas-bomb runs (D54, D57) require the reaction to have a negative slope. This positioning of the reaction cannot be consistent with a [bt, sa] point at 11kb, 950°C (Audibert et al. 1994) without extreme curvature and a sharp change of slope for the reaction.

2. The relation of the KFMASH-system and related sub-systems was shown by Audibert et al. (1994) and the diagram is reproduced as figure 7.11. The invariant point of interest is the KMAS-system [sa, grt, L, bt] point which lies in the high-pressure, low-temperature part of figure 7.11. It is labelled [spr] (i.e. [sa]) in figure 1 of Motoyoshi et al. (1993). This point marks the low-temperature termination of the KMAS reaction, os = en + sil + kfs + qz (sa, grt, L, bt, crd), which is also a degenerate KMASH-system reaction. The invariant point involves cordierite, which must be anhydrous as the KMAS-system is anhydrous. Figure 7.11 shows that the [sa, grt, L, bt] point must lie above the KFMASH (bt, sa, crd) reaction, which is constrained, according to the experiments of Audibert et al. (1994), to lie at just under 11kb at 950°C (figure 7.10). The best estimate of the high-pressure stability

---

[13] Audibert et al. (1994) did use carbon capsules potentially allowing the stabilisation of cordierite to higher pressures by the incorporation of CO_2 (see section 7.3). However, the reaction limiting the stability of garnet-osumilite does not involve cordierite and would be unaffected, but this reaction is also placed at significantly higher pressures than in this study. Motoyoshi et al. (1993) used platinum capsules.

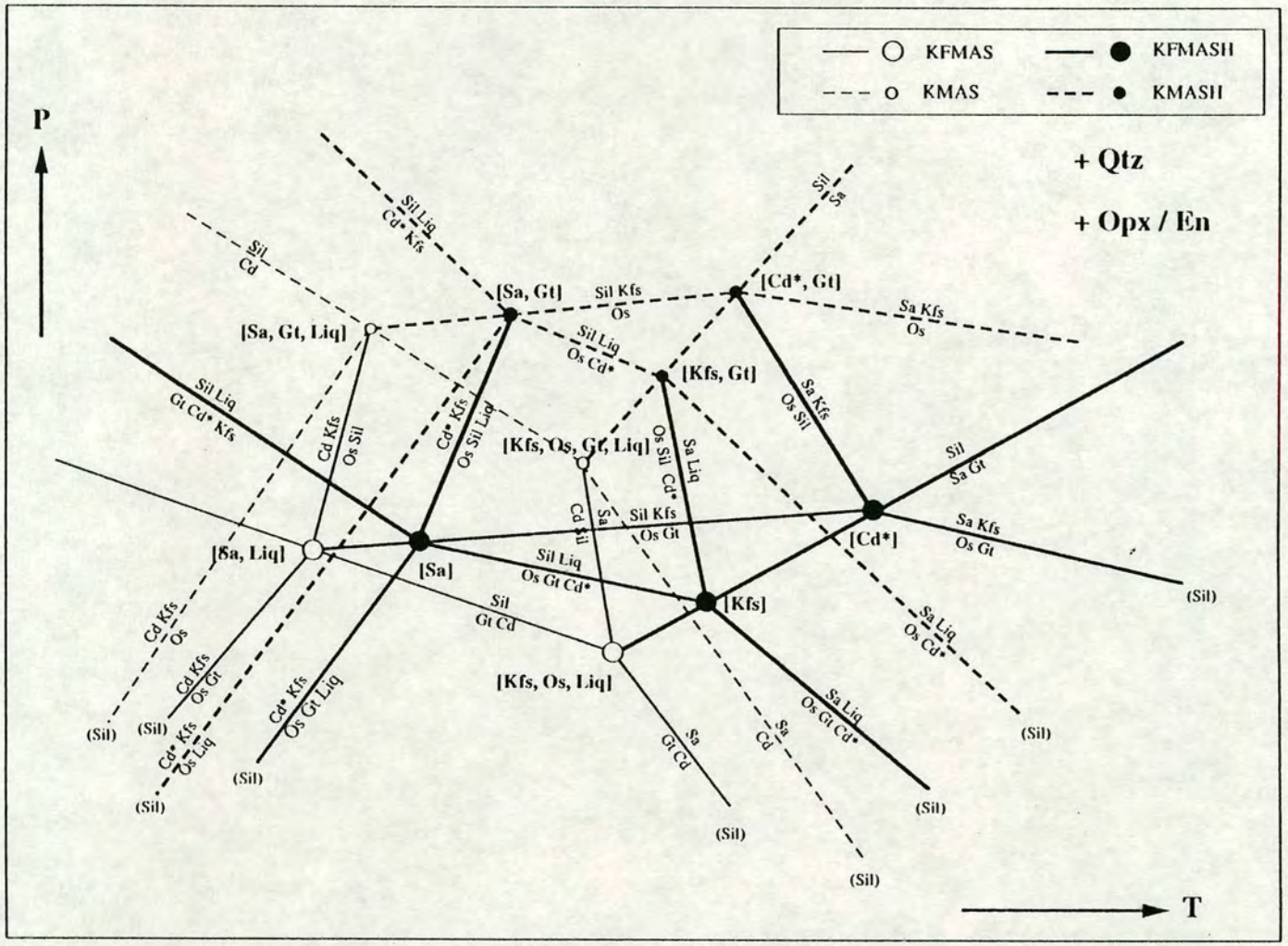

Figure 7.11. Reproduced from Audibert et al. (figure 3, 1994). Theoretical pressure -temperature diagram showing the phase relations with with quartz and orthopyroxene in excess, in the KFMASH (heavy solid lines), KFMAS (solid lines, after Grew, 1982). Dashed lines represent the iron-free sub-systems. "crd*" = water-undersaturated cordierite. "crd" - anhydrous cordierite.

limit of anhydrous cordierite at 950°C is 8.2kb (Newton 1972). Therefore the grid of Audibert et al. (1994) requires the stability of anhydrous cordierite at least 3kb above its high-pressure stability limit. The authors are aware of this contradiction and suggest the [sa, grt, L, bt] point lies at temperatures below 950°C. However, given that osumilite is only found in rocks formed at high-temperature (>850°C), this requires extreme curvature of the KMAS reaction os = en + sil + kfs + qz, which Motoyoshi et al. (1993) found to have zero dP/dT from 975 to 1100°C.

7.4.3 Combined osumilite phase relations using all the experimental data.

It seems very likely that the experimental pressure estimates of Audibert et al. (1994) are too high and that this results from an underestimated friction correction. The fact that the experimental temperatures of Audibert et al. (1994) match well with this study suggests that the underestimated friction correction is the sole cause of the pressure discrepancy. Another cause might well affect temperature as well as pressure. If this is the case then, if the pressures were adjusted, the results of that study could be combined with the current results. The minimum reduction in pressure necessary is 2kb, if the (bt, sa, crd) reaction of Audibert et al. (1994) is re-drawn with a higher dP/dT (figure 7.10). With this -2kb correction applied, the results of Audibert et al. (1994) are combined with the results of the current study, and a grid is drawn (figure 7.12).

The KMASH experiments of Motoyoshi et al. (1993) constrain the high pressure stability limit of magnesium osumilite, which breaks down via the degenerate (KMAS) reaction osumilite = enstatite + sillimanite + K-feldspar + quartz. The experiments were conducted using a similar cell to that of Audibert et al. (1994) and may therefore have also produced overestimated pressure estimates. Unfortunately, their experiments cannot be directly compared with the current experiments as no iron-free mixes were used in this study. However, extrapolation of the data of Chatterjee and Schreyer (1972) on the MAS system reaction sapphirine + quartz = enstatite + sillimanite[14] can be used to show that the required correction to the pressures of Mototyoshi et al. (1993) is less than that for Audibert et al. (1994). Due to compositional degeneracies, this MAS-system reaction passes through the KMASH invariant points [bt, crd, grt] and [bt, kfs, grt] (figure 7.12). The terminal

[14] The data of Chatterjee and Schreyer (1972) is believed to be reliable as the cell used was calibrated for pressure at 16.3kb and 600°C (see Seifert in Johannes et al. 1971), which is close to the run pressures in the study.

Figure 7.12. Interpretative pressure-temperature grid for the KFMASH- and KMASH-systems and degenerate systems arising from them. The phase relations below 1000°C are based on KFMASH-system experimental results from this study (INSERT A). The phase relations above 1000°C are based on experimental data from Audibert et al. (KFMASH, 1994) and Motoyoshi et al. (KMASH, 1993), though their experimental pressures have been reduced by 2kb and 0.75kb respectively (see text). Therefore, above 1000°C, the pressures are only approximate. The position of the MAS system reaction, enstatite + sillimanite = sapphirine + quartz, which passes through the [bt, crd, grt] and [bt, kfs, grt] points is extrapolated from the data of Chatterjee and Schreyer (1972). Phase-absent notation labels have been omitted for clarity but can easily be determined using the full list of phases given.

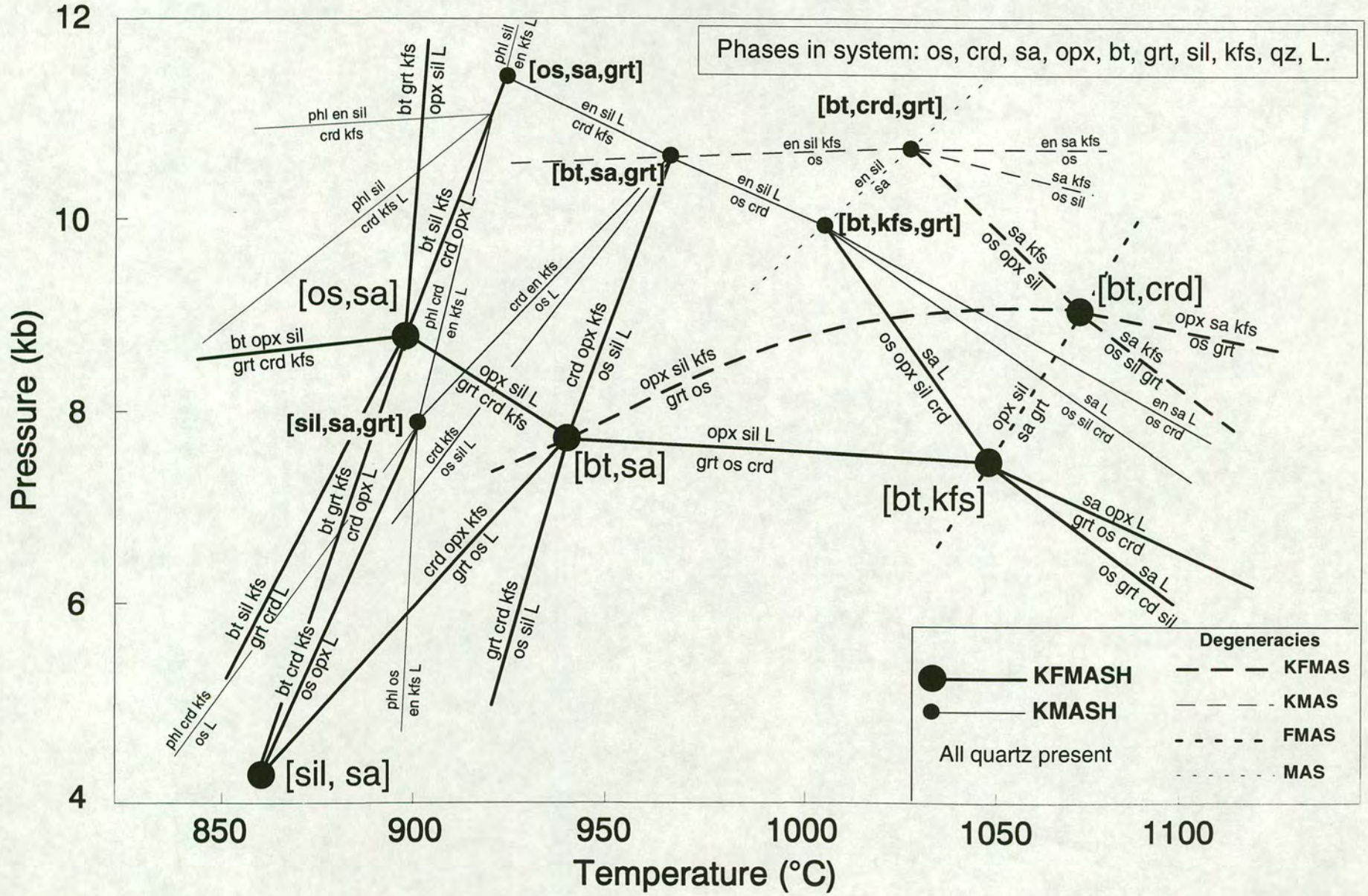
Phases in system: os, crd, sa, opx, bt, grt, sil, kfs, qz, L.
[os,sa,grt]
[bt,crd,grt]
[bt,sa,grt]
[bt,kfs,grt]
[os,sa]
[bt,crd]
[sil,sa,grt]
[bt,sa]
[bt,kfs]
[sil, sa]
phl en sil
crd kfs
bt grt kfs
opx sil L
phl sil
en kfs L
en sil L
crd kfs
en sil kfs
os
en sa kfs
os
sa kfs
os sil
en sil
sa
en sil L
os crd
sa kfs
os opx sil
bt sil kfs
crd opx L
phl sil
crd kfs L
bt opx sil
grt crd kfs
phl crd
en kfs L
crd en kfs
os L
crd opx kfs
os sil L
opx sil kfs
grt os
opx sil L
grt crd kfs
os opx sil crd
sa L
opx sa kfs
os grt
sa kfs
os sil grt
en sa L
os crd
opx sil
sa grt
sa L
os sil crd
opx sil L
grt os crd
bt grt kfs
crd opx L
bt sil kfs
grt crd L
crd kfs
os sil L
crd opx kfs
grt os L
bt crd kfs
os opx L
grt crd kfs
os sil L
phl os
en kfs L
phl crd kfs
os L
sa opx L
grt os crd
sa L
os grt cd sil
Degeneracies
KFMASH
KMASH
All quartz present
KFMAS
KMAS
FMAS
MAS
Pressure (kb)
12
10
8
6
4
Temperature (°C)
850
900
950
1000
1050
1100

osumilite reaction positioned by Motoyoshi et al. (1993) also passes through the [bt, crd, grt] point and has a very small dP/dT. Therefore, it must lie at around 10.75kb, which is 0.75kb below the estimate of Motoyoshi et al. (1993). This suggests that the friction correction used by Mototyoshi et al. (1993) was too small, but was not as large an underestimate as that made by Audibert et al. (1994). The reason for this difference is difficult to determine as neither study give diagrams of the cells used. The cell diameter is the only difference stated, 12.7mm for Motoyoshi et al. (1993) but 12.7mm *or* 19mm for Audibert et al. (1994). Alternatively, the extrapolation of the data of Chatterjee and Schreyer (1972) could be at fault (the lowest temperature reversal is at 1140 ± 10°C, 15kb) or the data itself could affected by the use of ideal stoichiometry sapphirine ($Mg_2Al_4SiO_{10}$) rather than a more realistic aluminous sapphirine.

The grid combining the experimental data from the current study and that of Audibert et al. (1994) and Motoyoshi et al. (1993) (figure 7.12) covers a large area of pressure-temperature space (850-1100°C, 5-12.5kb) and provides a powerful tool for the interpretation of high-grade metapelites. Figure 7.13 shows how pressure-temperature space can be divided into six fields each of which is defined by the stability of a simple diagnostic assemblage. The six KFMASH assemblages are listed below:

1. biotite-sillimanite-(± K-feldspar),
2. garnet-cordierite-K-feldspar,
3. orthopyroxene-sillimanite-melt,
4. garnet-osumilite-melt,
5. sapphirine-melt,
6. sapphirine-K-feldspar,

- all with quartz.

It should be remembered that the assemblages listed above are merely convenient for use with natural rocks. Other KFMASH assemblages also provide pressure-temperature constraints, e.g. cordierite-orthopyroxene-K-feldspar-quartz which cannot exist above 950°C at 9kb, 880°C at 5kb. This assemblage is important in natural rocks as a breakdown product after osumilite. The use of the phase diagrams in interpreting natural rocks, and the potential effects of the extra components present in the natural system is the subject of the next chapter.

Figure 7.13. Pressure-temperature diagram adapted from figure 7.12 showing the stability fields of six assemblages.

1. biotite-sillimanite-quartz (brown).
2. garnet-cordierite-K-feldspar-quartz (blue).
3. orthopyroxene-sillimanite-quartz-melt (red).
4. garnet-osumilite-quartz-melt (green).
5. sapphirine-quartz-melt (yellow).
6. sapphirine-K-feldspar-quartz (purple).

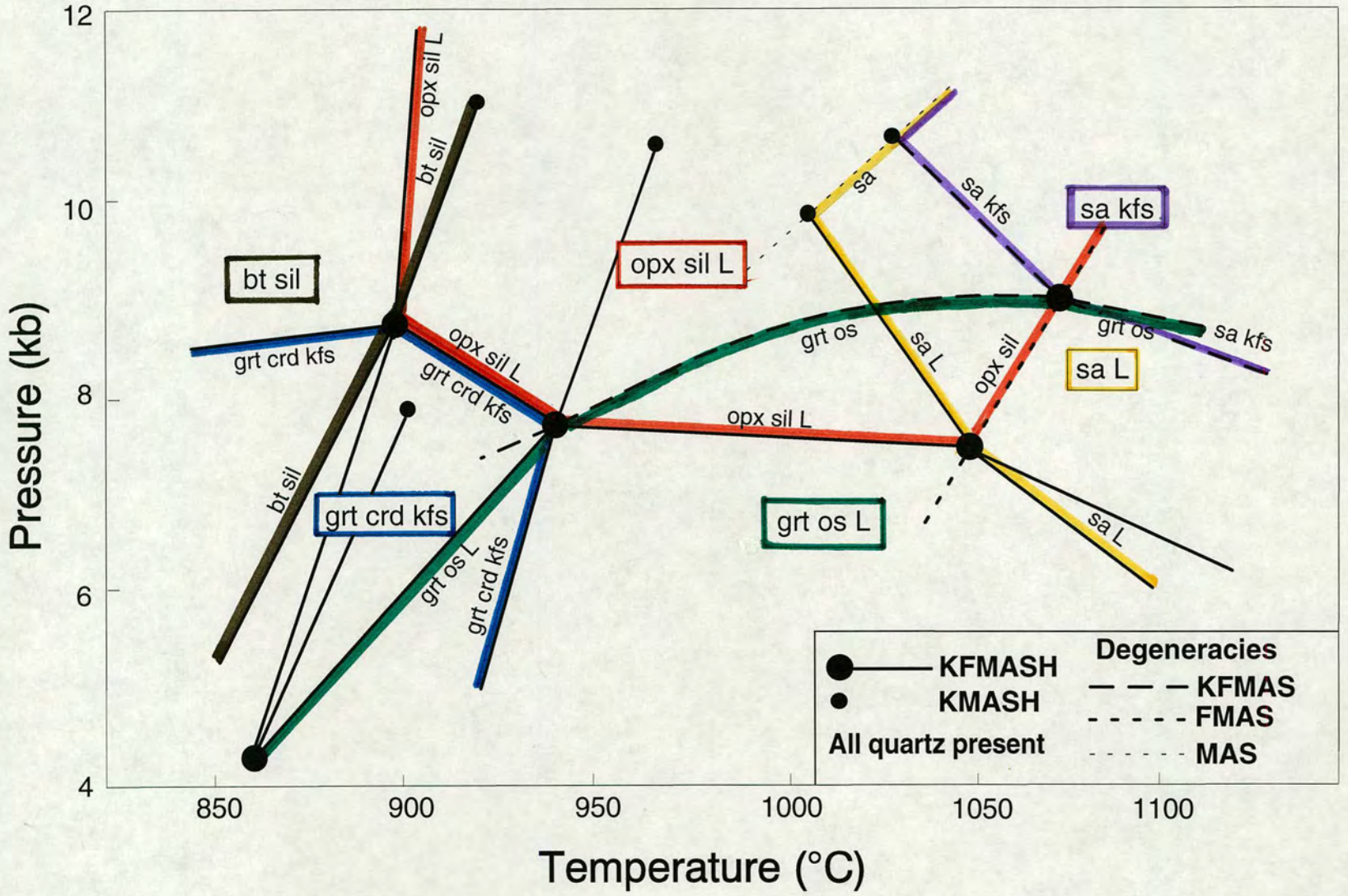
Pressure (kb)
12
10
8
6
4
850
900
950
1000
1050
1100
Temperature (°C)
bt sil
opx sil L
grt crd kfs
grt os L
sa kfs
sa L
KFMASH
KMASH
All quartz present
Degeneracies
KFMAS
FMAS
MAS

Chapter Eight.

APPLICATIONS OF PHASE DIAGRAMS TO NATURAL ROCKS.

Chapter Eight. Application of phase diagrams to natural rocks.

8.1. INTRODUCTION AND SYNOPSIS OF CHAPTER.

This chapter aims to illustrate the use of the phase relations derived in this thesis in estimating the pressure-temperature conditions of formation of some natural rocks. Cation exchange geothermometers and geobarometers are generally reset by re-equilibration after peak conditions and therefore usually give temperatures lower than estimates from phase assemblage constraints. For example, garnet-orthopyroxene Fe-Mg exchange geothermometry in the Napier Complex, Antarctica give temperatures around 900°C, rising towards 1000°C only when minimum K_D values are used, and even then in only three out of 42 cases (Harley and Hensen 1990). However, the regional occurrence of reduced sapphirine-quartz assemblages requires a minimum temperature of 1025°C (Hensen and Green, 1973, Chatterjee and Schreyer 1972). Therefore, phase relation data is particularly suited to constraining peak metamorphic conditions.

The grids derived here (INSERTS A, C, D, E, F) define the stability fields of many distinctive assemblages for rocks of appropriate composition which might not only give pressure-temperature estimates but also P-T-t path constraints. The natural rock data used in this chapter are from published studies which can only summarise the details of the occurrences, particularly phase and bulk compositions, and the interpretations made here are limited as a consequence of this. The grids will provide even more powerful constraints when studies are undertaken in the knowledge of what the most useful assemblages are, as these can then be specifically searched for. It is also important to obtain good bulk composition data to enable the judicious use of pseudosections.

An important assumption made in the application of the current phase relations at higher temperatures is that melt is present. Melts are not always easily identified in natural terrains as they may segregate and migrate away if the melt fraction is large. If only a small amount of melt was present it may crystallise back to phases which were previously present. These segregations may be too small to be unambiguously interpreted as melt. However, water will partition preferentially into a melt over other phases, in particular cordierite (see section 3.6.3). In many cases there will be no other hydrous phases. Therefore, if *any* water is present in a rock at a temperature

above the solidus, there will be some melt present. As it is very unlikely that any rock is *totally* anhydrous the assumption of a ubiquitous melt phase seems reasonable. It should be remembered that, in respect of phase relations, it is the presence or absence of melt which is crucial: the amount of melt is irrelevant[1].

The phase relations were derived in this study in the KFMASH system. It is therefore very important to be aware that reactions may well have different pressure-temperature positions when considered in the natural system, because of the effective addition of extra components. The most important elements omitted from the KFMASH system are sodium, calcium and titanium. Sodium will stabilise melt, alkali feldspar and osumilite, in that order. Calcium will form plagioclase and stabilise garnet, though most garnets in high-grade metapelitic granulites have very low grossular contents. In garnet-absent rocks calcium will be contained in plagioclase and fractionate only slightly into the melt. Titanium (and fluorine) can stabilise biotite to high temperatures and may result in formation of rutile or ilmenite. These considerations allow qualitative assessment of the effect of extra components.

	Original		**Revised**			
	P (kb)	**T (°C)**	**P (kb)**	**T (°C)**		
Nain	~5	645-915	4.5-5.0	840-880	Aureole	Low Fe
Namaqualand	~5	>800	5.5-6.5	840-900	Regional	High Fe^{3+}
SHBPGI	6.7-10	825-1000	7-10	900-950	Aureole	High Fe^{3+}
Rogaland	4 or 6-7	750-1000	4-5	875-1000	Aureole	High Fe^{3+}
Tula Mts, NC	6-9	IBC	<8kb	IBC	Regional	Low Fe
Scott Mts, NC	8-11	IBC	>8kb	IBC	Regional	Low Fe
Reference Peak, NC	~9kb	<1020	9-10kb	1030-1050	Regional	Low Fe

Table 8.1. Original pressure-temperature estimates for terrains considered in this chapter and revised estimates based on the current phase relation data for magnesian metapelites.
The type of terrain is specified: regional metamorphism or contact aureole metamorphism; high $(Mg^{2+}/Mg^{2+} + Fe^{2+})$ in rock due to low total iron contents ("low Fe") or due to oxidation of large proportion of iron to Fe^{3+} ("high Fe^{3+}"). SHBPGI - Sand Hill Big Pond Gabbronorite Intrusion. NC - Napier Complex, Antarctica. IBC - Isobaric cooling path delineated by rocks.

[1] Mouri et al. (1993) derived a KFMASH univariant grid based on that of Hensen and Harley (1990) but involving melt-absent equilibria. At high temperatures they state that the water present is held exclusively in cordierite. Section 3.6.3 shows that the partitioning coefficient of water between melt and cordierite undoubtedly favours the melt (K_w>1) and so the grid of Mouri et al. (1993) cannot be correct.

It is often possible for the KFMASH relations to place maximum or minimum constraints on natural rocks because the effect of extra components can only either lower or raise the position of the reaction.

An extra component will only lead to an increase in the variance of the system if no new phase is associated with it. Therefore, calcium (plagioclase), titanium (rutile/ilmenite) and sometimes ferric iron (magnetite) are unlikely to cause an increase in variance. Sodium, however, is not generally associated with a new phase and therefore, the presence of sodium is likely to lead to an extra degree of freedom.

A summary of the original pressure-temperature estimates for terrains considered in this chapter and revised estimates based on the current phase relation data for magnesian metapelites is given in table 8.1.

Two types of occurrences are distinguished in table 8.1 - contact aureole metamorphic terrains and regional metamorphic terrains, but no special correlations of phase assemblage with type of occurrence has been observed. Indeed, some phase assemblages have been found in both types: e.g. spinel-osumilite in Rogaland and Namaqualand (Kars et al. 1980, Waters 1991). All the rocks considered in this chapter have high $Mg/Mg^{2+}+ Fe^{2+}$ ratios but for two types of reason. Firstly there may be very little iron at all in the rock or, secondly, most of the iron present may be oxidised to ferric iron. Again, either can occur in contact or regionally metamorphosed terrains (table 8.1). A high ferric iron content will stabilise magnetite, but as spinel was not considered in this study the effect of its presence cannot be judged. Hensen (1986) showed that at high values of fO_2 metapelite phase relations could invert. However, this seems not to have occurred in the occurrences considered here as the low-fO_2 phase relations derived in this study adequately account for all the data.

8.2. NAIN COMPLEX, LABRADOR, CANADA AND NAMAQUALAND, SOUTH AFRICA.

Berg and Wheeler (1976) reported the first high-pressure[2] occurrence of osumilite from the contact aureole of the anorthositic Nain complex, Labrador, Canada. The osumilite occurs in an assemblage of cordierite-orthopyroxene-K-feldspar-quartz-plagioclase and nearby rocks contain the assemblage garnet-cordierite-orthopyroxene-K-feldspar-quartz-plagioclase (figure 8.1). Pyrrhotite, ilmenite and sometimes graphite are accessory phases. The bulk composition of the osumilite-bearing rock, whilst containing more alumina and less silica, is broadly similar to those used in the current experiments (BW, table 8.1). Calcium and sodium are the only major omissions from the synthetic experimental compositions and the potential effects of these are considered below. The rock has a bulk X_{Mg} of 0.67 which suggests the M62 or M74 pseudosections may be applicable.

Berg (1977) used garnet-cordierite and orthopyroxene-olivine-quartz assemblages to estimate the range of pressure-temperature conditions through the aureole as 645-915°C, 3.7-6.6 kb. Berg and Wheeler (1976) believed the osumilite-bearing assemblage formed at the hot end of the temperature range. The geographical distribution of the pressure estimates was systematic and the isobars defined an arch structure. The samples (2-625 and 2-1833) closest to the osumilite-bearing rock (2-1817) give pressures of 4.7 and 5.0 respectively (figure 10a, Berg 1977; figure 1, Berg and Wheeler 1976).

The osumilite-bearing (os-crd-opx-kfs-qz) and osumilite-absent (grt-crd-opx-kfs-qz) rock assemblages from the Nain aureole must occur between the (sil, grt) and (bt, sil) univariant reactions in the KFMASH system (INSERT A). At pressures of 4.7-5.0kb, as estimated by Berg (1977), this gives a very restricted temperature range in the KFMASH system. Experiment D51-17 (tables 3.1 and 4.1), run at 875°C and 5kb, produced the same assemblage as the natural osumilite-bearing rock and figure 8.1 shows the excellent correspondence of phase compositions. The phase compositions from the experiment are slightly higher suggesting a slightly higher pressure or temperature.

---

[2] The four previously reported occurrences came from erupted rhyolites or rhyodacites (Sakkabira, Japan; Monte Arci, Sardinia; Obsidian Cliffs, Oregon) and a fused hornfels (Tieveragh, Northern Ireland). The pressures of formation of each of these occurrences is less than 1kb. See Berg and Wheeler (1976) for references.

	M62	M74	M86	A90	REF	BW	AG1	AG2
SiO_2	66.00	67.13	68.44	70.45	75.46	57.14	51.05	70.35
TiO_2	0	0	0	0	0.53	0.08	1.17	0.57
Al_2O_3	18.84	18.73	18.40	15.73	13.94	22.26	21.88	14.80
Fe_2O_3	n.d.	n.d.	n.d.	n.d.	n.d.	n.d.	9.25	3.58
FeO	4.74	3.15	1.65	1.58	0.75	6.18	4.21	1.50
MgO	4.42	5.02	5.73	7.70	3.35	6.82	4.59	1.35
MnO	0	0	0	0	0.01	0.09	0.14	0.08
CaO	0.09	0.06	0.06	0	1.79	4.12	3.33	1.84
K_2O	4.95	4.97	4.81	4.54	1.12	1.16	0.49	2.84
Na_2O	0	0	0	0	3.02	2.203	2.44	2.45
P_2O_5	0	0	0	0	0.03	n.d.	0.06	0.08
H_2O	0.89	0.87	0.86	n.d.	n.d.	n.d.	n.d.	n.d.
Total	99.92	99.93	99.96	100.00	100.00	100.00	98.61	99.44
X_{Mg}	0.625	0.740	0.861	0.897	0.888	0.663	0.66	0.62

Table 8.2. Bulk compositions of rocks and experimental mixes.
M62, M74 and M86: synthetic compositions, this study. Determined by electron microprobe analysis of glasses and modal calculation.
A90: synthetic composition, Audibert et al. (1993). Method of determination not stated.
REF: Reference Peak, Antarctica, Grew (1982). Iron originally given as Fe_2O_3. Determined by X-ray fluorescence (XRF) analysis.
BW: Nain complex, Canada, Berg & Wheeler (1976). Calculated from given modes and compositions of phases, excluding 3.9 vol% graphite and 6.8 vol% alteration.
AG1 (sample 315c, osumilite-bearing) & **AG2** (sample 246, osumilite absent): Sand Hill Big Pond gabbronorite intrusion aureole, Canada, Arima & Gower (1991). Determined by XRF analysis. Method of determination of Fe^{2+}/Fe^{3+} ratio not stated.
N.B. $X_{Mg} = Mg/(Mg + Fe^{2+})$. "n.d." - not determined. "0" - not present in synthetic system.

D51-17 retained a small number of the garnet seeds whilst the Nain osumilite-bearing rock contained no garnet, despite having a lower bulk X_{Mg}. However, the seeds had very thin rims suggesting the experiment lay close to the low-pressure stability limit for that phase. In a composition with a bulk X_{Mg} of 0.70 (HG2, table 7.2) Hensen and Green (1970) also found the garnet low-pressure limit to lie at around 5kb at 900°C, although with relatively grossular--rich compositions compared to this study. Therefore, the pressure-temperature (P-T) conditions of formation of the Nain osumilite-bearing rock are interpreted to be close to, but slightly lower than D51-17, and in the garnet-absent field. This is consistent with the slight differences in the phase X_{Mg}'s. Figure 8.2b illustrates how the os-crd-opx-kfs-L divariant field, of large extent on the M86 pseudosection, may be present at low pressures on the M74 pseudosections. This field cannot extend down pressure below 4kb as the [sil] point

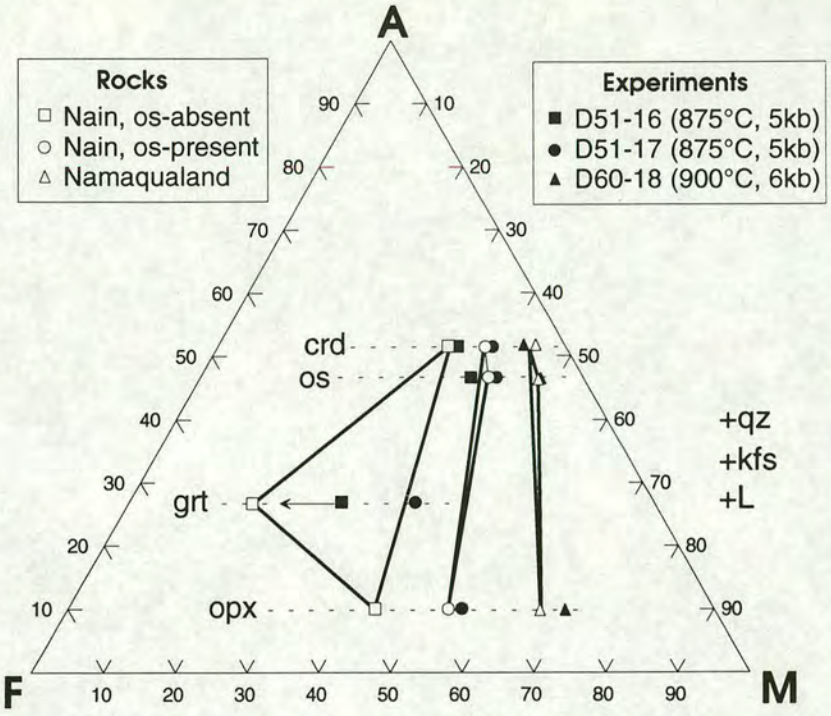

Figure 8.1. Three-component AFM projection comparing natural phase assemblages from the contact aureole of the Nain Complex, Labrador (Berg and Wheeler 1976) and from Namaqualand (figure 2c, Waters 1991) with the closest-matching results of experiments in this study. Full compositional data was not available for all the phases and so each phase is plotted at a constant A/AFM ratio (dotted lines). Garnet did not equilibrate well in many of the current experiments and it is likely that the garnets in D51-16 and D51-17 have too high an X_{Mg} (arrow).

intervenes on the grid derived in this study (INSERT A). The M62 pseudosection (figure 8.2a) can account for the Nain osumilite-absent assemblage, in the same P-T position as the osumilite-present rock. The P-T estimate for the Nain rocks based on the KFMASH phase relations from this study is 850-880°C, 4.5-5.0kb.

The assemblage os-crd-opx-kfs-qz has also been reported from Namaqualand (figure 2c, Waters 1991) but the co-existing phases have much higher X_{Mg}'s (figure 8.1) and these suggest that the M86 pseudosection may be applicable. The assemblage must certainly have formed at lower temperatures than the (bt, sil) reaction. The phase compositions from the rock are closely matched by those from D60-18, which was run at 900°C, 6kb. The AFM diagram presented by Waters (1991) shows the cordierite to have a higher X_{Mg} than the osumilite, but whether this is genuine or a result of projection from a hydrous phase is not given. Fluorine-rich biotite co-exists with the assemblage and a melt is almost certainly present also (Waters and Whales

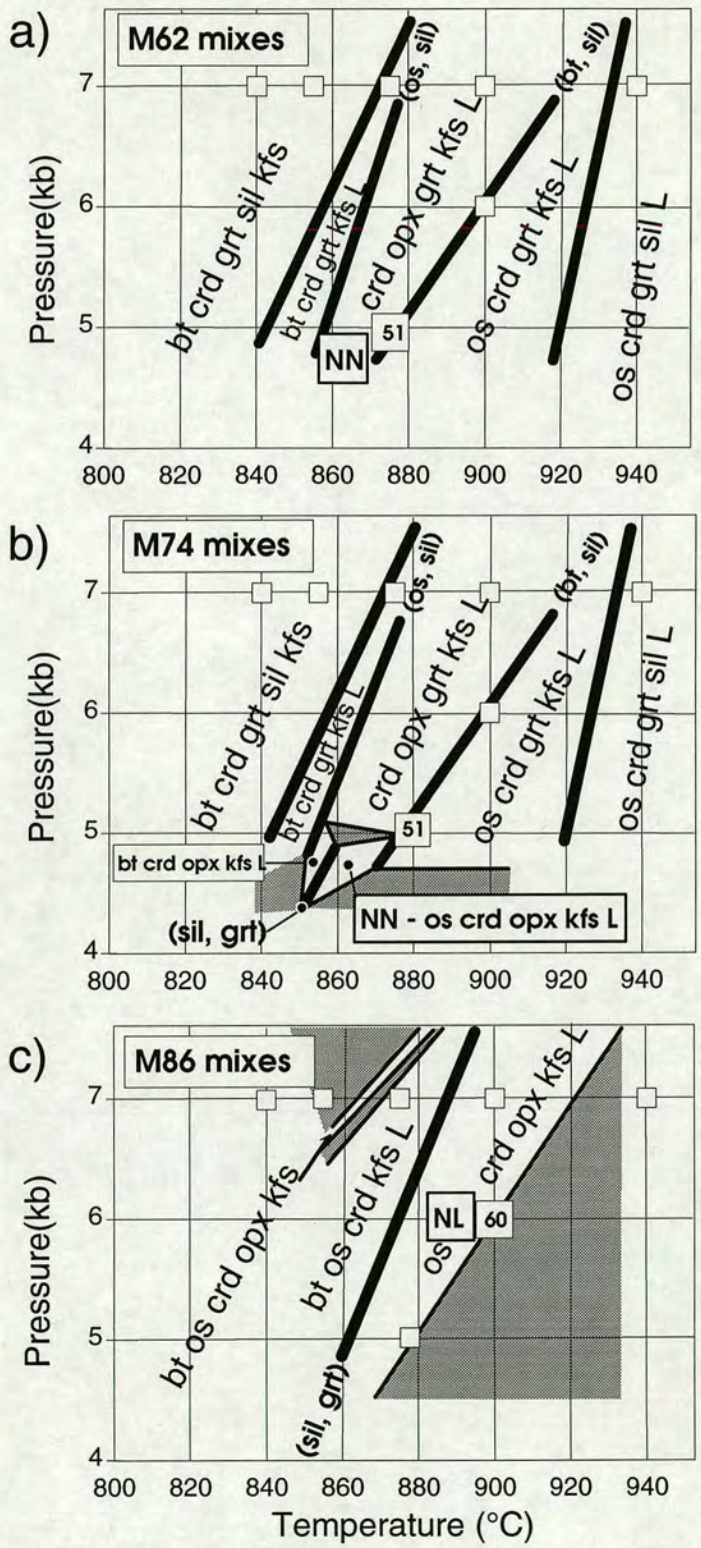

Figure 8.2. Details of the KFMASH pseudosections derived for the a) M62, b) M74 and c) M86 mixes (figures 6.13, 6.14 and 6.15) showing the interpreted positions of the rocks from the Nain complex contact aureole (NN, Berg and Wheeler 1976) and from Namaqualand (NL, Waters 1991). Also shown are the positions of the experimental runs D51 and D60. The small squares are the position of other experiments. In figure 8.2c, the (sil, grt) reactions is not used as a low-T limit as the biotite present in the rock had a high fluorine content which could considerably alter its stability. The low-T limit used is the position of the solidus near 840°C.

1986, Waters 1988). This would place the assemblage on the KFMASH (sil, grt) reaction. However, the presence of other components will make this reaction at least divariant in reality and the biotite will be stabilised up temperature by the fluorine (and titanium) it contains. Therefore, the interpreted position of the Namaqualand osumilite gneiss is placed near experiment D60-18 and ignores the fluorine rich biotite. The P-T estimate based on this is 840 (solidus)-900°C, 5.5-6.5kb, and considerably improves the estimate given by Waters (1988) of higher than 800°C at about 5kb.

The effect of sodium and calcium on the P-T estimates for the Nain and Namaqualand occurrences will depend on the displacement of the KFMASH relations these components cause. Calcium will stabilise garnet, but will be mostly present in plagioclase. The (sil, grt) reaction will therefore be unaffected. The (sil, bt) reaction would be shifted to lower temperatures, but as this reaction is the upper temperature limit, this will not broaden the P-T estimates. Sodium will partition into the melt most strongly, then the alkali feldspar and the osumilite. Therefore, the (sil, bt) reaction will again be shifted down temperature and will not broaden the P-T estimates. The (sil, grt) reaction would also shift down temperature with the addition of sodium but this reaction involves biotite, which is very likely to be stabilised up temperature by titanium and fluorine. The stabilisation of biotite is very strong (section 7.2) and would probably compensate for the effect of the sodium. The above considerations suggest that the P-T estimates are reasonable as given.

8.3 SAND HILL BIG POND GABBRONORITE INTRUSION AUREOLE, LABRADOR, CANADA .

Metamorphic osumilite was reported by Arima and Gower (1991) from a group of granulite-facies metasedimentary gneisses found in the aureole of the Sand Hill Big Pond gabbronorite intrusion (SHBPGI). A range of garnet-absent assemblages were found, virtually all of which occur on the M86 pseudosection (INSERT E). Arima and Gower (1991) give limited bulk rock XRF data, some of which is reproduced in table 8.2, and state that the total range of bulk X_{Mg} = 0.64-0.88[3].

[3] $X_{Mg} = Mg^{2+}/Mg^{2+} + Fe^{2+}$. As will be seen below, the rocks from the SHBPGI aureole formed at a high enough pressure for garnet to be stable at the lower end of the X_{Mg} range 0.64-0.88 but none is reported from the rocks. The high values of X_{Mg} result from high ferric-iron contents (hematite and magnetite are ubiquitously present) but the method of Fe^{3+}/Fe^{2+} determination is not given by Arima and Gower (1991). It is possible that the actual ferric-iron content is higher than estimated, so that the bulk X_{Mg} of all the rocks is too high for garnet to form.

The assemblages found enabled Arima and Gower (1991) to interpret a series of four KMAS or KMASH system reactions which accounted for the evolution of the rocks towards the intrusion. These reactions correspond exactly[4] to four KMASH reactions shown on INSERT F. The reactions emanate down pressure from the [os, sa, grt] and [bt, sa, grt] invariant points. In the KFMASH system these become divariant reactions and these are shown on an adapted version of the M86 pseudosection as reactions 1 to 4 (figure 8.3). Reactions 1 and 4 do not appear on the pseudosection derived for the M86 mixes as suitable bulk compositions were not used in these

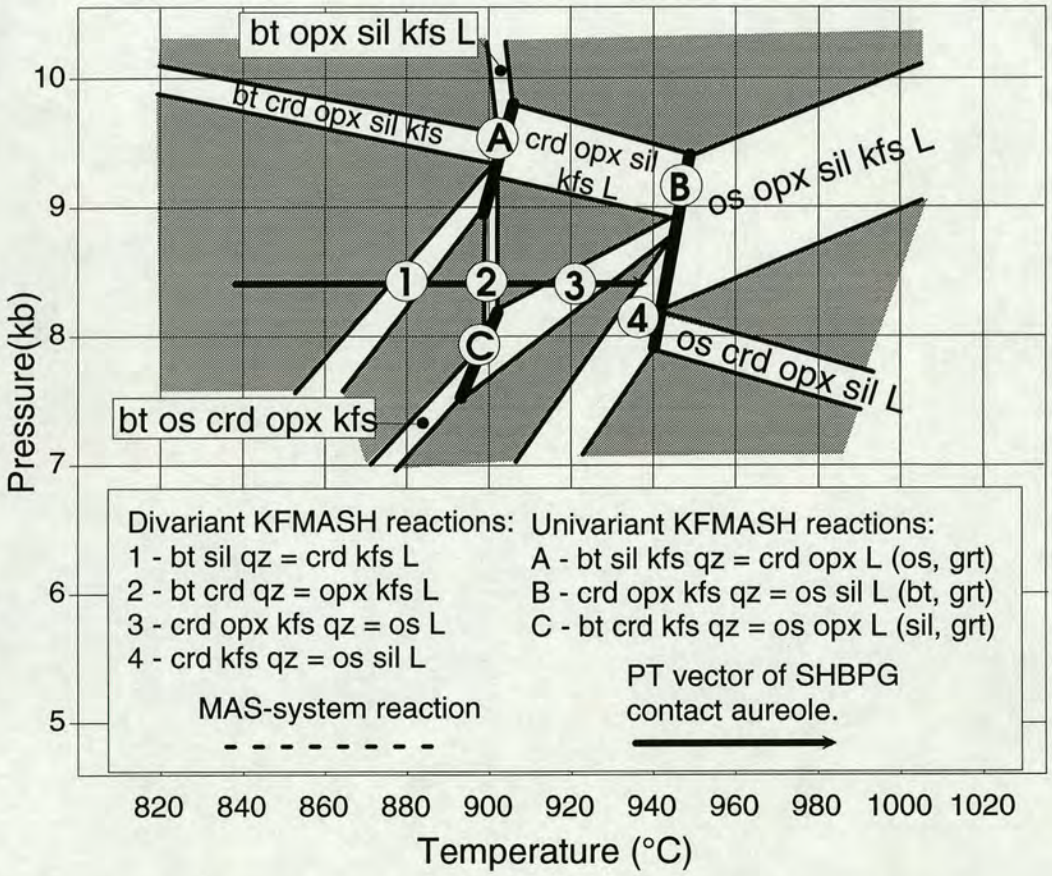

Figure 8.3. Pressure-temperature pseudosection for the SHBPGI aureole. Reactions 1 to 4 were interpreted by Arima and Gower (1991) from the rocks found in the aureole. The highest grade assemblage found corresponds to the KFMASH univariant reaction B, which will be at least divariant in the natural system. The pseudosection is adapted from INSERT E using the KMASH reactions shown on figure 7.12.

[4] Arima and Gower (1991) did not consider the possibility of a melt phase but noted that the bulk compositions became more silica-poor as the intrusion became nearer. Comparison of AG1, from near the intrusion, and AG2 (table 8.2), from further away, certainly suggests the original presence, and then removal, of a silica-rich melt from AG1.

experiments. Arima and Gower (1991) considered nearly sixty samples and therefore, presumably, a reasonable range of bulk compositions. This enabled the detection of all the reactions shown although a single rock may not have seen them all. For this reason, the pseudosection in figure 8.3 is not likely to be apply strictly to a single composition, although it is topologically correct. It is, however, a useful illustration.

According to figure 8.3, the highest grade unambiguous assemblage found is os-crd-opx-sil-kfs-qz (sample 354b). This is equivalent to the KFMASH univariant reaction B (figure 8.3) which would become at least divariant in the natural system. An isobaric path up-temperature to this reaction crosses the four reactions identified by Arima and Gower (1991) and suggests that temperatures in the area of the aureole sampled ranged from 850°C up to 950°C next to the intrusion. The assemblage in sample 354b formed above the temperature where biotite is lost, i.e. 900°C (figure 8.3). This is a good minimum estimate as natural biotites will be stabilised to higher temperatures relative to synthetic KFMASH biotites.

The upper pressure limit is constrained by the near ubiquitous presence of cordierite. The maximum stability of water-saturated magnesium cordierite is 11.2kb (Newton 1972). The electron microprobe analysis totals for cordierites close to the SHBPG intrusion are all between 99.3 and 99.9wt%, suggesting low volatile contents which will reduce the stability of cordierite, as will the small but significant iron-content (X_{Mg}=0.90-0.92). Experiments near univariant reaction B (figure 8.3) produced cordierites with very similar X_{Mg}'s but lower oxide totals, e.g. cordierite in D54-18, X_{Mg}=0.91, 98.2wt%. These should be stable to higher pressures than the SHBPGI aureole cordierite. In the experiments cordierite was lost between 9kb and 10kb and the higher pressure is used as an upper limit on the SHBPGI aureole rocks. The low pressure limit is constrained by the position of the [bt] point at 7.0-8.1kb (INSERT A, section 6.3.3) because the assemblage from sample 354b lies on reaction B (figure 8.3) which terminates down pressure at this invariant point. The assemblage must therefore have formed at a pressure above the invariant point.

Arima and Gower (1991) did not constrain the pressure and temperature conditions of the aureole further than stating that the peak conditions lay near an MAS invariant point involving enstatite, cordierite, sapphirine, sillimanite and quartz. This point was positioned at 825-950°C, 6.7-7.5kb by Newton et al. (1974) and about 1000°C,

10kb by Hensen (1987)[5]. The phase relations derived in this study constrain the rocks in the aureole of the SHBPGI to have formed at temperatures rising from 850°C to 950°C next to the intrusion at a pressure between 7kb and 10kb. This pressure bracket is generous and the preferred pressure estimate is 8.5kb (figure 8.3). The temperature of the peak assemblage lies between 900 and 950°C. There is no evidence to suggest that the rocks exposed at the surface were not formed at a single pressure.

The absence of garnet means that the addition of calcium to the system will largely be confined to plagioclase and will not significantly affect the P-T positions of the reactions. As in section 8.2, addition of sodium will lower the temperature of the reactions and so the phase relations used here provide good maximum temperature estimates.

8.4 ROGALAND, NORWAY.

Osumilite was reported from the contact aureole of the Rogaland anorthositic igneous complex by Maijer et al. (1977). Despite many studies of the area since that time, little data exists on the mineral assemblages present and their evolution. Original garnet-biotite-sillimanite-plagioclase-perthite-quartz assemblages give way to cordierite-orthopyroxene-spinel-plagioclase-perthite-quartz assemblages, also with osumilite nearer the pluton (Kars et al. 1980). As spinel was not included in the current study the assemblages cannot be constrained using the phase diagrams derived here, but remembering that D51-16 (875°C, 5kb) contained a trace of spinel, it is likely that the peak Rogaland assemblages formed below 5kb and near the [sil] point (INSERT A). Spinel occurs frequently in the Rogaland assemblages, as it does in the Namaqualand assemblages (Waters 1988, 1991).

The only assemblage for which compositional data was also reported was garnet-osumilite-orthopyroxene-K-feldspar-quartz (figure 4b, Waters 1991). The garnet has an X_{Mg} of 0.38, the orthopyroxene, 0.59, and the osumilite, 0.79. This assemblage does not appear on the current pseudosections as the experimental compositions used

[5] The P-T conditions estimated here suggest this MAS point lies at the high temperature end of the estimate of Newton et al. (1974). The pressure of the point as determined by Newton et al. (1974) is probably correct for the volatile-free cordierite they use. If volatile-bearing cordierite is considered the point becomes a MASH point and will lie at higher pressure.

have too high alumina contents, stabilising garnet-cordierite-osumilite instead (e.g. 60-17A, Appendix Three and INSERT D). D51-17 (5kb, 875°C) contains osumilite of X_{Mg} = 0.78 and orthopyroxene of X_{Mg} = 0.61, which compare favourably with the real phase compositions. The stability field of the garnet-osumilite assemblage is highlighted on figure 7.13 and shows that, at 5kb, the osumilite must have formed at temperatures above 875°C. It should be remembered that sodium and calcium present in the natural system will move the garnet-osumilite bounding reaction up and down temperature respectively.

Conventional geothermometry and geobarometry for the Rogaland rocks has not been very successful due to extensive re-equilibration of phases in later, lower grade metamorphic events (Jansen et al. 1985). The rocks are believed to have been formed at temperatures rising from 750 to 1000°C near the intrusions (Kars et al. 1980, Maijer et al. 1981, Jansen et al. 1985) at pressures of 4kb (Jansen et al. 1985) or 6-7kb (Henry 1974). No constraints on the peak conditions are given. The discussion above shows that the phase relations derived in this study constrain the P-T conditions of the Rogaland rocks to lie below 5kb and above 875°C.

8.5 NAPIER COMPLEX, EAST ANTARCTICA.

The regional occurrence of osumilite in magnesian pelites from the Napier Complex, in association with orthopyroxene-sillimanite-quartz, sapphirine-quartz and spinel-quartz assemblages, has stimulated interest in the high-grade phase relations of such rocks for many years. (Dallwitz 1968, Sheraton et al. 1980, Ellis 1980, Ellis et al. 1980, Grew, 1980, 1982, Motoyoshi and Hensen 1989, Harley and Hensen 1990, Hensen and Motoyoshi 1991). Harley and Hensen (figure 12.3c, 1990) summarised the pressure estimates made by Ellis (1980), Harley (1983, 1985), Ellis and Green (1985) and Sandiford (1985). The pressure increases from 5kb in the north to 11kb in the south of the Napier Complex with the interpreted isobars running roughly east-west. The temperature estimates are fairly even over the south-west part of the terrain (where the pressure varies from 7-11kb) and all the estimates imply very high-grade conditions: garnet-orthopyroxene geothermometers, 900-1000°C maximum; exsolved and inverted pigeonites in meta-ironstones, 970-1020°C; alkali-feldspar mesoperthites, ~1000°C (refs. in Harley and Hensen 1990, p329-331). The phase relations derived in this study enable these P-T estimates to be assessed and refined.

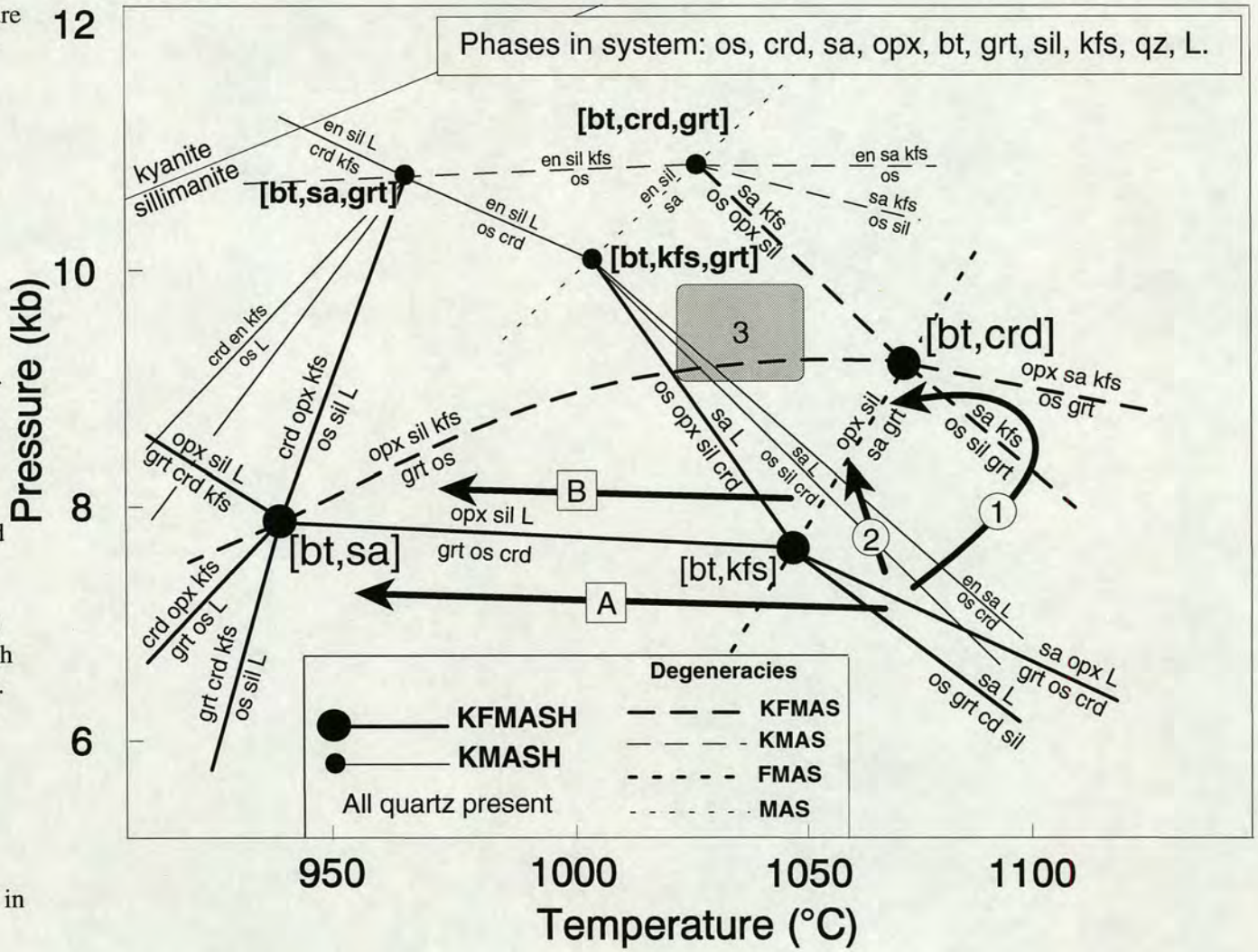

Figure 8.4. Pressure-temperature grid of KFMASH and simple-system reactions showing the P-T range of the Napier Complex, Antarctica (detail of figure 7.12). Paths A and B are schematic paths for the Tula Mountains and Scott Mountains respectively (Harley and Hensen 1990). P-T paths 1 and 2 are alternative interpretations of the rocks reported from Mt Riiser-Larsen (Motoyoshi and Hensen 1989, Hensen and Motoyoshi 1991).
1- assumes sa-kfs assemblage not significantly affected by high sodium content of the feldspar. 2 - recognises sa-kfs assemblage is stabilised to lower temperatures by a high sodium content in the feldspar. Path 2 is more consistent with geobarometric data given by (Harley and Hensen 1990). Shaded field 3 represents the approximate P-T location of the peak assemblages at Reference Peak as determined in section 8.4.2.

8.5.1 Pressure of formation of orthopyroxene-sillimanite and garnet-cordierite coronas after sapphirine-quartz assemblages.

Harley and Hensen (1990) noted that sapphirine-quartz assemblages in the Tula mountains (central-part of the Napier complex) were generally replaced by coronas involving garnet and cordierite whereas the same assemblages in the Scott Mountains (southern-part of the Napier complex) were replaced by coronas involving orthopyroxene-sillimanite. These observations suggest that the Tula Mountains and Scott Mountains cooled at pressures below and above the reactions separating garnet -cordierite and orthopyroxene-sillimanite-quartz respectively. However, Harley and Hensen (figure 12.4, 1990) placed the FMAS system reaction, garnet + cordierite = orthopyroxene + sillimanite + quartz at about 11kb, based on the data of Bertrand et al. (1991) which was shown previously to apply only to pure FMAS vapour-saturated systems (section 7.3). The current data places the analogous water-undersaturated KFMASH reactions[6] at 8-9kb (figure 7.7). This is in good agreement with the 8kb isobar lying between the Tula and Scott Mountains on figure 12.3c of Harley and Hensen (1990) and therefore the current data is in good agreement with the natural-rock barometric estimates. The position of the reactions and schematic cooling paths are shown in figure 8.4. A significant calcium-content in garnet would move the (bt, sa, kfs) reaction up pressure (c.f. section 7.3) but this might be partially offset by the partitioning of sodium into the melt.

8.5.2 The high pressure stability limit of osumilite.

The high-pressure stability limit of osumilite is an important constraint on the P-T conditions prevalent in the Napier complex. Osumilite is always the most magnesian phase in these rocks and therefore pure magnesium osumilite will be stable to higher pressures than osumilite with a lower X_{Mg}. Motoyoshi et al. (1993) found the high-pressure limit of Mg-osumilite to be at 11.5kb but it was shown in section 7.4.3 that their KMASH experiments probably overestimated pressures and an estimate of 10.75kb is preferred here. The osumilite-out isograd for rocks in the Napier complex lies close to 9kb according to Harley and Hensen (1990). Motoyoshi et al. (1993) thought this difference might be the result of errors in the geobarometry but it is more likely that the small iron-contents reduce the pressure stability of the natural

---

[6] At lower temperatures the appropriate KFMASH reaction is grt + crd + kfs + qz = opx + sil + L (os, bt, sa). At higher temperatures the reaction is garnet + osumilite + cordierite = orthopyroxene + sillimanite + quartz + melt (bt, sa, kfs) (figure 8.4 and 7.7)

osumilites. Alternatively, even the revised Mg-osumilite stability limit pressure of 10.75kb may be too high.

An osumilite-orthopyroxene-sillimanite-quartz assemblage[7] from Reference Peak in the Scott Mountains (Grew 1982) enables the P-T estimates for rocks near the osumilite-out isograd in the Napier Complex to be further constrained. The phases in

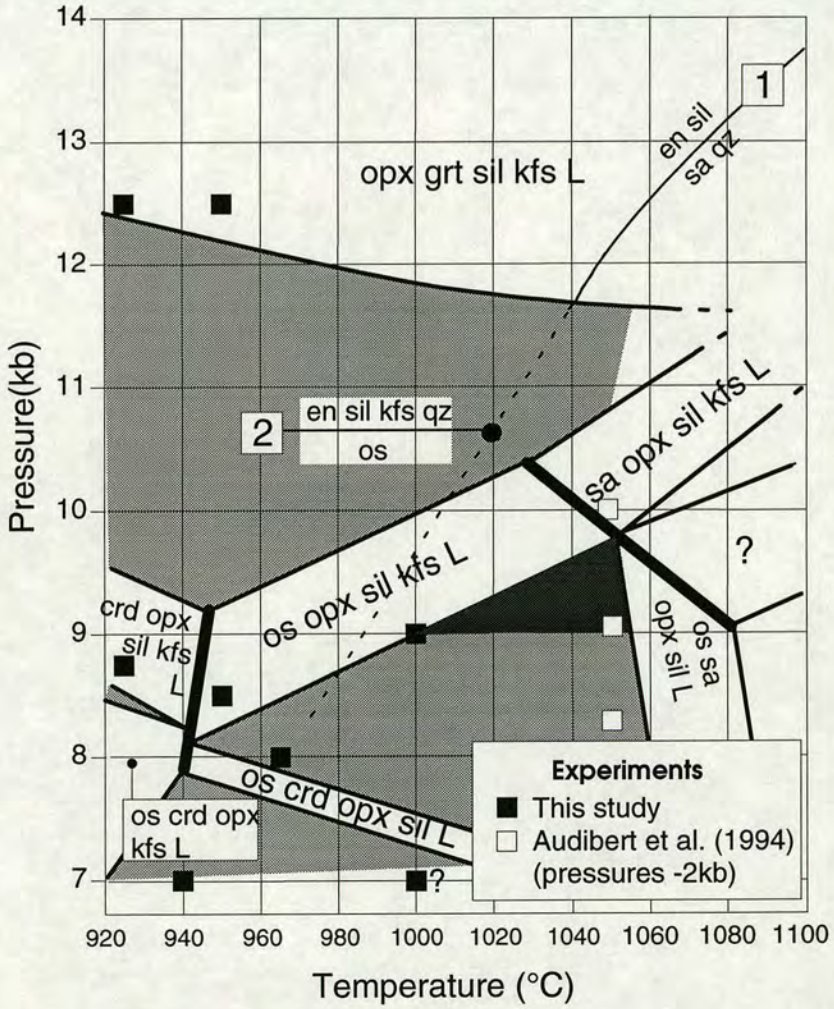

Figure 8.5. Pressure-temperature pseudosection for M86 mixes, extrapolated from figure 6.15 to include the phase relations derived in figure 7.12. The Reference Peak assemblage (os-opx-sil-qz) must lie an area higher pressure and/or temperature than the experiment at 1000°C, 9kb and in the os-opx-sil-qz trivariant field. This area is shaded dark grey. Reaction 1 - the MAS system reaction enstatite + sillimanite = sapphirine and quartz (extrapolated from Chatterjee and Schreyer 1972). Reaction 2 - osumilite = enstatite + sillimanite + K-feldspar + quartz (adjusted down pressure from Motoyoshi et al. 1993, see figure 7.12).

[7] This assemblage was also interpreted to have been stable in rocks from southern Algeria (Audibert et al. (1993).

the assemblage are extremely magnesian, with the X_{Mg} of osumilite being 0.97 and that of orthopyroxene being 0.92. This suggests the rock is near the KMASH high-pressure limit of osumilite. High temperatures are also suggested as Grew (1980) reported the sapphirine-quartz assemblage from a different sample from Reference Peak[8], although only 1 vol% sapphirine was present. The bulk composition of the osumilite-bearing sample (REF, table 8.2) is well approximated by the M86 mix used in this study. Figure 8.5 shows the maximum stability range of the divariant osumilite-orthopyroxene-sillimanite-K-feldspar-quartz assemblage for the M86 compositions but the Reference Peak assemblage does not include K-feldspar and must therefore lie in the trivariant field stable at lower pressures. However, the fact that osumilite and orthopyroxene formed in the experiment at 1000°C, 9kb (D65-18A) had X_{Mg}'s of 0.94 and 0.89 respectively, i.e. lower than those for the Reference Peak rock, means that the Reference Peak assemblage must have formed at a higher pressure and/or temperature. Also, the occurrence of sapphirine-quartz requires the P-T conditions to be above the trace of the (bt, kfs, grt) reaction (INSERT F). Therefore, the P-T estimate for Reference Peak based on figure 8.5 is 1030-1050°C, 9-10kb and, given the high X_{Mg}'s of the phases, the P-T estimate of Harley and Hensen (1990) of <1020°C, 9kb appears to be a little low. The involvement of sodium in the natural system could cause this discrepancy. The stability limit of Mg-osumilite cannot lie very far above that for X_{Mg}=0.97 osumilite and therefore probably lies between 10kb and 10.75kb (c.f. section 7.4).

The foregoing discussion assumes the presence of melt in the rocks during the main metamorphism in the Napier Complex. It was argued at the beginning of this chapter that this would generally be the case, and had to be if cordierite containing water was present. However, large areas of the Napier Complex contain no cordierite and therefore, in the absence of field evidence for melting, the possibility remains that no melt was present and the grids used are not strictly applicable.

8.5.3 Prograde path of metamorphism of the Napier Complex.

Sapphirine-orthopyroxene-quartz symplectites from Mount Riiser-Larsen, in the central part of the Napier Complex, have been interpreted as pseudomorphs after cordierite which formed near peak metamorphic conditions (Motoyoshi and

[8] The sapphirine-quartz assemblage from Reference Peak could only be stable at higher temperatures than the MAS system reaction enstatite + sillimanite = sapphirine + quartz shown on figure 8.5 (and extrapolated from Chatterjee and Schreyer 1972).

Matsueda 1984, Motoyoshi and Hensen 1989). This texture indicates a rise in pressure and was used to support the proposal of an anti-clockwise P-T-t prograde path (Motoyoshi and Hensen 1989). Furthermore, sapphirine-K-feldspar-quartz assemblages, replaced by garnet-osumilite-sillimanite, from Mt. Riiser-Larsen (Hensen and Motoyoshi 1992) imply that the rise in pressure was accompanied by a rise in temperature. This interpretation is shown in figure 8.4 (arrowed path 1). Osumilite plays only a minor role in the phase relations of these rocks as they are rather poor in potassium.

Hensen and Motoyoshi (1992) proposed that the anti-clockwise P-T-t path might result from the intrusion of hot magmas above the present level of erosion, i.e. to the north of the Napier Complex as it is now oriented. This would act to at least smooth out the geotherm so that the crust between 7 and 11kb was nearly isothermal[9] and perhaps even to invert the geotherm such that the lower levels (i.e. southern parts) of the Napier Complex were cooler. This hypothesis is consistent with the occurrence of the osumilite-orthopyroxene-sillimanite-quartz assemblage from Reference Peak (southern Napier Complex, higher pressure, Grew 1982, Harley and Hensen 1990) which must have formed below the stability of sapphirine-K-feldspar-quartz (field 3, figure 8.4). The negative dP/dT of the sapphirine-K-feldspar-quartz limiting reactions means that the rocks at Mt Riiser-Larsen may have experienced higher temperatures than those at Reference Peak. However, there are some difficulties with this hypothesis.

The geobarometry of Harley and Hensen (1990) implies that Mt. Riiser-Larsen experienced pressures between 7 and 8kb at peak metamorphism. Figure 8.4 shows that, at reasonable temperatures, a minimum pressure of 9kb is required to stabilise the sapphirine-K-feldspar-quartz assemblage in the KFMASH system (and the field is drawn at a maximum). The reason for the discrepancy lies in the composition of the feldspars which, at Mt. Riiser-Larsen, are not potassium-rich alkali-feldspars but usually contain around 40-60% albite-component (Motoyoshi and Matsueda 1984, S.L.Harley pers. comm.). The effect of sodium on the KFMASH system will be to expand the stability fields of assemblages containing alkali-feldspars at the expense of osumilite-bearing assemblages. This would expand the sapphirine-K-feldspar-quartz field down temperature and negate the necessity for a temperature rise and for pressures in excess of those estimated by Harley and Hensen (1990). P-T path 2

[9] An isothermal peak temperature over this pressure range was proposed by Harley (1983, 1985) and Harley and Black (1987).

(figure 8.4) demonstrates this and is therefore preferred as the P-T-t path of the assemblages at Mt. Riiser-Larsen.

Path 2 (figure 8.4) does require the more northerly regions of the Napier Complex (Reference Peak) to be at higher pressure but does not require them to be at lower temperature and so the magmatic "overplating" hypothesis of Hensen and Motoyoshi (1991) remains unproved. A temperature difference between the higher pressure and lower pressure regions of the Napier complex is still possible but must be smaller than the resolution observable with current methods of temperature estimation. Nonetheless, the new phase relations for osumilite presented here support the >1000°C temperatures invoked by previous work.

8.6 CONCLUSIONS.

The examples presented briefly above demonstrate the ability of the phase relations derived in this thesis, sometimes in combination with the data of Audibert et al. (1994, with pressures reduced by 2kb), to place useful constraints on the pressure-temperature conditions of formation of natural rocks. This has been possible solely from published data. It is anticipated that the KFMASH grids will prove even more useful in future studies in which vital assemblages and bulk composition data can be deliberately sought.

Chapter Nine

SUMMARY OF CONCLUSIONS

Chapter Nine. Summary of Conclusions.

9.1 SUMMARY OF CONCLUSIONS.

This thesis reports the results and implications of an extensive experimental study of phase relations in high-grade magnesian metapelites. The conclusions drawn from the study are summarised in this chapter.

The data set was derived from sixty four experiments on synthetic KFMASH system magnesian metapelites. Mineral mixes of three bulk compositions were used, with bulk X_{Mg}'s of 0.62, 0.74 and 0.86. The mixes were run simultaneously at various pressures and temperatures in the range 840-1000°C, 5-12.5kb. Both solid-media (salt-cell) and gas-media apparatus were used. Reproducibility of results was demonstrated by duplicate runs in different apparatus (D49 and D66, 875°C, 5kb), although with slight differences in phase compositions, most probably due to small differences in the ambient fO_2 conditions (table 2.3). Pressure uncertainties were ± 0.5kb for the solid-media salt cells and ± 0.2kb for the gas bombs. Temperature uncertainties were ± 5°C for both types of apparatus (table 2.1).

Phase assemblages and compositions were determined by electron microprobe analysis (table 3.1, 3.2) and the results were considered in detail, so as to fully characterise the run products. Some aspects of the mineral chemistry added to current knowledge:

- In biotite, the substitution identified by Patino Douce et al. (1993),

  $$Al[6] = -0.66\ (Fe+Mg),$$

  was qualitatively confirmed to occur to the right with increasing temperature and decreasing pressure. The absolute concentration of Al[6] depends on the silica-content of the biotite which can be affected by data selection procedure.

- The cordierites formed in the experiments were potassic, containing up to 0.10 cations per formula unit (18 oxygens, table 3.7). Schreyer et al. (1990) believed this type of cordierite to be characteristic of very low pressure environments but the current experiments produced them up to 8.5kb. It is suggested here that potassic cordierites are characteristic of environments in which the crystals form rapidly and in the presence of highly mobile

potassium. The assertion of Putnis and Holland (1986) that the formation of indialite, the hexagonal polymorph of cordierite, could lead to overstepping of cordierite-forming reactions by up to 3kb is not supported by the current data. (Section 3.4.1).

• Osumilite occurred in twenty experiments and so a large data set of experimental osumilite compositions has been produced. The Tschermak substitution operates. (Table 3.8).

• The partitioning of iron and magnesium between melt and crystals observed in the current experiments is different to that reported by Ellis (1986) and cannot be explained by reasonable uncertainties. In the current experiments the ln K_D values are higher, i.e. the difference in the X_{Mg}'s of the phases is larger. In particular, the Fe-Mg partitioning between melt and garnet does not support the conclusion of Ellis (1986) that below 900°C at 10kb the partitioning reverses and the melt becomes more magnesian than co-existing garnet. (Figures 3.20, 3.21, 3.22).

• Comparison of the melt compositions measured here and those published in the literature show that many compositional trends determined by electron microprobe analysis may be partly the result of potassium volatilisation under too powerful an electron beam (figures 3.23, 3.25).

• The water-contents of the melt and the cordierite were estimated by modal analysis, theory-based modelling and Secondary Ion Mass Spectrometry. The estimates were consistent with each other and gave melt water-contents of between 1 and 4wt%, increasing with pressure and decreasing with temperature. The partitioning coefficient of water between melt and cordierite ($K_w=H_2O^L/H_2O^{crd}$) was found to be 3 ± 0.3 for a water-rich, though still water-undersaturated, experiment which is considerably lower than the values of 5 to 7 predicted for the water-saturated case, calculated from literature data (table 3.13).

The product assemblages of the experiments were not always interpreted to be the equilibrium assemblages. Interpretation of the experiments was made by graphical mass balance using three-component projections (table 4.1, 4.2). Uncertainties arising from incomplete or poor knowledge of some of the phase compositions were

not large enough to affect these interpretations. Five reversal experiments, allied with other considerations, indicated that the experiments had closely approached equilibrium, with the exception of those run well below the solidus (table 5.1).

The results of the experiments were used to construct and constrain a univariant KFMASH petrogenetic grid (INSERT A) and a pseudosection for each bulk composition (INSERTS C, D, E). Phase composition variation and its effect on reaction stoichiometries and therefore grid topology was considered and allowed an evaluation of the role of K-feldspar in biotite dehydration melting reactions. The role of this phase is determined by the H_2O/K_2O ratio of the melt relative to that of biotite. If the ratio for the melt is higher then K-feldspar will be a product and vice versa. In the current experiments K-feldspar is a reactant.

Three major geological implications of the grids were apparent.

a) Biotite dehydration melting reactions.

The positioning of univariant biotite dehydration melting reactions in pressure-temperature space for the first time enables a more informed discussion of the controls on biotite dehydration melting. This is because the pressure-temperature positions of the reactions do not depend on a_{H2O} or on composition in the KFMASH system and so provide a fixed starting point for the consideration of lower crustal processes. A simple model can account for the data published to date (Vielzeuf and Holloway 1988, Le Breton and Thompson 1988, Patino Douce and Johnston 1991).

In the model, the width of the divariant temperature interval, which starts at the onset of melting and finishes with the disappearance of biotite, is inversely proportional to the bulk X_{Mg} of the rock and may depend on the pressure at which melting occurs. For a given rock, the absolute position of the melting interval in temperature is determined principally by the concentration of stabilising elements in the biotite, i.e. titanium and fluorine: the higher the concentration, the higher temperature the melting interval. The effects of titanium- and fluorine-contents of biotite and bulk rock X_{Mg} are unlikely to operate entirely independently: high concentrations of stabilising elements may help to broaden the melting interval in the same way as lowering the bulk X_{Mg} would.

The amount of melt produced when biotite dehydration melting reactions run to completion depends primarily on the initial amount of biotite as this limits the bulk water-content, although this assumes that sufficient quartz and alkali-feldspar is present to allow maximum melting. Therefore, in rocks of similar biotite concentration and bulk composition, but with different X_{Mg}'s, a similar total amount of melt will be produced through dehydration melting. However, the temperature intervals over which the rocks melt will be different and so the incremental melt production will vary, i.e. the volume of melt produced for a given rise in temperature will vary. As melting intervals are narrower for more magnesian rocks, these compositions will have a higher incremental melt production.

b) Garnet-cordierite and orthopyroxene-sillimanite-quartz assemblages.

The relation of the garnet-cordierite and orthopyroxene-sillimanite-quartz assemblages has been clarified. The variety of stoichiometries cited for the reaction between these assemblages has been reflected in the wide range of pressure-temperature positions it has been assigned (table 7.4). In this study, the reaction has been rigorously defined, constrained and reversed in the KFMASH system as,

garnet + cordierite + K-feldspar + quartz = orthopyroxene + sillimanite + melt.

which runs from 900°C, 8.8kb to 1000°C, 7.8kb. The reaction is essentially a dehydration melting reaction involving cordierite and producing a denser assemblage and thus the constrained negative dP/dT is appropriate.

The pressure-temperature position of the reaction as determined in this study is lower than other estimates for several reasons. Firstly, the cordierite is water-undersaturated and therefore has a lower high-pressure stability limit than vapour-saturated cordierite (figure 7.7, Newton 1972, Bertrand et al. 1991). Secondly, the involvement of a hydrous, potassic melt (and K-feldspar) may lower the pressure of the reaction as water will partition more strongly in the melt than the cordierite. The presence of the alkalis, potassium and particularly sodium, would have a similar effect as they also partition preferentially into the melt. Thirdly, the current experiments are essentially calcium-free: studies using mixes containing calcium report grossular-contents in garnet of up to 10 mol% which appear to stabilise that mineral and so displace the reaction up pressure (Hensen and Green 1970, 1971, 1973).

c) The stability of osumilite.

The phase relations of osumilite derived from the experiments shows that the mineral has a wide stability range in magnesian metapelites. They also clarify previous theoretical work (Ellis et al. 1980, Grew 1982) and provide powerful comparisons with the recent experimental work of Audibert et al. (1994) which was conducted at higher, but overlapping, temperatures. The topologies derived in the studies are very similar, as are the temperature estimates of a shared invariant point, but the pressure estimates for this point differ by 2-4kb. The experiments of Audibert et al. (1994) require higher pressures than the current experiments. A cross-calibration experiment conducted in this study using a talc-pyrex cell analogous to that used by Audibert et al. (1994) shows that the friction correction for that cell has been underestimated by at least 10%. The true friction correction for the cell at the pressures at which it was used is at least -20%. With this taken into account, the phase relations from both studies can be combined to produce a grid of univariant KFMASH reactions covering the range 840-1100°C, 5-12.5kb for pelitic compositions (INSERT F). This allows subdivision of the granulite facies by six simple quartz-bearing assemblages (figure 7.13);

biotite-sillimanite,
garnet-cordierite-K-feldspar,
orthopyroxene-sillimanite,
garnet-osumilite-melt,
sapphirine-melt,
sapphirine-K-feldspar-melt.

The wide stability range of osumilite demonstrated in this study at high temperature crustal conditions raises a question: why have only six high pressure occurrences of osumilite ever been reported? The answer is likely to be the fact that osumilite is hard to distinguish in thin section as it has first order grey interference colours, moderate relief and weak cleavage and therefore simply has not been seen. Also, osumilite is a high temperature mineral and frequently replaced by symplectites of quartz-K-feldspar and cordierite or orthopyroxene or both. This may not have been recognised in the past as forming after osumilite.

The phase relations derived in this thesis are demonstrated to be very useful in constraining the pressure-temperature conditions of metamorphism through the consideration of natural metapelites from five localities. The phase relations are of use because many distinctive low-variance assemblages occur with small stability ranges which are limited by the univariant reactions. Cation exchange geothermometers and geobarometers can only recover closure temperatures and can easily be reset by re-equilibration after peak conditions. Well-constrained phase relations are therefore particularly useful in estimating peak conditions. For example, peak conditions for the rocks from the contact aureole of the Sand Hill Big Pond Gabbronorite Intrusion, Canada (Arima and Gower 1991) were previously thought to have equilibrated somewhere in the range 825-1000°C. The current phase relations require that the rocks formed in the range 900-950°C (table 8.1).

It is vital to be aware of the possible effects on the phase relations that elements present in the natural system but not in the KFMASH system may have. As partitioning behaviour can be confidently predicted, the shift a reaction will experience on addition of another element can be qualitatively accounted for. In optimum cases, all extra elements shift the reaction in one direction so the phase relations derived in the KFMASH provide firm maximum or minimum constraints.

Conclusion.

This thesis has achieved its aim of developing a well-constrained petrogenetic grid for granulite-facies metapelites. This grid, and the pseudosections of it, allow a better understanding of the process of biotite dehydration melting and redefines or clarifies several topics of recurring interest, e.g. the role of K-feldspar in biotite dehydration melting and the relationship between the garnet-cordierite and orthopyroxene-sillimanite-quartz assemblages. The grid shows that in magnesian metapelites osumilite will have a wide stability range at high temperatures and moderate pressures, in water-undersaturated conditions. The experiments show a striking similarity to some natural rocks and as a consequence the phase relations can be powerful geothermometers and geobarometers.

9.2. FUTURE WORK.

This study has produced the first fully-constrained, experimentally-based, petrogenetic grid applicable to the dehydration melting of metapelites and higher grade conditions but much remains to be elucidated. These areas of future interest are discussed below.

Addition of components to the KFMASH system: sodium and calcium.

The current study was conducted in the KFMASH system and the effect of other important elements, present in the natural system, has only been accounted for qualitatively. Further experiments to determine the effect on phase relations resulting from the addition of sodium would be particularly interesting. This is because sodium is the only major element missing from the KFMASH system whose addition would not be accompanied by the formation of a new phase. This would therefore add a degree of freedom and result in invariant points becoming univariant reactions, univariant reactions becoming divariant reactions and so on. The addition of further, extra elements would be compensated for by the stabilisation of an extra phase. Addition of calcium would stabilise plagioclase and titanium would stabilise rutile or ilmenite. Therefore, a KNFMASH system grid would be an excellent tool for application to natural rocks as it would have the same level of variance.

Titanium and fluorine in biotite.

The presence of high concentrations of titanium and fluorine in biotite increases its temperature stability markedly. For example, at 10kb, biotite with 5.38wt% TiO_2 and 1.29wt% fluorine persisted in the experiments of Patino Douce and Johnston (1991) to 975°C, at least 75°C beyond the terminal stability of pure KFMASH biotite, as determined by this study. No quantitative study of this effect has yet been published despite its obvious importance in determining the temperature of melting, and therefore melt productivity, in metapelites.

Phase relations at lower pressures: spinel.

Many granulite-facies rocks at lower pressures involve spinel and experiments to extend the grid to include spinel-bearing assemblages would be a very valuable addition. The resultant grid would be applicable to magnesian metapelites from

virtually all low-fO_2 granulite terrains. Some progress could be possible without new experimental data as assemblages from Rogaland and Namaqualand both involve spinel and osumilite. Natural data on stable phase assemblages could be sufficient to constrain some further phase relations. The minor occurrence spinel found in the lowest pressure experiment (D51-16, 5kb, 875°C) would provide a good starting point.

Further field studies.

The examples of applications of the phase relations to real rocks given in this study were based on published work. Future investigations should prove even more fruitful as the significant assemblages are now better known and all the appropriate data could be collected for important specimens, e.g. bulk composition data, phase composition data.

Cordierite as a fluid-monitor in lower crustal melting.

This thesis has emphasised the sometimes neglected fact that cordierite is a vapour-bearing mineral. This implies lower melt production from reactions which also produce cordierite and the production of melt from cordierite breakdown reactions. Furthermore, this is the first major study of phase relations involving water-undersaturated cordierites and they have been shown to have a lower high pressure stability limit than vapour-saturated cordierites. Cordierite has significant potential as an indicator of fluid activity during lower crustal melting. However, this use cannot be implemented in the absence of experimental data on the partitioning of water and CO_2 between melt and cordierite in water-undersaturated systems. Obtaining this experimental data by using Secondary Ion Mass Spectrometry to determine volatile contents is the aim of post-doctoral research I will be conducting at the University of Edinburgh.

APPENDICES

Appendix One - Technical problems in the development of a salt-cell for the solid-media apparatus.

The original salt-cell used in the laboratory at Edinburgh was designed to hold one capsule just below the thermocouple, separated from it by an alumina disc. To enable the cell to hold more capsules, without them lying outside the hot-spot, the alumina disc was removed and the capsules arranged radially, as illustrated in figure 2.1. However, the adapted cell failed initially and it took nearly thirty attempted runs to overcome the various problems listed below.

1) *Thermocouple failure*. Examination of the first few runs showed that when the salt became hot, it softened and dyked up the bore of the ceramic thermocouple (TC) sheath, thereby shearing the wire. Heating of the cell must begin at 2-3kb, if the target pressure is 10kb, because salt expands considerably up temperature. The salt becomes soft enough to flow at 300-500°C which coincides with a pressure of about 3-4kb. At these relatively low pressures the void space in the bore of the ceramic TC sheath has not closed down and the salt can dyke up it. Two solutions were found. The first involved shaving the edges of the TC sheath using a diamond wheel, exposing the bore and wires, up to the level of the pyrophyllite. The pyrophyllite closes down round the TC sheath at very low pressures and seals the open end of the bore. The second solution was to use mullite TC sheaths. These cannot support void space in the bore to same pressures as the harder ceramic TC sheaths and therefore close down around the wires before the salt softens.

2) *Furnace breakage*. This was the most difficult problem encountered. The removal of the alumina disc, which originally sat just below the TC, seemed to destabilise the cell. During the run-up, a point would be reached where the temperature would suddenly drop by a hundred degrees or so, but not return to zero, and then start to slowly rise again. The resistance of the cell rose sharply after the drop in temperature. "Post-mortem" examination of the cell showed that the furnace had been badly fractured and salt had dyked through the cracks. Presumably this resulted from an excessive end-load pressure on the furnace, perhaps resulting from the salt compacting more than the furnace. Several changes were required to solve this problem. First, the component lengths were altered so that the salt pieces were longer than the furnace. It was hoped that this would allow for differential compaction of the salt pieces and the furnace. The original furnace wall thickness was 0.75mm and it

proved necessary to increase this to 1.2mm to produce a stable furnace. However, increasing the cross-sectional area of the furnace decreases its resistance. The resistance of the furnace is inversely proportional to the current required to heat the cell and doubling the furnace thickness caused the required current to become excessive. Therefore, a new grade of carbon, with a higher intrinsic resistance, was bought and used. The final shorter, thicker, higher-resistance furnace was robust and no further furnace problems were encountered.

3) *Salt melting*. Run failures also occurred at high temperatures as the result of the salt melting and dyking through the furnace. These occurred between 60 and 80°C below the ideal melting temperature of salt. Dummy runs were conducted to find out when the salt melted at three different pressures. In these, the cell was kept at constant pressure and heated until it failed. The results are given in table A1.1.

Pressure (kb)	**Ideal Melting T (°C) (Bohlen 1984)**	**Actual Melting T (°C) (this study)**
12.5	1040	980
10	1000	930
8	960	880

Table A1.1. Ideal and actual melting temperatures of salt in the solid-media cells at different pressures.

The actual melting temperature of the salt is low probably because of the presence of impurities in the salt, particularly water. Water is used in the pressing of the salt components and, despite the components being dried in an oven for weeks or months, some water must remain trapped in the salt.

Conclusion

The final cell design was very reliable: eight runs were attempted using it and none failed. Other workers in the laboratory have also used it successfully. The cell's limitation to relatively low temperatures is unavoidable with the present design. I would recommend the salt-pyrex-boron nitride cell reported by Boettcher et al. (1981) for higher temperature work. The talc-pyrex cell tested in this study (figure 2.2) is not suitable for work under 15kb without rigorous calibration (see sections 2.3.1 and 7.4).

Appendix Two: The implementation of fO_2 sensors in a low-temperature, quartz-saturated system.

A2.1 Introduction.

An accurate knowledge of the prevailing fugacity of oxygen (fO_2) is very valuable in any experimental study. The fO_2 could be important in this study as it may affect phase stabilities and compositions. At high fO_2 complete topological inversion of the univariant grid occurs (Hensen 1986). Traditionally, the fO_2 in experiments has been controlled by the use of buffer assemblages such as nickel-nickel oxide. The successful use of a buffer is only guaranteed when a free fluid phase is present and is the same in the buffer assemblage and in the experimental charge. For this reason the control of fO_2 in fluid-undersaturated experiments by a buffer assemblage is not guaranteed and is therefore frequently unconstrained. However, a new technique has been reported recently which enables the accurate and precise *measurement* of fO_2 in fluid-undersaturated, partially molten experiments (Gudmundsson and Holloway 1989, 1993, Jamieson et al. 1992).

The propensity of iron to alloy with platinum has been known for several decades and has seriously hampered experimentalists using platinum sample containers with iron-bearing mixes. This results from a large negative deviation from ideality in the Fe-Pt system which results in a high concentration of iron in platinum even at low activities of iron (Grove 1981). The technique of fO_2 measurement described here utilises this phenomenon to positive effect.

The technique involves the placement of short lengths of very thin (0.025mm diameter) platinum wire directly into iron-bearing experimental mixes[1]. This results in the formation of Pt-Fe alloys. The activity-composition (a-x) relations for Pt-Fe alloys are straightforward and relatively well known and therefore the activity of iron-metal can be calculated from the alloy composition as determined by electron microprobe analysis. Writing an O_2-dependant reaction involving iron-metal allows the calculation of fO_2 if the activities of the other phases are known and the equilibrium constant is calculated from standard phase data.

---

[1] Loops of wire are used as they were easy to load into the capsules and enabled easy electron microprobe analysis: when the charge was mounted and polished such that a lengthwise cross-section was exposed, two sections of the wire are certain to be intersected.

In partially molten systems the wires are believed to form equilibrium Fe-Pt alloys very rapidly, perhaps as quickly as one hour (Dr. M.Pownceby, pers. comm.) and therefore problems of disequilibrium are very unlikely. It should be noted however that the rapidity of equilibration of the wire means that the calculated fO_2 only reflects the value of fO_2 when an experiment is quenched. If the run is a long one, the initial value of fO_2 may have been different.

The technique has only been reported for experiments containing platinum wires which reproduced the conditions of the mantle, i.e. mafic compositions, 1100-1400°C, 1 atmosphere to 20kb (Gudmundsson and Holloway 1989, 1993, Jamieson et al. 1992). This appendix reports the attempts made to develop an analogous technique applicable to silicic compositions at lower crustal conditions.

A2.2 Strategy of fO_2 calculation.

Choice of reaction and silicate phase activity models.

In order to calculate the fO_2 from an experiment containing a wire it is necessary to chose a reaction for which the activities of all the phases can be calculated. Both Grove (1981) and Van der Laan and Koster van Groos (1991) chose the reactions[2]:

$$2Fe + SiO_2 + O_2 = Fe_2SiO_4 \quad (1)$$
$$Fe + {}^1/_2O_2 = FeO \quad (2),$$

Jamieson et al. (1992) used the olivine-pyroxene-Fe reaction:

$$2FeSiO_3 + 2Fe + O_2 = 2Fe_2SiO_4 \quad (3).$$

Reaction 1 has the advantage of being independent of the ferrous to ferric (Fe^{2+}/Fe^{3+}) iron ratio but requires a formulation for a_{Ol} and the a_{SiO2} in the melt. Reaction 2 requires an approximation of the Fe^{2+}/Fe^{3+} ratio and but does not involve olivine.

---

[2] Their goal was a method of calculating the Pt-Fe alloy composition in equilibrium with given experimental P-T-fO_2-composition conditions so that iron loss during experiments could be minimised by the use of suitable alloys as sample containers. It is the reverse problem to that considered here.

Ideally, the reaction chosen should be independent of Fe^{2+}/Fe^{3+} ratio and should not require a formulation of activity for a component in the melt, as these data are not easily obtained. Reaction 3 satisfies these conditions.

The O_2-dependent reaction chosen for the current study must involve one of the iron-bearing phases which occur in the experiments, i.e. orthopyroxene, garnet, cordierite, osumilite or melt. Only orthopyroxene and garnet have well-reported a-x relations and therefore possible reactions are:

$$3Fe + Al_2SiO_5 + 2SiO_2 + {}^3/_2O_2 = Fe_3Al_2Si_3O_{12} \quad (4)$$
$$Fe + SiO_2 + {}^1/_2O_2 = FeSiO_3 \quad (5)$$

The use of reaction 4 involves almandine which is advantageous because garnet is ubiquitously present in the experiments which used the M62 and M74 mixes. The a-x relations for almandine have been described by Newton and Hasleton (1981). However, it also requires a knowledge of the activities of quartz and sillimanite which are only easily obtained when those phases are present, as then their activities are unity. All the experiments are quartz-saturated but not all have sillimanite in excess. Another problem is that the garnets in the current experiments did not always equilibrate well (see section 3.4.2).

The formation of orthoferrosilite, reaction 5, is the simplest reaction and only requires the co-existence of quartz and orthopyroxene in the experiments. This is the case for nearly all the experiments which used the M86 mixes but because of the iron-loss associated with the use of the wires, only the M62 mixes are suitable for the fO_2 calculations[3]. However, some of the experiments which used the M62 mix produced orthopyroxene. Activity-composition relations in orthopyroxenes have been widely studied (e.g. Williams 1971, Nielsen and Drake 1979, Harley 1984). The orthopyroxenes formed in the experiments in the present study are aluminous and the model of Harley (1984) may be most appropriate, especially as it considers the relevant temperature interval. The model presented by Harley (1984) treats Fe-Mg-Al orthopyroxenes as two-site regular solutions with reciprocal interaction across the sites included in the activity expressions. Other authors (e.g. Jamieson et al. 1992,

[3] A 4mm piece of 0.025mm-diameter platinum wire will take up 6.4% of the total iron from 9mg of M86 mix, if the alloy is 60 mol% iron. If the wire were palladium, it would take up 8.8% of the total iron. By contrast, for the M62 mixes the platinum wire takes up 1.0% of the total iron, the palladium wire 1.1%. In fact, the alloys were generally less than 40 mol% iron. Iron-loss of less than 1% from the M62 mixes was deemed acceptable.

Nielsen and Drake 1979) have concluded that ideal solution models adequately describe the a-x relations. In the calculations below an ideal on-site mixing model was used (from a computer programme written by Dr. T.J.B.Holland). Section 3.4.1 showed that the alumina-contents of the orthopyroxenes were too high to be at equilibrium and this could result in high X_{Mg}'s (Harley 1984), though section 3.4.2 shows this to be unlikely.

Choice of Fe-Pt alloy activity model.

The accurate knowledge of the a-x relation of iron-metal in the Pt-Fe alloy is central to this technique of fO_2 measurement. Jamieson et al. (1992), van der Laan and Koster van Groos (1991) and Grove (1981) used the empirical model of Heald (1967). The model is based on two sets of experiments. The experiments of Heald (1967) covered the range 1131-1347°C at 1 atmosphere and have proved to be very reliable. The most thorough study of the Pt-Fe a-x relation at high temperature (>1300°C) is Gudmundsson and Holloway (1993) which reports data very similar to that of Heald (1967), but less scattered and with better constrained uncertainties. In the temperature range 800-950°C, Heald (1967) used data from Sundaresen et al. (1963) to derive the a-x relation. However, in a similar temperature range (coincident with that of this study, 850-1000°C), Alcock and Kubik (1969) produce a different relation which has a greater deviation from ideality. They argue that Sundaresen et al. (1963) failed to account for the non-stoichiometry of the wustite coexisting in their experiments and did not account for the formation of magnetite. Alcock and Kubik (1969) also produced an a-x relation for Pd-Fe alloys in the same temperature range. The a-x relations reported by Alcock and Kubik (1969) for both Pd-Fe and Pt-Fe alloys are in good agreement with unpublished data obtained by Dr M. Pownceby (pers. comm.) and are therefore used here. The effect of pressure on the a_{Fe} in Pt-Fe alloy is small. The change in a_{Fe} from 1 bar to 20kb is equivalent to about $^1/_2 \log_{10}$ fO_2 units (Gudmundsson and Holloway 1989, 1993).

Calculation of the equilibrium constant.

The Gibbs free energy for the reaction (ΔG_r) was calculated as a function of pressure and temperature using the form of the standard thermodynamic relation given in Holland and Powell (1990) where the contribution of each end-member phase is;

$$\Delta_f H_{1,298} - TS_{1,298} + \int_{298}^{T} C_p dT - T\int_{298}^{T} \frac{C_p}{T} dT + [V_{1,298} + \alpha V(T-298)]P - \frac{\beta V}{2} P^2 \qquad (7).$$

The thermodynamic data was taken from the internally consistent data set published in the same paper. The sum of individual phase energy contributions is ΔG_r and this equals -RTlnK, where K is the equilibrium constant. The effect of temperature on the ΔG_r of reaction 5 at constant pressure is slight: ΔG_r = -412.8 kJ at 800°C compared to ΔG_r = -393.3 kJ at 950°C, both at 10Kb. The effect of pressure at constant temperature is negligible; ΔG_r of reaction 4 is -621.4kJ at 840°C, 12.5kb, for example.

Calculation of fO_2.

For experiments containing garnet, sillimanite and quartz (reaction 4), these values of ΔG_r were then used to calculate the value of fO_2 via the relation:

$$fO_2 = \sqrt{\frac{a_{alm}}{a_{Fe.} e^{-(\frac{\Delta G_r}{RT})}}} \qquad (8),$$

where a_{alm} is the activity of almandine in garnet and a_{Fe} is the activity of iron in the Fe-Pt alloy, both as calculated above.

Similarly, the relation used for experiments containing orthopyroxene and quartz (reaction 5) is:

$$fO_2 = \sqrt{\frac{a_{fs}}{a_{Fe.} e^{-(\frac{\Delta G_r}{RT})}}} \qquad (9),$$

where a_{fs} is the activity of orthoferrosilite in the orthopyroxene.

The parameter uncertainties used to calculate the uncertainty in the fO_2 were: ΔG_r - ± 2 standard deviations; T - ± 5°C; a_{fs} - ± 10%; a_{alm} - ± 10%; a_{Fe} - ± 20%. The standard deviations of the ΔG_r's were calculated using the uncertainties given by

Holland and Powell (1990) and were about 11.8kJ for reaction 4 and 7.5kJ for reaction 5.

A2.3 Platinum wires: subsolvus or supersolvus?

Platinum was used initially in this investigation because it was the only metal used in the published studies. The experiments run at or above 900°C produced wires which were homogeneous in composition suggesting a single phase solid solution (plate 10b and table A2.1). However, those run at lower temperatures (850-875°C) produced wires that were not homogeneous. These had iron-rich rims of one composition and an iron-poor centre of a different composition. The composition seemed to change abruptly from the rim to the centre (plate 10a and table A2.1), but investigation of this was limited by the analytical resolution of the electron microprobe. The abrupt zoning suggested that at the temperatures of those experiments a solvus was operating, i.e. there was not a single phase for the bulk alloy composition produced. Consultation of the data tables of Hultgren et al. (1973) confirmed this but their data suggests that the solvus persists to 1350°C for alloys with X_{Fe} of 0.20-0.60, a far higher temperature than 900°C. The reason for this contradiction is not understood. The change from zoned to homogeneous wires also coincides with the solidus and so the zoned wires may simply have failed to equilibrate in the absence of a melt. However, the data of Hultgren et al. (1973) still require the homogeneous alloys to have formed below the solvus. Small amounts of silver (0.2-0.9wt%) were present in the Fe-Pt alloys derived from the silver-palladium capsule metal and perhaps this affected the equilibrium.

A2.4. Results of platinum wire experiments.

The results of the platinum wire experiments are summarised in table A2.1. The only experiment which contained orthopyroxene as well as garnet-sillimanite-quartz was D49-16. The data from this experiment was used to calculate two estimates of the fO_2. These do not lie within error of each other. The low levels of ferric iron in the experimental phases (evidenced by the consistently stoichiometric electron microprobe analyses) implies the fO_2 calculation based on reaction 4 is more accurate as it gives values just below the Quartz-Fayalite-Magnetite buffer. The calculation based on reaction 5 gives an fO_2 close to the Haematite-Magnetite buffer but this cannot be the case as the phase relations derived in this study are consistent with the low-fO_2 grid (~ QFM) of Hensen (1971, 1986) and not the high-fO_2 grid

Experiment	T (°C)	P (kb)	X_{Fe} Rim	X_{Fe} Centre	$log_{10}fO_2$
DS40-13	900	12.5	0.252	Homogeneous	-12.6_{alm}
DS41-13	950	12.5	0.316	Homogeneous	-13.0_{alm}
DS43-13	900	10	0.302	Homogeneous	-13.7_{alm}
DG47-16	940	7	0.250	Homogeneous	-11.8_{alm}
					-8.4_{fs}
DG49-16	875	7	0.230	0.025	n.c.
DG51-16	875	5	0.235	0.014	n.c.
DG39-13	850	5	0.215	0.15	-12.9_{alm}

Table A2.1. Summary of platinum wire experimental data. The values of $log_{10}fO_2$ were calculated as described in section A2.2 and have a calculated uncertainty of ±1 unit. Subscripts "alm" and "fs" show the value was calculated using reaction 4 or 5 respectively. "n.c." - not calculated, as no suitable assemblage was produced. Experiments labelled "DS**-**" were run in salt cells in the solid-media apparatus, those labelled "DG**-**" were run in the gas-bombs.

(~HM, Annersten and Seifert 1981, Hensen 1986). Disequilibrium orthopyroxene phase compositions are a likely reason for the discrepancy in the calculations, in particular the high alumina contents. The ideal a-x relation used could also be at fault. Also, the doubt described in the last section as to whether the alloy compositions represent equilibrium, single-phase solid-solution data complicates the situation by questioning whether any of the calculated fO_2's are valid. In the face of these difficulties the results must be treated very cautiously indeed.

A2.5 Palladium wires: the solution?

Palladium-iron alloys should exhibit a continual solid-solution from one pure end-member to the other at any temperature above 900°C, according to the data of Hultgren et al (1973). This is within the current experimental range and as the Pd-Fe a-x relation is as well known as that for Pt-Fe alloys at these temperatures (Alcock and Kubik 1969), palladium wires were tested. Supersolidus experiments D56-16 and D57-17 both contained palladium wires. However, when analysed after the run they had virtually zero iron-content (<0.25wt%) and contained 70wt% silver, 30wt% palladium: the same composition as the capsule metal. Direct contact of the experimental mix and the capsule metal buffered the a_{Pd} and a_{Ag} throughout the charge so that the palladium wire formed an alloy of the same composition as the capsule metal. The experiment did at least show the high mobility of the metals in the partially molten experiments.

In order to isolate the experimental mix and wire from the capsule metal and therefore allow a Pd-Fe alloy to form, a carbon capsule inside a platinum capsule was used[4]. This approach was successful in a gas bomb run (D68-16A, 875°C, 5kb) in as far as a Pd-Fe alloy did form but unfortunately the outer platinum capsule burst. This caused the sample to desiccate and therefore no melting occurred. The absence of melt prevented any of the co-existing silicates phases from equilibrating with the wire and so calculation of the fO_2 was not possible. It is interesting to note, however, that the palladium wire was absolutely homogeneous in composition (X_{Fe}=0.305) whereas a platinum wire placed in a separate part of the charge, for reference, was zoned (X_{Fe}=0.34-0.43[5]). These observations are consistent with the Pd-Fe wire being formed at supersolvus conditions and the Pt-Fe wire being formed at subsolvus conditions.

Time was not available for further investigation to be undertaken as part of this thesis. However, it is believed that palladium wires placed in supersolidus, vapour-undersaturated experiments above 900°C will be able to produce estimates of fO_2 accurate to ± 1 $\log_{10}$ unit, assuming good compositional data can be also be obtained for the silicate phases. A set of experiments designed such that the various parameters required for the calculation are easily obtained would be required to test the technique properly. For example, a more iron-rich bulk composition would be advantageous as the a_{Fe}-x relations are better known for iron-rich Pd-Fe alloys. Also a-x relations for the silicate phases need to be more fully investigated. Testing palladium wires in an appropriate bulk composition in a variety of experimental set-ups, e.g. gas-bombs with and without tantalum in the can, solid-media with and without external buffers, should enable the technique to be reliably assessed.

A2.5 References for Appendix Two.

Alcock, C.B. and Kubik, A., 1969. A thermodynamic study of the γ phase solid solutions formed between palladium, platinum and iron. *Acta Metallurgica*, **17**, 437-442.

---

[4] If carbon capsules were not desirable in a particular study, gold capsules could be appropriate as these do not generally alloy with iron. The affinity of gold for palladium would need to be checked.

[5] The higher proportion of iron in this alloy indicates a lower fO_2 than for the closed capsules (table A2.1). This would be expected if conditions in the can of the gas-bomb are more reducing than inside a closed capsule in the can. This was the expected effect of packing the can with tantalum.

Annersten H. & Seifert, F., 1981. Stability of the assemblage orthopyroxene-sillimanite-quartz in the system MgO-FeO-Al_2O_3-SiO_2-H_2O. *Contributions to Mineralogy and Petrology*, **77**, 158-165.

Grove, T.L., 1981. Use of FePt alloys to eliminate the iron loss problem in 1 atmosphere gas mixing experiments: theoretical and practical considerations. *Contributions to Mineralogy and Petrology*, **78**, 298-304.

Gudmundsson, G., Holloway J.R. and Carmichael, I.S.E., 1988. Pressure effect on the ferric/ferrous ratio in basaltic liquids, *EOS*, **69**, 1511.

Gudmundsson, G. & Holloway J.R., 1989. The activity coefficient of iron in platinum at 1400°C and from 1 atmosphere to 20kb, *EOS*, **69**, 1402.

Gudmundsson, G. & Holloway J.R., 1993. Activity-composition relationships in the system Fe-Pt at 1300 and 1400°C and at 1 atmosphere and 20kb. *American Mineralogist*, **78**, 178-186.

Harley, S.L.,1984. The solubility of alumina in orthopyroxene coexisting with garnet in FeO-MgO-Al_2O_3-SiO_2 and CaO-FeO-MgO-Al_2O_3-SiO_2, *Journal of Petrology*, **25** (3), 665-696.

Heald, E.F., 1967. Thermodynamics of iron-platinum alloys, *Transactions of the Metallurgical Society of AIME*, **239**, 1337-1340.

Hensen, B.J., 1986. Theoretical phase relations involving cordierite and garnet revisited: the influence of oxygen fugacity on the stability of sapphirine and spinel in the system Mg-Fe-Al-Si-O. *Contributions to Mineralogy and Petrology*, **92**, 362-367.

Holland, T.J.B., & Powell, R., 1990. An enlarged and updated internally consistent thermodynamic data set with uncertainties and correlations: the system K_2O-Na_2O-CaO-MgO-MnO-FeO-Fe_2O_3-Al_2O_3-TiO_2-SiO_2-C-H_2-O_2, *Journal of Metamorphic Geology*, **8**, 89-124.

Hultgren, R., Desai, P.D., Hawkins, D.T., Gleiser, M. and Kelley, K.K., 1973. Selected values of thermodynamic properties of binary alloys. American Society for Metals, Metals Park, Ohio, U.S.A.

Jamieson, H.E., Roeder, P.L. and Grant, A.H., 1992. Olivine-pyroxene-PtFe alloy as an oxygen geobarometer. *Journal of Geology*, **100**, 138-145.

van der Laan, S.R., & Koster van Groos, A.F., 1991. Pt-Fe alloys in experimental petrology applied to high-pressure research on Fe-bearing systems, *American Mineralogist*, **76**, 1940-1949.

Newton, R.C. and Hasleton, H.T., 1981. Thermodynamics of the garnet-plagioclase-Al_2SiO_5-quartz barometer. In: "*Thermodynamics of minerals and melts*", Advances in physical geochemistry, Volume **1**, 131-148. Springer Verlag, New York.

Nielsen, R.L., & Drake, M.J., 1979. Pyroxene-melt equilibria, *Geochimica et Cosmochimica Acta*, **43**, 1259-1272.

Sundaresen, M., Gerasimov, Ya.I., Geiderikh, V.A. and Vasil'eva, I.A., 1963. *Russian Journal of Physical Chemistry*, **37**, 1330-1333.

Williams, R.J., 1971. Reaction constants in the system Fe-MgO-SiO_2-O_2 at 1 atm. between 900°C and 1300°C. *American Journal of Science*, **270**, 334-360.

Appendix Three - Three-component projections of the experimental products.

In this appendix three-component projections are presented for every supersolidus experiment and the subsolidus experiments which were near the solidus. All the electron microprobe data gathered for each phase in each experiment is plotted on the diagram. The mean analysis for each phase is also plotted. The experiments well below the solidus were generally unchanged in phase assemblage and compositions and these are not plotted.

Most of the experiments produced the assemblage quartz-K-feldspar-melt and so the AFM projection is most commonly used, where each phase is projected from quartz, K-feldspar and melt. Projecting from the hydrous melt in this system is very close to projecting from pure water, as the melt plots very near the H (water) apex of the AFMH tetrahedron (see figure 4.5). Two other simple projections are used: KFM, for experiments lacking K-feldspar but containing quartz-sillimanite-melt, and HFM for experiments lacking a melt-phase but containing quartz-sillimanite-K-feldspar. The projections are summarised in the following table:

Projection	**Phases (Elements) projected from:**		
AFM	Quartz (SiO_2)	K-feldspar (K_2O)	Melt (H_2O)
KFM	Quartz (SiO_2)	Sillimanite (Al_2O_3)	Melt (H_2O)
HFM	Quartz (SiO_2)	Sillimanite (Al_2O_3)	K-feldspar (K_2O).

In a few rare cases none of these diagrams were suitable as the experiment did not have the any of the assemblages from which they are projected. Rather than introduce more complicated projections for unique cases, the data is simply plotted on the diagram anyway, thereby achieving one of the purposes of this appendix, which is to present all the electron microprobe data in a concise form. If an experiment is plotted on an unsuitable projection then no lines are drawn between the phases and no interpretation is made from it.

Various lines are drawn on the diagrams and represent the following:

———————	**tie-line indicating the phase assemblage interpreted to be in equilibrium,**
— — — — — —	**tie-line indicating a four-phase assemblage interpreted to be univariant or quasi-univariant,**
- - - - - - - - - - - -	**tie-line indicating a phase present in the experiment but interpreted to be metastable.**

The water-contents of the phases were estimated in section 3.6, but are subject to uncertainties which will translate into uncertainties in the position of hydrous phases and the bulk compositions on the projections. As these projections are used as interpretative tools (section 4.1) it is important to assess how large the uncertainty in projected position is for each type of diagram used. This is done in section 4.2, where it is concluded that, for AFM diagrams, the uncertainties in projected position are small enough not to affect the interpretation, whereas for KFM diagrams they are too large for the diagrams to be used for interpretative purposes.

The bulk composition of each mix is plotted as a box, representing the uncertainty in the composition. The uncertainty is assessed by plotting the measured bulk composition (from microprobe analyses of glass) and the calculated (ideal) composition on the diagram in use and encompassing them with a box. The bulk compositions are given in table 2.7.

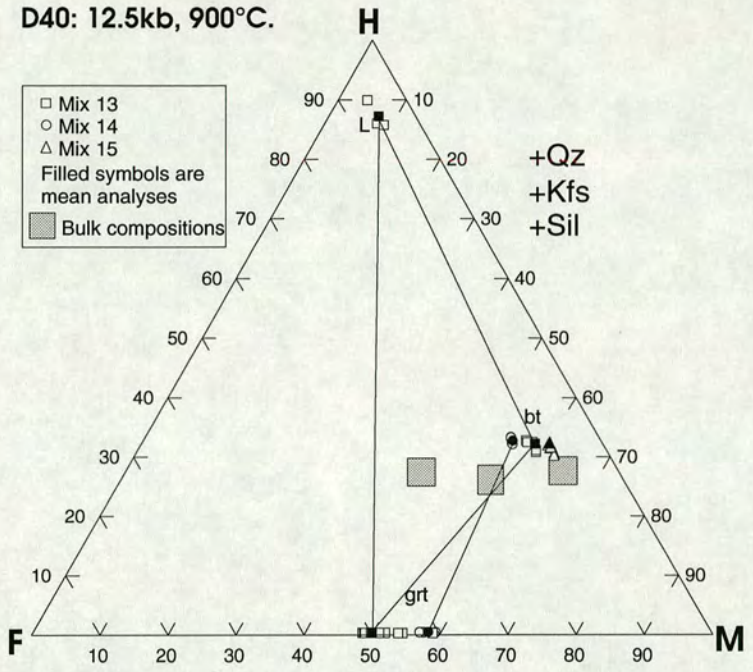

Note (D40): the crossing tie-line probably results from D40-14 having not melted whereas D40-13 did and the phases in the supersolidus experiment equilibrating further than those in the subsolidus run (see Chapter Two).

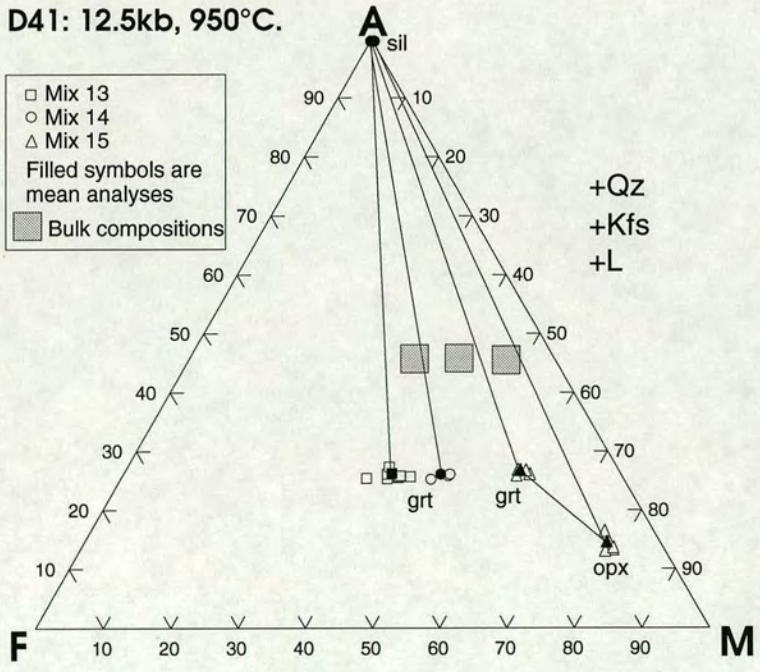

Note (D41): these are the only experiments in which trivariant tie-lines (here grt-sil) do not intersect the bulk compositions. The rim garnet is metastably iron rich, as reported in other studies (see section 3.4.2).

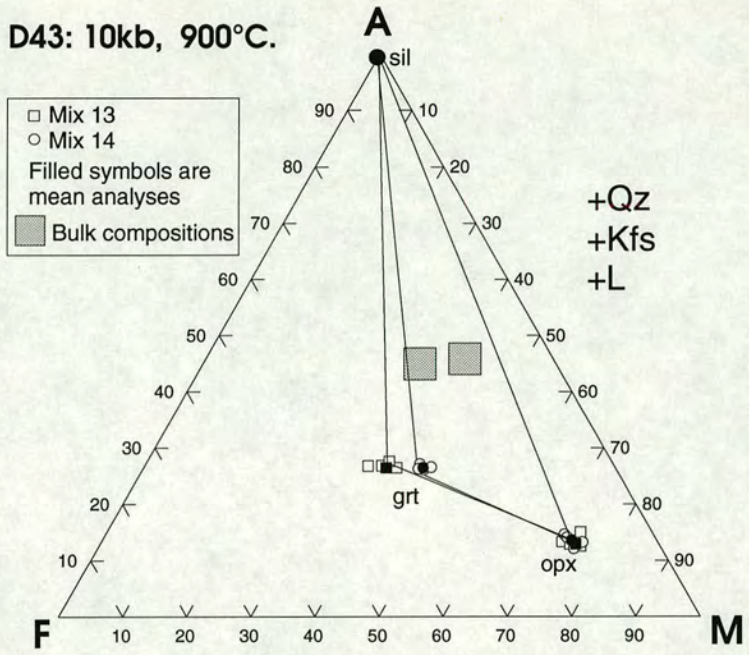

Note (D43): as the two bulk compositions produced the same assemblage at the same pressure and temperature the compositions should be the same. The fact that they are not the same for garnet shows that that phase did not equilibrate fully.

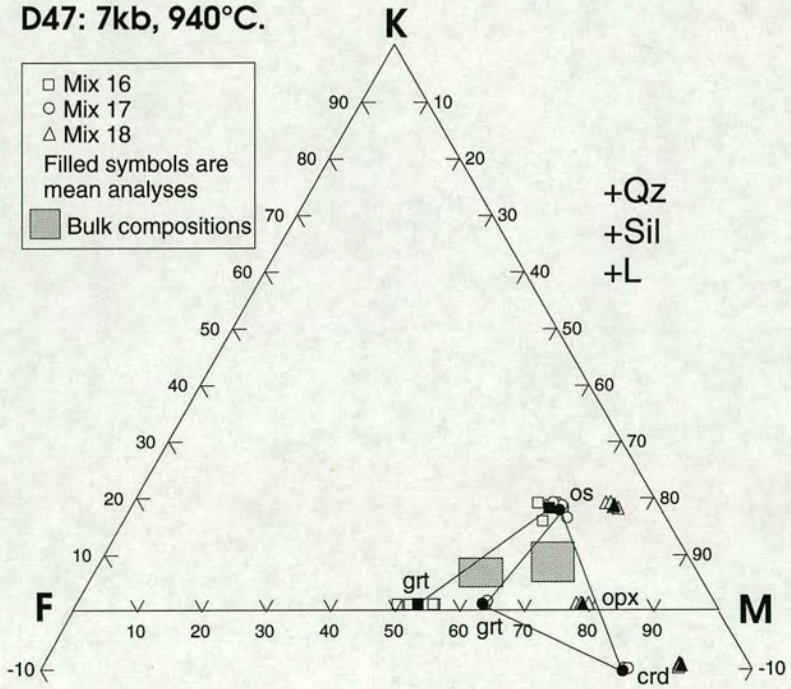

Note (D47): experiment D47-18 did not contain sillimanite and therefore cannot be legitimately plotted on this projection. The phase compositions from that experiment are plotted only so that all the data is displayed. The diagram is drawn for a melt water-content of 2wt% and a K_w of 3.0 (see section 3.6.3).

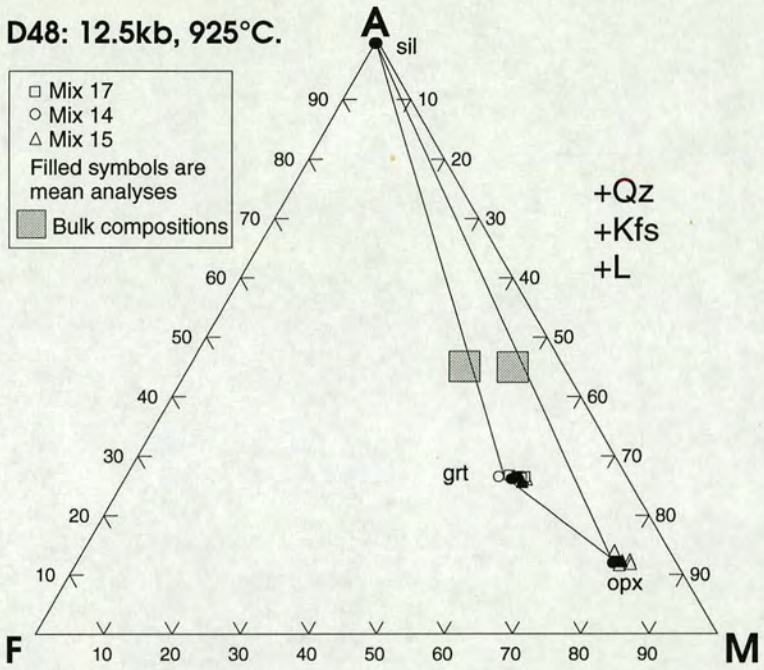

Note (D48): this experiment compared the two types of mix. The mixes with mineral-sillimanite (14, 15) compare very favourably with that with gel-sillimanite (17) at these pressures.

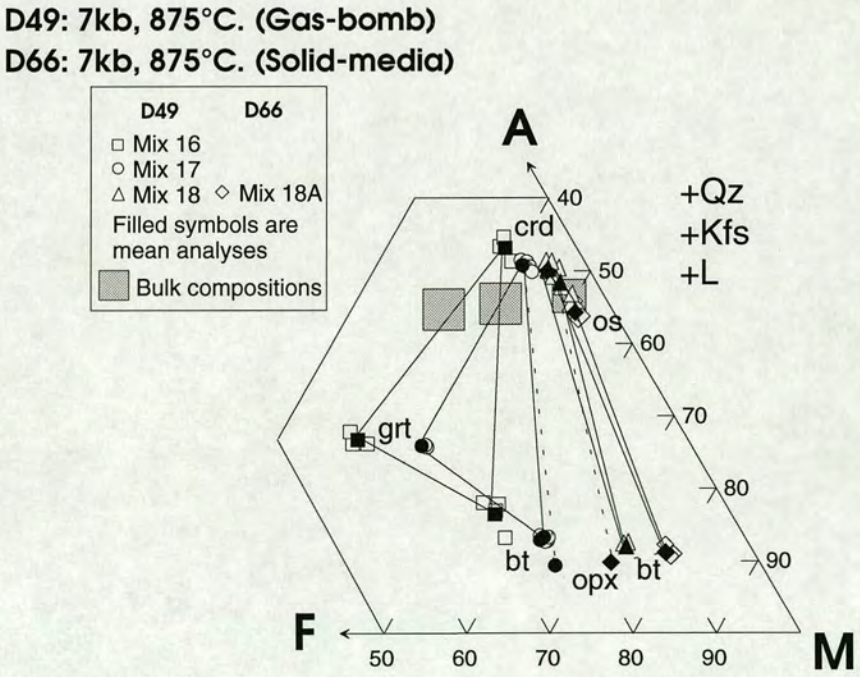

Note (D49 and D66): The M86 mixes in these runs provide a comparison of the gas bomb and solid-media apparatus. The same assemblage was produced in both experiments and the only noticeable difference in the phase compositions is in the biotite: this may reflect a difference in fO_2 in the two sets of apparatus (see section 2.3.4). Experiment D66-18A also produced metastable orthopyroxene.

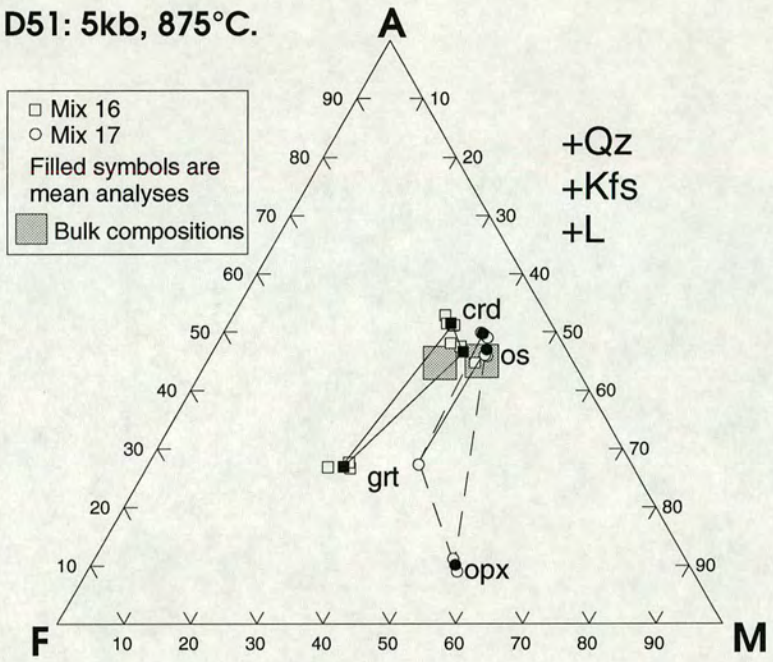

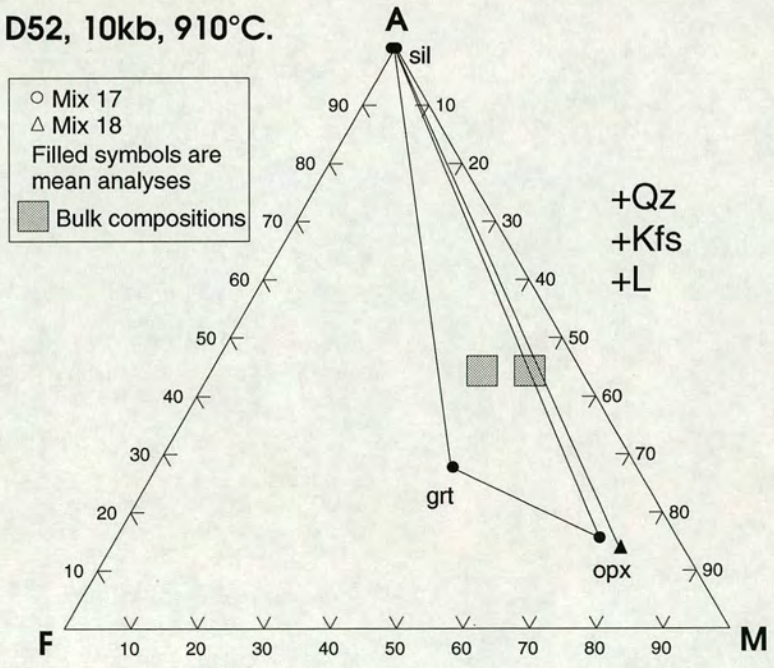

Note (D52): both the experiments from run D52 were contaminated with water and lost all their K-feldspar. Therefore they cannot be legitimately plotted on this projection, but are included for completeness.

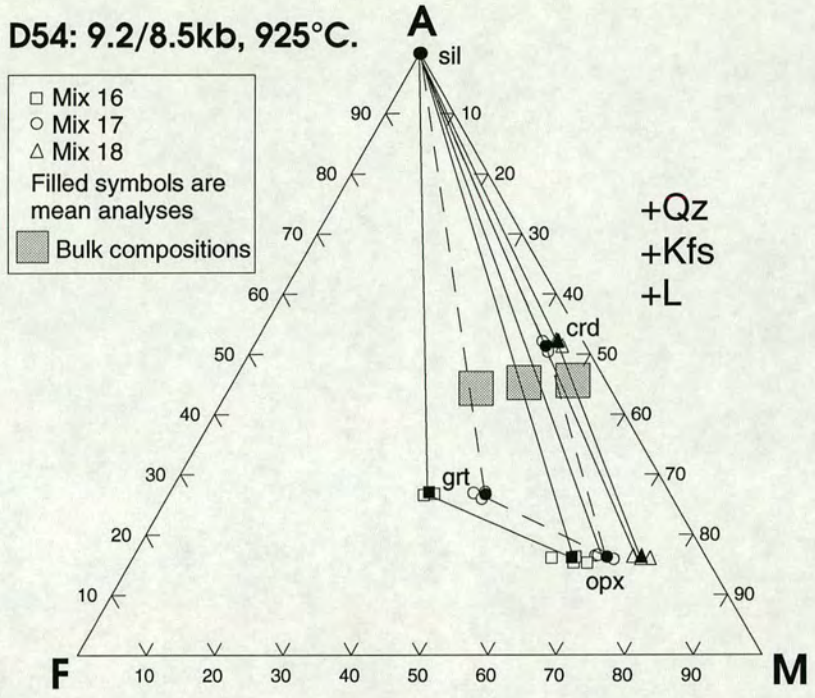

Note (D54): Due to leak in the gas-bomb apparatus the pressure drifted slowly down through this run from 9.2kb to 8.5kb.

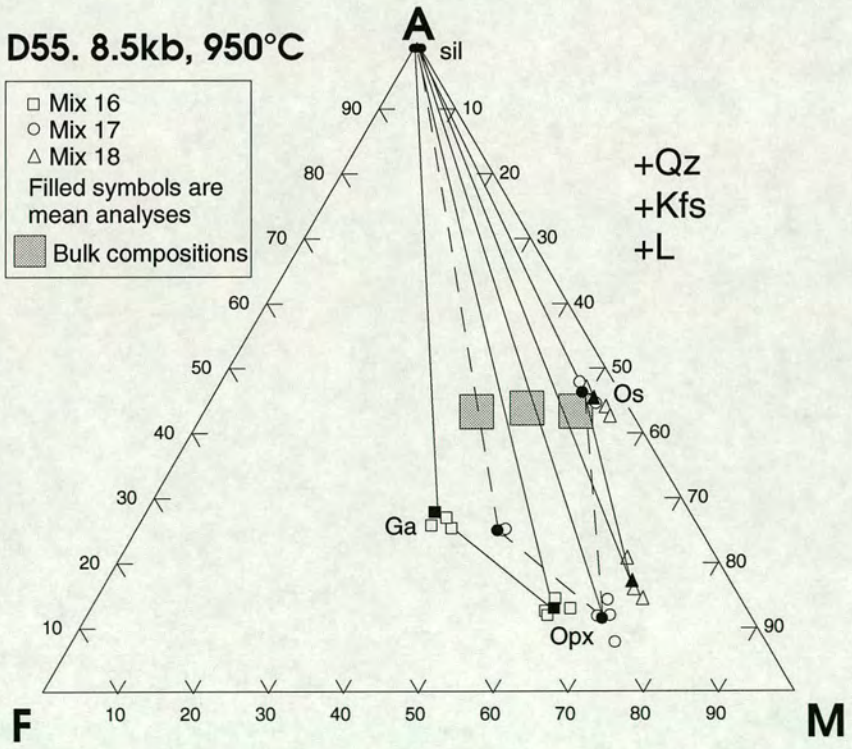

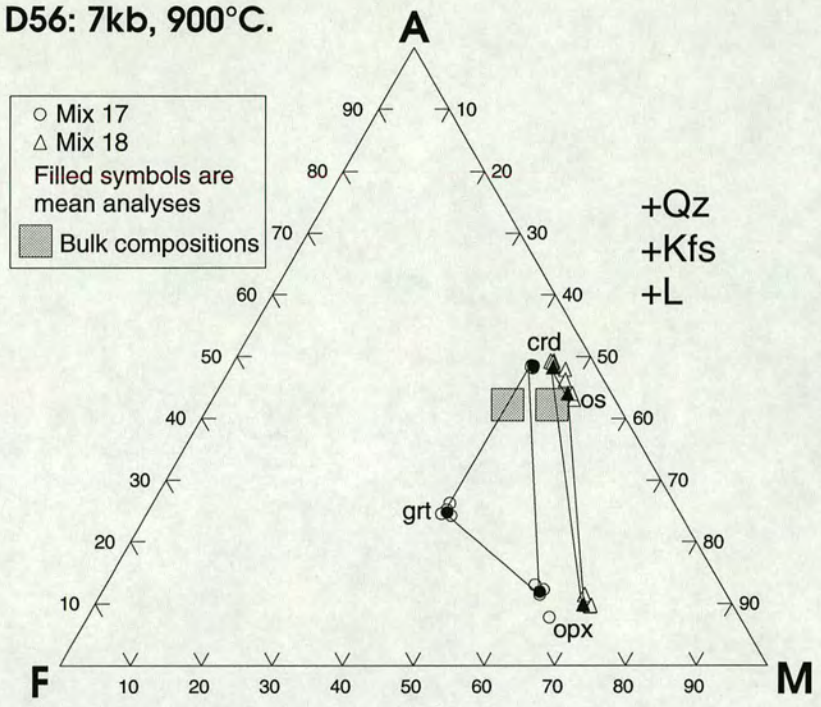

Note (D56): experiment D56-16 was seriously contaminated with water and contained no quartz or K-feldspar and so is not plotted on the projection (see 4.1).

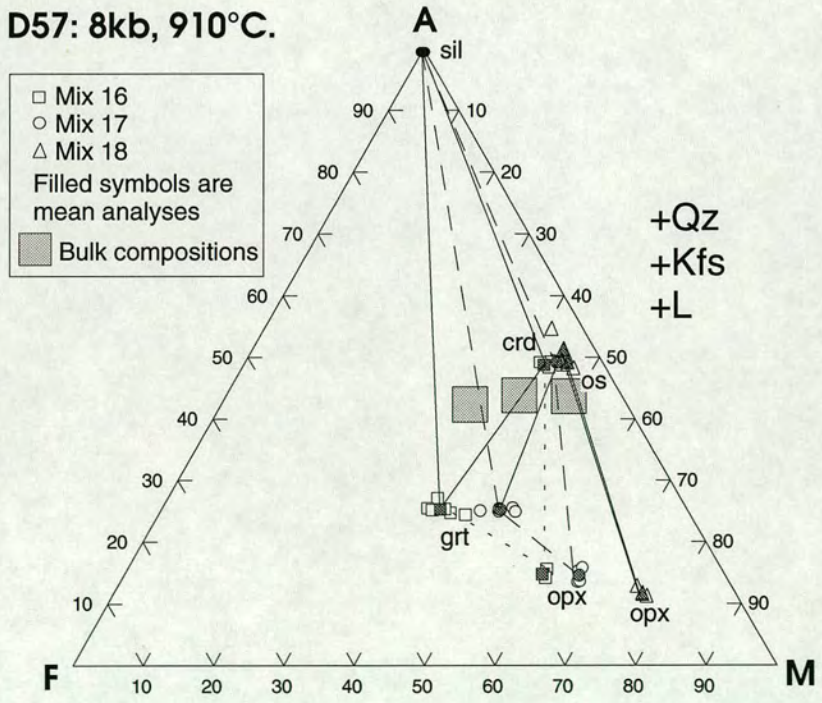

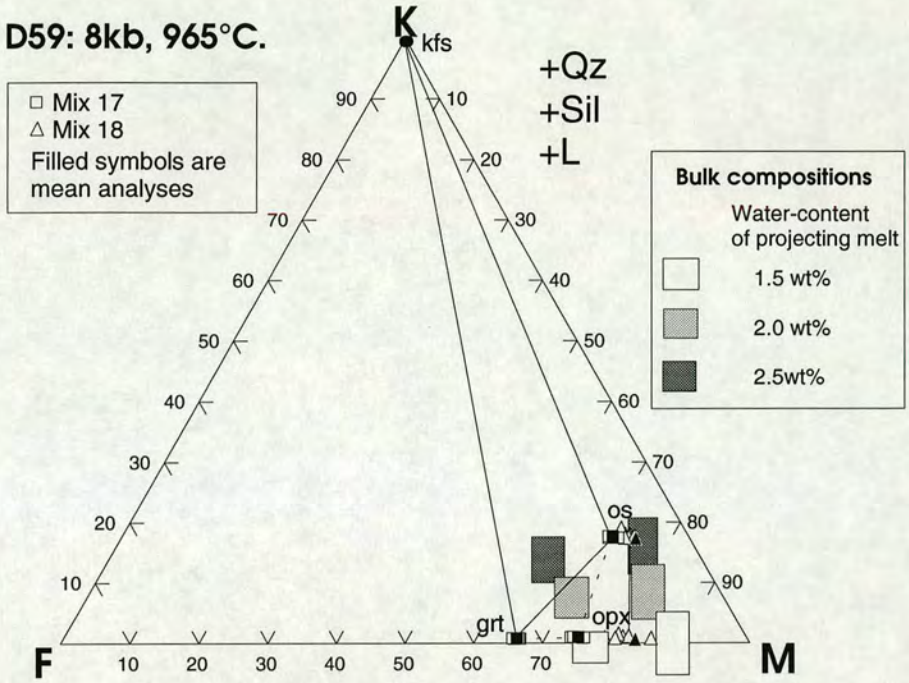

Note (D59): the sensitivity of the position of the bulk compositions to the water-content of the melt is shown by plotting them from three different water-contents (numbers in boxes, in wt%). This also shows how the KFM projection can be used to give constraints on melt water-contents. See section 3.6.2 for further explanation.

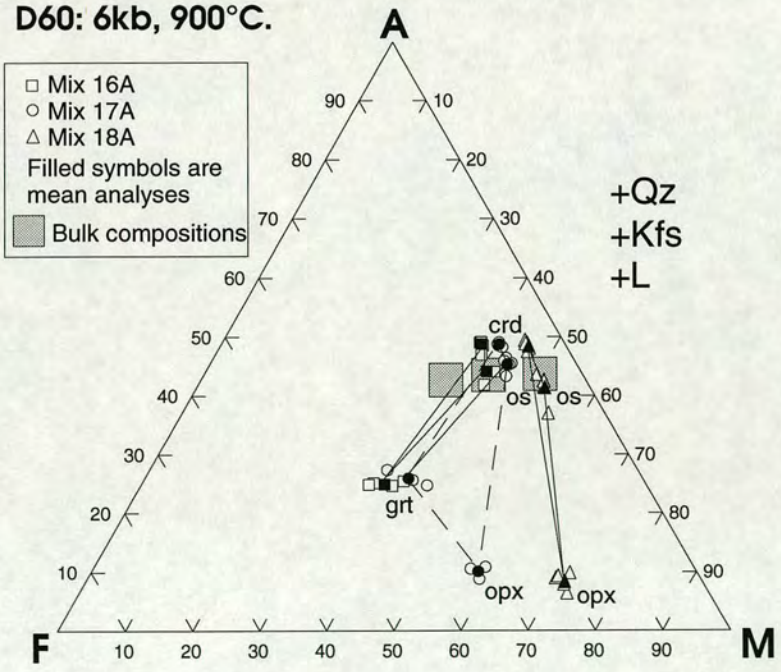

Note (D60): This run lies on the univariant (bt, sil) reaction. Mixes 16A, 17A: the assemblage grt-crd-os represents the low-T side of the reaction, the grt-os-opx assemblage the high-T side of the reaction. Mix 18A: the assemblage crd-os-kfs represents the low-temperature side of the reaction, the assemblage crd-os-opx (no kfs and therefore not properly represented on this diagram), the high-temperature side of the reaction.

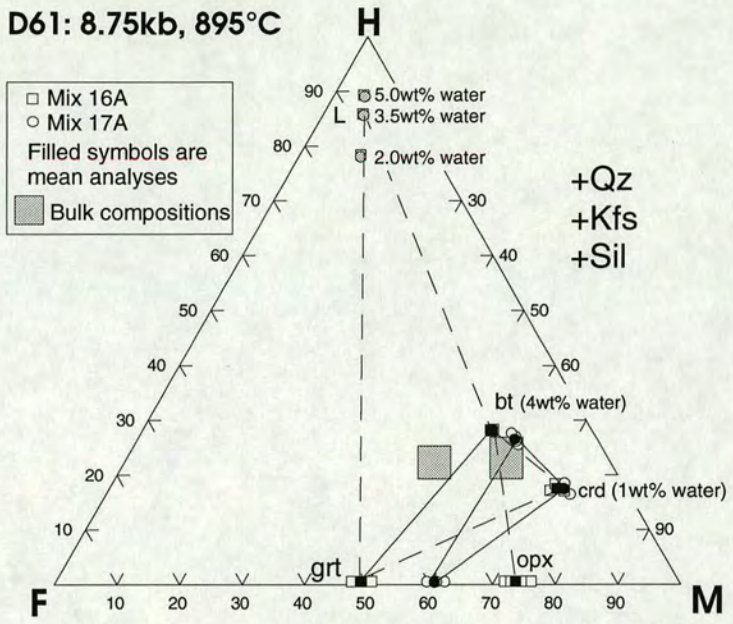

Note (D61): Experiment D61-16 produced eight phases, implying it lies very close to the [os] KFMASH invariant point in pressure-temperature-composition space. Water-contents for the hydrous phases are indicated. The water-content estimate (section 3.6.2) for the melt in D61-16 is 2.7wt% water.

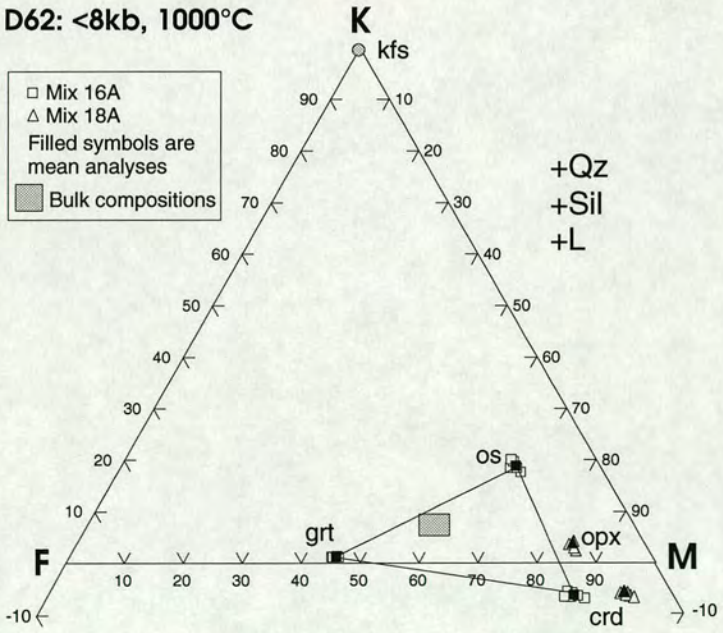

Note (D62): D62 was run in the solid-media apparatus using a talc-pyrex cell. Comparison with gas-bomb runs implies that the friction correction is much larger than previously thought (see 2.3.1). The pressure can only be constrained to be less than 8kb. D62-18 did not contain sillimanite and so cannot be legitimately plotted on this projection. The diagram is plotted for a melt-water content of 2.0 wt% and a K_w of 3.0 (see section 3.6.3).

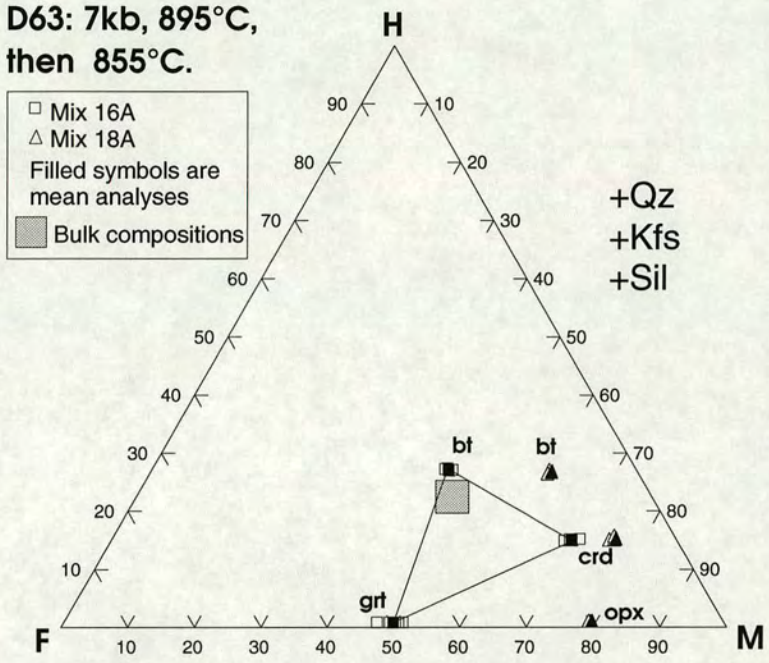

Note (D63): This run reversed the biotite dehydration melting equilibria at 7kb. D63-18 contained no sillimanite and so cannot be legitimately plotted on this projection.

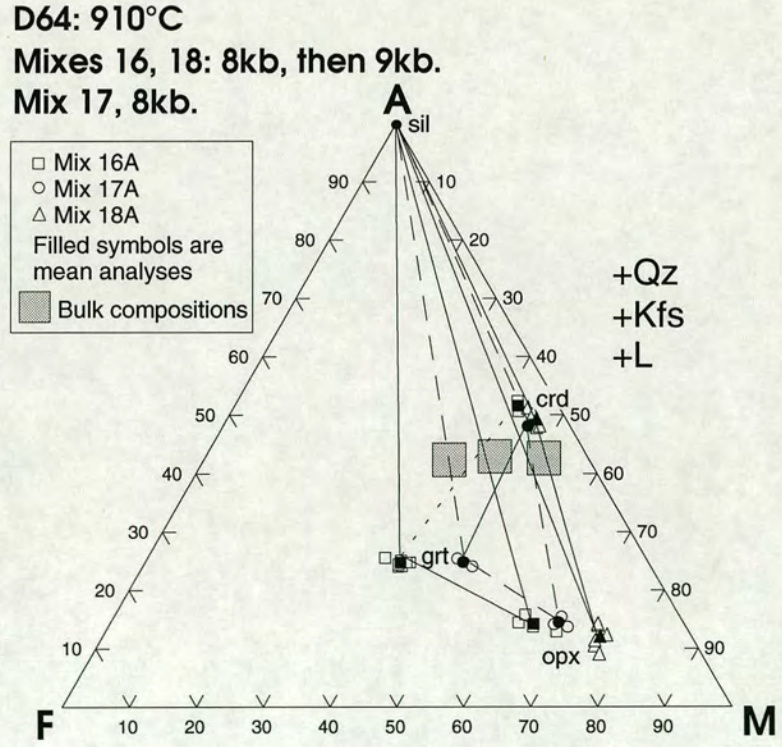

Note (D64): This run reversed the grt+crd+kfs+qz = opx+sil+L (os, bt) equilibrium at 910°C. Mix 17 was removed after the first of the two steps of the run.

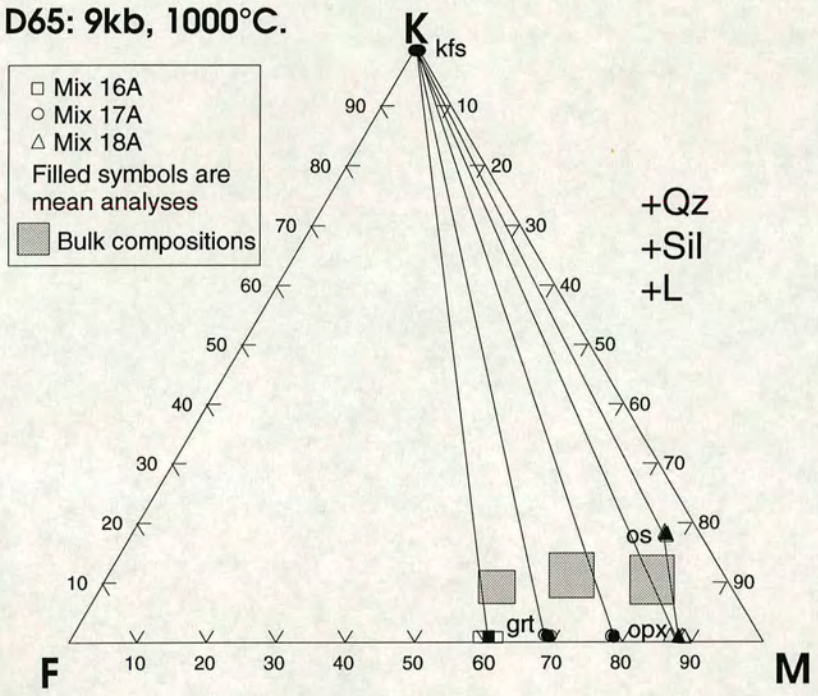

Note (D65): this run was conducted at the pressure and temperature which would normally be taken as the run conditions of run D62, but produces a higher pressure assemblage.

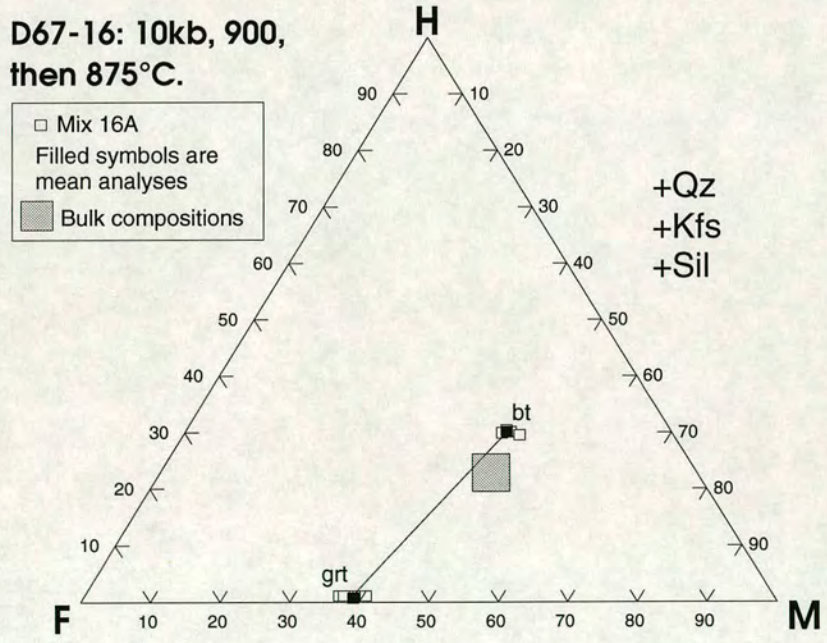

Note (D67): this run reversed the biotite dehydration melting equilibrium at 10kb.

REFERENCES

References.

Albee, A.L., 1965a. A petrogenetic grid for the Fe-Mg silicates of pelitic schists. *American Journal of Science*, **263**, 512-536.

Albee, A.L., 1965b. Distribution of Fe, Mg and Mn between garnet and biotite in natural mineral assemblages. *Journal of Geology*, **73**, 155-164.

Annersten H. and Seifert, F., 1981. Stability of the assemblage orthopyroxene-sillimanite-quartz in the system MgO-FeO-Al_2O_3-SiO_2-H_2O. *Contributions to Mineralogy and Petrology*, **77**, 158-165.

Aranovich, L.Ya. and Podlesskii, K.K., 1989. Geothermobarometry of high grade metapelites: simultaneously operating reactions. In: "*Evolution of metamorphic belts*", Daly, J.S., Cliff, R.A., Yardley, B.W.D. (eds.), Geological Society Special Publication, **43**, 45-61.

Arima, M. and Gower, C.F., 1991. Osumilite-bearing granulites in the eastern Grenville Province, Eastern Labrador, Canada: mineral parageneses and metamorphic conditions. *Journal of Petrology*, **32**, 29-61.

Armbruster, T. and Oberhansli, R., 1988. Crystal chemistry of double-ring silicates: structural, chemical and optical variation in osumilites. *American Mineralogist*, **73**, 585-594.

Audibert, N., Bertrand, P., Hensen, B., Kienast, J-R. and Ouzegane, Kh., 1993. Cordierite-K-feldspar-quartz-orthopyroxene symplectite from southern Algeria: new evidence for osumilite in high-grade metamorphic rocks. *Mineralogical Magazine*, **57**, 354-357.

Audibert, N., Hensen, B.J., and Bertrand P., 1994. Experimental study of phase relationships involving osumilite in the system K_2O-FeO-MgO-Al_2O_3-SiO_2-H_2O at high pressure and high temperature. Submitted to *Journal of Metamorphic Geology*.

Barbey, P., Macaudiere, J. and Nzenti, J.P., 1990. High-pressure dehydration melting of metapelites: evidence from the migmatites of Yaounde (Cameroon). *Journal of Petrology*, **31**, 401-427.

Bell, P., Mao, H. and England, J., 1971. A discussion of pressure distribution in modern solid-pressure-media apparatus. *Carnegie Institute of Washington Yearbook*, **70**, 277-281.

Berg, J.H., 1977. Regional geobarometry in the contact aureoles of the anorthositic Nain Complex, Labrador. *Journal of Petrology* **18**, 399-430.

Berg, J.J. and Wheeler, E.P., 1976. Osumilite of deep-seated origin in the contact aureole of the anorthositic Nain complex, Labrador. *American Mineralogist*, **61**, 29-37.

Bertrand, P., Ellis, D.J. and Green, D.H., 1991. The stability of sapphirine-quartz and hypersthene-sillimanite-quartz assemblages: an experimental investigation in the system FeO-MgO-Al_2O_3-SiO_2 under H_2O and CO_2 conditions. *Contributions to Mineralogy and Petrology*, **108**, 55-71.

Bertrand, P., Guiraud, M. and Ellis, D., 1993. Phase relations involving indialite in metamorphic rocks. Submitted to: *European Journal of Mineralogy.*

Bertrand, P., Ouzegane, Kh. and Kienast, J.R., 1992. P-T-X relationships in the Precambrian Al-Mg-rich granulites from In Ouzzal, Hoggar, Algeria. *Journal of Metamorphic Geology*, **10**, 17-31.

Bhattacharya, A., Mazumdak, A.C. and Sen, S.K., 1988. Fe-Mg mixing in cordierite: constraints from natural data and implications for cordierite-garnet geothermometry in granulites. *American Mineralogist*, **73**, 338-344.

Boettcher, A.I., Windom, K.E., Bohlen, S.R. and Luth, R.W., 1981. A low-friction, low-to-high-temperature furnace-sample assembly for piston-cylinder, high-pressure apparatus. *Reviews of Scientific Instruments*, **52**, 1903-1904.

Bohlen, S.R., 1984. Equlibria for precise pressure calibration and a frictionless furnace assembly for the piston-cylinder apparatus. *Neues Jarhb. Miner. Mh.*, **9**, 404-412.

Bohlen, S.R., Boettcher, A.L., Wall, V.J. and Clemens, J.D., 1983. Stability of phlogopite-quartz and sanidine-quartz: a model for melting in the lower crust. *Contributions to Mineralogy and Petrology*, **83**, 270-277.

Bowen, N.L., 1940. Progressive metamorphism of siliceous limestone and dolomite. *Journal of Geology*, **48**, 225-274.

Boyd, F.R. and England, J.L., 1960. Apparatus for phase-equilibrium measurements at pressures upto 50kb and temperatures upto 1,750°C. *Journal of Geophysical Research*, **65**, 741-748.

Caporuscio, F.A. and Morse, S.A., 1978. Ocurrence of sapphirine plus quartz at Peekshill, New York. *American Journal of Science*, **278**, 1334-1342.

Chatterejee, N.D. and Schreyer, W., 1972. The reaction enstatite$_{ss}$ + sillimanite = sapphirine$_{ss}$ + quartz in the system MgO-Al2O$_3$-SiO$_2$. *Contributions to Mineralogy and Petrology*, **36**, 49-62.

Clark, S.P., 1959. Effect of pressure on the melting points of eight alkali halides. *Journal of Chemical Physics*, **31**, 1526-1531.

Clemens, J.D., 1990. The granulite-granite connection. In: "*Granulites and Crustal Evolution*", Vielzeuf, D. and Vidal, Ph. (eds). Kluwer Academic Publishers. 25-36.

Clemens, J.D. and Vielzeuf, D., 1987. Constraints on melting and magma production in the crust. *Earth & Planetary Science Letters,* **86**, 287-306.

Dallwitz, W.B., 1968. Co-existing sapphirine and quartz in granulites form Enderby Land, Antarctica. *Nature*, **219**, 476-477.

Daniels et al. In preparation, referred to in Schreyer et al. 1990.

Deer. W.A., Howie, R.A. and Zussman, J., 1962. "*Rock-forming minerals, Volume 3: Sheet silicates*". London, Longmans/Green & Co.

Deer. W.A., Howie, R.A. and Zussman, J., 1986. "*Rock-forming minerals, Volume 1B: Disilicates and Ring Silicates*". Second edition, London, Longman.

Droop, G.T.R., 1987. A general equation for estimating Fe^{3+} concentrations in ferromagnesian minerals and oxides from microprobe analyses, using stoichiometric criteria. *Mineralogical Magazine*, **51**, 431-435.

Dyar, M., Guidotti, C., Holdaway, M. and Colucci, M., 1993. Nonstoichiometric hydrogen contents in common rock-forming hydroxyl silicates. *Geochimica et Cosmochimica Acta*, **57**, 2913-2918.

Ebadi, A. and Johannes, W., 1991. Experimental investigation of composition and beginning of melting in the system $NaAlSi_3O_8$-$KAlSi_3O_8$-SiO_2-H_2O-CO_2. *Contributions to Mineralogy and Petrology*, **106**, 286-295.

Eckert, J.O. and Bohlen, S.R., 1992. Reversed experimental determinations of the Mg-Fe^{2+} exchange equilibria in Fe-rich garnet-orthopyroxene pairs. *EOS*, **73**(43), 608.

Edgar, A.D., 1973. "*Experimental Petrology - Basic Principles and Techniques*". Oxford University Press, London.

Ellis, D.J., 1980. Osumulite-sapphirine-quartz granulites from Enderby Land, Antarctica: P-T conditions of metamorphism, implications for garnet-cordierite

equilibria and the evolution of the deep crust. *Contributions to Mineralogy & Petrology,* **74**, 201-210.

Ellis, D.J., 1986. Garnet-liquid Fe^{2+}-Mg equilibria and implications for the beginning of melting in the crust and subduction zones. *American Journal of Science*, **286**, 765-791.

Ellis, D.J., Sheraton, J.W., England, R.N. and Dallwitz, W.B., 1980. Osumilite-sapphirine-quartz granulites from Enderby Land, Antarctica: mineral assemblages and reactions. *Contributions to Mineralogy & Petrology*, **72**, 123-143.

Essene, E.J., 1989. The current status of thermobarometry in metamorphic rocks. In: "*Evolution of Metamorphic Belts*", Daly, J.S., Cliff, R.A. & Yardley, B.W.D., (eds), Geological Society Special Publication, **43**, 1-44.

Ferry, J.M. and Spear, F.S., 1978. Experimental calibration of the partitioning of Fe and Mg between biotite and garnet. *Contributions to Mineralogy and Petrology*, **66**, 113-117.

Ford, C.E., 1972. Furnace design, temperature distribution, calibration and seal design in internally heated pressure vessels. *Progress in Experimental Petrology, Natural Environment Research Council (Great Britain) Series D,* **2**(11), 89-96.

Fyfe, W.S., 1973. The granulite facies, partial melting and the Archaean crust. *Philosophical Transactions of the Royal Society of London A*, **273**, 457-461.

Graham, C.M. and Elphick, S.C.E., 1990. A re-examination of the role of hydrogen in Al-Si interdiffusion in feldspars. *Contributions to Mineralogy & Petrology*, **104**, 481-491.

Grant. J.A., 1973. Phase equilibria in high-grade metamorphism and partial melting of pelitic rocks. *American Journal of Science*, **273**, 289-317.

Grant, J.A., 1985. Phase equilibria in partial melting of pelitic rocks. In: "*Migmatites*", Ashworth, J.R. (ed), Blackie. 86-144.

Green, D.H. and Ringwood, A.E., 1967. An experimental investigation of the gabbro to eclogite transformation and its petrological applications. *Geochimica et Cosmochimica Acta*, **31**, 767-833.

Grew, E.S., 1980. Sapphirine + quartz association from Archaean rocks in Enderby Land, Antarctica. *American Mineralogist,* **65**, 821-836.

Grew, E.S., 1982. Osumilite in the sapphirine-quartz terrane of Enderby Land, Antarctica: implications for osumilite petrogenesis in the granulite facies. *American Mineralogist*, **67**, 762-787.

Gudmundsson, G. and Holloway, J.R., 1989. See appendix two.

Gudmundsson, G. and Holloway, J.R., 1993. See appendix two.

Guidotti, C.V., 1984. Micas in metamorphic rocks. In: "*Micas*", Bailey, S.W., (ed), *Mineralogical Society of America Reviews in Mineralogy*, **13**, 357-456.

Harley, S.L., 1983. Regional geobarometry-geothermometry and metamorphic evolution of Enderby Land, Antarctica. In: Oliver, R.L., James, P.R. & Jago, J.B. (eds) Antarctic Earth Science. Canberra: Australian Academy of Science, 25-30.

Harley, S.L., 1984a. An experimental study of the partitioning of Fe and Mg between garnet and orthopyroxene. *Contributions to Mineralogy & Petrology,* **86**, 359-373.

Harley, S.L., 1984b. The solubility of alumina in orthopyroxene coexisting with garnet in FeO-MgO-Al_2O_3-SiO_2 and CaO-FeO-MgO-Al_2O_3-SiO_2. *Journal of Petrology,* **25**, 665-696.

Harley, S.L., 1985. Garnet-orthopyroxene bearing granulites from Enderby Land, Antarctica: Metamorphic pressure-temperature-time evolution of the Archaean Napier Complex. *Journal of Petrology,* **26**, 819-856.

Harley, S.L., 1989. The origins of granulites: a metamorphic perspective. *Geological Magazine,* **126**, 215-247.

Harley, S.L. and Fitzsimons, I.C.W., 1991. Pressure-temperature evolution of metapelitic granulites in a polymetamorphic terrane: the Rauer Group, east Antarctica. *Journal of Metamorphic Geology,* **9**, 231-243.

Harley, S.L., Fitzsimons, I.C.W., Buick, I.S. and Watt, G.R., 1992. The significance of reworking, fluids and partial melting in granulite metamorphism, East Prydz Bay, Antarctica. In : "*Recent Progress in Antarctic Earth Science*", Yoshida, Y., Kaminuma, K. & Shiraishi, K. (eds), Terra Scientific Publishing Company, Tokyo, 119-127.

Harley, S.L. and Hensen, B.J., 1990. Archaean and Proterozoic high-grade terranes of East Antarctica (40-80E): a case study of diversity in granulite facies metamorphism. In: *"High-temperature Metamorphism and Crustal Anatexis"*, J.R. Ashworth & M. Brown, Eds., London, Unwin Hyman, 320-370.

Harley, S.L., Hensen, B.J. and Sheraton, J.W., 1990. Two-stage decompression in orthopyroxene-sillimanite granulites from Forefinger Point, Enderby Land, Antarctica: implications for the evolution of the Archean Napier Complex. *Journal of Metamorphic Petrology*, **8**, 591-613.

Henry, J, 1974. Garnet-cordierite gneisses near the Egersund-Ogna anorthositic intrusion, southwestern Norway. *Lithos*, **7**, 207-216.

Hensen, B.J., 1971. Theoretical phase relations involving cordierite and garnet in the system MgO-FeO-Al_2O_3-SiO_2. *Contributions to Mineralogy and Petrology*, **3**, 191-214.

Hensen, B.J., 1977. The stability of osumilite in high grade metamorphic rocks. *Contributions to Mineralogy and Petrology*, **64,** 197-204.

Hensen, B.J., 1986. Theoretical phase relations involving cordierite and garnet revisited: the influence of oxygen fugacity on the stability of sapphirine and spinel in the system Mg-Fe-Al-Si-O. *Contributions to Mineralogy and Petrology*, **92**, 362-367.

Hensen, B.J. and Essene, E.J., 1971. Stability of pyrope-quartz in the system MgO-Al_2O_3-SiO_2. *Contributions to Mineralogy and Petrology*, **30**, 72-83.

Hensen, B.J. and Green, D.H., 1970. Experimental data of co-existing cordierite and garnet under high grade metamorphic conditions. *Physics of Earth and Planetary Interiors*, **3**, 431-440.

Hensen, B.J. and Green, D.H., 1971. Experimental study of the stability of cordierite and garnet in pelitic compositions at high pressures and temperatures. I. Compositions with excess alumino-silicate. *Contributions to Mineralogy and Petrology*, **33**, 309-330.

Hensen, B.J. and Green, D.H., 1972. Experimental study of the stability of cordierite and garnet in pelitic compositions at high pressures and temperatures. II. Compositions without excess alumino-silicate. *Contributions to Mineralogy and Petrology*, **35**, 331-354.

Hensen, B.J. and Green, D.H., 1973. Experimental study of the stability of cordierite and garnet in pelitic compositions at high pressures and temperatures. III. Synthesis of experimental data and geological applications. *Contributions to Mineralogy and Petrology*, **38**, 151-166.

Hensen, B.J. and Harley, S.L., 1990. Graphical analysis of P-T-X relations in granulite facies metapelites. In: Ashworth, J.R. & Brown, M. (eds) "*High-temperature Metamorphism and Crustal Anatexis*". London: Unwin Hyman, p19-56.

Hensen, B.J. and Motoyoshi, Y., 1992. Osumilite-producing reactions in high-temperature granulites from the Napier Complex, East Antarctica: Tectonic implications. *Recent Progress in Antarctic Earth Science*. Yoshida, Y., Kaminuma, K. and Shiraishi, K. (eds), Terra Scientific Publishing Company, Tokyo. 87-92.

Holdaway, M.J. and Lee, S.M., 1977. Fe-Mg cordierite stability in high-grade pelitic rocks based on experimental, theoretical, and natural observations. *Contributions to Mineralogy and Petrology*, **63**, 175-198.

Holloway, J.R., 1971. Internally heated pressure vessels. In *"Research techniques for high temperature and pressure"*, G.C.Ulmer (ed), 217-257. New York, Springer.

Holloway, J.R. and Wood, B.J., 1988. *"Simulating the Earth: experimental geochemistry"*, Unwin Hyman.

Holness, M.B., 1992. Equilibrium dihedral angles in the system quartz-CO_2-H_2O-NaCl at 800°C and 1-15 kbar: the effects of pressure and fluid composition on the permeability of quartzites. *Earth and Planetary Science Letters*, **114**, 171-184.

Holness, M.B., 1993. Temperature and pressure dependence of quartz-aqueous fluid dihedral angles: the control of adsorbed water on the permeability of quartzites. *Earth and Planetary Science Letters*, **117**, 363-377.

Holtz, F. and Barbey, P., 1991. Genesis of peraluminous granites II. Mineralogy and chemistry of the Tourem Complex (North Portugal). Sequential melting versus restite unmixing. *Journal of Petrology*, **32**, 959-978.

Holtz, F., Behrens, H., Dingwell, D.B. and Taylor, R., 1992a. Water solubility in aluminosilicate melts of haplogranitic compositions at 2 kbar. *Chemical Geology*, **96**, 289-302.

Holtz, F., Johannes, W. and Pichavant, M., 1992b. Peraluminous granites: the effect of alumina on melt composition and coexisting minerals. *Transactions of the Royal Society of Edinburgh: Earth Sciences*, **83**, 409-416.

Holtz, F., Pichavant, M., Barbey, P. and Johannes, W., 1992c. Effects of water on liquidus phase relations in the haplogranitic system at 2 and 5 kilobars. *American Mineralogist*, **77**, 1223-1241.

Holtz, F. and Johannes, W., 1993. Maximum and minimum water contents of granitic melts: implications for chemical and physical properties of ascending magmas. Sumbmitted to Lithos.

Holtz, F., Behrens, H. and Dingwell, D.B., 1993. Water solubility in haplogranitic melts: compositional, pressure and temperature dependence. In preparation.

Huang, W.L. and Wyllie, P.J., 1975. Melting relations in the system $NaAlSi_3O_8$-$KAlSi_3O_8$-SiO_2 to 35kb, dry and with excess water. *Journal of Geology*, **83**, 737-748.

Jamieson et al. 1992. See appendix two.

Jansen, J.B.H., Blok, R.J.P., Bos, A. and Scheelings, M., 1985. Geothermometry and geobarometry in Rogaland and preliminary results from the Bamble area, southern Norway. In: "*The Deep Proterozoic Crust in the North Atlantic Provinces*", eds. Tobi, A.C. and Touret, J.L.R., pages 499-515. Published Reidel, Dordrecht.

Johannes, W., Bell, P.M., Mao, H.K., Boettcher, A.L., Chipman, D.W., Hays, J.F., Newton, R.C. and Seifert, F., 1971. An interlaboratory comparison of piston-cylinder pressure calibration using the albite breakdown reaction. *Contributions to Mineralogy Petrology*, **32**, 24-38.

Johannes, W. and Holtz, F., 1990. Formation and composition of water-undersaturated granitic melts. In: Ashworth, J.R. & Brown, M. (eds) "*High-temperature Metamorphism and Crustal Anatexis*", 87-104. London: Unwin Hyman.

Johannes, W. and Holtz, F., 1992. Melting of plagioclase in granite and related systems: composition of co-existing phases and kinetic observations. *Transactions of the Royal Society of Edinburgh: Earth Sciences*, **83**, 417-422.

Johannes, W. and Schreyer, W., 1981. Experimental introduction of CO_2 and H_2O into Mg-cordierite. *American Journal of Science*, **281**, 299-317.

Jones, K.A. and Brown, M., 1990. High-temperature 'clockwise' P-T paths and melting in the development of regional migmatites: an example from southern Brittany, France. *Journal of Metamorphic Geology*, **8**, 551-578.

Jurewicz, S.R. and Watson, E.B., 1985. Distribution of partial melt in a felsic system: importance of surface energy. *Contributions to Mineralogy and Petrology*, **84**, 66-72.

Kars, H., Jansen, J.B.H., Tobi, A.C. and Poorter, R.P.E., 1980. The metapelitic rocks of the polymetamorphic Precambrian of Rogaland, SW Norway (II). *Contributions to Mineralogy and Petrology*, **75**, 235-244.

Khlestov, V.V., 1964. Garnets from cordierite-bearing rocks of the Sharyzhalgay complex (southern Transbaikal). *Dokl. Akad. Nauk. SSSR*, **154**, 4, 842-845.

Kitamura, M. and Hiroi, Y., 1982. Indialite from Unazuki pelitic schists, Japan and its transition texture to cordierite. *Contributions to Mineralogy and Petrology*, **80**, 110-116.

Korzhinskii, D.S., 1959. "*Theory of Metasomatic Zoning*". (Translated by J.Agrell). Published 1970, Clarendon Press, Oxford.

Kretz, R., 1959. Chemical study of garnet, biotite and horneblende from gneisses of south-western Quebec, with emphasis on distribution of elements in co-existing minerals. *Journal of Geology,* **67**, 37-42.

Lamb, W.M. and Valley, J.W., 1985. C-O-H fluid calculations and granulite genesis. In: Tobi, A.C. & Touret, J.L.R. (eds) "*The Deep Proterozoic Crust in the North Atlantic Provinces*". Dordrecht: Reidel, 119-131.

Lamb, W.M., Valley, J.W. and Brown, P.E., 1987. Post-metamorphic CO_2-rich fluid inclusions in granulites. *Contributions to Mineralogy and Petrology* **96**, 485-495.

Le Breton, N. and Thompson, A.B., 1988. Fluid-absent (dehydration) melting of biotite in metapelites in the early stages of crustal anatexis. *Contributions to Mineralogy and Petrology*, **99**, 226-237.

Lee, H.Y. and Ganguly, J., 1988. Equlibrium compositions of co-existing garnet and orthopyroxene: reversed experimental determinations in the system FeO-MgO-Al_2O_3-SiO_2 and applications. *Journal of Petrology*, **29**, 93-114.

Luth, R.C., 1976. Granitic rocks. In: "*The evolution of the crystalline rocks*", Bailey, D.K. and MacDonalds, R., Eds., Academic Press, London, 335-417.

Maijer, C., Jansen, J.B.H., Wevers, J. and Poorter, R.P.E., 1977. Osumilite, a new mineral to Norway. *Norsk Geologisk Tidsskrift*, **57**, 187-188.

Maijer, C., Andriessen, P.A.M., Hebeda, E.H., Jansen, J.B.H. and Verschure, R.H. 1981. Osumilite, an approximately 970ma old high-temperature index mineral of the granulite-facies metamorphism in Rogaland, SW Norway. *Geologie en Mijnbouw*, **60**, 267-272.

Marakushev, A.A. and Kudryavtsev, V.A., 1965. Hypersthene-sillimanite paragenesis and its petrological implication. *Dokl. Akad. Nauk. SSSR*, **164**, 1, 179-182.

Martignole, J. and Sisi, J.C., 1981. Cordierite-garnet-H_2O equilibrium: a geological, thermometer, barometer and water-fugacity indicator. *Contributions to Mineralogy and Petrology*, **77**, 38-46.

Mirwald, P.W., Getting, I.C. and Kennedy, G.C., 1975. Low-friction cell for piston-cylinder high-temperature apparatus. *Journal of Geophysical Research*, **80**, 1519-1525.

Miyashiro, A., 1956. Osumilite, a new mineral and its crystal structure. *American Mineralogist*, **41**, 104-116.

Motoyoshi, Y. and Hensen, B.J., 1989. Sapphirine-quartz-orthopyroxene symplectites after cordierite in the Archaean Napier Complex, Antarctica: evidence for a counterclockwise P-T path? *European Journal of Mineralogy*, **1**, 467-471.

Motoyoshi, Y., Hensen, B.J. and Arima M., 1993. Experimental study of the high-pressure stability limit of osumilite in the system K_2O-MgO-Al_2O_3-SiO_2: implications for high-temperature granulites. *European Journal of Mineralogy*, **5**, 439-445.

Motoyoshi, Y. and Matsueda, H., 1984. Archean granulites from Mt. Riiser-Larsen in Enderby Land, East Antarctica. *Memoirs of National Institute of Polar Research (Tokyo): Special Issue*, **33**, 103-125.

Mottana, A., Fusi, A., Bianchi, Potenza, B., Crespi, R. and Liborio, G., 1983. Hydrocarbon-bearing cordierite from the Derivo-Colico road tunnel (Como, Italy). *Neues Jahrb. Min.*, **148**, 181-199.

Mouri, H., Guiraud, M. and Kienast, J-B., 1993. Al-Mg granulites of Ihouhaouene, Hoggar (Algeria): an example of phase relationships in the KFMASH system and melt-absent equilibria. *C. R. Acad. Sci. Paris*, **t.316**, Serie II, 1565-1572.

Nekvasil, H., 1988. Calculated effect of anorthite component on the crystallisation paths of water-undersaturated haplogranitic melts. *American Mineralogist*, **73**, 966-81.

Nekvasil, H. and Burnham, C.W., 1987. The calculated individual effects of pressure and water-content on phase equilibrium in the granite sysytem. In: "*Magmatic Processes: Physicochemical Principles*". B.O.Mysen (ed). Geochemical Society Special Publication, **1**, 433-445.

Newton, R.C., 1972. An experimental determination of the high-pressure stability limits of magnesian cordierite under wet and dry conditions. *Journal of Geology*, **80**, 398-420.

Newton, R.C. 1990. Fluids and melting in the Archean deep crust of southern India. In: "*High Temperature and Crustal Anatexis*", Ashworth, J.R. and Brown, M. (eds). Unwin Hyman Ltd. 149-179.

Newton, R.C., Smith, J.V. and Windley, B.F., 1980. Carbonic metamorphism, granulites and crustal growth. *Nature*, **288**, 45-50.

Newton, R.C. and Wood, B.J., 1979. Thermodynamics of water in cordierite and some petrologic consequences of cordierite as a hydrous phase. *Contributions to Mineralogy and Petrology*, **68**, 391-405.

Nichols, G.T., Berry, R.F. and Green, D.H., 1992. Internally-consistent gahnite spinel-cordierite-garnet equilibria in the FMASHZn system: geothermobarometry and applications. *Contributions to Mineralogy and Petrology*, **111**, 362-377.

Niggli, P., 1954. Rocks and mineral deposits. (Translated by R.L.Parker). W.H.Freeman and co., San Francisco, 559pp.

Olesch, M. and Seifert, F., 1981. The restricted stability of osumilite under hydrous conditions in the system K_2O-MgO-Al_2O_3-SiO_2-H_2O. *Contributions to Mineralogy and Petrology*, **76**, 362-367.

Patino Douce, A.E. and Johnston, A.D., 1991. Phase equilibria and melt productivity in the pelitic system: implications for the origin of peraluminous granitoids and aluminous granulites. *Contributions to Mineralogy and Petrology*, **107**, 202-218.

Patino Douce, A.E., Johnston, A.D. and Rice, J.M., 1993. Octahedral excess mixing properties in biotite: a working model with applications to geobarometry and geothermometry. *American Mineralogist*, **78**, 113-131.

Pattison, D.R.M. and Newton, R.C., 1989. Reversed experimental calibration of the garnet-clinopyroxene Fe-Mg exchange thermometer. *Contributions to Mineralogy and Petrology*, **101**, 87-103.

Pawley, A., 1989. "Experimental studies of the structure, stability and thermochemistry of amphiboles in the systems Na_2O-MgO-Al_2O_3-SiO_2-H_2O and Na_2O-CaO-MgO-SiO_2-H_2O." Unpublished PhD thesis, University of Edinburgh.

Peterson, J.W and Newton, R.C., 1989. Reversed experiments on biotite-quartz-feldspar melting in the system KMASH: implications for crustal anataxis. *Journal of Geology*, **97**, 465-485.

Phillips, G.N., 1980. Water activity changes across an amphibolite-granulite facies transition, Broken Hill, Australia. *Contributions to Mineralogy & Petrology*, **75**, 377-386.

Pichavant, M., Holtz, F. and McMillan, P., 1992. Phase relations and compositional dependence of H_2O solubility in quartz-feldspar melts.*Chemical Geology*, **96**, 303-319.

Powell, R., 1983. Processes in granulite-facies metamorphism. In: "*Migmatites, Melting and Metamorphism*", Atherton M.P. & Gribble, C.D. (eds). Nantwich: Shiva, 127-139.

Powell, R. and Downes, J., 1990. Garnet porphyroblast-bearing leucosomes in metapelites: mechanisms, phase diagrams and an example from Broken Hill, Australia. In: "*High-temperature Metamorphism and Crustal Anatexis*", Ashworth, J.R. & Brown, M. (eds). London, Unwin Hyman. p19-56.

Putnis, A. and Holland, T., 1986. Sector-trilling in cordierite and equilibrium overstepping in metamorphism. *Contributions to Mineralogy and Petrology*, **93**, 265-272.

Putnis, A., Salje, E., Redfern, S., Fyfe, C. and Strobl, H., 1987. Structural states of Mg-cordierite I: Order parameters from synchotron X-ray and NMR data. *Physics and Chemistry of Minerals*, **14**, 446-454.

Puziewicz, J. and Johannes, W., 1988. Phase equilibria and compositions of Fe-Mg-Al minerals and melts in water-saturated peraluminous granitic systems. *Contributions to Mineralogy and Petrology*, **100**, 156-168.

Puziewicz, J. and Johannes, W., 1990. Experimental study of a biotite-bearing granite system under water-saturated and water-undersaturated conditions. *Contributions to Mineralogy and Petrology*, **104**, 397-406.

Richardson, S., Bell, P. and Gilbert, M., 1968. Kyanite-sillimanite equilibria between 700°C and 1500°C. *American Journal of Science*, **266**, 513-541.

Sandiford, M.A., 1985. The metamorphic evolution of granulites at Fyfe Hills: implications for Archean crustal thickness in Enderby Land, Antarctica. *Journal of Metamorphic Geology*, **3**, 155-178.

Schreyer, W., Blumel, P. and Maresch, W., 1986. Cordierit und Osumilith aus den Buchiten der Blauen Kuppe bei Eschwege. *Aufschluss*, **37**, 353-367.

Schreyer, W., Maresch, W.V., Daniels, P. and Wolfsdorff, P., 1990. Potassic cordierites: characteristic minerals for high-temperature, very low-pressure environments. *Contributions to Mineralogy and Petrology*, **105**, 162-172.

Schreyer, W. and Yoder, H.S., 1960. Instability of anhydrous Mg-cordierite at high pressures. *Carnegie Institute of Washington Yearbook*, **59**, 90-91.

Schreyer, W. and Yoder, H.S., 1964. The system Mg-cordierite-water and related rocks. *Neues. Jahrb. Min. Abdhl.*, **101,** 271-342.

Sen, S. and Bhattacharya, A., 1984. An orthopyroxene-garnet thermometer and its application to the Madras charnockites. *Contributions to Mineralogy and Petrology*, **88**, 64-71.

Sheraton, J.W., Offe, L.A., Tingey, R.J. and Ellis, D.J., 1980. Enderby Land, Antarctica - an unusual Precambrian high-grade metamorphic terrain. *Journal of the Geological Society of Australia*, **27**, 1-18.

Shulters, J.C. and Bohlen, S.R., 1989. The stability of hercynite and hercynite-gahnite spinels in corundum- or quartz-bearing assemblages. *Journal of Petrology*, **30**, 1017-1031.

Skjerlie, K.P., Patino Douce, A.E. and Johnston A.D., 1993. Fluid absent melting of a layered crustal protolith: implications for the generation of anatectic granites. *Contributions to Mineralogy and Petrology*, **114**, 365-378.

Smith, D.C., 1984. Coesite in clinopyroxene in the Caledonides and its implications for geodynamics. *Nature*, **310**, 641-644.

Stevens, G. and Van Reenen, D., 1992. Partial melting and the origin of metapelitic granulites in the Southern Marginal Zone of the Limpopo Belt, South Africa. *Precambrian Research*, **55**, 303-319.

Stevens, G. and Clemens, J.D., 1993. Fluid-absent melting and the roles of fluids in the lithosphere: a slanted summary? *Chemical Geology*, **108**, 1-17.

Stuwe K. and Powell, R., 1989. Low-pressure granulite facies metamorphism in the Larsemann Hills area, East Antarctica; petrology and tectonic implications for the evolution of the Prydz Bay area. *Journal of Metamorphic Geology*, **7**, 465-483.

Thompson, A.B., 1976. Mineral reactions in pelitic rocks: 2. Calculation of some pressure-temperature-composition (Fe-Mg) phase relations. *American Journal of Science*, **276**, 425-454.

Thompson, A.B., 1982. Dehydration melting of pelitic rocks and the generation of H_2O-undersaturated granitic liquids. *American Journal of Science*, **282**, 1567-1595.

Thompson, A.B. and Algor, J.R., 1977. Model system for anatexis of pelitic rocks: 1. Theory of melting reactions in the system $KAlO_2$-$NaAlO_2$-Al_2O_3-SiO_2-H_2O. *Contributions to Mineralogy and Petrology*, **63**, 247-269.

Thompson, J.B., 1955. The thermodynamic basis for the mineral facies concept. *American Journal of Science*, **253**, 65-103.

Touret, J., 1971. Fluid inclusions in rocks from the lower continental crust. In "*The Nature of the Lower Continental Crust*", Dawson, J.B., Carswell, D.A., Hall, J. and Wedepohl, K.H. (eds). *Geological Society Special Publication*, **24**, 161-172.

Valley, J.W., Bohlen, S.R., Essene, E.J. and Lamb, W.M., 1990. Metamorphism in the Adirondacks: II. The role of fluids. *Journal of Petrology*, **31**, 555-596.

Valley, J.W. and O'Neil, J.R., 1984. Fluid heterogeneity during granulite facies metamorphism in the Adirondacks: stable isotope evidence. *Contributions to Mineralogy and Petrology*, **85**, 158-173.

Vernon, R.H. and Collins, W.J., 1988. Igneous microstructures in migmatites. *Geology*, **16**, 1126-1129.

Vielzeuf, D. and Boivin, P., 1984. An algorithm for the construction of petrogenetic grids - application to some equilibria in granulite paragneisses. *American Journal of Science*, **282**, 760-791.

Vielzeuf, D., Clemens, J.D., Pin, C. and Moinet, E., 1990. Granites, granulites and crustal differentiation. In: "*Granulites and Crustal Evolution*", Vielzeuf, D. and Vidal, Ph. (eds). Kluwer Academic Publishers. 59-85.

Vielzeuf, D. and Holloway, J.R., 1988. Experimental determination of the fluid-absent melting relations in the pelitic system: consequences for crustal differentiation. *Contributions to Mineralogy and Petrology*, **98**, 257-276.

Warren, R.G., 1983. Metamorphic and tectonic evolution of granulites, Arunta Block, central Australia. *Nature*, **305**, 300-303.

Waters, D.J., 1988. Partial melting and the formation of granulite facies assemblages in Namaqualand, South Africa. *Journal of Metamorphic Geology*, **6**, 387-404.

Waters, D.J., 1991. Hercynite-quartz granulites: phase relations, and implications for crustal processes. *European Journal of Mineralogy*, **3**, 367-386.

Waters, D.J. and Whales, C.L., 1984. Dehydration melting and the granulite transition in metapelites from southern Namaqualand, South Africa. *Contributions to Mineralogy and Petrology*, **88**, 269-275.

Watson, E.B. and Brenan, J.M., 1987. Fluids in the lithosphere, 1. Experimentally-determined wetting characteristics of CO_2-H_2O fluids and their implications for fluid transport, host-rock physical properties, and fluid inclusion formation. *Earth & Planetary Science Letters*, **85**, 497-515.

Wickham, S.M., 1987. The segregation and emplacement of granitic magmas. *Journal of the Geological Society*, **144**, 281-297.

Wones, D.R. and Eugster, H.P., 1965. Stability of biotite: experiment, theory and application. *American Mineralogist*, **50**, 1228-1272.

Wones, D.R., 1972. Stability of biotite: a reply. *American Mineralogist*, **57**, 316-317.

Wright, T.L., 1968. X-ray and optical study of alkali feldspar: II. An X-ray method for determining the composition and structural state from measurement of 2θ values for three reflections. *American Mineralogist*, **53**, 88-104.

Zen, E-An., 1966. Construction of pressure-temperature diagrams for multi-component systems after the method of Schreinemakers - a geometric approach. *US Geological Survey Bulletin*, **1225**, 56pp.

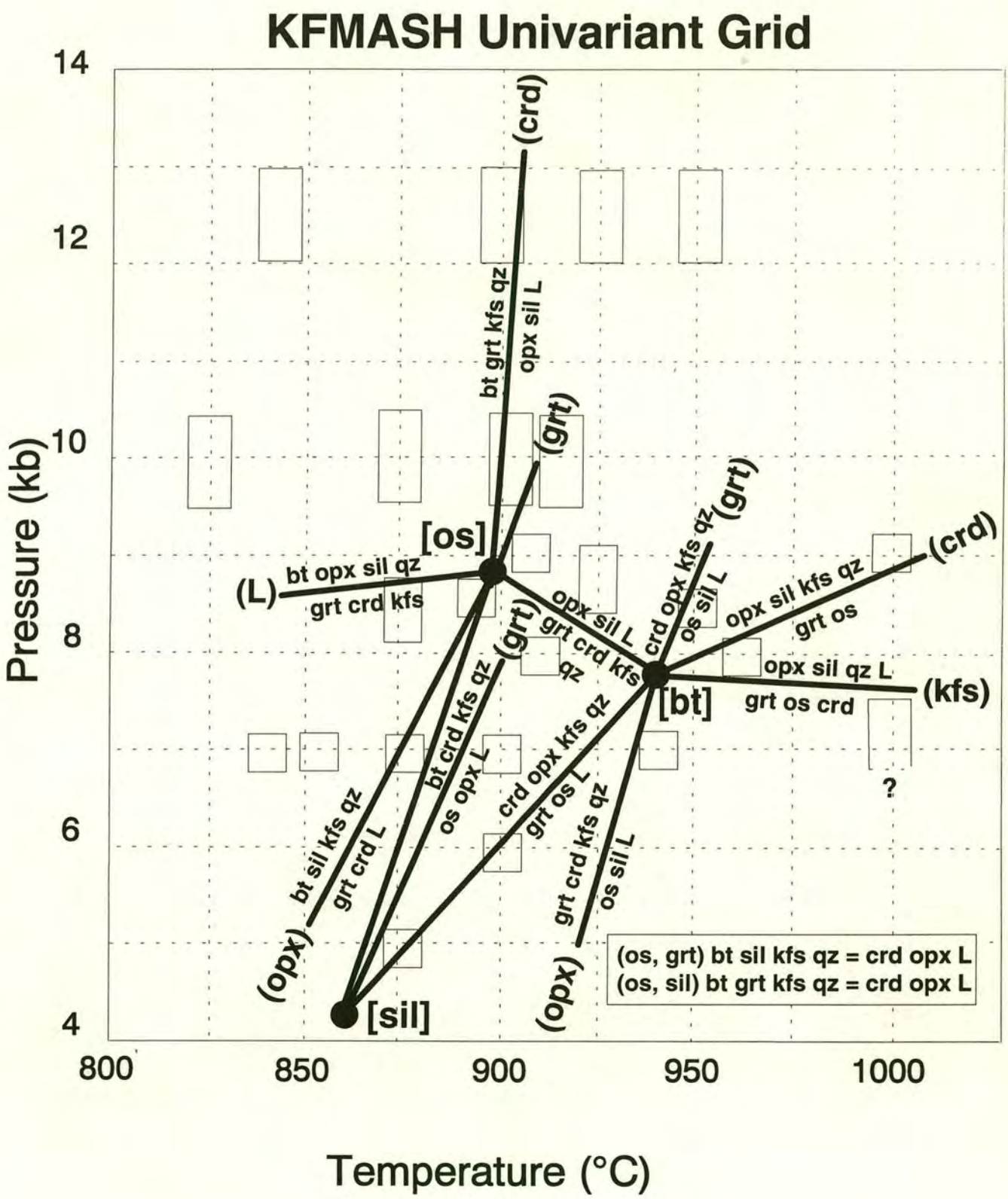

INSERT A. Univariant reaction pressure-temperature grid for the KFMASH system based on the current experimental data. The run conditions of the experiments are shown as rectangles, the size of which represent the uncertainty in the run conditions. INSERT B gives the run numbers of the experiments for reference. This diagram is reproduced from figure 6.11.

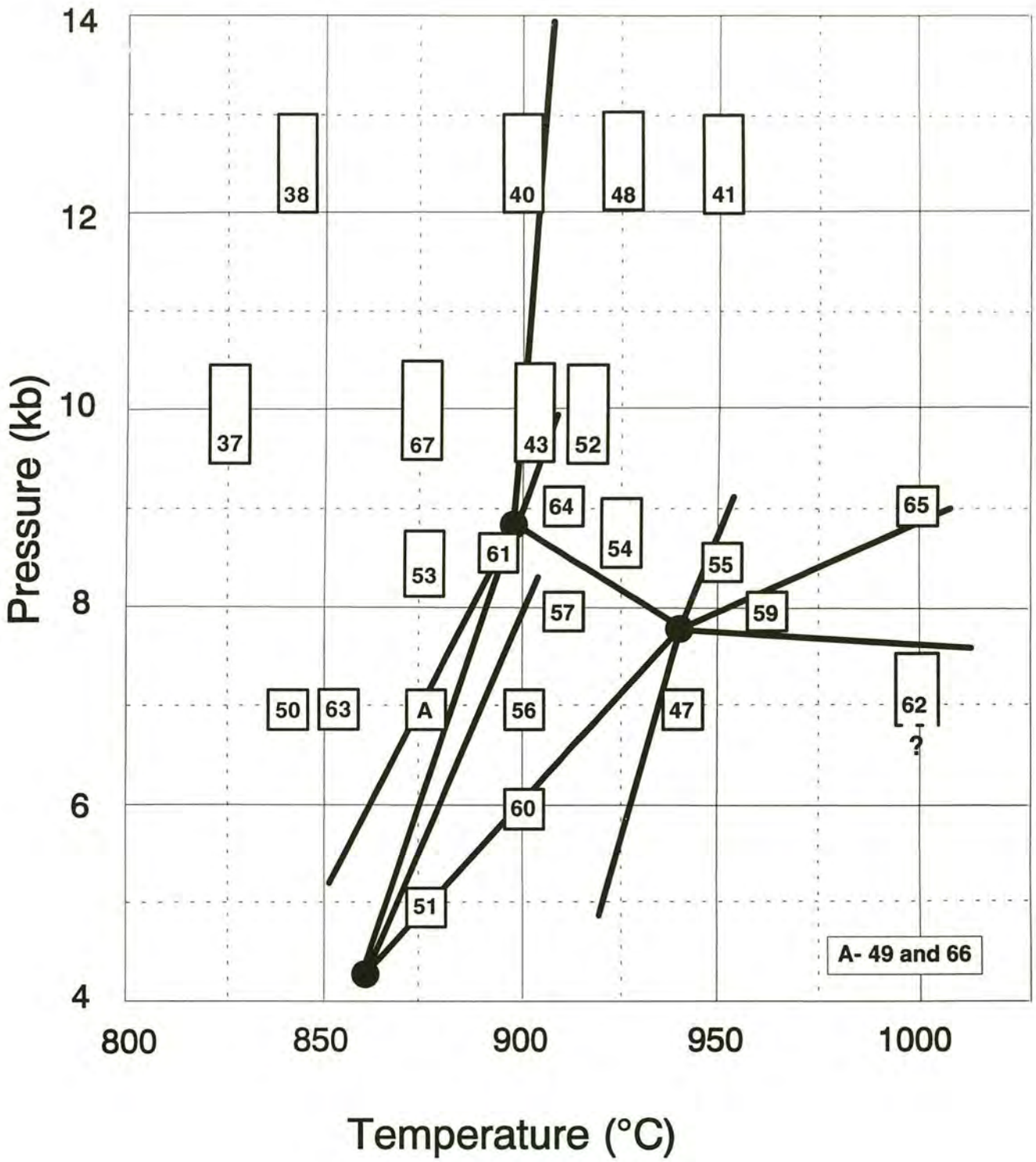

INSERT B. Pressure-temperature plot showing the position of the runs. The run numbers are given in the rectangles. The size of the rectangles represents the pressure-temperature uncertainty of the run conditions. N.B. D64-17A was removed after the first step of a isothermal reversal, having run at the same conditions as run 57. This diagram is reproduced from figure 6.12.

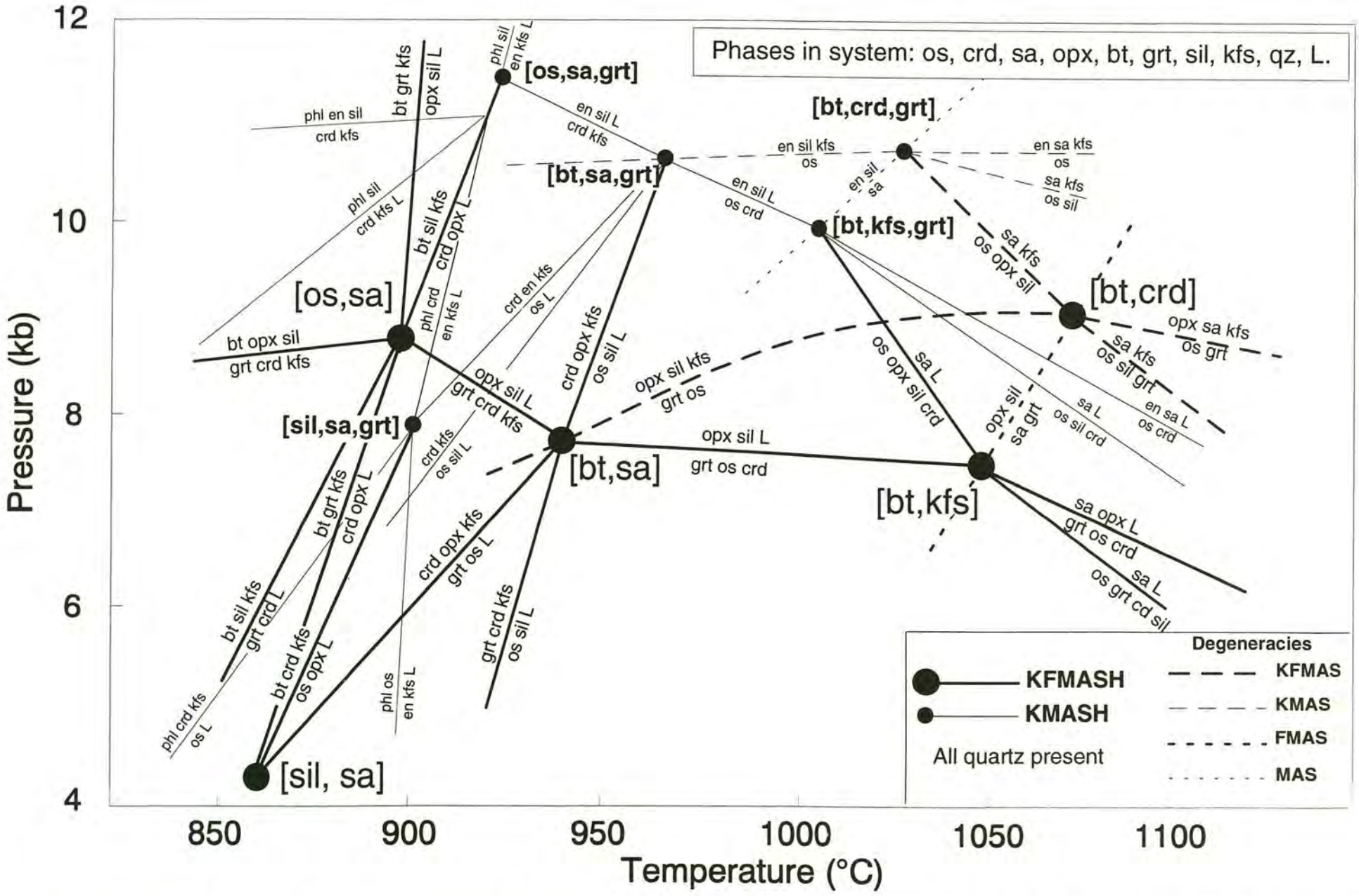

INSERT F. Pressure-temperature grid for the KFMASH and KMASH systems and degenerate systems arising from them, This diagram is reproduced from figure 7.12

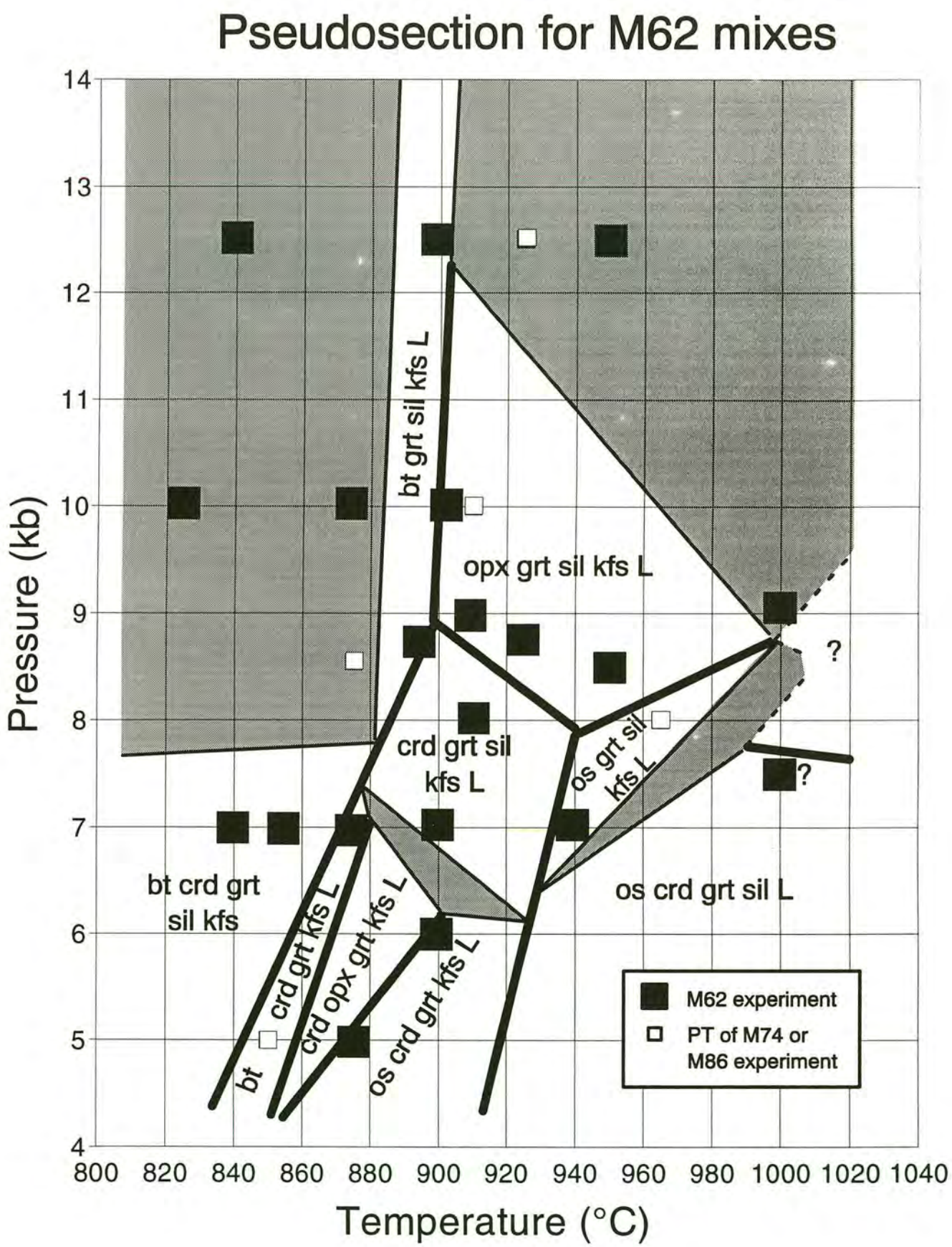

INSERT C. Pressure-temperature pseudosection for the M62 mixes (KFMASH system). The heavy lines are univariant reactions, the divariant fields are shaded white and are separated from the grey-shaded trivariant fields by lighter lines. This diagram is reproduced from figure 6.13.

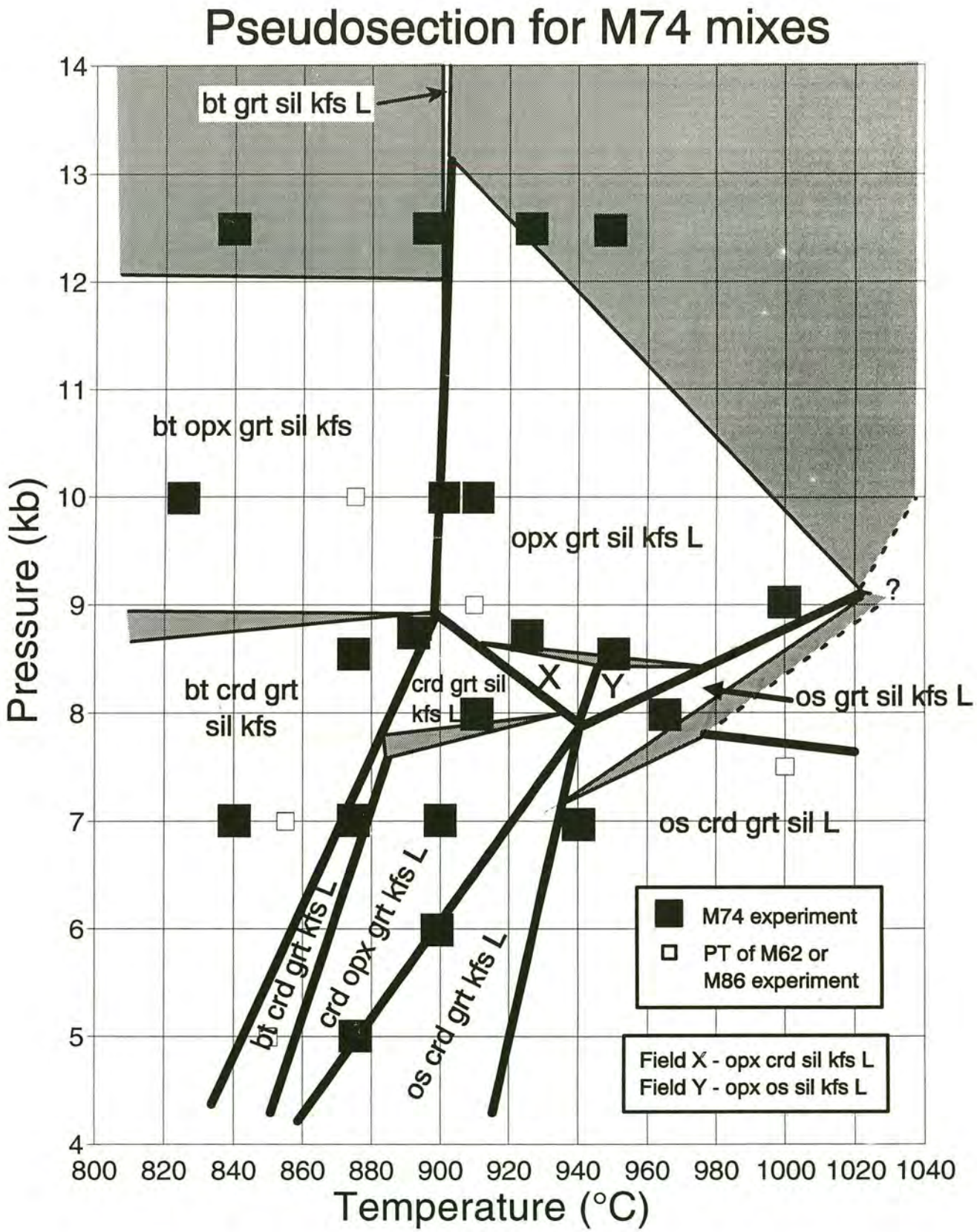

INSERT D. Pressure-temperature pseudosection for the M74 mixes (KFMASH system). The heavy lines are univariant reactions, the divariant fields are shaded white and are separated from the grey-shaded trivariant fields by lighter lines. This diagram is reproduced from figure 6.14.

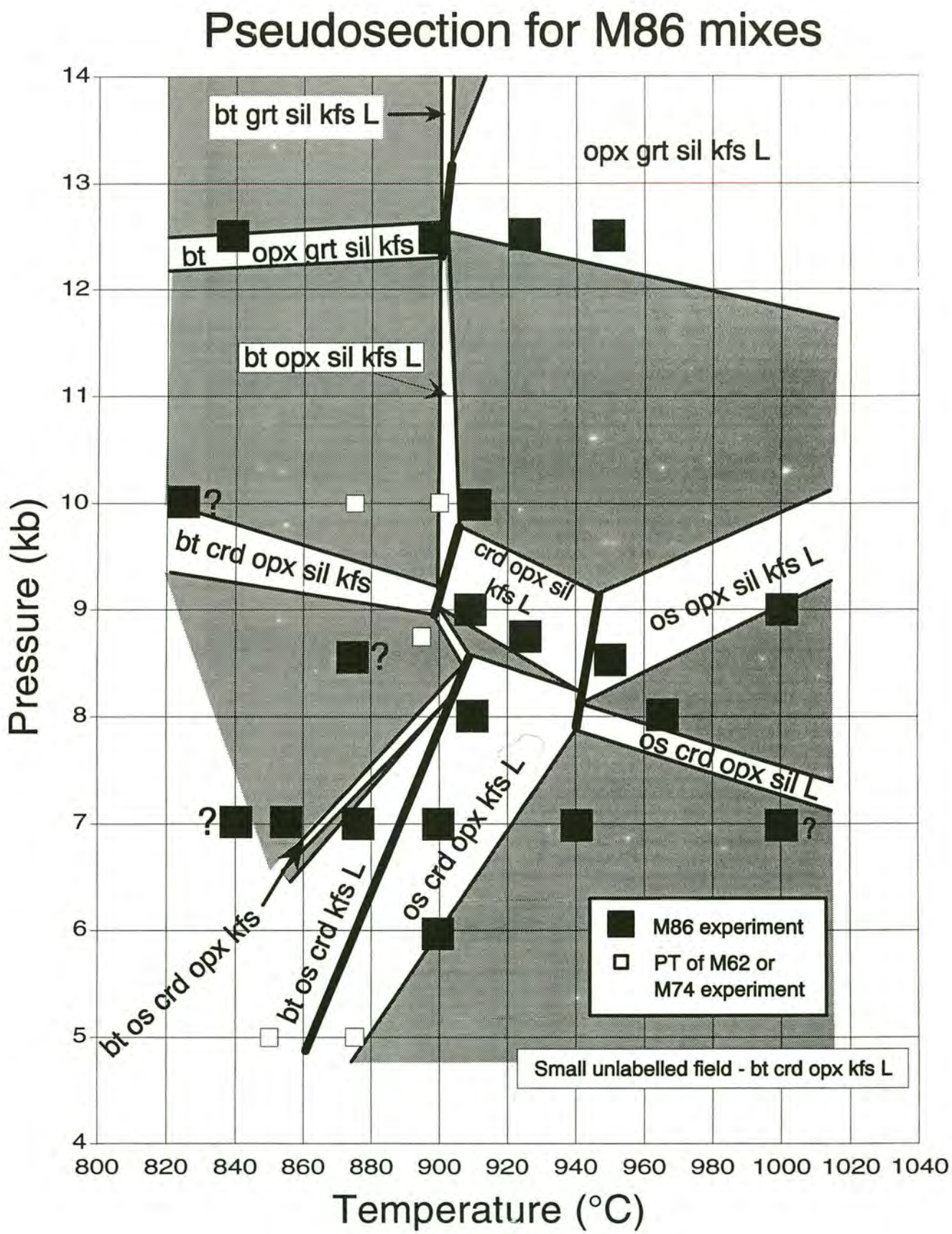

INSERT E. Pressure-temperature pseudosection for the M86 mixes (KFMASH system). The heavy lines are univariant reactions, the divariant fields are shaded white and are separated from the grey-shaded trivariant fields by lighter lines. This diagram is reproduced from figure 6.15.